

NanoScience and Technology

Series Editors

Phaedon Avouris
Bharat Bhushan
Dieter Bimberg
Klaus von Klitzing
Hiroyuki Sakaki
Roland Wiesendanger

For further volumes:
<http://www.springer.com/series/3705>

The series NanoScience and Technology is focused on the fascinating nano-world, mesoscopic physics, analysis with atomic resolution, nano and quantum-effect devices, nanomechanics and atomic-scale processes. All the basic aspects and technology-oriented developments in this emerging discipline are covered by comprehensive and timely books. The series constitutes a survey of the relevant special topics, which are presented by leading experts in the field. These books will appeal to researchers, engineers, and advanced students.

Zhifeng Ren · Yucheng Lan
Yang Wang

Aligned Carbon Nanotubes

Physics, Concepts, Fabrication and Devices

 Springer

Zhifeng Ren
Department of Physics
Boston College
Chestnut Hill, MA
USA

Yang Wang
Institute for Advanced Materials
Academy of Advanced Optoelectronics
South China Normal University
Guangzhou
People's Republic of China

Yucheng Lan
Department of Physics
Boston College
Chestnut Hill, MA
USA

ISSN 1434-4904

ISBN 978-3-642-30489-7

ISBN 978-3-642-30490-3 (eBook)

DOI 10.1007/978-3-642-30490-3

Springer Heidelberg New York Dordrecht London

Library of Congress Control Number: 2012945476

© Springer-Verlag Berlin Heidelberg 2013

This work is subject to copyright. All rights are reserved by the Publisher, whether the whole or part of the material is concerned, specifically the rights of translation, reprinting, reuse of illustrations, recitation, broadcasting, reproduction on microfilms or in any other physical way, and transmission or information storage and retrieval, electronic adaptation, computer software, or by similar or dissimilar methodology now known or hereafter developed. Exempted from this legal reservation are brief excerpts in connection with reviews or scholarly analysis or material supplied specifically for the purpose of being entered and executed on a computer system, for exclusive use by the purchaser of the work. Duplication of this publication or parts thereof is permitted only under the provisions of the Copyright Law of the Publisher's location, in its current version, and permission for use must always be obtained from Springer. Permissions for use may be obtained through RightsLink at the Copyright Clearance Center. Violations are liable to prosecution under the respective Copyright Law.

The use of general descriptive names, registered names, trademarks, service marks, etc. in this publication does not imply, even in the absence of a specific statement, that such names are exempt from the relevant protective laws and regulations and therefore free for general use.

While the advice and information in this book are believed to be true and accurate at the date of publication, neither the authors nor the editors nor the publisher can accept any legal responsibility for any errors or omissions that may be made. The publisher makes no warranty, express or implied, with respect to the material contained herein.

Printed on acid-free paper

Springer is part of Springer Science+Business Media (www.springer.com)

Foreword

Carbon nanotubes play a special role in the realm of carbon nanostructures. The field of carbon nanotube research took off in a serious way after Iijima's 1991 experimental paper on the structure of multiwall carbon nanotubes and the breakthroughs of the discovery of single wall carbon nanotube (SWNT) synthesis in 1993. It is noteworthy that the early 1993 SWNT synthesis was done in industrial laboratories (NEC for Iijima in Japan, and IBM/Almaden for Bethune in the US), with industrial interest in carbon nanotubes giving more importance and public interest to these discoveries. Following these discoveries, it took some time before others gained the know-how to make good quality nanotubes, so by 1996 the field took off seriously. The discovery of methods to grow forests of parallel carbon nanotubes came on the scene toward the end of the 1990s, opening up new directions for research but mainly for application's to electronics, energy, and the medical field because of the possibility of making a large number of aligned nanotubes. It is this topic which is especially elaborated and emphasized in this particular volume on carbon nanotubes. At the end of the decade a nanotube conference NT99 emerged and this conference series has also contributed to enhance nanotube research, which has been flourishing ever since, gathering more than 1000 attendees at the NT10 meeting in Beijing.

Many research fields grow rapidly at first and after a few years the field reaches its maximum interest and then decreases attracting broad attention. There are several reasons that carbon nanotubes have maintained a high interest level over a relatively long time. This relates to the complexity of SWNTs and the chirality variations of one nanotube to another. More explicitly, the carbon hexagons which are the fundamental building blocks of the carbon nanotubes can be oriented along any direction with respect to the nanotube axis and this relates to the (n, m) chirality property of nanotubes. During the first decade of the twenty-first century much attention was given to being able to sort nanotubes according to their (n, m) chirality, and even to developing strategies by which the chirality could be controlled during the growth process. The first of these challenges regarding nanotube chirality sorting has now been met head-on, and the sorting of individual nanotubes according to their chirality can now be accomplished on a commercial basis.

Significant progress has also been made in synthesizing specific (n, m) chirality nanotubes, though much further progress is still needed to address this challenge fully.

Many applications of carbon nanotubes have started coming to light in recent years and this is a research direction of great promise. Therefore, a book with an applications focus is especially timely. That the authors of the book have years of experience in applications research and in commercial exploitation of carbon nanotubes makes this volume of even greater importance and value, as they share this expertise and experience with students, researchers, and others.

Cambridge, MA, USA

Mildred S. Dresselhaus

Preface

Ever since the discovery of carbon nanotubes (CNTs) by Iijima in 1991, there have been extensive research efforts on their synthesis, physics, electronics, chemistry, and applications due to the fact that carbon nanotubes were predicted to have extraordinary physical, chemical, mechanical, optical, and electronic properties. Among the various forms of carbon nanotubes: single-walled and multi-walled, random and aligned, semiconducting and metallic, aligned carbon nanotubes are especially important since fundamental studies and many important applications will not be possible without the alignment. The CNTs have been aligned by various in situ and ex situ techniques. These aligned CNTs have been widely applied in various fields including high energy storage batteries, extremely strong composites, highly sensitive sensors and devices, etc., covering physics, chemistry, biology, engineering, and more. Up to now there have been thousands of scientific publications on fabrication, characterization, physical properties, and applications of aligned CNTs in various aspects. It is the right time now to review the accomplishments on aligned CNTs.

Although there have been significant endeavors on growing carbon nanotubes in an aligned configuration since their discovery in 1991, little success had been made before our first report on growing individually aligned carbon nanotubes on various substrates by plasma enhanced chemical vapor deposition (PECVD) [1]. Aligned CNT arrays have been extensively studied as field emission devices, optical devices, chemical sensors, and biosensors. Based on a recent review article [2], we further expanded to include more recent work on aligned CNTs to write this book. In the book, we introduce the main results of aligned CNTs including CNT growth mechanisms and techniques, CNT microstructures and physical properties, alignment techniques, applications of aligned CNTs, and related physical mechanisms.

In this book, we first review the fundamental structures of CNTs and their unique anisotropic properties in [Chap. 2](#) (*Carbon Nanotubes*), general growth methods in [Chap. 3](#) (*Growth Techniques of Carbon Nanotubes*) and in [Chap. 4](#) (*Chemical Vapor Deposition of Carbon Nanotubes*). Because of the wide and important application of DC-PECVD method to align CNTs, [Chap. 5](#) (*Physics of*

Direct Current Plasma-Enhanced Chemical Vapor Deposition) is specially dedicated to discuss the experimental setup, physical principle, and experimental parameters in more detail. Various in situ and ex situ alignment techniques are introduced in **Chap. 6** (*Technologies to Achieve Carbon Nanotube Alignment*). Major fabrication methods are illustrated in detail, particularly the most widely used PECVD growth technique on which various device integration schemes are based. The orientation of aligned CNT systems is vertical, parallel, or at other angles to the substrate surface. The techniques to examine the alignment of CNTs are discussed in **Chap. 7** (*Measurement Techniques of Aligned Carbon Nanotubes*). These chapters provide the necessary initial techniques for the following in-depth introduction of the state-of-the-art applications of aligned CNT arrays that we talk about in **Chap. 8** (*Properties and Applications of Aligned Carbon Nanotube Arrays*) and in **Chap. 9** (*Potential Applications of Carbon Nanotube Arrays*). In these two chapters, we introduce the applications of aligned CNTs in field emission, optical antennas, nanocoax solar cells, subwavelength light transmission, electrical interconnects, nanodiodes, and many others. At the end, the current limitations and challenges are discussed to lay down the foundation for future developments.

In the book, we list detailed experimental procedures and explain the physical mechanisms of sensors and devices to help the readers to understand the aligned CNTs for practical devices. At the same time, a lot of references including review papers and books are also listed. The book can be used as a textbook on aligned CNTs for beginners, and a reference book for advanced readers. In order to understand the aligned CNT well, we strongly encourage the readers, especially beginners on CNTs to first read other books on CNTs, such as *Carbon Nanotubes: Synthesis, Structure, Properties, and Applications* (Edited by M. S. Dresselhaus, G. Dresselhaus, and P. Avouris, Springer, 2000), *Carbon Nanotubes: Preparation and Properties* (Edited by T. W. Ebbesen, CRC Press, 1996), and *Physics of Carbon Nanotube Devices* (Authored by F. Léonard, William Andrew Inc., 2008).

The writing is partly supported by the US Department of Energy under Contract Number DOE DE-FG02-00ER45805 (Z.F.R.), partly by the Defense Threat Reduction Agency under grants HDTRA1-10-1-0001 and HDTRA122221 (YCL).

Chestnut Hill, MA

Zhifeng Ren
Yucheng Lan
Yang Wang

References

1. Z.F. Ren, et al., *Science* **282**, 1105–1108 (1998)
2. Y.C. Lan, et al., *Adv. Phys.* **60**, 553–678 (2011)

Contents

1	Introduction to Carbon	1
	References	4
2	Carbon Nanotubes	7
2.1	History of Carbon Nanotubes	8
2.1.1	History Before 1991	8
2.1.2	History Since 1991	10
2.1.3	History of Aligned Carbon Nanotubes	11
2.2	Structures of Carbon Nanotubes	16
2.2.1	Graphite	16
2.2.2	Single-Walled Carbon Nanotubes	17
2.2.3	Double-Walled Carbon Nanotubes	18
2.2.4	Multi-Walled Carbon Nanotubes	19
2.2.5	Bamboo-Like Carbon Nanotubes	19
2.2.6	CNT Y-Junctions	20
2.2.7	Carbon Nanobuds	21
2.2.8	CNT Nanotorus and Micro-Rings	23
2.2.9	Carbon Microtubes	24
2.2.10	Amorphous Carbon Nanotubes	25
2.2.11	Coiled Carbon Nanotubes	26
2.2.12	Flattened Carbon Nanotubes	26
2.2.13	Other Carbon Nanomaterials	28
2.3	Physical Properties of Carbon Nanotubes	30
2.3.1	Anisotropic Mechanical Properties	30
2.3.2	Anisotropic Electrical Properties	30
2.3.3	Anisotropic Thermal Conductivity	31
2.3.4	Anisotropic Thermal Diffusivity	32
2.3.5	Anisotropic Seebeck Coefficient	34
2.3.6	Other Anisotropic Physical Properties	34
	References	35

3	Growth Techniques of Carbon Nanotubes	45
3.1	Arc Discharge	45
3.2	Laser Ablation	47
3.3	Chemical Vapor Deposition	48
3.4	Hydrothermal Methods	52
3.5	Flame Method	56
3.6	Disproportionation of Carbon Monoxide	57
3.7	Catalytic Pyrolysis of Hydrocarbons	59
3.8	Electrolysis	59
3.9	Solar Energy	60
	References	61
4	Chemical Vapor Deposition of Carbon Nanotubes	67
4.1	Thermal Chemical Vapor Deposition	67
4.1.1	Hot-Wall Chemical Vapor Deposition	68
4.1.2	Hot-Wire Chemical Vapor Deposition	70
4.1.3	Thermal Chemical Vapor Deposition Growth Mechanism of Carbon Nanotubes	71
4.1.4	Experimental Condition of Carbon Nanotube Array Growth	73
4.2	Plasma-Enhanced Chemical Vapor Deposition	75
4.2.1	Direct Current Plasma-Enhanced Chemical Vapor Deposition	76
4.2.2	Radio-Frequency Plasma-Enhanced Chemical Vapor Deposition	78
4.2.3	Microwave Plasma-Assisted Chemical Vapor Deposition	78
4.2.4	Plasma-Enhanced Chemical Vapor Deposition Growth Mechanism of Carbon Nanotube Alignment . . .	80
4.2.5	Experimental Conditions of Plasma-Enhanced Chemical Vapor Deposition Growth	83
	References	86
5	Physics of Direct Current Plasma-Enhanced Chemical Vapor Deposition	93
5.1	Equipment Setup and Growth Procedure	93
5.2	Substrate and Underlayer	95
5.3	Growth Temperature	96
5.4	Plasma Heating and Etching Effects	97
5.5	Plasma States	99
5.6	Catalyst Crystal Orientation	100
5.7	Electric Field Manipulation	101
5.8	DC-PECVD Growth Mechanism	102
5.8.1	First Stage: Randomly Entangled CNT Growth	102

5.8.2	Second Stage: Partially Aligned CNT Growth	104
5.8.3	Third Stage: Fully Aligned CNT Growth	105
5.8.4	DC-PECVD Growth Mechanism	106
	References	107
6	Technologies to Achieve Carbon Nanotube Alignment	111
6.1	In Situ Techniques for Carbon Nanotube Alignment	112
6.1.1	Thermal Chemical Vapor Deposition with Crowding Effect	112
6.1.2	Thermal Chemical Vapor Deposition Growth with Imposed Electric Field	116
6.1.3	Thermal Chemical Vapor Deposition Growth Under Gas Flow Fields	119
6.1.4	Thermal Chemical Vapor Deposition Growth with Epitaxy	123
6.1.5	Thermal Chemical Vapor Deposition Under Magnetic Fields	128
6.1.6	Vertically Aligned Carbon Nanotube Arrays Grown by Plasma-Enhanced Chemical Vapor Deposition	128
6.1.7	Other In Situ techniques	140
6.2	Ex Situ Techniques for Carbon Nanotube Alignment	140
6.2.1	Ex Situ Alignment Under Electric Fields	141
6.2.2	Ex Situ Alignment Under Magnetic Fields	141
6.2.3	Ex Situ Mechanical Methods	143
6.2.4	Other Ex Situ Methods	147
	References	147
7	Measurement Techniques of Aligned Carbon Nanotubes	157
7.1	Scanning Electron Microscopy	157
7.2	Bragg Diffraction	160
7.2.1	X-Ray Diffraction	160
7.2.2	Neutron Diffraction	164
7.2.3	Electron Diffraction	164
7.2.4	Light Diffraction	166
7.3	Small-Angle Scattering	168
7.3.1	Small-Angle X-Ray Scattering	168
7.3.2	Small-Angle Neutron Scattering	172
7.4	Raman Spectroscopy	173
7.5	Transmission Electron Microscopy	176
7.6	Scanning Tunneling Microscopy	178
7.7	Atomic Force Microscopy	179
7.8	Other Techniques	179
	References	180

8	Properties and Applications of Aligned Carbon Nanotube Arrays	183
	Nanotube Arrays	183
8.1	Field Emission Devices	183
8.1.1	Field Emission of Aligned Carbon Nanotube Arrays	184
8.1.2	Carbon Nanotube Array Emitters	187
8.1.3	High-Intensity Electron Sources	188
8.1.4	Lighting	189
8.1.5	Field Emission Flat Panel Displays	191
8.1.6	Incandescent Displays	193
8.1.7	X-Ray Generators	194
8.1.8	Microwave Devices	195
8.1.9	Other Field Emission Devices	197
8.2	Optical Devices	198
8.2.1	Photonic Crystals	198
8.2.2	Optical Antennae	199
8.2.3	Optical Waveguides	202
8.2.4	SWCNT Array Solar Cells	204
8.2.5	Solar Cells Based on MWCNT Nanocoaxes	204
8.3	Nanoelectrode-Based Sensors	208
8.3.1	Nanoelectrode Arrays	208
8.3.2	Ion Sensors	213
8.3.3	Gas Sensors	215
8.3.4	Biosensors	222
8.4	Thermal Devices: Thermal Interface Materials	228
8.5	Electrical Interconnects and Vias	231
8.6	Templates	235
8.7	Aligned-CNT Composites and Applications	236
	References	236
9	Potential Applications of Carbon Nanotube Arrays	255
9.1	Mechanical Devices	255
9.1.1	Carbon Nanotube Ropes	256
9.1.2	TEM Grids	259
9.1.3	Artificial Setae	260
9.1.4	Piezoresistive Effects: Pressure and Strain Sensors	260
9.2	Electrical Devices	263
9.2.1	Random Access Memory	263
9.2.2	Low κ Dielectrics	264
9.2.3	Transistors	265
9.3	Acoustic Sensors	265
9.3.1	Artificial Ears	265
9.3.2	Thermoacoustic Loudspeakers	265
9.4	Electrochemical and Chemical Storage Devices	269
9.4.1	Fuel Cells	270

9.4.2	Supercapacitors	274
9.4.3	Lithium Ion Batteries	279
9.4.4	Hydrogen Storage	280
9.5	Electromechanical Devices: Actuators	280
9.6	Terahertz Sources	281
9.7	Other Applications.	282
	References	283
Epilogue		291
Index		293

Acronyms

1D	One-dimensional
2D	Two-dimensional
3D	Three-dimensional
AAO	Anodized aluminum oxide
AC	Alternating current
AFM	Atomic force microscopy
CMOS	Complementary metal–oxide semiconductor
CNF	Carbon nanofiber
CNT	Carbon nanotube
CRT	Cathode ray tube
CVD	Chemical vapor deposition
DC	Direct current
DNA	Deoxyribonucleic acid
DWCNT	Double-walled carbon nanotube
EDS	Energy X-ray dispersive spectrum
FED	Field emission display
FIB	Focused ion beam
HRTEM	High-resolution transmission electron microscopy
IC	Integrated circuit
ITO	Indium tin oxide
IR	Infrared
LCD	Liquid crystal display
MWCNT	Multi-walled carbon nanotube
PECVD	Plasma-enhanced chemical vapor deposition
ppm	Parts per million
PPn	Polyphenol
ppb	Parts per billion
PS	Polystyrene
PVA	Polyvinyl alcohol
RC delay	Resistive capacitive delay
RF	Radio frequency

RNA	Ribonucleic acid
SAED	Selected area electron diffraction
SEM	Electron scanning microscopy
S/N ratio	Signal-noise-ratio
STM	Scanning tunneling microscopy
STEM	Scanning transmission electron microscopy
SWCNT	Single-walled carbon nanotube
TCO	Transparent conductive oxide
TEM	Transmission electron microscopy
TIM	Thermal interface material
XRD	X-ray diffraction

Chapter 1

Introduction to Carbon

Carbon is a chemical element with symbol *C*, atomic number of 6, and electron configuration of $[\text{He}]2s^22p^2$. Its name originates from Latin *carbo* and French *charbon* meaning charcoal [1]. Carbon is the fourth most abundant chemical element in the universe by mass. It is also the second abundant element by mass in human body.

Carbon has been known since prehistoric time. Woods, mainly consisted of carbon, have been widely used for warming and cooking from prehistoric time. Diamond, another allotrope of carbon, has been treasured as gemstones because of remarkable optical characteristics and widely applied in industry because of superior hardness and good thermal conductivity. In the first chapter of this book, we briefly review the family of carbon.

The well-known allotropes of carbon are diamond, graphite, amorphous carbon, and fullerenes. Figure 1.1 shows crystallographic structures of these allotropes.

Diamond consists of pure sp^3 hybridized carbon atoms (Fig. 1.1a). It is renowned for its extreme hardness (hardest natural materials with Mohs hardness of 10 since antiquity) originating from the strong covalent bonding between carbon atoms and for its relatively high optical dispersion of visible spectrum covering 1–5.5 eV [2] and thermal conductivity (900–2,320 W/m/K [3]). Diamond is mainly applied in industrial cutting and polishing tools besides as the most popular gemstone in our life. There are many books which reviewed the properties and applications of diamond [4–8].

Graphite has a layered and planar structure (Fig. 1.1b). In each layer, the carbon atoms are arranged in a hexagonal lattice with a lattice parameter of 0.142 nm while the distance between planes is 0.335 nm, making it the softest natural materials with Mohs hardness of 1. Each graphite layer consists of pure sp^2 hybridized carbon atoms and van der Waals force holds the layers together. Graphite is mainly applied in industry for lubrication. Physical properties, preparation, and applications of graphite are summarized in some books [8–11].

Amorphous carbon, such as soot and black carbon, does not have any crystalline structure (Fig. 1.1c). Amorphous carbon can be used as inks, paints, and industrial

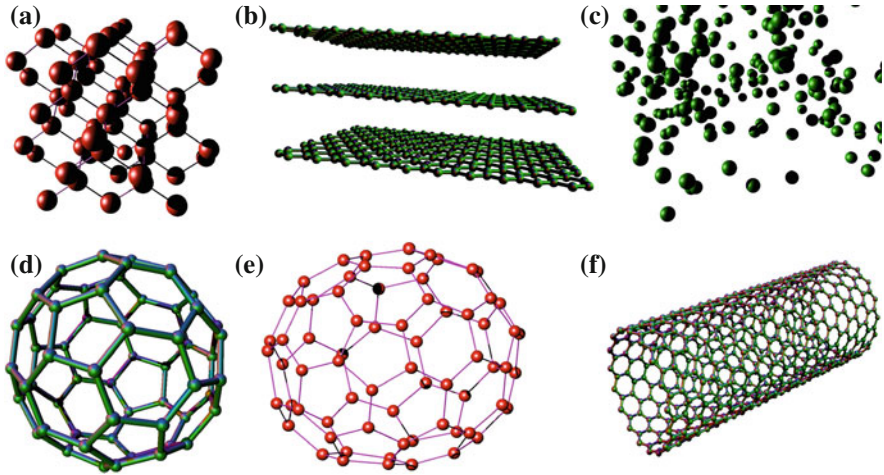


Fig. 1.1 Allotropes of carbon. **a** Diamond. The carbon atoms are bonded together in a tetrahedral lattice arrangement. The carbon atoms are sp^3 hybridized. **b** Graphite. The carbon atoms are bonded together in sheets of a hexagonal lattice. Van der Waals force bonds the sheets together. The atoms are sp^2 hybridized. **c** Amorphous carbon. The carbon atoms are randomly arranged. **d** Spherical fullerene, C_{60} . The carbon atoms of fullerenes are bonded together in pentagons and hexagons. **e** Ellipsoidal fullerene, C_{70} . The carbon atoms are bonded together in an ellipsoidal formation. **f** Tubular fullerene, SWCNT. The carbon atoms are in a tubular formation

rubber fillers. The detailed physical properties and applications of amorphous carbon are summarized in some books [12–14].

The fourth allotrope of carbon is fullerene that is at nanoscale. The physics, chemistry, properties, and applications of fullerenes are described in many books [8, 15–25]. In this chapter, we briefly introduce the family members of fullerenes and describe their crystallographic structures.

Figure 1.1d–f illustrates the structures of fullerene members. The family includes the spherical fullerene (buckyball), ellipsoidal fullerenes, elongated cylindrical carbon nanotubes, and planar graphene. With the development of nanotechnology and nanoengineering, fullerene plays an important role in the nanoapplications.

The existence of C_{60} , nanospheres formed by 60 carbon atoms, was proposed in 1970 [26] and first discovered in arc-discharged carbon-soot in laboratory in 1985 [27]. Later C_{60} was found in various natural environments, like in rocks [28] on the earth, and in space [29]. C_{60} is the simplest buckyball with each carbon atom covalently bonded to three adjacent carbon atoms (Fig. 1.1d). The diameter of C_{60} sphere is around 1 nm. The hardness of buckyballs is greater than that of diamond, promising applications as polymer fillers to increase mechanical strength. Functionalized buckyballs have been developed for targeted drug delivery and antioxidants. The interested readers can refer to some books [30] and reviews [31].

Besides spherical C_{60} , ellipsoidal fullerenes are also observed in nature and synthesized in laboratories, such as C_{70} (Fig. 1.1e), C_{72} , C_{76} , and C_{84} . Icosahedral

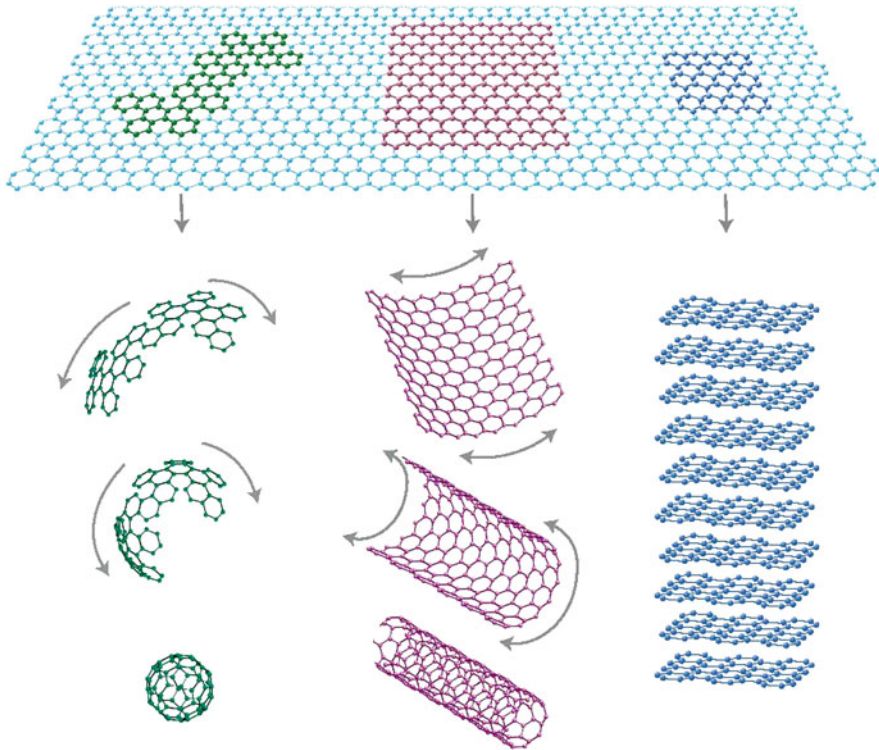


Fig. 1.2 Mother of all graphitic forms. Graphene is a 2D building material for carbon materials of other dimensionalities [36]. It can be wrapped up into 0D buckyballs (*left*), rolled into 1D nanotubes (*middle*) or stacked into 3D graphite (*right*)

fullerene, such as C_{540} , is also observed. The details of spherical-like fullerenes are summarized in some books and papers [32].

Carbon nanotubes (CNTs, also called buckytubes in earlier days) are elongated cylindrical fullerenes with diameters of nanometers and lengths of microns even millimeters. The carbon atoms in a CNT are bonded trigonally in a curved sheet (graphitic layer) that forms a hollow cylinder. Such unique nanostructures result in many extraordinary properties [33, 34], such as high tensile strength, high electrical and thermal conductivities, high ductility, high thermal and chemical stability, making them suitable for various applications.

CNTs are typically categorized as single-walled (SWCNTs), double-walled (DWCNTs), and multi-walled (MWCNTs) with respect to the number of graphitic layers. The nature of the atomic bonding in a CNT is described by applied quantum chemistry or, specifically, orbital hybridization. The chemical bonds in CNTs are sp^2 bonds, similar to those in graphite. More detailed atomic structures of individual CNTs are well described in many books [33, 34].

Graphene is a one-atom-thick planar sheet of carbon atoms with sp^2 hybridization (Fig. 1.2). The term *graphene* was coined as a combination of *graphite* and the suffix *-ene* to describe single-layer carbon foils in 1962 [35]. Graphene is most easily visualized as an atomic layer made of carbon atoms and their bonds. The sp^2 carbon atoms form a honeycomb crystal lattice [36].

Graphene is the basic structural element of some carbon allotropes and can be considered as mother of all graphitic forms. The graphene can be wrapped up into 0D buckyballs, rolled into 1D nanotubes, or stacked into 3D graphite (Fig. 1.2). For example, the crystalline form of graphite consists of many graphene sheets stacked together.

Graphene has potential applications in single molecule gas detection due to its 2D structure, in transistors because of its high electronic quality, in integrated circuits, in transparent conducting electrodes, as well as in solar cells, ultracapacitors, and biodevices because of its super physical properties in electric, electronic, optical, thermal, mechanical properties. The interested readers are referred to recent review papers [36].

References

1. H.W. Fowler, F.G. Fowler (eds.), *The Concise Oxford Dictionary of Current English* (Clarendon Press, Oxford, 1964)
2. J. Walker, Optical absorption and luminescence in diamond. *Rep. Prog. Phys.* **42**(10), 1605 (1979)
3. L. Wei, P.K. Kuo, R.L. Thomas, T.R. Anthony, W.F. Banholzer, Thermal conductivity of isotopically modified single crystal diamond. *Phys. Rev. Lett.* **70**(24), 3764–3767 (1993)
4. W. Hershey, *The Book of Diamonds* (Hearst Press, New York, 1940)
5. G. Harlow (ed.), *The Nature of Diamonds* (Cambridge University Press, Cambridge, 1998)
6. M.H. Nazaré, A.J. Neves (eds.), *Properties, Growth and Applications of Diamond* (INSPEC, Institution of Electrical Engineers, London, 2001)
7. K.E. Spear, J.P. Dismukes (eds.), *Synthetic Diamond: Emerging CVD Science and Technology* (Wiley, New York, 1994)
8. R. Setton, P. Bernier, S. Lefrant (eds.), *Carbon Molecules and Materials* (CRC Press, New York, 2002)
9. M. Inagaki, *New Carbon: Control of Structure and Functions* (Elsevier Science Ltd., Amsterdam, 2000)
10. P. Delhaés (ed.), *Graphite and Precursors* (Gordon and Breach Science Publishers, New York, 2001)
11. F. Cirkel, C.M. Branch, *Graphite: Its Properties, Occurrence, Refining and Uses* (Nabu Press, Charleston, SC 2010)
12. S.R.P. Silva (ed.), *Properties of Amorphous Carbon* (INSPEC, Institution of Electrical Engineers, London, 2003)
13. S.R.P. Silva, J. Roberts, G.A.J. Amaratunga (eds.), *Specialist Meeting on Amorphous Carbon* (World Scientific Publishing Company, Singapore 1998)
14. J. P. Sullivan, J. Robertson, O. Zhou, T. B. Allen, B. F. Coll, (eds.), *Amorphous and Nanostructured Carbon*, vol. 593 of Material Research Society Symposium Proceedings. Materials Research Society, Warrendale, PA 2000.
15. P.W. Stephens (ed.), *Physics and Chemistry of Fullerenes* (World Scientific Publishing Co., Singapore, 1994)

16. R. Taylor (ed.), *The Chemistry of Fullerenes* (World Scientific Publishing Co., Singapore, 1995)
17. M.S. Dresselhaus, G. Dresselhaus, P.C. Eklund, *Science of Fullerenes and Carbon Nanotubes: Their Properties and Applications* (Academic Press, San Diego, 1996)
18. R. Taylor (ed.), *Lecture Notes on Fullerene Chemistry: A Handbook for Chemists* (Imperial, London, 1999)
19. K.M. Kadish, R.S. Ruoff (eds.), *Fullerenes: Chemistry, Physics, and Technology* (Wiley-Interscience, New York, 2000)
20. T. Akasaka, S. Nagase (eds.), *Endofullerenes: A New Family of Carbon Clusters* (Kluwer Academic Publishers, Netherland, 2002)
21. P.W. Fowler, D.E. Manolopoulos, *An Atlas of Fullerenes* (Dover Publications, New York, 2007)
22. F. Langa, J. Nierengarten (eds.), *Fullerenes: Principles and Applications* (Royal Society of Chemistry, Cambridge, 2007)
23. E.F. Sheka, *Fullerenes: Nanochemistry, Nanomagnetism, Nanomedicine, Nanophotonics* (CRC, Boca Raton, 2011)
24. A. Hirsch, M. Brettreich, *Fullerenes: Chemistry and Reactions* (Wiley-VCH, Weinheim, 2005)
25. A. Krüger, *Carbon Materials and Nanotechnology* (Wiley-VCH, Weinheim, 2010)
26. E.K. Osawa, Kagaku (Kyoto) **25**, 854–863 (1970) (in Japanese)
27. H.W. Kroto, J.R. Heath, S.C. O'Brien, R.F. Curl, R.E. Smalley, C₆₀: Buckminsterfullerene. *Nature* **318**, 162–163 (1985)
28. P.R. Buseck, S.J. Tsipursky, R. Hettich, Fullerenes from the geological environment. *Science* **257**(5067), 215–217 (1992)
29. J. Cami, J. Bernard-Salas, E. Peeters, S.E. Malek, Detection of C₆₀ and C₇₀ in a young planetary nebula. *Science* **329**(5996), 1180–1182 (2010)
30. E. Ösawa (ed.), *Perspectives of Fullerene Nanotechnology* (Kluwer Academic Publishers, Netherland, 2002)
31. P. Ehrenfreund, B.H. Foing, Fullerenes and cosmic carbon. *Science* **329**(5996), 1159–1160 (2010)
32. G.B. Adams, O.F. Sankey, J.B. Page, M. O'Keeffe, D.A. Drabold, Energetics of large fullerenes: balls, tubes, and capsules. *Science* **256**(5065), 1792–1795 (1992)
33. T.W. Ebbesen (ed.), *Carbon Nanotubes: Preparation and Properties* (Chemical Rubber, Boca Raton, 1997) (And references therein)
34. M.S. Dresselhaus, G. Dresselhaus, P. Avouris (eds.), *Carbon Nanotubes: Synthesis, Structure, Properties, and Applications of Topics in Applied Physics*, vol. 80 (Springer, Heidelberg, 2001)
35. H.P. Boehm, A. Clauss, G.O. Fischer, U. Hofmann, Das adsorptionsverhalten sehr dünner kohlenstoff-folien. *Zeitschrift für anorganische und allgemeine Chemie* **316**(3–4), 119–127 (1962)
36. A.K. Geim, K.S. Novoselov, The rise of graphene. *Nat. Mater.* **6**, 183–191 (2007)

Chapter 2

Carbon Nanotubes

The carbon atoms in a carbon nanotube (CNT) are bonded trigonally in a curved sheet (graphite layer) that forms a hollow cylinder in nanoscale, similar to that in other fullerenes. The length of CNTs may range from less than a micron to several millimeters or even centimeters. Their unique nanostructures result in many extraordinary properties such as high tensile strength, high electrical and thermal conductivities, high ductility, high thermal and chemical stability, making them suitable for various applications as discussed in Chap. 8: *Properties and Applications of Aligned Carbon Nanotube Arrays* and Chap. 9: *Potential Applications of Carbon Nanotube Arrays*. In this chapter, we review the history and structures of carbon nanotubes.

CNTs are typically categorized as single-walled CNT (SWCNTs), double-walled CNT (DWCNTs), and multi-walled CNT (MWCNTs) with respect to the number of graphite layers. The nature of the atomic bonding in a CNT is described by applied quantum chemistry, or specifically, orbital hybridization. The chemical bonds in CNTs are all sp^2 bonds, similar to those of graphite. The atomic structure and physical properties of individual CNTs are well described in the previous review literatures [1–3].

Carbon nanotubes and related nanostructures have been one of the most scientifically studied material systems in the recent years ever since their well-known experimental discovery [4]. A large variety of potential applications have been envisioned, some of which have already been realized while others are still under study. As a necessary introduction, we will first review the history of CNTs and fundamental structures of CNTs.

The most intriguing properties of CNTs lie in their unique quasi one-dimensional nanoscale structures that are intrinsically anisotropic: properties in the longitudinal direction are drastically different from those in the azimuthal directions. At the end of this chapter, we introduce the anisotropic properties of CNTs. This will carry out the necessary preparation for the following in-depth review of the state-of-the-art fabrications and applications of aligned CNT arrays.

2.1 History of Carbon Nanotubes

It is a long story of CNT discovery. Table 2.1 lists the milestones of the CNT development. 1991 is a major milestone in the history of CNTs in which year Sumio Iijima published his high-resolution transmission electron microscopy (HRTEM) images of CNTs in journal *Nature* [4].

2.1.1 History Before 1991

The CNTs have an arguably long history of discovery. It was speculated [22] that the first carbon filament was possibly synthesized as early as 1889 [5] in Thomas Alva Edison's era when a light bulb filament was searched for incandescent lamps. Carbon filaments were produced by a thermal decomposition of gaseous hydrocarbon (methane) to make light bulb filaments. In that era, carbon filaments smaller than a few microns in diameter could not be observed because of the low resolution of the optical microscopes used at the time. Based on the experimental method and conditions described in the corresponding patent [5], it is conceivable that hollow carbon filaments were possibly produced at the era [22], although no images were recorded as direct evidences.

Some scientists even believed that CNTs were likely produced in ancient forging (AD 900–1800) although, of course, nobody noticed them at that time [23]. Although the opinion was questioned, it is possible from the view of present understanding of CNT synthesis conditions.

In fact, during these era, the nanoscaled materials cannot be observed even though the CNTs were synthesized. Only after the transmission electron microscope was invented in 1931 by Ernst Ruska and Max Knoll and commercialized in 1939 by Siemens Inc., direct visualization of the nanoscaled materials is possible.

The first transmission electron microscopy (TEM) evidence for the tubular nature of nanoscale carbon filaments was published in 1952 [8]. Clear TEM images of hollow carbon filaments were published, as shown in Fig. 2.1a, which clearly illustrates that the carbon filaments are hollow tubes with diameters of about 50 nm. The graphitic walls are clearly observed from the TEM image contrast. The structures seem to be multi-walled with 15–20 layers [22].

In 1973, Boehm reported hollow carbon fibers by catalytic disproportionation of carbon monoxide at 480–700 °C [25]. In 1976, hollow carbon fibers with nanometer-scale diameters were synthesized using a vapor-growth technique [10, 24]. HRTEM image (Fig. 2.1b) clearly shows the graphite walls and hollow core of a carbon fiber [24]. In another paper [10], it is reported that the carbon fibers can also be consisted of a single wall of graphite layer (Fig. 2.1c).

In 1979, hollow carbon fibers were produced on carbon anodes during arc discharge and presented in a conference [11, 12]. These hollow tubular nanostructures were grown in a nitrogen atmosphere at low pressures. In 1987, a patent to produce

Table 2.1 Milestones of carbon nanotubes.

Year	Authors	Contribution	Ref.
1889	Hughes and Chambers	Carbon filaments were synthesized from the thermal decomposition of gaseous hydrocarbon.	[5]
1890	Schützenberger	Carbon fibers were grown from thermal decomposition of hydrocarbon.	[6]
1903	Pélabon	Carbon fibers were grown from thermal decomposition of hydrocarbon.	[7]
1939	Siemens Inc.	TEM was commercialized, making the study on morphology and inner texture of carbon fibers possible in nanoscale.	[8]
1952	Radushkevich and Lukyanovich	First TEM evidence was published to show hollow graphitic carbon fibers with nanosized diameter.	[9]
1958	Hillert and Lang	Concentric texture of carbon fibers were determined from electron diffraction; bamboo textured carbon fibers were synthesized.	[10]
1976	Oberlin, Endo and Koyama	Carbon fibers were produced using a vapor-growth technique; TEM image of hollow carbon fiber with possibly one graphite layer was published.	[11, 12]
1979	Abrahamson	Hollow carbon fibers were produced on carbon anodes during arc-discharge.	[13]
1987	Tennent	A patent for graphitic, hollow core carbon fibrils was issued in US.	[4]
1991	Iijima	Carbon nanotubes were reported in the soot of arc discharge; Carbon nanotubes were brought into the awareness of the scientific community.	[14]
1992	Scuseria	Branched SWCNT was reported.	[15]
1992	Mintmire et al.	The electronic properties of SWCNTs were theoretically predicted.	[16]
	Hamada et al.		[17]
	Saito et al.		[18]
1993	Iijima and Ichihashi	SWCNTs were synthesized using Fe catalyst.	[19]
	Bethune et al.	SWCNTs were synthesized using Co catalyst.	[20]
2004	Hu et al.	Carbon microtubes were synthesized using templates.	[21]
2007	Nasibulin et al.	Carbon nanotube nanobuds were synthesized.	[21]

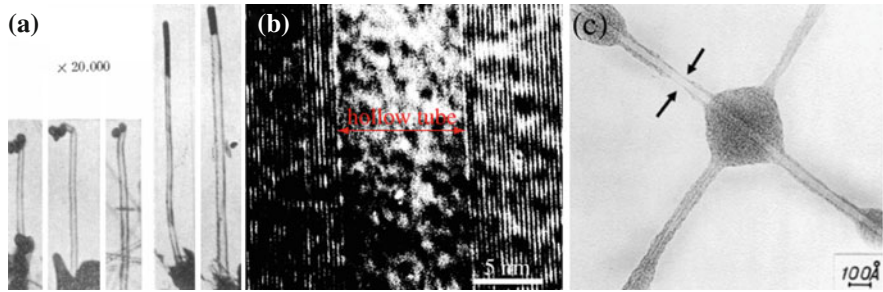


Fig. 2.1 Typical hollow carbon fiber images in the history. **a** First TEM images of possible MWCNTs published in 1952. Reprinted from Monthioux and Kuznetsov [22]. Copyright (2006), Elsevier. **b** First HRTEM image of a hollow fiber consisted of multilayers, published in 1976. Reprinted from Oberlin et al. [24]. **c** First TEM image of possible SWCNTs published in 1976. Reprinted from Oberlin et al. [10]. Copyright (1976), Elsevier

cylindrical discrete carbon fibrils with a constant diameter between about 3.5 and about 70 nm . . . , length 102 times the diameter, and an outer region of multiple essentially continuous layers of ordered carbon atoms and a distinct inner core . . . was issued [13].

Most of the work before 1991 was unfortunately not well known by the broader scientific community, nor was the hollow carbon structures called *carbon nanotubes*, and therefore not creating a significant impact.

2.1.2 History Since 1991

Since buckminster fullerene (shown in Fig. 1.1d) was discovered by arc discharge in 1985 [26], more and more scientists expressed interests in nanomaterials. Shortly after, Iijima, using the same method (arc discharge) to produce C_{60} , found that the central core of the cathodic deposit contained a variety of closed graphitic structures including nanoparticles and nanotubes [4]. The obtained CNTs were MWCNTs as shown in Fig. 2.2a. The work was published in *Nature* in 1991 and has been noticed worldwide in the scientific community. It is fair to say that the report of CNTs by Iijima strengthened the scientific community pursuit to nanoscience and nanotechnology. Readers interested in the CNT discovery stories are referred to the related literatures [22, 27, 28], especially the editorial paper written by Monthioux and Kuznetsov in *Carbon* journal [22].

Following the research of MWCNTs by Iijima in 1991, SWCNTs were independently synthesized using arc-discharge techniques (see Fig. 2.2b,c) by adding transition-metal catalysts (Fe [18] or Co [19]). The synthesis of SWCNTs is an important milestone in the development of CNT research because many theoretical predications of CNT properties can be more conveniently tested on the simplest SWCNT structures.

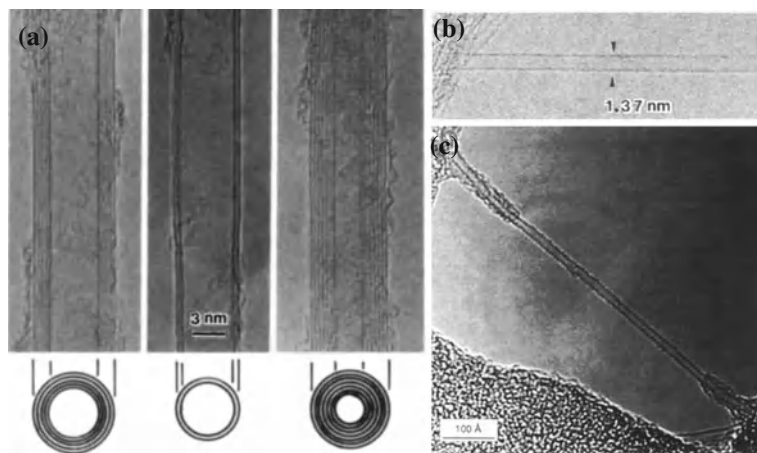


Fig. 2.2 High-resolution TEM images of the most well-known **a** MWCNTs published in 1991. From Iijima [4]. Copyright (1991), Macmillan Publishers Ltd. **b** SWCNTs published in 1993 grown from iron catalyst, From Iijima and Ichihashi [18]. Copyright (1993), Macmillan Publishers Ltd. and **c** SWCNTs published simultaneously with (b) using another catalyst, cobalt. From Bethune et al. [18]. Copyright (1993), Macmillan Publishers Ltd. All these CNTs were synthesized by DC arc-discharge evaporation of carbon.

The arc discharge-produced materials are mixtures of amorphous carbon, graphite, and CNTs with a low CNT yield. Pure CNTs are usually obtained by various purification methods [29–34]. Although the yield is low and the purification procedure is complex, the produced CNTs have good crystallinity and very few defects. So the method is still widely used today.

In 1995, an alternative method of preparing SWCNTs, laser vaporization of graphite, was discovered by Smalley's group [35]. This method resulted in a high yield of SWCNTs with unusually uniform diameters [36].

Besides the above classic CNT structures, hybrid CNTs, such as CNT Y-junctions [14, 37–39], CNT nanobuds [21, 40], CNT nanotorus [40], carbon microtubes with nano-wall [20] were also synthesized. The details of these hybrid structures are discussed in Chap. 2.2: *Structures of Carbon Nanotubes*.

2.1.3 History of Aligned Carbon Nanotubes

Along with the synthesis of individual CNTs, CNT arrays consisting of a number of individual CNTs were also fabricated at the same time.

CNT ropes consisting of 100–500 aligned SWCNTs in a closely stacked two-dimensional triangular lattice arrangement were reported as early as in 1996 using a laser ablation method (Fig. 2.3) [36]. SWCNT ropes were synthesized from a carbon-nickel-cobalt mixture at 1200°C. These SWCNTs are nearly uniform in diameter and

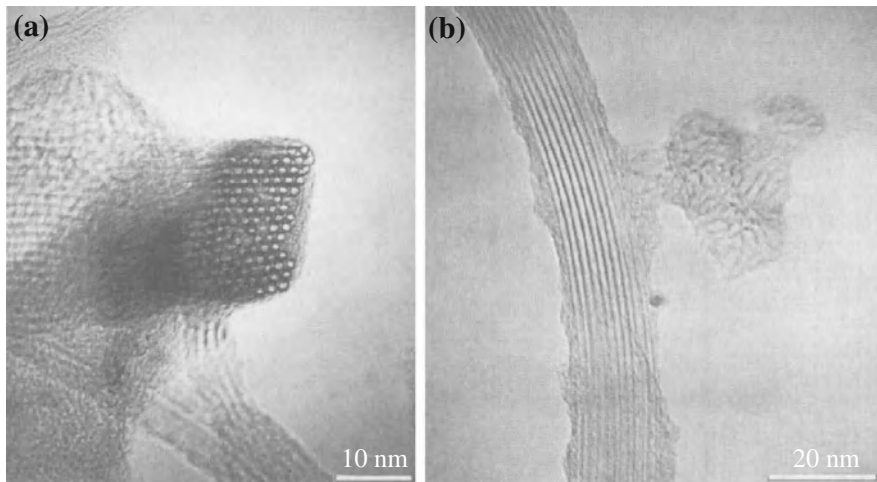


Fig. 2.3 TEM images of an SWCNT rope prepared by laser vaporization of graphite in 1996. **a** A single SWCNT rope made up of ~ 100 SWCNTs as it bends through the image plane of the microscope, showing uniform diameter and triangular packing of the tubes within the rope. **b** Side view of a rope segment. From Thess et al. [36].

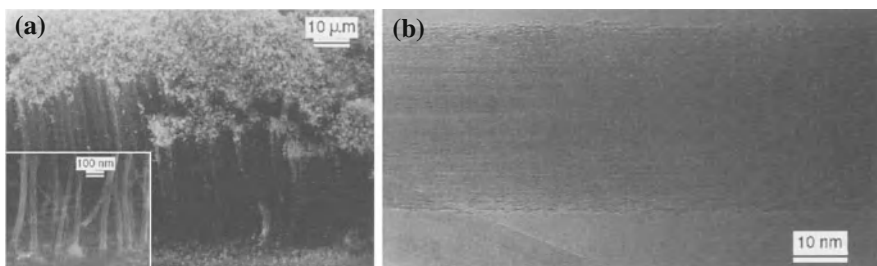


Fig. 2.4 **a** SEM image of a film composed of aligned CNTs prepared in 1996. This film with a thickness of $50\ \mu\text{m}$ was obtained by growing for 2 hr. *Inset*: high-magnification SEM image. **b** High-resolution TEM image of a CNT composing the CNT film in **a**, consisting of about 40 concentric shells of graphitic sheets with a sheet spacing of 0.34 nm. The inner and outer diameters of the tube are 4 and 34 nm, respectively. From Li et al. [42].

self-organize into ropes consisting of 100–500 SWCNTs with a SWCNT spacing of $17\ \text{\AA}$. Mechanical properties and applications of these CNT ropes are described in Chap. 9.1.1: *Carbon Nanotube Ropes*.

Later, large-scale MWCNTs were fabricated from iron nanoparticles embedded in mesoporous silica by pyrolysis of acetylene using a thermal chemical vapor deposition (CVD) method (Fig. 2.4) [42]. The MWCNTs grown from the iron nanoparticles embedded in mesoporous silica are approximately perpendicular to the surface of the silica and form an aligned array of isolated tubes with a tube spacing of about 100 nm [42]. It is believed that some catalytic iron nanoparticles were embedded in

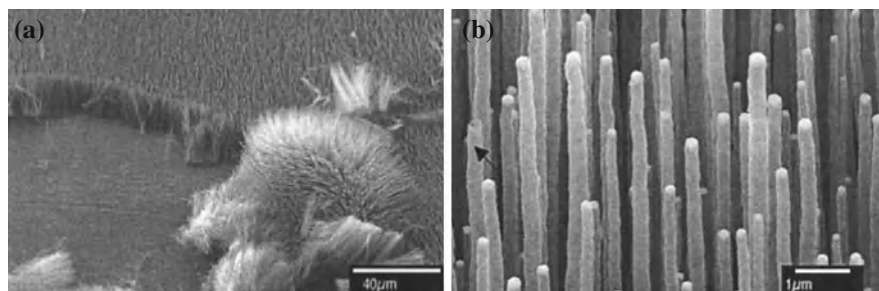


Fig. 2.5 **a** Low-magnification SEM image of an MWCNT array grown by PECVD in 1998. **b** High-magnification SEM image of MWCNTs shown in **a**. The CNTs are vertically grown on the substrate and the CNT sites are random. From Ren et al. [44]. Reprinted with permission from AAAS

the vertical cylindrical pores. When CNTs grew in these vertical pores, they became perpendicular to the surface of the silica substrate. Those CNTs formed on iron nanoparticles embedded in inclined cylindrical pores were tilted along the axes of the pores. The growth direction of the nanotubes can be controlled by the pores from which the nanotubes grow. These MWCNTs were randomly grown on the substrates, not very straight, and often entangled together.

Large-scale MWCNTs were also fabricated from thin films of cobalt catalysts patterned on a silica substrate by pyrolysis of 2-amino-4,6-dichloro-s-triazine [43] using thermal CVD method.

Straight, well-aligned, and separated CNT arrays were not successfully fabricated until 1998 using a plasma-enhanced chemical vapor deposition (PECVD) method below 666 °C (Fig. 2.5) [44]. CNTs were aligned over areas up to several square centimeters on nickel-coated glass. The diameter and length of the aligned CNTs are controllable from 20 to 400 nm and from 0.1 to 50 μm, respectively. The CNTs were very straight (Fig. 2.5b). Because the catalytic nickel nanoparticles were fabricated by radio frequency magnetron sputtering, the nanoparticles distributed randomly on the glass substrate. The vertical CNTs were then randomly grown on the glass surface.

Later, large periodic arrays of CNTs were grown by plasma-enhanced hot filament CVD on periodic arrays of nickel dots prepared by e-beam lithography [45] (Fig. 2.6). The sites of the CNTs depend on the sites of catalytic nickel nanodots. The nanotube growth process is compatible with silicon integrated circuit processing, and CNT devices requiring freestanding vertical CNTs can be readily fabricated since then.

In order to obtain periodic catalytic nanoparticles cheaply, polystyrene microsphere lithography was developed [46, 47]. Figure 2.7a shows aligned CNTs in a honeycomb lattice pattern. The CNTs grow from the periodically patterned catalysts prepared by microsphere lithography (Fig. 2.7b). From then on, the vertically grown CNTs are site controlled. These 3D aligned CNTs have wide applications, such as field-emission displays, physical and biological sensors, etc.

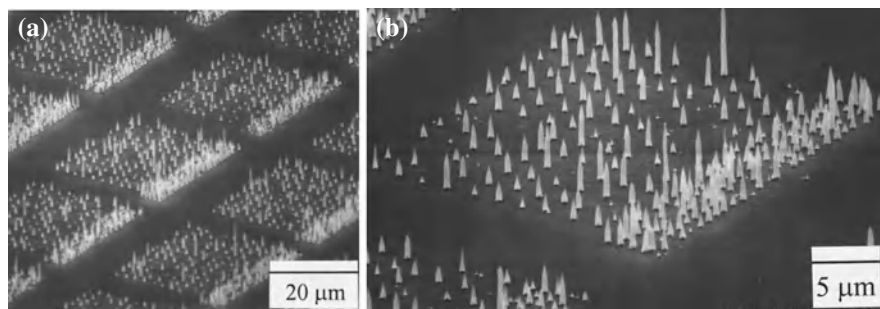


Fig. 2.6 SEM images of highly ordered arrays with the assistance of e-beam lithography for making the catalytic Ni dots. **a** A repeated CNT array pattern and **b** a CNT array pattern. From Ren et al. [45]. Reprinted with permission from American Institute of Physics

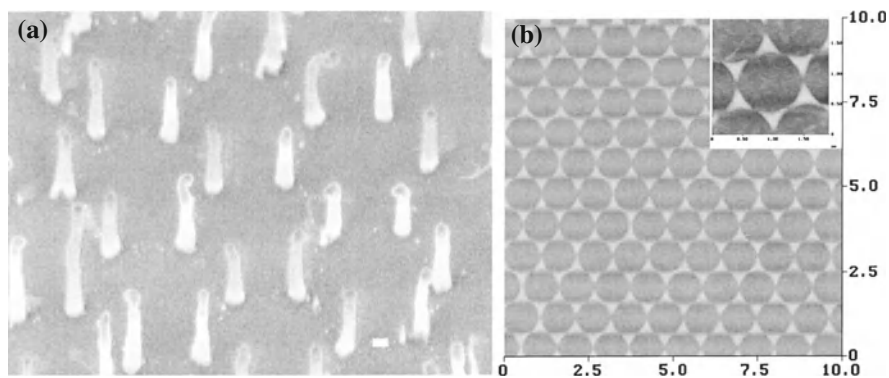


Fig. 2.7 **a** SEM images of a honeycomb array of aligned CNTs grown by PECVD. **b** AFM image of Ni catalytic dots used to grow CNTs in **(a)**. The Ni catalytic dots were prepared by polystyrene microsphere masks. *Inset*: higher magnification image of nickel dots. From Huang et al. [46]. Reprinted with permission from American Institute of Physics

At the same time, superlong CNT arrays were also grown vertical to the substrate surface using a thermal CVD method [48, 49], especially the water-assisted CVD method [50]. More details of the CVD technique are described in Chap. 6.1.1: *Thermal Chemical Vapor Deposition with Crowding Effect*. Table 2.2 lists the milestones of the CNT arrays.

Among the various CNT-related structures discovered, we mainly discuss here arrays of aligned CNTs which may be SWCNTs, DWCNTs, MWCNTs, and bamboo or fiber-like. Meanwhile, we recommend a handful of available books to interested readers for further reading and understanding on individual CNTs of more varieties [55–58].

Table 2.2 Milestones of CNT arrays

Year	Authors	CNT arrays	Techniques	Comments	Ref.
1994	Ajayan et al.	MWCNT in polymer	Ex: Arc-discharge + stretching	Stretching MWCNTs embedded in a polymer matrix	[51]
1995	de Heer et al.	MWCNT film	Ex: arc-discharge + filtering	Mechanical alignment of MWCNTs using nano-pore ceramic filter	[52]
1996	Li et al.	MWCNTs grown on porous SiO _x	In: thermal CVD	Acetylene (gas) as carbon source and Fe particles embedded in porous SiO _x as catalyst	[42]
1996	Thess et al.	SWCNT bundle	In: laser ablation	SWCNTs arrays in hexagonal structure	[36]
1997	Terrones et al.	Grown on patterned catalyst	In: pyrolysis over Co thin films	Triazine molecules as carbon-source and patterned Co as catalyst	[43]
1998	Ren et al.	Grown on large-area glass	In: hot-wire DC PECVD	Ni as catalyst and acetylene (gas) as carbon-source, and NH ₃ as plasma enhancing gas	[44]
1999	Ren et al.	3D ordered CNT arrays	In: DC PECVD	CNT vertically grown on 2D ordered catalytic Ni nanodots prepared by e-beam.	[45]
1999	Fan et al.	Grown on template	In: CVD	Fe in porous Si as catalyst and ethylene pyrolytically as carbon-source	[48]
2002	Wei et al.	Grow vertically or parallel to the substrate surface	In: CVD	Xylene as carbon-source and ferrocene as catalyst	[53]
2003	Huang et al.	Honeycomb array of aligned carbon nanotubes	In: DC PECVD	CNT grown on 2D ordered Ni nanodots with honeycomb-array.	[46]
2003	Rao et al.	SWCNT aligned on substrate surface	In: individual polar molecular marks	SWCNTs were attracted towards the polar regions and self-assemble to form pre-designed structure	[54]
2004	Hata et al.	SWCNT forest grown on substrate	In: water-assisted CVD method		[50]

Ex: ex situ method; In: in situ method

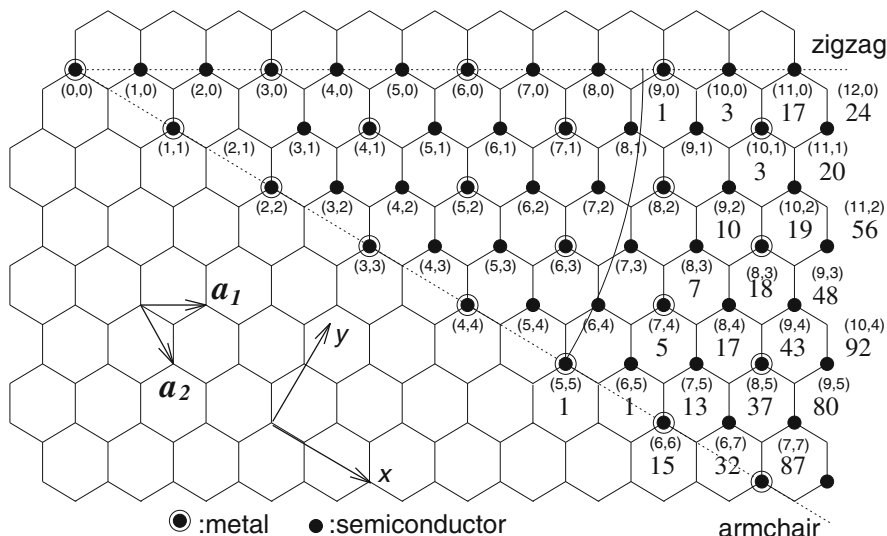


Fig. 2.8 The hexagonal honeycomb lattice of the graphite layer. From Dresselhouse et al. [55]

2.2 Structures of Carbon Nanotubes

Until now, various CNTs are synthesized, such as single-walled CNTs (SWCNTs), double-walled CNTs (DWCNTs), multi-walled CNTs (MWCNTs), and coiled CNTs, etc. The chemical bonds in CNTs are all sp^2 bonds, similar to those of graphite. Below we introduce CNTs with different morphology. The atomic structure details of individual CNTs are well described in the previous literatures [3, 55–63].

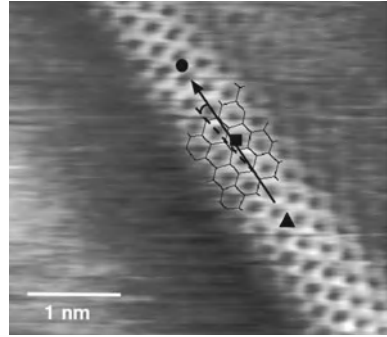
2.2.1 Graphite

Graphite layer is the basic structural element of CNTs. A graphitic layer is a one-atom-thick planar sheet of sp^2 -bonded carbon atoms with a honeycomb crystal lattice structure (Fig. 2.8). The hexagonal honeycomb lattice of the sheet can be defined by the unit vectors \mathbf{a}_1 and \mathbf{a}_2 [55, 64]. The carbon-carbon bond length is 0.142 nm. Its unique physical properties are reviewed in a collection of books and in a vast amount of literatures [65, 66].

According to the Russian Doll model, the sheets of graphite can be rolled into concentric cylinders to form CNTs. It can also form nanospheres, as show in Fig. 1.2.

Recently, SWCNTs were unzipped into single-layered graphite by an oxidative process [67] or plasma etching [68]. The structure and physical properties of the

Fig. 2.9 STM image of a SWCNT produced by laser vaporization. The tube axis is indicated with a *solid arrow* and the zigzag direction is highlighted by a *dashed line*. From Odom et al. [70]



unzipped sheets are very similar to these of single layer graphite. So the crystalline structure of graphite is closely related to that of CNTs [69].

2.2.2 Single-Walled Carbon Nanotubes

SWCNT consists of one layer of carbon sheet. Figure 2.9 shows the atomic structure of an SWCNT. SWCNTs can be synthesized by CVD [10], arc discharge [18, 19], and thermocatalytical disproportionation of carbon monoxide [71, 72]. Now massive amount of SWCNTs is produced mainly by CVD methods. Most SWCNTs have a diameter close to 1 nm, with length extendable up to millimeter or even centimeter scales.

The structure of an SWCNT can be conceptualized by wrapping a graphitic layer into a seamless cylinder. Figure 2.10a shows how an SWCNT is rolled up from a graphitic layer. The way the layer is wrapped is represented by a pair of indices (n, m) called the chiral vector $\mathbf{C}_h = n\mathbf{a}_1 + m\mathbf{a}_2$, where \mathbf{a}_1 and \mathbf{a}_2 are defined in Fig. 2.8. The integers n and m denote the number of unit vectors along two directions in the honeycomb crystal lattice of a graphitic layer. If $n = m$, the SWCNTs are called *arm-chair* (Fig. 2.10b). If $m = 0$, they are called *zig-zag* (Fig. 2.10c), and the rest are called *chiral* (Fig. 2.10d).

SWCNTs have unique electrical properties. For a given (n, m) SWCNT, if $n = m$, the CNT is metallic with low energy properties of a Tomonaga-Luttinger liquid [74], and the rest of the SWCNTs can be either metallic or semiconducting depending on their chirality (or equivalently speaking, their diameter), as theoretically predicted [16, 17, 75] and experimentally confirmed [70, 76]. The unique physical properties of SWCNTs are reviewed in various books [63] and literatures. For example, metallic CNTs can theoretically carry an electrical current density as high as $4 \times 10^9 \text{ A/cm}^2$ which is more than 1000 times greater than good metals such as copper [77].

The structure and properties of SWCNTs are reviewed in many books [78]. Here we do not cover the detailed properties of the SWCNTs.

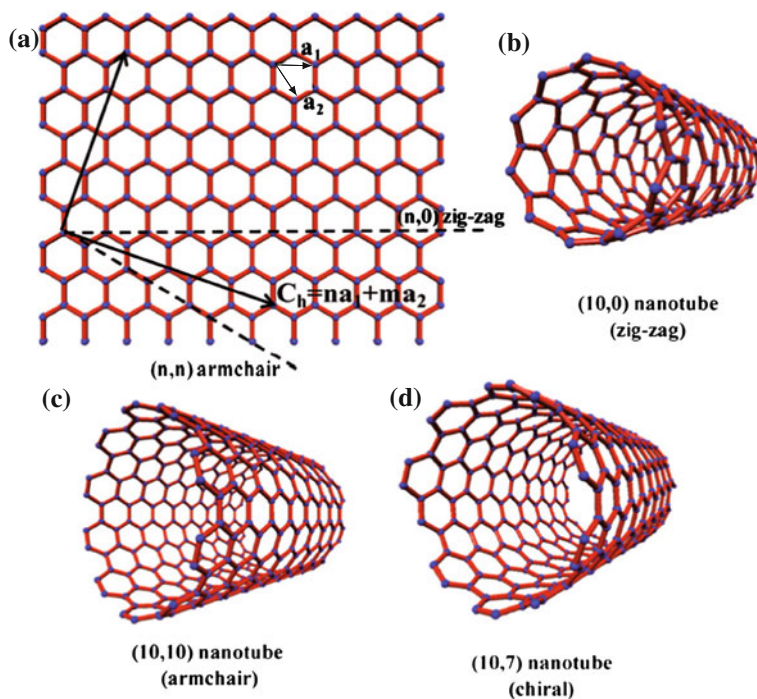


Fig. 2.10 **a** An infinite graphite layer with (n, m) nanotube naming scheme describing how a nanotube is rolled up. \mathbf{a}_1 and \mathbf{a}_2 are the unit vectors of graphite layer in real space. **b** SWCNT of zigzag structure, **c** SWCNT of armchair structure, and **d** SWCNT of chiral structure. From Rao et al. [73]. Copyright (2009), The Royal Society of Chemistry

2.2.3 Double-Walled Carbon Nanotubes

DWCNTs were observed during arc-discharge synthesis [4] and during the disproportionation of carbon monoxide [71]. The presence of DWCNTs was related to the nature of the catalyst [79]. Now DWCNTs can be synthesized by CVD methods [80, 81] and produced at gram scales [82].

DWCNTs are interesting members of the CNT family because their morphology and most physical properties are similar to those of SWCNTs, while their electrical and chemical properties are significantly improved for many application considerations. DWCNTs are especially important when functionalization is required to add new properties to the CNTs. In the case of SWCNTs, covalent functionalization will break some C=C bonds, leaving holes in the CNT structures and thus modifying both their mechanical and electrical properties. In the case of DWCNTs, only the outer walls are modified and therefore many properties are well preserved.

Fig. 2.11 3D model of an MWCNT



2.2.4 Multi-Walled Carbon Nanotubes

The MWCNT structure (Fig. 2.11) can be conceptualized by wrapping several graphite layers into a concentric seamless cylinder. Figure 2.1b shows an HRTEM image of an MWCNT.

There are two models, namely the Russian Doll model and the Parchment model [83], which can be used to describe the structures of MWCNTs. In the Russian Doll model, graphitic sheets are arranged in the form of concentric cylinders, for example, a (0, 8) SWCNT within a wider (0, 10) SWCNT. The inter-layer distance in an MWCNT is slightly above that in graphite, which is approximately 3.3 Å, suggesting a different layer-stacking mechanism. In the Parchment model proposed in 1960 [83] to explain the cylindrical structure of carbon fibers, a single continuous graphitic layer scrolls or rolls up to form concentric tubes.

2.2.5 Bamboo-Like Carbon Nanotubes

Bamboo-like CNTs are usually synthesized using thermal CVD methods. They are usually produced at low gas pressures and high temperatures or at high gas pressures regardless of temperature [84, 87]. As the pressure goes up, the wall and the inner diameter of the CNTs get thicker and larger, respectively, by increasing the number of graphitic layers. Once a layer forms in the bamboo-like structure, all the layers will terminate on the surface of the CNTs. Crystallinity of the bamboo-like CNTs usually becomes poorer with the increase in pressure due to higher growth rates. The inclination angle (the angle between the fringes of the wall and the axis of the CNT) increases with the pressure.

PECVD methods are also frequently employed to produce bamboo-like CNTs with even higher degree of deviations from the classic CNT structures. In some cases at low growth temperatures, the structure is composed of closely stacked graphitic

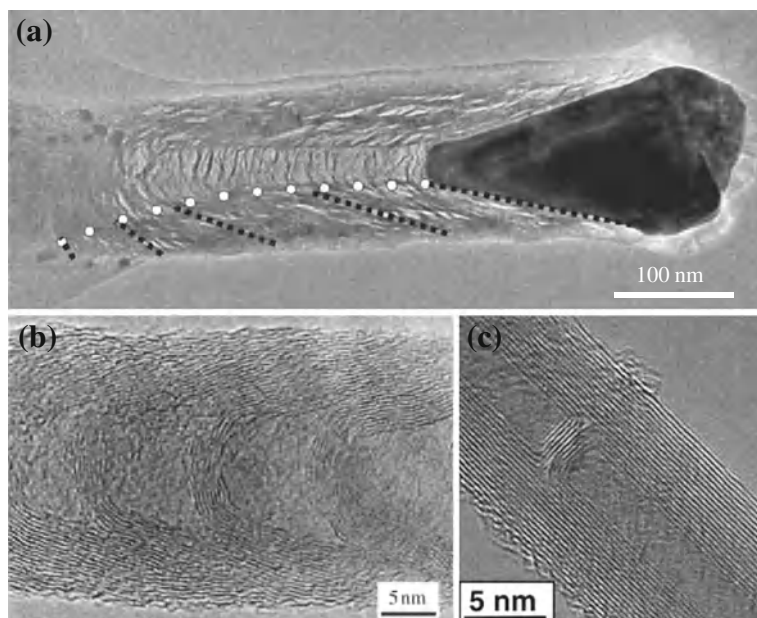


Fig. 2.12 Bamboo-like CNTs. **a** TEM image of a bamboo-like CNT after 5 min PECVD growth on silicon substrate. The *black dotted lines* indicate the wall angle in the sidewalls. The *white circular dots* mark the transition between the cup bottoms and cup walls. From Cui et al. [84]. Copyright (2004), American Institute of Physics. **b** HRTEM image of a bamboo-like CNT grown by thermal CVD. From Li et al. [85]. Copyright (2001), Springer. HRTEM image of a bamboo-like CNT with a zero inclination angle, synthesized by a Wolff-Kishner reduction process. From Wang et al. [86]. Copyright (2005) American Chemical Society

cups with very small hollow core or inner compartment space (Fig. 2.12). The cross-sectional views of these PECVD-produced nanostructures look very much like fishbones [85] and are therefore occasionally called fishbone CNTs, or stacked-cup CNTs, or simply carbon nanofibers (CNFs) to ignore its low level of hollowness altogether. Note that these CNFs sometimes may also have concentric outer walls with a zero inclination angle in addition to the fishbone structures [88].

2.2.6 CNT Y-Junctions

Carbon nanotubes are one of the most promising elements for the fabrication of nanoelectronic devices [89]. However, connection of two or more CNTs together to form an ideal junction is very challenging. A simple joint of two different carbon nanotubes can be formed by introducing a pair of pentagon and heptagon into the hexagonal network of a single carbon nanotube [90–93]. Until now, the formation of a three-point junction (T or Y-junction) has been achieved [38, 39, 41, 42, 94, 95].

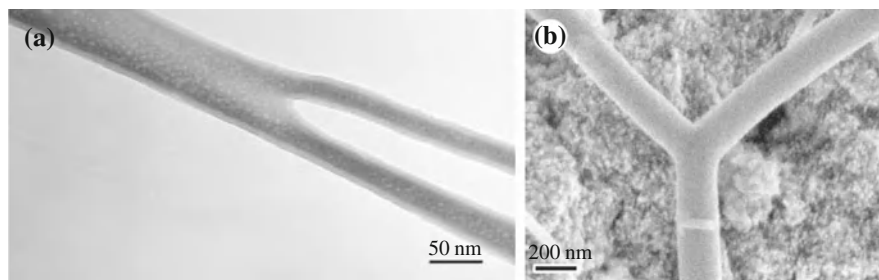


Fig. 2.13 **a** TEM image of CNT Y-junction. From Li et al. [37]. Copyright (1999), Macmillan Publishers Ltd. **b** SEM image of CNT Y-junction with smooth surface. From Li et al. [39]. Reprinted with permission from American Institute of Physics

Alumina membrane with splitting nanochannels has been attempted to grow Y-junctions [37]. The as-grown junctions have one big stem and two small branches oriented nearly in the same direction confined by the shape and size of the channels (Fig. 2.13a). Pyrolysis of organometallic precursor such as nickelocene along with thiophene has also been reported to result in Y-shaped junctions [38]. The angles between the arms vary in the range of 90–150° from junction to junction, and the arms are not straight while basic electronic properties as a junction have been observed. Single-walled Y-junctions have also been observed in the residue of the thermally decomposed C_{60} in the presence of transition metals [96].

Very straight carbon nanotube Y-junctions with fixed angles between the arms was synthesized by CVD by pyrolysis of methane over cobalt supported on magnesium oxide [39]. Figure 2.13b shows a Y-junction with neat smooth surface and uniform arms of about 200 nm in diameter. The angles between the three arms are close to 120°. All the Y-junctions have very similar shape regardless of their different diameters. TEM observations show that most Y-junctions have hollow cores in their three arms. High-resolution TEM of the Y-junction indicates the Y junction is well graphitized. The Y-junction consists of about 60 concentric graphite layers in its arms and a hollow core of 8.5 nm in diameter.

The Y-junctions possess unique electronic properties due to their structures, which may be a great advantage for practical applications. The Y-junctions offers more opportunities for the development of nanoelectronic devices and fiber-reinforced composites. The Y-junction fibers are expected to reinforce the composites better than the straight ones. The interested readers are referred to some review literatures on Y-junctions [95].

2.2.7 Carbon Nanobuds

Carbon nanobuds are a kind of hybridized carbon nanomaterials combining two previously discovered allotropes of carbon: carbon nanotubes and fullerenes. In this

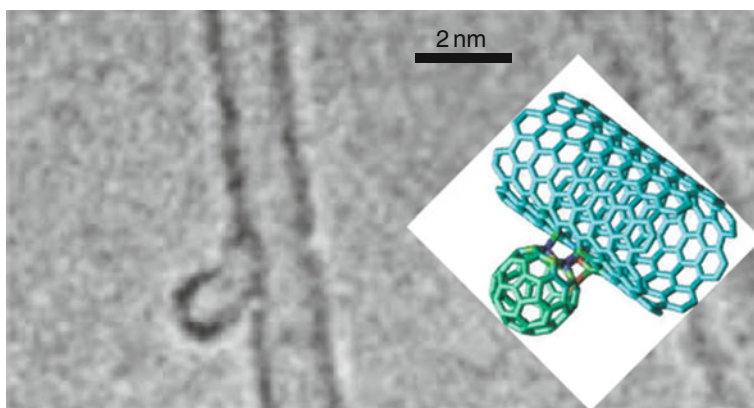


Fig. 2.14 TEM image of CNT nanobuds in which a fullerene is combined with a SWCNT and attached to the surface of the SWCNT. Inset is the structure of the nanobud on SWCNT. From Nasibulin et al. [41]. Copyright (2007). Macmillan Publishers Ltd

material, fullerene-like buds are covalently bonded to the outer sidewalls of the underlying carbon nanotubes (Fig. 2.14). In situ TEM studies show that the fullerenes are formed together with CNTs [21]. It is believed that the carbon atoms at the edge of the dynamic layer (with dangling bonds) can be attacked by etching agents, resulting in the closure of the rings consisting of five carbon atoms (pentagon formation). Further, the formed pentagon is surrounded by hexagons, producing nanobuds [21, 40]. The negative curvature carbon was proposed [14] ten years earlier than the experimental observation.

This hybrid material has useful properties of both fullerenes and carbon nanotubes. The mechanical properties and the electrical conductivity of the nanobuds are similar to those of corresponding carbon nanotubes. However, because of the higher reactivity of the attached fullerene molecules, the hybrid material can be further functionalized through known fullerene chemistry. Additionally, the attached fullerene molecules can be used as molecular anchors to prevent slipping of the nanotubes in various composite materials, thus enhancing the mechanical properties of CNT composites.

Due to the large number of highly curved fullerene surfaces acting as electron emission sites on conductive carbon nanotubes, nanobuds possess advantageous field electron emission characteristics. So they've been found to be exceptionally good field emitters. Randomly oriented nanobuds have already been demonstrated to have an extremely low work function for field electron emission [40]. The macroscopic field thresholds for field electron emission of the nanobuds are about $0.65 \text{ V}/\mu\text{m}$ while as high as $2 \text{ V}/\mu\text{m}$ of non-functionalized SWCNTs. The current density of the nanobuds is much higher than that of corresponding pure SWCNTs.

Fig. 2.15 Predicated CNT nanotorus. From Liu et al. [40]

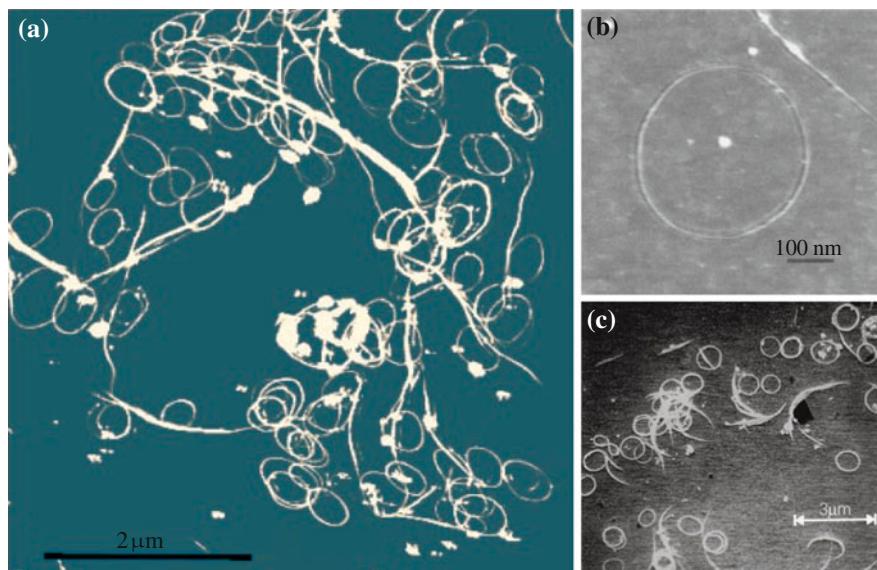
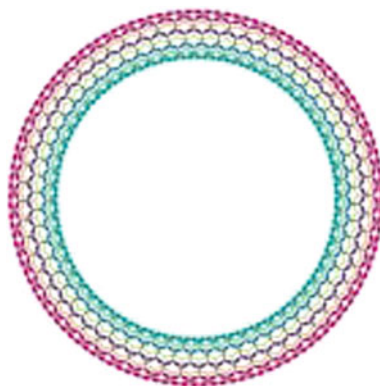


Fig. 2.16 **a** AFM image of carbon nanotube rings cast on mica. Sano et al. [102]. **b** Scanning force image of a bundle of CNT tori. From Liu et al. [103]. **c** SEM image of toroidal CNTs consisting of curled SWCNT bundles. From Martel et al. [104]

2.2.8 CNT Nanotorus and Micro-Rings

A nanotorus (Fig. 2.15) is theoretically described as carbon nanotube bent into a torus (doughnut shape) [41, 97, 98]. It is believed that the heptagon-pentagon construction in CNTs can explain the formation of curved nanotubes, tori, or coils [99–101].

In history, the existence of SWCNT bundle forming tori (Fig. 2.16) was reported as early as in 1997 [102–105]. The diameter of these tori is between 300 and 500 nm. SWCNTs with an average diameter of 1.4 nm were prepared using laser ablation,

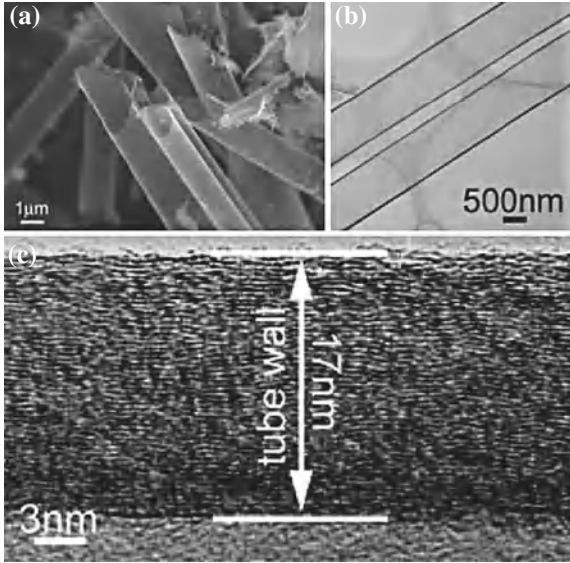


Fig. 2.17 Carbon microtubes. **a** SEM of microtubes; **b** TEM image showing the hollow; **c** HRTEM of a microtube wall. From Hu et al. [20]

then shortened and induced to coil by using an acid treatment with ultrasound. It is believed that the ring formation process has a SWCNT coiling over itself to form a loop.

These SWCNT tori exhibited negative magnetoresistance characteristic of weak one-dimensional localization [106].

Nanotori are predicted to have many unique properties, such as magnetic moments 1,000 times larger than previously expected for certain specific radii [99, 100]. Properties such as magnetic moment and thermal stability vary widely depending on radius of the torus and radius of the tube.

2.2.9 Carbon Microtubes

Figure 2.17 shows carbon microtubes grown from a thermal reaction between ZnS and activated carbon. The synthesized carbon microtubes have outer diameter of 1–2 μ , wall thickness of 10–20 nm, and lengths ranging from hundreds of micrometers to millimeters.

It is explained that the liquid droplet of Zn from ZnS powder provides an energetically favorable site for the absorption of the gaseous carbon. The carbon atoms diffuse and penetrate into the Zn liquid droplets, and precipitate from the Zn–C solution, giving rise to the growth of carbon microtubes at the solution boundary. Based

Fig. 2.18 HRTEM micrograph of an individual as-grown carbon nanotube by CVD method. The graphitic layers are oriented along the axle shown as a *arrow*. From Ciet et al. [107]

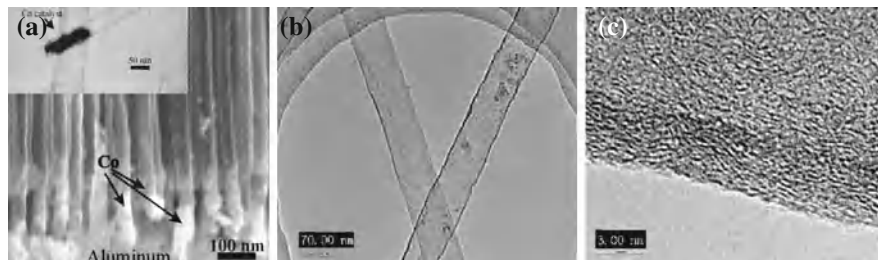
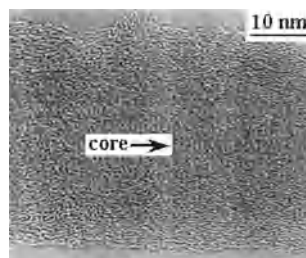


Fig. 2.19 **a** Cross-section SEM image of the nanotube array partially exposed from AAO template. The cobalt catalyst is at the base of the tubes separated from the aluminum substrate. From Li et al. [110]. The inset is a TEM image of a single nanotube showing the cobalt particle at the base. **b** TEM and **c** HRTEM images of amorphous CNTs synthesized from AAO templates. From Hu et al. [111]

on the growth mechanism, the diameter of the carbon microtubes is controlled by the diameter of the liquid Zn catalyst droplets, supported by the SEM observation.

2.2.10 Amorphous Carbon Nanotubes

Individual amorphous CNT can be synthesized by thermal CVD [107, 108] and by hydrothermal method [109]. Figure 2.18 shows the amorphous feature of an individual as-grown carbon nanotube grown by CVD method. The microstructure of the amorphous CNT is similar to that of bulk amorphous carbon, which is composed of nanoscaled graphitic sheets. The nanoscaled graphite sheets in wall of the carbon nanotube are roughly parallel to the tube axis while the central hole contrast is very low due to the poor crystallization.

The amorphous CNTs are not thermally stable. The nanoscaled graphitic sheets of the amorphous CNTs begin to grow at 1,700°C in flowing argon and totally crystallize into MWCNTs at 2,000°C for 2 h [107].

Amorphous CNT arrays can be synthesized from nanoporous anodic alumina templates [111, 112]. Figure 2.19a shows a SEM image of amorphous CNT array prepared from anodized aluminum oxide (AAO) templates. The CNT array has a very

high site-density of tubes, approximately 10^{10} tubes/cm² [110]. The tube diameter distribution throughout the CNT array is narrow, close to 5% of the mean diameter, depending on the diameter distribution of nanochannel in the AAO template. The nanotube diameter, CNT site density, and CNT array spacing are controllable by using different AAO template whose responding parameters can be easily adjustable by adjusting the anodizing voltage, electrolyte composition, and temperature resulting in ordered arrays with selectable diameters ranging from approximately 10 nm to several hundred nanometers and size-densities of up to 10^{11} tubes/cm². The CNT lengths of up to 100 μ m can be obtained by varying the length of the nanopores in the AAO template in which the CNT nanotubes are grown.

Figure 2.19b shows a TEM image of amorphous CNTs prepared from AAO templates. The diameter is several microns, agreed with SEM observation. Further HRTEM image (Fig. 2.19c) indicates the CNT wall is less than 20 nm and amorphous.

2.2.11 Coiled Carbon Nanotubes

Theoretically by combining heptagons and pentagons in the predominantly hexagonal carbon framework, helicoidal graphite or helically shaped carbon tubules can be generated (Fig. 2.20a) [97, 98]. Experimentally, the existence of helix-shaped MWCNTs have been reported by pyrolysis of hydrocarbons (such as acetylene) over catalyst [114–116] (Fig. 2.20b). During these thermolytic processes, the catalytic metal particle plays a key role in the nanotube growth because the accumulation of carbon atoms occurs on the particle surface, which is the most reactive. Due to the irregular morphology of some particles, different rates for carbon agglomeration might arise within the particle walls, which are responsible for the growth of bent structures such as spirals and helices.

More details of the synthesis, microstructure, and potential applications of coiled CNTs can be found in some review literatures [117, 118] and the references therefore.

2.2.12 Flattened Carbon Nanotubes

MWCNTs experience the shape deformation or flattening during their growth and the structure deformation of flattening can change their electronic properties.

Fully flattened MWCNTs were first observed in the CNTs prepared by carbon-arc discharge method [119], and these flattened MWCNTs had a outer width of 20–22 nm. It was postulated that the flattening was caused by external mechanical forces [120, 121].

Alternatively, large thick flattened MWCNTs were synthesized using hydrothermal method at autogenic pressure [122], and the flattened MWCNTs had layers of 13–40 and outer width of 43–121 nm. It was proposed that the high pressure at the

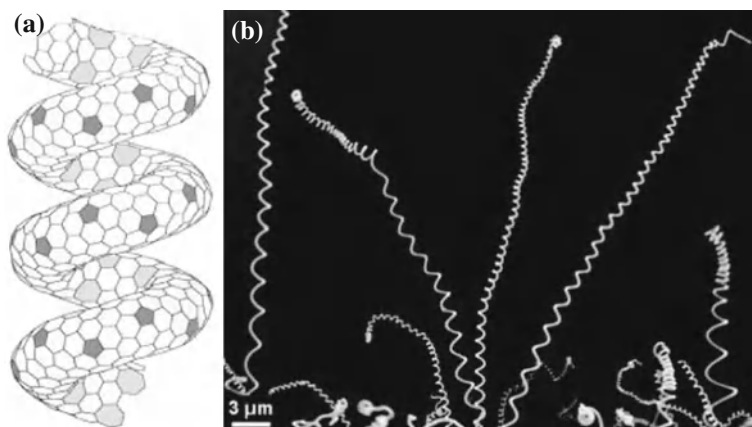


Fig. 2.20 **a** Molecular model of a helicoidal SWCNT, constructed by interspersing five- and seven-membered rings judiciously within the mainly hexagonal network. From Terrones et al. [113]; **b** Corkscrew-like carbon nanotubes produced by pyrolysis of melamine over CoO_x substrates at 1,000 °C. From Grobert et al. [114]

beginning of the reaction played an important role in the formation of the flattened MWCNTs.

Flattened MWCNTs were also synthesized from thermal CVD. The flattened nanotubes are capped with single crystal catalytic nanoparticles and sealed by these nanoparticles. Nanotubes were parallelly flattened and spirally flattened. It is speculated that the pressure difference between inside and outside the nanotube during the growth results in a compression on CNTs. The parallel flattening and spiral flattening of the nanotubes are formed due to the axial compression and torsion exerted on the nanotubes, respectively [123].

Figure 2.21 shows the shape change of a flattened nanotube when it is rotated in TEM. The outer diameter of the nanotube at point *A* is 25.0 nm before rotation (Fig. 2.21a) and does not change after the rotation (Fig. 2.21b), indicating that the nanotube has a circular cross-section at point *A*. Therefore, the carbon nanotube surrounding the catalyst at point *A* is in cylindrical shape. However this nanotube is completely flattened at point *B*. In Fig. 2.21a, the outer diameter and wall thickness of the nanotube at point *A* is 25.0 and 3.5 nm, respectively. At point *B* the width of the nanotube is 35.7 nm. From a simple calculation [120], a cylindrical nanotube with outer diameter of 25.0 nm and wall thickness of 3.5 nm will form a ribbon with width of 35.2 nm if it is completely flattened. This calculated data matches very well with the measured width of 35.7 nm at point *B* of the flattened nanotube in Fig. 2.21a. So the nanotube is completely flattened at point *B* [123]. It can be seen in Fig. 2.21a that the nanotube is also flattened at point *M* in a direction different from that at point *B*. The two local flattenings at points *B* and *M* are all parallel to the long axis of the nanotube.

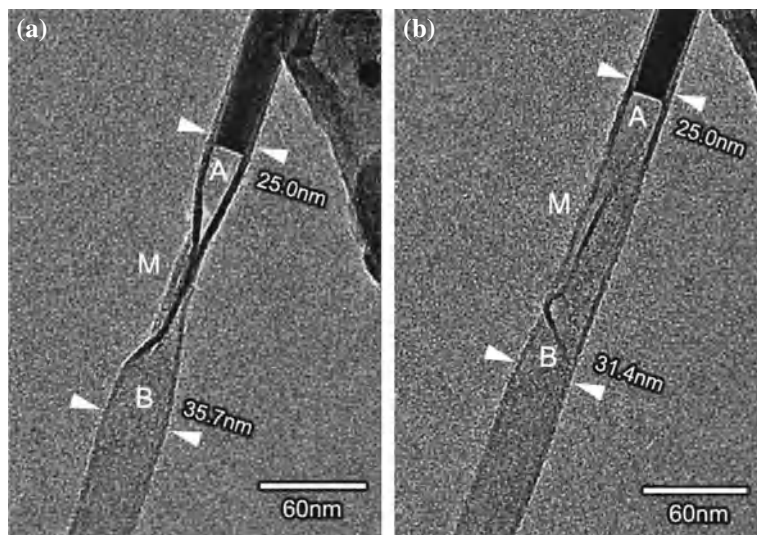
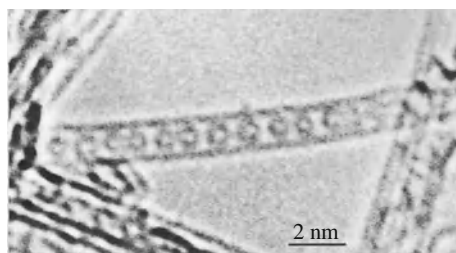


Fig. 2.21 TEM images of flattened CNTs **a** before and **b** after rotation of 35° . The inside end (denoted by letter *A*) of the catalyst particle does not change its diameter during the rotation, but the nanotube changes its shape dramatically at points *M* and *B*. From Li et al. [123]. Reprinted with permission from Elsevier

Fig. 2.22 Single-walled carbon nanotube containing a row of closed carbon shells concentric with the tubule axis. The diameter and center-to-center spacing of the internal shells are consistent with a chain of C_{60} molecules. The nanotube is surrounded by vacuum. From Smith et al. [124]



2.2.13 Other Carbon Nanomaterials

Besides the carbon nanomaterials described above, there are other carbon nanomaterials, such as CNT peapods, carbon nanofibers, and carbon nano-onions, etc.

CNT Peapods. Some nanomaterials, such as C_{60} can be inserted into SWCNTs [124], forming CNT peapods (Fig. 2.22). Besides C_{60} , gadolinium metallofullerenes (GdC_{82} [125, 126], Gd_2C_{92} [127]) can be encapsulated in single-walled carbon nanotubes too.

Additional, water and metal nanoparticles can also be encapsulated in CNTs, like tin nanowires encapsulated in amorphous carbon nanotubes [128], gallium in CNTs [129], liquids in CNTs [130, 131]. CNTs have also been applied to encapsulate

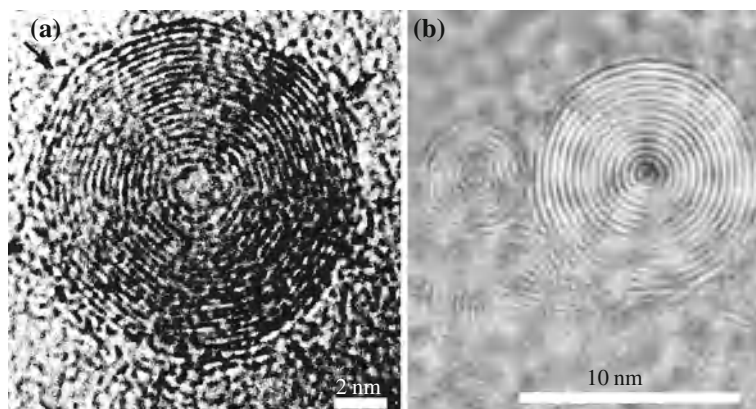


Fig. 2.23 HRTEM images of carbon nano-onions. **a** Produced by vacuum deposition. From Iijima [141]. **b** Produced by arc discharge in water. From Sano et al. [142]

other materials, such as metals, carbides, oxides, gases, etc. Various of CNT peapods and related physical properties are summarized in some books [57, 132] and review literatures [133, 134].

The temperature-dependent thermal conductivity of the CNT peapod shows a qualitatively similar behavior to that of an unfilled carbon nanotube while is higher than that of the nanotube at all temperatures [135].

Carbon Nanofiber. Carbon fibers have been industrially synthesized by pyrolysis of natural gas [136] and vapor method [137] and applied in plastics, concretes, ceramics, metal carbides to reinforce the mechanical properties of composite [137]. Now carbon nanofibers have been synthesized by PECVD method [138]. Compared with CNTs, the carbon nanofibers are solid, not hollow. The interested readers on physical properties and applications of carbon fibers are referred to some books [1, 2] and some review papers on vertically aligned carbon nanofibers [139, 140].

Carbon Nano-onion. Carbon nano-onion was found in arc-discharged carbon root (Fig. 2.23a) in 1980 [141] by Iijima before C_{60} fullerene was discovered in 1985. Later such carbon nano-onions were produced in water (Fig. 2.23b). Carbon nano-onions can also be produced in vacuum under the irradiation of nanotubes and nanoparticles [143, 144]. The average diameter of the nano-onions is several ten nanometers. Discovery history, microscale structures, physical properties, and growth mechanism of the carbon nano-onions are reviewed in books [57].

Other Carbon Nanomaterials. Besides above carbon nanostructures, other interesting carbon nanostructures are also reported, such as carbon nano-cones with conical structures [145, 146] and fullerene nanohorns [147].

2.3 Physical Properties of Carbon Nanotubes

The CNTs with length ranging from less than a micron to several millimeters is a kind of hollow cylinder consisted of trigonally bonded carbon atoms in a curved sheet. Their unique nanostructures result in many extraordinary properties such as high tensile strength, high electrical and thermal conductivities, high ductility, high thermal and chemical stability, which make them suitable for various applications. For an overview of the basic physical properties of SWCNTs, we refer the readers to some excellent books and review articles on electronic properties [60, 63, 148–157], on structure properties [60, 63, 151, 153, 158], on optical properties [58, 63, 152, 153, 159–166], on electrical properties [58, 60, 63, 151, 153, 167], on thermal properties [58, 152, 153, 168, 169], on mechanical properties [58, 150, 151, 153, 169, 170], on atomic properties [58, 153], on magnetic properties [60, 150, 171], and on vibrational properties [60, 154, 172–174]. Based on the unique physical properties, individual CNTs have wide applications. The applications of individual CNTs are reviewed in many review papers and books [62, 113, 175–178].

Because of the anisotropic properties of graphite along a -plane and c -plane directions, the physical properties of CNTs are also anisotropic. The diameter of a CNT is several nanometers, while the length may be in millimeters even centimeters [50, 179, 180]. In these cases, the high aspect ratios of individual CNTs can go up to $\sim 10^7$, further enhancing the degree of anisotropy of CNTs. The anisotropic properties and high aspect ratios make the aligned CNTs necessary in many applications. Below we briefly introduce the anisotropic properties of aligned CNTs.

2.3.1 Anisotropic Mechanical Properties

Simple geometrical considerations suggest that CNTs should be much softer in the radial direction than along the tube axis. Experimental Young's modulus of SWCNT ropes is 1,002 GPa [105] along the SWCNT axis (Fig. 2.24). At the same time, TEM observation of radial elasticity suggested that even the van der Waals forces can deform two adjacent CNTs [119]. Nanoindentation experiments performed on MWCNTs indicated that Young's modulus is in the order of several GPa, confirming that CNTs are indeed rather soft in the radial direction [52].

2.3.2 Anisotropic Electrical Properties

The electrical resistivity in the CNT axis direction is much lower than that in the radial direction. Figure 2.25 shows the electrical resistance along and perpendicular to the MWCNT tube axis. When the electrons travel perpendicular to the CNT tube axis, the electrons need to hop from one graphitic layer to another, causing a higher electrical resistivity. For MWCNT arrays, the electrical conductivity is an order of

Fig. 2.24 Eight stress versus strain curves obtained from the tensile-loading experiments on individual SWCNT ropes. From Yu et al. [105]. Copyright (2000), the American Physical Society

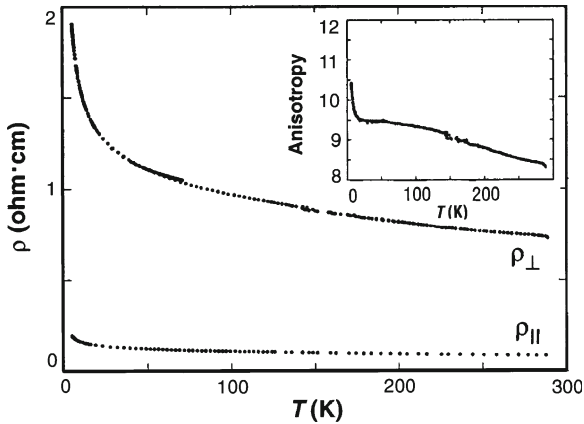
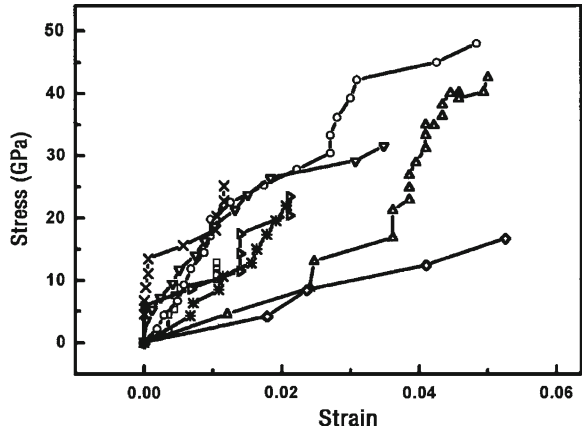


Fig. 2.25 Electrical resistance of a CNT array. *Inset:* resistivity anisotropy $\rho_{\perp}/\rho_{\parallel}$. From de Heer et al. [52]

magnitude lower in the perpendicular direction of CNT arrays. The electrical conductivity is 7–14 S/cm at room temperature along the direction of CNT arrays while about 1 S/cm perpendicular to CNT arrays [181]. SWCNT films also show similar anisotropy [182, 183].

The anisotropic electrical resistance is also observed in SWCNT/epoxy nanocomposites [184].

2.3.3 Anisotropic Thermal Conductivity

All CNTs are expected to be very good thermal conductors along the axis direction, sometimes exhibiting ballistic transports, but are simultaneously good thermal insu-

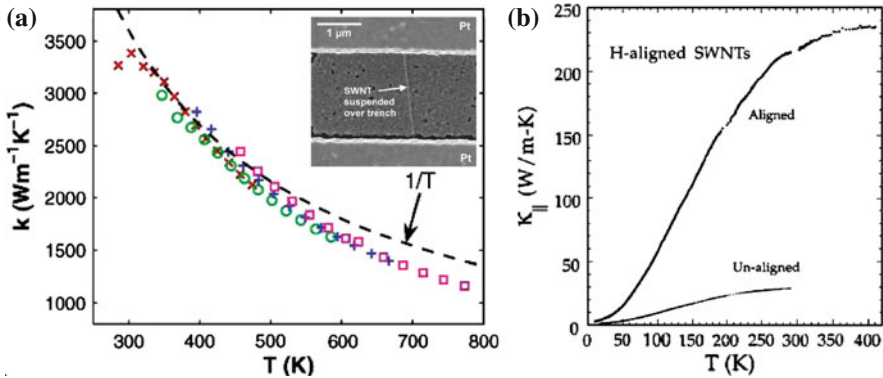


Fig. 2.26 **a** Thermal conductivity of an SWCNT versus temperature. The *dashed line* marks the $1/T$ trend expected due to Umklapp phonon–phonon scattering. *Inset*: SEM image of a typical SWCNT used for thermal conductivity measurement, freely suspending across a trench and lying on top of the Pt contacts. From Pop et al. [185]. Copyright (2006) American Chemical Society. **b** Thermal conductivity of aligned SWCNTs. From Hone et al. [182]. Copyright (2000), American Physical Society

lators perpendicular to the CNT axis. Measurements show that thermal conductivity of SWCNTs is about 3,500 W/mK (Fig. 2.26a) along CNT axis direction, or even to 6,600 W/mK for an isolated (10, 10) SWCNT at room temperature [186]. The value is much higher than that of copper, a metal well known for its good thermal conductivity of 385 W/mK.

Figure 2.26b shows the thermal conductivity of SWCNT films prepared by filtration deposition from suspension in strong magnetic fields. Thermal conductivity exhibits anisotropy with respect to the alignment axis [182]. The alignment of CNTs induces an order of magnitude increase in thermal conductivity when compared with randomly aligned samples.

Thermal conductivity of aligned MWCNTs have been reported in many scientific papers [181, 187–189]. The range for thermal conductivity at 300 K is about 0.5–1.2 W/mK along the MWCNT growth direction, with the shortest CNT array having the highest thermal conductivity, and an order of magnitude lower in the direction perpendicular to the MWCNTs [181]. It is also found that the defects of the CNTs affect the thermal properties.

2.3.4 Anisotropic Thermal Diffusivity

The structure of aligned CNT arrays is expected to induce a large anisotropy of the thermal diffusivity along the directions parallel and perpendicular to the CNT alignment direction. Figure 2.27 shows the anisotropic thermal diffusivity of MWCNT arrays grown by CVD method. The thermal diffusivity of the MWCNT arrays is

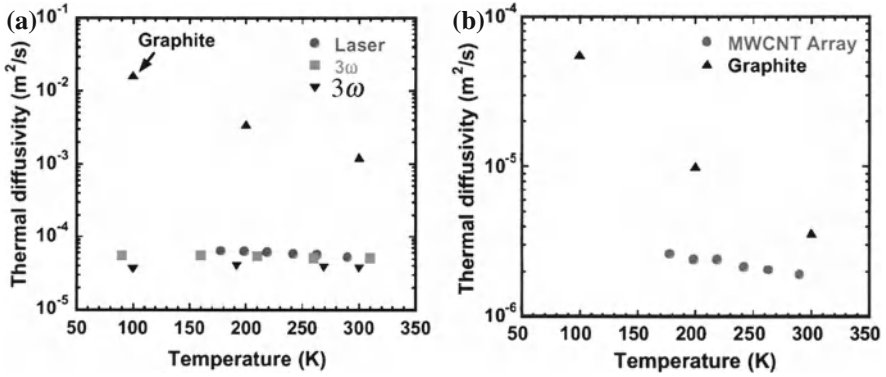


Fig. 2.27 Measured thermal diffusivity **a** along the carbon nanotube alignment direction compared with the thermal diffusivity along the graphite layers and **b** perpendicular to the carbon nanotube alignment direction compared with the thermal diffusivity perpendicular to the graphite layers. \blacktriangledown : from Yi et al. [187]; \blacktriangle : from Borca-Tasciuc et al. [190]

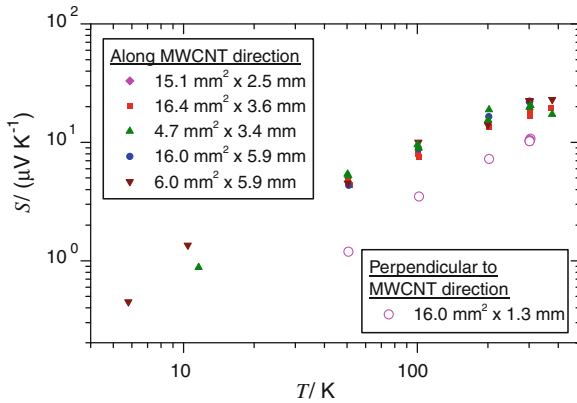


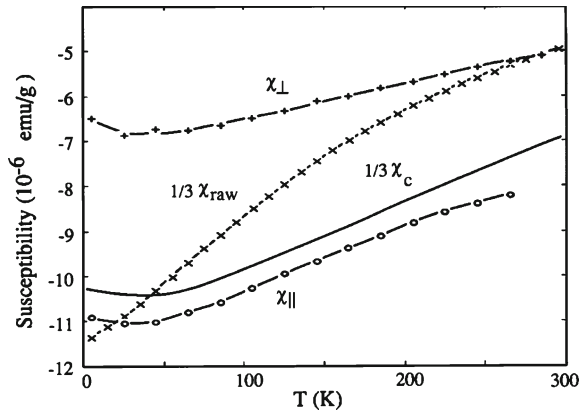
Fig. 2.28 Seebeck coefficient of the MWCNT arrays under vacuum 10^{-4} Torr as a function of temperature. Cross-sectional areas and heights of MWCNT arrays are indicated. From Jakubinek et al. [181]

measured by the photothermoelectric technique (labeled laser in Fig. 2.27a), or determined using the self-heating method (labeled 3ω in Fig. 2.27a).

Figure 2.27a shows the measured thermal diffusivity along the CNT alignment direction compared with the thermal diffusivity along the graphite layers. The measured thermal diffusivity decreases only slightly with temperature and is two orders of magnitude smaller than the thermal diffusivity along the layers of graphite.

Figure 2.27b shows the thermal diffusivity perpendicular to the CNT alignment direction, compared with the thermal diffusivity perpendicular to the graphite layers. The thermal diffusivity across the alignment direction is 25 times smaller than along

Fig. 2.29 Static magnetic susceptibilities of CNTs versus temperature, for field parallel (χ_{\parallel}) and perpendicular (χ_{\perp}) to the CNTs. χ_{raw} , unprocessed CNTs; χ_c , planar graphite. From Chauvet et al. [191]. Copyright (1995), American Physical Society



the alignment direction and is between 50% and five times smaller than the thermal diffusivity across the planes of graphite.

2.3.5 Anisotropic Seebeck Coefficient

Figure 2.28 shows the Seebeck coefficient of MWCNT arrays, parallel (Fig. 2.28a) and perpendicular (Fig. 2.28 b) to the CNT direction. The Seebeck coefficient is $20 \mu\text{V/K}$ at 300 K [181]. At lower temperature, the Seebeck coefficient is higher along the MWCNT direction than perpendicular to the MWCNT direction.

2.3.6 Other Anisotropic Physical Properties

Ellipsometry experiments of aligned MWCNT films indicated that the dielectric function parallel to the CNT axis resembles that of graphite parallel to the graphitic planes, while the dielectric function perpendicular to the CNT axis shows features characteristic of the dielectric function of graphite perpendicular to the graphitic planes [52].

Figure 2.29 shows the anisotropic magnetic susceptibility of CNTs. A calculation using the tight-binding model and the London approximation shows that the magnetic susceptibility χ is a sensitive function of the magnetic field direction θ [192]. Numerically, the θ dependence is well approximated by a function $\chi(\theta) = a + b \cos(2\theta)$. Experiments also show that the magnetic susceptibility of CNT bundles is more diamagnetic when the magnetic field is parallel to the CNT axis than when the field is perpendicular to the CNT axis [193]. The magnetic behavior of CNT bundles is different from that of random CNTs [194].

Besides these anisotropic properties above, anisotropic thermopower is also observed in SWCNT films [182].

References

1. B. Rand, S.P. Appleyard, M.F. Yardim (eds.) *Design and Control of Structure of Advanced Carbon Materials for Enhanced Performance*. NATO Science Series E: applied sciences, vol. 374 (Kluwer Academic Publishers, Dordrecht, 2001)
2. L.P. Biró, C.A. Bernardo, G.G. Tibbetts, P. Lambin (eds.) *Carbon Filaments and Nanotubes: common origins, differing applications?*. NATO Science Series E: applied sciences, vol. 372 (Kluwer Academic Publishers, Dordrecht, 2001)
3. S. Saito, A. Zettl (eds.) *Carbon Nanotubes: quantum cylinders of graphene*. Contemporary Concepts of Condensed Matter Science (Elsevier, Netherlands, 2008)
4. S. Iijima, Helical microtubules of graphitic carbon. *Nature* **354**, 56–58 (1991)
5. T.V. Hughes, C.R. Chambers, Manufacture of carbon filaments, U.S. Patent 000405480, 1889
6. P. Schützenberger, L. Schützenberger, Sur quelques faits relatifs à l'histoire du carbone. *C. R. Acad. Sci. Paris* **111**, 774–778 (1890)
7. C. Pélabon, H. Pélabon, Sur une variété de carbone filamenteux. *C. R. Acad. Sci. Paris* **137**, 706–708 (1903)
8. L.V. Radushkevich, V.M. Lukyanovich, About the carbon structure, thermal CO decomposition on metal contact synthesized. *J. Phys. Chem. Russia* **26**, 88–95 (1952)
9. M. Hillert, N. Lange, The structure of graphite filaments. *Z. Kristallogr.* **111**, 24–34 (1958)
10. A. Oberlin, M. Endo, T. Koyama, Filamentous growth of carbon through benzene decomposition. *J. Cryst. Growth* **32**(3), 335–349 (1976)
11. J. Abrahamson, P.G. Wiles, B.L. Rhoades, Structure of carbon fibers found on carbon arc anodes. in *14th Biennial Conference on Carbon* American Carbon Society, University Park, PA, June 1979
12. J. Abrahamson, P. Wiles, B. Rhoades, Structure of carbon fibers found on carbon arc anodes. *Carbon* **37**(11), 1873–1874 (1999)
13. H.G. Tennent, Carbon fibrils, method for producing same and compositions containing same. U.S. Patent 4663230 (Kennett Square, PA, 1987)
14. G.E. Scuseria, Negative curvature and hyperfullerenes. *Chem. Phys. Lett.* **195**(5–6), 534–536 (1992)
15. J.W. Mintmire, B.I. Dunlap, C.T. White, Are fullerene tubules metallic? *Phys. Rev. Lett.* **68**(5), 631–634 (1992)
16. N. Hamada, S.-I. Sawada, A. Oshiyama, New one-dimensional conductors: graphitic microtubules. *Phys. Rev. Lett.* **68**(10), 1579–1581 (1992)
17. R. Saito, M. Fujita, G. Dresselhaus, M.S. Dresselhaus, Electronic structure of graphene tubules based on C_{60} . *Phys. Rev. B* **46**(3), 1804–1811 (1992)
18. S. Iijima, T. Ichihashi, Single-shell carbon nanotubes of 1-nm diameter. *Nature* **363**(6430), 603–605 (1993)
19. D.S. Bethune, C.H. Klang, M.S. de Vries, G. Gorman, R. Savoy, J. Vazquez, R. Beyers, Cobalt-catalysed growth of carbon nanotubes with single-atomic-layer walls. *Nature* **363**(6430), 605–607 (1993)
20. J.Q. Hu, Y. Bando, F.F. Xu, Y.B. Li, J.H. Zhan, J.Y. Xu, D. Golberg, Growth and field-emission properties of crystalline, thin-walled carbon microtubes. *Adv. Mater.* **16**(2), 153–156 (2004)
21. A.G. Nasibulin, A.S. Anisimov, P.V. Pikhitsa, H. Jiang, D.P. Brown, M. Choi, E.I. Kauppinen, Investigations of nanobud formation. *Chem. Phys. Lett.* **446**(1–3), 109–114 (2007)
22. M. Monthieux, V.L. Kuznetsov, Who should be given the credit for the discovery of carbon nanotubes? *Carbon* **44**(9), 1621–1623 (2006)

23. M. Reibold, P. Paufler, A.A. Levin, W. Kochmann, N. Patzke, D.C. Meyer, Materials: carbon nanotubes in an ancient damascus sabre. *Nature* **444**(7117), 286–286 (2006)
24. A. Oberlin, M. Endo, T. Koyama, High resolution electron microscope observations of graphitized carbon fibers. *Carbon* **14**(2), 133–135 (1976)
25. H. Boehm, Carbon from carbon monoxide disproportionation on nickel and iron catalysts: morphological studies and possible growth mechanisms. *Carbon* **11**(6), 583–586 (1973)
26. H.W. Kroto, J.R. Heath, S.C. O'Brien, R.F. Curl, R.E. Smalley, C₆₀: Buckminsterfullerene. *Nature* **318**, 162–163 (1985)
27. J.A.E. Gibson, Early nanotubes? *Nature* **359**(6394), 369–369 (1992)
28. H.P. Boehm, The first observation of carbon nanotubes. *Carbon* **35**(4), 581–584 (1997)
29. X.H. Chen, C.S. Chen, Q. Chen, F.Q. Cheng, G. Zhang, Z.Z. Chen, Non-destructive purification of multi-walled carbon nanotubes produced by catalyzed CVD. *Mater. Lett.* **57**(3), 734–738 (2002)
30. P. Chaturvedi, P. Verma, A. Singh, P.K. Chaudhary, P.K. Harsh, P.K. Basu, Carbon nanotube—purification and sorting protocols, *Defence Sci. J.* **58**(5), 591–599, 2008
31. K. MacKenzie, O. Dunens, A.T. Harris, A review of carbon nanotube purification by microwave assisted acid digestion. *Sep. Purif. Technol.* **66**(2), 209–222 (2009)
32. S.K. Pillai, S.S. Ray, M. Moodley, Purification of single-walled carbon nanotubes. *J. Nanosci. Nanotechnol.* **7**(9), 3011–3047 (2007)
33. S.K. Pillai, S.S. Ray, M. Moodley, Purification of multi-walled carbon nanotubes. *J. Nanosci. Nanotechnol.* **8**(12), 6187–6207 (2008)
34. X. Song, Y. Fang, A technique of purification process of single-walled carbon nanotubes with air. *Spectrochim. Acta A* **67**(3–4), 1131–1134 (2007)
35. T. Guo, P. Nikolaev, A. Thess, D. Colbert, R. Smalley, Catalytic growth of single-walled nanotubes by laser vaporization. *Chem. Phys. Lett.* **243**(1–2), 49–54 (1995)
36. A. Thess, R. Lee, P. Nikolaev, H. Dai, P. Petit, J. Robert, C. Xu, Y.H. Lee, S.G. Kim, A.G. Rinzler, D.T. Colbert, G.E. Scuseria, D. Tománek, J.E. Fischer, R.E. Smalley, Crystalline ropes of metallic carbon nanotubes. *Science* **273**(5274), 483–487 (1996)
37. J. Li, C. Papadopoulos, J. Xu, Nanoelectronics: growing Y-junction carbon nanotubes. *Nature* **402**(6759), 253–254 (1999)
38. B.C. Satishkumar, P.J. Thomas, A. Govindaraj, C.N.R. Rao, Y junction carbon nanotubes. *Appl. Phys. Lett.* **77**(16), 2530–2532 (2000)
39. W.Z. Li, J.G. Wen, Z.F. Ren, Straight carbon nanotube Y junctions. *Appl. Phys. Lett.* **79**(12), 1879–1881 (2001)
40. A.G. Nasibulin, P.V. Pikhitsa, H. Jiang, D.P. Brown, A.V. Krashennnikov, A.S. Anisimov, P. Queipo, A. Moisala, D. Gonzalez, G. Lientschnig, A. Hassaniien, S.D. Shandakov, G. Lolli, D.E. Resasco, M. Choi, D. Tománek, E.I. Kauppinen, A novel hybrid carbon material. *Nat. Nanotechnol.* **2**(3), 156–161 (2007)
41. L. Liu, G.Y. Guo, C.S. Jayanthi, S.Y. Wu, Colossal paramagnetic moments in metallic carbon nanotubes. *Phys. Rev. Lett.* **88**, 217206 (2002)
42. W.Z. Li, S.S. Xie, L.X. Qian, B.H. Chang, B.S. Zou, W.Y. Zhou, R.A. Zhao, G. Wang, Large-scale synthesis of aligned carbon nanotubes. *Science* **274**(5293), 1701–1703 (1996)
43. M. Terrones, N. Grobert, J. Olivares, J.P. Zhang, H. Terrones, K. Kordatos, W.K. Hsu, J.P. Hare, P.D. Townsend, K. Prassides, A.K. Cheetham, H.W. Kroto, D.R.M. Walton, Controlled production of aligned-nanotube bundles. *Nature* **388**(6637), 52–55 (1997)
44. Z.F. Ren, Z.P. Huang, J.W. Xu, J.H. Wang, P. Bush, M.P. Siegal, P.N. Provencio, Synthesis of large arrays of well-aligned carbon nanotubes on glass. *Science* **282**, 1105–1107 (1998)
45. Z.F. Ren, Z.P. Huang, D.Z. Wang, J.G. Wen, J.W. Xu, J.H. Wang, L.E. Calvet, J. Chen, J.F. Klemic, M.A. Reed, Growth of a single freestanding multiwall carbon nanotube on each nanonickel dot. *Appl. Phys. Lett.* **75**(8), 1086–1088 (1999)
46. Z.P. Huang, D.L. Carnahan, J. Rybczynski, M. Giersig, M. Sennett, D.Z. Wang, J.G. Wen, K. Kempa, Z.F. Ren, Growth of large periodic arrays of carbon nanotubes. *Appl. Phys. Lett.* **82**(3), 460–462 (2003)

47. K. Kempa, B. Kimball, J. Rybczynski, Z.P. Huang, P.F. Wu, D. Steeves, M. Sennett, M. Giersig, D.V.G.L.N. Rao, D.L. Carnahan, D.Z. Wang, J.Y. Lao, W.Z. Li, Z.F. Ren, Photonic crystals based on periodic arrays of aligned carbon nanotubes. *Nano Lett.* **3**(1), 13–18 (2003)
48. S. Fan, M.G. Chapline, N.R. Franklin, T.W. Tomblor, A.M. Cassell, H. Dai, Self-oriented regular arrays of carbon nanotubes and their field emission properties. *Science* **283**(5401), 512–514 (1999)
49. G-Y. Xiong, D. Wang, Z. Ren, Aligned millimeter-long carbon nanotube arrays grown on single crystal magnesia. *Carbon* **44**(5), 969–973 (2006)
50. K. Hata, D.N. Futaba, K. Mizuno, T. Namai, M. Yumura, S. Iijima, Water-assisted highly efficient synthesis of impurity-free single-walled carbon nanotubes. *Science* **306**(5700), 1362–1364 (2004)
51. P.M. Ajayan, O. Stephan, C. Colliex, D. Trauth, Aligned carbon nanotube arrays formed by cutting a polymer resin-nanotube composite. *Science* **265**(5176), 1212–1214 (1994)
52. W.A. de Heer, W.S. Bacsá, A. Châtelain, T. Gerfin, R. Humphrey-Baker, L. Forro, D. Ugarte, Aligned carbon nanotube films: production and optical and electronic properties. *Science* **268**(5212), 845–847 (1995)
53. B.Q. Wei, R. Vajtai, Y. Jung, J. Ward, R. Zhang, G. Ramanath, P.M. Ajayan, Microfabrication technology: organized assembly of carbon nanotubes. *Nature* **416**(6880), 495–496 (2002)
54. S.G. Rao, L. Huang, W. Setyawan, S. Hong, Nanotube electronics: large-scale assembly of carbon nanotubes. *Nature* **425**(6953), 36–37 (2003)
55. M.S. Dresselhaus, G. Dresselhaus, P.C. Eklund, *Science of Fullerenes and Carbon Nanotubes: their properties and applications* (Academic Press, New York, 1996)
56. R. Saito, G. Dresselhaus, M. S. Dresselhaus, *Physical Properties of Carbon Nanotubes* (World Scientific, Singapore, 1998)
57. P.J.F. Harris, *Carbon Nanotubes and Related Structures: new materials for the twenty-first century* (Cambridge University Press, Cambridge, 1999)
58. M.S. Dresselhaus, G. Dresselhaus, P. Avouris (eds.), *Carbon Nanotubes: synthesis, structure, properties, and applications*. Topics in Applied Physics, vol. 80 (Springer, Berlin, 2001)
59. T.W. Ebbesen (ed.), *Carbon Nanotubes: preparation and properties* (Chemical Rubber, Boca Raton, 1997)
60. K. Tanaka, T. Yamabe, K. Fukui (eds.), *The Science and Technology of Carbon Nanotubes* (Elsevier, Amsterdam, 1999)
61. C. Hierold (ed.), *Carbon Nanotube Devices: properties, modeling, integration and applications*. Advanced Micro & Nanosystems, vol. 8 (Wiley-VCH, Weinheim, 2008)
62. M. Meyyappan (ed.), *Carbon Nanotubes: Science and Applications* (CRC Press, Boca Raton, 2004)
63. S. Reich, C. Thomsen, J. Maultzsch, *Carbon Nanotubes: basic concepts and physical properties* (Wiley-VCH, Germany, 2004)
64. M.S. Dresselhaus, G. Dresselhaus, R. Saito, Carbon fibers based on C₆₀ and their symmetry. *Phys. Rev. B* **45**(11), 6234–6242 (1992)
65. P. Delhaés (ed.), *Graphite and Precursors* (Gordon and Breach Science Publishers, New York, 2001)
66. F. Cirkel, C.M. Branch, *Graphite: Its Properties, Occurrence, Refining and Uses* (Nabu Press, North Carolina, 2010)
67. D.V. Kosynkin, A.L. Higginbotham, A. Sinitzskii, J.R. Lomeda, A. Dimiev, B.K. Price, J.M. Tour, Longitudinal unzipping of carbon nanotubes to form graphene nanoribbons. *Nature* **458**, 872–876 (2009)
68. L. Jiao, L. Zhang, X. Wang, G. Diankov, H. Dais, Narrow graphene nanoribbons from carbon nanotubes. *Nature* **458**, 877–880 (2009)
69. M. Terrones, Materials science: nanotubes unzipped. *Nature* **458**, 845–846 (2009)
70. T.W. Odom, J-L. Huang, P. Kim, C.M. Lieber, Atomic structure and electronic properties of single-walled carbon nanotubes. *Nature* **391**(6662), 62–64 (1998)
71. H. Dai, A.G. Rinzler, P. Nikolaev, A. Thess, D.T. Colbert, R.E. Smalley, Single-wall nanotubes produced by metal-catalyzed disproportionation of carbon monoxide. *Chem. Phys. Lett.* **260**(3–4), 471–475 (1996)

72. M. Audier, M. Coulon, Kinetic and microscopic aspects of catalytic carbon growth. *Carbon* **23**(3), 317–323 (1985)
73. C.N.R. Rao, R. Voggu, A. Govindaraj, Selective generation of single-walled carbon nanotubes with metallic, semiconducting and other unique electronic properties. *Nanoscale* **1**(1), 96–105 (2009)
74. C. Kane, L. Balents, M.P.A. Fisher, Coulomb interactions and mesoscopic effects in carbon nanotubes. *Phys. Rev. Lett.* **79**, 5086–5089 (1997)
75. R. Saito, M. Fujita, G. Dresselhaus, M.S. Dresselhaus, Electronic structure of chiral graphene tubules. *Appl. Phys. Lett.* **60**(18), 2204–2206 (1992)
76. J.W.G. Wildöer, L.C. Venema, A.G. Rinzler, R.E. Smalley, C. Dekker, Electronic structure of atomically resolved carbon nanotubes. *Nature* **391**(6662), 59–62 (1998)
77. S. Hong, S. Myung, Nanotube electronics: a flexible approach to mobility. *Nat. Nanotechnol.* **2**, 207–208 (2007)
78. J. Han, in *Carbon Nanotubes: science and applications*, ed. by M. Meyyappan. Structure and Properties of Carbon Nanotubes (CRC Press, Boca Raton, 2004)
79. J.H. Hafner, M.J. Bronikowski, B.R. Azamian, P. Nikolaev, A.G. Rinzler, D.T. Colbert, K.A. Smith, R.E. Smalley, Catalytic growth of single-wall carbon nanotubes from metal particles. *Chem. Phys. Lett.* **296**(1–2), 195–202 (1998)
80. G.Y. Xiong, Y. Suda, D.Z. Wang, J.Y. Huang, Z.F. Ren, Effect of temperature, pressure, and gas ratio of methane to hydrogen on the synthesis of double-walled carbon nanotubes by chemical vapour deposition. *Nanotechnology* **16**(4), 532–535 (2005)
81. O.M. Dunens, K.J. MacKenzie, A.T. Harris, Large-scale synthesis of double-walled carbon nanotubes in fluidized beds. *Ind. Eng. Chem. Res.* **49**(9), 4031–4035 (2010)
82. E. Flahaut, R. Bacsa, A. Peigney, C. Laurent, Gram-scale CCVD synthesis of double-walled carbon nanotubes. *Chem. Commun.* **2003**(12), 1442–1443 (2003)
83. R. Bacon, Growth, structure, and properties of graphite whiskers. *J. Appl. Phys.* **31**(2), 283–290 (1960)
84. H. Cui, X. Yang, M.L. Simpson, D.H. Lowndes, M. Varela, Initial growth of vertically aligned carbon nanofibers. *Appl. Phys. Lett.* **84**(20), 4077–4079 (2004)
85. W. Li, J. Wen, Y. Tu, Z. Ren, Effect of gas pressure on the growth and structure of carbon nanotubes by chemical vapor deposition. *Appl. Phys. A* **73**(2), 259–264 (2001)
86. W. Wang, B. Poudel, D.Z. Wang, Z.F. Ren, Synthesis of multiwalled carbon nanotubes through a modified Wolff-Kishner reduction process. *J. Am. Chem. Soc.* **127**(51), 18018–18019 (2005)
87. W. Li, J. Wen, Z. Ren, Effect of temperature on growth and structure of carbon nanotubes by chemical vapor deposition. *Appl. Phys. A* **74**(3), 397–402 (2002)
88. Y. Ominami, Q. Ngo, A.J. Austin, H. Yoong, C.Y. Yang, A.M. Cassell, B.A. Cruden, J. Li, M. Meyyappan, Structural characteristics of carbon nanofibers for on-chip interconnect applications. *Appl. Phys. Lett.* **87**(23), 233105 (2005)
89. P.L. McEuen, Nanotechnology: carbon-based electronics. *Nature* **393**(6680), 15–17 (1998)
90. R. Saito, G. Dresselhaus, M.S. Dresselhaus, Tunneling conductance of connected carbon nanotubes. *Phys. Rev. B* **53**(4), 2044–2050 (1996)
91. L. Chico, V.H. Crespi, L.X. Benedict, S.G. Louie, M.L. Cohen, Pure carbon nanoscale devices: nanotube heterojunctions. *Phys. Rev. Lett.* **76**(6), 971–974 (1996)
92. Z. Yao, H.W.C. Postma, L. Balents, C. Dekker, Carbon nanotube intramolecular junctions. *Nature* **402**(6759), 273–276 (1999)
93. Y. Yao, Q. Li, J. Zhang, R. Liu, L. Jiao, Y.T. Zhu, Z. Liu, Temperature-mediated growth of single-walled carbon-nanotube intramolecular junctions. *Nat. Mater.* **6**(4), 283–286 (2007)
94. M.S. Fuhrer, J. Nygård, L. Shih, M. Forero, Y.-G. Yoon, M.S.C. Mazzoni, H.J. Choi, J. Ihm, S.G. Louie, A. Zettl, P.L. McEuen, Crossed nanotube junctions. *Science* **288**(5465), 494–497 (2000)
95. P.R. Bandaru, Electrical characterization of carbon nanotube Y-junctions: a foundation for new nanoelectronics. *J. Mater. Sci.* **42**(5), 1809–1818 (2007)
96. P. Nagy, R. Ehlich, L. Biró, J. Gyulai, Y-branching of single walled carbon nanotubes. *Appl. Phys. A* **70**(4), 481–483 (2000)

97. S. Itoh, S. Ihara, J.-I. Kitakami, Toroidal form of carbon C₃₆₀. *Phys. Rev. B* **47**(3), 1703–1704 (1993)
98. S. Ihara, S. Itoh, J.-I. Kitakami, Toroidal forms of graphitic carbon. *Phys. Rev. B* **47**, 12908–12911 (1993)
99. B.I. Dunlap, Connecting carbon tubules. *Phys. Rev. B* **46**(3), 1933–1936 (1992)
100. B.I. Dunlap, Relating carbon tubules. *Phys. Rev. B* **49**(8), 5643–5651 (1994)
101. A. Fonseca, K. Hernadi, J. Nagy, P. Lambin, A. Lucas, Growth mechanism of coiled carbon nanotubes. *Synth. Met.* **77**(1–3), 235–242 (1996)
102. M. Sano, A. Kamino, J. Okamura, S. Shinkai, Ring closure of carbon nanotubes. *Science* **293**(5533), 1299–1301 (2001)
103. J. Liu, H. Dai, J.H. Hafner, D.T. Colbert, R.E. Smalley, S.J. Tans, C. Dekker, Fullerene ‘crop circles’. *Nature* **385**, 780–781 (1997)
104. R. Martel, H.R. Shea, P. Avouris, Rings of single-walled carbon nanotubes. *Nature* **398**, 299 (1999)
105. M-F. Yu, B.S. Files, S. Arepalli, R.S. Ruoff, Tensile loading of ropes of single wall carbon nanotubes and their mechanical properties. *Phys. Rev. Lett.* **84**(24), 5552–5555 (2000)
106. H.R. Shea, R. Martel, P. Avouris, Electrical transport in rings of single-wall nanotubes: one-dimensional localization. *Phys. Rev. Lett.* **84**(19), 4441–4444 (2000)
107. L. Ci, B. Wei, C. Xu, J. Liang, D. Wu, S. Xie, W. Zhou, Y. Li, Z. Liu, D. Tang, Crystallization behavior of the amorphous carbon nanotubes prepared by the CVD method. *J. Cryst. Growth* **233**, 823–828 (2001)
108. H. Nishino, R. Nishida, T. Matsui, N. Kawase, I. Mochida, Growth of amorphous carbon nanotube from poly(tetrafluoroethylene) and ferrous chloride. *Carbon* **41**(14), 2819–2823 (2003)
109. T. Luo, L. Chen, K. Bao, W. Yu, Y. Qian, Solvothermal preparation of amorphous carbon nanotubes and Fe/C coaxial nanocables from sulfur, ferrocene, and benzene. *Carbon* **44**(13), 2844–2848 (2006)
110. J. Li, C. Papadopoulos, J.M. Xu, M. Moskovits, Highly-ordered carbon nanotube arrays for electronics applications. *Appl. Phys. Lett.* **75**(3), 367–369 (1999)
111. Y.F. Hu, X.L. Liang, Q. Chen, L.-M. Peng, Z.D. Hu, Electrical characteristics of amorphous carbon nanotube and effects of contacts. *Appl. Phys. Lett.* **88**(6), 063113 (2006)
112. W.Y. Jang, N.N. Kulkarni, C.K. Shih, Z. Yao, Electrical characterization of individual carbon nanotubes grown in nanoporous anodic alumina templates. *Appl. Phys. Lett.* **84**(7), 1177–1179 (2004)
113. M. Terrones, Science and technology of the twenty-first century: synthesis, properties, and applications of carbon nanotubes. *Annu. Rev. Mater. Res.* **33**, 419–501 (2003)
114. N. Grobert, M. Terrones, S. Trasobares, K. Kordatos, H. Terrones, J. Olivares, J. Zhang, P. Redlich, W. Hsu, C. Reeves, D. Wallis, Y. Zhu, J. Hare, A. Pidduck, H. Kroto, D. Walton, A novel route to aligned nanotubes and nanofibres using laser-patterned catalytic substrates. *Appl. Phys. A: Mater.* **70**(2), 175–183 (2000)
115. S. Amelinckx, X.B. Zhang, D. Bernaerts, X.F. Zhang, V. Ivanov, J.B. Nagy, A formation mechanism for catalytically grown helix-shaped graphite nanotubes. *Science* **265**(5172), 635–639 (1994)
116. H. Hou, Z. Jun, F. Weller, A. Greiner, Large-scale synthesis and characterization of helically coiled carbon nanotubes by use of Fe(CO)₅ as floating catalyst precursor. *Chem. Mater.* **15**(16), 3170–3175 (2003)
117. K. Lau, C. Gu, D. Hui, A critical review on nanotube and nanotube/nanoclay related polymer composite materials. *Compos. Part B Eng.* **37**(6), 425–36 (2006)
118. M.J. Hanus, A.T. Harris, Synthesis, characterisation and applications of coiled carbon nanotubes. *J. Nanosci. Nanotechnol.* **10**(4), 2261–2283 (2010)
119. R.S. Ruoff, J. Tersoff, D.C. Lorents, S. Subramoney, B. Chan, Radial deformation of carbon nanotubes by van der Waals forces. *Nature* **364**, 514–516 (1993)
120. N.G. Chopra, L.X. Benedict, V.H. Crespi, M.L. Cohen, S.G. Louie, A. Zettl, Fully collapsed carbon nanotubes. *Nature* **377**(6545), 135–138 (1995)

121. L.X. Benedict, N.G. Chopra, M.L. Cohen, A. Zettl, S.G. Louie, V.H. Crespi, Microscopic determination of the interlayer binding energy in graphite. *Chem. Phys. Lett.* **286**(5–6), 490–496 (1998)
122. S. Liu, J. Yue, R.J. Wehmschulte, Large thick flattened carbon nanotubes. *Nano Lett.* **2**(12), 1439–1442 (2002)
123. W.Z. Li, X. Yan, K. Kempa, Z.F. Ren, M. Giersig, Structure of flattened carbon nanotubes. *Carbon* **45**(15), 2938–2945 (2007)
124. B.W. Smith, M. Monthioux, D.E. Luzzi, Encapsulated C₆₀ in carbon nanotubes. *Nature* **396**(6709), 323–324 (1998)
125. K. Hirahara, K. Suenaga, S. Bandow, H. Kato, T. Okazaki, H. Shinohara, S. Iijima, One-dimensional metallofullerene crystal generated inside single-walled carbon nanotubes. *Phys. Rev. Lett.* **85**(25), 5384–5387 (2000)
126. K. Suenaga, M. Tencé, C. Mory, C. Colliex, H. Kato, T. Okazaki, H. Shinohara, K. Hirahara, S. Bandow, S. Iijima, Element-selective single atom imaging. *Science* **290**(5500), 2280–2282 (2000)
127. K. Suenaga, R. Taniguchi, T. Shimada, T. Okazaki, H. Shinohara, S. Iijima, Evidence for the intramolecular motion of Gd atoms in a Gd₂C₉₂ nanopeapod. *Nano Lett.* **3**(10), 1395–1398 (2003)
128. R. Li, X. Sun, X. Zhou, M. Cai, X. Sun, Aligned heterostructures of single-crystalline tin nanowires encapsulated in amorphous carbon nanotubes. *J. Phys. Chem. C* **111**(26), 9130–9135 (2007)
129. Y. Gao, Y. Bando, Carbon nanothermometer containing gallium. *Nature* **415**, 599 (2002)
130. Y. Gogotsi, J.A. Libera, M. Yoshimura, Hydrothermal synthesis of multiwall carbon nanotubes. *J. Mater. Res.* **15**(12), 2591–2594 (2000)
131. D. Mattia, Y. Gogotsi, Review: static and dynamic behavior of liquids inside carbon nanotubes. *Microfluid. Nanofluid.* **5**(3), 289–305 (2008)
132. S.B. Chikkannanavar, B.W. Smith, D.E. Luzzi, in *Carbon Nanotubes Properties and Applications*, ed. by M.J.O’Connell. Carbon Nanotube Peapod Materials (CRC Press, Taylor & Francis, Boca Raton, 2006)
133. R. Kitaura, H. Shinohara, Carbon-nanotube-based hybrid materials: nanopeapods. *Chem. Asian J.* **1**(5), 646–655 (2006)
134. M. Monthioux, Filling single-wall carbon nanotubes. *Carbon* **40**(10), 1809–1823 (2002)
135. E. González Noya, D. Srivastava, L.A. Chernozatonskii, M. Menon, Thermal conductivity of carbon nanotube peapods. *Phys. Rev. B* **70**(11), 115416 (2004)
136. G.G. Tibbetts, Carbon fibers produced by pyrolysis of natural gas in stainless steel tubes. *Appl. Phys. Lett.* **42**(8), 666–668 (1983)
137. M. Inagaki, *New Carbon: control of structure and functions*. (Elsevier Science, Amsterdam, 2000)
138. S. Hofmann, C. Ducati, J. Robertson, B. Kleinsorge, Low-temperature growth of carbon nanotubes by plasma-enhanced chemical vapor deposition. *Appl. Phys. Lett.* **83**(1), 135–137 (2003)
139. A.V. Melechko, V.I. Merkulov, T.E. McKnight, M.A. Guillorn, K.L. Klein, D.H. Lowndes, M.L. Simpson, Vertically aligned carbon nanofibers and related structures: controlled synthesis and directed assembly. *J. Appl. Phys.* **97**(4), 041301/1–041301/39 (2005)
140. M. Tanemura, T. Okita, J. Tanaka, M. Kitazawa, K. Itoh, L. Miao, S. Tanemura, S.P. Lau, H.Y. Yang, L. Huang, Room-temperature growth and applications of carbon nanofibers: a review. *IEEE Trans. Nanotechnol.* **5**(5), 587–594 (2006)
141. S. Iijima, Direct observation of the tetrahedral bonding in graphitized carbon black by high resolution electron microscopy. *J. Cryst. Growth* **50**(3), 675–683 (1980)
142. N. Sano, H. Wang, M. Chhowalla, I. Alexandrou, G.A.J. Amaratunga, Synthesis of carbon ‘onions’ in water. *Nature* **414**, 506–507 (2001)
143. D. Ugarte, Curling and closure of graphitic networks under electron-beam irradiation. *Nature* **359**, 707 (1992)

144. D. Ugarte, Formation mechanism of quasi-spherical carbon particles induced by electron bombardment. *Chem. Phys. Lett.* **207**, 473 (1993)
145. M. Ge, K. Dattler, Observation of fullerene cones. *Chem. Phys. Lett.* **220**, 192 (1994)
146. A. Krishman, E. Dujardin, M.M.J. Treacy, J. Jigdahl, S. Lynum, T.W. Ebbesen, Graphitic cones and the nucleation of curved carbon surfaces. *Nature* **388**, 451 (1997)
147. S. Iijima, M. Yudasaka, R. Yamada, S. Bandow, K. Suenaga, F. Kokai, K. Takahashi, Nano-aggregates of single-walled graphitic carbon nano-horns. *Chem. Phys. Lett.* **309**(3–4), 165–170 (1999)
148. S.G. Louie, in *Carbon Nanotubes: synthesis, structure, properties, and applications*, ed. by M.S. Dresselhaus, G. Dresselhaus, P. Avouris. Electronic Properties, Junctions, and Defects of Carbon Nanotubes, Topics in Applied Physics, vol. 80 (Springer, Berlin, 2001) pp. 113–146
149. Z. Yao, C. Dekker, P. Avouris, in *Carbon Nanotubes: synthesis, structure, properties, and applications*, ed. by M.S. Dresselhaus, G. Dresselhaus, P. Avouris. Electronic Transport Through Single-Wall Carbon Nanotubes, Topics in Applied Physics, vol. 80 (Springer, Berlin, 2001) pp. 147–172
150. L. Forró, C. Schönenberger, in *Carbon Nanotubes: synthesis, structure, properties, and applications*, ed. by M.S. Dresselhaus, G. Dresselhaus, P. Avouris. Physical Properties of Multi-Wall Nanotubes, Topics in Applied Physics, vol. 80 (Springer, Berlin, 2001) pp. 329–390
151. J. Bernholc, D. Brenner, M.B. Nardelli, V. Meunier, C. Roland, Mechanical and electrical properties of nanotubes. *Annu. Rev. Mater. Res.* **32**, 347–375 (2002)
152. V.N. Popov, Carbon nanotubes: properties and application. *Mat. Sci. Eng. R Rep.* **43**(3), 61–102 (2004)
153. M. Dresselhaus, G. Dresselhaus, A. Jorio, Unusual properties and structure of carbon nanotubes. *Annu. Rev. Mater. Res.* **34**(1), 247–278 (2004)
154. M. Burghard, Electronic and vibrational properties of chemically modified single-wall carbon nanotubes. *Surf. Sci. Rep.* **58**(1–4), 1–109 (2005)
155. P. Avouris, J. Chen, Nanotube electronics and optoelectronics. *Mater. Today* **9**, 46–54 (2006)
156. P. Avouris, Z.H. Chen, V. Perebeinos, Carbon-based electronics. *Nat. Nanotechnol.* **2**, 605–615 (2007)
157. P. Avouris, M. Freitag, V. Perebeinos, Carbon-nanotube photonics and optoelectronics. *Nat. Photonics* **2**(6), 341–350 (2008)
158. C.N.R. Rao, B.C. Satishkumar, A. Govindaraj, M. Nath, Nanotubes. *Chem. Phys. Chem.* **2**, 78–105 (2001)
159. M.S. Dresselhaus, P.C. Eklund, Phonons in carbon nanotubes. *Adv. Phys.* **49**(6), 705–814 (2000)
160. R. Saito, H. Kataura, in *Carbon Nanotubes: synthesis, structure, properties, and applications*, ed. by M.S. Dresselhaus, G. Dresselhaus, P. Avouris. Optical Properties and Raman Spectroscopy of Carbon Nanotubes, Topics in Applied Physics, vol. 80 (Springer, Berlin, 2001) pp. 213–246
161. H. Dai, Carbon nanotubes: opportunities and challenges. *Surf. Sci.* **500**(1–3), 218–241 (2002)
162. M. Dresselhaus, G. Dresselhaus, R. Saito, A. Jorio, Raman spectroscopy of carbon nanotubes. *Phys. Rep.* **409**(2), 47–99 (2005)
163. J.J. Zhao, X.S. Chen, J.R.H. Xie, Optical properties and photonic devices of doped carbon nanotubes. *Anal. Chim. Acta* **568**(1–2), 161–170 (2006)
164. M.S. Dresselhaus, G. Dresselhaus, R. Saito, A. Jorio, Exciton photophysics of carbon nanotubes. *Annu. Rev. Phys. Chem.* **58**, 719–747 (2007)
165. M.S. Dresselhaus, A. Jorio, M. Hofmann, G. Dresselhaus, R. Saito, Perspectives on carbon nanotubes and graphene raman spectroscopy. *Nano Lett.* **10**(3), 751–758 (2010)
166. R. Saito, M. Hofmann, G. Dresselhaus, A. Jorio, M.S. Dresselhaus, Raman spectroscopy of graphene and carbon nanotubes. *Adv. Phys.* **60**(3), 413–550 (2011)
167. M. Biercuk, S. Ilani, C. Marcus, P. McEuen, in *Carbon Nanotubes: advanced topics in the synthesis, structure, properties and applications*, ed. by A. Jorio, G. Dresselhaus, M.S. Dresselhaus. Electrical Transport in Single-Wall-Carbon-Nanotubes, Topics in Applied Physics, vol. 111 (Springer, Heidelberg, 2008) pp. 455–493

168. J. Hone, in *Carbon Nanotubes: synthesis, structure, properties, and applications*, ed by M.S. Dresselhaus, G. Dresselhaus, P. Avouris. Phonons and Thermal Properties of Carbon Nanotubes, Topics in Applied Physics, vol. 80 (Springer, Berlin, 2001) pp. 273–286
169. Y. Lan, Y. Wang, Z.F. Ren, Physics and applications of aligned carbon nanotubes. *Adv. Phys.* **60**(4), 553–678 (2011)
170. B.I. Yakobson, P. Avouris, in *Carbon Nanotubes: synthesis, structure, properties, and applications*, ed by M.S. Dresselhaus, G. Dresselhaus, P. Avouris. Mechanical Properties of Carbon Nanotubes, Topics in Applied Physics, vol. 80 (Springer, Berlin, 2001) pp. 287–328
171. J. Kono, S. Roche, in *Carbon Nanotubes Properties and Applications*, ed by M.J. O’Connell. Magnetic Properties (CRC Press/Taylor & Francis, Boca Raton/FL, 2006) pp. 119–152
172. S.K. Doorn, D. Heller, M. Usrey, P. Barone, M.S. Strano, in *Carbon Nanotubes Properties and Applications*, ed by M.J. O’Connell. Raman Spectroscopy of Single-Walled Carbon Nanotubes: probing electronic and chemical behavior (CRC Press/Taylor & Francis, Boca Raton/FL, 2006) pp. 153–186
173. R.F. Gibson, E.O. Ayorinde, Y.F. Wen, Vibrations of carbon nanotubes and their composites: a review. *Compos. Sci. Technol.* **67**(1), 1–28 (2007)
174. S. Kilina, S. Tretiak, Excitonic and vibrational properties of single-walled semiconducting carbon nanotubes. *Adv. Funct. Mater.* **17**(17), 3405–3420 (2007)
175. M. Daenen, R.D. de Fouw, B. Hamers, P.G.A. Janssen, K. Schouteden, M.A.J. Veld, The wondrous world of carbon nanotubes: a review of current carbon nanotube technologies. Technical report, Eindhoven University of Technology, 2003
176. P. Bernier, D. Carroll, G. Kim, S. Roth (eds.), *Nanotube-Based Devices*, Materials Research Society Symposium Proceedings. Materials Research Society, vol. 772 (2003)
177. C.P. Collier, in *Carbon Nanotubes Properties and Applications*, ed by M.J. O’Connell. Carbon Nanotube Tips for Scanning Probe Microscopy, (CRC Press/Taylor & Francis, Boca Raton/FL, 2006) pp. 295–309
178. P.R. Bandaru, Electrical properties and applications of carbon nanotube structures. *J. Nanosci. Nanotechnol.* **7**(4–5), 1239–1267 (2007)
179. H.W. Zhu, C.L. Xu, D.H. Wu, B.Q. Wei, R. Vajtai, P.M. Ajayan, Direct synthesis of long single-walled carbon nanotube strands. *Science* **296**(5569), 884–886 (2002)
180. Z.W. Pan, S.S. Xie, B.H. Chang, C.Y. Wang, L. Lu, W. Liu, W.Y. Zhou, W.Z. Li, L.X. Qian, Very long carbon nanotubes. *Nature* **394**(6694), 631–632 (1998)
181. M.B. Jakubinek, M.A. White, G. Li, C. Jayasinghe, W. Cho, M.J. Schulz, V. Shanov, Thermal and electrical conductivity of tall, vertically aligned carbon nanotube arrays. *Carbon* **48**(13), 3947–3952 (2010)
182. J. Hone, M.C. Llaguno, N.M. Nemes, A.T. Johnson, J.E. Fischer, D.A. Walters, M.J. Casavant, J. Schmidt, R.E. Smalley, Electrical and thermal transport properties of magnetically aligned single wall carbon nanotube films. *Appl. Phys. Lett.* **77**(5), 666–668 (2000)
183. J.E. Fischer, W. Zhou, J. Vavro, M.C. Llaguno, C. Guthy, R. Haggemueller, M.J. Casavant, D.E. Walters, R.E. Smalley, Magnetically aligned single wall carbon nanotube films: preferred orientation and anisotropic transport properties. *J. Appl. Phys.* **93**(4), 2157–2163 (2003)
184. Q. Wang, J. Dai, W. Li, Z. Wei, J. Jiang, The effects of CNT alignment on electrical conductivity and mechanical properties of SWNT/epoxy nanocomposites. *Compos. Sci. Technol.* **68**(7–8), 1644–1648 (2008)
185. E. Pop, D. Mann, Q. Wang, K. Goodson, H. Dai, Thermal conductance of an individual single-wall carbon nanotube above room temperature. *Nano Lett.* **6**(1), 96–100 (2006)
186. S. Berber, Y.-K. Kwon, D. Tománek, Unusually high thermal conductivity of carbon nanotubes. *Phys. Rev. Lett.* **84**(20), 4613–4616 (2000)
187. W. Yi, L. Lu, D.-I. Zhang, Z. W. Pan, S. S. Xie, Linear specific heat of carbon nanotubes. *Phys. Rev. B* **59**(14), R9015–R9018 (1999)
188. D.J. Yang, Q. Zhang, G. Chen, S.F. Yoon, J. Ahn, S.G. Wang, Q. Zhou, Q. Wang, J.Q. Li, Thermal conductivity of multiwalled carbon nanotubes. *Phys. Rev. B* **66**(16), 165440 (2002)
189. X. Wang, Z. Zhong, J. Xu, Noncontact thermal characterization of multiwall carbon nanotubes. *J. Appl. Phys.* **97**(6), 064302 (2005)

190. T. Borca-Tasciuc, S. Vafaei, D.-A. Borca-Tasciuc, B.Q. Wei, R. Vajtai, P.M. Ajayan, Anisotropic thermal diffusivity of aligned multiwall carbon nanotube arrays. *J. Appl. Phys.* **98**(5), 054309 (2005)
191. O. Chauvet, L. Forro, W. Bacsa, D. Ugarte, B. Doudin, W.A. de Heer, Magnetic anisotropies of aligned carbon nanotubes. *Phys. Rev. B* **52**, R6963 (1995)
192. J.P. Lu, Novel magnetic properties of carbon nanotubes. *Phys. Rev. Lett.* **74**(7), 1123–1126 (1995)
193. X.K. Wang, R.P.H. Chang, A. Patashinski, J.B. Ketterson, Magnetic susceptibility of buckytubes. *J. Mater. Res.* **9**(6), 1578–1582 (1994)
194. A.P. Ramirez, R.C. Haddon, O. Zhou, R.M. Fleming, J. Zhang, S.M. McClure, R.E. Smalley, Magnetic susceptibility of molecular carbon: Nanotubes and fullerite. *Science* **265**(5168), 84–86 (1994)

Chapter 3

Growth Techniques of Carbon Nanotubes

CNTs have been synthesized by arc discharge, laser ablation, chemical vapor deposition (CVD), and flame method, etc. Most of these processes take place in vacuum or with process gases. CNTs have been produced in massive quantities, making them available to industrial-scale applications. Table 3.1 lists some synthesis methods. Below we will briefly discuss these techniques.

3.1 Arc Discharge

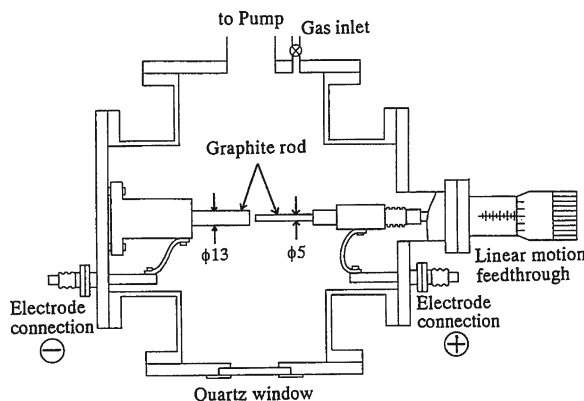
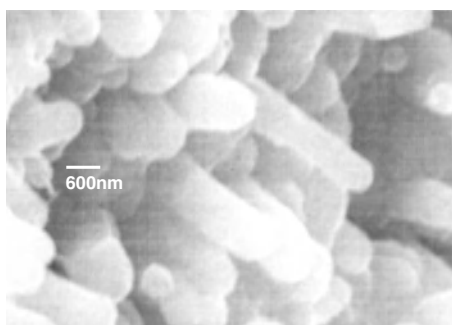
Figure 3.1 shows a growth setup of arc discharge [1]. The arc-discharge is produced under high current [2]. The arc-discharge technique was first established to synthesize carbon nano-onions in 1980 [3] and Buckminsterfullerenes in 1985 [4]. During this process, the carbon contained in the negative electrode sublimates because of the high discharge temperature (above 1,200 °C). In 1991, Iijima used the method [5] to synthesize MWCNTs in the carbon soot of graphite electrodes using a current of 100 A. Bulk quantities of MWCNTs can be produced by this method under suitable arc-evaporation conditions [6]. After adding catalysts, SWCNTs were also produced [7, 8] and sometimes even in large quantities [9].

The method has been most widely used for CNT synthesis because of the simple setup. The yield is up to 30 % by weight and both SWCNTs and MWCNTs of lengths up to 50 μm can be produced. Industrially, the CNTs are usually separated from the amorphous carbon by-products through purification processes found in some review literatures [10–14] for SWCNTs [11, 15] and MWCNTs [12]. The diameter and the length of the CNTs are hard to control because of the temperature nonuniformity and pressure instability issues [16]. The CNTs synthesized by arc discharge have very few structural defects and are quite straight. The method is reviewed in some books and literatures [13, 17, 18].

Although the yield is low and the purification procedure is complex, the produced CNTs have good crystallinity and very few defects. So the method is still widely used

Table 3.1 Synthesis methods of CNTs

Method	Reaction Temperature (°C)	CNT Length (μm)	CNT Growth Rate (μm/s)	CNT Yield	CNT Quality	CNT Purity
Arc discharge	4,000	1	Up to 10 ⁷	Low	High	Low
Laser ablation	RT–1,000	1	0.1	Low	High	Med
Flame	500–1,200	1–10	10–100	Low	High	Med
Thermal CVD	500–1,200	0.1–10 ⁵	0.1–10	High	Med	Med-high
PECVD	100–800	0.1–10	0.01–1	Low	Low–med	Med

**Fig. 3.1** Setup of an arc-discharge technique. Reproduced from Saito and Inagaki [1]**Fig. 3.2** SEM image of aligned CNTs prepared by arc-discharge method. From Ahmad et al. [19]

today. Large-scale production of single-walled carbon nanotubes can be produced by the electric arc-discharge technique [9].

Usually, the arc-discharge produced CNTs are random. Recently, it was reported that self-aligned CNTs were synthesized [19] in the soot deposited at the carbon cathode by a DC arc discharge method using copper catalysts (Fig. 3.2). The average diameter of these aligned CNTs is about 400–600 nm. These nanotubes are closed from the ends with half of the fullerene.

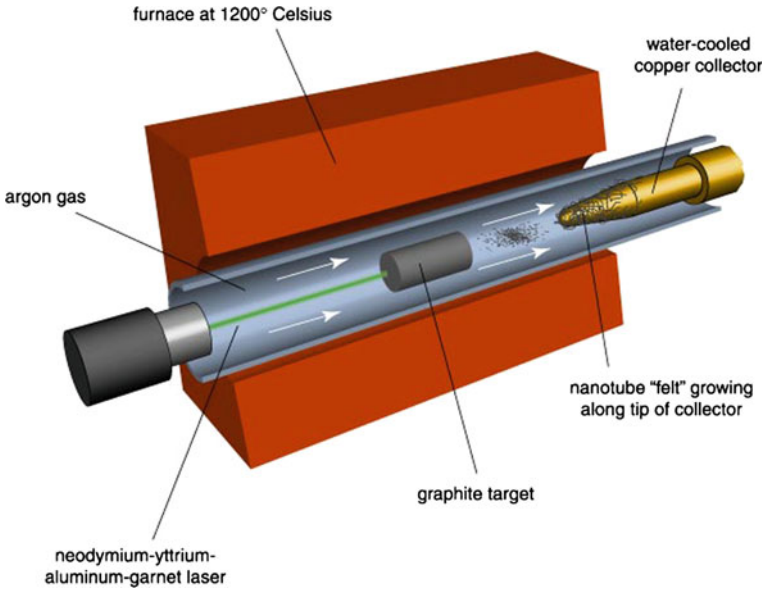


Fig. 3.3 Laser ablation equipment to produce CNTs. From Yakobson and Smalley [23]. Copyright (1997) American Scientist

Under certain experimental setups, uniform arrays of multi-walled CNTs can also be grown from a hydrogen–methane gas mixture activated by a DC discharge without catalyst [20]. It is proposed that the hydrogen plasma induces the formation of nanopores in silicon substrate. The inner pore surface serves as a mask during multi-walled nanotube growth, playing an important role in the formation of aligned nanotubes.

The arc-discharge method is summarized in many books [2, 13, 21] and review literatures [18]. The CNT growth mechanism of arc-discharge is also reviewed [22]. The interested readers are referred to these references for further reading.

3.2 Laser Ablation

Laser ablation is a process of removing materials from a solid surface by irradiating the surface with a laser beam. At low laser flux, the solid material is heated by the absorbed laser energy to evaporate or sublimate.

Laser ablation was developed in 1995 to produce CNTs [24, 25]. Figure 3.3 illustrates the growth setup of laser ablation. In a typical laser ablation process for CNT growth, a graphite block is placed inside an oven and irradiated by a pulsed laser, and Ar gas is pumped along the direction of the laser point. The oven temperature is set approximately to 1,200°C. As the laser ablates the target, carbon is

vaporized and carried by the flowing gas onto a cool copper collector. CNTs grow on the cooler surfaces of the reactor as the vaporized carbon condenses. Sometimes, a water-cooled surface may be included in the system to collect the CNTs. SWCNTs are formed from a composite block of graphite and metal catalyst particles [24], whereas MWCNTs form from pure graphite as the starting material [25].

It is proposed that the laser heats and vaporizes the target surface containing graphite and catalytic metal (nickel and cobalt). As the vaporized species cool, small carbon molecules and atoms quickly condense to form larger clusters, including possibly fullerenes. The catalysts also begin to condense, but more slowly at first and attach to carbon clusters preventing their closing into cage structures. From these initial clusters, tubular molecules grow into SWCNTs until the catalyst particles become too large, or until conditions have cooled sufficiently down so that carbon can no longer diffuse through or on the catalyst particles. It is also possible that the particles become completely coated with a carbon layer such that no more carbon atoms can be absorbed and therefore nanotube growth ceases.

The growth mechanism of CNT in laser ablation process was experimentally examined by spectral emission and fluorescence measurement [26]. The interested readers are referred to some books on CNT growth by laser ablation method [21] and review literatures [22] for further reading.

The laser ablation method yields around 70–90 wt% MWCNTs in the growth product [27]. Compared to arc discharge, the diameter of the laser-ablation produced CNTs can be better controlled by the reaction temperature. However, laser ablation is more expensive than either arc discharge or CVD due to the need for high-power lasers.

Ordered CNT bundles can also be synthesized using this method. Figure 2.3 shows a SWCNT ropes. SWCNTs compact in a hexagonal structure in the rope.

Besides laser heating, other heating methods can also be employed, such as using an electron beam to evaporate graphite blocks in high vacuum to grow CNTs [28] or to evaporate ultrathin graphite foils in ultrahigh vacuum [29].

3.3 Chemical Vapor Deposition

Chemical vapor deposition (CVD) is a chemical process used to produce high-purity, high-performance solid materials. The process is often used in the semiconductor industry to produce thin films. The advantages of CVD are easy setup and operation, and easy scale-up at low cost. Therefore, the CVD method has been widely used, and considerable progress has been made in the past decades.

The catalytic vapor-phase deposition of carbon was first reported in 1959 using carbon monoxide–hydrogen mixtures over Fe [31]. In 1993, CNTs were synthesized by this process from acetylene over Fe particles at 700 °C [32]. Large-scale aligned CNTs were synthesized by thermal CVD catalyzed by iron nanoparticles embedded in mesoporous silica [30]. The aligned nanotubes are approximately perpendicular to the surface of the silica and form an aligned array of isolated tubes with inter-tube

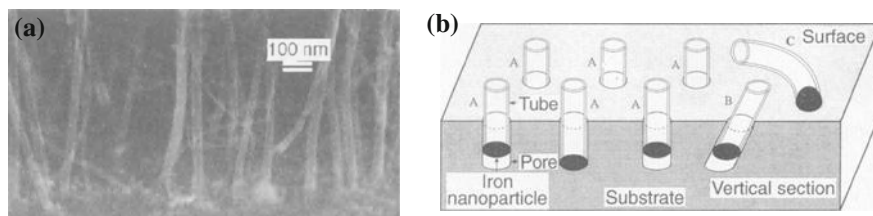


Fig. 3.4 CNT array grown by thermal CVD method. **a** High-magnification SEM image of CNTs growing out from the mesoporous iron/silica substrate and forming an array. **b** Possible growth model of CNTs formed on iron nanoparticles embedded in mesoporous silica. From Li et al. [30]. Copyright (1996), AAAS

spacings of about 100 nm (Fig. 3.4a). The growth direction of the nanotubes may be controlled by orientation of the pores from which the nanotubes grow (Fig. 3.4b). The length of such grown aligned MWCNTs can be about 2 mm [33].

Using mask techniques, the MWCNTs can self-assemble into CNT towers on catalyst patterns deposited on porous silicon substrate by a base growth mechanism [34]. Aligned nanotube bundles were also grown by the CVD method over thin films of a cobalt catalyst patterned on a silica substrate [35].

Of the various means for nanotube synthesis, CVD shows the most promise for industrial-scale deposition, because of its price per unit ratio, and because CVD is capable of growing nanotubes directly on a desired substrate, whereas the nanotubes must be collected in the other growth techniques. Tons of CNTs are commercially synthesized using CVD method.

Although CVD offers the benefit of significantly lower synthesis temperatures than arc-discharge and laser ablation techniques, it still requires a growth temperature of 600–950 °C. In order to decrease the growth temperature, an important approach in CVD method is to employ plasma. CNT arrays can be grown on glass under the assistance of plasma at 660 °C [36]. Large-scale CNT arrays are well synthesized (Fig. 3.5). Until now, this PECVD process has become the most popular method to synthesize SWCNTs and MWCNTs [37], MWCNT arrays [36] and ordered SWCNT strands [38] on various substrates. After employing various plasma techniques, the growth temperature can be further lowered down to 300 °C. There are many types of CVD and the details of these CVD are discussed in Chap. 4: *Chemical Vapor Deposition*. During a standard thermal CVD or PECVD procedure, a substrate is coated with a layer of metal catalytic nanoparticles, most commonly nickel, cobalt, iron, or a combination. The metal nanoparticles can also be produced by other ways, such as reduction of oxides or oxides solid solutions. The size of the catalytic nanoparticles can be controlled by patterned (or masked) deposition of the metal, annealing, or by plasma etching of a metal layer. The substrate with catalytic particles is usually heated to approximately 700 °C in a protective gas. To initiate the growth of nanotubes, two gases are bled into the reactor: a process gas (such as ammonia, nitrogen or hydrogen) and a carbon-containing gas (such as acetylene, ethylene, ethanol or methane). Nanotubes grow at the sites of the metal catalyst: the carbon-containing

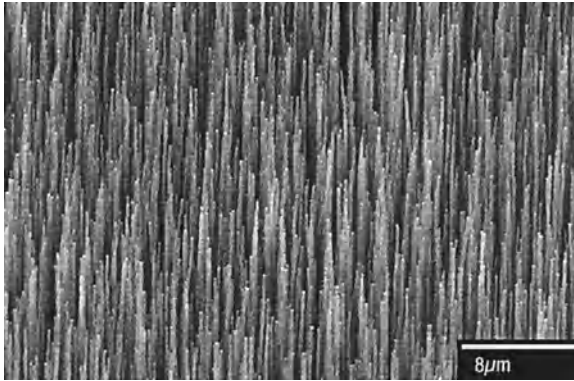


Fig. 3.5 SEM micrograph of CNTs grown by DC PECVD on glass. From Ren et al. [36]. Reprinted with permission from AAAS

gas is broken apart first at the surface of the catalytic nanoparticles, and the obtained carbon fragments are transported to the edges of the catalytic nanoparticles, where the carbon fragments form into the carbon nanotubes. The catalytic nanoparticles can stay at the tips of the growing nanotubes during the growth process, or remain at the nanotube bases, depending on the adhesion between the catalytic nanoparticles and the substrate. The diameters of the nanotubes that are to be grown are related to the size of the metal particles.

In the CVD process, the catalyst is one of the key factors for CNT growth. Nickel [36, 39–43], cobalt [44–46], iron [30, 34, 47, 48], stainless steel [49, 50], gold, platinum, and their alloys have been successfully used as catalysts. Some catalysts used for CNT growth were summarized recently [51].

There are many proposed formation mechanisms for catalytically grown CNTs in the literatures [52–58], such as covering bulk diffusion mechanisms [58, 59], surface diffusion mechanisms [52], spatial velocity hodograph [53] and catalyst surface step edge effects [55]. There also exists a two-step growth mechanism: the first step corresponding to the catalytic growth of a CNT and the second step corresponding to a thickening step via a catalyst-free pyrolytic carbon deposition mechanism [60–64].

In a CVD growth, hydrocarbon (such as methane, benzene, acetylene, naphthalene, ethylene, etc.) pyrolyzes over metal catalysts (such as Co, Ni, Fe, Pt, and Pd) deposited on various substrates. Here, we mainly discuss the pyrolytic CNT growth mechanism to show how CNT grow in a CVD procedure. Various pyrolytic CNT growth mechanisms were described in some literatures [58, 60, 65–69]. At present, the three following mechanisms of the carbon nanotubes via pyrolytic growth have been widely recognized.

(1) *Top carbon diffusion through catalytic particles.* The mechanism [58, 66–68] proposed that the decomposition of hydrocarbons (such as acetylene C_2H_2) on the top surfaces of the metal catalyst results in the creation of H_2 and C_n species. The

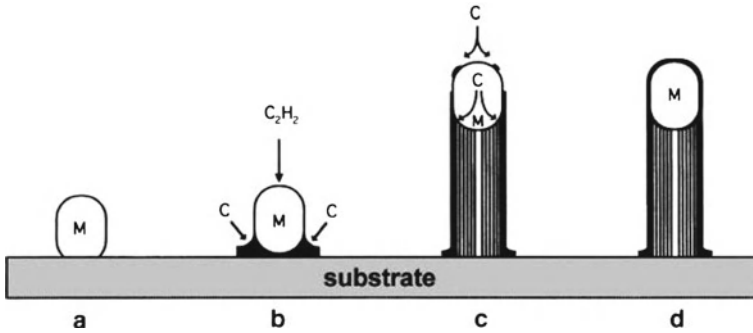


Fig. 3.6 Growth mechanism postulated in 1975 for the formation of carbon filaments by pyrolysis of acetylene (C_2H_2) on a metal particle (M); Letter C denotes carbon. From Baker et al. [66]. The model proposes that carbon is cracked on the catalytic particle and diffuses through the metal, then precipitates at the other end in the form of graphite and the metal particle always remain at the top of the tubule

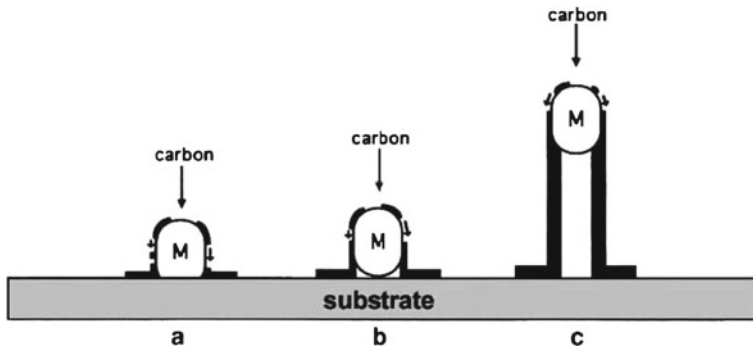


Fig. 3.7 Schematic illustration of the growth mechanism proposed in 1976 for carbon fibers and filaments from benzene pyrolysis over catalytic particles. From Oberlin et al. [52]. Here, the hydrocarbon cracks on the surface of the metal and diffuses on the surface of the particle. Carbon then precipitates to the colder end in the form of graphitic domains

carbon fragments then diffuse through the catalytic nanoparticles and precipitate at another side of the catalytic particles (Fig. 3.6) with a lower temperature, thereby allowing the carbon nanotubes to grow. This process continues until the catalytic activity of the leading particle is neutralized or the carbon species stop reacting with the exposed end (Fig. 3.6 d).

(2) *Surface carbon diffusion on catalytic particles.* As earlier as in 1970s, it is postulated [52, 70] that carbon filaments grow through carbon diffusion on the surface of the metal particle, thus precipitating at the other end of the particle (Fig. 3.7).

(3) *Bottom carbon diffusion through catalytic particles.* In particular, this mechanism is based on pyrolysis experiments of acetylene over Fe-Pt substrates [65], and by natural gas passing over stainless steel surfaces at high temperatures [71, 72].

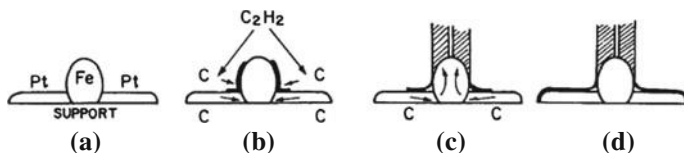


Fig. 3.8 Representation proposed in 1980 for carbon filament growth from Fe-Pt/ C_2H_2 systems. From Baker and Chludzinski [68]. Carbon also diffuses through the metal, but the particle always remains at the bottom of the filament

Filament growth occurs due to the rapid movement of carbon species through the catalyst by a diffusion process (Fig. 3.8b–c), thus segregating a filament (Fig. 3.8d). In this model, tubes grow from their bases rather than from their tips.

The nucleation and growth process of carbon nanotubes are in situ examined in TEM recently [73]. CNTs grow from iron carbide nanocatalysts in a CVD procedure with C_2H_2 as carbon source, observed on a in situ environmental transmission electron microscopy. It is found that graphitic networks are formed on the fluctuating iron carbide nanoparticles and subsequently CNTs are expelled from them [73]. The atomic scale in situ observations suggest that carbon atoms diffuse through the bulk of catalytic nanoparticles during the growth of CNTs.

Up to now, some books are published on CNT growth from CVD methods. The readers are referred to these books [74].

3.4 Hydrothermal Methods

Hydrothermal processing is traditionally defined as any heterogeneous reaction in the presence of aqueous solvents or mineralizers under high pressure and temperature conditions to dissolve and recrystallize materials that are relatively insoluble under ordinary conditions [75]. Recently, hydrothermal is re-defined as any heterogeneous chemical reaction in the presence of a solvent (whether aqueous or non-aqueous) above the room temperature and at pressure greater than 1 atm in a closed system, covering the terms of solvothermal, alcohothermal, glycolthermal, ammonothermal, and so on, to describe all the heterogeneous chemical reactions taking place in a closed system in the presence of a solvent, whether it is aqueous or nonaqueous, under supercritical or non-supercritical conditions.

Figure 3.9 shows the most popular autoclave designs such as Morey autoclaves (Fig. 3.9a) and the popularly known stirred autoclaves (Fig. 3.9b). These hydrothermal reactors have been used for a variety of applications like materials synthesis, crystal growth, and hydrothermal phase equilibrium studies, and so on.

Until now, there are hundreds of nanomaterials processed using hydrothermal technologies in the past decades, covering metals, metal oxides, and semiconductors, such as PbSe nanocubes [76] and nitride nanomaterials [77, 78]. CNTs have also been synthesized using the technique.

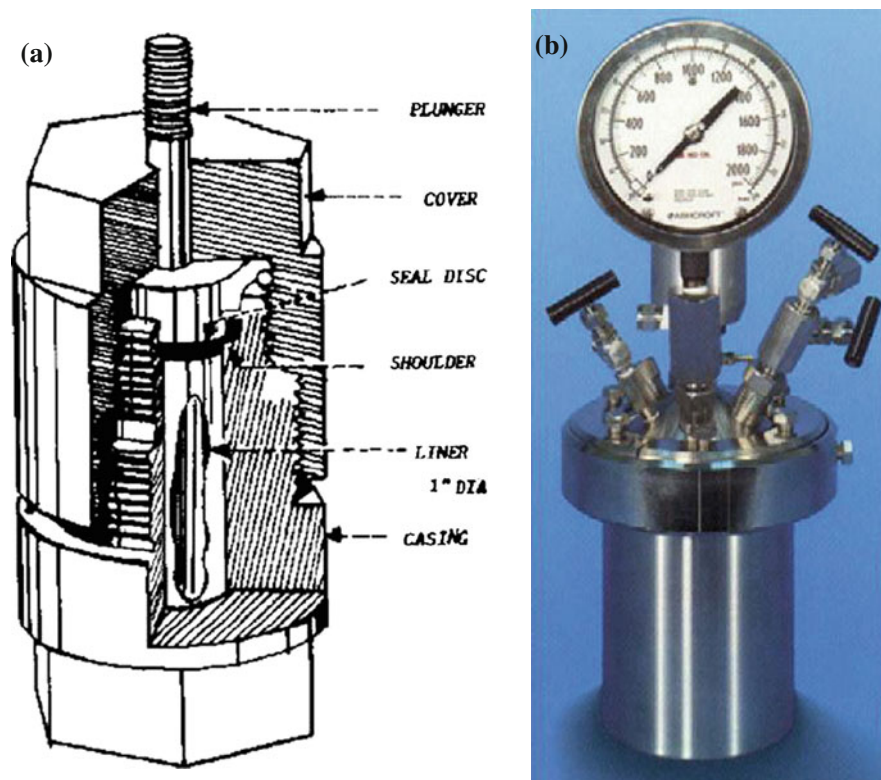


Fig. 3.9 Hydrothermal reactors. From Byrappa and Adschiri [75]. **a** Morey autoclave commonly used as reactors in hydrothermal processing of materials. **b** Commercially available stirred reactors with facilities to withdraw the fluids and externally pump the desired gas into the autoclave, coupled magnetic stirrer assembly

In a hydrothermal procedure, temperature and pressure affect the dissolution greatly and are very important parameters in the hydrothermal growth. The temperature can be measured and controlled easily by an external heater. In most of these autoclaves, the pressure can be either directly measured using the Bourdon gauge fixed to the autoclaves, or it can be calculated using the pressure-vapor-temperature (PVT) relations of solvents. Figure 3.10 is the experimental pressure of water at different temperatures in an autoclave.

In the previous CNT synthesis methods such as arc discharge and laser ablation methods, high reaction temperature and metal catalysts are usually needed. Hydrothermal method is capable to synthesize CNTs at relatively lower temperatures. It is reported that CNTs were synthesized at 1,000 °C [81] from supercritical CO₂, at 700–800 °C [82, 83] (60–100 MPa) from polyethylene and ethylene glycol carbon sources, at 600 °C [84] from ethanol, at 600 °C [85] (12.4 MPa, Fe alloys as catalysts) from toluene, at 350 °C [86] (Co/Ni as catalysts) from hexachlorobenzene and

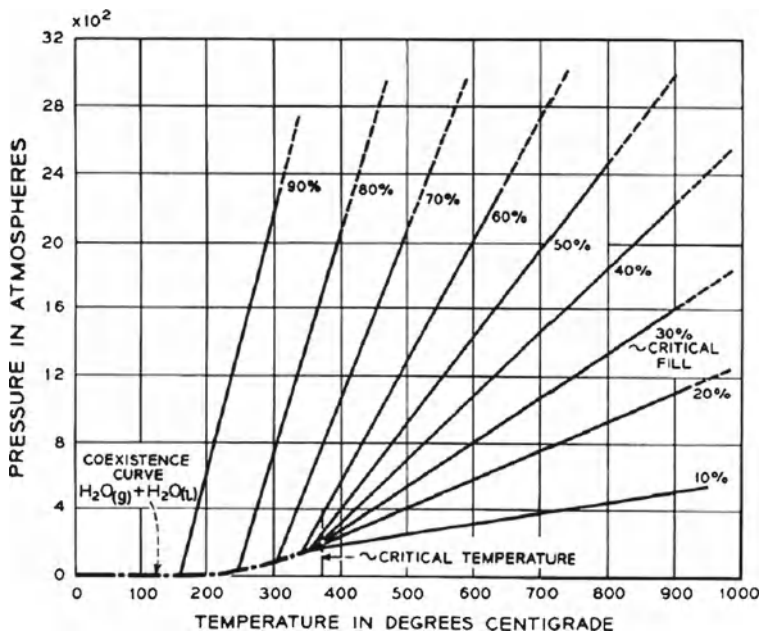


Fig. 3.10 PVT diagram of H_2O in a closed system. From Kennedy [79]

tetrachloroethylene, at 310 °C [87], at 180 °C [80] from ethyl alcohol, at 175 °C [88] (iron-encapsulated poly-propyleneimine dendrimers as catalyst) from CCl_4 in supercritical carbon dioxide medium, at even 160 °C [87] from ethyl alcohol/polyethylene glycol in a basic aqueous solution, and at other temperatures [89].

In a typical CNT synthesis of hydrothermal method [90], 60 mL hexane as non-aqueous solvents, 0.6 mL $SiCl_4$, 3 g ethoxylated alcohol polyoxyethylene ether used as a carbon source, and 6 mL Na (25 wt%) dispersion in toluene were added to a 200 mL flask. The mixture was stirred in a magnetic stirrer for 10 min, and then transferred to a Parr reactor with a capacity of 125 mL. The Parr reactor was sealed and then kept at 310 °C for 72 h in a furnace, and then cooled to room temperature. The pressure in the Parr reactor can be calculated from PVT diagram of hexane in a closed system. The products were washed with hexane, alcohol and distilled water several times, and then dried in a vacuum oven at 60 °C for 6 h. The synthesized CNTs are MWCNT, as shown in Fig. 3.11. The multi-walled carbon nanotubes have outer diameters between 5 nm and 20 nm, and inner diameters between 2 nm and 8 nm. The length of the multi-walled carbon nanotubes is of several microns. The CNTs usually graphitized well (Fig. 3.11).

It is worth pointing out that the diameters of the as-prepared MWCNTs by the low-temperature hydrothermal route are much smaller than those prepared by high-temperature hydrothermal method [83]. For example, the inner diameter of CNTs prepared at 700–800 °C under 60–100 MPa pressure is 20–800 nm [83]. The in-

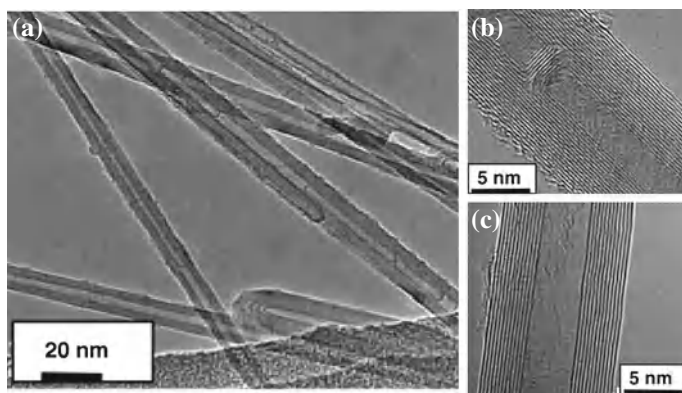


Fig. 3.11 CNTs synthesized by hydrothermal method. **a** TEM image of CNTs and **b–c** HRTEM images of CNTs. From Wang et al. [80]. Copyright (2005), American Chemical Society

ner diameter of CNTs is 5–8 nm when hydrothermally synthesized at 310 °C [90], 4–8 nm when produced at 160 °C [80]. The outer-diameters of hydrothermal grown CNTs are about 100 nm [83] at 700–800 °C while 10–40 nm when reacted at 180 °C [80].

Although the hydrothermal technique offers some special advantages for processing such advanced materials, there are some disadvantages with respect to the CNTs. For example, hydrothermal condition affects the stability of CNTs. Detailed hydrothermal experiments indicated that SWCNTs slowly change over to MWCNTs and polyhedral graphitic nanoparticles under hydrothermal conditions above 550 °C [91] or 800 °C [92] in pure water under 100 MPa pressure. SWCNTs can completely transform into MWCNTs and polyhedral carbon nanoparticles after 48 h treatment at these hydrothermal conditions. The presence of oxygen in super-critical water greatly thins the MWCNTs. So far there are no reports in the literature on the preparation of SWCNTs and the commercial production of CNTs from hydrothermal technique [75]. However, the hydrothermal technique definitely provides some high quality CNTs with a control over the tube diameter and tube structures [75].

Hydrothermal syntheses of aligned arrays of carbon nanotubes were reported via anodic aluminum oxide (AAO) templates [93]. Glucose was polymerized in the pores of the AAO template under hydrothermal conditions to form a mixture of organic polymers, resulting in the uniform coating of the inner surfaces of the AAO nanochannels with a carbonaceous film. The carbonaceous films on the AAO template were carbonized at 900 °C under a flow of N₂ to obtain CNTs. Figure 3.12 shows aligned CNTs grown by this method. The as-prepared CNTs are about 200 nm in diameter and have cylinders with a wall thickness of about 10 nm.

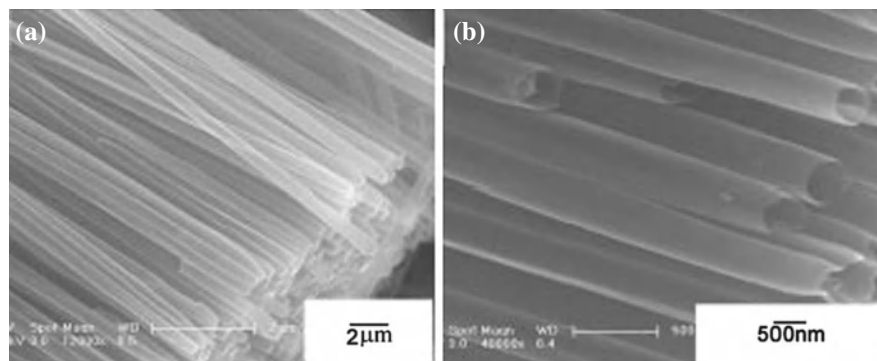


Fig. 3.12 FESEM images of aligned CNTs grown by hydrothermal method at **a** low and **b** high magnification. From When et al. [93]

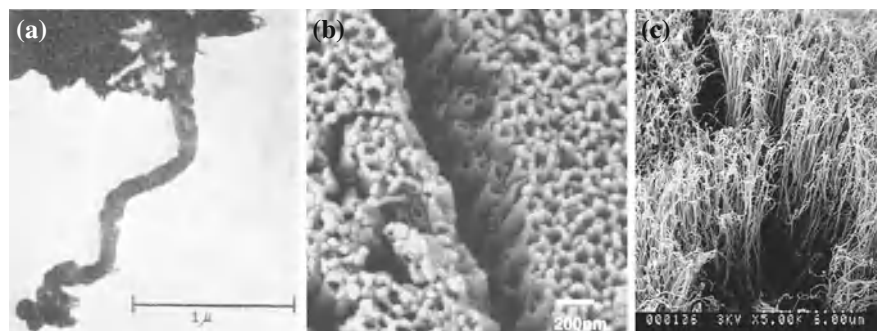


Fig. 3.13 MWCNTs grown by flame method. **a** TEM image of curved carbon vermicules obtained in the brickwork of blast furnace, published in 1953. From Davis et al. [94]. **b** Top-view SEM image of CNT arrays with length of about 500 nm via a flame method on silicon substrates using a nanoporous template of anodized aluminum oxide. From Hu et al. [95]. **c** SEM image of vertically oriented MWCNTs synthesized by an ethylene-air diffusion flame without template. From Yuan et al. [96]

3.5 Flame Method

The flame method should be the oldest method to artificially produce CNTs. The scientists suspected that CNTs were synthesized in the ancient forging if catalyst exists and it was reported that CNTs were discovered in ancient Damascus sabers forged more than 400 years ago [97].

Different from the above-described state-of-the-art techniques used in the laboratories, CNTs are commonly formed in such mundane places as ordinary flames, produced by burning methane, ethylene, and benzene, found in soot from both indoor and outdoor air in the natural, incidental, and controlled flame environments.

Curved carbon vermicules with thickness of 10 nm to 200 nm were found in the bricks of blast furnaces at 450 °C from carbon monoxide [94] (Fig. 3.13a). It was

suggested that CO was catalyzed by iron to carbon and the particles of catalyst were located at the ends of the carbon products [94]. The early chemical reaction of the soot formation in various hydrocarbon diffusion flames was carefully studied recently to disclose the CNT grown in flame [96, 98, 99]. SWCNTs [99, 100] and bamboo-like CNTs [101] were synthesized by the flame method. However, these naturally occurring varieties can be highly irregular in size and quality because the environment in which they are produced is often highly uncontrolled.

Recently, aligned CNTs, such as well-aligned MWCNT arrays [95, 96] and SWCNT arrays [102, 103], are produced in controlled flame environments. For example, MWCNT arrays were grown using a laminar ethylene/air co-flow diffusion flame using AAO templates (Fig. 3.13b). The basal plane of the AAO template (with Co nanoparticles at the bottom of nanopore as catalyst) was placed perpendicular to the gas flow direction and a layer of smooth and shiny black CNTs was deposited on the AAO template [95]. The sample was then dipped into the chromic and phosphoric acid mixture to partially remove the AAO template.

Figure 3.13c shows a CNT array produced by the flame method without template. The CNTs are aligned vertically to the substrate surface [96].

3.6 Disproportionation of Carbon Monoxide

As discussed in Chap. 2, the first possible CNTs, hollow carbon nanofilaments published in 1952, were synthesized using this method [104]. Carbon vermicules were also produced from carbon monoxide at about 450 °C on the surface of iron oxide [94] in 1953. The carbon threads is twisted with diameter of less than one micron. Later hollow carbon fibers were produced by catalytic disproportionation of carbon monoxide [105] as well as SWCNTs [106]. The setup of the method is illustrated in some literatures [107].

Figure 3.14a shows carbon products prepared in 1973 by passing 80 % CO / 20 % H₂ over Raney nickel at 600 °C using carbon monoxide disproportionation [105]. The synthesized carbon products are hollow and curved. Straight carbon tubes were reported in 1985 from the disproportion of CO in CO-CO₂ gas mixtures over FeNi alloy between 500 °C and 650 °C [59], see Fig. 3.14b. The HRTEM image indicates the atomic carbon layers are parallel to the side surface of the catalyst.

In the disproportionation method, carbon monoxide is subject to disproportionation according to the Boudouard equilibrium:



The equilibrium favors the right side at temperatures below 700 °C in the presence of catalysts like iron, cobalt, and nickel [105]. Usually the CO gas passes over fine iron, cobalt or nickel powders, resulting in CNT growth.

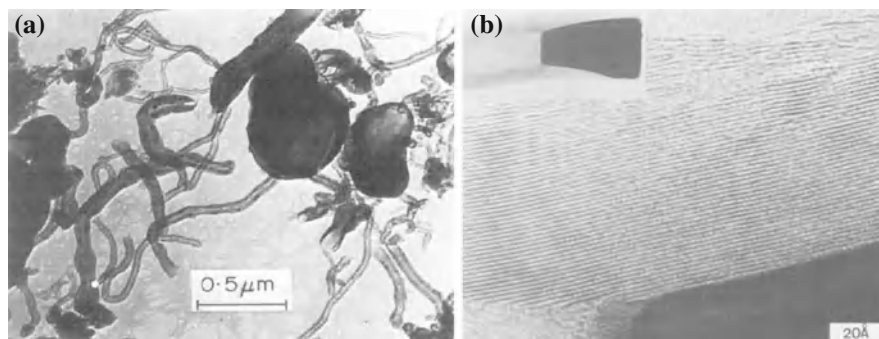
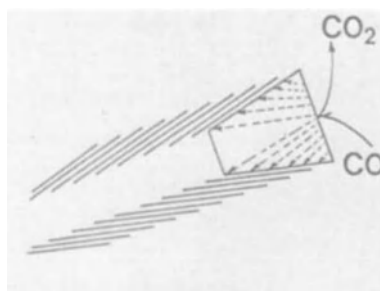


Fig. 3.14 Electron microphotographs of carbon synthesized by carbon monoxide disproportionation method. **a** Hollow carbon fiber published in 1973. From Boehm [105]. **b** Carbon tubes published in 1985. From Audier and Coulon [59]. Inset: TEM image of the catalyst on carbon tip

Fig. 3.15 Schematic drawing of tubular carbon growth from the disproportionation of Co. From Audier and Coulon [59]. The conical particle at end is catalyst



Detailed TEM observation suggested that the dissociative chemisorption of the carbon monoxide on the NiFe alloy surface leads to bulk diffusion of carbon atoms into the alloy, as shown in Fig. 3.15. The bulk diffusion of carbon is driven by an isothermal gradient with local equilibria at both metal–carbon and metal–gas interfaces. Then the carbon atoms precipitate at the metal–carbon interface to form carbon tubes.

At present, it is possible to generate SWCNTs using pyrolysis of various carbon sources in the presence of metals and/or metal alloys [106, 107]. Under high pressures, bulk CNTs with production rate of g/h can be produced using this method [107]. It is reported that the SWCNTs are extremely efficiently produced from CO at elevated pressures (1–10 atm) and temperatures (800–1,200 °C) under the thermolysis of Fe(CO)₅. Because of the high pressure, the technique is also named as the HiPco (*high-pressure CO*) process. The interested readers on HiPco process are referred to a review literature and references therefore [108].

3.7 Catalytic Pyrolysis of Hydrocarbons

Pyrolysis is an old method to grow CNTs. As we discussed in Chap. 2, carbon filaments were produced by the thermal decomposition of methane before 1900 [109] and CNTs were probably synthesized through benzene decomposition in 1976 [52]. Pyrolytic CNT growth mechanism was described in some literatures [59, 60].

Recently, well-aligned CNT forests were grown by hydrogen-free spray pyrolysis CVD method under optimal experimental parameters such as temperature, injection speed, precursor volume, and catalyst concentration [110]. Experimental observations and characterizations reveal that the growth rate, size, and quality of the carbon nanotubes are significantly dependent on the reaction parameters. The grown MWCNTs are over 1 mm.

3.8 Electrolysis

CNTs can also be prepared through electrolysis in molten alkali halide salts [111, 112].

In a typical experiment, lithium chloride was filled into a carbon crucible and heated to its melting point in air [111] or under an Ar atmosphere [112]. Then a carbon rod was immersed in the melt to form the cathode of an electrolysis cell (crucible acts as the anode). When a DC voltage between the electrodes was applied (Fig. 3.16), the immersed surface of the cathode rod was eroded during electrolysis and some materials dispersed throughout the melt. After purification, the obtained products were MWCNTs and onion-like polyhedral particles. The CNTs are not always straight, but tend to form loops. With this technique and under optimal conditions, it is possible to generate up to 20–40% of MWCNTs.

During the growth of MWCNTs using the liquid phase approach, it was identified from electron diffraction [113] that carbon dissolves into molten Li to yield Li_2C_2 above 600 °C:

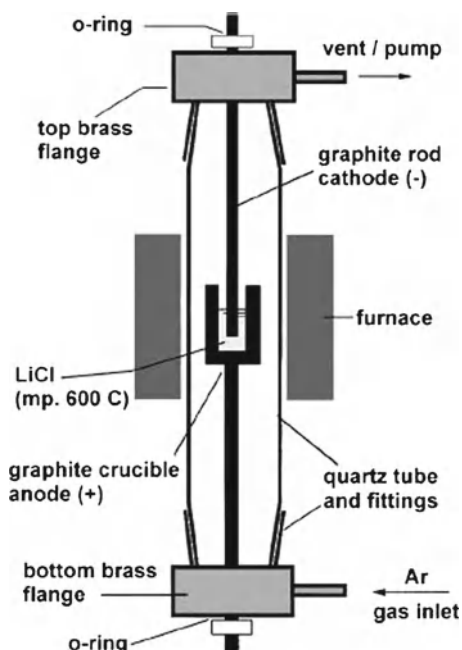


The yielded Li_2C_2 was found to be encapsulated within well-graphitized CNTs [111, 112]. The formation of Li_2C_2 may be a key step in cathode dissolution and subsequent nanotube formation. It was proposed that carbon atoms extrude or segregate as an ordered hexagonal array, thus resulting in carbon nanotubes [113].

The studies indicated that the carbon nanotube production strongly depends on the molten salt and the temperature of the electrolyte [114]. In particular, it was suggested that the carbon nanotube formation is caused by graphite intercalation processes occurring at the cathode [114].

Until now, various salts have been successfully employed to produce carbon nanotubes by electrolysis, such as LiCl, KCl, NaCl, and LiBr [115].

Fig. 3.16 Schematic diagram of the electrolysis set-up used to produce CNTs in the liquid phase. From Hsu et al. [112]



The liquid-phase electrolytic method has not been widely used probably because the nanotube yield is difficult to control. In addition, the technique has not been able to produce SWCNTs [115]. More details of the synthesis of CNTs are found in the review literature and related books [115–117].

3.9 Solar Energy

In addition to high-energy lasers, arc-discharge, and thermal routes, solar energy offers an alternative to produce SWCNTs and MWCNTs.

In the technique the solar light was focused on a carbon-metal target in an inert atmosphere [118]. Solar energy is capable of vaporizing graphite-metal targets because the average incident solar flux in such experiments is close to 500 W/cm^2 and can reach a front temperature of $2,800 \text{ K}$ [115]. It has proved possible to generate a more powerful solar furnace ($1,000 \text{ kW}$) that results in temperatures close to $3,400 \text{ K}$, which can increase significantly the yields of fullerenes and nanotubes [119]. Higher solar flux densities in the range of $600\text{--}920 \text{ W/cm}^2$ successfully generated carbon soot (production rate of 2 g/h) rich in fullerenes and nanotubes [115].

It is also possible to carry out pyrolytic processes using a solar furnace in order to produce MWCNTs. In particular, the catalytic decomposition of CH_4 and C_4H_{10}

in the presence of Ni/Al₂O₃ or Co/MgO is able to generate carbon filaments and nanotubes [115].

This method is potentially advantageous but further research needs to be carried out because the quality of the products is highly sensitive to the pressure, carrier gas, and carbon-metal ratio [115].

Up to now, many books review the CNT growth method and growth mechanism. Interested readers are referred to these excellent books [13, 63, 117] and review literatures [69, 120–122].

References

1. Y. Saito, M. Inagaki, Optical emission studies on chemical species in an arc flame of fullerene/metallofullerene generator. *Jpn. J. Appl. Phys.* **32**(Part 2, No. 7A), L954–L957 (1993)
2. A. Anders, *Cathodic Arcs: From Fractal Spots to Energetic Condensation*. Atomic, Optical, and Plasma Physics, (Springer, 2010)
3. S. Iijima, Direct observation of the tetrahedral bonding in graphitized carbon black by high resolution electron microscopy. *J. Cryst. Growth* **50**(3), 675–683 (1980)
4. H.W. Kroto, J.R. Heath, S.C. O'Brien, R.F. Curl, R.E. Smalley, C₆₀: Buckminsterfullerene. *Nature* **318**, 162–163 (1985)
5. S. Iijima, Helical microtubules of graphitic carbon. *Nature* **354**, 56–58 (1991)
6. T.W. Ebbesen, P.M. Ajayan, Large-scale synthesis of carbon nanotubes. *Nature* **358**(6383), 220–222 (1992)
7. S. Iijima, T. Ichihashi, Single-shell carbon nanotubes of 1-nm diameter. *Nature* **363**(6430), 603–605 (1993)
8. D.S. Bethune, C.H. Klang, M.S. de Vries, G. Gorman, R. Savoy, J. Vazquez, R. Beyers, Cobalt-catalysed growth of carbon nanotubes with single-atomic-layer walls. *Nature* **363**(6430), 605–607 (1993)
9. C. Journet, W.K. Maser, P. Bernier, A. Loiseau, M.L. de la Chapelle, S. Lefrant, P. Deniard, R. Leek, J.E. Fischer, Large-scale production of single-walled carbon nanotubes by the electric-arc technique. *Nature* **388**, 756–768 (1997)
10. P. Chaturvedi, P. Verma, A. Singh, P.K. Chaudhary, Harsh, P.K. Basu, Carbon nanotube - purification and sorting protocol. *Defence Sci. J.* **58**(5), 591–599 (2008)
11. S.K. Pillai, S.S. Ray, M. Moodley, Purification of single-walled carbon nanotubes. *J. Nanosci. Nanotechnol.* **7**(9), 3011–3047 (2007)
12. S.K. Pillai, S.S. Ray, M. Moodley, Purification of multi-walled carbon nanotubes. *J. Nanosci. Nanotechnol.* **8**(12), 6187–6207 (2008)
13. M. Daenen, R.D. de Fouw, B. Hamers, P.G.A. Janssen, K. Schouteden, M.A.J. Veld, *The Wondrous World of Carbon Nanotubes: A Review of Current Carbon Nanotube Technologies*, Technical Report, (Eindhoven University of Technology, Eindhoven, 2003)
14. K. MacKenzie, O. Dunens, A.T. Harris, A review of carbon nanotube purification by microwave assisted acid digestion. *Sep. Purif. Technol.* **66**(2), 209–222 (2009)
15. X. Song, Y. Fang, A technique of purification process of single-walled carbon nanotubes with air. *Spectrochim. Acta A* **67**(3–4), 1131–1134 (2007)
16. M. Ushio, D. Fan, M. Tanaka, A method of estimating the space-charge voltage drop for thermionic arc cathodes. *J. Phys. D: Appl. Phys.* **27**(3), 561–566 (1994)
17. E.G. Gamaly, Growth mechanism of carbon nanotubes, in *Carbon Nanotubes: Preparation and Properties*, ed. by T.W. Ebbesen. (Chemical Rubber, Boca Raton, 1997), pp. 164–190
18. S. Farhat, C.D. Scott, Review of the arc process modeling for fullerene and nanotube production. *J. Nanosci. Nanotechnol.* **6**(5), 1189–1210 (2006)

19. B. Ahmad, M. Ahmad, J. Akhter, N. Ahmad, Formation of diamond-like carbon balls, self aligned and nonaligned nanotubes at the tip of the cathode during the synthesis of fullerenes in the DC arc discharge experiment. *Mater. Lett.* **59**(12), 1585–1588 (2005)
20. R. Ismagilov, P. Shvets, A. Kharin, A. Obraztsov, Noncatalytic synthesis of carbon nanotubes by chemical vapor deposition. *Crystallogr. Rep.* **56**(2), 310–314 (2011)
21. A.P. Moravsky, E.M. Wexler, R.O. Loutfy, Growth of carbon nanotubes by arc discharge and laser ablation, in *Carbon Nanotubes: Science and Applications*, ed. by M. Meyyappan. (CRC Press, Boca Raton, 2004 pp. 80–121)
22. P.J.F. Harris, Solid state growth mechanisms for carbon nanotubes. *Carbon* **45**(2), 229–239 (2007)
23. B. Yakobson, R. Smalley, Fullerene nanotubes: C1,000,000 and beyond. *Am. Sci.* **85**, 324–337 (1997)
24. T. Guo, P. Nikolaev, A. Thess, D. Colbert, R. Smalley, Catalytic growth of single-walled nanotubes by laser vaporization. *Chem. Phys. Lett.* **243**(1–2), 49–54 (1995)
25. T. Guo, P. Nikolaev, A.G. Rinzler, D. Tomanek, D.T. Colbert, R.E. Smalley, Self-assembly of tubular fullerenes. *J. Phys. Chem.* **99**(27), 10694–10697 (1995)
26. C. Scott, S. Arepalli, P. Nikolaev, R. Smalley, Growth mechanisms for single-wall carbon nanotubes in a laser-ablation process. *Appl. Phys. A: Mater.* **72**, 573–580 (2001)
27. A. Thess, R. Lee, P. Nikolaev, H. Dai, P. Petit, J. Robert, C. Xu, Y.H. Lee, S.G. Kim, A.G. Rinzler, D.T. Colbert, G.E. Scuseria, D. Tománek, J.E. Fischer, R.E. Smalley, Crystalline ropes of metallic carbon nanotubes. *Science* **273**(5274), 483–487 (1996)
28. Z.Y. Kosakovskaya, L.A. Chemozatonskii, E.A. Fedorov, Nanofilament carbon structure. *JETP Lett.* **56**(1), 26–30 (1992)
29. M. Ge, K. Sattler, Vapor-condensation generation and STM analysis of fullerene tubes. *Science* **260**(5107), 515–518 (1993)
30. W.Z. Li, S.S. Xie, L.X. Qian, B.H. Chang, B.S. Zou, W.Y. Zhou, R.A. Zhao, G. Wang, Large-scale synthesis of aligned carbon nanotubes. *Science* **274**(5293), 1701–1703 (1996)
31. P.L. Walker, J.F. Rakszawski, G.R. Imperial, Carbon formation from carbon monoxide-hydrogen mixtures over iron catalysts. I. properties of carbon formed. *J. Phys. Chem. B* **63**(2), 133–140 (1959)
32. M. José-Yacamán, M. Miki-Yoshida, L. Rendón, J.G. Santiesteban, Catalytic growth of carbon microtubules with fullerene structure. *Appl. Phys. Lett.* **62**(6), 657–659 (1993)
33. Z.W. Pan, S.S. Xie, B.H. Chang, C.Y. Wang, L. Lu, W. Liu, W.Y. Zhou, W.Z. Li, L.X. Qian, Very long carbon nanotubes. *Nature* **394**(6694), 631–632 (1998)
34. S. Fan, M.G. Chapline, N.R. Franklin, T.W. Tomblor, A.M. Cassell, H. Dai, Self-oriented regular arrays of carbon nanotubes and their field emission properties. *Science* **283**(5401), 512–514 (1999)
35. M. Terrones, N. Grobert, J. Olivares, J.P. Zhang, H. Terrones, K. Kordatos, W.K. Hsu, J.P. Hare, P.D. Townsend, K. Prassides, A.K. Cheetham, H.W. Kroto, D.R.M. Walton, Controlled production of aligned-nanotube bundles. *Nature* **388**(6637), 52–55 (1997)
36. Z.F. Ren, Z.P. Huang, J.W. Xu, J.H. Wang, P. Bush, M.P. Siegal, P.N. Provencio, Synthesis of large arrays of well-aligned carbon nanotubes on glass. *Science* **282**, 1105–1107 (1998)
37. A. Peigney, P. Coquay, E. Flahaut, R.E. Vandenberghe, E. De Grave, C. Laurent, A study of the formation of single- and double-walled carbon nanotubes by a CVD method. *J. Phys. Chem. B* **105**(40), 9699–9710 (2001)
38. H.W. Zhu, C.L. Xu, D.H. Wu, B.Q. Wei, R. Vajtai, P.M. Ajayan, Direct synthesis of long single-walled carbon nanotube strands. *Science* **296**(5569), 884–886 (2002)
39. Z.F. Ren, Z.P. Huang, D.Z. Wang, J.G. Wen, J.W. Xu, J.H. Wang, L.E. Calvet, J. Chen, J.F. Klemic, M.A. Reed, Growth of a single freestanding multiwall carbon nanotube on each nanonickel dot. *Appl. Phys. Lett.* **75**(8), 1086–1088 (1999)
40. Y.C. Choi, Y.M. Shin, S.C. Lim, D.J. Bae, Y.H. Lee, B.S. Lee, D.C. Chung, Effect of surface morphology of Ni thin film on the growth of aligned carbon nanotubes by microwave plasma-enhanced chemical vapor deposition. *J. Appl. Phys.* **88**, 4898–4903 (2000)

41. H.T. Ng, M.L. Foo, A.P. Fang, J. Li, G.Q. Xu, S. Jaenicke, L. Chan, S.F.Y. Li, Soft-lithography-mediated chemical vapor deposition of architected carbon nanotube networks on elastomeric polymer. *Langmuir* **18**(1), 1–5 (2002)
42. Z.P. Huang, J.W. Xu, Z.F. Ren, J.H. Wang, M.P. Siegal, P.N. Provencio, Growth of highly oriented carbon nanotubes by plasma-enhanced hot filament chemical vapor deposition. *Appl. Phys. Lett.* **73**(26), 3845–3847 (1998)
43. Z.P. Huang, D.L. Carnahan, J. Rybczynski, M. Giersig, M. Sennett, D.Z. Wang, J.G. Wen, K. Kempa, Z.F. Ren, Growth of large periodic arrays of carbon nanotubes. *Appl. Phys. Lett.* **82**(3), 460–462 (2003)
44. M.W. Li, Z. Hu, X.Z. Wang, Q. Wu, Y. Chen, Low-temperature synthesis of carbon nanotubes using corona discharge plasma reaction at atmospheric pressure. *J. Mater. Sci. Lett.* **22**(17), 1223–1224 (2003)
45. J. Li, C. Papadopoulos, J.M. Xu, M. Moskovits, Highly-ordered carbon nanotube arrays for electronics applications. *Appl. Phys. Lett.* **75**(3), 367–369 (1999)
46. J. Li, C. Papadopoulos, J. Xu, Nanoelectronics: Growing Y-junction carbon nanotubes. *Nature* **402**(6759), 253–254 (1999)
47. Y.Y. Wei, G. Eres, V.I. Merkulov, D.H. Lowndes, Effect of catalyst film thickness on carbon nanotube growth by selective area chemical vapor deposition. *Appl. Phys. Lett.* **78**(10), 1394–1396 (2001)
48. X. Xu, G.R. Brandes, A method for fabricating large-area, patterned, carbon nanotube field emitters. *Appl. Phys. Lett.* **74**(17), 2549–2551 (1999)
49. E.T. Thostenson, W.Z. Li, D.Z. Wang, Z.F. Ren, T.W. Chou, Carbon nanotube/carbon fiber hybrid multiscale composites. *J. Appl. Phys.* **91**(9), 6034–6037 (2002)
50. W.Z. Li, D.Z. Wang, S.X. Yang, J.G. Wen, Z.F. Ren, Controlled growth of carbon nanotubes on graphite foil by chemical vapor deposition. *Chem. Phys. Lett.* **335**, 141–149 (2001)
51. A.V. Melechko, V.I. Merkulov, T.E. McKnight, M.A. Guillorn, K.L. Klein, D.H. Lowndes, M.L. Simpson, Vertically aligned carbon nanofibers and related structures: controlled synthesis and directed assembly. *J. Appl. Phys.* **97**(4), 041301/1–041301/39 (2005)
52. A. Oberlin, M. Endo, T. Koyama, Filamentous growth of carbon through benzene decomposition. *J. Cryst. Growth* **32**(3), 335–349 (1976)
53. S. Amelinckx, X.B. Zhang, D. Bernaerts, X.F. Zhang, V. Ivanov, J.B. Nagy, A formation mechanism for catalytically grown helix-shaped graphite nanotubes. *Science* **265**(5172), 635–639 (1994)
54. J.B. Nagy, G. Bister, A. Fonseca, D. Méhn, Z. Kónya, I. Kiricsi, Z.E. Horváth, L.P. Biró, On the growth mechanism of single-walled carbon nanotubes by catalytic carbon vapor deposition on supported metal catalysts. *J. Nanosci. Nanotechnol.* **4**(4), 4326–4345 (2004)
55. S. Helveg, C. López-Cartes, J. Sehested, P.L. Hansen, B.S. Clausen, J.R. Rostrup-Nielsen, F. Abild-Pedersen, J.K. Nørskov, Atomic-scale imaging of carbon nanofibre growth. *Nature* **427**, 426–429 (2004)
56. H. Zhu, K. Suenaga, A. Hashimoto, K. Urita, K. Hata, S. Iijima, Atomic-resolution imaging of the nucleation points of single-walled carbon nanotubes. *Small* **1**(12), 1180–1183 (2005)
57. F. Ding, K. Bolton, A. Rosén, Nucleation and growth of single-walled carbon nanotubes: A molecular dynamics study. *J. Phys. Chem. B* **108**(45), 17369–17377 (2004)
58. R.T.K. Baker, M.A. Barber, P.S. Harris, F.S. Feates, R.J. Waite, Nucleation and growth of carbon deposits from the nickel catalyzed decomposition of acetylene. *J. Catal.* **26**(1), 51–62 (1972)
59. M. Audier, M. Coulon, Kinetic and microscopic aspects of catalytic carbon growth. *Carbon* **23**(3), 317–323 (1985)
60. M. Endo, K. Takeuchi, K. Kobori, K. Takahashi, H.W. Kroto, A. Sarkar, Pyrolytic carbon nanotubes from vapor-grown carbon fibers. *Carbon* **33**(7), 873–881 (1995)
61. J.-C. Charlier, A. De Vita, X. Blase, R. Car, Microscopic growth mechanisms for carbon nanotubes. *Science* **275**(5300), 647–649 (1997)
62. M. Yudasaka, R. Kikuchi, Y. Ohki, E. Ota, S. Yoshimura, Behavior of Ni in carbon nanotube nucleation. *Appl. Phys. Lett.* **70**(14), 1817–1818 (1997)

63. J.C. Charlier, S. Iijima, Growth mechanisms of carbon nanotubes. in *Carbon Nanotubes: Synthesis, Structure, Properties, and Applications*, vol. 80, ed. by M.S. Dresselhaus, G. Dresselhaus, P. Avouris. Topics in Applied Physics, (Springer, Berlin, 2001), pp. 55–81
64. T.W. Ebbesen (ed.), *Carbon Nanotubes: Preparation and Properties*. (Chemical Rubber, Boca Raton, 1997)
65. R.T.K. Baker, P.S. Harris, R.B. Thomas, R.J. Waite, Formation of filamentous carbon from iron, cobalt and chromium catalyzed decomposition of acetylene. *J. Catal.* **30**(1), 86–95 (1973)
66. R.T.K. Baker, R.J. Waite, Formation of carbonaceous deposits from the platinum-iron catalyzed decomposition of acetylene. *J. Catal.* **37**(1), 101–105 (1975)
67. R.T.K. Baker, P.S. Harris, *Chemistry and Physics of Carbon*, (Dekker, New York, 1978)
68. R.T.K. Baker, J.J. Chludzinski, Filamentous carbon growth on nickel-iron surfaces: The effect of various oxide additives. *J. Catal.* **64**(2), 464–478 (1980)
69. R. Baker, Catalytic growth of carbon filaments. *Carbon* **27**(3), 315–323 (1989)
70. T. Baird, J. Fryer, B. Grant, Carbon formation on iron and nickel foils by hydrocarbon pyrolysis-reactions at 700°C. *Carbon* **12**(5), 591–602 (1974)
71. G.G. Tibbetts, Carbon fibers produced by pyrolysis of natural gas in stainless steel tubes. *Appl. Phys. Lett.* **42**(8), 666–668 (1983)
72. J. Bradley, G. Tibbetts, Improved yield of carbon fibers by pyrolysis of natural gas in stainless steel tubes. *Carbon* **23**(4), 423–430 (1985)
73. H. Yoshida, S. Takeda, T. Uchiyama, H. Kohno, Y. Homma, Atomic-scale in-situ observation of carbon nanotube growth from solid state iron carbide nanoparticles. *Nano Lett.* **8**(7), 2082–2086 (2008)
74. M. Meyyappan, (ed.) *Carbon Nanotubes: Science and Applications* (CRC Press, Boca Raton, 2004)
75. K. Byrappa, T. Adschiri, Hydrothermal technology for nanotechnology. *Prog. Cryst. Growth Charact. Mater.* **53**(2), 117–166 (2007)
76. B. Poudel, W.Z. Wang, D.Z. Wang, J.Y. Huang, Z.F. Ren, Shape evolution of lead telluride and selenide nanostructures under different hydrothermal synthesis conditions. *J. Nanosci. Nanotechnol.* **6**(4), 1050–1053 (2006)
77. Y. Lan, X. Chen, Y. Cao, Y. Xu, L. Xun, T. Xu, J. Liang, Low-temperature synthesis and photoluminescence of AlN. *J. Cryst. Growth* **207**(3), 247–250 (1999)
78. X. Chen, Y. Cao, Y. Lan, X. Xu, J. Li, K. Lu, P. Jiang, T. Xu, Z. Bai, Y. Yu, J. Liang, Synthesis and structure of nanocrystal-assembled bulk GaN. *J. Cryst. Growth* **209**(1), 208–212 (2000)
79. G.C. Kennedy, Pressure-volume-temperature relations in water at elevated temperatures and pressures. *Am. J. Sci.* **248**(8), 540–564 (1950)
80. W. Wang, B. Poudel, D.Z. Wang, Z.F. Ren, Synthesis of multiwalled carbon nanotubes through a modified Wolff-Kishner reduction process. *J. Am. Chem. Soc.* **127**(51), 18018–18019 (2005)
81. M. Motiei, Y. Rosenfeld Hacoheh, J. Calderon-Moreno, A. Gedanken, Preparing carbon nanotubes and nested fullerenes from supercritical CO₂ by a chemical reaction. *J. Am. Chem. Soc.* **123**(35), 8624–8625 (2001)
82. J.M. Calderon Moreno, M. Yoshimura, Hydrothermal processing of high-quality multiwall nanotubes from amorphous carbon. *J. Am. Chem. Soc.* **123**(4), 741–742 (2001)
83. Y. Gogotsi, J.A. Libera, M. Yoshimura, Hydrothermal synthesis of multiwall carbon nanotubes. *J. Mater. Res.* **15**(12), 2591–2594 (2000)
84. J. Liu, M. Shao, X. Chen, W. Yu, X. Liu, Y. Qian, Large-scale synthesis of carbon nanotubes by an ethanol thermal reduction process. *J. Am. Chem. Soc.* **125**(27), 8088–8089 (2003)
85. D.C. Lee, F.V. Mikulec, B.A. Korgel, Carbon nanotube synthesis in supercritical toluene. *J. Am. Chem. Soc.* **126**(15), 4951–4957 (2004)
86. Y. Jiang, Y. Wu, S. Zhang, C. Xu, W. Yu, Y. Xie, Y. Qian, A catalytic-assembly solvothermal route to multiwall carbon nanotubes at a moderate temperature. *J. Am. Chem. Soc.* **122**(49), 12383–12384 (2000)
87. W. Wang, S. Kunwar, J.Y. Huang, D.Z. Wang, Z.F. Ren, Low temperature solvothermal synthesis of multiwall carbon nanotubes. *Nanotechnology* **16**(1), 21–23 (2005)

88. J.K. Vohs, J.J. Brege, J.E. Raymond, A.E. Brown, G.L. Williams, B.D. Fahlman, Low-temperature growth of carbon nanotubes from the catalytic decomposition of carbon tetrachloride. *J. Am. Chem. Soc.* **126**, 9936–9937 (Aug. 2004)
89. S. Liu, J. Yue, R.J. Wehmschulte, Large thick flattened carbon nanotubes. *Nano Lett.* **2**(12), 1439–1442 (2002)
90. W. Wang, J. Huang, D. Wang, Z. Ren, Low-temperature hydrothermal synthesis of multiwall carbon nanotubes. *Carbon* **43**(6), 1328–1331 (2005)
91. S.S. Swamy, J.M. Calderon-Moreno, M. Yoshimura, Stability of single-wall carbon nanotubes under hydrothermal conditions. *J. Mater. Res.* **17**(4), 734–737 (2002)
92. J.-Y. Chang, B. Lo, M. Jeng, S.-H. Tzing, Y.-C. Ling, Morphological variation of multiwall carbon nanotubes in supercritical water oxidation. *Appl. Phys. Lett.* **85**(13), 2613–2615 (2004)
93. Z. Wen, Q. Wang, J. Li, Template synthesis of aligned carbon nanotube arrays using glucose as a carbon source: Pt decoration of inner and outer nanotube surfaces for fuel-cell catalysts. *Adv. Funct. Mater.* **18**(6), 959–964 (2008)
94. W.R. Davis, R.J. Slawson, G.R. Rigby, An unusual form of carbon. *Nature* **171**, 756–756 (1953)
95. W. Hu, D. Gong, Z. Chen, L. Yuan, K. Saito, C.A. Grimes, P. Kichambare, Growth of well-aligned carbon nanotube arrays on silicon substrates using porous alumina film as a nanotemplate. *Appl. Phys. Lett.* **79**(19), 3083–3085 (2001)
96. L. Yuan, K. Saito, W. Hu, Z. Chen, Ethylene flame synthesis of well-aligned multi-walled carbon nanotubes. *Chem. Phys. Lett.* **346**(1–2), 23–28 (2001)
97. M. Reibold, P. Paufler, A.A. Levin, W. Kochmann, N. Patzke, D.C. Meyer, Materials: Carbon nanotubes in an ancient damascus sabre. *Nature* **444**(7117), 286–286 (2006)
98. L. Yuan, K. Saito, C. Pan, F.A. Williams, A.S. Gordon, Nanotubes from methane flames. *Chem. Phys. Lett.* **340**(3–4), 237–241 (2001)
99. M.J. Height, J.B. Howard, J.W. Tester, J.B.V. Sande, Flame synthesis of single-walled carbon nanotubes. *Carbon* **42**(11), 2295–2307 (2004)
100. M.D. Diener, N. Nicholson, J.M. Alford, Synthesis of single-walled carbon nanotubes in flames. *J. Phys. Chem. B* **104**(41), 9615–9620 (2000)
101. L. Yuan, T. Li, K. Saito, Growth mechanism of carbon nanotubes in methane diffusion flames. *Carbon* **41**(10), 1889–1896 (2003)
102. R.L. Vander Wal, G.M. Berger, L.J. Hall, Single-walled carbon nanotube synthesis via a multi-stage flame configuration. *J. Phys. Chem. B* **106**, 3564–3567 (2002)
103. W. Merchan-Merchan, A. Saveliev, L.A. Kennedy, A. Fridman, Formation of carbon nanotubes in counter-flow, oxy-methane diffusion flames without catalysts. *Chem. Phys. Lett.* **354**(1–2), 20–24 (2002)
104. L.V. Radushkevich, V.M. Lukyanovich, About the carbon structure, thermal CO decomposition on metal contact synthesized. *J. Phys. Chem. Russia* **26**, 88–95 (1952)
105. H. Boehm, Carbon from carbon monoxide disproportionation on nickel and iron catalysts: Morphological studies and possible growth mechanisms. *Carbon* **11**(6), 583–586 (1973)
106. H. Dai, A.G. Rinzler, P. Nikolaev, A. Thess, D.T. Colbert, R.E. Smalley, Single-wall nanotubes produced by metal-catalyzed disproportionation of carbon monoxide. *Chem. Phys. Lett.* **260**(3–4), 471–475 (1996)
107. P. Nikolaev, M.J. Bronikowski, R.K. Bradley, F. Rohmund, D.T. Colbert, K.A. Smith, R.E. Smalley, Gas-phase catalytic growth of single-walled carbon nanotubes from carbon monoxide. *Chem. Phys. Lett.* **313**(1–2), 91–97 (1999)
108. P. Nikolaev, Gas-phase production of single-walled carbon nanotubes from carbon monoxide: A review of the HiPco process. *J. Nanosci. Nanotechnol.* **4**(4), 307–316 (2004)
109. T.V. Hughes, C.R. Chambers, Manufacture of carbon filaments”, in U.S. Patent 000405480, 1889
110. M.I. Ionescu, Y. Zhang, R. Li, X. Sun, H. Abou-Rachid, L.-S. Lussier, Hydrogen-free spray pyrolysis chemical vapor deposition method for the carbon nanotube growth: Parametric studies. *Appl. Surf. Sci.* **257**(15), 6843–6849 (2011)

111. W.K. Hsu, J. Hare, M. Terrones, H. Kroto, D.R. Walton, P.J. Harris, Condensed-phase nanotubes. *Nature* **377**(6551), 687–687 (1995)
112. W. Hsu, M. Terrones, J. Hare, H. Terrones, H. Kroto, D. Walton, Electrolytic formation of carbon nanostructures. *Chem. Phys. Lett.* **262**(1–2), 161–166 (1996)
113. W.K. Hsu, J. Li, H. Terrones, M. Terrones, N. Grobert, Y.Q. Zhu, S. Trasobares, J.P. Hare, C.J. Pickett, H.W. Kroto, D.R.M. Walton, Electrochemical production of low-melting metal nanowires. *Chem. Phys. Lett.* **301**(1–2), 159–166 (1999)
114. G.Z. Chen, I. Kinloch, M.S.P. Shaffer, D.J. Fray, A.H. Windle, Electrochemical investigation of the formation of carbon nanotubes in molten salts. *High Temp. Mater. Process.* **2**(4), 459–469 (1998)
115. M. Terrones, Science and technology of the twenty-first century: Synthesis, properties, and applications of carbon nanotubes. *Annu. Rev. Mater. Res.* **33**, 419–501 (2003)
116. H. Dai, Carbon nanotubes: Opportunities and challenges. *Surf. Sci.* **500**(1–3), 218–241 (2002)
117. H.J. Dai, Nanotube growth and characterization, in *Carbon Nanotubes: Synthesis, Structure, Properties, and Applications*, vol. 80, ed. by M.S. Dresselhaus, G. Dresselhaus, P. Avouris, Topics in Applied Physics, (Springer, Berlin, 2001), pp. 29–53
118. D. Laplaze, P. Bernier, W. Maser, G. Flamant, T. Guillard, A. Loiseau, Carbon nanotubes: The solar approach. *Carbon* **36**(5–6), 685–688 (1998)
119. L. Alvarez, T. Guillard, J. Sauvajol, G. Flamant, D. Laplaze, Solar production of single-wall carbon nanotubes: growth mechanisms studied by electron microscopy and raman spectroscopy. *Appl. Phys. A: Mater. Sci. Process.* **70**(2), 169–173 (2000)
120. C. Baddour, C. Briens, Carbon nanotube synthesis: a review. *Int. J. Chem. Reactor Eng.* **3**, R3 (2005)
121. N. Bajwa, X. S. Li, P.M. Ajayan, R. Vajtai, Mechanisms for catalytic CVD growth of multi-walled carbon nanotubes. *J. Nanosci. Nanotechnol.* **8**(11), 6054–6064 (2008)
122. Q. Zhang, J.-Q. Huang, M.-Q. Zhao, W.-Z. Qian, F. Wei, Carbon nanotube mass production: Principles and processes. *ChemSusChem* **4**, 864–889 (2011)

Chapter 4

Chemical Vapor Deposition of Carbon Nanotubes

Chemical vapor deposition (CVD) has been a chemical process used to produce high-purity, high-performance thin films in the semiconductor industry. Now, CVD is a promising method to grow carbon nanotubes (CNTs) because it is easy to be scaled up to produce CNTs with different area to meet different requirements. Moreover, the lower reaction temperature in the CVD process also makes it possible to synthesize CNTs directly on many substrates. Large scale of aligned CNT arrays have been grown by either thermal CVD [1–4] or plasma-enhanced CVD [5–8].

In a typical CVD process of CNTs, a substrate is coated with a nanolayer of metal catalyst particles, most commonly nickel, cobalt, iron, or a combination. The substrate is exposed to one or more volatile precursors. The metal catalytic nanoparticles can be prepared by many methods as discussed in Sect. 6.1.6. The carbon-containing gas is broken apart by heating or plasma during CVD procedure. The carbon is transported to the surface of the catalytic nanoparticles, where it forms the CNTs at the sites of the metal catalyst. The by-products are usually removed by gas flow through the reaction chamber.

According to the decomposition method of carbon-containing gasses, the CVDs can be categorized into thermal CVD and plasma-enhanced CVD (PECVD). In this chapter, we introduce the variety of CVD techniques, including thermal CVD and various plasma-enhanced CVD, the CVD growth mechanism, and alignment of CNTs using these methods.

4.1 Thermal Chemical Vapor Deposition

The design of thermal CVD is simple. The carbon-containing gasses (such as acetylene, ethylene, ethanol, and methane) are pyrolyzed by high temperature. The growth temperature is usually high, 700–1,200 °C, in order to pyrolyze the reaction gas. According to the type of heating, there are two kinds of thermal CVD. One is hot-wall CVD and another is hot-wire CVD.

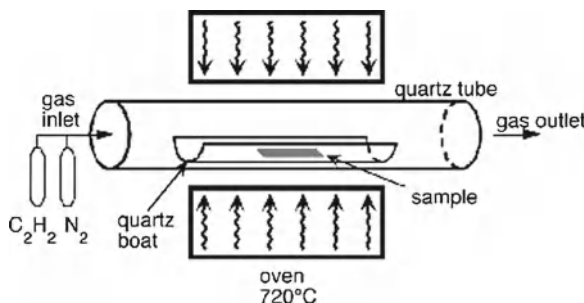


Fig. 4.1 Hot-wall thermal CVD experimental setup. The chamber reactor is heated by an electrical furnace during the hot-wall CVD process

Large arrays of vertically aligned carbon nanotubes with anisotropic properties have been successfully synthesized by the thermal CVD, such as the water-assisted thermal CVD and atmosphere thermal CVD because of a crowding effect coming from the van der Waals force among neighbors in the dense CNTs [4, 9]. The details are described in Sect. 6.1.1. The thermal CVD grown CNTs are widely considered suitable for direct integration into various functional systems, like gecko tape [10] and black body absorber [11], as talked about in Chap. 9.

4.1.1 Hot-Wall Chemical Vapor Deposition

Figure 4.1 shows the equipment of hot-wall CVD. It is consisted of a reaction chamber and a heating furnace. The reaction chamber normally consists of a quartz tube and the CVD growth process is performed in the tube. A high-temperature electric tube furnace provides energy to heat the reaction chamber to pyrolyze the gasses. The reaction temperature range is usually higher than 700 °C, even up to 1,250 °C.

In a typical hot-wall CVD growth under vacuum, the catalyst is coated on substrates first before being loaded into the quartz-tube reactor. Then, the chamber is pumped down to 0.1 Torr before raising the temperature to 750 °C [13]. Once the temperature of the reactor reaches 750 °C, NH₃ gas is delivered to the reactor at 80 standard cubic centimeter per minute (sccm) for 10 min, and then C₂H₂ (feed gas) is introduced at 20 sccm for the duration of the growth. Growth times of 10, 30, and 60 min are used. After the growth, the samples are cooled down to 250 °C under vacuum and then removed from the reactor. Usually, the grown CNTs are curved [12, 14], as shown in Fig. 4.2. Bamboo-like CNTs can be synthesized using the thermal CVD [15].

There are hundreds of papers reported CNT growth using the method. The interested readers are referred to some review papers and books.

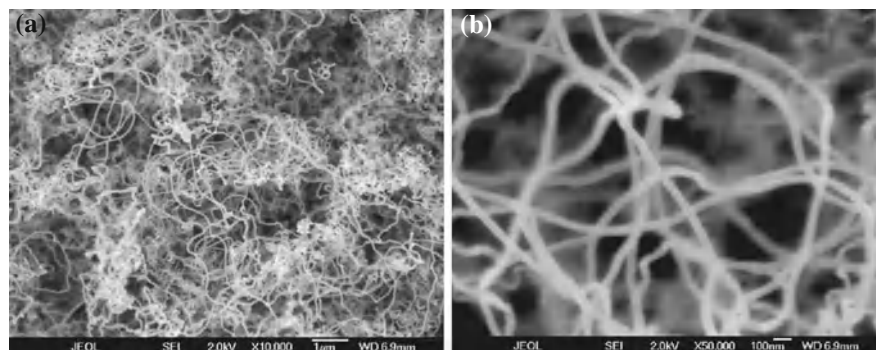


Fig. 4.2 SEM images of curved CNTs grown by hot-wall CVD. From Chen et al. [12]. Reprinted with permission from Elsevier. **a** Low, and **b** high magnification

If an external field, such as electric field or force field, is applied in the thermal CVD process, straight CNTs can be grown along a certain direction. We will talk about it in Chap. 6.

Without the external fields, the thermal grown nanotubes are usually randomly oriented besides the curved morphology. Only under some certain reaction conditions without a external field, closely spaced nanotubes can maintain a vertical growth direction resulting in a dense array of nanotubes resembling a carpet or forest [10, 11, 16–20]. Such certain reaction conditions can be created by a hot-wall CVD growth under atmosphere or by a water-assisted thermal CVD growth.

Figure 4.3 shows CNT arrays grown under atmosphere using the hot-wall CVD method. The CNT arrays are several millimeters [18]. In the CNT array growth, immediately after annealing of catalyst, the quartz tube is pumped down to about 1 mTorr, followed by introducing flowing gasses of H_2 (100 sccm) and C_2H_4 (110 sccm) with the pump turned off. When the pressure reaches at one atmosphere (about 760 Torr), a valve is open to atmosphere to maintain the pressure inside the tube at 760 Torr. The thermal CVD growth is carried out at 715–760 °C for 5–60 min. The grown CNTs are macroscopic straight and vertical to the substrate, as shown in Fig. 4.3a, b. The longest CNTs is about 2.2 mm (Fig. 4.3a), achieved with an optimal annealing pressure at 200 Torr with the optimal growth parameters of 100 sccm H_2 , 110 sccm C_2H_4 at 745 °C, 760 Torr, and for 45 min [18]. Higher magnification SEM (Fig. 4.3c) and HRTEM image (Fig. 4.3d) indicate that the diameter of the thermal CVD grown CNTs are very small. The CNT growth is very sensitive to the growth conditions including flow rate of feeding gasses, gas pressure and temperature at the growth zone during growth, and growth time [18, 20].

As a variation of thermal CVD, water-assisted chemical vapor deposition can grow super-long CNT arrays [19]. In this kind of process, the activity and lifetime of the catalyst are enhanced by addition of water into the thermal CVD reactor. Vertically aligned SWCNT nanotube forests with millimeter length can be synthesized on the substrate surface [21]. The growth sites are controllable by careful deposition of the catalyst. Various shapes of single-walled nanotube structures were successfully

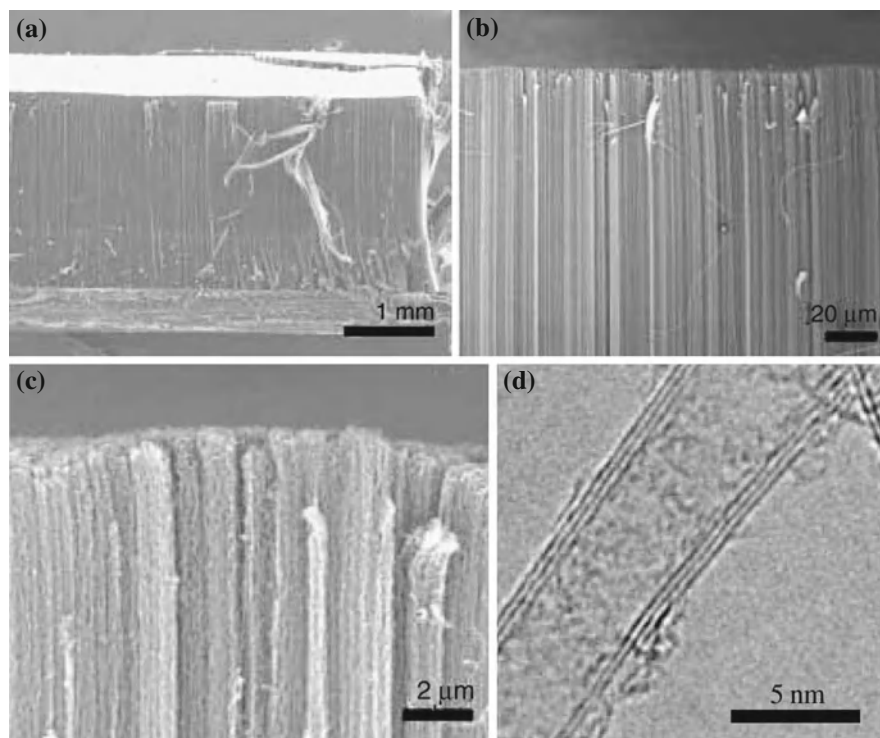


Fig. 4.3 SEM images of CNTs grown under atmosphere on single crystal MgO substrates coated with Fe film. From Xiong et al. [18]. Reprinted with permission from Elsevier. **a** Low magnification showing the length of CNTs and the thickness of MgO substrate. **b** Medium magnification showing the good alignment. **c** High magnification showing the wavy nature of the alignment. **d** HRTEM of a typical MWCNT

fabricated on patterned catalysts using the super-growth technique. The details of CNT forests grown by thermal CVD are discussed in Sect. 6.1.1.

The synthesis efficiency of thermal CVD is about 100 times higher than that of the laser ablation method. The time required to make SWCNT forests of the height of 2.5 mm by the water-assisted CVD method is 10 min [19]. Those CVD grown SWCNT forests can be easily separated from the catalyst, yielding clean SWCNT material (purity > 99.98 %) without further purification.

4.1.2 Hot-Wire Chemical Vapor Deposition

The equipment of hot-wire CVD is similar to the hot-wall CVD while a hot-wire (sometimes termed as hot-filament) instead of an electric furnace is employed to chemically pyrolyze the source gasses. The hot-wire CVD costs less energy than the hot-wall CVD.

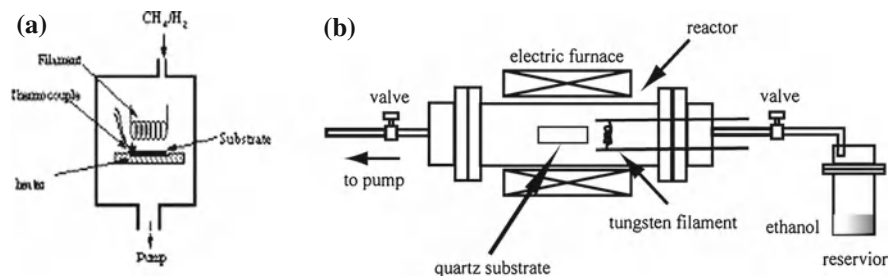


Fig. 4.4 Hot-wire thermal CVD experimental setup. **a** Hot-wire CVD without an external heater. **b** Hot-wire CVD with a furnace heater. From Sugai et al. [22]

In the simplest hot-wire CVD without heater, the gas activation required for CVD process is achieved by heating the filament (typically, tungsten) up to 2,200 °C. The CNTs are deposited on the substrate surface directly (Fig. 4.4a). Usually, the substrate is heated by the thermal irradiation from the filament.

In a hot-wire CVD with a heater, the substrate is heated by an electric furnace, shown in Fig. 4.4b, and the substrate temperature is independently controlled using an external heater. The distance between the filament and the substrate, a crucial parameter, can be adjusted from a few millimeters to a few centimeters to produce CNTs [22].

The growth mechanism of hot-wire CVD is the same as that of hot-wall CVD and will be discussed in Sect. 4.1.3

4.1.3 Thermal Chemical Vapor Deposition Growth Mechanism of Carbon Nanotubes

In the thermal CVD process, the catalyst is one of the key factors in CNT growth. Nickel, cobalt [24], stainless steel [25, 26], gold, platinum, and even tungsten have been the catalyst for CNT growth. Recent study shows that most metals can be used as catalyst to grown CNTs. A summary of the catalysts of CNT growth can be found in the literatures [27]. Usually, catalyst Ni, Co, their alloys or oxides are used as catalyst. Figure 4.5 shows the phase diagram of carbon with nickel. Nickel decreases the growth temperature of CNTs. The phase diagrams of carbon with other metals are similar [23].

In a conventional thermal CVD, the growth of CNTs occurs in three main steps [28]: (i) decomposition/pyrolysis of the carbonaceous gas molecules; (ii) diffusion of the resultant carbon atoms through the catalytic nanoparticle from the nanoparticle/gas interface toward the nanoparticle/nanotube interface due to the concentration gradient; and (iii) precipitation of carbon atoms at the nanoparticle/nanotube interface. In the third main step, CNTs grow catalytically and then thicken via a catalyst-free pyrolytic carbon deposition mechanism [29–33]. Each of these steps

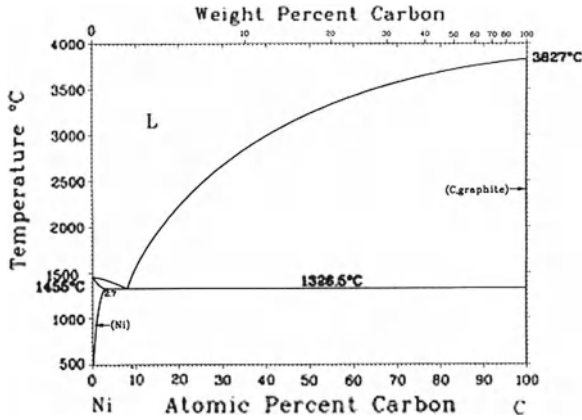


Fig. 4.5 Carbon–nickel phase diagram. From Bassalski and Okamoto [23]

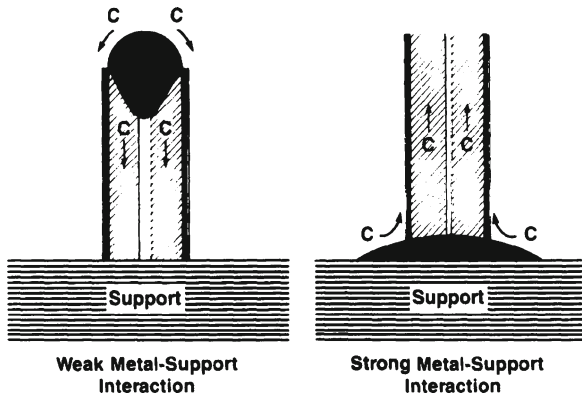


Fig. 4.6 Influence of the metal-support interaction on the mode of growth of filamentous carbon. From Baker [28]

can be a complex process. Recent in situ HRTEM analysis during the CNT growth confirmed the growth mechanism [34].

In the thermal CVD process based on vapor–liquid–solid model, the catalytic nanoparticles become liquid droplets at high enough temperature. These droplets accept carbon atoms from vapor and get saturated. CNTs grow by precipitation of dissolved carbon atoms in the droplets. Meanwhile, the droplets are lifted up by growing CNTs (Fig. 4.6a) or still adhere to the substrate surface (Fig. 4.6b), depending on the interaction between catalyst and substrate. If the catalytic droplets are lifted up, the droplets are elongated to form pear-shaped or rod-like at the top of the CNTs because of the gravity.

The time-resolved, high-resolution in situ transmission electron microscope observations [35] of the formation of carbon nanofibres from methane decomposition

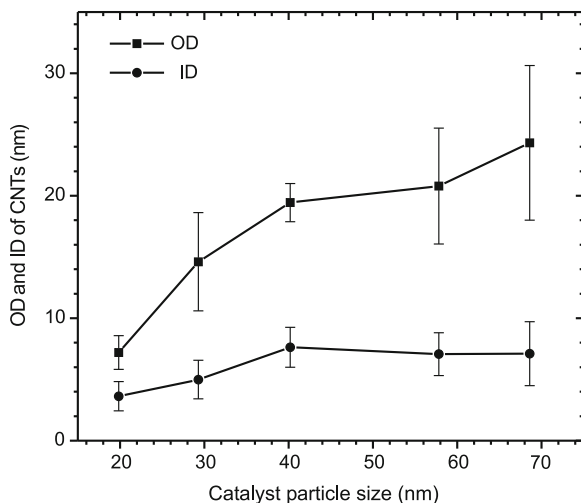


Fig. 4.7 Dependence of outer diameter (OD) and inner diameter (ID) of CNTs (with error bar) on the diameter of catalytic nanoparticles. From Li et al. [37]. Reprinted with permission from Elsevier. The CNTs were synthesized by thermal CVD method using stainless steel as catalyst

over nickel nanocrystals indicates that graphene layers nucleate and grow on the monoatomic step edges at the nickel surface. The carbon nanofiber growth depends on the surface diffusion of carbon and nickel atoms and the nickel metallic step edges act as spatiotemporal dynamic growth sites.

4.1.4 Experimental Condition of Carbon Nanotube Array Growth

Many experimental parameters, catalyst, gasses, temperature, and pressure, affect the CNT growth in the thermal CVD process. Below we talk about the effects of each of these parameters briefly. The readers are referred to some review literatures on CVD growth [36].

Catalyst. The diameter of thermal CVD grown CNTs depends on the catalyst size. The average outer diameter of MWCNTs increases with the diameter of the catalytic nanoparticles (Fig. 4.7). Compared with outer diameter, the inner diameter of MWCNTs increases slightly with the size of catalytic nanoparticles and saturates faster. CNTs cannot grow on catalyst particles with very small diameter. At a reaction temperature of 660 °C in CVD process, the optimum catalyst particle diameter is 40 nm for the growth of CNTs with high density and purity [25].

Detailed experimental data show that there is an effective diameter range of catalyst particles for growing CNTs. Theoretical work [38] indicates that energy of the carbon atoms on the nanotube wall is inversely proportional to the square of the radius of CNTs. In other words, the smaller the diameter of the CNTs, the more

energy the carbon atoms need to form the nanotube wall. In order to grow CNTs on small catalytic nanoparticles, much higher temperature is necessary in CNT growth process [39, 40]. In a thermal CVD, the smallest inner diameter of the MWCNTs is about 3 nm at 660 °C [25]. Single-walled CNTs with diameter ranging from 1 to 5 nm have also been synthesized by CVD at 1,000 °C [39, 41]. However, the smallest inner diameter of the CNTs from arc-discharge is about 0.7 nm, which is compatible with the diameter of C₆₀ [42]. It is believed that the temperature in arc-discharge process is as high as 3,000 °C and carbon atoms evaporated from the graphite rod can obtain enough energy at such high temperature to form CNTs with small diameter.

It is noted that CNTs with smaller diameter can be synthesized by increasing the growth temperature in the CVD process. The average inner diameter of the CNTs is smaller than that of the corresponding catalyst particles, in thermal CVD process [37] as well as in microwave PECVD process [6].

The CNT growth sites are controllable by deposition of the catalyst. Various shapes of CNT films can be grown from the patterned catalyst. The role of catalyst on CNT growth is reviewed recently [43–45].

Gasses. The gas precursors affect the quality of CNTs. If the C₂H₂ concentration is higher, like the ratio of acetylene and ammonia is 40:160 sccm, many CNTs are encircled by amorphous carbon and carbon nanoparticles that result in a rough surface [46]. This observation is explained as carbon over-supply during the CNT growth. In Based on the catalytic growth mechanism, the difference of carbon concentrations across the catalyst surface makes carbon diffuses in and segregates from catalytic nanoparticles. However, it is well known that the carbon concentration inside the catalyst, for any certain temperature, is limited by carbon solid solubility. Once the maximum concentration of carbon has been reached in the catalytic nanoparticles, the extra carbon will directly deposit on CNT surfaces. Therefore, a decrease in the gas ratio of acetylene to ammonia should reduce or remove amorphous carbon and carbon nanoparticles on CNTs.

Gas purification is also an essential step in obtaining reliable nanotube growth [47]. Even subparts per million levels of oxygen-containing species in gasses can significantly modify the vertically aligned CNT growth kinetics.

Pressure and temperature. In the thermal CVD method, the temperature is 600–1,050 °C and the pressure is 0.6–760 Torr [48]. The growth temperature is crucial in synthesizing CNTs with different structures [37]. At low gas pressure, the CNTs are completely hollow at low growth temperature and bamboo-like structure at high growth temperature. While at high gas pressure, all the CNTs are bamboo-like structure regardless of growth temperature [48]. Bamboo-like CNTs are usually synthesized above 600 °C [49].

The effect of pressure and temperature on the CNT structure can be explained by the growth mechanism of CNTs in CVD. It is generally accepted that CNTs are formed by carbon atom dissolving, diffusing, and precipitating through the catalyst droplets in CVD process [28, 50, 51]. The dissolving, diffusing and precipitating rates of the carbon atoms are affected by both the carbon atom concentration and the temperature. The carbon precipitation region on the catalytic droplets can be distinguished into two areas, side area and back area [50]. At low gas pressure, such

as 0.6 Torr, the carbon concentration from the decomposition of C_2H_2 is certainly low. At growth temperature lower than $700^\circ C$, the dissolving and diffusing rates are limited by the low concentration of carbon atoms so that carbon atoms can only precipitate on the side area of the catalyst droplets to form completely hollow CNTs. With the increase of the temperature, the dissolving and diffusing rates of carbon atoms will increase, and carbon atoms can get to the back area of the catalyst droplet to form bamboo-like CNTs. At high gas pressure of 760 Torr, the carbon concentration is high enough for the precipitating at both side and back areas of the catalytic droplets to form bamboo-like CNTs [48].

Temperature and pressure affect the CNT yield too. Experiments indicate that the CNT yield decreases with temperatures higher than $800^\circ C$ at 0.6 Torr and $900^\circ C$ at 760 Torr. The yield decrease can be explained from two aspects [48]. First, if the temperature is too high, chemical reaction between carbon and catalyst may take place to form catalyst carbide, causing the catalysts to lose catalytic activity for growing CNTs. Second, the high carbon concentration resulted from high temperature may cause the dissolving rate higher than diffusing and precipitating rates, carbon atoms will accumulate on the surface of catalysts to form a carbon shell, as a result, the catalysts lose their catalytic activity. Once the catalysts lose activity, the growth of CNTs stops.

4.2 Plasma-Enhanced Chemical Vapor Deposition

PECVD utilizes plasma to enhance chemical reaction rates of the precursors and to deposit thin films from a vapor to a solid state on a substrate. PECVD processing allows deposition at lower temperatures, which is often critical in the manufacture of semiconductors. Compared with the thermal CVD method, the growth temperature is insignificantly decreased by the plasma in PECVD method [52, 53].

Chemical reactions involved in the deposition process occur after the creation of plasmas of the reacting gasses. The plasma is generally created by radio frequency (RF) or direct current (DC) discharge between two electrodes, the space between which is filled with the reacting gasses.

The physical properties of the grown CNTs are easily influenced by PECVD than by the thermal CVD deposition technique, because more process parameters can be varied in PECVD. Additionally, the hydrogen content, etching ability, etching rate and selectivity in etching, step coverage as well as stoichiometry, etc., can be adjusted during the PECVD growth.

There are many kinds of PECVD to synthesize CNTs [54, 55]. Based on heating methods, there are back-heated PECVD, hot-filament PECVD, and the simplest PECVD without heating source. Based on plasma sources, PECVD can be categorized as DC PECVD, RF-PECVD, microwave PECVD, etc. The actual PECVD system can be any combination of a plasma source and an external heating source.

In the simplest DC PECVD without heating source, the gas precursors are decomposed by the DC plasma and the produced radicals are deposited on the substrate

surface. The substrate temperature (growth temperature) is usually higher than room temperature because the substrate is heated by the plasma, depending on the intensity and energy of plasma.

In most of the PECVD processes reported in the literatures, the substrate is usually heated by an external heating source and the substrate temperature is controlled by the heating sources. In principle, an electric furnace or an IR lamp can be used as the external heating source. In all these PECVD with heating sources, the substrates are normally heated not only directly by the plasma but also by these external heating sources when used or activated. In the back-heated PECVD, the substrate is heated by a resistance heater beneath the substrate-holding platform in order to control the growth temperature accurately [56, 57]. In the case of the hot-filament PECVD, a hot filament hanging over the substrate has been employed as the heating source [5, 58–60].

Below, we introduce PECVD according to the plasma sources. The advantage of PECVD over thermal CVD is that a plasma is generated in the PECVD growth process to lower the growth temperature while the voltage potential used to produce the plasma directs the CNT growth. CNT arrays have been successfully synthesized using these PECVD techniques. The applications of the aligned CNTs grown by PECVD will be introduced in Chaps. 8, and 9.

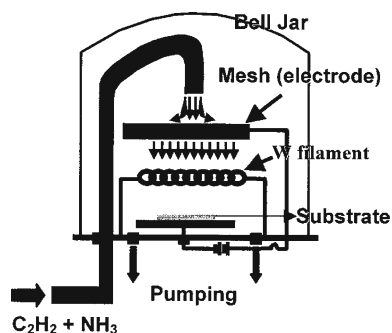
4.2.1 Direct Current Plasma-Enhanced Chemical Vapor Deposition

A DC PECVD is mainly consisted of a DC power supply and a vacuum system. The substrate can be heated by a heater located at the back of the substrate (back-heated PECVD) or by a hot-filament (hot-filament PECVD). A typical DC hot-filament PECVD system with a plate–plate electrode configuration is shown in Fig. 4.8. Sometimes, a rod–plate electrode configuration is employed [61] to decrease the voltage potential used to produce plasma between the electrodes. The anode-to-cathode distance is in centimeters. A DC power supply, configured to a constant-current mode, is used to control the discharge current level whose intrinsically associated bias voltage is automatically supplied.

During the DC PECVD growth, ammonia (NH₃) and acetylene (C₂H₂) gasses may, theoretically, generate more than 100 species by almost 900 chemical reactions [59]. Regardless of the trace species and extremely slow reactions, it was suggested that the remained 175 reactions could produce 20 neutral species as [59]:



Fig. 4.8 Schematic diagram of DC plasma enhanced hot-filament chemical vapor deposition reactor. From Han et al. [60]



plus CN, HCN, and HC_3N formed as the result of further reaction of the above products. In addition, there are four kinds of charged species (NH_3^+ , NH_2^+ , C_2H_2^+ , and e^-) generated from the chemical reactions. It is noted [62] that the CNT growth by PECVD processing is under a very complicated environment, in addition to the effects of other working parameters such as heating temperature, gas flow speed, gas ratio ($\text{C}_2\text{H}_2/\text{NH}_3$), gas pressure, and the strength of plasma etching.

Aligned CNTs have been grown in PECVD chambers, running gasses, such as an acetylene–ammonia gas mixture (80:160 sccm) with a heated cathode at 500°C and a DC power source for plasma ignition operating at 515 V [63]. Vertically aligned CNT arrays have been produced by the DC PECVD method [7, 8, 15, 52, 53, 60, 64–68].

The typical DC current density is in the range of $0.1\text{--}1\text{ mA/cm}^2$ [5, 52, 59, 65, 68–70] when vertically aligned CNT arrays are synthesized. In some cases, well-aligned CNTs can also grow at a very low current (2–3 orders of magnitude lower, $<6.2\text{ }\mu\text{A/cm}^2$) at a dark discharge condition [61, 64, 65].

Usually, the base pressure of the deposition chamber is $<6 \times 10^{-6}$ Torr and CNT arrays are grown in a pressure of 1–20 Torr maintained by flowing gasses with a total flow rate of 120–200 sccm.

Besides the growth temperature and growth time, the plasma intensity affects the morphology of CNT greatly. The CNT diameter increases with the plasma intensity. The growth rate is also higher at higher plasma intensity.

Well-aligned CNT arrays have been fabricated by PECVD method. Figures 2.5, 2.6, and 2.7 show SEM images of the aligned CNT arrays grown by DC PECVD. The grown CNTs are straight, well ordered on substrates.

Below, we give two typical experimental conditions of PECVD to grow aligned CNTs.

During a typical back-heated DC PECVD experiment, NH_3 and C_2H_2 are first introduced into the vacuum chamber ($\sim 10^{-2}$ Torr base pressure) after the substrate is loaded with catalyst. The system pressure is held at ~ 8 Torr during the whole CNT growth. Then a DC discharge is initiated between two electrodes, glowing in a whitish-blue color covered the whole cathode surface, and manipulated in the PECVD procedure. At same time, the temperature of the cathode surface, monitored

by a thermocouple, is kept at several hundred Celsius by adjusting the heater backing the cathode plate.

In a typical hot-filament PECVD procedure, the PECVD system is pumped down to 2×10^{-6} Torr, then 160 sccm ammonia gas is introduced into the chamber and the temperature is increased by applying current on the tungsten filament [49]. 100 W DC plasma is applied for 10–20 s first to pre-etch the catalytic nanoparticles, then 40 sccm acetylene gas is introduced and the plasma intensity is increased to 170 W for the aligned CNTs growth. The pressure during growth is about 15 Torr. Both acetylene and ammonia have minimum purity of 99.99%. CNT arrays with length of microns can be grown using the procedure when the growth time is 5 min and the growth temperature is below 660 °C. The growth durations are from 10 min to 5 h depending on the desired CNT lengths [71]. The CNTs are oriented perpendicular to the substrate surface and are quite uniform in height.

4.2.2 Radio-Frequency Plasma-Enhanced Chemical Vapor Deposition

Figure 4.9 shows the structure of a radio-frequency PECVD (RF-PECVD) [72]. The RF-PECVD equipment is consisted of a reactor formed by a metal cathode and a metal anode, a solid state RF generator, and pumping systems. The substrate is located on the cathode whose temperature can be controlled using a resistive heater and measured by a thermocouple. The substrate temperature is also the growth temperature. Using a RF generator, the plasma is formed in the reaction chamber. The produced plasma contains reactive ions and radicals. The CNT growth starts easily because of the activation and cleaning of the surface by less intense bombarding with ions from the plasma.

MWCNT arrays can be synthesized using the RF-PECVD (Fig. 4.10). The grown CNT arrays are dense and aligned vertically to the substrate surface [73, 74].

4.2.3 Microwave Plasma-Assisted Chemical Vapor Deposition

Besides DC and RF sources, microwave can also be used to produce plasma to grow CNT arrays [6–8, 76–79].

A microwave plasma-enhanced CVD mainly consists of a microwave magnetron, a circulator, a four-stub tuner, a cavity, and a waveguide [75]. Figure 4.11a illustrates the structure of a microwave-assisted PECVD system. The microwave power can be adjusted from 0 to 3,000 W at the frequency of 2.45 GHz generated from the microwave magnetron. The function of the circulator is to prevent power being reflected by the load, thus avoiding overheating of the magnetron. The four-stub tuner, consisting of four threaded stubs spaced three-eighth of a wavelength apart, is

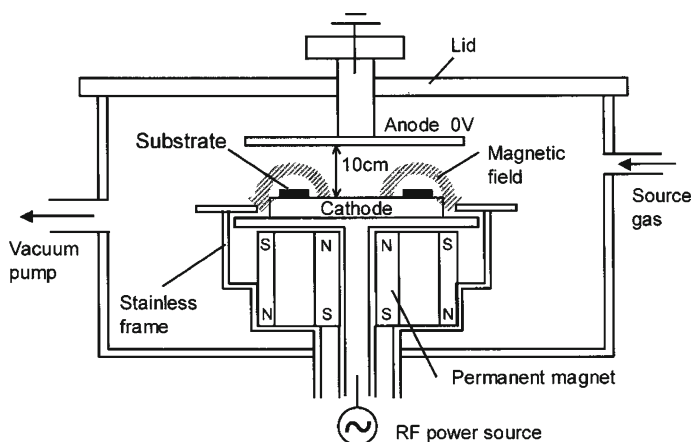


Fig. 4.9 Schematic illustration of a RF-PECVD system. From Shiratori et al. [72]. The substrate is back-heated

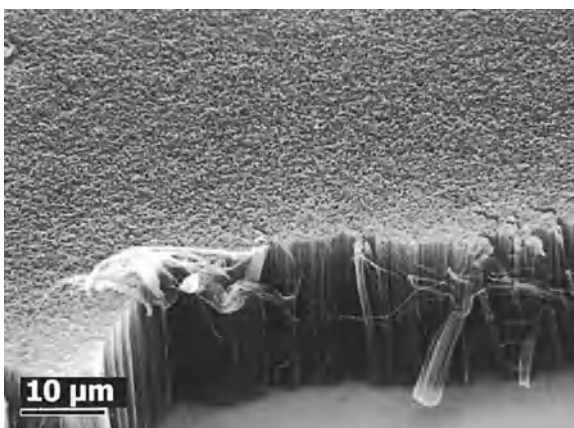


Fig. 4.10 SEM image of MWCNTs grown by RF-PECVD method. From Delzeit et al. [73]. Growth pressure: 20 Torr; growth temperature: 800 °C; growth time: 10 min; CH₄/H₂/Ar: 50/50/1,000 sccm; inductive power: 100 W; RF power to the substrate: 100 W; self-bias: 25 V; catalyst: Fe(10 nm)/Al(10 nm)

an additional device used to optimize impedance matching. Sliding short is used to adjust the length of the cavity such that the cavity can resonate at 2.45 GHz. High field intensity could be attained when the cavity resonates. A quartz tube, which is used as the reaction chamber, passes through the cavity. Reaction gasses are introduced at one end of the quartz tube and exhausted at the other end. The flow rates are controlled by the set of the mass/master flow controller.

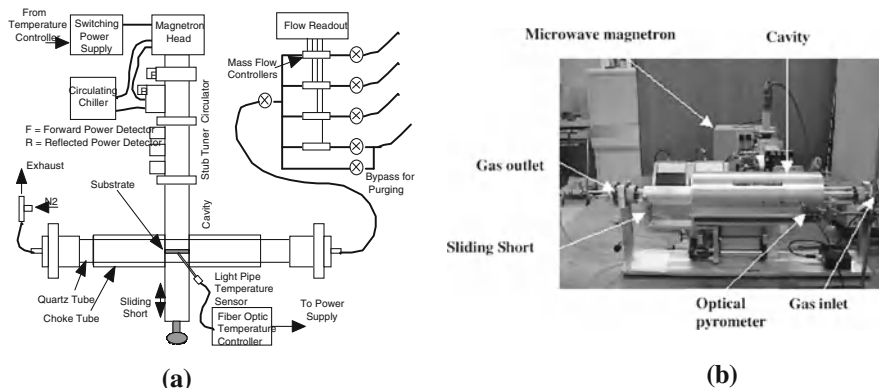


Fig. 4.11 **a** Microwave-assisted CVD system for large-scale fabrication of CNTs. **b** Actual microwave-assisted CVD system for CNT fabrication. From Varadan and Xie [75]

In the microwave CVD system, SiC is usually chosen as the substrate due to its moderate loss tangent, thus it could absorb microwave energy effectively. An actual photograph of the system is shown in Fig. 4.11b.

In a typical case, after substrates are placed in a RF-PECVD chamber with the pressure reduced to below 1 Pa, a reaction gas is introduced to maintain a working pressure of $1 \times 10^2 - 4 \times 10^3$ Pa [77]. The total flow rate of methane and hydrogen is about 100 sccm and the microwave power is 500 W. The reaction time is 30 min, during the course of a negative voltage of -250 V is applied, and the CNTs grow to about 30 μm .

Microwave-assisted CVD is considered as a cost-effective method to synthesize large-scale CNTs in the order of kilograms due to the fast heating and cooling processes. The microwave-assisted CVD method can also produce coiled multi-walled nanotubes [75], as shown in Fig. 2.20b.

4.2.4 Plasma-Enhanced Chemical Vapor Deposition Growth Mechanism of Carbon Nanotube Alignment

Before the famous work of Iijima in 1991, the thermal CVD growth mechanism of carbon hollow nanofibers have been widely studied [80, 81], as discussed in Sect. 3.3. The PECVD growth mechanism of CNTs are similar to that of thermal CVD. The readers are referred to the related literatures.

The thermal CVD grown CNTs are usually curved [82], as shown in Fig. 4.2. In the water-assisted thermal CVD and atmosphere thermal CVD, the grown CNTs are still curved while these cured CNTs are aligned vertically to the substrate surface because of the crowding effect. On the contrast, PECVD can produce vertical and straight CNT.

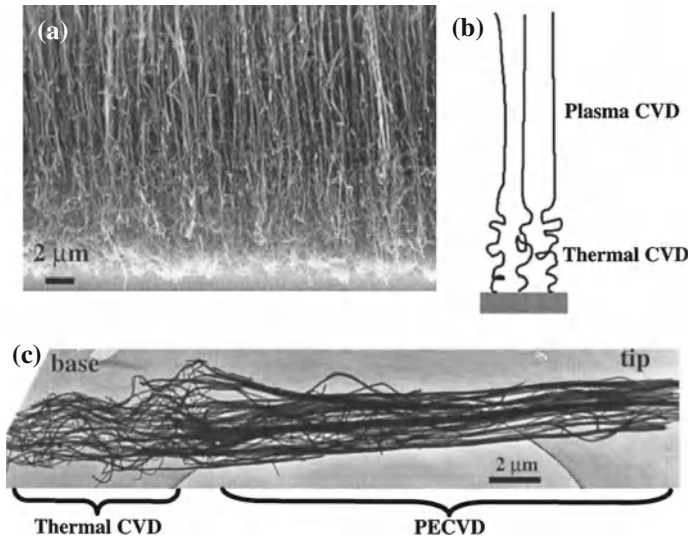


Fig. 4.12 **a** SEM micrograph and **b** schematic illustration showing the aligned nanotube structure produced by a 2 min thermal CVD process followed by a 70-min PECVD process, indicating both the electric-field induced alignment effect and the base growth mechanism. **c** TEM micrograph showing a bundle of nanotubes with the *upper portion* straight and the *lower portion* curled. From Bower et al. [7]

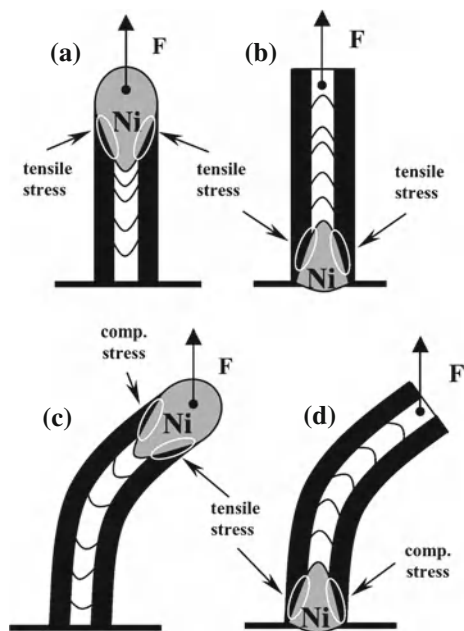
In Fig. 4.12, the CNTs are grown first by a thermal CVD without a plasma (lower portion of CNTs shown in Fig. 4.12) followed by a PECVD with a plasma (shown as the upper portion in Fig. 4.12). The PECVD grown CNTs are straight while the thermal CVD grown CNTs are curved while both of them are aligned vertically to the substrate surface.

The electric field affects the alignment of CNT during CVD growth. It is observed that aligned straight CNTs can be grown when a positive bias is applied to the substrate in a thermal CVD procedure whereas no aligned growth occurs under a negative bias or no bias [83, 84] (details are discussed in Chap. 6). Other experiments also confirm that the CNTs mainly grow along electric fields [85]. These observations indicate that the electric field plays an important role in the alignment of CNTs. There is a strong electric field during the PECVD growth process when a plasma is generated and the CNTs should grow along the direction of the plasma in a CNT growth.

Therefore, it is reasonable to mention [54] that CNTs grown by PECVD are more vertically aligned than thermal CVD grown structures, as shown in Fig. 4.12, because the entire growing CNTs are submerged inside the large electric field existing in the direction normal to the substrate. The achievement of CNT alignment comes from the electric field induced electrostatic force in the negative sheath of a glow discharge initiated during conventional PECVD.

Figure 4.13 qualitatively depicts a CNT alignment mechanism of DC PECVD growth [86]. The electrostatic force F creates a uniform tensile stress across the

Fig. 4.13 CNT alignment mechanism in PECVD growth process. From Merkulov et al. [86]. Ni nanoparticle works as catalyst, locating at tip (a) and (c) or at base (b) and (d) of a CNT



entire nanoparticle–CNT interface, regardless of where the catalytic nanoparticle is located (tip or base). As growth proceeds, CNTs may bend if there are spatial fluctuations in the carbon precipitation; this would lead to nonuniform stresses at the nanoparticle–CNT interface. When the nanoparticle is at the top, the electrostatic force \mathbf{F} produces a compressive force at the CNT–particle interface where a greater growth rate is seen (Fig. 4.13c); on the side where less growth rate happens, a tensile stress is applied at the interface. This opposite behavior favors subsequent carbon precipitation at the interface with tensile stress (and a smaller rate of growth). The net result is a stable, negative feedback that works to equalize the growth rate everywhere, and vertical orientation is maintained (Fig. 4.13a). When the catalytic nanoparticle is at the base (Fig. 4.13d), the stress at the interface with the higher growth rate is tensile; this acts to further increase the rate at the same location, causing further bending of the structure. Stress fluctuation developed around catalytic nanoparticles by the electric field can modulate the diffusion rate of carbon atoms [86], so as to prevent the deviation of the direction of CNT growth from the electric-field direction (Fig. 4.13b).

The CNT vertical growth in a PECVD growth process can also be quantitatively explained. The substrate acts as the cathode electrode in DC discharge and is negatively charged. Some negative charges are collected at the top of grown nanotubes by the sheath electric field. The electric field \mathbf{E} is strengthened near the top of nanotubes. The local electric field E_{local} can be calculated by an equation $E_{\text{local}} = \beta \times V/r$, where V is the voltage potential on the sheath, r is the radius of the nanotube, and β is a form factor of 0.2–0.3. When $V = 200$ V, $r = 50$ nm, and $\beta = 0.25$,

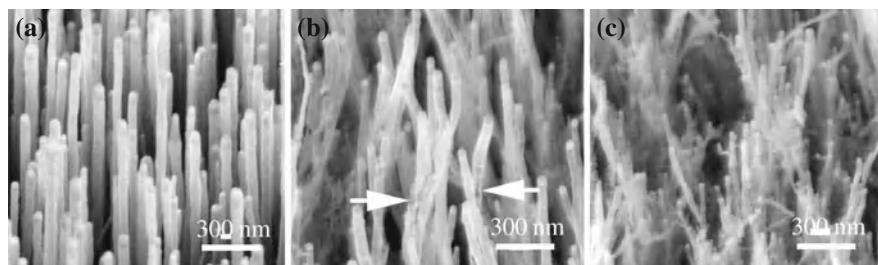


Fig. 4.14 SEM images of as-grown CNTs grown from catalyst **a** Ni, **b** Fe, and **c** Co. From Huang et al. [93]. Reprinted with permission from Springer. The CNTs were grown by a hot-filament PECVD method and the catalyst films are deposited by a magnetron sputtering on titanium substrates

$E_{\text{local}} = 1 \text{ MV/mm}$. If the top of a nanotube is negatively charged by one unit charge, a force of 0.2 nN acts on the top toward the plasma. It is suggested that such force assists the nanotubes to grow well aligned and perpendicular to the substrate in a DC discharge [87].

When the DC bias in DC-PECVD is low or there is no DC bias in RF-PECVD or microwave PECVD [88–92], the explanation is also successful because there are always catalytic nanoparticles at the base or at the top of CNTs to collect charges.

4.2.5 Experimental Conditions of Plasma-Enhanced Chemical Vapor Deposition Growth

Manly experimental conditions affect the morphology of CNT arrays, such as carbon source, catalyst, growth temperature, and plasma conditions, in the PECVD growth. Here, we briefly review these experimental parameters.

Gas. Up until now, many gasses, such as carbon monoxide (CO) and acetylene (C_2H_2), have been used as the carbon sources [5, 71] in PECVD growth. Ammonia (NH_3) and hydrogen (H_2) are widely used for dilution gases [14]. The gases to grow CNTs are summarized in some review literatures.

Catalyst. In the PECVD method, the catalytic nanoparticles direct the CNT growth direction along the plasma fields. Many metallic nanoparticles have been tested for catalyst to grow CNTs. Some tested metal catalysts are summarized in some reviews [27].

The catalyst element affects the alignment of CNTs. Detailed experiments show that Ni is the most suitable catalyst for growth of aligned CNTs among Ni, Co, and Fe catalysts [93]. The CNTs catalyzed by Ni have the best alignment and the smoothest and cleanest wall surface, whereas those from Co are covered with amorphous carbon and nanoparticles on the outer surface. The CNTs produced from Ni catalyst also exhibit a reasonably good graphitization.

Figure 4.14 shows the SEM images of as-grown CNT arrays from 25 nm thick Ni, Fe, and Co catalyst films, respectively. The morphology of the CNT arrays are very different. The nanotubes grown from the Ni film (Fig. 4.14a) exhibit a straight alignment perpendicular to the substrate, whereas that from the Fe film (Fig. 4.14b) and that from the Co film (Fig. 4.14c) are crooked or twisted. According to the proposed catalytic growth mechanism [94], the crooked, twisted, or helical CNTs may be the result of a variation of carbon segregation or catalytic activity on the active sites around the catalyst periphery during nanotube growth. Therefore, it can be deduced that Co and Fe exhibit nonuniform catalytic activity and carbon segregation. In contrast, the catalytic activity of Ni and carbon segregation from Ni are uniform and stable across the catalyst surface. As a result, CNTs grown from Ni have fairly good alignment and regular tubular structure.

The catalyst element not only affects the nanotube alignment, but also affects the diameter of nanotubes. For the same thickness of catalyst film (25 nm), the nanotubes grown from Co have the smallest diameter, whereas those grown from Fe have a diameter between those from Ni and Co. Although the growth behavior is very much different in terms of nanotube alignment and diameter, they share the same tip-growth mechanism because there is a catalyst particle on the tip of every nanotube, regardless of which catalyst is used.

Besides the effects on the nanotube diameter, wall thickness, morphology, and microstructure, the catalyst element affects the growth rate of CNTs. Ni yields the highest growth rate, largest diameter and thickest wall, whereas Co results in the lowest growth rate, smallest diameter, and thinnest wall.

Substrates. Various kind of substrates have been used to grow vertically aligned CNT arrays. It is reported that glasses [5], Si wafers, quartz wafers, various metals (Al foils [95, 96], Ni–Cr–Co alloys [97], stainless steel sheet [98]) are employed as substrates to grow CNT arrays.

Barrier layer. Usually, various materials, such as Al, Al₂O₃, Ti, TiO₂, TiN, Cr, SiO₂ and MgO are deposited on the substrates to act as barrier layers, forming sandwich structure, like aluminum foil laminated on stainless steel [99] to grow vertically aligned CNTs. The substrates withstand CNT growth temperature and support the barrier layer, catalyst, and CNTs while the barrier layers prevent Ostwald ripening and catalyst diffusion into the substrates, improve the adhesion of CNTs with the substrates, and affect the physical characteristics of the grown CNTs.

In general, spin coating, spray coating, sputtering deposition, or e-beam deposition are the strategies adopted for the barrier layer deposition.

Temperature. The morphology of the CNTs is related to the size of the catalytic nanoparticles and growth temperature. PECVD growth typically involves processing temperatures over 500 °C while CNT arrays can also be grown at much lower temperatures, such as 120, 200, or 400 °C [100]. When the diameter of the catalytic nanoparticles is smaller than 50 nm, usually either no CNTs or only short and curved CNTs are grown at 600 °C by PECVD [49]. When the size of the catalytic nanoparticles is large, well-aligned CNTs with uniform length distribution were grown. Because the reaction gasses are decomposed by the plasma, not pyrolyzed by heating, the growth temperature of PECVD is usually lower than that of thermal CVD.

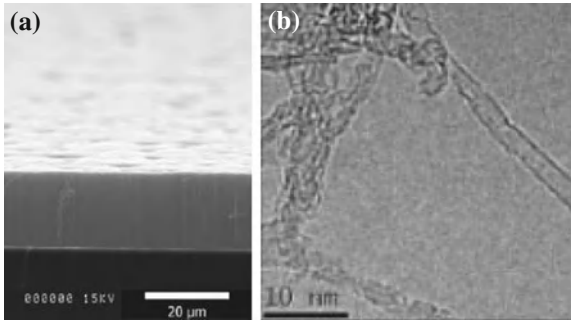


Fig. 4.15 **a** SEM, and **b** HRTEM images of SWCNTs grown by glow discharge at the atmospheric pressure. From Nozaki and Okazaki [101]

Plasma. In the PECVD method, the catalytic nanoparticles are subjected to the plasma. The plasma etches the catalyst and at the same time assists the CNT growth.

The plasma etching benefits the uniformity of the catalytic nanoparticles. Usually, the size of the prepared 2D catalyst is not uniform while distributed on a Gauss function, especially when the catalyst is produced from electrochemical deposition method [49] or sputtering method. In order to grow CNT arrays with uniform diameter, the uniform diameter of catalytic nanoparticles is necessary. During a PECVD process, the smaller catalytic nanoparticles can be removed by plasma etching before the growth of CNTs [49]. In order to completely eliminate the smaller catalytic nanoparticles, the pre-etching is employed by applying low intensity plasma to the substrate for a short time before the introduction of carbon source gas, such as acetylene. After the pre-etching, those smaller nanoparticles are removed and the survived nanoparticles are uniform. Compared with the average size of the un-etched nanoparticles, the average size of the survived nanoparticles becomes smaller.

Plasma also causes some inherent problems in the PECVD process, such as overheating [59] and over-etching [70]. These two cumulative results come from the bombardment of a massive ion flux onto the substrate surface, which can lead to a significant discrepancy between real and readout surface temperatures and severe mechanical and chemical damages of the substrate [85].

Pressure. In most cases, the vertical CNTs are synthesized in a low-pressure plasma chamber. The produced CNTs are usually CNFs or MWCNTs.

Atmospheric pressure glow discharge is another kind PECVD method to grow CNTs in a broad range of operating pressures from 10^{-1} to 10^5 Pa [101–104]. The produced CNTs are pure SWCNTs or pure MWCNTs, vertically aligned on the substrate, as shown in Fig. 4.15.

Additionally, CNTs have also been synthesized at other atmospheric pressure PECVD such as microwave plasma jet and atmospheric pressure plasma jet.

Achievements. Besides MWCNT arrays, vertical bamboo-structured CNT arrays [15], well aligned DWCNTs [77], vertical SWCNT forest [101], and carbon

nanofibers [105] have been produced using PECVD technique. The diameter and the length of aligned CNTs can be easily controlled by changing the size of the catalytic nanoparticles and the growth time, respectively [106]. The site density of CNTs is controlled by the site density of catalyst [49]. Currently the catalyst arrays with different site density have been prepared by electron-beam lithography [5], photolithography [77], micro contact printing [107], and shadow mask [4] etc.

References

1. W.Z. Li, S.S. Xie, L.X. Qian, B.H. Chang, B.S. Zou, W.Y. Zhou, R.A. Zhao, G. Wang, Large-scale synthesis of aligned carbon nanotubes. *Science* **274**(5293), 1701–1703 (1996)
2. Z.W. Pan, S.S. Xie, B.H. Chang, C.Y. Wang, L. Lu, W. Liu, W.Y. Zhou, W.Z. Li, L.X. Qian, Very long carbon nanotubes. *Nature* **394**(6694), 631–632 (1998)
3. M. Terrones, N. Grobert, J. Olivares, J.P. Zhang, H. Terrones, K. Kordatos, W.K. Hsu, J.P. Hare, P.D. Townsend, K. Prassides, A.K. Cheetham, H.W. Kroto, D.R.M. Walton, Controlled production of aligned-nanotube bundles. *Nature* **388**(6637), 52–55 (1997)
4. S. Fan, M.G. Chapline, N.R. Franklin, T.W. Tomblor, A.M. Cassell, H. Dai, Self-oriented regular arrays of carbon nanotubes and their field emission properties. *Science* **283**(5401), 512–514 (1999)
5. Z.F. Ren, Z.P. Huang, J.W. Xu, J.H. Wang, P. Bush, M.P. Siegal, P.N. Provencio, Synthesis of large arrays of well-aligned carbon nanotubes on glass. *Science* **282**, 1105–1107 (1998)
6. Y.C. Choi, Y.M. Shin, Y.H. Lee, B.S. Lee, G.-S. Park, W.B. Choi, N.S. Lee, J.M. Kim, Controlling the diameter, growth rate, and density of vertically aligned carbon nanotubes synthesized by microwave plasma-enhanced chemical vapor deposition. *Appl. Phys. Lett.* **76**(17), 2367–2369 (2000)
7. C. Bower, W. Zhu, S. Jin, O. Zhou, Plasma-induced alignment of carbon nanotubes. *Appl. Phys. Lett.* **77**(6), 830–832 (2000)
8. C. Bower, O. Zhou, W. Zhu, D.J. Werder, S. Jin, Nucleation and growth of carbon nanotubes by microwave plasma chemical vapor deposition. *Appl. Phys. Lett.* **77**(17), 2767–2769 (2000)
9. B.J. Hinds, N. Chopra, T. Rantell, R. Andrews, V. Gavalas, L.G. Bachas, Aligned multiwalled carbon nanotube membranes. *Science* **303**(5654), 62–65 (2004)
10. L. Ge, S. Sethi, L. Ci, P.M. Ajayan, A. Dhinojwala, Carbon nanotube-based synthetic gecko tapes. *Proc. Natl. Acad. Sci. USA* **104**(26), 10792–10795 (2007)
11. K. Mizuno, J. Ishii, H. Kishida, Y. Hayamizu, S. Yasuda, D.N. Futaba, M. Yumura, K. Hata, A black body absorber from vertically aligned single-walled carbon nanotubes. *Proc. Natl. Acad. Sci. USA* **106**(15), 6044–6047 (2009)
12. J.H. Chen, W.Z. Li, D.Z. Wang, S.X. Yang, J.G. Wen, Z.F. Ren, Electrochemical characterization of carbon nanotubes as electrode in electrochemical double-layer capacitors. *Carbon* **40**(8), 1193–1197 (2002)
13. R.D. Bennett, G.Y. Xiong, Z.F. Ren, R.E. Cohen, Using block copolymer micellar thin films as templates for the production of catalysts for carbon nanotube growth. *Chem. Mater.* **16**(26), 5589–5595 (2004)
14. S.H. Jo, J.Y. Huang, S. Chen, G.Y. Xiong, D.Z. Wang, Z.F. Ren, Field emission of carbon nanotubes grown on carbon cloth. *J. Vac. Sci. Technol. B* **23**(6), 2363–2368 (2005)
15. C.J. Lee, J.H. Park, J. Park, Synthesis of bamboo-shaped multiwalled carbon nanotubes using thermal chemical vapor deposition. *Chem. Phys. Lett.* **323**(5–6), 560–565 (2000)
16. M. Zhang, S. Fang, A.A. Zakhidov, S.B. Lee, A.E. Aliev, C.D. Williams, K.R. Atkinson, R.H. Baughman, Strong, transparent, multifunctional, carbon nanotube sheets. *Science* **309**(5738), 1215–1219 (2005)

17. G. Zhang, D. Mann, L. Zhang, A. Javey, Y. Li, E. Yenilmez, Q. Wang, J.P. McVittie, Y. Nishi, J. Gibbons, H. Dai, Ultra-high-yield growth of vertical single-walled carbon nanotubes: hidden roles of hydrogen and oxygen. *Proc. Nat. Acad. Sci. USA* **102**(45), 16141–16145 (2005)
18. G.-Y. Xiong, D. Wang, Z. Ren, Aligned millimeter-long carbon nanotube arrays grown on single crystal magnesia. *Carbon* **44**(5), 969–973 (2006)
19. K. Hata, D.N. Futaba, K. Mizuno, T. Namai, M. Yumura, S. Iijima, Water-assisted highly efficient synthesis of impurity-free single-walled carbon nanotubes. *Science* **306**(5700), 1362–1364 (2004)
20. G.Y. Xiong, Y. Suda, D.Z. Wang, J.Y. Huang, Z.F. Ren, Effect of temperature, pressure, and gas ratio of methane to hydrogen on the synthesis of double-walled carbon nanotubes by chemical vapour deposition. *Nanotechnology* **16**(4), 532–535 (2005)
21. K. Hasegawa, S. Noda, Moderating carbon supply and suppressing ostwald ripening of catalyst particles to produce 4.5-mm-tall single-walled carbon nanotube forests. *Carbon* **49**(13), 4497–4504 (2011)
22. T. Sugai, T. Okazaki, H. Yoshida, H. Shinohara, Syntheses of single- and double-wall carbon nanotubes by the HTPAD and HFCVD methods. *New J. Phys.* **6**, 21 (2004)
23. T.B. Massalski, H. Okamoto (eds.), *Binary Alloy Phase Diagrams* (ASM International, Materials Park, 1996)
24. H. Ago, T. Komatsu, S. Ohshima, Y. Kuriki, M. Yumura, Dispersion of metal nanoparticles for aligned carbon nanotube arrays. *Appl. Phys. Lett.* **77**(1), 79–81 (2000)
25. Y. Li, W. Kim, Y. Zhang, M. Rolandi, D. Wang, H. Dai, Growth of single-walled carbon nanotubes from discrete catalytic nanoparticles of various sizes. *J. Phys. Chem. B* **105**(46), 11424–11431 (2001)
26. E.T. Thostenson, W.Z. Li, D.Z. Wang, Z.F. Ren, T.W. Chou, Carbon nanotube/carbon fiber hybrid multiscale composites. *J. Appl. Phys.* **91**(9), 6034–6037 (2002)
27. A.V. Melechko, V.I. Merkulov, T.E. McKnight, M.A. Guillorn, K.L. Klein, D.H. Lowndes, M.L. Simpson, Vertically aligned carbon nanofibers and related structures: controlled synthesis and directed assembly. *J. Appl. Phys.* **97**(4), 041301/1–041301/39 (2005)
28. R. Baker, Catalytic growth of carbon filaments. *Carbon* **27**(3), 315–323 (1989)
29. M. Endo, K. Takeuchi, K. Kobori, K. Takahashi, H.W. Kroto, A. Sarkar, Pyrolytic carbon nanotubes from vapor-grown carbon fibers. *Carbon* **33**(7), 873–881 (1995)
30. J.-C. Charlier, A. De Vita, X. Blase, R. Car, Microscopic growth mechanisms for carbon nanotubes. *Science* **275**(5300), 647–649 (1997)
31. M. Yudasaka, R. Kikuchi, Y. Ohki, E. Ota, S. Yoshimura, Behavior of Ni in carbon nanotube nucleation. *Appl. Phys. Lett.* **70**(14), 1817–1818 (1997)
32. J.C. Charlier, S. Iijima, Growth Mechanisms of Carbon Nanotubes, in *Carbon Nanotubes: Synthesis, Structure, Properties, and Applications*, ed by M.S. Dresselhaus, G. Dresselhaus, P. Avouris. Topics in Applied Physics, vol 80 (Springer, Berlin, 2001), pp. 55–81
33. T.W. Ebbesen (ed.), *Carbon Nanotubes: Preparation and Properties* (Chemical Rubber, Boca Raton, 1997)
34. H. Yoshida, S. Takeda, T. Uchiyama, H. Kohno, Y. Homma, Atomic-scale in-situ observation of carbon nanotube growth from solid state iron carbide nanoparticles. *Nano Lett.* **8**(7), 2082–2086 (2008)
35. S. Helveg, C. López-Cartes, J. Sehested, P.L. Hansen, B.S. Clausen, J.R. Rostrup-Nielsen, F. Abild-Pedersen, J.K. Nørskov, Atomic-scale imaging of carbon nanofibre growth. *Nature* **427**, 426–429 (2004)
36. K. Awasthi, A. Srivastava, O.N. Srivastava, Synthesis of carbon nanotubes. *J. Nanosci. Nanotechnol.* **5**(10), 1616–1636 (2005)
37. W.Z. Li, D.Z. Wang, S.X. Yang, J.G. Wen, Z.F. Ren, Controlled growth of carbon nanotubes on graphite foil by chemical vapor deposition. *Chem. Phys. Lett.* **335**, 141–149 (2001)
38. G.B. Adams, O.F. Sankey, J.B. Page, M. O’Keeffe, D.A. Drabold, Energetics of large fullerenes: balls, tubes, and capsules. *Science* **256**(5065), 1792–1795 (1992)
39. J.F. Colomer, C. Stephan, S. Lefrant, G. Van Tendeloo, I. Willems, Z. Kónya, A. Fonseca, C. Laurent, J.B. Nagy, Large-scale synthesis of single-wall carbon nanotubes by catalytic chemical vapor deposition (CCVD) method. *Chem. Phys. Lett.* **317**(1–2), 83–89 (2000)

40. B. Kitiyanan, W.E. Alvarez, J.H. Harwell, D.E. Resasco, Controlled production of single-wall carbon nanotubes by catalytic decomposition of CO on bimetallic Co–Mo catalysts. *Chem. Phys. Lett.* **317**(3–5), 497–503 (2000)
41. J. Kong, H.T. Soh, A.M. Cassell, C.F. Quate, H. Dai, Synthesis of individual single-walled carbon nanotubes on patterned silicon wafers. *Nature* **395**(6705), 878–881 (1998)
42. S. Iijima, T. Ichihashi, Single-shell carbon nanotubes of 1-nm diameter. *Nature* **363**(6430), 603–605 (1993)
43. J. Gavillet, J. Thibault, O. Stephan, H. Amara, A. Loiseau, C. Bichara, J.P. Gaspard, F. Ducastelle, Nucleation and growth of single-walled nanotubes: the role of metallic catalysts. *J. Nanosci. Nanotechnol.* **4**(4), 346–359 (2004)
44. A.R. Harutyunyan, The catalyst for growing single-walled carbon nanotubes by catalytic chemical vapor deposition method. *J. Nanosci. Nanotechnol.* **9**(4), 2480–2495 (2009)
45. C.T. Wirth, S. Hofmann, J. Robertson, State of the catalyst during carbon nanotube growth. *Diam. Relat. Mater.* **18**(5–8), 940–945 (2009)
46. Z.P. Huang, D.L. Carnahan, J. Rybczynski, M. Giersig, M. Sennett, D.Z. Wang, J.G. Wen, K. Kempa, Z.F. Ren, Growth of large periodic arrays of carbon nanotubes. *Appl. Phys. Lett.* **82**(3), 460–462 (2003)
47. J.B. In, C.P. Grigoropoulos, A.A. Chernov, A. Noy, Hidden role of trace gas impurities in chemical vapor deposition growth of vertically-aligned carbon nanotube arrays. *Appl. Phys. Lett.* **98**(15), 153102 (2011)
48. W. Li, J. Wen, Z. Ren, Effect of temperature on growth and structure of carbon nanotubes by chemical vapor deposition. *Appl. Phys. A* **74**(3), 397–402 (2002)
49. Y. Tu, Z.P. Huang, D.Z. Wang, J.G. Wen, Z.F. Ren, Growth of aligned carbon nanotubes with controlled site density. *Appl. Phys. Lett.* **80**(21), 4018–4020 (2002)
50. W. Li, J. Wen, Y. Tu, Z. Ren, Effect of gas pressure on the growth and structure of carbon nanotubes by chemical vapor deposition. *Appl. Phys. A* **73**(2), 259–264 (2001)
51. R.S. Wagner, W.C. Ellis, Vapor-liquid-solid mechanism of single crystal growth. *Appl. Phys. Lett.* **4**(5), 89–90 (1964)
52. S. Hofmann, C. Ducati, J. Robertson, B. Kleinsorge, Low-temperature growth of carbon nanotubes by plasma-enhanced chemical vapor deposition. *Appl. Phys. Lett.* **83**(1), 135–137 (2003)
53. S. Hofmann, C. Ducati, B. Kleinsorge, J. Robertson, Direct growth of aligned carbon nanotube field emitter arrays onto plastic substrates. *Appl. Phys. Lett.* **83**(22), 4661–4663 (2003)
54. M. Meyyappan, L. Delzeit, A. Cassell, D. Hash, Carbon nanotube growth by PECVD: a review. *Plasma Sources Sci. Technol.* **12**(2), 205–216 (2003)
55. M. Meyyappan, A review of plasma enhanced chemical vapour deposition of carbon nanotubes. *J. Phys. D: Appl. Phys.* **42**(213001), 15 (2009)
56. K.B.K. Teo, M. Chhowalla, G.A.J. Amaratunga, W.I. Milne, D.G. Hasko, G. Pirio, P. Legagneux, F. Wyczisk, D. Pribat, Uniform patterned growth of carbon nanotubes without surface carbon. *Appl. Phys. Lett.* **79**(10), 1534–1536 (2001)
57. V.I. Merkulov, A.V. Melechko, M.A. Guillorn, D.H. Lowndes, M.L. Simpson, Growth rate of plasma-synthesized vertically aligned carbon nanofibers. *Chem. Phys. Lett.* **361**(5–6), 492–498 (2002)
58. B.A. Cruden, A.M. Cassell, Q. Ye, M. Meyyappan, Reactor design considerations in the hot filament/direct current plasma synthesis of carbon nanofibers. *J. Appl. Phys.* **94**(6), 4070–4078 (2003)
59. K.B.K. Teo, D.B. Hash, R.G. Lacerda, N.L. Rupasinghe, M.S. Bell, S.H. Dalal, D. Bose, T.R. Govindan, B.A. Cruden, M. Chhowalla, G.A.J. Amaratunga, M. Meyyappan, W.I. Milne, The significance of plasma heating in carbon nanotube and nanofiber growth. *Nano Lett.* **4**(5), 921–926 (2004)
60. J.-H. Han, W.-S. Yang, J.-B. Yoo, C.-Y. Park, Growth and emission characteristics of vertically well-aligned carbon nanotubes grown on glass substrate by hot filament plasma-enhanced chemical vapor deposition. *J. Appl. Phys.* **88**(12), 7363–7365 (2000)

61. Y. Wang, Nanophotonics of vertically aligned carbon nanotubes: two-dimensional photonic crystals and optical dipole antenna. Ph.D. Thesis, Boston College, 2006
62. H. Wang, Z.F. Ren, The evolution of carbon nanotubes during their growth by plasma enhanced chemical vapor deposition. *Nanotechnology* **22**(40), 405601 (2011)
63. T.A. El-Aguizy, J. hyun Jeong, Y.-B. Jeon, W.Z. Li, Z.F. Ren, S.-G. Kim, Transplanting carbon nanotubes. *Appl. Phys. Lett.* **85**(24), 5995–5997 (2004)
64. V.I. Merkulov, D.H. Lowndes, Y.Y. Wei, G. Eres, E. Voelkl, Patterned growth of individual and multiple vertically aligned carbon nanofibers. *Appl. Phys. Lett.* **76**(24), 3555–3557 (2000)
65. M. Chowalla, K.B.K. Teo, C. Ducati, N.L. Rupesinghe, G.A.J. Amaratunga, A.C. Ferrari, D. Roy, J. Robertson, W.I. Milne, Growth process conditions of vertically aligned carbon nanotubes using plasma enhanced chemical vapor deposition. *J. Appl. Phys.* **90**(10), 5308–5317 (2001)
66. S.H. Jo, Y. Tu, Z.P. Huang, D.L. Carnahan, D.Z. Wang, Z.F. Ren, Effect of length and spacing of vertically aligned carbon nanotubes on field emission properties. *Appl. Phys. Lett.* **82**(20), 3520–3522 (2003)
67. S.H. Jo, Y. Tu, Z.P. Huang, D.L. Carnahan, J.Y. Huang, D.Z. Wang, Z.F. Ren, Correlation of field emission and surface microstructure of vertically aligned carbon nanotubes. *Appl. Phys. Lett.* **84**(3), 413–415 (2004)
68. R.E. Morjan, V. Maltsev, O. Nerushev, Y. Yao, L.K.L. Falk, E.E.B. Campbell, High growth rates and wall decoration of carbon nanotubes grown by plasma-enhanced chemical vapour deposition. *Chem. Phys. Lett.* **383**(3–4), 385–390 (2004)
69. Y. Tu, Y. Lin, Z.F. Ren, Nanoelectrode arrays based on low site density aligned carbon nanotubes. *Nano Lett.* **3**(1), 107–109 (2003)
70. Y. Wang, J. Ryczynski, D.Z. Wang, K. Kempa, Z.F. Ren, W.Z. Li, B. Kimball, Periodicity and alignment of large-scale carbon nanotubes arrays. *Appl. Phys. Lett.* **85**(20), 4741–4743 (2004)
71. Z.P. Huang, J.W. Xu, Z.F. Ren, J.H. Wang, M.P. Siegal, P.N. Provencio, Growth of highly oriented carbon nanotubes by plasma-enhanced hot filament chemical vapor deposition. *Appl. Phys. Lett.* **73**(26), 3845–3847 (1998)
72. Y. Shiratori, H. Hiraoka, Y. Takeuchi, S. Itoh, M. Yamamoto, One-step formation of aligned carbon nanotube field emitters at 400 °C. *Appl. Phys. Lett.* **82**(15), 2485–2487 (2003)
73. L. Delzeit, I. McAninch, B.A. Cruden, D. Hash, B. Chen, J. Han, M. Meyyappan, Growth of multiwall carbon nanotubes in an inductively coupled plasma reactor. *J. Appl. Phys.* **91**(9), 6027–6033 (2002)
74. H.S. Kang, H.J. Yoon, C.O. Kim, J.P. Hong, I.T. Han, S.N. Cha, B.K. Song, J.E. Jung, N.S. Lee, J.M. Kim, Low temperature growth of multi-wall carbon nanotubes assisted by mesh potential using a modified plasma enhanced chemical vapor deposition system. *Chem. Phys. Lett.* **349**(3–4), 196–200 (2001)
75. V.K. Varadan, J. Xie, Large-scale synthesis of multi-walled carbon nanotubes by microwave CVD. *Smart Mater. Struct.* **11**(4), 610 (2002)
76. H. Cui, O. Zhou, B.R. Stoner, Deposition of aligned bamboo-like carbon nanotubes via microwave plasma enhanced chemical vapor deposition. *J. Appl. Phys.* **88**(10), 6072–6074 (2000)
77. H. Murakami, M. Hirakawa, C. Tanaka, H. Yamakawa, Field emission from well-aligned, patterned, carbon nanotube emitters. *Appl. Phys. Lett.* **76**(13), 1776–1778 (2000)
78. M. Okai, T. Muneyoshi, T. Yaguchi, S. Sasaki, Structure of carbon nanotubes grown by microwave-plasma-enhanced chemical vapor deposition. *Appl. Phys. Lett.* **77**(21), 3468–3470 (2000)
79. L.C. Qin, D. Zhou, A.R. Krauss, D.M. Gruen, Growing carbon nanotubes by microwave plasma-enhanced chemical vapor deposition. *Appl. Phys. Lett.* **72**(26), 3437–3439 (1998)
80. H. Boehm, Carbon from carbon monoxide disproportionation on nickel and iron catalysts: Morphological studies and possible growth mechanisms. *Carbon* **11**(6), 583–586 (1973)
81. R.T.K. Baker, P.S. Harris, R.B. Thomas, R.J. Waite, Formation of filamentous carbon from iron, cobalt and chromium catalyzed decomposition of acetylene. *J. Catal.* **30**(1), 86–95 (1973)

82. L. Huang, B. White, M. Y. Sfeir, M. Huang, H. X. Huang, S. Wind, J. Hone, S. O'Brien, Cobalt ultrathin film catalyzed ethanol chemical vapor deposition of single-walled carbon nanotubes. *J. Phys. Chem. B* **110**(23), 11103–11109 (2006)
83. Y. Zhang, A. Chang, J. Cao, Q. Wang, W. Kim, Y. Li, N. Morris, E. Yenilmez, J. Kong, H. Dai, Electric-field-directed growth of aligned single-walled carbon nanotubes. *Appl. Phys. Lett.* **79**(19), 3155–3157 (2001)
84. Y. Avigal, R. Kalish, Growth of aligned carbon nanotubes by biasing during growth. *Appl. Phys. Lett.* **78**(16), 2291–2293 (2001)
85. J. G. Wen, Z. P. Huang, D. Z. Wang, J. H. Chen, S. X. Yang, Z. F. Ren, J. H. Wang, L. E. Calvet, J. Chen, J. F. Klemic, M. Reed, Growth and characterization of aligned carbon nanotubes from patterned nickel nanodots and uniform thin films. *J. Mater. Res.* **16**(11), 3246–3253 (2001)
86. V. I. Merkulov, A. V. Melechko, M. A. Guillorn, D. H. Lowndes, M. L. Simpson, Alignment mechanism of carbon nanofibers produced by plasma-enhanced chemical-vapor deposition. *Appl. Phys. Lett.* **79**(18), 2970–2972 (2001)
87. Y. Hayashi, T. Negishi, S. Nishino, Growth of well-aligned carbon nanotubes on nickel by hot-filament-assisted DC plasma chemical vapor deposition in a CH₄/H₂ plasma. *J. Vac. Sci. Technol. A* **19**(4), 1796–1799 (2001)
88. K. MacKenzie, O. Dunens, A. T. Harris, A review of carbon nanotube purification by microwave assisted acid digestion. *Sep. Purif. Technol.* **66**(2), 209–222 (2009)
89. X. Song, Y. Fang, A technique of purification process of single-walled carbon nanotubes with air. *Spectrochim. Acta A* **67**(3–4), 1131–1134 (2007)
90. T. Guo, P. Nikolaev, A. Thess, D. Colbert, R. Smalley, Catalytic growth of single-walled nanotubes by laser vaporization. *Chem. Phys. Lett.* **243**(1–2), 49–54 (1995)
91. A. Thess, R. Lee, P. Nikolaev, H. Dai, P. Petit, J. Robert, C. Xu, Y. H. Lee, S. G. Kim, A. G. Rinzler, D. T. Colbert, G. E. Scuseria, D. Tománek, J. E. Fischer, R. E. Smalley, Crystalline ropes of metallic carbon nanotubes. *Science* **273**(5274), 483–487 (1996)
92. A. G. Nasibulin, P. V. Pikhitsa, H. Jiang, D. P. Brown, A. V. Krashennikov, A. S. Anisimov, P. Queipo, A. Moisala, D. Gonzalez, G. Lientschnig, A. Hassani, S. D. Shandakov, G. Lolli, D. E. Resasco, M. Choi, D. Tománek, E. I. Kauppinen, A novel hybrid carbon material. *Nat. Nanotechnol.* **2**(3), 156–161 (2007)
93. Z. Huang, D. Wang, J. Wen, M. Sennett, H. Gibson, Z. Ren, Effect of nickel, iron and cobalt on growth of aligned carbon nanotubes. *Appl. Phys. A* **74**(3), 387–391 (2002)
94. S. Amelinckx, X. B. Zhang, D. Bernaerts, X. F. Zhang, V. Ivanov, J. B. Nagy, A formation mechanism for catalytically grown helix-shaped graphite nanotubes. *Science* **265**(5172), 635–639 (1994)
95. N. Yoshikawa, T. Asari, N. Kishi, S. Hayashi, T. Sugai, H. Shinohara, An efficient fabrication of vertically aligned carbon nanotubes on flexible aluminum foils by catalyst-supported chemical vapor deposition. *Nanotechnology* **19**(24), 245607 (2008)
96. C.-C. Su, S.-H. Chang, Effective growth of vertically aligned carbon nanotube turfs on flexible Al foil. *Mater. Lett.* **65**(17–18), 2700–2702 (2011)
97. T. Hiraoka, T. Yamada, K. Hata, D. N. Futaba, H. Kurachi, S. Uemura, M. Yumura, S. Iijima, Synthesis of single- and double-walled carbon nanotube forests on conducting metal foils. *J. Am. Chem. Soc.* **128**(41), 13338–13339 (2006)
98. X. Lepró, M. D. Lima, R. H. Baughman, Spinnable carbon nanotube forests grown on thin, flexible metallic substrates. *Carbon* **48**(12), 3621–3627 (2010)
99. S. P. Patole, H.-I. Kim, J.-H. Jung, A. S. Patole, H.-J. Kim, I.-T. Han, V. N. Bhoraskar, J.-B. Yoo, The synthesis of vertically-aligned carbon nanotubes on an aluminum foil laminated on stainless steel. *Carbon* **49**, 3522–3528 (2011)
100. M. K. Tabatabaei, H. Ghafouri fard, J. Koohsorkhi, S. Khatami, S. Mohajerzadeh, Remote and direct plasma regions for low-temperature growth of carbon nanotubes on glass substrates for display applications. *J. Phys. D: Appl. Phys.* **44**(11), 115401 (2011)
101. T. Nozaki, K. Okazaki, Carbon nanotube synthesis pressure glow discharge: a review. *Plasma Processes Polym.* **5**(4), 301–321 (2008)

102. T. Nozaki, T. Goto, K. Okazaki, K. Ohnishi, L. Mangolini, J. Heberlein, U. Kortshagen, Deposition of vertically oriented carbon nanofibers in atmospheric pressure radio frequency discharge. *J. Appl. Phys.* **99**(2), 024310-1–024310-7 (2006)
103. T. Nozaki, K. Ohnishi, K. Okazaki, U. Kortshagen, Fabrication of vertically aligned single-walled carbon nanotubes in atmospheric pressure non-thermal plasma CVD. *Carbon* **45**(2), 364–374 (2007)
104. T. Nozaki, Y. Kimura, K. Okazaki, Carbon nanotubes deposition in glow barrier discharge enhanced catalytic CVD. *J. Phys. D: Appl. Phys.* **35**(21), 2779–2784 (2002)
105. L. Zheng, G. Sun, Z. Zhan, Tuning array morphology for high-strength carbon-nanotube fibers. *Small* **6**(1), 132–137 (2010)
106. S. Huang, L. Dai, A. Mau, Controlled fabrication of aligned carbon nanotube patterns. *Phys. B* **323**(1–4), 333–335 (2002)
107. L. Nilsson, O. Groening, C. Emmenegger, O. Kuettel, E. Schaller, L. Schlapbach, H. Kind, J.-M. Bonard, K. Kern, Scanning field emission from patterned carbon nanotube films. *Appl. Phys. Lett.* **76**(15), 2071–2073 (2000)

Chapter 5

Physics of Direct Current Plasma-Enhanced Chemical Vapor Deposition

Probably the most widely used growth method for aligned CNTs is DC-PECVD due to its effectiveness in alignment control and equipment setup simplicity. It is, therefore, worth to dedicate this chapter to review this technique in more thorough details while also not limit the discussion to a single type of electrical discharge (plasma). Besides, comprehensive reviews on various aspects of PECVD techniques for aligned CNT growth is already available [1, 2].

Although it has been reported that, in DC configurations, CNTs can be grown under either a positive or negative bias, the most popular choice is applying a negative bias on the substrate probably to utilize the ion bombardment effects that will be discussed in the following paragraphs. Unlike in the cases of AC plasmas where identical parallel plate electrodes are predominantly used for growth uniformity, DC plasmas require a higher breakdown voltage to initiate and therefore the electrode shapes need to be modified to facilitate the initiation. The simplest and most popular option is to have the positive electrode of a much smaller effective surface area, e.g., a small plate or even a rod end with a flat or pointy tip, so that its local sharp edges can more easily induce strong local electric fields to initiate the plasma. Besides, this configuration can also provide relatively uniform CNT growth over centimeter scales, sufficient for laboratory research. There are also specific characteristics of DC plasma growth such as the substrate conductivity requirement and dark discharge plasma states, which will be demonstrated together with some general growth aspects in all PECVD processes.

5.1 Equipment Setup and Growth Procedure

An exemplary schematic setup of the DC-PECVD apparatus is illustrated in Fig. 5.1 [3, 4]. Inside a vacuum chamber (1), a rod-shaped molybdenum anode (2) hangs vertically about 1–2 cm over a horizontal molybdenum cathode plate (3) which also serves as a sample stage. The diameters of the rod and the plate are 0.25 mm and 4 mm,

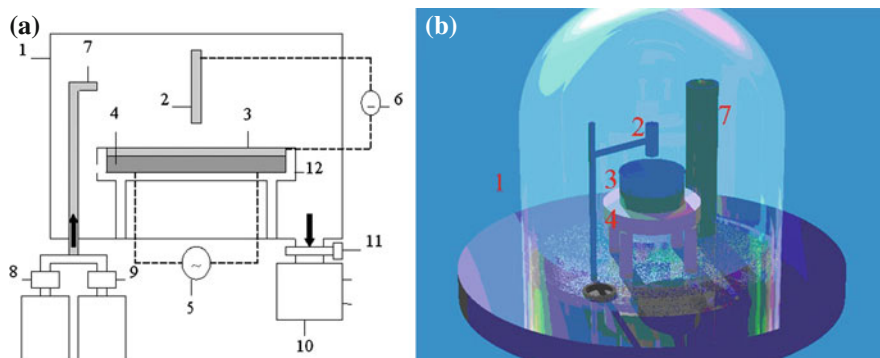


Fig. 5.1 **a** Setup of DC-PECVD system. From Wang [3]. **b** 3D structure of the PECVD growth chamber to align CNTs

respectively. Underneath the cathode plate is a resistive plate heater (4) powered by an external AC voltage source (5). The two electrodes are connected to an external power supply (6), MDX-1K Magnetron Drive (The Advanced Energy Inc.), which runs on a constant voltage, current or power mode. Feedstock gases are introduced into the chamber via a single gas pipe (7) after going through respective flow controllers (8, 9), and the chamber evacuation is solely executed by a mechanical pump (10). The evacuation speed and therefore the system pressure are manually controlled by a gate valve (11) which throttles the evacuation channel. In addition to the basic structure in Fig. 5.1, a pressure sensor is installed in the chamber base plate, and a thermocouple is first insulated in a thin quartz tube and then brought into contact to the cathode for temperature monitoring. Compared to the other plasma sources which are mostly AC, the major setup difference is that the anode surface is shrunk into a much smaller size than the cathode. This makes the sharp edges of the anode to be almost the closest geometrical point to the cathode where the plasma should initiate and the edges allow a relatively low breakdown voltage due to local field enhancement.

The DC-PECVD process for vertically aligned CNT arrays includes four basic steps, namely evacuation, heating, plasma generation, and cooling. A typical procedure can be described as follows. After samples are loaded onto the sample stage, the chamber is evacuated to a base pressure of around 10^{-2} Torr. NH_3 is then introduced into the chamber to reach a pressure of 8 Torr and the heater is turned on to gradually elevate the stage temperature. Typical growth temperatures used are in the range of 450–600 °C which can be normally reached in a period of 15–30 min. The pressure is maintained by adjusting the aperture of the gate valve. As soon as the temperature and pressure are stabilized, a DC bias voltage of 450–650 V is applied to the gap between the two electrodes to ignite an electrical discharge (plasma) over the sample. The plasma current intensity may typically vary within 0.1–0.5 A. C_2H_2 is then introduced to trigger the CNT growth. The flow rate ratio of $\text{NH}_3:\text{C}_2\text{H}_2$ is

usually around 4:1 which results in a minimum amount of amorphous carbon formation. And the growth time may vary from a couple of minutes to hours depending on the growth rate and desired CNT length. When the end of growth time is reached, the bias voltage is turned off immediately to terminate the plasma. Meanwhile, the gases are discontinued and the gate valve is fully opened to evacuate the chamber. The heater is also turned off for the samples to cool down naturally. Inert gases such as N_2 or Ar can also be fed into the chamber to speed up the cooling process if desired.

Again, the above setup and procedure should be taken as a basic example with room for variations in peripheral aspects such as triode-type electrode setups, different mechanisms for substrate heating, and application of other reacting gases such as CH_4 and H_2 . The apparatus and process simplicity has greatly facilitated the adoption of this technique by many research groups around the globe and has helped to push the aligned CNT research forward rapidly and significantly.

5.2 Substrate and Underlayer

For any growth process of CNTs, the general requirements for the underlying substrate (or underlayer coated onto the substrate) are that (1) it has to be both physically and chemically stable for up to the growth temperature and (2) its surface must not poison the catalyst particles in contact (such as by forming an inactive alloy) which can be frequently avoided by an inert buffer layer coating. For PECVD processes, the substrate must also be chemically stable under the plasma which is rich of H-species. Some weakly bonded oxides such as indium oxide can be quickly reduced in this plasma and is therefore usually not applicable as the substrate or underlayer. And for DC-PECVD, in particular, the substrate must be electrically conductive to sustain a continuous DC current flow through its surface where the CNTs grow from. Most metals and semiconductors (such as silicon wafers) are very good substrate materials, and insulating substrates such as glass [5] and polyimide [6] can be first coated with a conductive layer to work properly (requiring electrical contact of the conductive layer to the cathode during growth). Although it has been reported [5] that directly depositing catalyst films onto glass may still result in aligned CNT growth, this phenomenon should be due to the formation of a conductive amorphous carbon layer which connects the narrow spacing among the dewetted catalyst particles, which is more directly observed on polyimide substrates [6]. Indeed, large-spacing catalyst particles are found to always require a conductive substrate or underlayer for CNT alignment. Common transparent conductive oxide (TCO) thin films can also be applied as conductive underlayers on insulating glass substrates for aligned CNT growth by DC-PECVD, although it requires proper choice of the discharge conditions [6], which will be discussed in detail later.

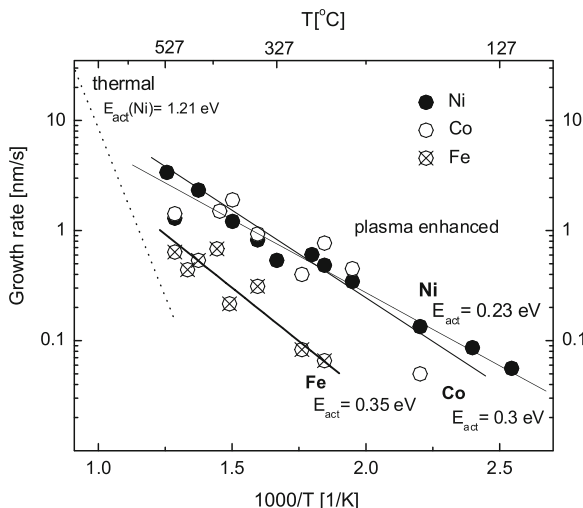


Fig. 5.2 Arrhenius plots for CNT growth rates on different catalysts in NH_3 diluted C_2H_2 . From S. Hofmann et al. [7]. Copyright (2005), American Physical Society

5.3 Growth Temperature

One of the major advantages of using PECVD growth techniques is the low growth temperature. The ionization of the neutral hydrocarbon molecules inside the plasma facilitates the breaking of the CH bonds and lowers the activation energy of the CNT growth, E_{act} . Indeed, the activation energy for PECVD processes is experimentally measured to be ~ 0.3 eV, much lower than the ~ 1.2 eV for thermal CVD processes [7]. Figure 5.2 shows the extrapolated activation energy values for DC-PECVD and thermal CVD growth based on experimental data. DC-PECVD growth temperature has successfully been demonstrated to be as low as 390 °C for bamboo-like CNTs and 120 °C for amorphous carbon nanofibers (CNFs) [8], compared to thermal CVD growth temperatures in the 500–700 °C range.

Although at very low temperatures the carbon-atoms in the grown structure begin to be more disordered (Fig. 5.3), the fact that carbon atoms can still diffuse and precipitate along the catalyst surfaces to result in nanostructure growth demonstrates that carbon diffusivity is just the limiting factor for low-temperature growth rate, whereas the feed-stock hydrocarbon dissociation is really the bottle-neck process for growth initiation. This understanding leads to remote-plasma CVD processes for growth temperature lowering [9, 10], which is beyond the scope of this book. Since alignment can still be achieved at these low temperatures (Fig. 5.3), many application opportunities open up, especially in templating on plastic substrates where temperature is sensitive and morphology is more essential than crystallinity.

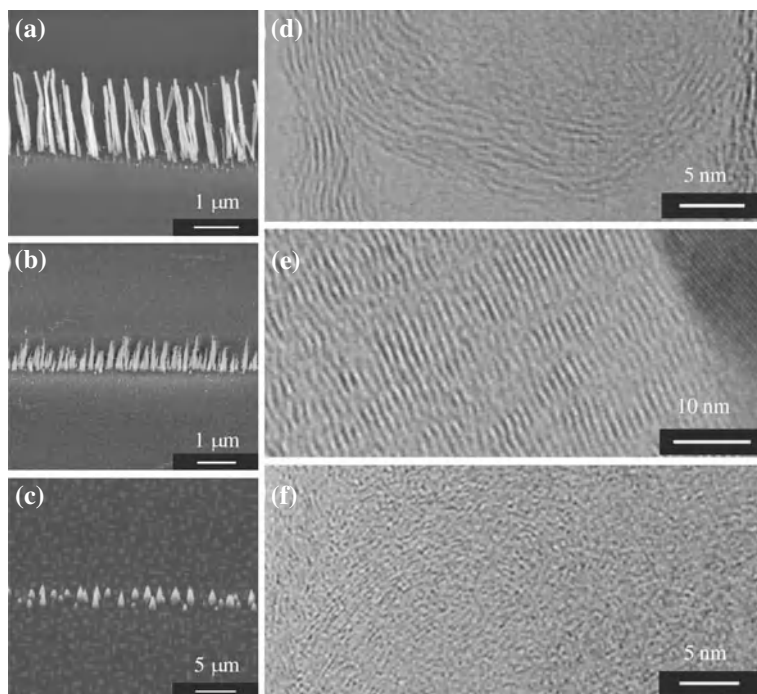


Fig. 5.3 CNF arrays PECVD grown at (a, d) 500 °C, (b, e) 270 °C, and (c, f) 120 °C. a–c SEM images of CNF arrays and d–f HRTEM images of CNFs. From S. Hofmann et al. [8]. Copyright (2003), American Institute of Physics

5.4 Plasma Heating and Etching Effects

Although the primary intention to introduce plasma in CNT growth is to reduce the activation energy by facilitating hydrocarbon dissociation as stated above, the plasma has two other major collateral effects which must be taken into consideration and sometimes utilization: heating and etching. As a DC voltage higher than the breakdown threshold on the Paschen curve is applied across the electrodes, free electrons are energized and subsequently ionize neutral species through elastic collisions, generating more free electrons. Such an avalanche process causes an electrical discharge state of a collection of free electrons, ions, and neutral species, which is called plasma.

The collisions among energized charged particles and neutral molecules inside the plasma body raise the gas temperature which can be conducted to the substrate. Also the ionic bombardment onto the substrate surface (sitting at a negative potential on the cathode) caused by positive ions accelerated across the plasma sheath field incurs ohmic heating of the substrate. Both processes together can lead to significant substrate heating to above 700 °C in real growth chambers without a separate heater

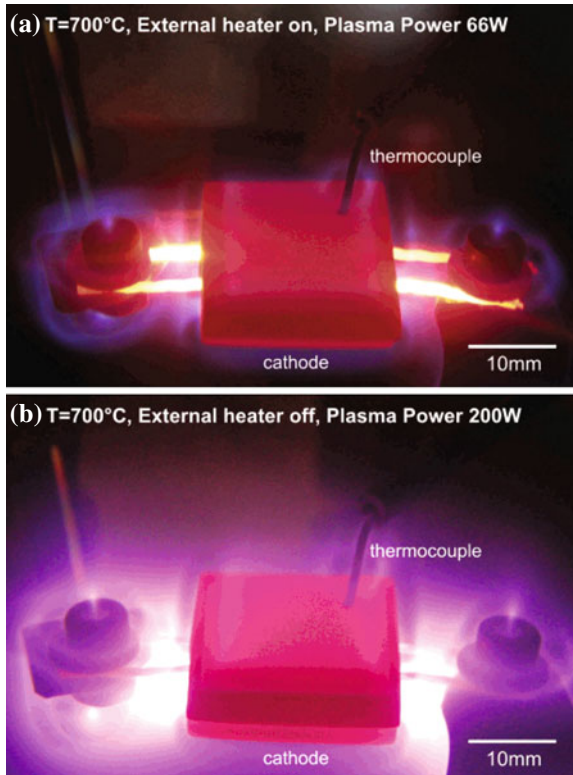


Fig. 5.4 **a** Photograph showing combined resistive heating using an external tungsten heater beneath the electrode and plasma heating at 700 °C. **b** Plasma heating of the cathode at 700 °C, using 200 W of plasma power with the external heater off. The chamber is filled with a mixture of gases of 54:200 sccm of C_2H_2/NH_3 at a pressure of 12 mbar. From Teo et al. [11]. Copyright (2004) American Chemical Society

[11]. Figure 5.4 shows that plasma heating can raise the substrate temperature as much as using a separate heater. Aligned CNTs can grow with such plasma heating just as well as with separate heating mechanisms. It is also this plasma heating effect that puts the accuracy of many low-temperature PECVD growth results into question. Special care has to be taken during the experimental setup to measure the substrate temperature which includes the heating contribution from the plasma.

Besides partially causing the plasma heating effect, the ion bombardment on the substrate surface exposed to the plasma also causes physical or chemical mass removal, especially at locations where the local field strength is high. Such a plasma etching effect is widely conceived to account for the removal of amorphous carbon during CNT growth and facilitate the catalyst thin-film dewetting prior to CNT growth. One of the clearest demonstrations of the plasma etching effect is done using 2D periodic catalyst particle arrays where particle size (and the resulting CNT

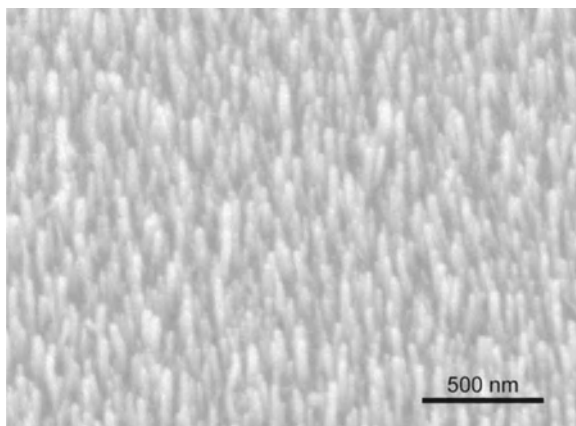


Fig. 5.5 An SEM image of aligned CNF arrays grown from a 6 nm thick Ni film at 400 °C for 1 h by a dark-discharge current density of $<6.2 \mu\text{A}/\text{cm}^2$. From Wang et al. [6]. Reprinted with permission from Institute of Physics

diameter) is shown to decrease with increasing time of plasma exposure before CNT growth [12, 13]. This provides an opportunity to tailor the catalyst particle size and control the resulting CNT diameter by exposing the particles to a certain period of plasma etching prior to CNT growth. Besides reducing the particle size, the plasma etching also rounds off any sharp edges of the original particle shape and, in some cases, facilitates and modifies the breaking down (dewetting) of a continuous film [6, 14–16].

5.5 Plasma States

For DC plasmas, there exists a series of discharge states with different current density levels. From current density levels of low to high, a DC plasma can experience dark discharge, glow discharge, and arc-discharge states [17]. Since right after gas breakdown, the plasma directly enters the glow discharge state which is most frequently used for most PECVD growth processes. If the current density of a glow discharge state is continuously lowered crossing a critical point when the bias voltage experiences an abrupt increase, the plasma enters a new state of dark discharge. The extremely low current density level of dark discharges can significantly reduce the plasma heating and etching effects, which may be beneficial to aligned CNT growth in many scenarios where such effects are detrimental. For instance, aligned CNF arrays with exceptionally small diameters (10 nm) are successfully grown using a dark discharge plasma (Fig. 5.5), and the process also allowed direct CNF growth on TCO underlayers such as ITO and ZnO at a moderately low temperature [6].

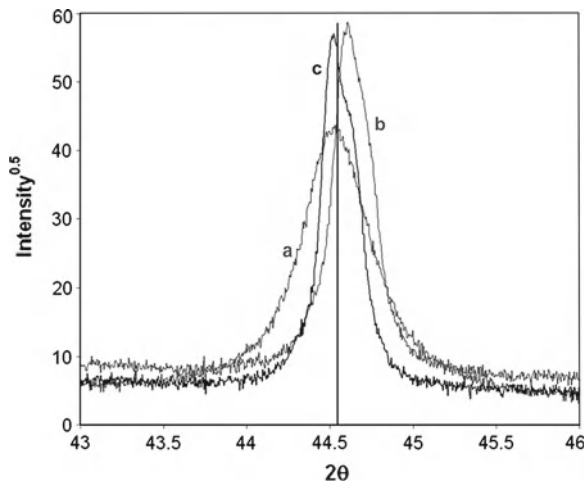


Fig. 5.6 Ni (111) reflection following **a** initial thin-film deposition at room temperature, **b** the pre-etch to break-up the film into discrete nanoparticles associated with a 2° peak shift to the right indicating a tensile, biaxial stress that developed in the film due to the thermal cycle, and **c** suspension of the nanoparticle film above the substrate surface by the aligned CNFs. From Fowlkes et al. [18]. Copyright (2006), Elsevier

Counterintuitively, dark discharges have a highly uniform nature which is suitable for large-scale applications.

5.6 Catalyst Crystal Orientation

It is almost always preferable to have identical CNTs or CNFs in an aligned array over a macroscopic distance. Further work needs to be done to improve the uniformity across an array by starting from catalyst particles of identical morphology and crystallographic orientation. It has been shown that during CNT growth by DC-PECVD, the crystallographic orientations of the catalyst particles are preserved [18]. Figure 5.6 shows the X-ray diffraction (XRD) comparison among the original Ni film (curve *a*), the dewetted Ni particles (curve *b*), and the Ni particles embedded in the CNTs (curve *c*) after growth. The Ni crystal orientation is preserved. Such preservation means that it is useful to prepare catalyst particles all with the same crystallographic orientation by epitaxial growth methods [19, 20] or graphoepitaxy [21–23], etc.

The motivations for such epitaxial control of the catalyst particles are: (1) carbon diffusion rates along different catalyst crystal planes are different, meaning that catalyst particles with the same orientation might provide the same CNT growth rate [18, 24]; (2) CNT cap formation is determined by the surface facets of the catalyst particles, meaning that catalyst particles with the same orientation might yield CNTs with the same atomic structure (chirality, diameter, etc.) [25–27]. Of course, precise

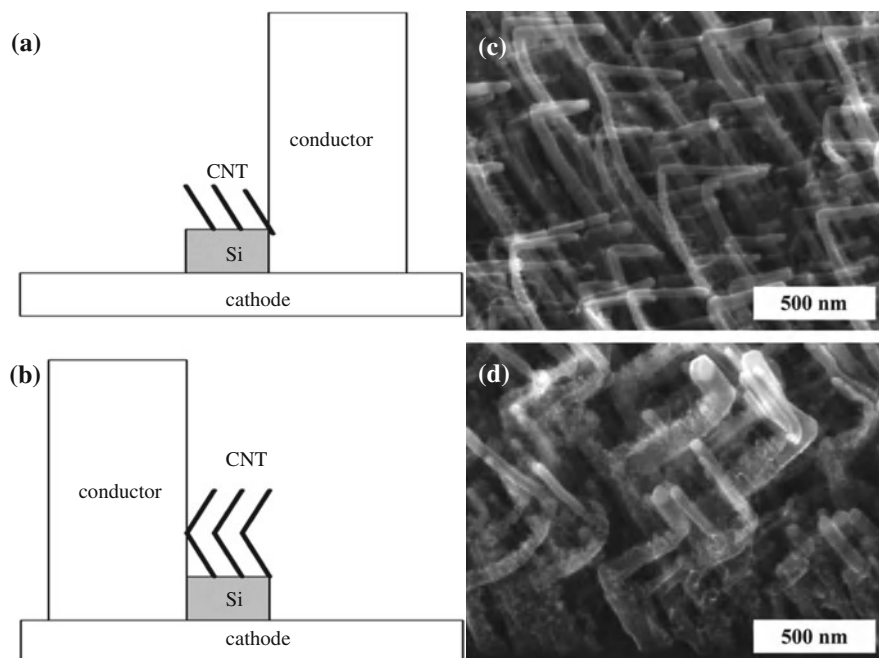


Fig. 5.7 a, b Mechanism of carbon capping. CNT growth direction is changed by modifying local electric field direction using a conductor block. SEM images of CNTs with over 90° bends (c) and longer CNTs with multiple bends to produce a zigzag structure (d). c and d From AuBuchon et al. [28]. Copyright (2005) American Chemical Society

control of CNT structures on the atomic level in an aligned array will involve much more than controlling the crystallographic orientation of the catalyst particles, but this is certainly a first and necessary step to take. And the orientation preservation of the catalyst particles during the DC-PECVD process provides the prerequisite condition for achieving this ambitious goal.

5.7 Electric Field Manipulation

Since CNTs grow along the electric field lines in the DC-PECVD process, one can impose special conditions where CNTs grow at an angle to the substrate plane. This is usually done at a relatively small scale by modifying the local field direction using a second conductor block during the PECVD growth in the chamber, such as that shown in Fig. 5.7a and c. Furthermore, once the first inclined CNT growth is completed, the setup can be changed to result in a different field direction and then the growth can be restarted by re-activating the catalyst particles [28] or introducing new catalysts [29]. Repeating the above procedure may result in zigzag-shaped bent CNT arrays

(Fig. 5.7b and d), which exemplifies the degree of alignment manipulation using variations of conventional DC-PECVD methods.

Such techniques are valuable for the study of catalytic properties of nanoparticles and the electric field effects on CNT growth and, most importantly, widen the possibilities to achieve more complicated and well-controlled CNT morphologies. One can imagine that in an advanced PECVD setup where the substrate is surrounded by various conductors whose positions and shapes can be remotely controlled at all time during the growth by an external controller, CNTs can be accurately grown into almost arbitrary shapes with even more variety and complexity in a quite straightforward way.

5.8 DC-PECVD Growth Mechanism

In a plasma enhanced chemical vapor deposition, carbon nanotubes are grown through the repeated accumulation of carbon atoms from the decomposition of gasses upon a catalyst particle, as described in Chap. 3.3. The alignment mechanism of millions of carbon nanotubes upon the substrates is generally attributed to the electric field caused by the plasma, as discussed in Chap. 4.2.4. CNTs grow parallel to the electric field to form aligned CNT arrays.

However the plasma etching complicates the CNT growth procedure, yielding three stages of a CNT alignment growth. In the first stage, the budding tubes appear randomly entangled; then partially aligned tubes appear in a second stage, then tubes in full alignment in the third final stage. In the process of achieving the third stage of nanotube growth, the two earlier stages of CNT growth have usually been overlooked as each stage is etched away by the next application of plasma.

Below we talk about the whole CNT growth procedure using a thin Ni catalyst coating film with a thickness of 5 nm under DC-PECVD conditions.

5.8.1 First Stage: Randomly Entangled CNT Growth

The first stage tubes, produced in zero to four minutes (growth time: $\tau = 0\text{--}4$ min), are described as a tangle of random large and small diameter carbon nanotubes.

With growth time $\tau = 1$ min, Fig. 5.8a shows that CNT growth by PECVD can rapidly generate lots of randomly entangled CNTs that are composed of thick and short CNTs (diameter $\phi \sim 100$ nm, length $L \sim 1$ μm), plus some thin and long CNTs ($\phi \sim 20$ nm, $L \sim 4$ μm). These first-stage-CNTs are randomly entangling and partially standing (some CNTs lying down) on the surface of the substrate, which is totally different from the vertically aligned CNTs [5, 12, 14, 31–35]. Based on the morphology of the first-stage-CNTs in Fig. 5.8a and the fast growth rate (around 1–4 $\mu\text{m}/\text{min}$), it is suggested that the CNT growth is dominated by a thermal CVD processing rather than a PECVD processing (standard growth rate at 0.1–0.2 $\mu\text{m}/\text{min}$ [36]), which probably resulted from the strong catalytic capability of the nanoscale

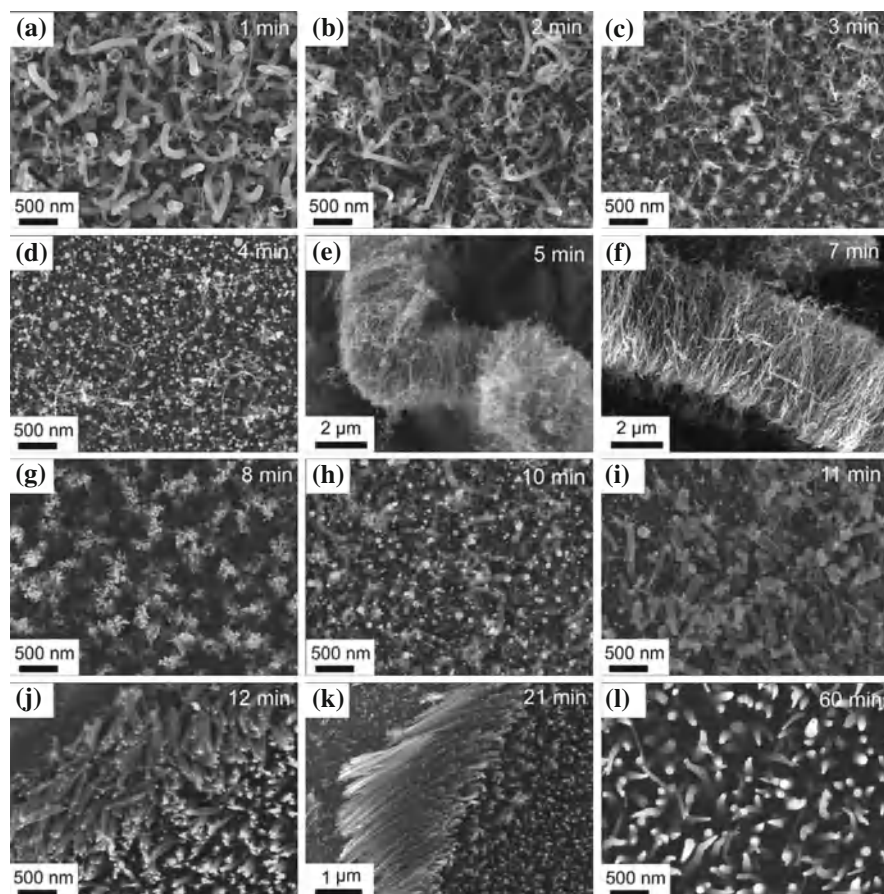


Fig. 5.8 SEM microphotographs showing the effect of plasma etching on the CNT growth evolution in a PECVD system (Ni catalyst thickness: 5 nm, growth time: $\tau = 1\text{--}60$ min). From Wang et al. [30]. Reprinted with permission from IOP Publishing

Ni particles at high temperature, and the sufficient supply of carbon sources that came from the decomposition of the feedgas C_2H_2 . Interestingly, Fig. 5.8a and TEM images show that the catalyst particles (Ni) only locate on the top end of each CNT, which agrees with the most common CNT growth mode by PECVD (tip-mode) [5, 12, 14, 31–35], but disagrees with the standard CNT growth mode by thermal CVD (base- or root-mode) [37]. Under this circumstance, it is supposed that these isolated Ni particles are mainly granulated by the NH_3 annealing (more than 30 min at high temperature), rather than by the plasma etching (more details are discussed later).

However, the first-stage-CNTs cannot grow further due to the effect of the subsequent plasma etching. Figure 5.8b shows that more than half of the CNTs (thick

and short) are etched away by the plasma at $\tau = 2$ min, and Fig. 5.8c shows that most of the CNTs disappear at $\tau = 3$ min. It is interesting to note that the thin and long CNTs can survive for a longer period of time than the thick and short ones. This phenomenon could be attributed to the fact that the thin and long CNTs have better crystallization than the thick and short ones [30]. Accordingly, the former has higher strength than the latter to withstand the plasma etching. At $\tau = 4$ min, Fig. 5.8d shows that there are a few thick and short CNTs left plus some thin and long CNTs remaining. At the early stage ($\tau = 0\text{--}4$ min) of CNT growth, the first-stage-CNTs experienced fast growth (within the first 1 min) and then were gradually etched away (within the following 3 min), which may lead to two dramatic changes on the surface of the substrate. One is the relocation of the nanosized catalyst particles that lifted off the substrate by CNT growth and returned to the surface owing to the removal of the first-stage-CNTs. Another is the deposition of the decomposed first-stage-CNT fragments on the surface of the substrate, which is consistent with the previous finding of the 5 nm amorphous carbon film covering on the substrate surface in PECVD operation [38]. As a result, it is suggested that most of the catalyst particles (see Fig. 5.8d) were partially embedded into the amorphous carbon coating on the substrate with their top surface open due to the plasma etching. Additionally, it is seen that the areal density of Ni particles in Fig. 5.8d looks much higher than that in Fig. 5.8a. These extra Ni particles in Fig. 5.8d are supposed to come from the crumbed Ni particles on the tips of thick and short CNTs (see Fig. 5.8a) and some small Ni nanoparticles which were previously embedded in the body of the thick and short CNTs [39].

5.8.2 Second Stage: Partially Aligned CNT Growth

The second stage tubes, created in four to ten minutes ($\tau = 4\text{--}10$ min), are generally smaller in diameter, but taller and only partially aligned.

Originating from the high areal density of the small Ni particles shown in Fig. 5.8d, the second-stage-CNTs can partially align due to a crowding effect or van der Waals forces [1], as shown in Fig. 5.8e and f. At $\tau = 4\text{--}10$ min, the second-stage-CNT growth rate is around $2\text{--}4\ \mu\text{m}/\text{min}$, which is almost 5–10 times slower than the CNT growth rate by thermal CVD [37], but more than 20 times faster than a standard CNT growth rate by PECVD [36]. Accordingly, it is suggested that this second-stage-CNT growth may also be regarded as a kind of thermal CVD processing under plasma etching, as a result of the strong catalytic ability of the small Ni particles. TEM images show that the second-stage-CNTs (Fig. 5.8f) are very uniform in diameter ($\phi \approx 20$ nm), and the multi-walled second-stage-CNTs have much better crystallization or graphitization [30] than that obtained by normal PECVD growth [5, 31]. Actually, these second-stage-CNTs grown by PECVD have a very similar morphology to those CNTs grown by thermal CVD [37, 40], except for the fact that the second-stage-CNTs grown by PECVD have the catalyst particles (Ni) located on the CNT top ends (tip-mode [1, 34]), but the CNTs grown by thermal CVD always keep the catalyst particles (Fe) at the bottom (base-mode [1, 34]). When the CNT

growth time reached 8 min, as shown in Fig. 5.8g, the topview SEM image shows that some second-stage-CNTs top tips aggregated to form clusters as a result of plasma etching. Moreover, at $\tau = 10$ min, Fig. 5.8h shows that most of the second-stage-CNTs were removed by plasma etching. That is, the lifetime of second-stage-CNTs is less than 6 min. During this period of time, second-stage-CNTs might effectively protect (covering) the remaining first-stage-CNTs from the plasma etching. Therefore, it is noted that Fig. 5.8h and d have similar morphologies. Figure 5.8h and TEM images [30] clearly show that the remaining thick CNTs (leftover from the incomplete etching of the big diameter first-stage-CNTs shown in Fig. 5.8a) have been seriously damaged by the plasma etching. Additionally, it is noted that the areal density of Ni particles in Fig. 5.8h is a little bit smaller than that shown in Fig. 5.8d. While the second-stage-CNTs were etched out, most of the etched carbon species were evaporated and pumped out, but some CNT debris could directly fall down to the substrate surface to form the amorphous layer [38]. In this case, some small Ni particles may have been embedded into the carbon layer and thus cannot be imaged by the SEM shown in Fig. 5.8h.

5.8.3 Third Stage: Fully Aligned CNT Growth

After ten minutes of plasma etching ($\tau = 10$ –60 min), the early stage nanotubes have been washed away and the third stage tubes begin to emerge in tall, ordered rows upon the substrate. At this stage, the tubes themselves are shielded by makeshift *helmets* of catalyst particles, which effectively protect them during the last part of the growth process. Eventually, these last bits of catalyst are etched away as well.

While the second-stage-CNTs were being etched out, a new kind of CNTs (third-stage-CNTs) started to nucleate and grow. It is seen that the third-stage-CNTs align perpendicularly to the substrate with their catalyst particles facing the plasma ion bombardment. As shown from TEM images, the very limited carbon deposition layer on the top surface should be identified as the third-stage-CNT growth direction. In this case, the metal particle (Ni) can act as a *safety helmet* to withstand the plasma etching, which protects the main body of the third-stage-CNTs. Accordingly, it is reasonable that all of the third-stage-CNTs are fully perpendicular to the substrate, with the growth direction along the axis line of the third-stage-CNTs only. Once some third-stage-CNTs lose the shielding heads (Ni) or deviate from the growth direction, the CNTs will be cut/etched away by the plasma. In other words, the plasma etching only allows the vertically aligned CNTs to survive and grow longer (see Fig. 5.8i–l).

As for the third-stage-CNT growth, Fig. 5.8k and TEM images [30] show that each third-stage-CNT grows perpendicularly to the substrate. TEM images clearly shows the tip-mode growth with the catalyst particles on the top ends of third-stage-CNTs [30]. The disordered *bamboo* structure inside the third-stage-CNTs is the proof of the growth direction, which is consistent with the previous studies [31, 41]. During the third-stage-CNT growth, some parts of the catalytic particles may break away due to the plasma etching and be embedded inside the third-stage-CNT body, but others may

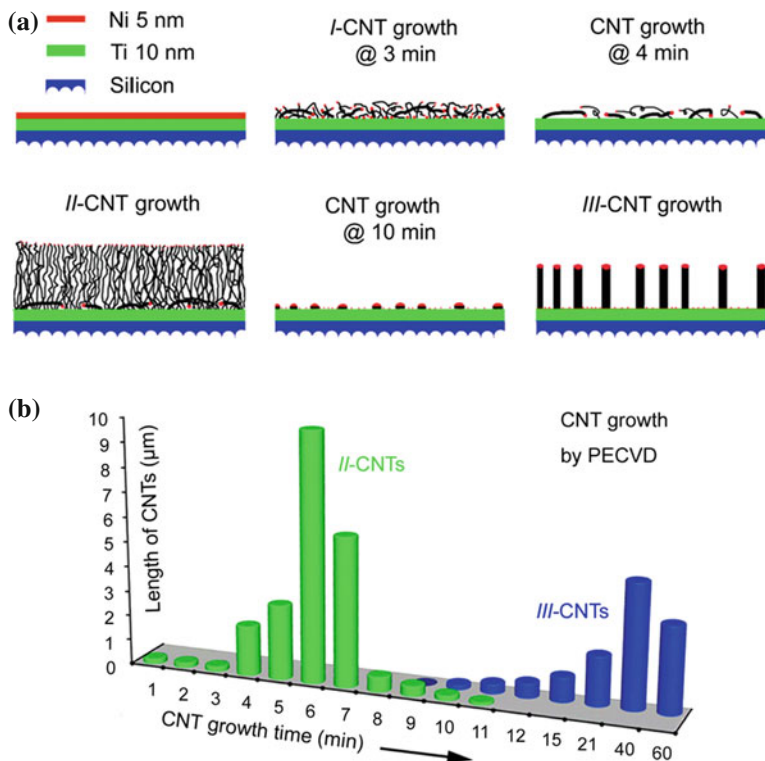


Fig. 5.9 **a** A model showing the evolution of CNTs from first-stage-CNTs (I-CNTs) to second-stage-CNTs (II-CNTs) to third-stage-CNTs (III-CNTs) during their growth by the PECVD system. **b** Diagram showing the CNT length versus growth time and the starting and ending of the growth of the partially aligned II-CNTs and the fully aligned III-CNTs. From Wang et al. [30]. Reprinted with permission from IOP Publishing

be etched off by plasma. Eventually, the catalytic particles will be completely gone and the growth stops. The TEM images clearly showed that one catalytic particle has been completely removed by the plasma etching [30], resulting in a sharp end of the third-stage-CNTs, which means the CNT cannot get further growth and start to be shortened due to further plasma etching.

5.8.4 DC-PECVD Growth Mechanism

In summary of the above evolution of CNT growth (with catalyst Ni thickness of 5 nm) in a DC-PECVD system, an illustrating model in Fig. 5.9a could help to elucidate the effect of plasma etching on the evolution of first-stage- and second-stage-CNTs and the final growth of third-stage-CNTs. Additionally, through careful

measurements of the CNTs length at certain growth time, the growth evolution of second-stage-CNTs and third-stage-CNTs can be found, as shown in Fig. 5.9b. It clearly shows the starting and ending of each growth stage and the evolution of the growth with time.

References

1. A.V. Melechko, V.I. Merkulov, T.E. McKnight, M.A. Guillorn, K.L. Klein, D.H. Lowndes, M.L. Simpson, Vertically aligned carbon nanofibers and related structures: controlled synthesis and directed assembly. *J. Appl. Phys.* **97**(4), 041301/1–041301/39 (2005)
2. M. Meyyappan, L. Delzeit, A. Cassell, D. Hash, Carbon nanotube growth by PECVD: a review. *Plasma Sources Sci. Technol.* **12**(2), 205–216 (2003)
3. Y. Wang, Nanophotonics of vertically aligned carbon nanotubes: two-dimensional photonic crystals and optical dipole antenna. Ph.D. thesis, Boston College, 2006
4. Persistence of Vision Pty. Ltd, Persistence of Vision Raytracer (Version 3.6) (2004)
5. Z.F. Ren, Z.P. Huang, J.W. Xu, J.H. Wang, P. Bush, M.P. Siegal, P.N. Provencio, Synthesis of large arrays of well-aligned carbon nanotubes on glass. *Science* **282**, 1105–1107 (1998)
6. Y. Wang, S.H. Jo, S. Chen, D.Z. Wang, Z.F. Ren, Aligned carbon nanofibres by a low-energy dark discharge for field emission and optoelectronics. *Nanotechnology* **17**(2), 501–505 (2006)
7. S. Hofmann, G. Csányi, A.C. Ferrari, M.C. Payne, J. Robertson, Surface diffusion: the low activation energy path for nanotube growth. *Phys. Rev. Lett.* **95**(3), 036101/1–036101/4 (2005)
8. S. Hofmann, C. Ducati, J. Robertson, B. Kleinsorge, Low-temperature growth of carbon nanotubes by plasma-enhanced chemical vapor deposition. *Appl. Phys. Lett.* **83**(1), 135–137 (2003)
9. Z. Yu, S. Li, P.J. Burke, Synthesis of aligned arrays of millimeter long, straight single-walled carbon nanotubes. *Chem. Mater.* **16**(18), 3414–3416 (2004)
10. E.J. Bae, Y.-S. Min, D. Kang, J.-H. Ko, W. Park, Low-temperature growth of single-walled carbon nanotubes by plasma enhanced chemical vapor deposition. *Chem. Mater.* **17**(20), 5141–5145 (2005)
11. K.B.K. Teo, D.B. Hash, R.G. Lacerda, N.L. Rupesinghe, M.S. Bell, S.H. Dalal, D. Bose, T.R. Govindan, B.A. Crudden, M. Chhowalla, G.A.J. Amaratunga, M. Meyyappan, W.I. Milne, The significance of plasma heating in carbon nanotube and nanofiber growth. *Nano Lett.* **4**(5), 921–926 (2004)
12. Z.P. Huang, J.W. Xu, Z.F. Ren, J.H. Wang, M.P. Siegal, P.N. Provencio, Growth of highly oriented carbon nanotubes by plasma-enhanced hot filament chemical vapor deposition. *Appl. Phys. Lett.* **73**(26), 3845–3847 (1998)
13. X. Wang, K. Kempa, Z.F. Ren, B. Kimball, Rapid photon flux switching in two-dimensional photonic crystals. *Appl. Phys. Lett.* **84**(11), 1817–1819 (2004)
14. J.H. Choi, T.Y. Lee, S.H. Choi, J.-H. Han, J.-B. Yoo, C.-Y. Park, T. Jung, S. Yu, W. Yi, I.T. Han, J.M. Kim, Density control of carbon nanotubes using NH₃ plasma treatment of Ni catalyst layer. *Thin Solid Films* **435**(1–2), 318–323 (2003)
15. S.H. Lim, K.C. Park, J.H. Moon, H.S. Yoon, D. Pribat, Y. Bonnassieux, J. Jang, Controlled density of vertically aligned carbon nanotubes in a triode plasma chemical vapor deposition system. *Thin Solid Films* **515**(4), 1380–1384 (2006)
16. J.H. Choi, T.Y. Lee, S.H. Choi, J. Han, J. Yoo, C. Park, T. Jung, S.G. Yu, W. Yi, I. Han, J.M. Kim, Control of carbon nanotubes density through ni nanoparticle formation using thermal and NH₃ plasma treatment. *Diamond Relat. Mater.* **12**(3–7), 794–798 (2003)
17. J.R. Roth, *Industrial Plasma Engineering* (Institute of Physics Publishing, Bristol, 1995), Chap. 8–9
18. J. Fowlkes, A. Melechko, K. Klein, P. Rack, D. Smith, D. Hensley, M. Doktycz, M. Simpson, Control of catalyst particle crystallographic orientation in vertically aligned carbon nanofiber synthesis. *Carbon* **44**(8), 1503–1510 (2006)

19. F. Silly, M.R. Castell, Fe nanocrystal growth on SrTiO₃ (001). *Appl. Phys. Lett.* **87**(6), 063106 (2005)
20. H. Zhou, D. Kumar, A. Kvit, A. Tiwari, J. Narayan, Formation of self-assembled epitaxial nickel nanostructures. *J. Appl. Phys.* **94**(8), 4841–4846 (2003)
21. M.W. Geis, D.C. Flanders, H.I. Smith, Crystallographic orientation of silicon on an amorphous substrate using an artificial surface-relief grating and laser crystallization. *Appl. Phys. Lett.* **35**(1), 71–74 (1979)
22. A.L. Giermann, C.V. Thompson, Solid-state dewetting for ordered arrays of crystallographically oriented metal particles. *Appl. Phys. Lett.* **86**(12), 121903 (2005)
23. Y.-J. Oh, C.A. Ross, Y.S. Jung, Y. Wang, C.V. Thompson, Cobalt nanoparticle arrays made by templated solid-state dewetting. *Small* **5**(7), 860–865 (2009)
24. T.E. McKnight, A.V. Melechko, D.W. Austin, T. Sims, M.A. Guillorn, M.L. Simpson, Microarrays of vertically-aligned carbon nanofiber electrodes in an open fluidic channel. *J. Phys. Chem. B* **108**(22), 7115–7125 (2004)
25. S. Hong, Y.-H. Shin, J. Ihm, Crystal shape of a nickel particle related to carbon nanotube growth. *Jpn. J. Appl. Phys.* **41**(Part 1, 10), 6142–6144 (2002)
26. S. Reich, L. Li, J. Robertson, Control the chirality of carbon nanotubes by epitaxial growth. *Chem. Phys. Lett.* **421**(4–6), 469–472 (2006)
27. S. Reich, L. Li, J. Robertson, Structure and formation energy of carbon nanotube caps. *Phys. Rev. B* **72**(16), 165423/1–165423/8 (2005)
28. J.F. AuBuchon, L. Chen, S. Jin, Control of carbon capping for regrowth of aligned carbon nanotubes. *J. Phys. Chem. B* **109**(13), 6044–6048 (2005)
29. J.F. AuBuchon, L. Chen, C. Daraio, S. Jin, Multibranching carbon nanotubes via self-seeded catalysts. *Nano Lett.* **6**(2), 324–328 (2006)
30. H. Wang, Z.F. Ren, The evolution of carbon nanotubes during their growth by plasma enhanced chemical vapor deposition. *Nanotechnology* **22**(40), 405601 (2011)
31. Z. Huang, D. Wang, J. Wen, M. Sennett, H. Gibson, Z. Ren, Effect of nickel, iron and cobalt on growth of aligned carbon nanotubes. *Appl. Phys. A* **74**(3), 387–391 (2002)
32. M. Chhowalla, K.B.K. Teo, C. Ducati, N.L. Rupasinghe, G.A.J. Amaratunga, A.C. Ferrari, D. Roy, J. Robertson, W.I. Milne, Growth process conditions of vertically aligned carbon nanotubes using plasma enhanced chemical vapor deposition. *J. Appl. Phys.* **90**(10), 5308–5317 (2001)
33. A. Gohier, T.M. Minea, M.A. Djouadi, A. Granier, Impact of the etching gas on vertically oriented single wall and few walled carbon nanotubes by plasma enhanced chemical vapor deposition. *J. Appl. Phys.* **101**(5), 054317 (2007)
34. V.I. Merkulov, A.V. Melechko, M.A. Guillorn, D.H. Lowndes, M.L. Simpson, Alignment mechanism of carbon nanofibers produced by plasma-enhanced chemical-vapor deposition. *Appl. Phys. Lett.* **79**(18), 2970–2972 (2001)
35. A.V. Melechko, V.I. Merkulov, D.H. Lowndes, M.A. Guillorn, M.L. Simpson, Transition between ‘base’ and ‘tip’ carbon nanofiber growth modes. *Chem. Phys. Lett.* **356**(5–6), 527–533 (2002)
36. Y. Wang, J. Rybczynski, D.Z. Wang, K. Kempa, Z.F. Ren, W.Z. Li, B. Kimball, Periodicity and alignment of large-scale carbon nanotubes arrays. *Appl. Phys. Lett.* **85**(20), 4741–4743 (2004)
37. C. Zhang, S. Pisana, C. Wirth, A. Parvez, C. Ducati, S. Hofmann, J. Robertson, Growth of aligned millimeter-long carbon nanotube by chemical vapor deposition. *Diam. Relat. Mater.* **17**(7–10), 1447–1451 (2008)
38. K.B.K. Teo, M. Chhowalla, G.A.J. Amaratunga, W.I. Milne, G. Pirio, P. Legagneux, F. Wycisk, J. Olivier, D. Pribat, Characterization of plasma-enhanced chemical vapor deposition carbon nanotubes by Auger electron spectroscopy. *J. Vac. Sci. Technol. B* **20**(1), 116–121 (2002)
39. S.H. Jo, Y. Tu, Z.P. Huang, D.L. Carnahan, J.Y. Huang, D.Z. Wang, Z.F. Ren, Correlation of field emission and surface microstructure of vertically aligned carbon nanotubes. *Appl. Phys. Lett.* **84**(3), 413–415 (2004)

40. L. Qu, L. Dai, M. Stone, Z. Xia, Z.L. Wang, Carbon nanotube arrays with strong shear binding-on and easy normal lifting-off. *Science* **322**(5899), 238–242 (2008)
41. V.I. Merkulov, D.H. Lowndes, Y.Y. Wei, G. Eres, E. Voelkl, Patterned growth of individual and multiple vertically aligned carbon nanofibers. *Appl. Phys. Lett.* **76**(24), 3555–3557 (2000)

Chapter 6

Technologies to Achieve Carbon Nanotube Alignment

Because of the strong anisotropy of CNT properties, it is always necessary to consider the orientation of its longitudinal direction when a CNT component is considered for both scientific studies and practical applications. Knowing the orientation is also a prerequisite to locate the two ends of a CNT that usually needs to be physically contacted by instrumental probing during characterizations or device integration. For a group of CNTs, the anisotropic nature of individual CNTs is best preserved and explicitly conceived when all the CNTs are aligned in the same direction as an array. Also, as opposed to many random CNT ensembles where individual CNTs are frequently bundled and twisted around one another, aligned CNT arrays usually are composed of isolated straight individual CNTs, making it possible to control the morphology of each of them, the spatial arrangement among them, the uniformity across the entire array, etc. This degree of detailed control is critically required for many major applications in electronics, optics, and others.

There are a handful of experimental technologies available to align a single or an array of CNTs along a predetermined orientation. The techniques rely on different mechanisms and therefore are applicable to different situations. These techniques are categorized into two groups pertaining to when the alignment is achieved: (a) *in situ* techniques where alignment is achieved during the CNT growth process and (b) *ex situ* techniques where CNTs are originally grown in random orientations and alignment is achieved afterwards such as during the device integration process. Such categorization is not out of absolute necessity but emphasizes those differences between the two schemes that are more important for potential large-scale manufacturing. While the *in situ* techniques bear the benefit of straightforwardness and simplicity, the *ex situ* techniques are free of growth restrictions such as substrate material and temperature. As process simplicity always comes first by the consideration of a manufacturer, the majority of alignment techniques invented so far are *in situ* techniques.

6.1 In Situ Techniques for Carbon Nanotube Alignment

In situ techniques directly align CNTs during the CNT growth process. It is straightforward and simple. Till date, aligned CNTs are most frequently grown using the in situ techniques. Here, we focus on the in situ CNT alignment from thermal CVD and plasma-enhanced chemical vapor deposition (PECVD) methods assisted by catalytic nanoparticles. Other in situ techniques, such as arc discharge method, laser ablation method, hydrothermal method, and flame method, are briefly discussed in Chap. 3.

6.1.1 Thermal Chemical Vapor Deposition with Crowding Effect

CNTs can be grown vertically on substrates using thermal CVD when the site density of catalyst is high enough. In a catalytic CVD growth process employing crowding effect, CNTs are grown from catalyst nanoparticles deposited on a substrate. One of the most common scenarios is that the nanoparticles are formed through a solid-state dewetting process [1, 2] of a continuous polycrystalline thin film deposited by physical vapor deposition, magnetron sputtering, thermal evaporation, etc. When a thin film of catalytic material (such as Fe) is heated under a non-reactive gas ambient or vacuum, voids will first appear at grain boundary triple junctions and grow larger driven by surface energy minimization. According to the Rayleigh instability theory [3], the continuation of such a dewetting process will lead to fingering morphology at the void rims and edges of the film and eventually result in isolated particle formation with both particle size and spacing determined by the film thickness. For CNT growth by CVD, catalytic nanoparticle size is usually only 0.5–10 nm, which requires very thin starting catalyst films and consequently very tight particle spacing.

High growth yield is also important in CNT alignment. As CNTs begin to grow from these densely distributed catalyst particles, it is generally conceived that van der Waals forces among close-by CNT neighbors cause them to all grow vertically to the substrate. Indeed, when certain growth conditions lead to a low growth yield, i.e., CNTs only grow from a small fraction of all the catalyst particles, the decrease in CNT site density (or increase in CNT spacing) results in complete randomness of CNT orientations [4], which confirms the crowding effect as the alignment mechanism for densely packed CNT arrays.

Since catalyst particles prepared by dewetting of thin films from physical vapor deposition usually have small interparticle spacing, the task to achieve aligned CNT growth solely relies on high growth yield by optimal CVD growth control. Such high yield growth has been repeatedly achieved throughout the CNT research community, for SWCNTs [4, 5], DWCNTs [6], and MWCNTs [7], and the wall number control is a complicated topic including factors of catalyst particle size and growth conditions, which are not the intended focus of this chapter.

There are many reports on how to increase the yield growth of CNTs from catalyst. The key to realize high yield growth is a proper introduction of oxidative agents

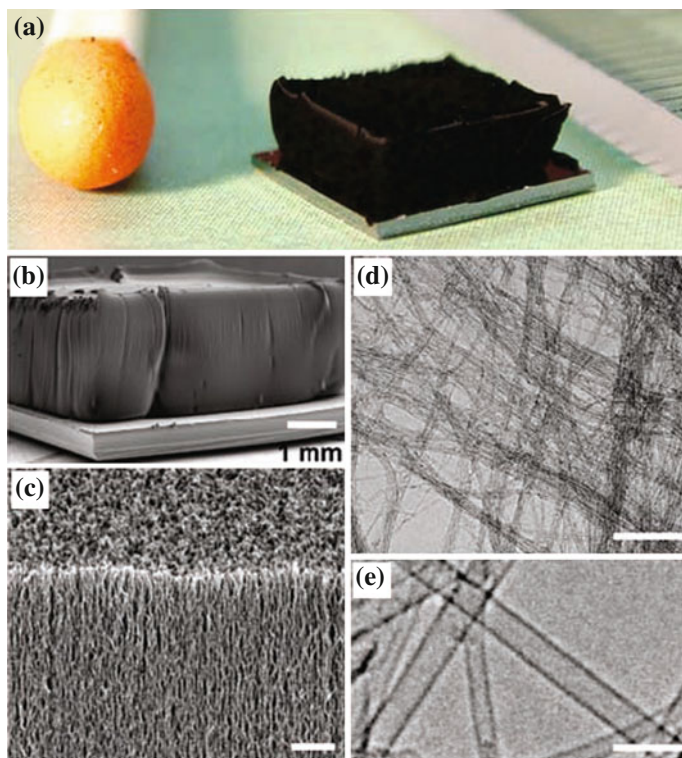


Fig. 6.1 SWCNT forest grown with water-assisted CVD. **a** Optical image of a 2.5 mm tall SWCNT forest on a 7×7 mm silicon wafer. **b** SEM image of the same SWCNT forest. **c** SEM image of the SWCNT forest ledge. **d** Low-resolution TEM image of the nanotubes. **e** HRTEM image of the SWCNTs. From Hata et al. [5]. Copyright (2004), AAAS

(O_2 , H_2O , etc.) under the gas ambient so that the catalyst particle surfaces remain active for the longest possible period, which is presumably achieved by balancing the competition between amorphous carbon growth and sp^2 graphitic crystal formation on the catalyst particles. Oxidants can not only remove or prevent amorphous carbon growth, but may also etch into graphite layers when used at higher than favorable concentrations. Another important function of oxidants is to remove excessive H_2 which is found to have negative effects on CNT growth during the incubation stage [4]. Controlling the proper level of oxidants in the growth environment depends on the specific deposition apparatus configuration and in some cases the timing and duration of oxidant introduction. When alignment is achieved, it is possible to grow aligned arrays of very long CNTs up to multiple millimeters (Fig. 6.1) as the growth front is kept unblocked [8], not possible in the case of unaligned growth.

If the starting catalyst thin film is patterned, aligned CNTs can grow into interesting vertical bundles with pre-designed shape and coordinate. Also, because such an aligned growth is independent of the substrate macroscopic morphology, one can use

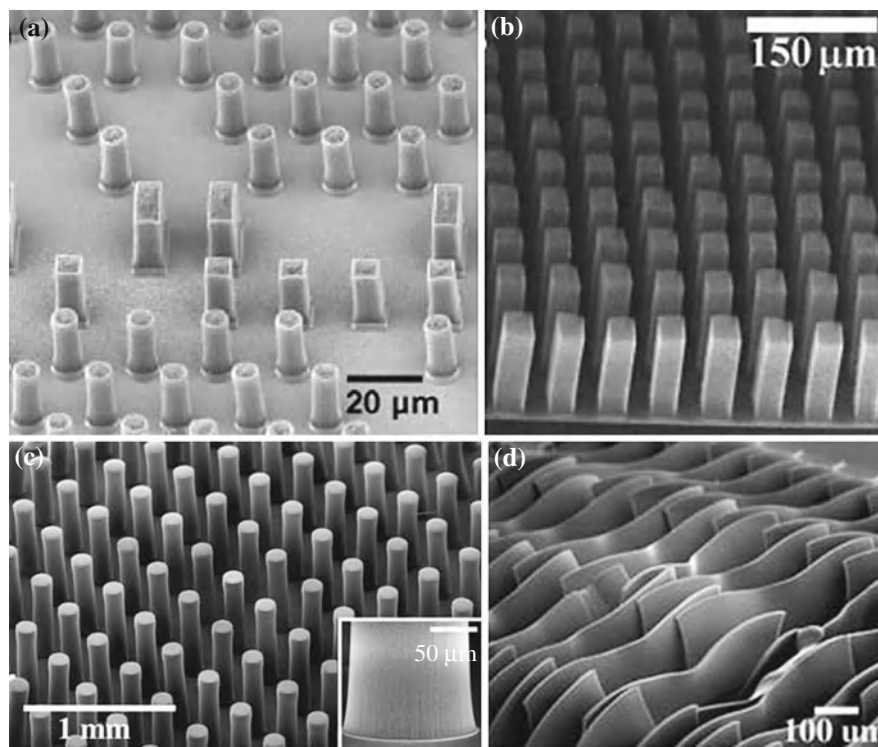


Fig. 6.2 SEM images of vertical CNT arrays with various shapes. **a** Molecular O_2 -assisted growth of vertical SWCNT square and circular towers. **b** CNT tower synthesized by thermal CVD on $38 \times 38 \mu\text{m}$ catalyst patterns. **c** SWCNT cylindrical pillars with $150 \mu\text{m}$ radius, $250 \mu\text{m}$ pitch, and 1 mm height, grown by water-assisted CVD on patterned catalyst. *Inset* SEM image of a root of a pillar. **d** SWCNT sheets with $10 \mu\text{m}$ thickness, grown by water-assisted CVD on catalytic stripe patterns. **a** From Zhang et al. [4]. Copyright (2005), National Academy of Sciences, USA. **b** From Fan et al. [9]. Copyright (1999), AAAS. **c, d** From Hata et al. [5]. Copyright (2004), AAAS

shaped substrates to obtain CNT arrays oriented in different directions according to local substrate surface curvature. Figure 6.2 shows SEM images of CNT arrays with different shapes. These CNT arrays are aligned by crowding effect during thermal CVD.

Besides the thin-film dewetting technique to obtain high-density catalyst particles, there are other ways to deposit pre-prepared catalyst nanoparticles at a high density onto growth substrates such as solution-based techniques [10], sublimation techniques [11], and deposition techniques [12]. As long as the CNTs are grown at a high enough areal density with a tight spacing, crowding effect will be effective to ensure vertical alignment of all individual CNTs.

CNT arrays can also be grown on micron-sized substrates using the crowding effect. The nanobrush shown in Fig. 6.3 demonstrates the versatility of this crowding

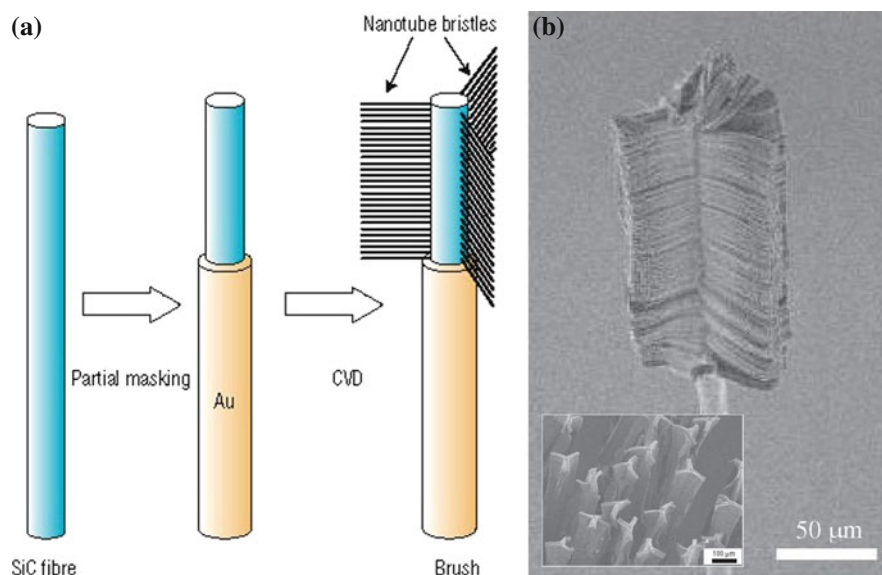
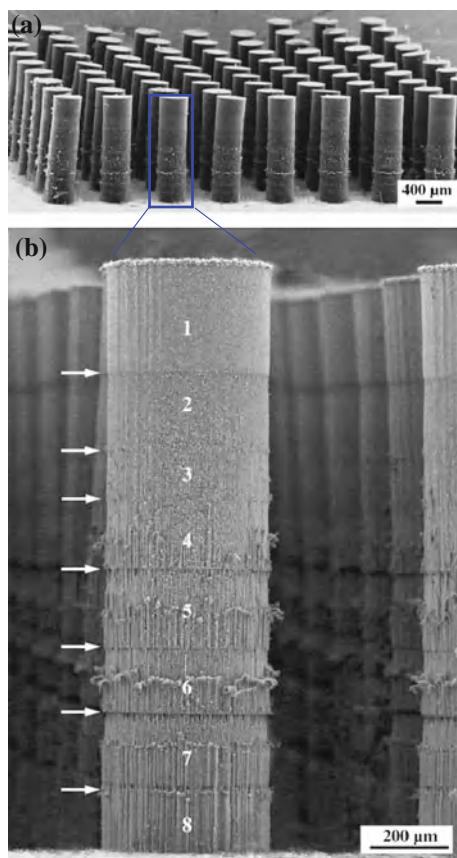


Fig. 6.3 CNT brushes grown by crowding effect. **a** Illustration of partial masking of SiC fibers in order to grow carbon nanotubes only on the fiber top. **b** A single brush (resembling a dust sweeper) consisting of nanotube bristles and a fiber handle. The bristles have a height (nanotube length) of 60 μm , and span of over 300 μm along the handle. *Inset* top-view of CNT brushes. From Cao et al. [7]. Copyright (2005), Macmillan Publishers Ltd: Nature Materials

effect method. Aligned CNTs can be grown on various substrate surface geometries, as long as the catalyst particle spacing and high yield growth conditions are met [7].

In addition, there is a so-called *regrowth* technique where one aligned CNT array as a layer of thick microscopic forests can be grown on top of another [13, 14] with the top array having its spacing and alignment inherited from the bottom one. Figure 6.4 shows a series of multiply stacked nanotube towers selectively grown on SiO_2 substrate with Au patterns. The vertically aligned nanotube arrays are perfectly stacked on top of one another, each grown on the substrate via CVD and vapor-phase catalyst delivery. During the growth, each layer, consisting of uniformly aligned arrays of hundreds of micron-long multi-walled nanotubes, nucleates and grows from the buried original substrate plane (silicon oxide) even after the substrate gets completely covered by continuous and multiple layers of nanotubes deposited during previous growth sequences. In order for this to happen, it is imperative that the hydrocarbon and the catalyst metal precursors diffuse through several hundreds of microns of porous nanotube films and start growing on top of the buried substrate, underneath the bottom of the multilayered stack of nanotubes. It also means that, every time a fresh layer is nucleated and grown from the bottom, the rest of the layers in the stack get lifted up from the substrate, moving up with the freshly growing nanotubes, from the bottom-up.

Fig. 6.4 **a** SEM image showing a 2D array of CNT pillars, each made of eight stacks of aligned nanotube layers. Eight separate growth sequences (CVD steps) were used to grow the eight stack pillars. **b** High-magnification SEM image showing the interfaces (positions indicated by *arrows*) between the separate stacks of nanotubes in a single pillar. The stacks are numbered 1–8, corresponding from the first to the eighth stack grown sequentially. From Li et al. [13]. Copyright (2005), American Chemical Society

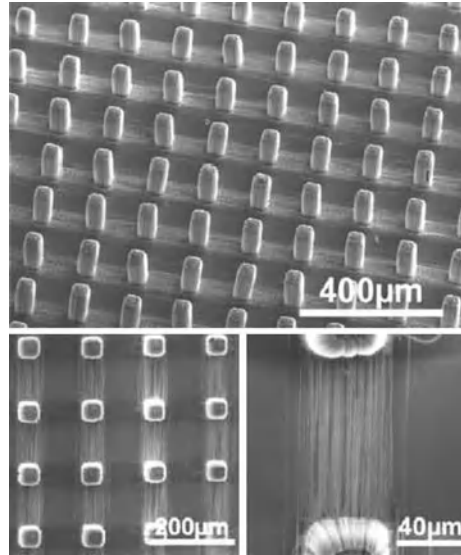


Employed a two-step CVD growth, 3D CNT architectures shown in Fig. 6.5 can be produced. The vertical MWCNT forests are first grown by crowding effect and then horizontal SWCNT arrays are grown on the substrate. The horizontal SWCNT arrays are synthesized orthogonally, connecting carbon nanotube forest islands on the substrate surface.

6.1.2 Thermal Chemical Vapor Deposition Growth with Imposed Electric Fields

Since CNTs are all electrically conductive (although with varying conductivities), a growing CNT under an external electric field can be treated as an induced electric dipole having a tendency to align with the electric field lines. Various methods have been developed to apply a strong enough electric field during the CNT growth process

Fig. 6.5 SEM images of 3D CNT architectures on quartz wafers by an orthogonally directed CVD growth. Horizontal SWCNTs are connecting MWCNT forest islands [15]. *Top* side view. *Bottom* top view



to achieve uniform alignment of CNTs based on this principle. Such field-directed growth is a useful technique to organize CNTs into horizontally aligned arrays.

Electric fields can orient CNTs owing to their large and highly anisotropic polarizability [17]. Figure 6.6b shows parallel SWCNTs directed by an electric field between a pair of electrodes on a dielectric substrate [16]. In the absence of an electric field, the CNTs grow into random CNT networks (Fig. 6.6a). SWCNTs can be field directed along the electric field direction above $0.13 \text{ V}/\mu\text{m}$ direct-current (DC) field strength or above $0.25 \text{ V}/\mu\text{m}$ AC field strength. Highly aligned suspended SWCNTs can be grown under field strength in the range of $0.5\text{--}2 \text{ V}/\mu\text{m}$ [16]. Field-directed growth has been employed to grow SWCNTs between electrodes to produce self-assembled field-effect transistors [15].

The field-alignment effect originates from the highly anisotropic polarizability of CNTs. The electric field E produces a dipole moment P on a CNT, that is, $P = \alpha E$. The polarizability along the tube axis α_{\parallel} is much higher than that perpendicular to the tube axis α_{\perp} [17]. For a nanotube oriented at an angle θ with respect to E , the dipole moment of the nanotube is along the tube axis with $P = \alpha_{\parallel} E \cos \theta$. The torque on the dipole moment is $\tau = |P \times E| = \alpha_{\parallel} E^2 \sin \theta \cos \theta$. Correspondingly, a force is applied to the dipole to rotate and align the tube with E (see inset in Fig. 6.6b). Calculation indicated that the induced large dipole moments lead to large aligning torques and forces F on the CNT and totally prevent randomization of nanotube orientation by thermal fluctuations when the electric field E is $0.5 \text{ V}/\mu\text{m}$ and the length of CNT is about $20 \mu\text{m}$ at $900 \text{ }^{\circ}\text{C}$ [16]. The grown CNTs suspend across the electrodes [16] or lie on the substrate surface [18, 19].

In a detailed discussion, it is accepted that two important factors control the aligned growth of CNTs on substrates under electric fields. The *first* is the aligning ability of

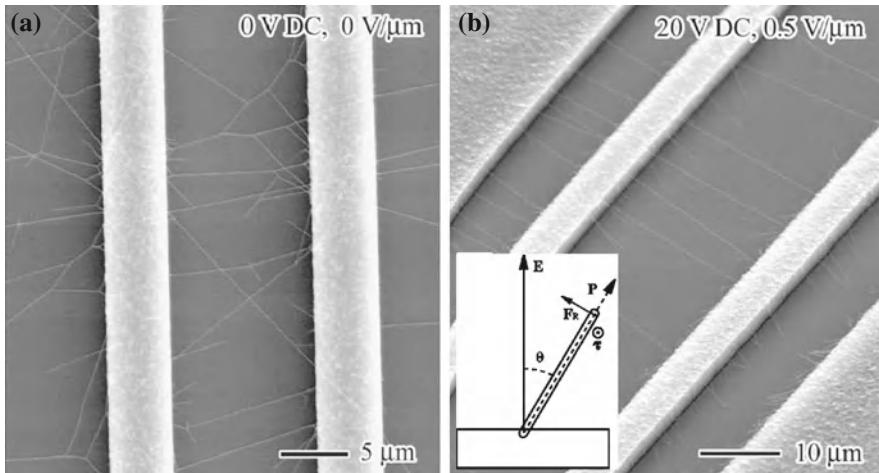


Fig. 6.6 The electric field-directed SWCNTs. **a** $E = 0 \text{ V}/\mu\text{m}$ and **b** $E = 0.5 \text{ V}/\mu\text{m}$. Inset force applied on a CNT in an electric field. From Zhang et al. [16]. Copyright (2001), American Institute of Physics

the external electric fields. For a $10 \mu\text{m}$ SWCNT, a $1 \text{ V}/\text{m}$ field strength would induce a dipole of 10 Debye, sufficient to overcome most of the orientation randomizing forces such as thermal vibration [16]. A statistical analysis of the nanotube orientation indicates that the direction of the aligned CNT axis is not parallel to the electric field perfectly, but slightly deviates by several degrees off the direction of the electric fields [19]. Besides the external electric field, the local electric field caused by static charging can also orient the CNTs grown by CVD [20]. For example, when aluminum nano-islands are patterned on oxidized silicon substrates, a large local electric field can be created by surface charging in the hot, reactive conditions of the CVD growth, and/or by an unbalanced charge at the alumina/oxide interface. Negative charge densities as high as $7 \times 10^{12} \text{ electron}/\text{cm}^2$ can be produced at the alumina/oxide interfaces [21]. CNTs grow on the silicon oxide surface near an alumina boundary, orienting perpendicularly to the boundary.

The *second* factor is the strong van der Waals interaction between the CNTs and the substrate. It is observed that field-directed CNTs suspend over quartz substrate [16] while lying on the SiO_2/Si substrate surface [18]. The van der Waals force should cause the different phenomenon. It is generally believed that during growth and lengthening of CNTs, the nanotubes stay away from substrate surfaces and the nanotubes fully experience the aligning effect of the electric field. CNTs do not contact the substrate surface until CNTs have been fully aligned to the electric field and guided onto the substrate surface. Under a certain electric field strength, the longer the CNTs, the better the alignment [16].

Plasma in the PECVD process also induces a self-biased electric field imposed on the substrate surfaces. The induced local electric fields can also direct the CNT

growth along local electric field directions in PECVD growth [22, 23]. The details are discussed in Sects. 4.2.4 and 6.1.6.

Attempts to organize CNTs into 2D crossbar structures by electric field-directed growth in two dimensions have also been carried out [24, 25]. Usually, CNT crossbar architectures are achieved by combining field-directed growth with surface-directed growth [26] (see Sect. 6.1.4). The two alignment mechanisms take place simultaneously to produce the dense nanotube crossbars.

6.1.3 Thermal Chemical Vapor Deposition Growth Under Gas Flow Fields

When CNTs grow at high temperatures, a feeding gas mixture (including reactive gases such as C_2H_4 and carrying gases such as H_2) passes over the growing CNTs. The feeding gas produces a flow field, causing CNTs to grow along the direction of the gas flow. So the flow field caused by the feeding gas can in situ orient the CNTs along the flow direction. Usually such grown CNTs are roughly parallel to the substrate surfaces.

There are two key components in the alignment mechanism. First, the growing fronts of nanotubes should be free above the substrate surface. This may happen due to fast heating under high gas flow, due to buoyant effect at low gas flow, or due to elevated sites over the substrate ground-level surface. Second, there should be a gas flow field to direct the CNT growth. A flow field always exists in the thermal CVD growth. Once the flow gas can carry CNTs (or their growing fronts) to overcome gravity, CNTs will grow along the gas flow direction.

6.1.3.1 Fast Heating Under High Gas Flow

The flow-directed method is first employed to orient CNTs in a fast-heating CVD process [27–30]. In a typical case, Si wafer substrates with catalysts are heated quickly to the reaction temperature in a CVD reaction chamber. Some resulting CNTs are long and oriented, while the short ones are random in orientation. The orientation of the long nanotubes is controlled by the gas flow direction.

It is believed that the fast-heating process causes a convection of the gas flow due to the temperature difference between the substrate and the feed gas. Such a convection flow of the feed gas lifts the nanotubes upward and keeps them floating and waving in the feed gas until CNTs are caught by the substrate because of van der Waals forces. During the whole growth process, the nanotubes are floating in the feed gas and growing along the gas flow direction.

In the fast-heating growth process, the flow rate is typically about 1,000 sccm [30]. Such a high-rate flow would cause local flow turbulences. The stability of the gas flow depends on the inner diameter ϕ of the quartz tube of the CVD furnace and the gas

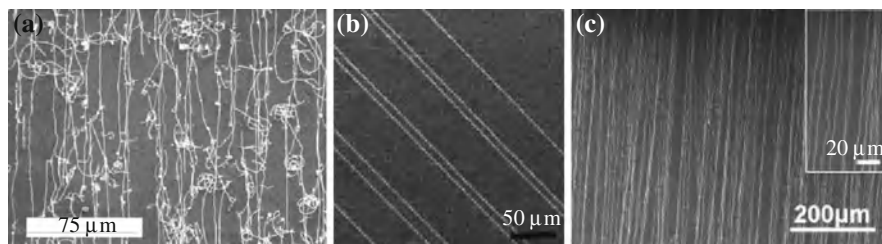


Fig. 6.7 SEM image of long CNTs oriented in a flow field. **a** SWCNTs grown under laminar flow ranges (Reynolds number = 50–2,000). **b** MWCNTs grown at Reynolds number of 50. **c** SWCNTs grown from Cu catalysts. **a** From Huang et al. [27]. Copyright (2003), American Chemical Society. **b** From Hong et al. [31]. Copyright (2005), American Chemical Society. **c** From Zhou et al. [32]. Copyright (2006), American Chemical Society

flow speed v , and can be characterized by the Reynolds number $Re = \rho v \phi / \gamma$, where ρ is the density and γ the viscosity coefficient of the feed gas. The turbulent flow causes some CNTs to touch the substrate surface and terminates the CNT growth, producing short CNTs. So the synthesized CNTs in a fast-heating growth usually consist of well-oriented long CNTs and short ones that are randomly oriented [28] as shown in Fig. 6.7a. At a higher Reynolds number, such as in the case of a large-diameter quartz tube and a high flow rate, relatively short and disordered CNTs are produced [27].

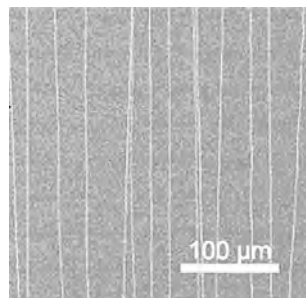
In order to grow long CNTs with alignment, a stable laminar gas flow is required to stabilize the catalytic tip of the growing CNTs, making CNT tips travel longer distances over the substrate surface. When using a small-diameter quartz tube and a low flow rate (such as less than 200 sccm), the Reynolds number can be reduced down to 50, near the lower limit of conventional laminar flow ranges. Better aligned CNTs can be achieved at low laminar flow rates (Fig. 6.7b). Obviously stable laminar flows with low Reynolds numbers are favorable for growing aligned CNT arrays [31].

The catalyst also affects the alignment of CNTs. It is reported that high-quality horizontally aligned SWCNT arrays can be prepared when Cu is used as the catalyst (Fig. 6.7c) [32].

6.1.3.2 Buoyant Effect at Low Gas Flow

When a feeding gas reaches the center region of a quartz tube from the relatively cooler end during CVD growth, a temperature difference between the substrate surface and the nearby gas will generate a vertical gas density difference (buoyant effect). The buoyant effect of convection flow induced by such gas density gradient can lift the CNTs up above the substrate, and the growth direction of CNTs can then be guided by a shear flow near the substrate surface [33].

Fig. 6.8 SEM image of SWCNT arrays obtained with 0.5 sccm of CH₄ and 1.0 sccm of H₂ at 970 °C. Reynolds number is 0.76 during CNT growth. From Jin et al. [33]. Copyright (2007) American Chemical Society



When the gas velocity is sufficiently low, the buoyant force will dominate. Figure 6.8 shows an SEM image of CNT arrays aligned by the buoyant effect. The CNTs are well aligned in parallel arrays. In order to improve the stability of the feed gas, the Reynolds number is decreased to below 1.0 by employing a very low gas flow rate and a narrow CVD quartz tube [33].

6.1.3.3 Trench Structure

The CNTs can also be oriented by a gas flow without a lift force when the catalysts are deposited on a high platform fabricated on a substrate surface [27, 34, 35]. Figure 6.9a shows a microtrench substrate surface structure. Catalytic nanoparticles are deposited on top of the microtrench. During the CNT growth, the nanotubes are freely suspended over the substrate surface and oriented along the flow direction. When CNTs grow long enough, they would touch another microtrench (see Fig. 6.9b) or settle down to the substrate surface due to gravity.

The key point of the method is to elevate the catalytic site. The catalysts can be deposited on top of the microtrenches fabricated by photolithography [34, 35]. A slight tilting of the substrate also raises the catalysts. Long and oriented CNTs grow in the gas flow direction from the substrate edge when a laminar flow dominates the growth dynamics inside the CVD reaction tube [36].

The laminar flow is also important in the growth process. If turbulent flow occurs, the CNTs would grow short and randomly, as observed in the fast-heating method. Depending on the experimental conditions, the flow rate can be 1,200 sccm [34], 60–300 sccm [36], or much lower (6 sccm) [33].

In some cases, the catalytic patterns produced by photolithography work similarly and SWCNTs are horizontally aligned between patterns [37].

Compared with other methods, CNTs grown in a gas flow are not only well oriented, but also frequently exceptionally long (in centimeters). So the method has also been used to grow long SWCNTs [31, 32].

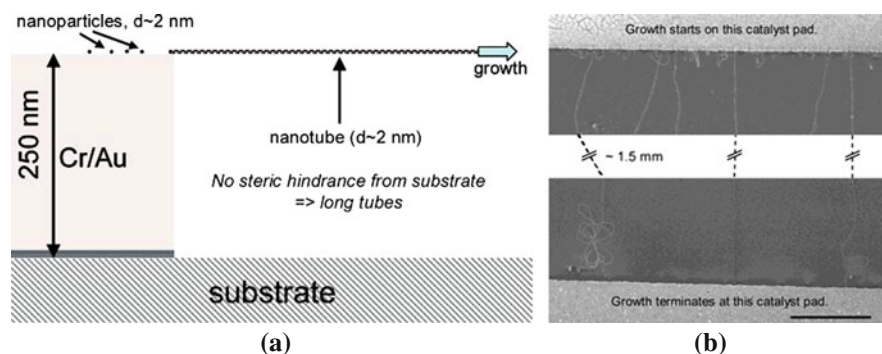


Fig. 6.9 A CNT array grown from trench structure. **a** Schematic drawing of nanotube growth from elevated catalyst sites. **b** An SEM image of initial and terminal points of long nanotubes. Scale bar: 50 μm . From Yu et al. [34]. Copyright (2004) American Chemical Society

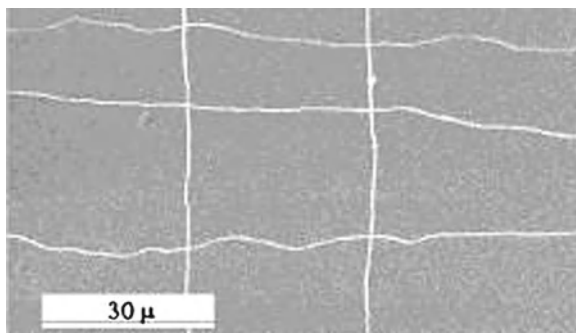


Fig. 6.10 An SEM image of a 2D nanotube network grown by multi-step growth in a flow field. From Huang et al. [28]. Copyright (2003) American Chemical Society

6.1.3.4 Two Dimensional Carbon Nanotube Networks Grown by Two-Step Process

When a multi-step growth is carried out, crossed CNT arrays can be produced using the flow method. Figure 6.10 shows an SEM image of crossed nanotube arrays grown by a two-step growth process. The CNTs are grown first along one direction under a flow field. Then catalysts are deposited on the substrate and the substrate is rotated 90° to grow another CNT array in a perpendicular direction.

Combined with the epitaxy technique (see Sect. 6.1.4), 2D crossed CNT arrays can also be synthesized by a one-step CVD procedure, as discussed in Sect. 6.1.4.4. *Two Dimensional Carbon Nanotube Networks Grown by One-Step Procedure.*

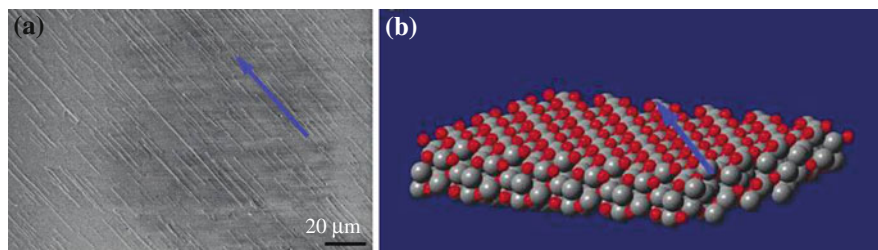


Fig. 6.11 **a** An SEM image of SWCNTs grown in direction $[1\bar{1}0\bar{1}]$ on R -plane sapphire substrate. **b** Simulation of the surface structure of the oxygen-depleted R -plane sapphire. The *red* and *gray* atoms indicate Al and O, respectively. The *blue arrows* indicate the direction $[1\bar{1}0\bar{1}]$. From Yu et al. [39]. Copyright (2006) American Chemical Society

6.1.4 Thermal Chemical Vapor Deposition Growth with Epitaxy

Epitaxy is another promising approach to align CNTs horizontally. There are three different types of epitaxial growth of CNTs [38]: (1) lattice-directed epitaxy by atomic rows, taking place on atomically flat surfaces; (2) ledge-directed epitaxy by atomic steps, taking place on vicinal surfaces; and (3) graphoepitaxy by nanofacets, taking place on nanostructured surfaces.

6.1.4.1 Lattice Directed Growth

The lattice directed growth of CNTs have been first observed along the low-index directions of Si(100) [40], Si(111) [40], Au(111) [41], and 6H-SiC(0001) [42, 43] surfaces. The synthesized CNTs are usually short. Later, long SWCNTs are horizontally aligned in parallel on $(1\bar{1}02)$ R -plane [15, 39, 44, 45] and $(11\bar{2}0)$ a -plane [45, 46] sapphire. In the lattice-directed growth, sapphire without intentional miscut (less than 0.5°) is usually used as the substrate. SWCNTs grow on atomically flat surfaces. Figure 6.11a shows SWCNTs grown on an R -plane sapphire surface. SWCNTs are aligned in parallel to the $[1\bar{1}0\bar{1}]$ -direction.

It is believed that the original surface layer of oxygen atoms of the sapphire substrate may be depleted in the CVD process leaving the surface terminated by aluminum atoms, as shown in Fig. 6.11b. In this case, $[1\bar{1}0\bar{1}]$ surface is the compact arrangement of Al atoms on the sapphire surface and the arrangement of Al atoms builds the pseudo-one-dimensional arrays, shown as a series of grooves aligned in the direction of $[1\bar{1}0\bar{1}]$, as shown in Fig. 6.11b. The CNTs grow along the unique one-dimensional (1D) array of surface atoms [45, 47, 48].

Besides, along the $[1\bar{1}0\bar{1}]$ -direction on $(1\bar{1}02)$ R -plane sapphire [39, 44, 47], it is also observed that SWCNTs are aligned along the $[1\bar{1}00]$ -direction on $(11\bar{2}0)$ a -plane [46, 49]. The preferential growth of SWCNTs along these lattice directions

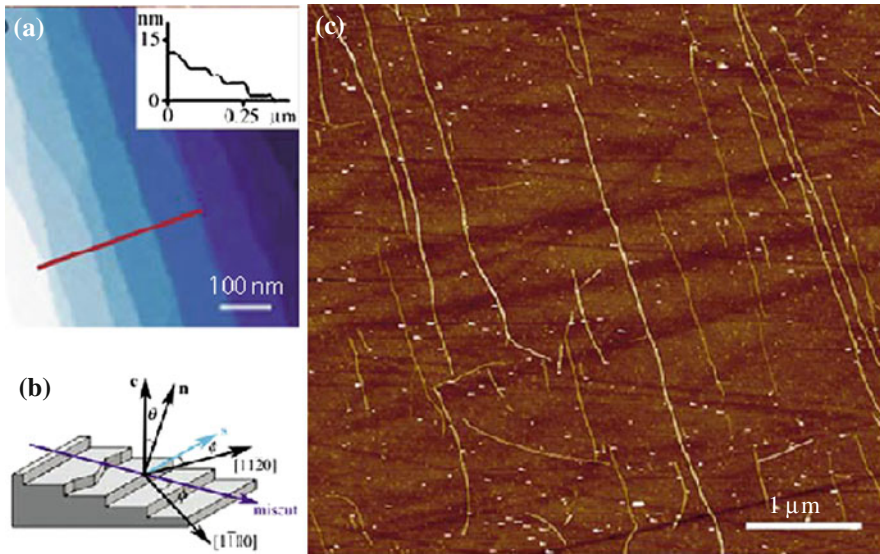


Fig. 6.12 **a** AFM topographic image of α - Al_2O_3 substrate surface after annealing at $1,100^\circ\text{C}$. The darker blue indicates lower terraces, whose edges correspond to the microsteps. The inset shows a section analysis along the red line. **b** Schematic representation of the atomic steps on vicinal α - Al_2O_3 (0001), and definition of the step vector $\mathbf{s} = (\mathbf{c}/c) \times \mathbf{n}$. **c** AFM topographic image of the aligned SWCNTs on miscut c -plane sapphire. Note that both the \mathbf{s} vector and the \mathbf{n} vector of microsteps are parallel to the SWCNTs in **c**. From Ismach et al. [51]. Copyright (2004), John Wiley and Sons

is attributed to higher charge densities along these atomic rows due to electrostatic and van der Waals forces.

Lattice-directed epitaxial growth of SWCNTs also takes place on other atomically flat single crystal substrates. Recently, for instance, SWCNTs were observed to grow on $\text{MgO}(001)$ substrates preferentially along the $[110]$ and $[1\bar{1}0]$ directions, and on single crystal quartz substrates [48, 50].

6.1.4.2 Ledge Directed Growth

The formation of highly aligned and dense arrays of long SWCNTs was first observed on c -plane sapphires in a CVD process [51]. Experimentally, the c -plane sapphire wafers turn out to have a miscut of a few degrees off the c -plane to produce atomic steps of the vicinal α - Al_2O_3 (0001) surfaces (Fig. 6.12) after being annealed at high temperature in vacuum. The atomic steps, with a height equal to one-sixth of the hexagonal unit cell ($h = c/6 = 0.219 \text{ nm}$), follow a general direction perpendicular to the miscut direction (Fig. 6.12b). Their average spacing is $d = h/\sin\theta$, where θ is the miscut inclination. CNTs grow along the atomic steps of the vicinal α - Al_2O_3 (0001) surfaces and form highly aligned dense arrays (Fig. 6.12c).

In the ledge directed growth, it is proposed that the higher contact area at the step edge causes the alignment of the CNTs along the edge direction. The uncompensated surface dipoles at the step edges induce electrostatic interactions and enhance the van der Waals force at the step edge, resulting in the alignment of CNTs [51].

Besides *c*-plane sapphire substrates, ledge directed CNT growth at step edges is also observed on *a*-plane sapphires [46], on *R*-plane sapphires [52, 53], and on SiO₂/Si wafers [54–56].

Ledge directed growth of CNTs is also observed on miscut quartz [37, 57]. In this case, the surface consists of vicinal α -SiO₂ ($1\bar{1}0\bar{1}$) with steps running along the [2110]-direction.

6.1.4.3 Graphoepitaxy

Graphoepitaxy generally refers to the incommensurate orientation of crystals [58] or periodic molecular assemblies [59] by relief features of the substrate, such as nanosteps or nanogrooves, which can be significantly larger than the lattice parameter.

Figure 6.13b–d shows AFM images of the graphoepitaxial growth of CNTs at nanosteps spontaneously self-assembled on the surface of thermally annealed miscut *c*-plane sapphire [58]. In the ledge directed growth talked about above, the *c*-plane sapphire wafers are miscut and mechanically polished to produce atomic steps toward the [1 $\bar{1}00$] or [1 $\bar{2}10$] directions with a height of $h = c/6 = 0.21$ nm [51]. In the graphoepitaxy growth here, the sapphire substrates are further thermally annealed at high temperature. Upon the further annealing, the thermodynamically unstable atomic steps tend to reduce the surface energy by bunching atomic steps together into faceted nanosteps spaced by flat *c*-plane terraces (Fig. 6.13a). It means that the atomic steps along [10 $\bar{1}0$] initially bunch into metastable *P*-faceted nanosteps (inset in Fig. 6.13a), which leads to graphoepitaxial nanotube growth along [10 $\bar{1}0$] (Fig. 6.13b). The height of the nanosteps is between one and three times larger than the unit cell, i.e., 1.3–3.8 nm.

The atomic steps along [11 $\bar{2}0$] can bunch into stable *R*-faceted nanosteps (inset in Fig. 6.13c) and the CNTs grow on this surface graphoepitaxially to form CNT arrays along the [11 $\bar{2}0$]-direction (Fig. 6.13c).

Upon further annealing, the metastable *P*-faceted nanosteps break into sawtooth-shaped *S*/*R*-bifaceted nanosteps (inset in Fig. 6.13d) and graphoepitaxy produces nanotubes loosely conformal to alternate *S*- and *R*-facets along [11 $\bar{2}0$] and [2 $\bar{1}\bar{1}0$], respectively, as shown in Fig. 6.13d.

Using artificial nanosteps, SWCNTs can also be horizontally aligned on other substrates. For example, plasma treatment creates some steps with several nanometers height on Si/SiO₂ wafer surfaces [54]. SWCNTs with a site density of 3–8 tubes/ μm^2 can be horizontally aligned on such substrate surfaces. SWCNTs can also be directly aligned along the trenches created by electron beam lithography on SiO₂/Si substrates [55], or along the patterned steps of sapphire [52]. Different from the flow directed growth where CNTs are grown across the microtrenches, here the graphoepitaxy grown CNTs are grown along the nanotrenches.

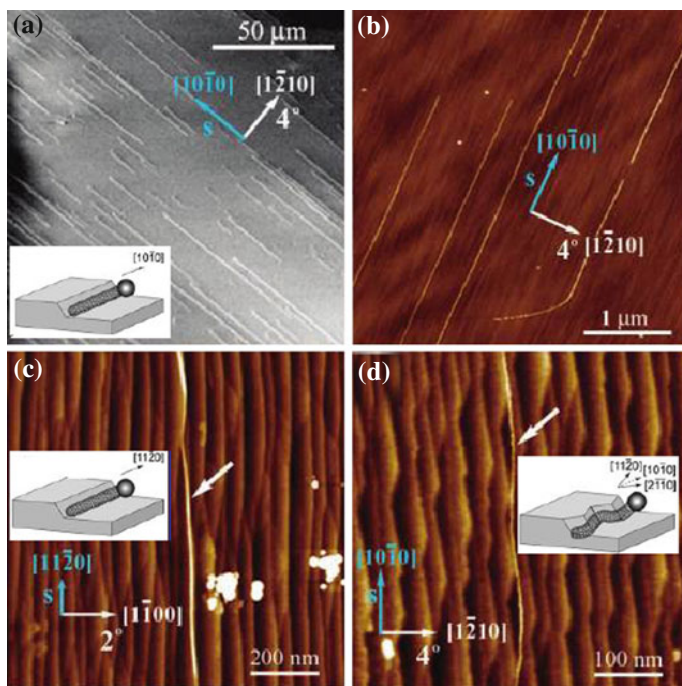


Fig. 6.13 Graphoepitaxial SWCNT growth on different annealed miscut *c*-plane sapphire substrates. **a** SEM image of straight nanosteps along $[10\bar{1}0]$. **b** AFM image of CNTs grown on the nanosteps along $[10\bar{1}0]$. **c** Nanosteps along $[11\bar{2}0]$ and **d** the highly faceted sawtooth-shaped nanosteps along $[10\bar{1}0]$. *Insets* the possible morphologies of CNTs grown along the faceted nanosteps of sapphire substrates. The *white arrows* in **c** and **d** mark the grown CNTs. From Ismach et al. [58]. Copyright (2005) American Chemical Society

6.1.4.4 Two-Dimensional Carbon Nanotube Networks Grown by One-Step Procedure

Combinations of the CNT epitaxial growth with the field-directed growth (see Sect. 6.1.2) or flow directed growth (see Sect. 6.1.3) can produce 2D crossbar arrays of CNTs in a one-step CVD procedure.

Figure 6.14 shows a crossbar array of SWCNTs spontaneously produced in a one-step CVD procedure by simultaneous graphoepitaxy growth and field directed growth, perpendicular to each other. The miscut *c*-plane sapphire is annealed to produce the nanosteps along the $[11\bar{2}0]$ -direction, while an electric field is applied perpendicularly to the nanosteps. The nanotubes originating from catalyst nanoparticles lying on the sapphire grow along the faceted nanosteps with an epitaxial growth, while the nanotubes emerging from the catalyst on patterned metallic stripes grow freely (with a field directed growth) without interacting with the substrate surface,

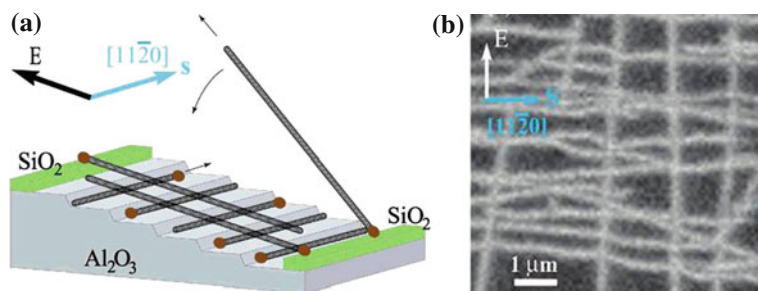


Fig. 6.14 Orthogonal self-assembly of SWCNT crossbar architectures by simultaneous graphoepitaxy growth and field directed growth in a one-step CVD procedure. **a** Schematic representation of the orthogonal self-assembly. **b** SEM image of a dense SWCNT grid obtained by simultaneous graphoepitaxy growth and field directed growth. From Ismach et al. [26]. Copyright (2006) American Chemical Society

in a way that allows the aligned CNTs grow along the electric field to eventually fall across the epitaxially grown nanotubes on the sapphire.

In the graphoepitaxial growth, SWCNTs grow along the atomic steps of miscut *c*-plane sapphire surfaces [51], or along the 1.3–4 nm high-faceted nanosteps of annealed miscut *c*-plane sapphire [60]. The alignment of the graphoepitaxial SWCNTs is unaffected by external forces, such as electric field and gas flow field [51, 60]. So the nanotubes originating from the catalyst nanoparticles lying on the bare sapphire grow along the nanosteps, while the nanotubes originating from catalyst nanoparticles lying on the SiO₂ islands grow up freely and are aligned by the electric field perpendicular to the nanosteps. The two alignment mechanisms take place selectively on miscut *c*-plane sapphire and patterned SiO₂ strips, respectively, without mutual interference, producing dense nanotube grids.

Similar to the combination of lattice directed growth and electric field directed growth, 2D crossbar structured CNTs can also be produced in a one-step CVD process from a combination of lattice-directed growth and flow-directed growth [61]. Figure 6.15 shows the mechanism and an SEM image of SWCNT crossbar structures grown on quartz substrates in this way. The average length of lattice-orientated SWCNTs can reach hundreds of microns, and the spacing between the nanotubes is about several microns. Gas flow directed SWCNTs are millimeters long and the spacing between nanotubes can be reduced to about 10 μm. The CNT node density of the crossbar structure is about 10⁷ tubes/cm².

Combining lattice directed growth and graphoepitaxial growth, bent CNTs can be horizontally grown on crystal substrates, like on *R*-plane sapphire with artificial nanosteps [52]. SWCNTs first grow along the specific crystallographic [1 $\bar{1}0\bar{1}$]-direction on *R*-plane sapphire due to the lattice oriented growth and then grow along artificial nanosteps, perpendicular to the first SWCNT growth direction [1 $\bar{1}0\bar{1}$]. These nanosteps change the nanotube growth direction from [1 $\bar{1}0\bar{1}$] to the nanostep direction with the bending angle of nearly 90°.

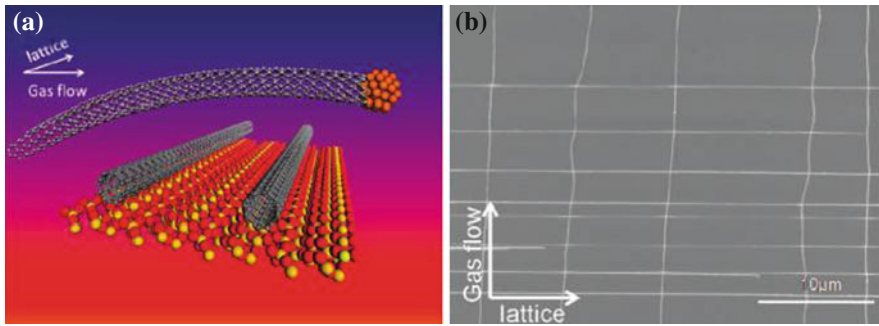


Fig. 6.15 2D CNT networks produced from a combination of lattice directed growth and flow directed growth. **a** Illustration of the mechanism for the growth of crossbar structured CNTs based on lattice directed and flow directed growth. **b** SEM image of SWCNT crossbar structure on quartz. From Zhang et al. [61]. Copyright (2009) American Chemical Society

6.1.5 Thermal Chemical Vapor Deposition Under Magnetic Fields

Another approach to align CNTs is to control the orientation of catalyst nanoparticles [62, 63]. Because only a certain nanocrystalline facet of catalytic nanoparticles is catalytically active and the diffusion rate of carbon atoms on the facet is the highest [such as (220) of Ni] [22, 64], the CNTs preferentially grow from the certain facet of the catalytic nanoparticles and the grown CNTs are oriented at a certain angle.

Ferromagnetic materials, such as iron, nickel, and cobalt that have been used for CNT catalysts, have one crystallographic magnetic easy axis. The magnetic easy axis tends to be parallel to the magnetic field. As a result, an external magnetic force can orient these magnetic catalytic nanoparticles, like catalytic iron nanoparticles [63] and Fe_3O_4 nanoparticles [62].

Figure 6.16 shows the histogram distribution of CNTs synthesized with or without an external magnetic field. When a magnetic field is applied during the CNT growth, CNTs grow preferentially along two certain directions.

6.1.6 Vertically Aligned Carbon Nanotube Arrays Grown by Plasma-Enhanced Chemical Vapor Deposition

CNT arrays have been in situ fabricated more successfully by PECVD method. The CNT arrays were first in situ aligned vertically on glass substrates using DC PECVD method [65–68]. Later a variety of PECVD methods, such as radio-frequency PECVD, hot-filament PECVD, microwave PECVD, electron cyclotron PECVD, etc., have been developed to grow aligned CNTs. DC PECVD was discussed in details in Chap. 5, including the experimental setup and experimental

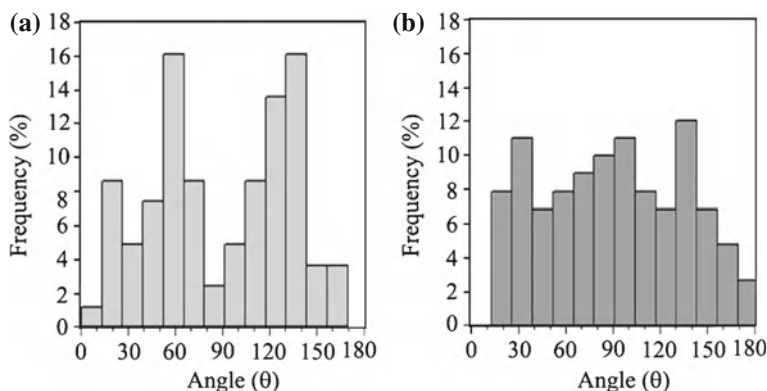


Fig. 6.16 **a** Histogram distribution of CNTs obtained by analyzing as-synthesized CNT growth angles in the presence of a magnetic field. The histogram displays two preferred growth directions centering at 60° and 130° . **b** Histogram distribution attained by analyzing as-synthesized CNT growth angles prepared in the absence of a magnetic field. No preferential growth angle is observable from these samples. From Kumar et al. [62]. Copyright (2005), American Institute of Physics

conditions. Other PECVD methods are similar to the DC PECVD method and were discussed in Sect. 4.2.

In these PECVD processes, DC electric fields, radio-frequency electric fields, or microwaves produce plasmas to primarily lower the synthesis temperature of CNTs. At the same time, an electric field (DC or AC) is also produced over the substrate surface, directing the CNT growth similar to the electric field effect discussed in Sect. 6.1.2. The straight CNTs grow along the direction of the parasitic electric field in the plasma [22, 23].

Besides the 1D CNT alignment along the plasma induced electric field, CNTs can also be 2D arranged on the substrate surface to form 3D CNT arrays. During the growth of 1D aligned CNTs or 3D CNT arrays, the spatial ordering of catalysts on the substrates plays an important role. Because the CNTs grow only from the catalytic nanoparticles in a PECVD process, the sites of catalytic nanoparticles are the spatial locations of CNTs. So the preparation of catalytic nanoparticles is very important on the fabrication of vertical CNT arrays. Table 6.1 summarizes several methods for preparing catalytic nanoparticles.

After the catalysts are deposited on the substrate surfaces, the aligned CNTs can be grown from these catalysts to form 1D or 3D CNT arrays using the PECVD method. The PECVD growth techniques were discussed in Sect. 4.2 and Chap. 5. Here, we mainly talk about the methods to prepare catalysts used for PECVD growth of aligned CNTs.

Table 6.1 Preparation methods of catalytic nanoparticles used for aligned CNTs

Method	Catalyst			Advantage & shortcoming
	Position	Size	Site density	
Solution method	Random	Several nm	Low, controllable	Simple, easy, cheap
Sputtering deposition	Random	Controllable	High, controllable	Easy, cheap
Electrochemical deposition	Random	Narrow	Controllable	Easy
Photo-lithography	Controllable	Controllable	Controllable	2D order, predesigned 2D structure, time-consuming, expensive
Microsphere lithography	Controllable	Controllable	Controllable	2D order, hexagonal structure, <3 types of patterns
E-beam lithography	Controllable	Controllable	Controllable	2D order, predesigned 2D structure, expensive, time-consuming
Micro-stamp	Controllable	Controllable	Controllable	2D order, predesigned structure, one type of pattern, cheap

6.1.6.1 One-Dimensionally Ordered Carbon Nanotube Arrays

Usually the PECVD grown CNTs are 1D ordered: the aligned CNTs are vertical to the substrate surface while the CNT sites on the substrates are random because of the random locations of catalytic nanoparticles on the substrate. The catalytic nanoparticles can be prepared by many methods, such as solution method [69–72], sputtering deposition [6, 65, 73], and electrochemical deposition [74]. The average number of catalytic nanoparticles per unit area can be controlled while the site locations of the nanoparticles remain random on the substrate surface. When the CNTs are grown along the plasma from these catalytic nanoparticles in a PECVD procedure, the synthesized CNTs are 1D ordered.

Solution method is the simplest way for producing catalysts which have been widely employed in preparing catalysts for various nanowire growths. Usually the substrate is soaked in water or alcohol solution of catalytic compound (such as NiNO_3 solution) for several minutes and then dried at room temperature. The deposited ions or ion clusters work as catalysts. In some cases, the deposited catalyst particles are reduced in hydrogen to activate their catalytic activity. CNTs are grown from these catalysts. The catalysts prepared by the solution method randomly distribute on the substrate surfaces and the PECVD grown CNTs are 1D ordered along the plasma-induced electric field.

As an example, iron catalysts have been prepared by this method. Iron nanoclusters with diameters between 3 and 13 nm were synthesized in organic solvents by thermal decomposition of iron pentacarbonyl and then were deposited onto a silicon substrate [69]. Iron-based catalytic nanoparticles with diameters of 1–2 nm were synthesized by soaking silicon oxide substrates in a solution of hydroxylamine and FeCl_3 [70]. Iron catalysts were also prepared by the iron-storage protein, ferritin [71], and by the polystyrene-block-polyferrocenyldimethylsilane diblock copolymer [72]. 1D CNT arrays have been successfully grown from these catalysts [69–72].

Magnetron sputtering deposition is usually employed to coat thin metal films on substrates and now is one of the most commonly used methods to synthesize the surface arrays of metal particles. The sputtered film is usually continuous at a thickness above 1 nm. Such as-coated films are not good catalysts for CNT growth. However, the continuous films are always coarsened into discrete nanoparticles under annealing or through a solid-state dewetting process if the thickness is several nanometers. Such annealed nanoparticles are usually well capable of catalyzing the growth of CNTs.

The catalyst preparation procedure of sputtering is simple and effective to grow catalytic nanoparticles for the growth of vertically aligned CNTs [6, 65, 73]. Till date, catalytic nanoparticles have been DC magnetron sputtered or radio frequency sputtered on substrates. Although this method is straightforward, it offers little control over the size or spacing of the metal nanoparticles, and patterned nanoparticle arrays are not achievable without additional modifications such as templating.

In a typical DC magnetron sputtering process, substrates are cleaned in alcohol by ultrasonication first, and then loaded into the sputtering chamber for catalyst film deposition. The chamber is evacuated to a base pressure of 5×10^{-7} Torr to 3×10^{-6} Torr. Then the pressure is maintained at 3–6 mTorr by introducing Ar gas. The catalyst target is Ar^+ bombarded for a few minutes to remove the oxidized surface layer on the target. Then the substrate temperature is maintained at 0–300 °C during deposition. The sputtering normally takes a few seconds to about 20 min to achieve catalyst film thickness of 2–100 nm.

The as-deposited films are normally smooth and continuous. However the as-deposited film is usually amorphous, no catalytic activity. In order to enhance the catalytic activity, the as-sputtered films are always annealed at high temperature before CVD growth. The annealing is usually carried out in the same CVD chamber for CNT growth. After the catalyst coated substrates are loaded into the chamber, the chamber is pumped down to about 1 mTorr or less, followed by heating to several hundred Celsius degrees. If the catalyst films have been exposed to air, annealing in hydrogen may remove the oxidized surface layer on the catalyst films. Depending on the annealing temperature and time, the continuous film develops into many individual nanoparticles, as shown in Fig. 6.17. Similar to other thin films on substrates, the amorphous continuous layer is coarse and grows at high temperature because of morphology instability. Statistical analysis of nanoparticle sizes indicates that the catalyst nanoparticle size increases linearly with the increase of the sputtered film thickness when it is below 100 nm, as theoretically predicted by Rayleigh instability theory.

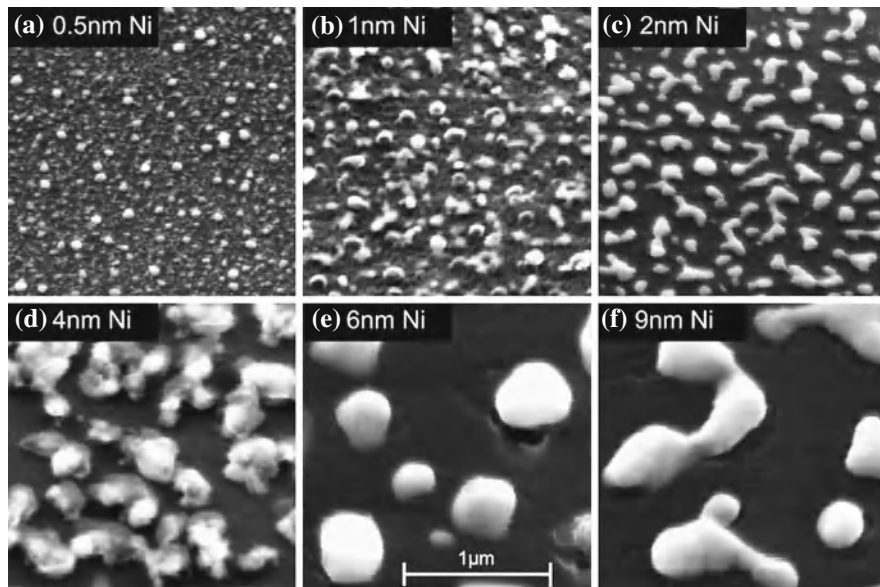


Fig. 6.17 SEM photographs of Ni particles with varying thicknesses deposited using magnetron sputtering on SiO₂ and then annealed at 750 °C in 20 Torr of H₂ for 15 min. From Chhowalla et al. [75]. Copyright (2001), American Institute of Physics

Aligned CNTs are usually grown by PECVD methods immediately after the annealing step. During the PECVD growth, the plasma intensity should be well controlled for optimal results. If not, those catalytic nanoparticles would either be quickly knocked off the substrate (over-etched) or agglomerate (over-heated) into bigger ones to survive under a strong plasma (glow discharge) in PECVD growth.

In order to grow isolated aligned CNTs as shown in Fig. 6.18f, discrete catalytic nanoparticles shown in Fig. 6.18c, not adjacent ones shown in Fig. 6.18a and b, are needed. Otherwise, more than one CNTs will grow closely together to form CNT bundles as shown in Fig. 6.18d and e. Plasma is a good method to achieve discrete catalytic nanoparticles. In a typical procedure, the catalysts are etched by plasma before introducing reaction gases. The smaller nanoparticles are over-etched while the bigger ones survive. At the same time, the diameter of the survived catalytic nanoparticles becomes more uniform, benefiting the growth of uniform CNTs.

Electrochemical deposition has been employed to prepare Ni [66, 74, 77], Ag [78–80], Au [80], and Pt [81] catalytic nanoparticles with different nucleation site densities and different particle diameters for CNT array growth. Similar to the catalysts prepared by the sputtering method, the electrochemically deposited nanoparticles are random. The catalyst site density and diameter of catalytic nanoparticles can be adjusted straightforwardly. Compared with the catalysts prepared by the sputtering methods, the electrochemically deposited metal nanoparticles could have a lower site density, smaller sizes, more uniform diameters, and can be well con-

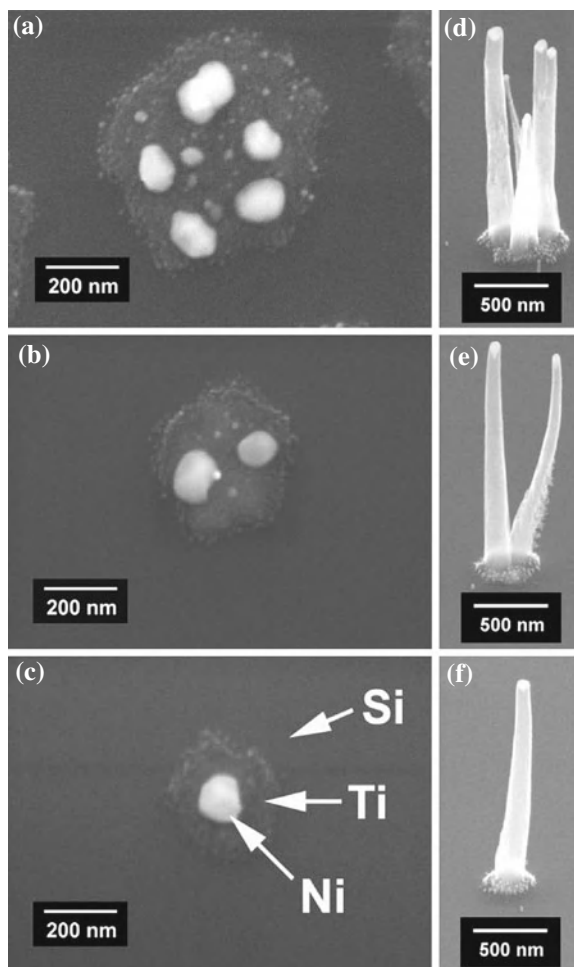


Fig. 6.18 Formation of **a** multiple, **b** double, and **c** single Ni catalytic nanoparticles on a substrate and subsequent growth of **d** multiple, **e** double, and **f** single vertical MWCNTs from the catalytic nanoparticles shown in **a–c**, respectively. From Merkulov et al. [76]. Copyright (2000), American Institute of Physics

trolled. For Ni catalytic nanoparticles, the site density can be easily tuned between about 10^6 particles/cm² and 10^8 particles/cm² and the diameter can be finely tuned from less than 50 up to 200 nm [74, 82]. Figure 6.19 shows the CNTs grown from different catalytic site densities.

The electrochemical deposition of catalytic nanoparticles is a cheap, effective technique, and is scalable to tens of inches. The CNT arrays grown from catalysts prepared by electrochemical depositions are therefore also inexpensive and in-scalable although the CNTs are randomly arranged on the substrate surface.

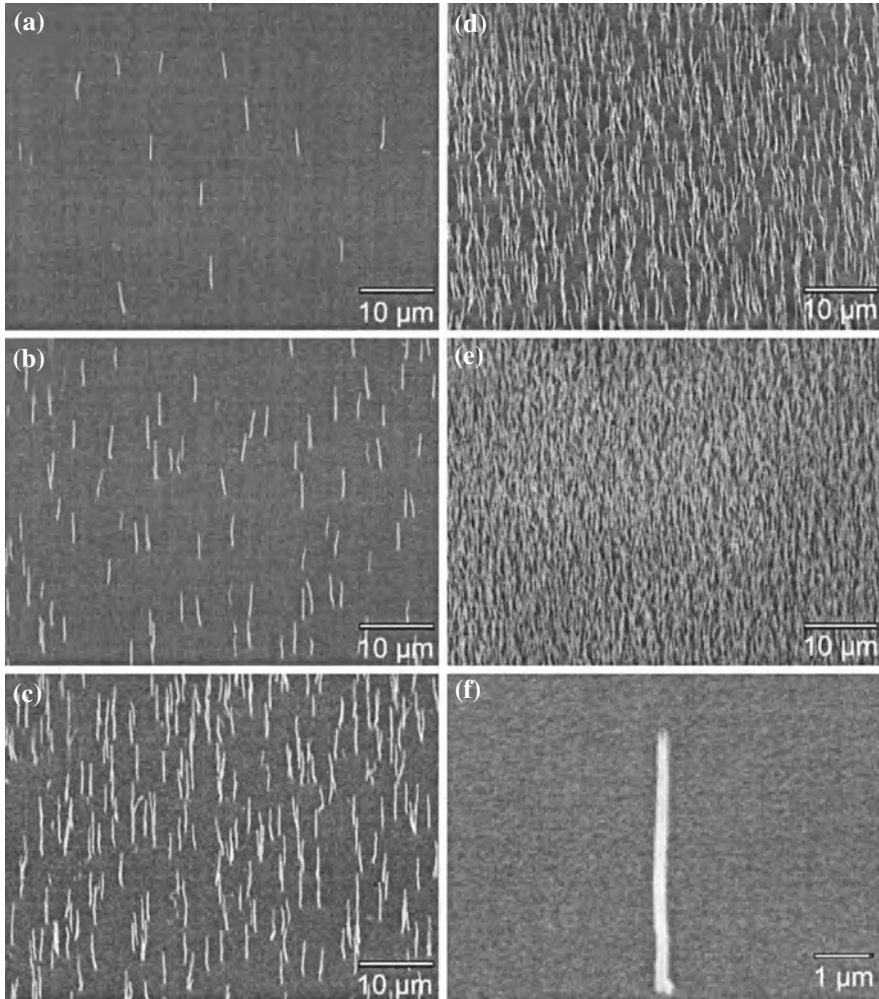


Fig. 6.19 SEM images of CNT arrays grown on Ni nanoparticles deposited electrochemically with a site density of **a** $7.5 \times 10^5/\text{cm}^2$, **b** $2 \times 10^6/\text{cm}^2$, **c** $6 \times 10^6/\text{cm}^2$, **d** $2 \times 10^7/\text{cm}^2$, **e** $3 \times 10^8/\text{cm}^2$, and **f** a freestanding CNT. From Yu et al. [74]. Reprinted with permission from American Institute of Physics

Atomic layer deposition is also used to deposit uniform and smooth Fe_2O_3 films for CNT growth. The highly oriented CNT arrays can be grown on the substrates with curved surface [83].

6.1.6.2 Three-Dimensionally Ordered Carbon Nanotube Arrays

In order to synthesize 3D ordered CNTs, 2D ordered catalytic nanoparticles are required on substrates. The 2D ordered catalytic nanoparticles can be prepared by conventional photolithography, X-ray photolithography, e-beam lithography [9, 84], nanosphere lithography [73, 85–89], anodized aluminum oxide (AAO) templating [90–92], and micro-stamp method [93], etc. Among them, the nanosphere lithography technique is a simple, cheap, and effective method to produce 2D ordered catalytic nanoparticles in inch scale. After the 2D catalytic nanoparticles are prepared, the CNTs can be vertically grown from them using PECVD method to form 3D CNT arrays.

Polystyrene nanosphere lithography has been proved to be a very simple, economic, and effective technique to fabricate large-scale nanoparticle arrays with long-range periodicity [73, 85–89]. It utilizes sub-micron latex beads hexagonally arranged into a monolayer as a shadow mask for further evaporation of various materials. As-deposited catalytic nanoparticles have a quasi-triangular shape, caused by the aperture shape in the nanospheres mask, and their size is tunable by the use of different sphere diameters. The technique has been used to prepare 2D catalytic nanoparticles to grow 3D CNT arrays [73, 85], to prepare 2D ordered catalyst patterns for ZnO nanorod arrays [94], and to grow TiO₂ nano-bowl arrays [95].

The nanosphere lithography process involves three main steps [86, 87, 94].

First, a 2D self-assembled and periodically ordered monolayer of nanospheres is formed on a substrate surface (Fig. 6.20). Several drops of the nanosphere suspension are applied to the surface of a substrate and then spread using a pipette tip. After being held stationary for about 1 min to obtain good dispersion of the suspension, the substrate is then slowly immersed into deionized water. Once the nanosphere-coated surface is immersed, nanospheres lift off from the substrate and form an unordered monolayer floating on the water surface. Then, a few drops of 2% dodecylsodium-sulfate solution are added to the water surface to change the surface tension (surface tension of water is 72.8 dynes/cm² at 20 °C while that of sodium dodecylsulfate solution is 40–70 dynes/cm² [96]). After the surface tension is reduced, all nanospheres immediately assemble into a close-packed monolayer. At the same time, the monolayer is pushed aside due to the change in the surface tension. The prior substrate is then removed through a clear area. The nanosphere monolayer is picked up by another clean substrate that is then slowly dried.

Figure 6.20a shows a monolayer of polystyrene nanospheres deposited on a 10 × 10 mm Si substrate. The uniform diffraction color in Fig. 6.20b shows that the coated nanospheres are indeed highly ordered without major defects over a long distance. This is further confirmed by a fast Fourier transform analysis [85]. The area of a single domain can reach a few square centimeters.

Second, the nanosphere monolayer is subsequently used as a shadow mask for physical vapor deposition of the catalyst (such as Fe, Co, or Ni). During this deposition process, the metal vapor can go through apertures in hexagonally packed nanospheres leading to a honeycomb lattice array of quasi-triangular particles.

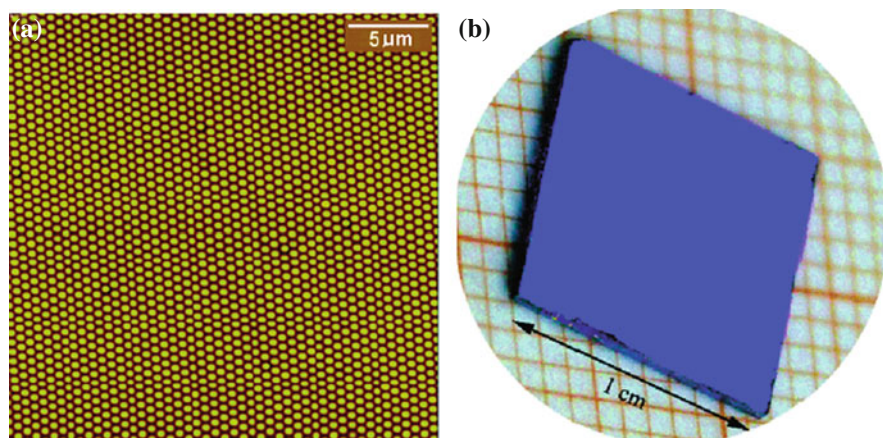


Fig. 6.20 Highly ordered monolayer of polystyrene nanospheres (diameter of $0.5\ \mu\text{m}$) on an Si substrate made by the self-assembly nanosphere lithography. **a** AFM image of the *closely packed hexagonal nanospheres*. **b** Optical image of an Si substrate coated with nanospheres. From Kempa et al. [85]. Reprinted with permission from American Chemical Society

Various deposition techniques such as e-beam deposition, magnetron sputtering, and thermal evaporation can be used to deposit metal catalysts through the nanospheres.

The deposition methods affect the final morphology of the deposited catalyst particle. During a sputtered process or an e-beam deposition, the isotropic velocity of the adatoms results in catalysts covering all opening areas, even beneath the nanospheres. During a thermal evaporation process, the deposition is line-of-site and the catalytic material is only deposited onto the areas of the substrate that are not shadowed vertically by the nanospheres. After the removal of the nanospheres, a highly ordered hexagonal array of catalyst particles is formed on the substrate. The sputtering technique usually produces a honeycomb-like catalyst network. The catalyst particles are connected. The thermal evaporation always produces isolated catalyst particles.

Third, the nanospheres are chemically etched away in toluene or tetrahydrofuran or mechanically by ultrasonication, leaving a patterned catalyst array on the substrate surface. Figure 6.21a shows the triangular particles deposited after nanosphere mask removal. The interparticle spacing can be adjusted by adopting nanospheres of different diameters.

More detailed procedure of the nanosphere lithography can be found in the related literatures [86, 87, 89] and books [97].

After the 2D catalyst arrays are prepared, 3D ordered CNT arrays can be grown from them using PECVD methods, as shown in Fig. 6.21b.

The as-evaporated catalysts are usually well ordered, triangular-shaped particles, as shown in Fig. 6.22a. In order to grow only one CNT from a catalyst site, it is very important to anneal the catalyst before CNT growth. After annealing, the quasi-triangular nanoparticles should become quasi-spherical with homogenous structure

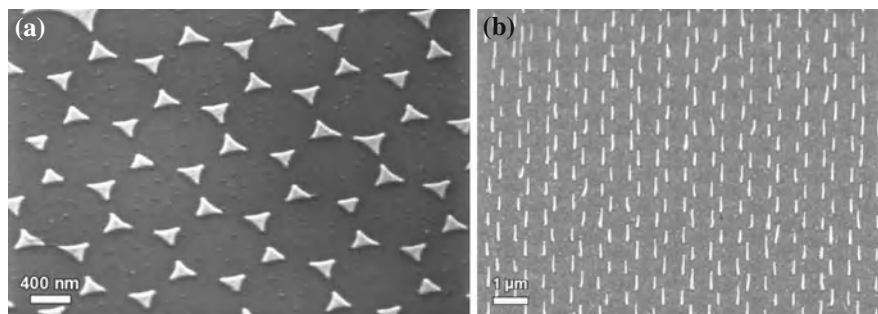


Fig. 6.21 **a** SEM image of honeycomb array of nickel catalytic particles evaporated through the 980 nm diameter nanosphere mask. **b** SEM image of the 45° tilted view of the honeycomb array of aligned CNTs grown on the nickel particle array shown in **a**. From Rybczynski et al. [89]. Reprinted with permission from American Institute of Physics

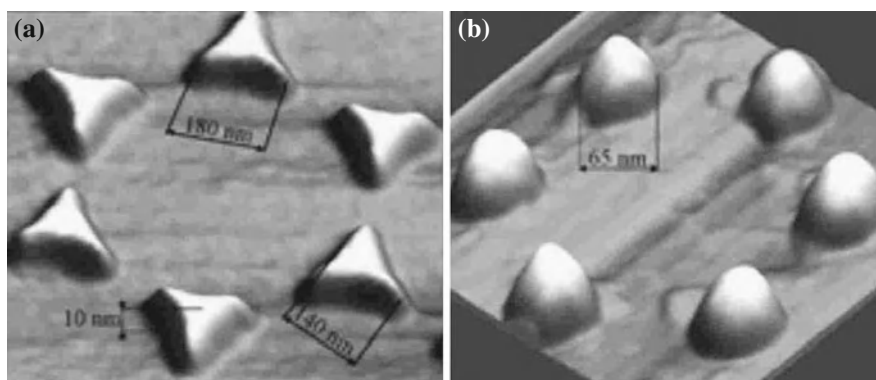


Fig. 6.22 AFM images of **a** as-evaporated and **b** annealed nickel nanoparticles evaporated through the 496 nm PS nanosphere mask. Annealing temperature: 900 °C; annealing time: 40 min. From Rybczynski et al. [86]

(Fig. 6.22b). The annealing temperature should be at least 65–70% of the melting point temperature of catalyst. Otherwise, multi-CNTs would grow from a catalytic site, as shown in Fig. 6.18d–e.

Sometimes, the annealed catalytic particles are further etched before PECVD procedures to remove the produced smaller nanoparticles. The mechanism of the plasma etching is discussed in Sect. 5.4.

Electron beam lithography can also produce catalytic patterns within a scanning electron microscope. In a typical procedure, the substrates coated with e-beam resists are loaded into SEM. A pattern is pre-designed on computer and the electron beam (e-beam) of SEM bombards on the substrate to expose the e-beam resists along the designed pattern. Then the bilayer e-beam resist is developed in a solution of methyl isobutyl ketone and isopropyl alcohol. Subsequently, catalytic nanoparticles are produced to form the designed pattern. The final catalyst pattern remains after

the resist liftoffs in acetone. Then the patterned substrate is loaded into a PECVD system for CNT array growth. CNTs grow accurately on the catalytic dots and not on the Si substrate, forming CNT arrays based on the spacing and periodicity of the lithographically patterned catalytic dots, as shown in Fig. 2.6.

Till date, many kinds of catalyst patterns have been prepared using the e-beam lithography to grow CNT arrays [9, 22, 75, 84, 98–101]. The CNT arrays grown from catalytic patterns made by e-beam lithography are periodic, but are limited to a very small area and are very expensive.

Other lithography techniques can also be used to prepare catalytic patterns besides the electron beam lithography, such as photolithography [102], phase shifting optical lithography, X-ray lithography, focused ion beam lithography, neutral atomic beam lithography.

Compared with the electron beam lithography, the conventional lithographies have a similar principle with e-beam lithography while the conventional lithographies are capable of larger fabricating features of ~ 200 nm and above [103, 104]. The e-beam lithography can fabricate features as small as 3–5 nm [110, 111]. Optical lithography can produce patterns with a minimal size of 100 nm when deep ultra-violet light is employed [105, 106] and down to 70 nm when extreme ultra-violet light is employed [107]. The resolution limit of the X-ray lithography is 25 nm [108, 109]. Focused ion beam lithography and neutral atomic beam lithography are seldom employed to prepare catalytic patterns because of cost. Nevertheless, electron beam lithography is the most powerful tool among these lithography techniques.

Anodized aluminum oxide (AAO), also named as anodic porous alumina, is described as a close-packed array of pores of which the size and interval can be controlled by changing the anodization conditions. The pores are organized spontaneously into close-packed hexagonal arrays. The defect-free area of naturally occurring ordering appears in a domain structure and is usually limited to the size of several micrometers. Employing some techniques, the long-range-ordered channel-array architecture is achieved on the millimeter scale [112].

It has been found that the AAO with pore diameters ranging from several nanometers to 200 nm is stable at high temperature and in organic solvents [113], and that the pore channels in AAO films are uniform, parallel, and perpendicular to the membrane surface. These physical properties make the AAO as ideal templates for the synthesis of oxide nanowire [114] and CNT arrays [90–92, 112, 115–117]. It is very useful in controlling the diameter and length of the nanomaterials through control of the nanochannels of anodic aluminum oxide.

The porous AAO templates can be fabricated by anodizing pure aluminum foils (purity 99.5%) directly in a sulfuric acid solution using a two-step process [118, 113]. Aluminum foils are annealed at 500 °C for 4 h to form texture, then degreased in acetone. After 2 h anodization at 27 V in 0.4 M sulfuric acid solution at 0 °C, an anodic oxide layer in microns is formed in a mixture of 0.4 M H_3PO_4 and 0.2 M H_2CrO_4 . Then the aluminum metal is removed in a saturated CuCl_2 solution. The pore diameter in the anodic oxide layer is finely adjusted in 6 wt % H_3PO_4 solution at 30 °C for 30 min, forming a through-hole membrane with pore diameters of about 50 nm.

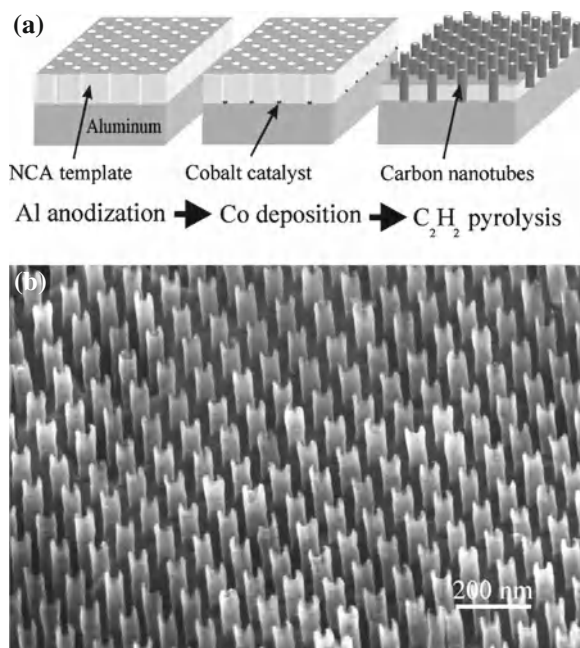


Fig. 6.23 **a** Schematic fabrication process of CNT array grown from AAO templates. **b** SEM image of the hexagonally ordered array of carbon nanotubes fabricated using the AAO template. From Lie et al. [115]

AAO templates can also be prepared from Al films directly. Aluminum of one micron thickness is deposited on an Si(100) wafer via sputtering. Then AAO templates of uniform and highly ordered nanopores are prepared by a two-step anodization process.

Additionally ordered pits can also be produced on aluminum before the two-step anodization process and high ordered holes can be prepared. The details of the AAO preparation are reviewed recently [114].

Many groups have employed the AAO templates to grow high-ordered CNT arrays [90–92, 112, 115–117, 119]. The catalytic nanoparticles are deposited in the nanochannels in AAO templates and the CNTs are grown from these ordered catalysts (Fig. 6.23). After growth, the filled templates are immersed in a 4 M NaOH solution for 12 h to free the carbon nanotubes and the final products are washed thoroughly with deionized water to obtain pure CNT arrays.

The use of such AAO templates for CNT synthesis guarantees a highly ordered vertical array of isolated CNTs with uniform diameter and length. However, CNTs synthesized on AAO templates show poor crystalline quality than those synthesized via arc-discharge method and CVD method.

Lateral porous anodic alumina templates can be used to grow ordered carbon nanotubes parallel to the substrate surface by a hot-filament assisted chemical vapor

deposition [120]. Such grown CNT arrays can be used as a channel for further development of electronic applications such as interconnects, field-effect transistors, sensors, and photonic devices.

Block copolymer micelles can be also used as a catalyst template [121, 122]. The amphiphilic block copolymer poly(styrene-block-acrylic acid) (PS-b-PAA) toluene solution is spin-casted onto the substrates. The film thickness is approximately 20 nm. The PS-b-PAA micelles in solution are capable of self-organizing into ordered structures on surfaces, creating quasi-hexagonal arrays of PAA spheres within a PS matrix. The film is then submerged in an NaOH water solution. When the thin film is exposed to the NaOH water solution, the PAA domains swell, and the swelling leads to the rupture of the PAA domains to the surface.

These cavitated polymer thin films are then rinsed in deionized water for 1 min, submerged in an FeCl_3 solution, and then rinsed in deionized water. In the cavitated thin films, the Fe^{3+} ions in solution exchange directly with the Na^+ ions of the carboxylic acid groups. The substrates are heated in air at 550°C for 20 min to degrade the polymer and to convert the iron ions into iron oxide nanoclusters. The resulting iron-containing nanoclusters are nearly monodisperse in size (diameter about 8 nm) and the substrates are patterned at a site density of approximately 10^{11} nanoparticles per squared centimeters. CNT arrays can be grown from the iron-oxide nanoclusters.

Other methods. Besides the above methods, there are many other methods to produce 2D ordered catalyst patterns, like micro-contact printing and micro-stamp method [93, 123, 124], shadow mask method [9, 75]. The interested readers are referred to the books [104] and review papers. All these 2D ordered catalyst patterns can be used to grow 3D CNT arrays through the PECVD procedures talked about in Sect. 4.2 and Chap. 5.

6.1.7 Other In Situ techniques

Additionally, there are many other in situ methods to grow CNT arrays, such as vapor-phase catalyst delivery [125]. Here, we do not cover these techniques because of space limitations.

6.2 Ex Situ Techniques for Carbon Nanotube Alignment

Ex situ assembly of CNTs is a post-synthesis method for CNT alignment. CNTs are first synthesized by the arc discharge method, CVD, or other growth methods talked about in Chap. 3, and then are assembled by electric fields, magnetic fields, force fields, or other methods. Compared with the in situ techniques, the ex situ techniques are free of collateral growth restrictions such as substrate material and growth temperature. Here, we talk about some ex situ techniques to align CNTs.

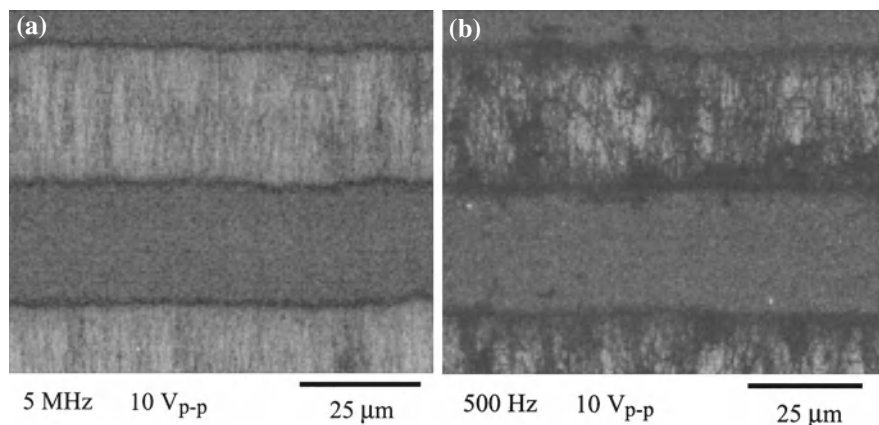


Fig. 6.24 SEM images of the SWCNTs aligned under AC electric fields. **a** Aligned by applying an AC electric field with a frequency of 5 MHz and a voltage of 10 V peak to peak. **b** Aligned by applying an AC electric field with a frequency of 500 Hz and a voltage of 10 V peak to peak. From Chen et al. [126]. Copyright (2001), American Institute of Physics

6.2.1 Ex Situ Alignment Under Electric Fields

CNTs can be aligned under electric fields in liquids [126–132]. The electric fields can be DC or AC fields. Figure 6.24 shows SEM images of aligned CNTs between two electrodes. Gold interdigitated electrodes are fabricated by vacuum deposition on Si/SiO₂ substrates. Then the substrates are immersed in the SWCNT suspension and an electric field is generated between the electrodes [126]. The CNTs are polarized in the suspension by the electric field because of dielectric mismatch between CNTs and the liquid. The polarization moment rotates the CNTs toward the direction of electric field lines, therefore aligning them in a common direction. After being aligned, the CNTs are taken out with the substrates and dried in air.

Another approach to align random CNTs, also related to electric field induced alignment, is the orientationally selective ablation of random networks with a planar polarized laser [133]. SWCNTs oriented with a projection in the plane of polarization were selectively ablated, leaving on the surface only those that are oriented perpendicular to the plane of polarization.

6.2.2 Ex Situ Alignment Under Magnetic Fields

Calculations reveal that CNTs exhibit diamagnetic or paramagnetic responses depending on the magnetic field direction, the helicity of CNTs, the Fermi energy of CNTs, and the radius [136]. Metallic SWCNTs are paramagnetic in the direction of their long axes, confirmed by experimental data (Fig. 6.25a). Under a magnetic

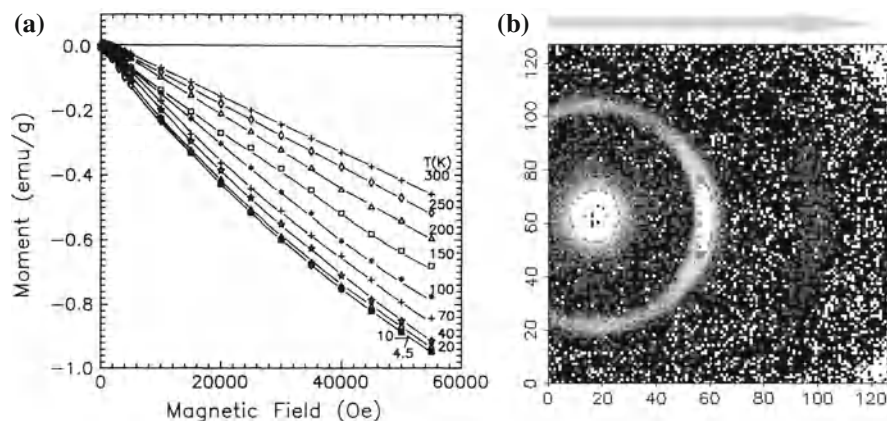


Fig. 6.25 **a** Field dependence of the magnetic moment of CNTs at high fields. The CNTs with diameter of 2–10 nm are grown by the arc discharge technique. **b** Small-angle neutron scattering pattern of CNTs aligned in magnetic fields. **a** From Heremans et al. [134]. Copyright (1994), American Physical Society. **b** From Yoon et al. [135]. Copyright (2006), John Wiley and Sons

field B , the CNTs with magnetic dipole moment P receive a torque vector given by $\tau = P \times B$. At high magnetic fields, the magnetic force applied on the CNTs can align the whole CNTs along the magnetic field direction.

Usually the purified CNTs are dispersed ultrasonically in a liquid epoxy resin and then the mixture is kept in a magnetic field at room temperature before the epoxy resin is cured. The CNTs are aligned in the liquid under a magnetic field due to the cooperative effect of the magnetic torque exerted by the magnetic field directly on the nanotubes and by the hydrodynamic torque and viscous shear (i.e., drag forces) exerted on the nanotubes by the polymer chains [137–142]. Small-angle neutron scattering of CNTs indicates that the CNTs really rotate and align in the magnetic field (Fig. 6.25b). The calculation of SWCNT susceptibilities predicts that a magnetic field of the order of 10 T can produce an observable alignment in a liquid suspension of SWCNTs [143]. Transmitted light measurement indicates that 90% of purified SWCNTs can be aligned in dimethylformamide along a magnetic field (19 T) axis with a CNT axial orientation within $17 \pm 1^\circ$ [144]. The alignment energy from CNT susceptibility should be much higher ($>5\kappa_B T$) to overcome the Brownian motion with an average energy of $\kappa_B T$, where T is the experimental temperature. Additionally, X-ray diffraction experiments also confirm that CNTs can align along the magnetic field direction.

The as-synthesized CNTs are usually aligned better under magnetic fields. The as-synthesized CNTs are usually paramagnetic because of the entrapped catalytic nanoparticles in the CNTs [134, 137]. The magnitude of magnetization of the as-synthesized CNTs is typically several orders of magnitude higher than the purified CNTs. Under a magnetic field, the as-synthesized CNTs tend to align CNTs parallel to the external magnetic field B easily.

In order to increase the susceptibility of individual CNTs, CNTs are coated or filled with magnetic nanoparticles [145]. The treated CNTs have stronger torque under magnetic field and a higher alignment degree of CNTs is expected. When magnetic particles (micro to nano in diameter) are deposited on CNTs as accelerator, the CNTs can be aligned at very low magnetic fields (0.02–0.89 T) at room temperature [146]. By changing the orientation and location of the substrates, crossed-networks of SWNTs-magnetic particle complex could easily be fabricated.

Such aligned CNTs show strong anisotropic physical properties [147–149], including structure, electrical conductivity, thermal conductivity, and thermopower, as talked about in Sect. 2.3.

6.2.3 Ex Situ Mechanical Methods

CNTs can be effectively aligned by various mechanical methods. Below, we briefly introduce some mechanical methods.

6.2.3.1 Stretching Method

The stretching method is probably the simplest ex situ method to align CNTs. CNTs are aligned under an external force field.

Figure 6.26 shows a simple stretching method to align CNTs on substrates. The CNTs are synthesized first on a substrate. The as-synthesized CNTs are random, tangled, and curved (Fig. 6.26a). Once the substrate is broken in the middle, a force pulls the CNTs on the substrate and the CNTs are aligned (Fig. 6.26b). The aligned CNTs are parallel to each other and perpendicular to the crack.

CNTs are also aligned in polymers by a shear field. The CNTs are first embedded in a polymer matrix, and aligned CNTs can be obtained by cutting thin slices of the CNT/polymer composites to align CNTs [151]. CNTs can also be aligned by mechanical shearing of CNT liquid crystal phase [152].

The CNT composites are also cast into films and then cut into small strips. The cast strips are mechanically stretched to a desired stretching ratio at high temper and CNTs are aligned parallel to the stretching direction [153]. 2D X-ray diffraction patterns indicate that the CNTs are aligned with their longitudinal axes parallel to the stretching direction. The mechanical method has been used to align SWCNTs in polymeric composite films successfully [154, 155].

Different from the force field produced by stretching, a spinning produces a radial force field. When CNTs are dispersed in a thermoplastic resin and melt-spun at high temperatures, the CNTs can be well aligned in the composite along the spinning direction [156].

The stretching method can macroscopically align the CNTs while not providing deterministic control over individual CNT alignment or position during assembly. The direction of CNTs cannot be aligned along the force field perfectly.

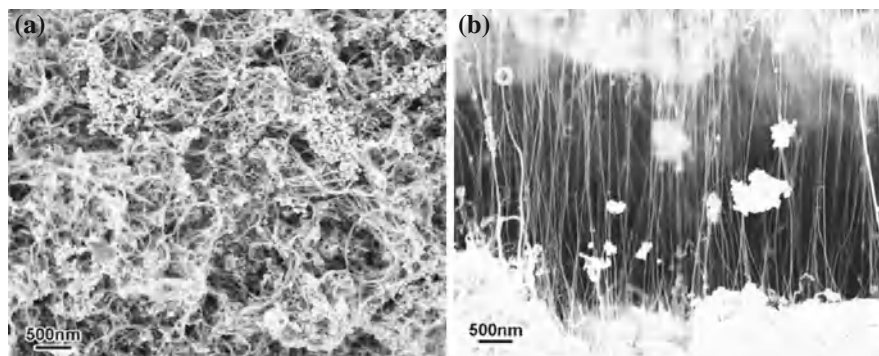


Fig. 6.26 **a** Thermal CVD grown MWCNTs deposited on the substrate. The grown CNTs are curled and randomly distributed on substrate surface. **b** Aligned DWCNTs after being pulled out. The CNTs are straight and parallel to the substrate surface. From Li et al. [150]. Reprinted with permission from Elsevier

6.2.3.2 Spinning Methods

The spinning method has been successfully used to fabricate CNT ropes and CNT clothes [157–165]. Till date, two main kinds of spinning methods, wet spinning method and dry spinning method, have been invented.

In a wet-spinning process, the synthesized CNTs are dispersed in a melt or a liquid/solution, aligned by flow processing, and then converted into a fiber through cooling or solvent removal [157]. The dry-spinning method directly spins the CNT forests synthesized by CVD [158], a CNT aerogel formed in the reaction zone [160], or cotton-like raw CNTs to form CNT yarns or continuous fibers.

In the *wet-spinning method*, the CNTs tend to form bundles rather than dispersed well in a liquid or solution because of the strong van der Waals forces between their sidewalls. There are many review literatures published on the wet-spinning method [164, 165]. In order to disperse CNTs, surfactants are used to stabilize CNT dispersions because surfactants can form micellar structures around individual CNTs. Surfactant such as sodium dodecyl sulfate, tetra-tri methylammonium bromide and lithium dodecyl sulfate [159, 166] have been used to disperse CNTs in an aqueous solution. The solution is then sonicated to allow the surfactant micelle to encase the CNTs. The surfactant concentration is critical for the formation of a good dispersion of CNTs. An optically homogeneous SWCNT solution can be formed with 0.35 wt % SWCNTs and 1 wt % sodium dodecyl sulfate in water.

Figure 6.27a shows a setup to produce SWCNT fibers with SWCNT content of 60 wt % using the wet-spinning method. In the process, an aqueous suspension of carbon nanotubes, stabilized by a surfactant, is injected into a flowing solution of polyvinyl alcohol which causes the CNT fiber to coagulate [157]. Then the CNT fibers are removed from the bath and washed to remove excess polymer. The resultant fiber

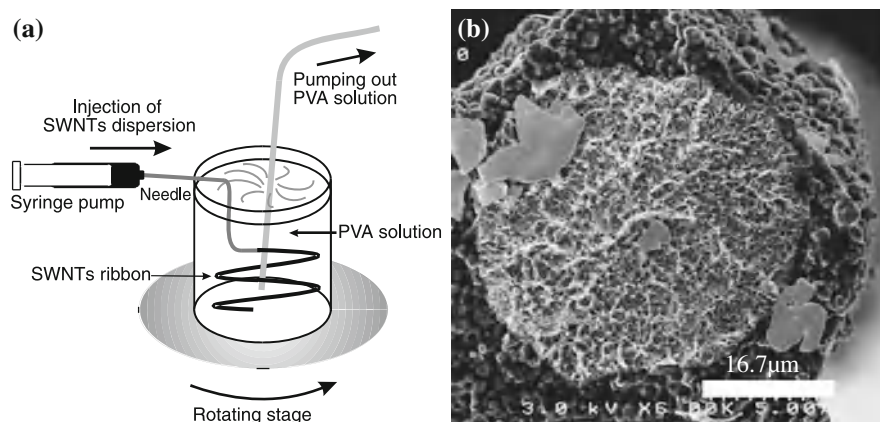


Fig. 6.27 The wet spinning method to align CNTs. From Vigolo et al. [157]. **a** Schematic of a rotating bath used for coagulating surfactant-dispersed SWCNTs into a fiber. **b** SEM image of cross section of a nanotube fiber made from the wet spinning method. The brighter region is mostly composed of SWCNTs while the surrounded *darker region* is mostly composed of carbon impurities

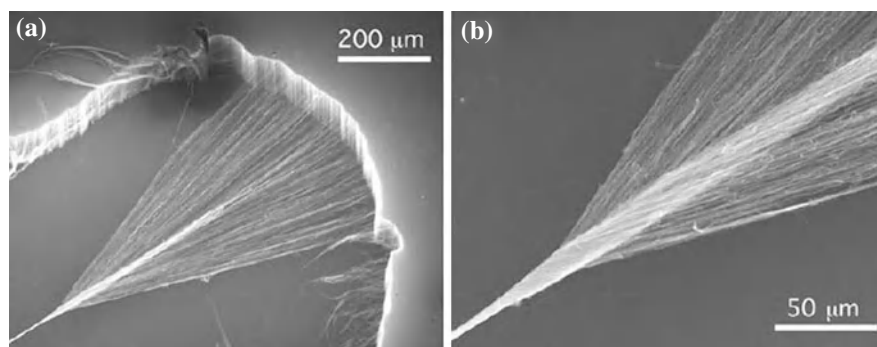


Fig. 6.28 SEM images of a carbon nanotube yarn twisted by dry-spinning method from CNT forest. From Zhu et al. [168]

is a composite of CNT and polymer, as shown in Fig. 6.27b. XRD indicates that the CNTs in such wet-spun CNT fibers are aligned.

Polymer-free CNT fibers can be produced using low-viscosity, polymer-free acids or bases as coagulant. For example, neat SWCNT fibers have been produced by the conventional wet spinning from sulfuric acid solution [167]. Purified SWCNTs were first mixed with acid solution and then extruded from a capillary tube. The produced SWCNT ropes are 200–600 nm in diameter and meters in length. After drying, the fibers show a high degree of alignment of SWCNTs.

The *dry-spinning* method directly spin the CNTs synthesized by a CVD method to form CNT yarns [158], being different from the wet spinning method in which

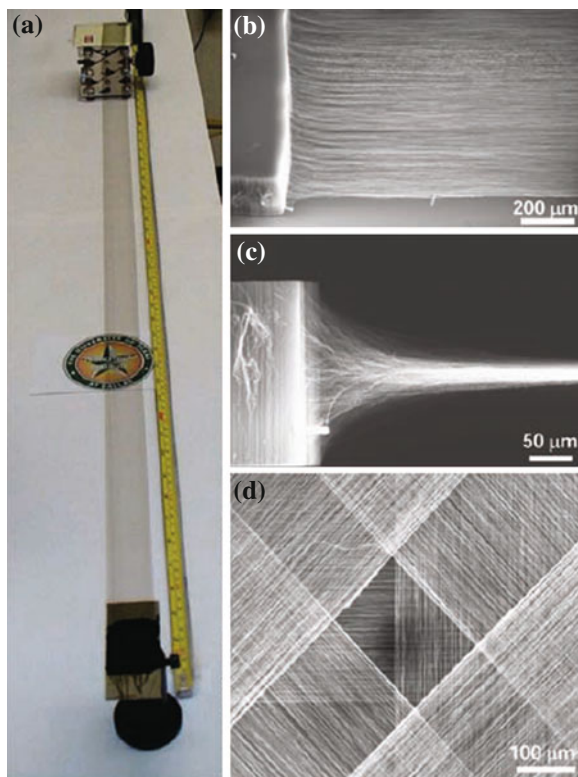


Fig. 6.29 MWCNT forest conversion into sheets and assemblies of those sheets. **a** Photograph of a self-supporting 3.4 cm-wide, meter-long MWCNT sheet that has been hand-drawn from a nanotube forest; it is transparent. **b** SEM image, at a 35° angle with respect to the forest plane, capturing an MWCNT forest being drawn into a sheet. **c** SEM micrograph showing the cooperative 90° rotation of MWCNTs in a forest to form a sheet. **d** SEM micrograph of a 2D reinforced structure fabricated by overlaying four nanotube sheets with a 45° shift in orientation between successive sheets. From Zhang et al. [162]. Copyright (2005), AAAS

process the CNTs are dispersed in a liquid. The dry-spun CNT yarns are pure CNTs without impurities. The such spun yarns are typically 10–20 cm in length and 5–20 μm in diameter. Their electrical resistivity is $5 \Omega \cdot \text{cm}$ and tensile strength is 0.8 GPa, lower than those of individual CNTs.

Using the similar dry spinning technique, continuous CNT fibers have also been directly spun from the CNT aerogel formed in the reaction zone into continuous fibers [160, 161]. CNT yarns have also been dry-spun from the cotton-like raw CNTs.

Besides the dry-spinning of the random CNTs, vertically grown CNT forests are also dry spun [169] and CNT ropes has been successfully produced [163, 168]. Figure 6.28 shows SEM images of a procedure to spin CNTs from a CNT forest. Till

date, many kinds of CNT yarns have been produced [170–174]. Interested readers are referred to the review publications [175].

The CNT thin sheets have been further assembled from these dry-spun yarns. Figure 6.29 shows a CNT sheet assembled by a dry-spinning method from MWCNT forests. The CNTs are well aligned along the force direction. The transparent thin CNT sheets are fabricated in meters. The CNT sheets have wide applications in transistor, transparent electrodes, displays, and actuators etc [176]. For example, these kinds of nanosheets can be used for TEM grids (see Sect. 9.1.2), incandescent displays and lighting (see Sect. 8.1.4), thermoacoustic loudspeakers (see Sect. 9.3.2), etc.

Here, we do not review these spinning methods in detail since there are already some thorough reviews on wet-spinning from solution [38, 159, 164, 165], on dry-spinning [38, 164], and on electrospinning from CNT composites [162].

6.2.4 Other Ex Situ Methods

Besides the ex situ methods discussed above, CNTs can also be aligned by fluidic methods [177, 178], electrophoresis [179, 180], surface forces [181], surface acoustic waves [182], by chemically directed assembly [183, 184], and by capillary action [185].

Till date, there are some review papers [176, 186–190] and books [191] focusing on the alignment of CNTs. The readers are referred to these literatures and references therein for detailed information.

References

1. E. Jiran, C. Thompson, Capillary instabilities in thin films. *J. Electron. Mater.* **19**(11), 1153–1160 (1990)
2. E. Jiran, C.V. Thompson, Capillary instabilities in thin, continuous films. *Thin Solid Films* **208**(1), 23–28 (1992)
3. L. Rayleigh, On the instability of jets. *Proc. Lond. Math. Soc.* **s1–10**(1), 4–13 (1878)
4. G. Zhang, D. Mann, L. Zhang, A. Javey, Y. Li, E. Yenilmez, Q. Wang, J.P. McVittie, Y. Nishi, J. Gibbons, H. Dai, Ultra-high-yield growth of vertical single-walled carbon nanotubes: hidden roles of hydrogen and oxygen. *Proc. Nat. Acad. Sci. U.S.A.* **102**(45), 16141–16145 (2005)
5. K. Hata, D.N. Futaba, K. Mizuno, T. Namai, M. Yumura, S. Iijima, Water-assisted highly efficient synthesis of impurity-free single-walled carbon nanotubes. *Science* **306**(5700), 1362–1364 (2004)
6. G.-Y. Xiong, D. Wang, Z. Ren, Aligned millimeter-long carbon nanotube arrays grown on single crystal magnesite. *Carbon* **44**(5), 969–973 (2006)
7. A. Cao, V.P. Veedu, X. Li, Z. Yao, M.N. Ghasemi-Nejhad, P.M. Ajayan, Multifunctional brushes made from carbon nanotubes. *Nat. Mater.* **4**(7), 540–545 (2005)
8. S. Chakrabarti, T. Nagasaka, Y. Yoshikawa, L. Pan, Y. Nakayama, Growth of super long aligned brush-like carbon nanotubes. *Jpn. J. Appl. Phys.* **45**(28), L720–L722 (2006)

9. S. Fan, M.G. Chapline, N.R. Franklin, T.W. Tomblor, A.M. Cassell, H. Dai, Self-oriented regular arrays of carbon nanotubes and their field emission properties. *Science* **283**(5401), 512–514 (1999)
10. J. Kong, H.T. Soh, A.M. Cassell, C.F. Quate, H. Dai, Synthesis of individual single-walled carbon nanotubes on patterned silicon wafers. *Nature* **395**(6705), 878–881 (1998)
11. R. Andrews, D. Jacques, A.M. Rao, F. Derbyshire, D. Qian, X. Fan, E.C. Dickey, J. Chen, Continuous production of aligned carbon nanotubes: a step closer to commercial realization. *Chem. Phys. Lett.* **303**(5–6), 467–474 (1999)
12. S. Sato, A. Kawabata, M. Nihei, Y. Awano, Growth of diameter-controlled carbon nanotubes using monodisperse nickel nanoparticles obtained with a differential mobility analyzer. *Chem. Phys. Lett.* **382**(3–4), 361–366 (2003)
13. X. Li, A. Cao, Y.J. Jung, R. Vajtai, P.M. Ajayan, Bottom-up growth of carbon nanotube multilayers: unprecedented growth. *Nano Lett.* **5**(10), 1997–2000 (2005)
14. L. Zhu, D.W. Hess, C.-P. Wong, Monitoring carbon nanotube growth by formation of nanotube stacks and investigation of the diffusion-controlled kinetics. *J. Phys. Chem. B* **110**(11), 5445–5449 (2006)
15. W. Zhou, L. Ding, S. Yang, J. Liu, Orthogonal orientation control of carbon nanotube growth. *J. Am. Chem. Soc.* **132**(1), 336–341 (2010)
16. Y. Zhang, A. Chang, J. Cao, Q. Wang, W. Kim, Y. Li, N. Morris, E. Yenilmez, J. Kong, H. Dai, Electric-field-directed growth of aligned single-walled carbon nanotubes. *Appl. Phys. Lett.* **79**(19), 3155–3157 (2001)
17. L.X. Benedict, S.G. Louie, M.L. Cohen, Static polarizabilities of single-wall carbon nanotubes. *Phys. Rev. B* **52**(11), 8541–8549 (1995)
18. A. Ural, Y. Li, H. Dai, Electric-field-aligned growth of single-walled carbon nanotubes on surfaces. *Appl. Phys. Lett.* **81**(18), 3464–3466 (2002)
19. E. Joselevich, C.M. Lieber, Vectorial growth of metallic and semiconducting single-wall carbon nanotubes. *Nano Lett.* **2**(10), 1137–1141 (2002)
20. I. Radu, Y. Hanein, D.H. Cobden, Oriented growth of single-wall carbon nanotubes using alumina patterns. *Nanotechnology* **15**(5), 473 (2004)
21. R.S. Johnson, G. Lucovsky, I. Baumvol, Physical and electrical properties of noncrystalline Al_2O_3 prepared by remote plasma enhanced chemical vapor deposition. *J. Vac. Sci. Technol. A* **19**(4), 1353–1360 (2001)
22. J.G. Wen, Z.P. Huang, D.Z. Wang, J.H. Chen, S.X. Yang, Z.F. Ren, J.H. Wang, L.E. Calvet, J. Chen, J.F. Klemic, M. Reed, Growth and characterization of aligned carbon nanotubes from patterned nickel nanodots and uniform thin films. *J. Mater. Res.* **16**(11), 3246–3253 (2001)
23. C. Bower, O. Zhou, W. Zhu, D.J. Werder, S. Jin, Nucleation and growth of carbon nanotubes by microwave plasma chemical vapor deposition. *Appl. Phys. Lett.* **77**(17), 2767–2769 (2000)
24. A. Nojeh, A. Ural, R.F. Pease, H. Dai, Electric-field-directed growth of carbon nanotubes in two dimensions. *J. Vac. Sci. Technol. B* **22**(6), 3421–3425 (2004)
25. Y. Gao, Y.S. Zhou, W. Xiong, M. Mahjouri-Samani, M. Mitchell, Y.F. Lu, Controlled growth of carbon nanotubes on electrodes under different bias polarity. *Appl. Phys. Lett.* **95**(14), 143117 (2009)
26. A. Ismach, E. Joselevich, Orthogonal self-assembly of carbon nanotube crossbar architectures by simultaneous graphoepitaxy and field-directed growth. *Nano Lett.* **6**(8), 1706–1710 (2006)
27. S. Huang, X. Cai, C. Du, J. Liu, Oriented long single walled carbon nanotubes on substrates from floating catalysts. *J. Phys. Chem. B* **107**(48), 13251–13254 (2003)
28. S. Huang, X. Cai, J. Liu, Growth of millimeter-long and horizontally aligned single-walled carbon nanotubes on flat substrates. *J. Am. Chem. Soc.* **125**(19), 5636–5637 (2003)
29. S. Huang, Q. Fu, L. An, J. Liu, Growth of aligned swnt arrays from water-soluble molecular clusters for nanotube device fabrication. *Phys. Chem. Chem. Phys.* **6**(6), 1077–1079 (2004)
30. S. Huang, B. Maynor, X. Cai, J. Liu, Ultralong, well-aligned single-walled carbon nanotube architectures on surfaces. *Adv. Mater.* **15**(19), 1651–1655 (2003)
31. B.H. Hong, J.Y. Lee, T. Beetz, Y. Zhu, P. Kim, K.S. Kim, Quasi-continuous growth of ultralong carbon nanotube arrays. *J. Am. Chem. Soc.* **127**(44), 15336–15337 (2005)

32. W. Zhou, Z. Han, J. Wang, Y. Zhang, Z. Jin, X. Sun, Y. Zhang, C. Yan, Y. Li, Copper catalyzing growth of single-walled carbon nanotubes on substrates. *Nano Lett.* **6**(12), 2987–2990 (2006)
33. Z. Jin, H. Chu, J. Wang, J. Hong, W. Tan, Y. Li, Ultralow feeding gas flow guiding growth of large-scale horizontally aligned single-walled carbon nanotube arrays. *Nano Lett.* **7**(7), 2073–2079 (2007)
34. Z. Yu, S. Li, P.J. Burke, Synthesis of aligned arrays of millimeter long, straight single-walled carbon nanotubes. *Chem. Mater.* **16**(18), 3414–3416 (2004)
35. Y. Li, D. Mann, M. Rolandi, W. Kim, A. Ural, S. Hung, A. Javey, J. Cao, D. Wang, E. Yenilmez, Q. Wang, J.F. Gibbons, Y. Nishi, H. Dai, Preferential growth of semiconducting single-walled carbon nanotubes by a plasma enhanced CVD method. *Nano Lett.* **4**(2), 317–321 (2004)
36. L. Huang, B. White, M. Y. Sfeir, M. Huang, H.X. Huang, S. Wind, J. Hone, S. O'Brien, Cobalt ultrathin film catalyzed ethanol chemical vapor deposition of single-walled carbon nanotubes. *J. Phys. Chem. B* **110**(23), 11103–11109 (2006)
37. C. Kocabas, M. Shim, J.A. Rogers, Spatially selective guided growth of high-coverage arrays and random networks of single-walled carbon nanotubes and their integration into electronic devices. *J. Am. Chem. Soc.* **128**(14), 4540–4541 (2006)
38. E. Joselevich, H. Dai, J. Liu, K. Hata, and A. H. Windle, Carbon nanotube synthesis and organization in Carbon Nanotubes. in *Advanced Topics in the Synthesis, Structure, Properties and Applications*, vol. 111 of Topics in Applied Physics (Springer, Berlin, 2008), pp. 101–164
39. Q. Yu, G. Qin, H. Li, Z. Xia, Y. Nian, S.-S. Pei, Mechanism of horizontally aligned growth of single-wall carbon nanotubes on *r*-plane sapphire. *J. Phys. Chem. B* **110**(45), 22676–22680 (2006)
40. M. Su, Y. Li, B. Maynor, A. Buldum, J.P. Lu, J. Liu, Lattice-oriented growth of single-walled carbon nanotubes. *J. Phys. Chem. B* **104**(28), 6505–6508 (2000)
41. M. Tominaga, A. Ohira, A. Kubo, I. Taniguchi, M. Kunitake, Growth of carbon nanotubes on a gold (111) surface using two-dimensional iron oxide nano-particle catalysts derived from iron storage protein. *Chem. Commun.* **2004**(13), 1518–1519 (2004)
42. V. Derycke, R. Martel, M. Radosavljević, F.M. Ross, P. Avouris, Catalyst-free growth of ordered single-walled carbon nanotube networks. *Nano Lett.* **2**(10), 1043–1046 (2002)
43. L.B. Ruppalt, P.M. Albrecht, J.W. Lyding, Atomic resolution scanning tunneling microscope study of single-walled carbon nanotubes on GaAs(110). *J. Vac. Sci. Technol. B* **22**(4), 2005–2007 (2004)
44. N. Ishigami, H. Ago, T. Nishi, K.-i. Ikeda, M. Tsuji, T. Ikuta, K. Takahashi, Unidirectional growth of single-walled carbon nanotubes. *J. Am. Chem. Soc.* **130**(51), 17264–17265 (2008)
45. S. Han, X. Liu, C. Zhou, Template-free directional growth of single-walled carbon nanotubes on *a*- and *r*-plane sapphire. *J. Am. Chem. Soc.* **127**(15), 5294–5295 (2005)
46. H. Ago, K. Imamoto, N. Ishigami, R. Ohdo, K.-I. Ikeda, M. Tsuji, Competition and cooperation between lattice-oriented growth and step-templated growth of aligned carbon nanotubes on sapphire. *Appl. Phys. Lett.* **90**(12), 123112 (2007)
47. H. Ago, K. Nakamura, K.-I. Ikeda, N. Uehara, N. Ishigami, M. Tsuji, Aligned growth of isolated single-walled carbon nanotubes programmed by atomic arrangement of substrate surface. *Chem. Phys. Lett.* **408**(4–6), 433–438 (2005)
48. A. Rutkowska, D. Walker, S. Gorfman, P.A. Thomas, J.V. Macpherson, Horizontal alignment of chemical vapor-deposited swnts on single-crystal quartz surfaces: further evidence for epitaxial alignment. *J. Phys. Chem. C* **113**(39), 17087–17096 (2009)
49. H. Ago, N. Uehara, K.-I. Ikeda, R. Ohdo, K. Nakamura, M. Tsuji, Synthesis of horizontally-aligned single-walled carbon nanotubes with controllable density on sapphire surface and polarized raman spectroscopy. *Chem. Phys. Lett.* **421**(4–6), 399–403 (2006)
50. T. Ozel, D. Abdula, E. Hwang, M. Shim, Nonuniform compressive strain in horizontally aligned single-walled carbon nanotubes grown on single crystal quartz. *ACS Nano* **3**(8), 2217–2224 (2009)
51. A. Ismach, L. Segev, E. Wachtel, E. Joselevich, Atomic-step-templated formation of single wall carbon nanotube patterns. *Angew. Chem. Int. Ed.* **43**(45), 6140–6143 (2004)

52. H. Ago, K. Imamoto, T. Nishi, M. Tsuji, T. Ikuta, K. Takahashi, M. Fukui, Direct growth of bent carbon nanotubes on surface engineered sapphire. *J. Phys. Chem. C* **113**(30), 13121–13124 (2009)
53. H. Ago, T. Nishi, K. Imamoto, N. Ishigami, M. Tsuji, T. Ikuta, K. Takahashi, Orthogonal growth of horizontally aligned single-walled carbon nanotube arrays. *J. Phys. Chem. C* **114**(30), 12925–12930 (2010)
54. N. Yoshihara, H. Ago, K. Imamoto, M. Tsuji, T. Ikuta, K. Takahashi, Horizontally aligned growth of single-walled carbon nanotubes on a surface-modified silicon wafer. *J. Phys. Chem. C* **113**(19), 8030–8034 (2009)
55. C.M. Orofeo, H. Ago, N. Yoshihara, M. Tsuji, Top-down approach to align single-walled carbon nanotubes on silicon substrate. *Appl. Phys. Lett.* **94**(5), 053113 (2009)
56. T. Kamimura, K. Matsumoto, Controlling direction of growth of carbon nanotubes on patterned SiO₂ substrate. *Appl. Phys. Express* **2**(1), 015005 (2009)
57. C. Kocabas, S. Hur, A. Gaur, M.A. Meitl, M. Shim, J.A. Rogers, Guided growth of large-scale, horizontally aligned arrays of single-walled carbon nanotubes and their use in thin-film transistors. *Small* **1**(11), 1110–1116 (2005)
58. A. Ismach, D. Kantorovich, E. Joselevich, Carbon nanotube graphoepitaxy: highly oriented growth by faceted nanosteps. *J. Am. Chem. Soc.* **127**(33), 11554–11555 (2005)
59. H.I. Smith, D.C. Flanders, Oriented crystal growth on amorphous substrates using artificial surface-relief gratings. *Appl. Phys. Lett.* **32**(6), 349–350 (1978)
60. R.A. Segalman, H. Yokoyama, E.J. Kramer, Graphoepitaxy of spherical domain block copolymer films. *Adv. Mater.* **13**(15), 1152–1155 (2001)
61. B. Zhang, G. Hong, B. Peng, J. Zhang, W. Choi, J.M. Kim, J.-Y. Choi, Z. Liu, Grow single-walled carbon nanotubes cross-bar in one batch. *J. Phys. Chem. C* **113**(14), 5341–5344 (2009)
62. N. Kumar, W. Curtis, J.-I. Hahm, Laterally aligned, multiwalled carbon nanotube growth using magnetospirillum magnetotacticum. *Appl. Phys. Lett.* **86**(17), 173101 (2005)
63. K.-H. Lee, J.-M. Cho, W. Sigmund, Control of growth orientation for carbon nanotubes. *Appl. Phys. Lett.* **82**(3), 448–450 (2003)
64. M.H. Kuang, Z.L. Wang, X.D. Bai, J.D. Guo, E.G. Wang, Catalytically active nickel 110 surfaces in growth of carbon tubular structures. *Appl. Phys. Lett.* **76**(10), 1255–1257 (2000)
65. Z.F. Ren, Z.P. Huang, J.W. Xu, J.H. Wang, P. Bush, M.P. Siegal, P.N. Provencio, Synthesis of large arrays of well-aligned carbon nanotubes on glass. *Science* **282**, 1105–1107 (1998)
66. Y. Tu, Y. Lin, Z.F. Ren, Nanoelectrode arrays based on low site density aligned carbon nanotubes. *Nano Lett.* **3**(1), 107–109 (2003)
67. Y. Wang, J. Rycbczynski, D.Z. Wang, K. Kempa, Z.F. Ren, W.Z. Li, B. Kimball, Periodicity and alignment of large-scale carbon nanotubes arrays. *Appl. Phys. Lett.* **85**(20), 4741–4743 (2004)
68. K.B.K. Teo, D.B. Hash, R.G. Lacerda, N.L. Rupesinghe, M.S. Bell, S.H. Dalal, D. Bose, T.R. Govindan, B.A. Cruden, M. Chhowalla, G.A.J. Amaratunga, M. Meyyappan, W.I. Milne, The significance of plasma heating in carbon nanotube and nanofiber growth. *Nano Lett.* **4**(5), 921–926 (2004)
69. C.L. Cheung, A. Kurtz, H. Park, C.M. Lieber, Diameter-controlled synthesis of carbon nanotubes. *J. Phys. Chem. B* **106**(10), 2429–2433 (2002)
70. H.C. Choi, S. Kundaria, D. Wang, A. Javey, Q. Wang, M. Rolandi, H. Dai, Efficient formation of iron nanoparticle catalysts on silicon oxide by hydroxylamine for carbon nanotube synthesis and electronics. *Nano Lett.* **3**(2), 157–161 (2003)
71. Y. Li, W. Kim, Y. Zhang, M. Rolandi, D. Wang, H. Dai, Growth of single-walled carbon nanotubes from discrete catalytic nanoparticles of various sizes. *J. Phys. Chem. B* **105**(46), 11424–11431 (2001)
72. C. Hinderling, Y. Keles, T. Steckli, H. Knapp, T. de los Arcos, P. Oelhafen, I. Korczagin, M. Hempenius, G. Vancso, R. Pugin, H. Heinzelmann, Organometallic block copolymers as catalyst precursors for templated carbon nanotube growth. *Adv. Mater.* **16**(11), 876–879 (2004)

73. Z.P. Huang, J.W. Xu, Z.F. Ren, J.H. Wang, M.P. Siegal, P.N. Provencio, Growth of highly oriented carbon nanotubes by plasma-enhanced hot filament chemical vapor deposition. *Appl. Phys. Lett.* **73**(26), 3845–3847 (1998)
74. Y. Tu, Z.P. Huang, D.Z. Wang, J.G. Wen, Z.F. Ren, Growth of aligned carbon nanotubes with controlled site density. *Appl. Phys. Lett.* **80**(21), 4018–4020 (2002)
75. M. Chowalla, K.B.K. Teo, C. Ducati, N.L. Rupesinghe, G.A.J. Amaratunga, A.C. Ferrari, D. Roy, J. Robertson, W.I. Milne, Growth process conditions of vertically aligned carbon nanotubes using plasma enhanced chemical vapor deposition. *J. Appl. Phys.* **90**(10), 5308–5317 (2001)
76. V.I. Merkulov, D.H. Lowndes, Y.Y. Wei, G. Eres, E. Voelkl, Patterned growth of individual and multiple vertically aligned carbon nanofibers. *Appl. Phys. Lett.* **76**(24), 3555–3557 (2000)
77. M.P. Zach, R.M. Penner, Nanocrystalline nickel nanoparticles. *Adv. Mater.* **12**(12), 878–883 (2000)
78. J.V. Zoval, R.M. Stiger, P.R. Biernacki, R.M. Penner, Electrochemical deposition of silver nanocrystallites on the atomically smooth graphite basal plane. *J. Phys. Chem.* **100**(2), 837–844 (1996)
79. G. Sandmann, H. Dietz, W. Plieth, Preparation of silver nanoparticles on ito surfaces by a double-pulse method. *J. Electroanal. Chem.* **491**(1–2), 78–86 (2000)
80. H. Liu, R.M. Penner, Size-selective electrodeposition of mesoscale metal particles in the uncoupled limit. *J. Phys. Chem. B* **104**(39), 9131–9139 (2000)
81. J.V. Zoval, J. Lee, S. Gorer, R.M. Penner, Electrochemical preparation of platinum nanocrystallites with size selectivity on basal plane oriented graphite surfaces. *J. Phys. Chem. B* **102**(7), 1166–1175 (1998)
82. S.H. Jo, Y. Tu, Z.P. Huang, D.L. Carnahan, D.Z. Wang, Z.F. Ren, Effect of length and spacing of vertically aligned carbon nanotubes on field emission properties. *Appl. Phys. Lett.* **82**(20), 3520–3522 (2003)
83. K. Zhou, J.-Q. Huang, Q. Zhang, F. Wei, Multi-directional growth of aligned carbon nanotubes over catalyst film prepared by atomic layer deposition. *Nanoscale Res. Lett.* **5**(10), 1555–1560 (2010)
84. T.A. El-Aguizy, J. hyun Jeong, Y.-B. Jeon, W. Z. Li, Z. F. Ren, S.-G. Kim, Transplanting carbon nanotubes. *Appl. Phys. Lett.* **85**(24), 5995–5997 (2004)
85. K. Kempa, B. Kimball, J. Rybczynski, Z.P. Huang, P.F. Wu, D. Steeves, M. Sennett, M. Giersig, D.V.G.L.N. Rao, D.L. Carnahan, D.Z. Wang, J. Y. Lao, W. Z. Li, Z.F. Ren, Photonic crystals based on periodic arrays of aligned carbon nanotubes. *Nano Lett.* **3**(1), 13–18 (2003)
86. J. Rybczynski, U. Ebels, M. Giersig, Large-scale, 2D arrays of magnetic nanoparticles. *Colloid. Surface. A* **219**(1–3), 1–6 (2003)
87. J. Rybczynski, D. Banerjee, A. Kosiorek, M. Giersig, Z.F. Ren, Formation of super arrays of periodic nanoparticles and aligned zno nanorods: simulation and experiments. *Nano Lett.* **4**(10), 2037–2040 (2004)
88. A. Kosiorek, W. Kandulski, P. Chudzinski, K. Kempa, M. Giersig, Shadow nanosphere lithography: simulation and experiment. *Nano Lett.* **4**(7), 1359–1363 (2004)
89. J. Rybczynski, K. Kempa, Y. Wang, Z.F. Ren, J.B. Carlson, B.R. Kimball, G. Benham, Visible light diffraction studies on periodically aligned arrays of carbon nanotubes: Experimental and theoretical comparison. *Appl. Phys. Lett.* **88**(20), 203122 (2006)
90. W. Hu, D. Gong, Z. Chen, L. Yuan, K. Saito, C.A. Grimes, P. Kichambare, Growth of well-aligned carbon nanotube arrays on silicon substrates using porous alumina film as a nanotemplate. *Appl. Phys. Lett.* **79**(19), 3083–3085 (2001)
91. J.S. Suh, J.S. Lee, Highly ordered two-dimensional carbon nanotube arrays. *Appl. Phys. Lett.* **75**(14), 2047–2049 (1999)
92. W.J. Yu, Y.S. Cho, G.S. Choi, D. Kim, Patterned carbon nanotube field emitter using the regular array of an anodic aluminium oxide template. *Nanotechnology* **16**(5), S291–S295 (2005)
93. L. Nilsson, O. Groening, C. Emmenegger, O. Kuettel, E. Schaller, L. Schlapbach, H. Kind, J.-M. Bonard, K. Kern, Scanning field emission from patterned carbon nanotube films. *Appl. Phys. Lett.* **76**(15), 2071–2073 (2000)

94. X. Wang, C.J. Summers, Z.L. Wang, Large-scale hexagonal-patterned growth of aligned ZnO nanorods for nano-optoelectronics and nanosensor arrays. *Nano Lett.* **4**(3), 423–426 (2004)
95. X.D. Wang, E. Graugnard, J.S. King, Z.L. Wang, C.J. Summers, Large-scale fabrication of ordered nanobowl arrays. *Nano Lett.* **4**(11), 2223–2226 (2004)
96. K.J. Mysels, Surface tension of solutions of pure sodium dodecyl sulfate. *Langmuir* **2**, 423–428 (July 1986)
97. M. Hilgendorff, M. Giersig, Assemblies of magnetic particles: synthesis and production. in *Nanoscale Materials*, ed. by L.M. Liz-Marzán, P.V. Kamat (Kluwer Academic Publishers, Boston, 2003)
98. Z.F. Ren, Z.P. Huang, D.Z. Wang, J.G. Wen, J.W. Xu, J.H. Wang, L.E. Calvet, J. Chen, J.F. Klemic, M.A. Reed, Growth of a single freestanding multiwall carbon nanotube on each nanonickel dot. *Appl. Phys. Lett.* **75**(8), 1086–1088 (1999)
99. Y.Y. Wei, G. Eres, V.I. Merkulov, D.H. Lowndes, Effect of catalyst film thickness on carbon nanotube growth by selective area chemical vapor deposition. *Appl. Phys. Lett.* **78**(10), 1394–1396 (2001)
100. K.B.K. Teo, M. Chhowalla, G.A.J. Amaratunga, W.I. Milne, D.G. Hasko, G. Pirio, P. Legagneux, F. Wyczisk, D. Pribat, Uniform patterned growth of carbon nanotubes without surface carbon. *Appl. Phys. Lett.* **79**(10), 1534–1536 (2001)
101. J. Moser, R. Panepucci, Z.P. Huang, W.Z. Li, Z.F. Ren, A. Usheva, M.J. Naughton, Individual free-standing carbon nanofibers addressable on the 50 nm scale. *J. Vac. Sci. Technol. B* **21**(3), 1004–1007 (2003)
102. H. Cong, L. Hong, R.S. Harake, T. Pan, CNT-based photopatternable nanocomposites with high electrical conductivity and optical transparency. *J. Micromech. Microeng.* **20**(2), 025002 (2010)
103. D. Qin, Y.N. Xia, J.A. Rogers, R.J. Jackman, X.M. Zhao, G.M. Whitesides, Microfabrication, microstructures and microsystems. *Top. Curr. Chem.* **194**, 1–20 (1998)
104. G. Cao, *Nanostructures and Nanomaterials: Synthesis, Properties & Applications* (Imperial College Press, London, 2004)
105. C.C. Davis, W.A. Atia, A. Güngör, D.L. Mazzoni, S. Pilevar, I.I. Smolyaninov, Scanning near-field optical microscopy and lithography with bare tapered optical fibers. *Laser Phys.* **7**(1), 243–248 (1997)
106. M.K. Herndon, R.T. Collins, R.E. Hollinsworth, P.R. Larson, M.B. Johnson, Near-field scanning optical nanolithography using amorphous silicon photoresists. *Appl. Phys. Lett.* **74**(1), 141–143 (1999)
107. T. Ito, S. Okazaki, Pushing the limits of lithography. *Nature* **406**(6799), 1027–1031 (2000)
108. G. Simon, A.M. Haghiri-Gosnet, J. Bourneix, D. Decanini, Y. Chen, F. Rousseaux, H. Lounios, B. Vidal, Sub-20 nm x-ray nanolithography using conventional mask technologies on monochromatized synchrotron radiation. *J. Vac. Sci. Technol. B* **15**(6), 2489–2494 (1997)
109. T. Kitayama, K. Itoga, Y. Watanabe, S. Uzawa, Proposal for a 50 nm proximity x-ray lithography system and extension to 35 nm by resist material selection. *J. Vac. Sci. Technol. B* **18**(6), 2950–2954 (2000)
110. C. Vieu, F. Carcenac, A. Pepin, Y. Chen, M. Mejias, A. Lebib, L. Manin-Ferlazzo, L. Couraud, H. Lunois, Electron beam lithography: resolution limits and applications. *Appl. Surf. Sci.* **164**(1–4), 111–117 (2000)
111. S. Yesin, D.G. Hasko, H. Ahmed, Fabrication of <5 nm width lines in poly(methylmethacrylate) resist using a water: isopropyl alcohol developer and ultrasonically-assisted development. *Appl. Phys. Lett.* **78**(18), 2760 (2001)
112. H. Masuda, H. Yamada, M. Satoh, H. Asoh, M. Nakao, T. Tamamura, Highly ordered nanochannel-array architecture in anodic alumina. *Appl. Phys. Lett.* **71**(19), 2770–2772 (1997)
113. Z. Chen, D. den Engelsen, P.K. Bachmann, V. van Elsbergen, I. Koehler, J. Merikhi, D.U. Wiechert, High emission current density microwave-plasma-grown carbon nanotube arrays by postdepositional radio-frequency oxygen plasma treatment. *Appl. Phys. Lett.* **87**(24), 243104 (2005)

114. C.R. Martin, Nanomaterials: a membrane-based synthetic approach. *Science* **266**(5193), 1961–1966 (1994)
115. J. Li, C. Papadopoulos, J.M. Xu, M. Moskovits, Highly-ordered carbon nanotube arrays for electronics applications. *Appl. Phys. Lett.* **75**(3), 367–369 (1999)
116. J.S. Suh, K.S. Jeong, J.S. Lee, I. Han, Study of the field-screening effect of highly ordered carbon nanotube arrays. *Appl. Phys. Lett.* **80**(13), 2392–2394 (2002)
117. F. Gao, Y. Yuan, K.F. Wang, X.Y. Chen, F. Chen, J.-M. Liu, Z.F. Ren, Preparation and photoabsorption characterization of BiFeO₃ nanowires. *Appl. Phys. Lett.* **89**(10), 102506 (2006)
118. R.C. Furneaux, W.R. Rigby, A.P. Davidson, The formation of controlled-porosity membranes from anodically oxidized aluminium. *Nature* **337**(6203), 147–149 (1989)
119. X. Chen, K. Cendrowski, J. Srenscek-Nazzal, M. Rümmele, R.J. Kalenczuk, H. Chen, P.K. Chu, E. Borowiak-Palen, Fabrication method of parallel mesoporous carbon nanotubes. *Colloid. Surface. A* **377**(1–3), 150–155 (2011)
120. K.-H. Kim, E. Lefevre, M. Châtelet, D. Pribat, C.S. Cojocaru, Laterally organized carbon nanotube arrays based on hot-filament chemical vapor deposition. *Thin Solid Films* **519**(14), 4598–4602 (2011)
121. R.D. Bennett, G.Y. Xiong, Z.F. Ren, R.E. Cohen, Using block copolymer micellar thin films as templates for the production of catalysts for carbon nanotube growth. *Chem. Mater.* **16**(26), 5589–5595 (2004)
122. E. Mendoza, S. Henley, C. Poa, G. Chen, C. Giusca, A. Adikaari, J. Carey, S. Silva, Large area growth of carbon nanotube arrays for sensing platforms. *Sens. Actuat. B Chem.* **109**(1), 75–80 (2005)
123. W. Chang, J. Kim, D. Choi, C. Han, Fabrication of nano-electrode arrays of free-standing carbon nanotubes on nano-patterned substrate by imprint method. *Appl. Surf. Sci.* **257**(7), 3063–3068 (2011)
124. W. Chang, J. Kim, D. Choi, C. Han, Fabrication of free-standing carbon nanotube electrode arrays on a quartz wafer. *Thin Solid Films* **518**(22), 6624–6629 (2010)
125. S. Talapatra, S. Kar, S.K. Pal, R. Vajtai, L. Ci, P. Victor, M.M. Shaijumon, S. Kaur, O. Nalamasu, M.P. Ajayan, Direct growth of aligned carbon nanotubes on bulk metals. *Nat. Nanotechnol.* **1**(2), 112–116 (2006)
126. X.Q. Chen, T. Saito, H. Yamada, K. Matsushige, Aligning single-wall carbon nanotubes with an alternating-current electric field. *Appl. Phys. Lett.* **78**(23), 3714–3716 (2001)
127. K. Yamamoto, S. Akita, Y. Nakayama, Orientation of carbon nanotubes using electrophoresis. *Jpn. J. Appl. Phys. Part 2* **35**(7B), L917–L918 (1996)
128. K. Bubke, H. Gnewuch, M. Hempstead, J. Hammer, M.L.H. Green, Optical anisotropy of dispersed carbon nanotubes induced by an electric field. *Appl. Phys. Lett.* **71**(14), 1906–1908 (1997)
129. J. Chung, K.-H. Lee, J. Lee, R.S. Ruoff, Toward large-scale integration of carbon nanotubes. *Langmuir* **20**(8), 3011–3017 (2004)
130. S.M. Jung, H.Y. Jung, J.S. Suh, Horizontally aligned carbon nanotube field emitters fabricated on ito glass substrates. *Carbon* **46**(14), 1973–1977 (2008)
131. S. Shekhar, P. Stokes, S.I. Khondaker, Ultrahigh density alignment of carbon nanotube arrays by dielectrophoresis. *ACS Nano* **5**(3), 1739–1746 (2011)
132. B.K. Sarker, M.R. Islam, F. Alzubi, S.I. Khondaker, Fabrication of aligned carbon nanotube array electrodes for organic electronic devices. *Mater. Express* **1**(1), 80–85 (2011)
133. C. Kocabas, M.A. Meitl, A. Gaur, M. Shim, J.A. Rogers, Aligned arrays of single-walled carbon nanotubes generated from random networks by orientationally selective laser ablation. *Nano Lett.* **4**(12), 2421–2426 (2004)
134. J. Heremans, C.H. Olk, D.T. Morelli, Magnetic susceptibility of carbon structures. *Phys. Rev. B* **49**(21), 15122–15125 (1994)
135. D.K. Yoon, S.R. Lee, Y.H. Kim, S.-M. Choi, H.-T. Jung, Large-area, highly aligned cylindrical perfluorinated supramolecular dendrimers using magnetic fields. *Adv. Mater.* **18**(4), 509–513 (2006)

136. J.P. Lu, Novel magnetic properties of carbon nanotubes. *Phys. Rev. Lett.* **74**(7), 1123–1126 (1995)
137. K. Kordás, T. Mustonen, G. Tóth, J. Vähäkangas, A. Uusimäki, H. Jantunen, A. Gupta, K.V. Rao, R. Vajtai, P.M. Ajayan, Magnetic-field induced efficient alignment of carbon nanotubes in aqueous solutions. *Chem. Mater.* **19**(4), 787–791 (2007)
138. G. Korneva, H. Ye, Y. Gogotsi, D. Halverson, G. Friedman, J.-C. Bradley, K.G. Kornev, Carbon nanotubes loaded with magnetic particles. *Nano Lett.* **5**(5), 879–884 (2005)
139. C. Gao, W. Li, H. Morimoto, Y. Nagaoka, T. Maekawa, Magnetic carbon nanotubes: synthesis by electrostatic self-assembly approach and application in biomanipulations. *J. Phys. Chem. B* **110**(14), 7213–7220 (2006)
140. S.C. Youn, D.-H. Jung, Y.K. Ko, Y.W. Jin, J.M. Kim, H.-T. Jung, Vertical alignment of carbon nanotubes using the magneto-evaporation method. *J. Am. Chem. Soc.* **131**(2), 742–748 (2009)
141. M.A. Correa-Duarte, M. Grzelczak, V. Salgueiriño Maceira, M. Giersig, L.M. Liz-Marzán, M. Farle, K. Sieradzki, R. Diaz, Alignment of carbon nanotubes under low magnetic fields through attachment of magnetic nanoparticles. *J. Phys. Chem. B* **109**(41), 19060–19063 (2005)
142. J.S. Shim, Y.-H. Yun, W. Cho, V. Shanov, M.J. Schulz, C.H. Ahn, Self-aligned nanogaps on multilayer electrodes for fluidic and magnetic assembly of carbon nanotubes. *Langmuir* **26**(14), 11642–11647 (2010)
143. M.F. Lin, K.W.K. Shung, Magnetization of graphene tubules. *Phys. Rev. B* **52**(11), 8423–8438 (1995)
144. D.A. Walters, M.J. Casavant, X.C. Qin, C.B. Huffman, P.J. Boul, L.M. Ericson, E.H. Haroz, M.J. O’Connell, K. Smith, D.T. Colbert, R.E. Smalley, In-plane-aligned membranes of carbon nanotubes. *Chem. Phys. Lett.* **338**(1), 14–20 (2001)
145. X.L. Xie, Y.W. Mai, X.P. Zhou, Dispersion and alignment of carbon nanotubes in polymer matrix: a review. *Mat. Sci. Eng. R Rep.* **49**(4), 89–112 (2005)
146. T.J. Park, J.P. Park, S.J. Lee, D.-H. Jung, Y.K. Ko, H.-T. Jung, S.Y. Lee, Alignment of SWNTs by protein-ligand interaction of functionalized magnetic particles under low magnetic fields. *J. Nanosci. Nanotechnol.* **11**(5), 4540–4545 (2011)
147. J.E. Fischer, W. Zhou, J. Vavro, M.C. Llaguno, C. Guthy, R. Haggenueller, M.J. Casavant, D.E. Walters, R.E. Smalley, Magnetically aligned single wall carbon nanotube films: preferred orientation and anisotropic transport properties. *J. Appl. Phys.* **93**(4), 2157–2163 (2003)
148. B.W. Smith, Z. Benes, D.E. Luzzi, J.E. Fischer, D.A. Walters, M.J. Casavant, J. Schmidt, R.E. Smalley, Structural anisotropy of magnetically aligned single wall carbon nanotube films. *Appl. Phys. Lett.* **77**(5), 663–665 (2000)
149. J. Hone, M.C. Llaguno, N.M. Nemes, A.T. Johnson, J.E. Fischer, D.A. Walters, M.J. Casavant, J. Schmidt, R.E. Smalley, Electrical and thermal transport properties of magnetically aligned single wall carbon nanotube films. *Appl. Phys. Lett.* **77**(5), 666–668 (2000)
150. W.Z. Li, J.G. Wen, M. Sennett, Z.F. Ren, Clean double-walled carbon nanotubes synthesized by CVD. *Chem. Phys. Lett.* **368**(3–4), 299–306 (2003)
151. P.M. Ajayan, O. Stephan, C. Colliex, D. Trauth, Aligned carbon nanotube arrays formed by cutting a polymer resin-nanotube composite. *Science* **265**(5176), 1212–1214 (1994)
152. L. Lu, W. Chen, Large-scale aligned carbon nanotubes from their purified, highly concentrated suspension. *ACS Nano* **4**(2), 1042–1048 (2010)
153. L. Jin, C. Bower, O. Zhou, Alignment of carbon nanotubes in a polymer matrix by mechanical stretching. *Appl. Phys. Lett.* **73**(9), 1197–1199 (1998)
154. M. Ichida, S. Mizuno, H. Kataura, Y. Achiba, A. Nakamura, Anisotropic optical properties of mechanically aligned single-walled carbon nanotubes in polymer. *Appl. Phys. A Mater.* **78**(8), 1117–1120 (2004)
155. Y. Kim, N. Minami, S. Kazaoui, Highly polarized absorption and photoluminescence of stretch-aligned single-wall carbon nanotubes dispersed in gelatin films. *Appl. Phys. Lett.* **86**(7), 073103 (2005)
156. X. Yuan, A.F.T. Mak, K.W. Kwok, B.K.O. Yung, K. Yao, Characterization of poly(L-lactic acid) fibers produced by melt spinning. *J. Appl. Polym. Sci.* **81**(1), 251–260 (2001)

157. B. Vigolo, A. Pénicaud, C. Coulon, C. Sauder, R. Pailler, C. Journet, P. Bernier, P. Poulin, Macroscopic fibers and ribbons of oriented carbon nanotubes. *Science* **290**(5495), 1331–1334 (2000)
158. H.W. Zhu, C.L. Xu, D.H. Wu, B.Q. Wei, R. Vajtai, P.M. Ajayan, Direct synthesis of long single-walled carbon nanotube strands. *Science* **296**(5569), 884–886 (2002)
159. P. Poulin, B. Vigolo, P. Launois, Films and fibers of oriented single wall nanotubes. *Carbon* **40**(10), 1741–1749 (2002)
160. F. Ko, Y. Gogotsi, A. Ali, N. Naguib, H. Ye, G. Yang, C. Li, P. Willis, Electrospinning of continuous carbon nanotube-filled nanofiber yarns. *Adv. Mater.* **15**(14), 1161–1165 (2003)
161. Y.-L. Li, I.A. Kinloch, A.H. Windle, Direct spinning of carbon nanotube fibers from chemical vapor deposition synthesis. *Science* **304**(5668), 276–278 (2004)
162. M. Zhang, S. Fang, A.A. Zakhidov, S.B. Lee, A.E. Aliev, C.D. Williams, K.R. Atkinson, R.H. Baughman, Strong, transparent, multifunctional, carbon nanotube sheets. *Science* **309**(5738), 1215–1219 (2005)
163. X. Zhang, Q. Li, T.G. Holesinger, P.N. Arendt, J. Huang, P.D. Kirven, T.G. Clapp, R.F. DePaula, X. Liao, Y. Zhao, L. Zheng, D. Peterson, Y. Zhu, Ultrastrong, stiff, and lightweight carbon-nanotube fibers. *Adv. Mater.* **19**(23), 4198–4201 (2007)
164. M.B. Bazbouz, G.K. Stylios, Novel mechanism for spinning continuous twisted composite nanofiber yarns. *Eur. Polym. J.* **44**(1), 1–12 (2008)
165. N. Behabtu, M.J. Green, M. Pasquali, Carbon nanotube-based neat fibers. *Nano Today* **3**(5–6), 24–34 (2008) and references therein
166. K. Koziol, J. Vilatela, A. Moissala, M. Motta, P. Cunniff, M. Sennett, A. Windle, High-performance carbon nanotube fiber. *Science* **318**(5858), 1892–1895 (2007)
167. L.M. Ericson, H. Fan, H. Peng, V.A. Davis, W. Zhou, J. Sulpizio, Y. Wang, R. Booker, J. Vavro, C. Guthy, A.N.G. Parra-Vasquez, M.J. Kim, S. Ramesh, R.K. Saini, C. Kittrell, G. Lavin, H. Schmidt, W.W. Adams, W.E. Billups, M. Pasquali, W.-F. Hwang, R.H. Hauge, J.E. Fischer, R.E. Smalley, Macroscopic, neat, single-walled carbon nanotube fibers. *Science* **305**(5689), 1447–1450 (2004)
168. M. Zhang, K.R. Atkinson, R.H. Baughman, Multifunctional carbon nanotube yarns by downsizing an ancient technology. *Science* **306**(5700), 1358–1361 (2004)
169. K. Jiang, Q. Li, S. Fan, Nanotechnology: spinning continuous carbon nanotube yarns. *Nature* **419**(6909), 801–801 (2002)
170. K. Liu, Y. Sun, X. Lin, R. Zhou, J. Wang, S. Fan, K. Jiang, Scratch-resistant, highly conductive, and high-strength carbon nanotube-based composite yarns. *ACS Nano* **4**(10), 5827–5834 (2010)
171. K. Liu, Y. Sun, R. Zhou, H. Zhu, J. Wang, L. Liu, S. Fan, K. Jiang, Carbon nanotube yarns with high tensile strength made by a twisting and shrinking method. *Nanotechnology* **21**(4), 045708 (2010)
172. M.D. Lima, S. Fang, X. Lepró, C. Lewis, R. Ovalle-Robles, J. Carretero-González, E. Castillo-Martínez, M.E. Kozlov, J. Oh, N. Rawat, C.S. Haines, M.H. Haque, V. Aare, S. Stoughton, A.A. Zakhidov, R.H. Baughman, Biscrolling nanotube sheets and functional guests into yarns. *Science* **331**(6013), 51–55 (2011)
173. W. Li, C. Jayasinghe, V. Shanov, M. Schulz, Spinning carbon nanotube nanothread under a scanning electron microscope. *Materials* **4**(9), 1519–1527 (2011)
174. W. Liu, X. Zhang, G. Xu, P.D. Bradford, X. Wang, H. Zhao, Y. Zhang, Q. Jia, F.-G. Yuan, Q. Li, Y. Qiu, Y. Zhu, Producing superior composites by winding carbon nanotubes onto a mandrel under a poly(vinyl alcohol) spray. *Carbon* **49**(14), 4786–4791 (2011)
175. K. Jiang, J. Wang, Q. Li, L. Liu, C. Liu, S. Fan, Superaligned carbon nanotube arrays, films, and yarns: a road to applications. *Adv. Mater.* **23**(9), 1154–1161 (2011)
176. L. Hu, D.S. Hecht, G. Grüner, Carbon nanotube thin films: fabrication, properties, and applications. *Chem. Rev.* **110**, 5790–5844 (2010)
177. W.A. de Heer, W.S. Bacsá, A. Châtelain, T. Gerfin, R. Humphrey-Baker, L. Forro, D. Ugarte, Aligned carbon nanotube films: production and optical and electronic properties. *Science* **268**(5212), 845–847 (1995)

178. Y.H. Yan, S. Li, L.Q. Chen, M.B. Chan-Park, Q. Zhang, Large-scale submicron horizontally aligned single-walled carbon nanotube surface arrays on various substrates produced by a fluidic assembly method. *Nanotechnology* **17**(22), 5696 (2006)
179. Y. Huang, X. Duan, Q. Wei, C.M. Lieber, Directed assembly of one-dimensional nanostructures into functional networks. *Science* **291**(5504), 630–633 (2001)
180. S.J. Oh, Y. Cheng, J. Zhang, H. Shimoda, O. Zhou, Room-temperature fabrication of high-resolution carbon nanotube field-emission cathodes by self-assembly. *Appl. Phys. Lett.* **82**(15), 2521–2523 (2003)
181. S.G. Rao, L. Huang, W. Setyawan, S. Hong, Nanotube electronics: large-scale assembly of carbon nanotubes. *Nature* **425**(6953), 36–37 (2003)
182. K.M. Seemann, J. Ebbecke, A. Wixforth, Alignment of carbon nanotubes on pre-structured silicon by surface acoustic waves. *Nanotechnology* **17**(17), 4529 (2006)
183. Y. Wang, D. Maspoch, S. Zou, G.C. Schatz, R.E. Smalley, C.A. Mirkin, Controlling the shape, orientation, and linkage of carbon nanotube features with nano affinity templates. *Proc. Natl. Acad. Sci. U.S.A.* **103**(7), 2026–2031 (2006)
184. P. Diaio, Z. Liu, Vertically aligned single-walled carbon nanotubes by chemical assembly—methodology, properties, and applications. *Adv. Mater.* **22**, 1430–1449 (2010)
185. J. Qu, Z. Zhao, X. Wang, J. Qiu, Tailoring of three-dimensional carbon nanotube architectures by coupling capillarity-induced assembly with multiple CVD growth. *J. Mater. Chem.* **21**(16), 5967–5971 (2011)
186. L. Dai, A. Patil, X. Gong, Z. Guo, L. Liu, Y. Liu, D. Zhu, Aligned nanotubes. *Chem. Phys. Chem.* **4**, 1150–1169 (2003)
187. Y.H. Yan, M.B. Chan-Park, Q. Zhang, Advances in carbon-nanotube assembly. *Small* **3**(1), 24–42 (2007)
188. L. Huang, Z. Jia, S. O'Brien, Orientated assembly of single-walled carbon nanotubes and applications. *J. Mater. Chem.* **17**, 3863–3874 (2007)
189. H. Chen, A. Roy, J.-B. Baek, L. Zhu, J. Qu, L. Dai, Controlled growth and modification of vertically-aligned carbon nanotubes for multifunctional applications. *Mat. Sci. Eng. R Rep.* **70**(3–6), 63–91 (2010)
190. C.-M. Seah, S.-P. Chai, A.R. Mohamed, Synthesis of aligned carbon nanotubes. *Carbon* **49**(14), 4613–4635 (2011)
191. S. Neupane, W. Li, Carbon nanotube arrays: synthesis, properties and applications. in *Three-Dimensional Nanoarchitectures: Designing Next-Generation Device*, ed. by W. Zhou, Z.L. Wang (Springer, London, 2011)

Chapter 7

Measurement Techniques of Aligned Carbon Nanotubes

In the previous chapters, structure and growth of carbon nanotubes, especially the aligned carbon nanotubes have been discussed. Some characterization methods of carbon nanotubes are also covered in these chapters. For example, electron microscopy, especially transmission electron microscopy (TEM), plays an important role in the discovery and development on CNTs. The hollow properties of CNTs and crystallographic structures have been successfully analyzed by TEM. Tomographic morphology of the CNTs have been characterized by scanning electron microscopy (SEM), scanning tunneling microscopy (STM), and atomic force microscopy (AFM). Among these microscopy techniques, SEM is the most popular method to characterize the CNT arrays. TEM is the powerful method to analyze CNTs with high resolution while STM and AFM are the important tools to study the surface structure of CNTs at atomic scale. Interested readers on characterization method of individual CNTs are referred to the review literatures [1] and the references therein.

These characterization methods are very powerful to determine the physical properties of individual CNTs. However, these methods have some limits to fully characterize the morphological and structural properties of aligned CNTs. In this chapter, we introduce the electron microscopy and other techniques, such as small-angle scattering and X-ray diffraction (XRD), to characterize the unique properties of aligned CNTs, such as degree of alignment. Qualitative or quantitative information of the alignment can be obtained from these techniques.

7.1 Scanning Electron Microscopy

The basic concept of the scanning electron microscopes was proposed by M. Knoll in 1935 [2] and various experimental SEMs were constructed in the late 1930s and early 1940s. For example, M. von Ardenne constructed a scanning transmission electron microscope (STEM) by adding scan coils to a transmission electron microscope in 1938 [3, 4]. The first SEM used to examine the surface of a solid specimen was

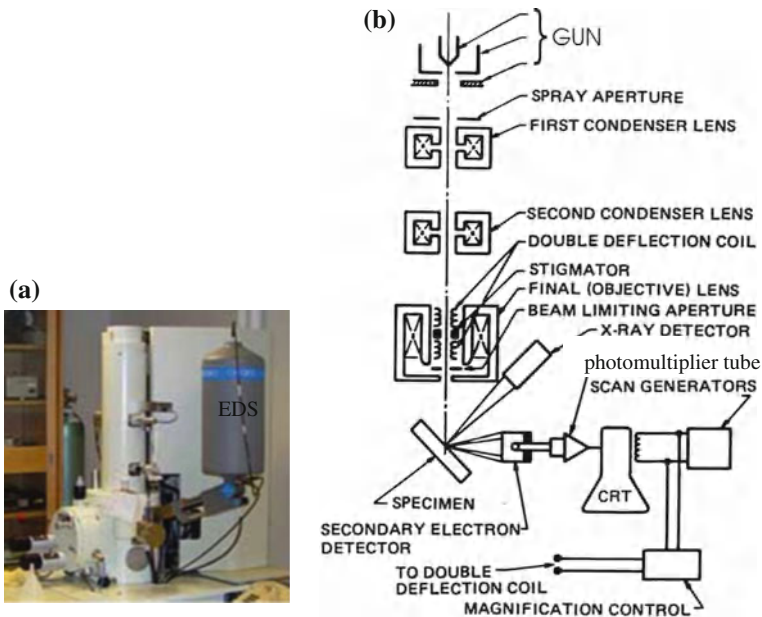


Fig. 7.1 a SEM equipped with an energy dispersive X-ray spectrometer in Boston College. b The electron and X-ray optics of SEM equipped with an energy dispersive X-ray spectrometer. From Goldstein et al. [7]

described by Zworykin in 1942 [5]. The resolution of SEM was achieved at 50 nm in 1952 [6] and even 1 nm at present. Up to now, SEM has been widely employed to detect the surface of various materials.

An SEM is a type of electron microscope to image a specimen by a high-energy beam of electrons in a raster scan mode. The high-energy electrons interact with the specimen atoms to produce signals that contain information about the specimen's surface topography, composition, and electrical conductivity etc. The types of signals produced by an SEM include secondary electrons, back-scattered electrons, characteristic X-rays, cathodoluminescence, specimen current, etc. Secondary electron imaging (SEI) is the most common detection mode in SEM and widely employed to observe the morphology of CNTs. We mainly focus on the SEI in this chapter. The interesting readers on other type of imaging and related principles are referred to some textbooks [7–12] and references therein.

The basic principle of the SEI is illustrated schematically in Fig. 7.1. A very fine beam of high-energy electrons (20–40 keV) is focused on the specimen surface and scanned across the specimen in a raster. When the high-energy electrons of the beam bombard onto the specimen, some incident electrons will strike the electrons in the k -orbits of the specimen atoms (inelastic scattering) to release free electrons with very low energy (<50 eV), secondary electrons, while some are elastically scattered by the specimen atoms. When the high-energy electrons travel deeper into the specimen

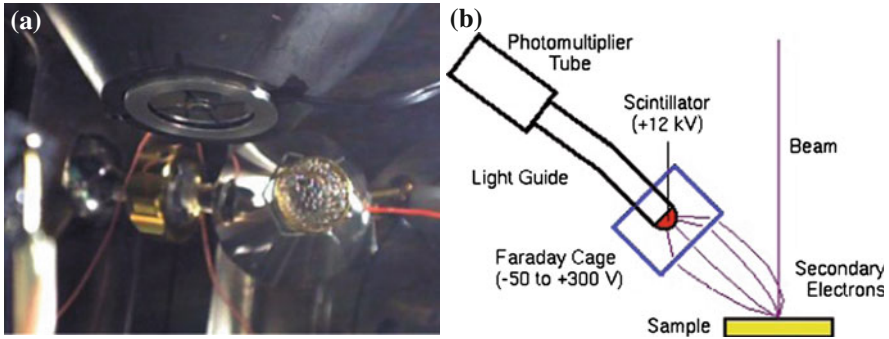


Fig. 7.2 Everhart–Thornley detector. **a** Optical image of E–T detector inside an SEM chamber in MSU. **b** Principle of E–T detector. From Everhart and Thornley [13]

undergoing multiple inelastic collisions, more secondary electrons will be released until the high-energy electrons devoid of energy. These released secondary electrons can only travel a few or tens nanometers from the specimen surface [7]. So SEI can give the tomographic information (several nanometers) of samples.

The secondary electrons can be collected to show the tomographic information of the specimen. The most frequently used detector of secondary electrons are the Everhart–Thornley (E–T) detector [13] with light-guide and highly efficient photomultiplier (Fig. 7.2). A typical E–T detector consists primarily of a scintillator inside a Faraday cage inside the specimen chamber of the electron scanning microscope. A low positive voltage (about 400 V) is applied to the Faraday cage to collect most of the relatively low energy secondary electrons emitted from the specimen surface. Other electrons within the SEM specimen chamber are not attracted by this low positive voltage. The scintillator is typically coated a conducting thin film and positively biased to a high positive voltage (up to 12,000 V) to accelerate the attracted secondary electrons through the Faraday cage to emit flashes of light, which are coupled to a light-guide conducted to a photomultiplier tube outside the SEM column for amplification.

The amplified electrical signal output by the photomultiplier is viewed and photographed on an analog video display, or subjected to analog-to-digital conversion and displayed and saved as a digital image.

When the electron beam raster scan the specimen surface, a 2D brightness distribution (electrical signal distribution) is produced in synchronism with the electron beam. There is thus a direct positional correspondence between the electron beam scanning across the specimen and the screen image.

The deflection coil controls the magnification of SEI. The magnification produced by an SEM is the ratio between the dimensions of the final image display and the field scanned on the specimen. In practice, the magnification switch varies the current of the double deflection coil to change the angle through which the electron beam is deflected (see Fig. 7.1b). The magnification ranges from 20 to 30,000 \times or higher

with spatial resolution of nanometers. The SEI can produce very high-resolution images of a specimen surface, revealing details down to 1 nm in size. The image resolution of SEI less than 0.5 nm is also possible. The observed areas range from several square centimeters to square microns or nanometers.

At the same time, SEI has a large depth of field on the order of millimeters due to the very narrow electron beam. SEI is a no-destroyed method. The observation method is direct and simple. Due to these advantages, SEI has been widely used to study the structures of aligned CNTs, including CNT length, diameters, and CNT site spacings.

Usually the SEM operates at 20 kV for better resolution depending on the electrical conductivity of CNT and substrates. 5 kV or lower is also used to avoid the electric discharging during observation.

SEI provides a direct examination of the CNT alignment and has been widely employed to determine the aligned CNTs, as shown in Fig. 2.5, Fig. 2.26, Fig. 6.21, and Fig. 6.24. Qualitative measurements on the CNT length, diameter, CNT site spacings have been successfully carried out on the aligned CNTs. However, the qualitative measurement of CNT alignment degree from SEI images are time-consuming.

7.2 Bragg Diffraction

In classical physics, the diffraction phenomenon is described as the bending of waves around small obstacles and the spreading out of waves through small openings. Diffraction from a 3D periodic structure, such as atoms arranged in a crystal, is called Bragg diffraction. Bragg diffraction is a consequence of interference between waves reflecting from different crystal planes. The condition of constructive interference can be expressed by Bragg's law:

$$2d \sin \theta = n\lambda \quad (7.1)$$

where λ is the wavelength, d is the distance between crystal planes, θ is the angle of the diffracted wave, and n is an integer known as the order of the diffracted beam. Bragg diffraction may be carried out using X-rays, neutrons, electrons, and light. The produced patterns contain the information of the periodic structures.

7.2.1 X-Ray Diffraction

The physical basics of X-ray diffraction (XRD) were formulated by Max von Laue, William H. Bragg and William L. Bragg at the beginning of the twentieth century, based on the X-ray findings of W. Conrad Röntgen. Characteristic X-rays are emitted when the high-energy electrons knock off an inner-shell electron from the specimen, causing an out-shell electron to fill the inner shell to release energy. When such an

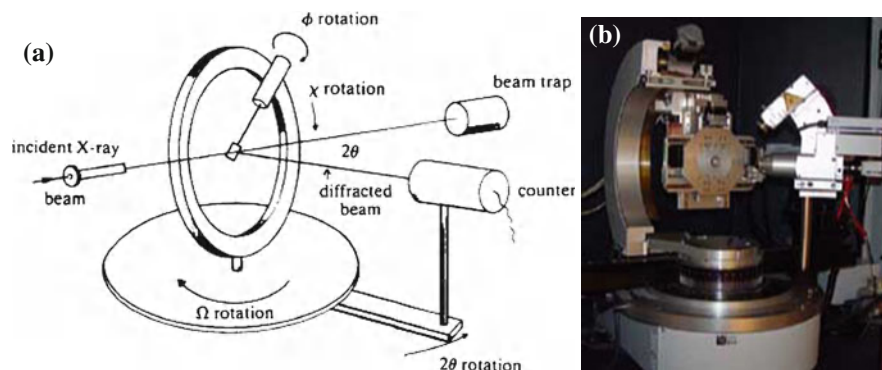


Fig. 7.3 Four-circle X-ray diffractometer. **a** Schematics of four-circle diffractometer with Bragg-Brentano geometry. From Cullity [14]. **b** An advanced diffractometer equipped with a 2D detector in Boston College

X-ray beam incidents on a crystalline samples, X-ray is diffracted by the crystallographic planes of the sample, as described by Braggs law expressed in Eq. (7.1). The XRD has been widely used to detect the crystallographic structures of the new compounds as well as to identificate the unknown compounds, study crystallinity, measure lattice parameters, size and strain, etc [14–16].

An X-ray diffractometer basically consists of an X-ray source (an X-ray tube or a synchrotron radiation source), a sample stage, and a detector. The X-ray is focused on the sample at an incident angle θ , while the detector received the X-ray intensity at 2θ away from the incident X-ray path, as shown in Fig. 7.3a. An X-ray diffractometer can be equipped with a point detector, a linear detector, or a 2D area detector depending on the experimental requirements. Figure 7.3b shows an advanced four-circle diffractometer with a 2D detector.

X-rays interact primarily with the electron cloud surrounding each atom. The contribution to the diffracted X-ray intensity is therefore larger for atoms with a large atomic number (Z) than that for atoms with a small Z . Carbon atoms have a small Z and intensity of X-ray is weak. At the same time, the diameter of CNTs is very small (in nanometers), inducing the broadening X-ray peaks. Based on these facts, X-ray powder diffraction is not a powerful tool to study the crystallographic structures of CNTs. However, the powder XRD is still a powerful tool to determine the orientation and alignment degree of aligned CNTs. Below we introduce how to employ XRD to characterize the alignment of CNTs.

7.2.1.1 X-ray Diffraction Patterns Recorded by 2D Detectors

Figure 7.4 shows typical 2D XRD patterns of MWCNT/polymer composites recorded by a 2D detector. When the CNTs are random, the diffraction rings are uniform (Fig. 7.4a). The diffraction intensity is essentially a constant over the whole azimuth

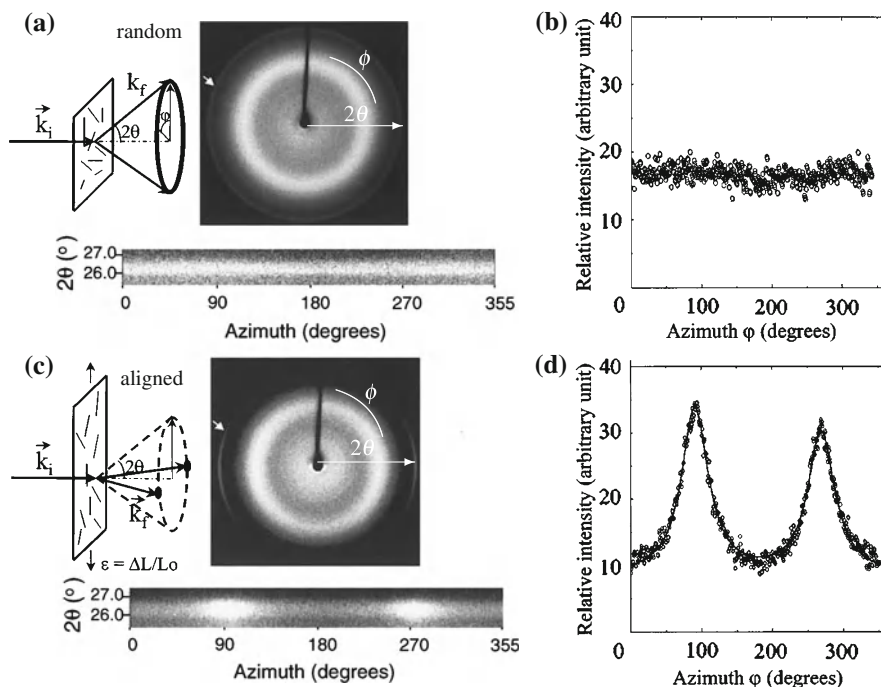


Fig. 7.4 2D X-ray diffraction patterns of MWCNT/polymer composites. (a, b) Random CNTs suspended in polymer. (c, d) Aligned CNTs suspended in polymer. The CNTs are aligned by a stretching method. *Left column*: the rectangular panels showing the intensity versus 2θ and azimuth ϕ plots. The white arrows in (a, c) mark the (002) Bragg peak of the CNTs. *Insets*: Schematics of the X-ray diffraction geometry. \mathbf{K}_i : the incident X-ray beam; \mathbf{K}_f : the scattered X-ray beam. The *right column*: integrated X-ray intensity (integrated along the 2θ axis) versus the azimuth. From Jin et al. [17]

ϕ range (Fig. 7.4b), indicating random orientation of the nanotubes. After the CNTs are aligned, the (002) Bragg intensity is concentrated at two spots centered at $\phi = 90^\circ$ and $\phi = 270^\circ$ (Fig. 7.4c). The non-uniform (002) intensity in the diffraction pattern indicates that the carbon nanotubes in the polymer are aligned.

In order to estimate the fraction of the aligned nanotubes that are aligned and the degree of alignment, the XRD intensity in Fig. 7.4c is integrated along the 2θ axis and plotted as intensity I versus azimuth ϕ (see Fig. 7.4d) after subtracting out the background intensity shown in Fig. 7.4b for the CNT composites without alignment [17]. The spectrum shown in Fig. 7.4d can be fitted using two Lorentzian functions with the same width and a constant background. The two peaks are centered at 90.9° and 270.1° , respectively, and are 179.2° apart. The fitted full width at half maximum of the two Lorentzian functions is 46.4° , which means that the aligned nanotubes have a mosaic angle of 23.2° around the stretching axis.

The amount of aligned nanotubes is proportional to the total integrated intensity of the two Lorentzian peaks shown Fig. 7.4d. Compared with the constant intensity

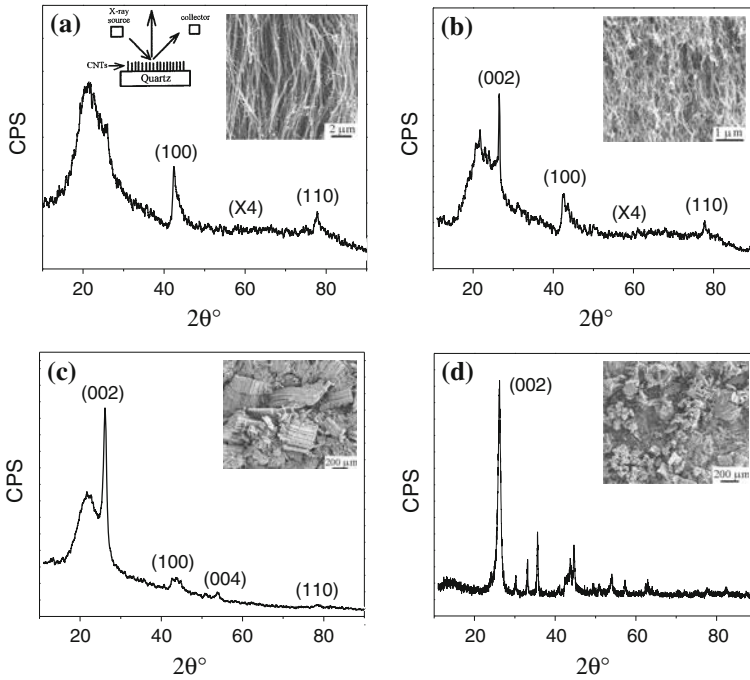


Fig. 7.5 XRD patterns of CNT arrays with different alignment degree. **a** As-grown straight CNT arrays with well-alignment. **b** As-grown curled CNTs with less alignment. **c** Disordered CNT arrays. The well-aligned straight CNT arrays are peeled off the substrate and ball-milled slightly. **d** Disordered CNT arrays. The well-aligned straight CNT arrays are peeled off the substrate and ball-milled heavily. The broaden peak at 20° comes from the substrate. The intensities in **(a)** and **(b)** are enlarged four times. Insets are SEM images of measured CNTs with different alignment degree. From Cao et al. [18]

of randomly dispersed nanotubes shown in Fig. 7.4b, the data in Fig. 7.4d imply that 58% of the nanotubes in the MWCNT/polymer composite are partially aligned along the stress direction [17].

7.2.1.2 X-ray Diffraction Patterns Recorded by Linear Detectors

The alignment degrees of CNT arrays can also be revealed by the XRD peak intensities I versus 2θ recorded by point detectors or linear detectors. Particularly, the intensity of the (002) peak decreases considerably with higher nanotube alignment [18] when the X-ray beam incidents along CNT growth direction.

Figure 7.5 shows the XRD patterns of CNT arrays with different alignment degrees [18]. Figure 7.5a, b show the XRD patterns directly measured on the as-grown CNT arrays on quartz substrates. For the well-aligned straight CNT arrays, no (002) peak of CNTs is observed (Fig. 7.5a) while a weak (100) peak at 42.4° and a (110) peak

at 77.7° are detected. With a less CNT alignment (Fig. 7.5b), the (002) peak emerges at 26° . Obviously the alignment affects the intensity of the (002) peak.

Once the aligned CNT arrays are peeled off the substrates and ball-milled, the alignment of CNTs becomes worse, as shown by the SEM images (insets in Fig. 7.5c, d). At the same time, a strong and sharp (002) peak appears (Fig. 7.5c, d). The intensity of the (002) peak increases monotonically with the decreasing alignment degree. So the alignment degree of CNT arrays can be determined from the (002) diffraction intensity.

Nanotube alignment of carbon nanotube fibers was also studied by X-ray micro-diffraction using synchrotron radiation [19], opening a way for micrometer scale analyses of nanotube-based materials.

7.2.2 Neutron Diffraction

The neutron diffraction is similar to XRD, following the same Bragg's law that describes XRD. A neutron diffraction measurement requires a neutron source (usually a nuclear reactor), a studied sample, and a detector. Free neutrons coming from the neutron source exhibit wave phenomena. When a beam of neutrons is slowed down and selected properly by their speed, the neutrons with a wavelength near one Angström can be diffracted by atoms in a solid material,

Different from X-ray, neutrons interact directly with the nucleus of the atoms, not the electron clouds. So it is the case that light atoms with low Z also contribute strongly to the diffracted intensity even in the presence of large Z atoms. Therefore, neutron diffraction is a better tool of crystallography to investigate the light atoms, such as hydrogen, carbon, and oxygen, in the materials, giving very precise data for the atomic positions in the structure.

Very similar to XRD, the structural information of aligned CNTs can be obtained from neutron diffraction. All the techniques can be copied directly from XRD method. Here we do not talk about details of neutron diffraction because of its high similarity with XRD.

7.2.3 Electron Diffraction

Electron diffraction is similar to XRD and neutron diffraction. An electron can be regarded as a wave much like sound or water waves because of its wave-particle duality. The wavelength of an electron is given by the de Broglie equation,

$$\lambda = \frac{h}{p} \quad (7.2)$$

Here h is Planck's constant and p the relativistic momentum of the electron. λ is called the de Broglie wavelength.

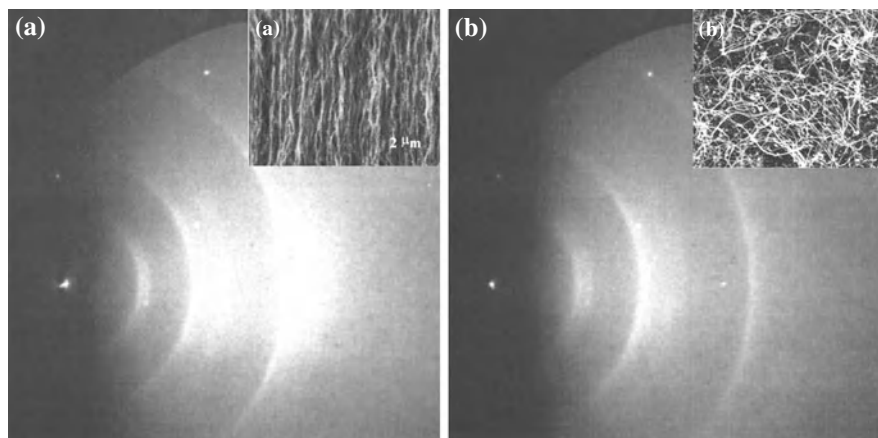


Fig. 7.6 Reflection high-energy electron diffraction images of the **a** vertically aligned and **b** randomly oriented multi-walled carbon nanotube samples. *Inset*: SEM images of examined aligned multi-walled carbon nanotubes. From Drotar et al. [20]

Below we introduce several electron diffraction techniques used to characterize the alignment of CNTs.

7.2.3.1 Reflection High-Energy Electron Diffraction

Reflection high-energy electron diffraction (RHEED) is a technique to characterize the surface of crystalline materials. RHEED gathers the information only from the surface layer of the sample, which distinguishes RHEED from other materials characterization methods that also rely on diffraction.

A RHEED system requires an electron source (gun), photoluminescent detector screen, and a sample with a clean surface. The electron gun generates a beam of electrons which strike the sample at a very small angle relative to the sample surface. Incident electrons diffract from atoms at the surface of the sample, and a small fraction of the diffracted electrons interfere constructively at specific angles and form regular patterns on the detector. For general surface characterization, the electron gun is operated at the range of 10–30 keV.

Figure 7.6 shows RHEED patterns for both the vertically aligned and randomly oriented samples. The SEM images of the aligned and randomly oriented CNTs are shown as insets in Fig. 7.6a, b, respectively. The RHEED patterns, for both samples, consist of concentric rings whose radii are roughly consistent with powder diffraction from graphite [20]. From the RHEED patterns, the lattice parameters of CNTs can be calculated.

In principle, the RHEED patterns can also contain information about the orientation of the nanotubes. However, the measured angular intensity profile along the (002) ring for both the vertically aligned and randomly oriented samples cannot give

such information [20]. There is a long way to obtain the orientation information from RHEED.

7.2.3.2 Selected Area Electron Diffraction

Selected area electron diffraction (SAED) has also been used to investigate the structure of CNT bundles [21]. Information on the helicity and the lattice packing has been obtained from SAED patterns.

7.2.3.3 Other Electron Diffraction Techniques

Besides the RHEED and SAED techniques, the low-energy electron diffraction and converged beam electron diffraction have also been used to determine the crystallographic structures of CNTs. However, these techniques have not been used to determine the alignment of CNTs.

7.2.4 Light Diffraction

A aligned CNT array is a highly ordered CNTs that are periodic over a long range (from a few nanometers to microns). The ordered CNT arrays appear analogs to crystal counterparts and can be determined from the Bragg diffractions of light. Here we introduce the application of light diffraction on the degree of CNT alignment.

Figure 7.7a–b show a periodic array of aligned carbon nanotubes grown by the PECVD method. CNTs are grown from the honeycomb pattern of catalytic Ni dots (inset in Fig. 7.7a) into the periodic CNT array with a hexagonal structure. The distance between two CNTs (catalytic Ni dots) is $1\mu\text{m}$. When a visible light (wavelength of 390–750 nm) passes through the CNT arrays, the light diffraction occurs [22].

Figure 7.7c shows a diffraction pattern obtained from the nanotube array shown in Fig. 7.7a. The pattern is obtained by shining green (560 nm) and blue (454 nm) laser light perpendicular to the plane of the hexagonal lattice. The projection is made onto an almost flat screen, which allowed for an observation of a large portion of the projected reciprocal space but causes a distortion of the triangular symmetry of the pattern. Apart from this, the pattern is highly rotationally symmetric (except for the third-order blue diffraction spots), showing that the carbon nanotubes are circularly symmetric in the plane. Note that there is a rather small hexatic distortion of the pattern, indicating presence of a possible formation of misaligned crystalline macro regions. There is also a small diffusive scattering (nonzero Ursell function) resulting from the fact that the nanotubes are not perfectly straight (see Fig. 7.7b). For perfectly straight nanotubes the diffraction spots would be points, and the green background around the central spot would disappear. The amount of the spot broadening can be estimated using the Debye–Waller factor and assuming that bent nanotubes can be

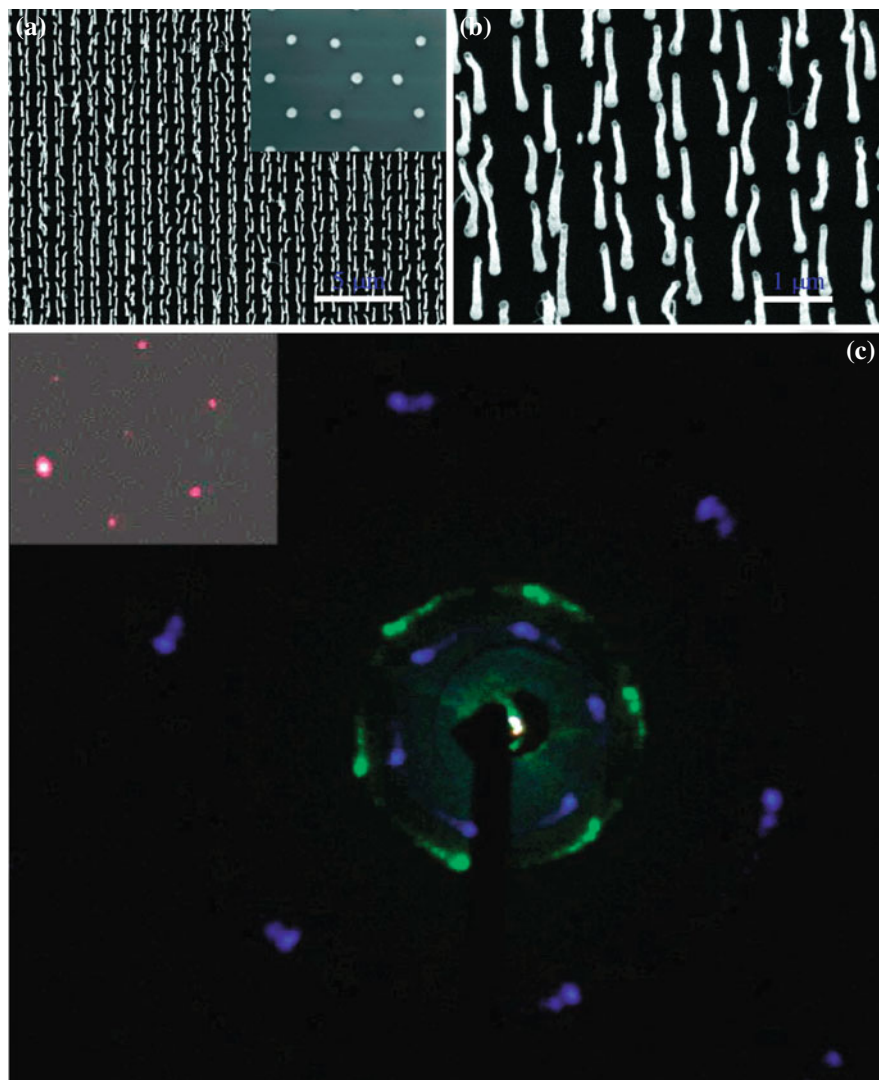


Fig. 7.7 SEM images of the highly ordered honeycomb array of aligned carbon nanotubes at low **a** and high **b** magnification, grown by PECVD. **c** Diffraction pattern of light at different frequencies by the nanotube arrays shown in **a**, **b**. Inset in **a**: SEM image of patterned Ni catalysts prepared by nanosphere lithography and electron beam evaporation. The distance between *two dots* are 1 μm. Inset in **c**: diffraction pattern of red light. From Kempa et al. [22]. Reprinted with permission from American Chemical Society

viewed as effectively displaced from the lattice sites. We estimate from Fig. 7.7a–b that the mean relative (to lattice constant) displacement of nanotubes is about 10%, and thus expect a similar degree of spot broadening relative to the spot distance, in agreement with Fig. 7.7c.

Figure 7.7c shows that in addition to highly symmetric first- and second-order spots of the blue light, there are visible four third-order spots, asymmetrically distributed on the lower right half of the diffractogram. These peaks result from the fact that the incoming light was not strictly normal to the plane, which shifts the Ewald sphere away from a reciprocal lattice point.

The visible light diffraction on honeycomb arrays of aligned carbon nanotubes can also be quantitatively measured by an optical spectrometer [23]. The information of the CNT alignment would be extracted from the diffraction spectra, as did from XRD patterns (see Sect. 7.2.1) and from neutron diffraction patterns (see Sect. 7.2.2).

Therefore, the alignment of CNT arrays can be characterized by light diffraction when the spacing of CNTs is closed to the wavelength of visible light.

Besides light diffraction, the quality of CNT arrays can also be roughly estimated from visible light reflection. The periodic arrays of aligned carbon nanotubes appear colorful [22, 23]. The CNT arrays with a high degree of ordering would reflect visible light uniformly, resulting in the uniform interference color. Any defects in the CNT arrays would cause the local change of the interference color.

7.3 Small-Angle Scattering

Small-angle scattering is a scattering technique with a small deflection angle ($0.1\text{--}10^\circ$), giving information about the size, shape, and orientation of surface structures. The deflected beams can be particles, such as neutron, or an electromagnetic or acoustic wave, such as X-ray. Small-angle scattering is a powerful while not a direct visualization technique to examine the orientation of the aligned CNTs.

7.3.1 *Small-Angle X-Ray Scattering*

Small-angle X-ray scattering (SAXS) is a small-angle scattering technique to elastically scatter X-rays by a sample which has inhomogeneities in the nanometer-range, and record the X-ray intensity at very low angles (typically $0.1\text{--}10^\circ$). SAXS has been used for the determination of the microscale or nanoscale structure, such as the shape, size, characteristic distances of partially ordered materials, pore sizes, and other information of nanoscaled materials. SAXS is capable of delivering structural information of materials between 5 and 25 nm, of repeat distances in partially ordered systems of up to 150 nm [24]. The method is accurate and non-destructive.

In a typical SAXS instrument, a monochromatic beam of X-rays incidents on a sample from which some X-rays are scattered. The scattered X-rays form a scattering

pattern which is then detected by a detector that is typically a 2D flat X-ray detector situated behind the sample perpendicular to the direction of the primary beam that initially incidents the sample. The scattering pattern contains the information of the structural information of the sample.

SAXS patterns are typically represented as scattered intensity I as a function of the magnitude of the scattering vector

$$q = 4 \pi \sin(\theta)\lambda \quad (7.3)$$

where 2θ is the angle between the incident X-ray beam and the detector measuring the scattered intensity, and λ is the wavelength of the X-rays.

The SAXS intensity can be expressed as

$$I(q) = P(q)S(q) \quad (7.4)$$

where $I(q)$ is the intensity as a function of the magnitude of the scattering vector \mathbf{q} , $P(q)$ is the form factor (scattering factor), a measure of the scattering amplitude of a wave by an isolated atom, and $S(q)$ is the structure factor, a mathematical description of how a material scatters incident radiation.

SAXS provides quantitative morphological insight into both nanoscopic properties such as average CNT diameters and ensemble properties such as CNT orientation. This arises from the mesoscopic size of the X-ray beam which is typically on the order of a few hundred microns. This dimension is simultaneously small in relation to the typical millimeter scale of the whole aligned CNT sample and large relative to the nanometer scale of individual CNTs. Thus the SAXS beam can probe a small region of the CNTs to yield data that reflect information about millions of CNTs.

The mesoscopic size scale of scattering techniques has been used successfully to demonstrate the average diameter and orientation of MWCNTs grown on substrates [25, 26], alignment of CNTs in CNT fibers with diameter of 10–100 μm [27], alignment of CNTs in CNT bundles [28], structure of semidilute SWCNT suspensions and gels [29], and dispersion of CNT in liquids [30].

Figure 7.8 illustrates one case of SAXS application to quantitatively characterize the morphology and alignment of vertically aligned MWCNT arrays. X-ray beam incidents on the carbon nanotubes perpendicular to the growth direction of the carbon nanotube. The beam diameter is 200 μm . The two dimensional SAXS patterns at varying distances from the substrate to the top are shown in Fig. 7.8a–e while SEM images illustrating the local morphologies are shown in Fig. 7.8f–j. From the 2D patterns, the orientation and diameter of CNTs can be calculated.

Degree of alignment. The SAXS patterns in Fig. 7.8a–e show anisotropic. The distinct higher cloud along y direction indicates vertical alignment of CNTs. Apparently with the improvement of the alignment, the anisotropy of the 2D SAXS patterns in Fig. 7.8a–e increases and the scattering along the y axis intensifies. In other words, the alignment degree of CNTs can be qualitatively described by the anisotropy of the 2D SAXS patterns.

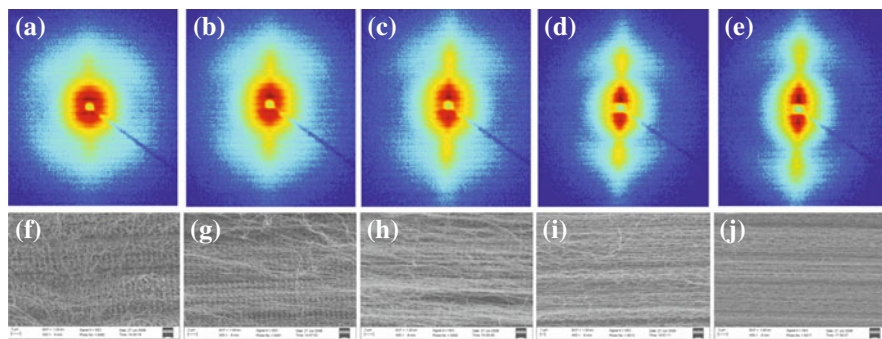


Fig. 7.8 a–e 2D SAXS scattering patterns of the aligned CNTs at 0.5, 2.0, 3.5, 5.0, and 6.0 mm from the substrate, f–j SEM images of CNT morphology at 0.5, 2.0, 3.5, 5.0, and 6.0 mm from the substrate. From Das et al. [26]

The alignment degree of the CNTs can be quantitatively fitted from the intensity of SAXS patterns. Figure 7.9a shows the azimuthal scan of the 2D SAXS patterns shown in Fig. 7.8a–e. The scattering intensity is azimuthally averaged to yield the scattering cross-section at $q = 0.001/\text{\AA}$ after subtraction of background. The presence of peaks at $\phi = 90^\circ$ and $\phi = 270^\circ$ corresponds to vertical alignment of the CNTs. The angular profiles are fitted with a two-peak model with a Lorentzian function and a Gaussian. The decrease in Lorentz width with increasing distance (Fig. 7.9b) indicates enhancement of alignment of the CNTs from the substrate.

The degree of alignment, f , is quantitatively estimated by examining Hermans orientation parameter, which can be defined for axially oriented systems as [31]

$$f = \frac{3\langle \cos^2 \phi \rangle - 1}{2}$$

$$\langle \cos^2 \phi \rangle = \frac{\int_0^{\pi/2} I(\phi) \cos^2 \phi \sin \phi d\phi}{\int_0^{\pi/2} I(\phi) \sin \phi d\phi} \quad (7.5)$$

The degree of alignment $f = -1/2, 0, 1$ correspond to perfect horizontal alignment, random orientation, and perfect vertical alignment, respectively. Based on Eq. (7.5) and data in Fig. 7.9a, the degree of alignment of CNTs can be calculated, shown in Fig. 7.9b. Figure 7.9b clearly indicates the degree of alignment (order parameter) f increases linearly with the distance h from substrate, in good correspondence with the SEM images shown in Fig. 7.8f–j.

Diameter of CNTs. In addition to quantifying the orientation of the aligned CNTs, the structural parameter such as the diameter and wall-thickness of CNTs can also be extracted from the SAXS patterns analysis.

First the average diameter of the CNTs can be roughly measured from the azimuthal integration along \mathbf{q} scattering vector. Figure 7.10a shows azimuthally integrated SAXS intensity as a function of scattering vector \mathbf{q} extracted from the 2D

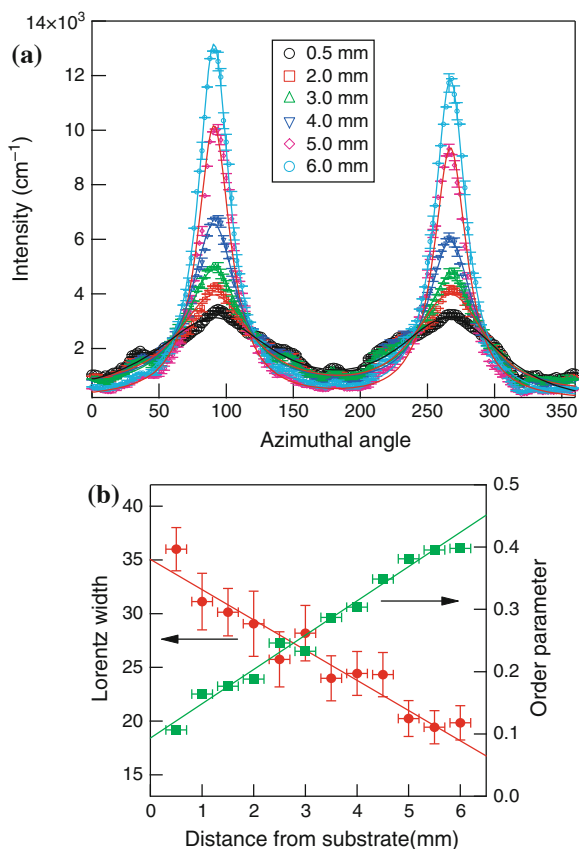


Fig. 7.9 **a** Azimuthal scans obtained from the 2D patterns at varying distances from the substrate at $q = 0.01/\text{\AA}$. Sharp peaks at $\phi = 90^\circ$ and 270° indicate preferential alignment of the carbon nanotubes. **b** Hermans orientation parameter (order parameter) and Lorentz width as a function of distance from the substrate. The decrease of Lorentz width and increase of the order parameter indicate the improvement of alignment of CNTs with increasing distance from the substrate. From Das et al. [26]

SAXS patterns (shown as Fig. 7.8a–e) over $\pm 10^\circ$ conical slices around $\phi = 90^\circ$ in the $x - y$ plane of detector at different distance of CNTs from the substrate. The peak lies near $q \sim 0.04/\text{\AA}$ indicates outer diameter of CNTs. The peak shifts to higher scattering angles with increased distance implies that the object responsible for the scattering decrease in size with distance from the substrate.

Furthermore the diameter can be accurately calculated from the profile fitting of the intensity shown in Fig. 7.10a. The SAXS intensities can be expressed as in Eq. (7.4). For a CNT with a core–shell cylinder structure, the form factor $P(q)$ can be expressed as a complex function of the radius and wall-thickness of CNTs [26].

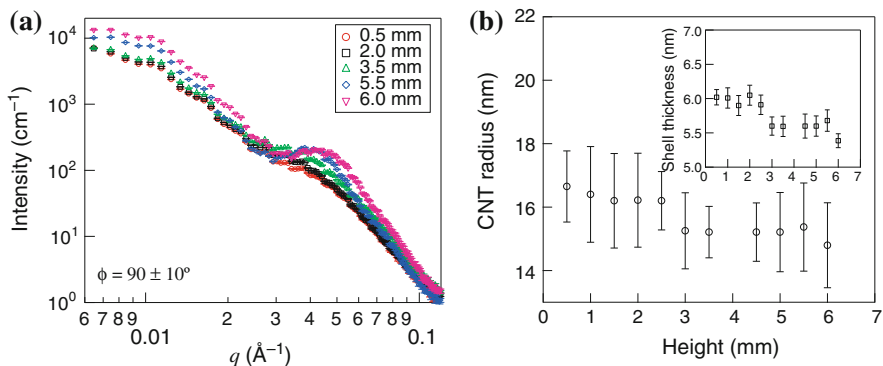


Fig. 7.10 **a** SAXS intensity as a function of scattering vector q by integrating over $\pm 10^\circ$ conical slices around $\phi = 90^\circ$ at different vertical distance of CNTs from the substrate. A peak lies near $q \sim 0.045/\text{\AA}$ that shifts to higher scattering angles with increasing distance. The broadening of the shoulder is due to the increased polydispersity of CNT diameters at longer distance from the substrate. **b** Average CNT radius and shell thickness (*inset*) at varying distance from the substrate as obtained by model fitting. From Das et al. [26]

After model fitting of the intensity, the average CNT radii and wall-thickness can be calculated from the SAXS intensity, as show in Fig. 7.10b.

More detailed work shows that the calculated CNT diameters from SAXS intensity fitting are slightly higher than that obtained from HRTEM investigations [32].

7.3.2 Small-Angle Neutron Scattering

Similar to SAXS, small-angle neutron scattering (SANS) is also a powerful tool to characterize the order and alignment of CNT arrays [33] besides to characterize the dispersion of CNTs in surfactant solutions [34, 35]. The alignment of CNTs is characterized by the Lorentzian width of SANS, similar to that of SAXS. The degree of the alignment can also be described by a nematic order parameter using Hermans orientation function ($f = 0$ for random orientation and $f = 1$ for perfect alignment), expressed by Eq. (7.5).

Figure 7.11a–f show the 2D scattering patterns for a vertically aligned CNTs shown in Fig. 7.11I. Local morphology of the aligned CNTs are shown in Fig. 7.11g–k. From left to right, the scattering intensity is anisotropic, enhanced along the y direction and suppressed along the x coordinate, indicating better vertical alignment of CNTs. The conclusion is in agreement with SEM images (Fig. 7.11g–k), indicating that the alignment is improving from left to right.

Similar to the SAXS technique, the azimuthal plot can also be obtained from the SANS 2D patterns, as shown in Fig. 7.11m at $q = 0.01 \text{ \AA}^{-1}$. The angular profiles are fitted with a two-peak model with a Lorentzian function for the narrow peak and a

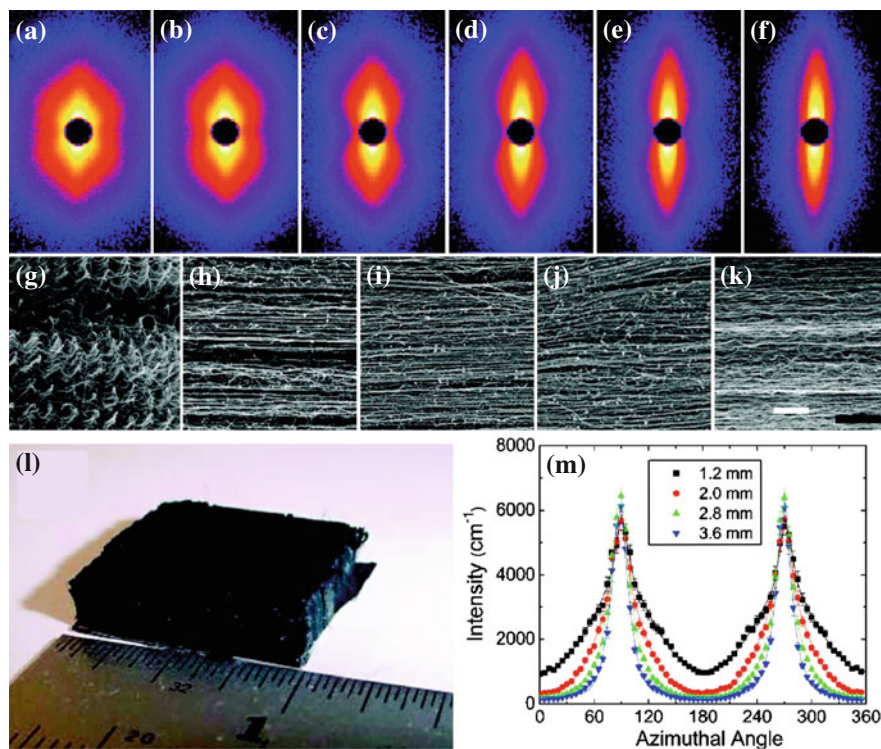


Fig. 7.11 a–f 2D SANS scattering patterns of the aligned CNTs at 0.4, 1.2, 2.0, 2.8, 3.6, and 4.4 mm from the substrate, respectively. g–k SEM images of CNT morphology near the substrate and at 1, 2, 3, and 4 mm from the substrate. l An optical image of the vertically aligned CNT sample. m Azimuthal plot of selected SANS patterns at $q = 0.01/\text{\AA}$. The solid lines through symbols are the best fit with superimposed Lorentz and Gauss functions. From Wang et al. [33]

Gaussian function for the broad peak. The fitting solid lines in Fig. 7.11m indicate that the Lorentzian width of the narrow peak remains constant at $17^\circ \pm 3^\circ$, whereas the Gaussian full width at half maximum decreases with the order of alignment [33]. The degree of the alignment could be calculated by a nematic order parameter using Hermans orientation function, as described in the SAXS technique.

7.4 Raman Spectroscopy

When photons are scattered from an atom or molecule, most photons are elastically scattered, Rayleigh scattering. The frequency and wavelength of the Rayleigh scattered photons are same as that of the incident photons. At the same time, a small fraction (approximately 1 in 10 million photons) of the scattered photons is inelasti-

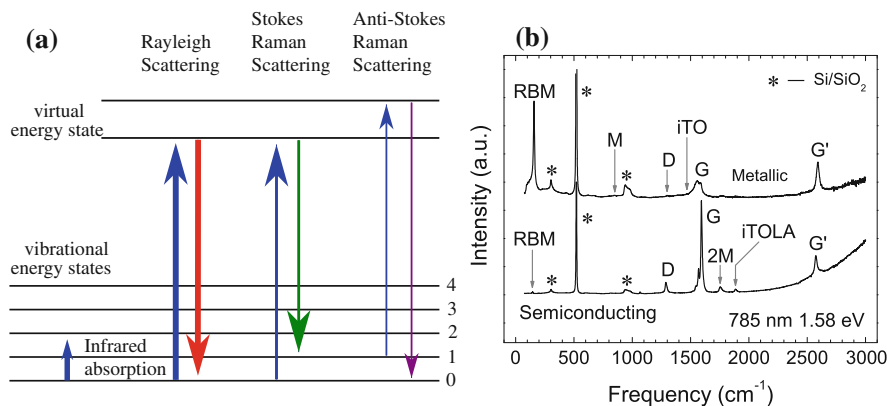


Fig. 7.12 Raman scattering. **a** A scheme of Raman excitation for a CNT. **b** Raman spectra from a metallic (*top*) and a semiconducting (*bottom*) SWCNT at the single nanotube level. The spectra show the RBM, D band, G band, and G' band features, in addition to weak double resonance features associated with the *M*-band and second-order modes (*i*TOLA). The isolated carbon nanotubes are sitting on an oxidized silicon substrate. From Saito et al. [40]

cally scattered by an excitation. The frequency of the inelastically scattered photons is different from the incident photons.

The inelastic scattering of light was predicted by Adolf Smekal [36] in 1923. Later the effect, named as Raman effect, was first observed in liquid [37, 38] by C. V. Raman and K. S. Krishnan, and in solid [39] independently by Grigory Landsberg and Leonid Mandelstam in 1928. Up to now, the Raman spectroscopy has been widely used in chemistry to identify the molecules, in solid state physics to characterize inorganic materials, etc.

There are two types of Raman scattering, Stokes scattering, and anti-Stokes scattering. The Raman effect occurs when a light beam impinges upon a molecule to excite the molecule from the ground state to a virtual energy state (Fig. 7.12a). When the molecule relaxes, a photon is emitted and the molecule returns to a different rotational or vibrational state. The difference in energy between the original state and the new state leads to a shift in the emitted photon's frequency away from the excitation wavelength. If the new state of the molecule is more energetic than the initial state, the emitted photon shifts to a lower frequency. This shift in frequency is designated as a Stokes shift. If the new state is less energetic than the initial state, the emitted photon shifts to a higher frequency. It is an Anti-Stokes scattering.

Figure 7.12b shows Raman spectra of CNTs. The spectra consisted of the radial breathing mode (RBM), tangential mode (G band), disorder-induced mode (D band), and other Raman features. Physical properties of CNTs can be characterized from these Raman features. The Raman scattering of CNTs are reviewed recently [40–45]. Here we focus on the G band of Raman scattering of aligned CNTs.

The electronic nature of aligned carbon nanotubes can be revealed by analyzing the two most intense peaks in the tangential vibration mode (G⁺ and G⁻ bands) of the

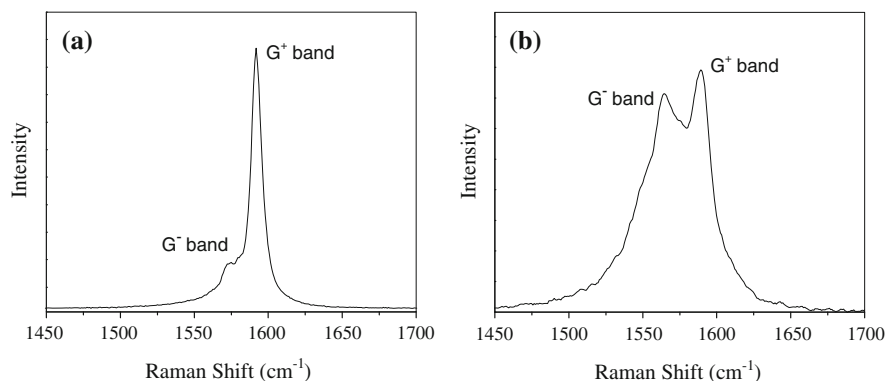
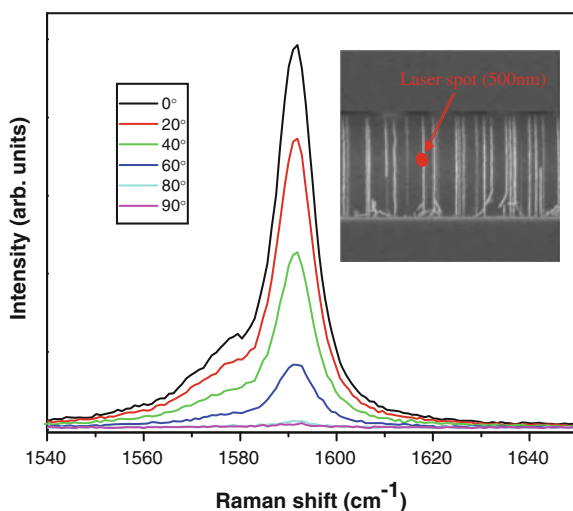


Fig. 7.13 Typical Raman spectrum of **a** semiconducting SWCNTs characterized as Lorentzian line-shape and **b** metallic SWCNTs characterized as Breit–Wigner–Fano line-shape. From Lei et al. [46]

Fig. 7.14 G band intensity as a function of the angle of polarization for individual nanotubes. *Inset*: SEM image of aligned nanotubes between source and drain electrodes, where the red dot stands for laser spot with $0.5\mu\text{m}$ in diameter. From Lei et al. [46]



nanotube arrays [46]. The G band of semiconducting carbon nanotubes (Fig. 7.13a) exhibits a typical Lorentzian line-shape while metallic nanotubes (Fig. 7.13b) shows a broadened Breit–Wigner–Fano line-shape due to the presence of free electrons in the conduction band. A metallic to semiconducting ratio of aligned CNTs can be determined from the ratio of G– band and G+ band of the nanotubes.

As a 1D system, the excitation of normal vibration modes along the axis of aligned carbon nanotubes exhibits a strong dependence on the linear polarization direction of the laser excitation source [46]. Figure 7.14 shows Raman spectra of the aligned carbon nanotubes grown by a CVD method, taken at six different angles of incidence of the laser polarization plane with respect to the nanotube principal axis. The Raman

intensity of the G band is a function of the angle of polarization. The Raman resonance is strongly suppressed when the light is polarized perpendicular to the carbon nanotube axis.

Therefore, from the Raman intensity, the degree of alignment of carbon nanotubes should be calculated. For random CNT bulks, the G band intensity is not dependent on the angle of the polarization. The G band intensity of well aligned CNT bulks depends on the angle of the polarization while the intensity should be higher than that of less aligned CNTs.

7.5 Transmission Electron Microscopy

Electron was discovered as a kind of particles by J. J. Thomson in 1897. Later de Broglie suggested the wave-particle duality in 1927. According to de Broglie's hypothesis, all particles, including electrons, can act as waves. The wavelength of electrons can be expressed in Eq. (7.2). After taking relativistic effects into account, the electron wavelength is

$$\lambda = \frac{h}{\sqrt{2m_0eU}} \frac{1}{\sqrt{1 + \frac{eU}{2m_0c^2}}} \quad (7.6)$$

where c is the speed of light, h is Planck's constant, U is the electric potential to accelerate the electrons, m_0 is the mass of the electron, and e is the elementary charge. The wavelength of the electrons is $12.3 \times 10^{-12} \text{m}$ (1.23\AA) in a 10 kV SEM while the wavelength is 0.25\AA in a 200 kV TEM. The de Broglie wavelength of electrons is many orders of magnitude smaller than that for light, theoretically allowing for imaging at atomic scales.

The first TEM was built by Max Knoll and Ernst Ruska in 1931 and the first commercial TEM was installed in 1939 by Siemens [47]. More recently, a resolution below 0.5\AA is achieved in an aberration corrector design [48].

Figure 7.15 shows an advanced TEM and optical components in a basic TEM. The details have been described in many text books [8, 49–52].

As we talked about in Chap. 2, TEM plays a very importance role on the discovery of CNTs. TEM firstly shows the direct proof of the hollow properties of CNTs, as shown in Figs. 2.1 and 2.2. Later TEM, especially high-resolution TEM (HRTEM) has been widely employed to study the structures of the CNTs, including the diameters, lengths, number of walls, etc.

Figure 7.16a shows the HTTEM image of the SWCNT bundles synthesized by the laser ablation method. The HRTEM image clearly shows that the carbon tubes are perfectly aligned in the bundle, with no twisting or bending of the bundle [21]. Figure 7.16b shows a cross-sectional view of the CNT bundle oriented with its axis parallel to the electron beam direction. This figure reveals the close-packed triangular arrangements of CNTs in the bundle. The triangular arrangement appears

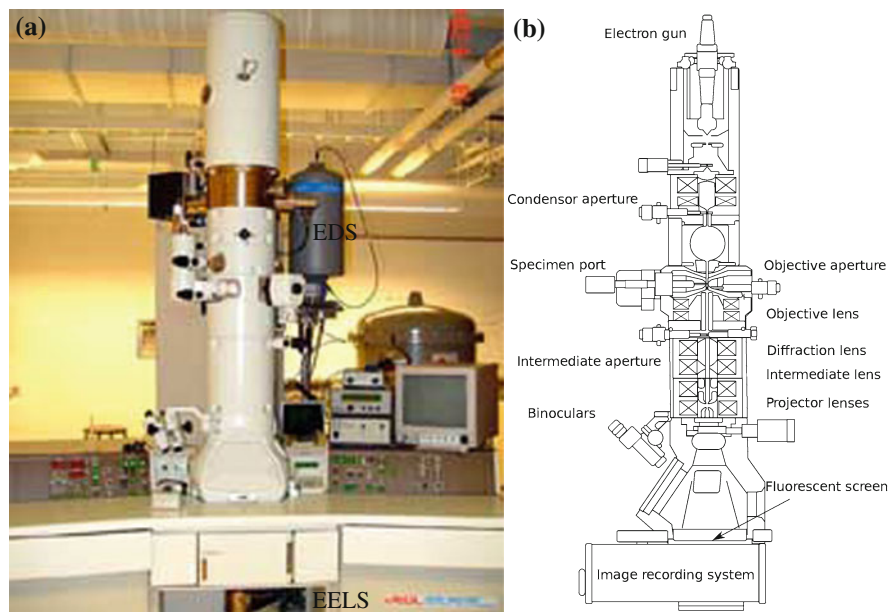
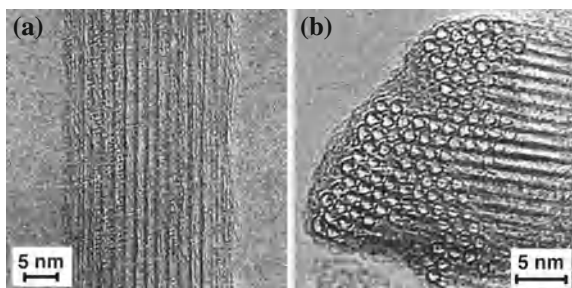


Fig. 7.15 **a** Advanced TEM equipped with EDS and EELS in Boston College. **b** Optical components in a basic TEM

Fig. 7.16 HRTEM images of SWCNT bundles synthesized by laser ablation. The CNT bundle axis is **a** parallel and **b** perpendicular to the image plane. From Colomer et al. [21]



to be perfect. Additionally the inter-tube distance can be directly measured from the HRTEM image.

Similar HRTEM images of CNT ropes are also shown in Fig. 2.3. Additionally, the aligned CNTs grown by the CVD method were also observed on TEM, as shown in Fig. 4.12. The alignment of CNTs can be directly observed from the TEM images [53].

Therefore TEM, especially HRTEM, is also a powerful tool to directly observe the alignment of CNTs. The measurement resolution is down to nanometers.

However, TEM is a destructive technique. When we scratch the CNTs off from the substrates for TEM specimens, the alignment structure of CNTs, especially the relative position between aligned CNTs, are usually changed. In order to keep the

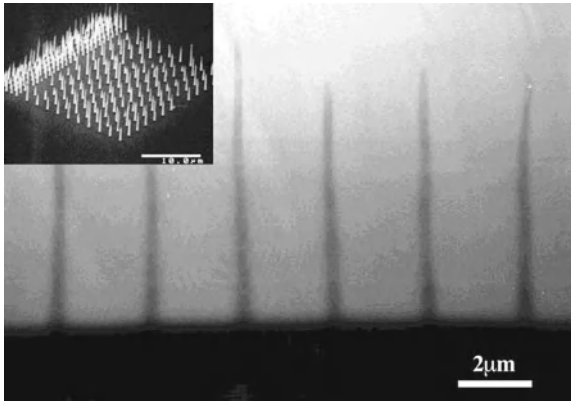


Fig. 7.17 TEM image of an array of single freestanding MWCNTs grown by PECVD. *Inset:* SEM image of the aligned freestanding CNT array. From Wen et al. [54]. Reprinted with permission from Cambridge University Press

original spatial structure of aligned CNTs, the aligned CNTs can be immersed in an epoxy. After cured, the aligned CNTs/epoxy is mechanically polished and ion milled to be TEM specimen, as in a traditional cross-sectional TEM specimen preparation procedure. In a typical procedure [54], (1) the as-grown CNT arrays are penetrated with a mixture of M-Bond 610 epoxy resin and acetone to provide mechanical stiffness, (2) the sample is first mechanically ground close to an array of the carbon nanotubes by a tripod (a precise grinding tool), then thinned from another side to about $10\mu\text{m}$ thick, (3) during the ion milling process, the ion beam etches only the substrate side such that the tip structure of CNTs is prevented from direct ion milling.

Figure 7.17 shows the cross-sectional microstructures of an array of single freestanding MWCNTs with a diameter of about 200nm and spacing of about $24\mu\text{m}$. The CNT array is grown from patterned catalysts prepared by electron beam lithography [54]. The microstructures of the tip, the middle part, and the interface between substrate and carbon nanotubes can be investigated beside the alignment of CNTs.

Compared with other techniques, the TEM technique can give direct results with much higher resolution and precision. However, the preparation of TEM specimen and the observation are time-consuming.

7.6 Scanning Tunneling Microscopy

A scanning tunneling microscope (STM), developed in 1986 [55], can image clean surfaces at the atomic level. A good resolution is achieved to be 0.1nm lateral resolution and 0.01nm depth resolution in an advanced STM [56]. The STM can be used

in ultra high vacuum, in air, even in water, and various other liquids at temperatures ranging from near zero kelvin to a few hundred degrees Celsius [57].

The STM principle is based on the concept of quantum tunneling. When a conducting tip is very close to a sample surface, a voltage bias can cause electrons to tunnel through the vacuum between the tip and the sample. The resulting tunneling current is a function of tip position and the local density of states of the sample. When the tip scans across the sample surface in the $X - Y$ plane, the changes in surface height and density of states cause the changes in currents. 2D images are acquired by monitoring the current as the tip scans across the surface. Scanning tunneling microscopy of SWCNTs are reviewed [58] on the electronic properties. Figure 2.9 shows a STM image of a SWCNT.

Based on the principle and experimental conditions, STM is suitable to observe the horizontally aligned CNT arrays grown on the substrate surface (see Chaps. 6.1.2, 6.1.3, and 6.1.4).

7.7 Atomic Force Microscopy

Atomic force microscopy (AFM) is a very high-resolution type of scanning probe microscopy discovered in 1986, with demonstrated resolution on the order of Ånström. The AFM mainly consists of a cantilever with a sharp tip as probe to scan the specimen surface. When the tip scans the specimen surface, forces between the tip and the specimen cause a deflection of the cantilever, which can be measured using a laser reflection, optical interferometry, or other methods.

The AFM provides a 3D surface profile, give true atomic resolution in ultra-high vacuum, and usually image a maximum height on the order of 10–20 μm and a maximum scanning area of about 150 \times 150 μm .

Similar to STM, AFM is suitable to characterize horizontally aligned CNTs, such as CNTs horizontally grown on quartz [59].

7.8 Other Techniques

Besides above techniques, there are many other methods to characterize the alignment of CNTs from their physical properties, such as 3ω technique [60], photothermo-electric technique [61], and fluorescence spectroscopy [62], etc. These techniques are not widely used by CNT scientists and will not talk about here for details. The interested readers are referred to some related literatures.

References

1. T. Belin, F. Epron, Characterization methods of carbon nanotubes: a review. *Mat. Sci. Eng. B: Solid* **119**, 105–118 (2005)
2. M. Knoll, Aufladepotential und sekundäremission elektronenbestrahlter körper. *Z. Tech. Phys.* **16**, 467–475 (1935)
3. M. von Ardenne, Das elektronen-rastermikroskop. theoretische grundlagen. *Z. Phys* **109**, 553–572 (1938)
4. M. von Ardenne, Das elektronen-rastermikroskop. praktische ausführung. *Z. Tech. Phys.* **19**, 407–416 (1938)
5. V.A. Zworykin, J. Hillier, R.L. Snyder, A scanning electron microscope. *ASTM Bull.* **117**, 15–23 (1942)
6. D. McMullan, An improved scanning electron microscope for opaque specimens. *Proc. Inst. Electr. Engrs.* **100**(Part II) 245–249 (1953)
7. G.I. Goldstein, D.E. Newbury, P. Echlin, D.C. Joy, C. Fiori, E. Lifshin, *Scanning Electron Microscopy and X-ray Microanalysis* (Plenum Press, New York, 1981)
8. I.M. Watt, *The Principles and Practice of Electron Microscopy* (Cambridge University Press, Cambridge, 1985)
9. L. Reimer, *Scanning Electron Microscopy: Physics of Image Formation and Microanalysis* (Springer, Heidelberg, 1998)
10. A. R. Clarke, C. Eberhardt, *Microscopy Techniques for Materials Science* (CRC Press, Boca Raton, 2002)
11. J. Goldstein, *Scanning Electron Microscopy and X-ray Microanalysis* (Kluwer Academic/Plenum Publishers, New York, 2003)
12. R.F. Egerton, *Physical Principles of Electron Microscopy: An Introduction to TEM, SEM, and AEM* (Springer, New York, 2005)
13. T.E. Everhart, R.F.M. Thornley, Wide-band detector for micro-microampere low-energy electron currents. *J. Sci. Instrum.* **37**(7), 246–248 (1960)
14. B.D. Cullity, *Elements of X-Ray Diffraction* (Addison-Wesley Publishing Company, Reading, Massachusetts, 1978)
15. R.A. Young (ed.), *The Rietveld Method* (Oxford University Press, Oxford, 1993)
16. V. Pecharsky, P. Zavalij, *Fundamentals of Powder Diffraction and Structural Characterization of Materials* (Springer, Berlin, 2008)
17. L. Jin, C. Bower, O. Zhou, Alignment of carbon nanotubes in a polymer matrix by mechanical stretching. *Appl. Phys. Lett.* **73**(9), 1197–1199 (1998)
18. A. Cao, C. Xu, J. Liang, D. Wu, B. Wei, X-ray diffraction characterization on the alignment degree of carbon nanotubes. *Chem. Phys. Lett.* **344**(1–2), 13–17 (2001)
19. V. Pichot, M. Burghammer, S. Badaire, C. Zakri, C. Riekel, P. Poulin, P. Launois, X-ray microdiffraction study of single-walled carbon nanotube alignment across a fibre. *EPL Europhys. Lett.* **79**(4), 46002 (2007)
20. J.T. Drotar, B.Q. Wei, Y.-P. Zhao, G. Ramanath, P.M. Ajayan, T.-M. Lu, G.-C. Wang, Reflection high-energy electron diffraction from carbon nanotubes. *Phys. Rev. B* **64**(12), 125417 (2001)
21. J.-F. Colomer, L. Henrard, P. Lambin, G. Van Tendeloo, Electron diffraction and microscopy of single-wall carbon nanotube bundles produced by different methods. *Euro. Phys. J. B.* **27**(1), 111–118 (2002)
22. K. Kempa, B. Kimball, J. Rybczynski, Z.P. Huang, P.F. Wu, D. Steeves, M. Sennett, M. Giersig, D.V.G.L.N. Rao, D.L. Carnahan, D.Z. Wang, J.Y. Lao, W.Z. Li, Z.F. Ren, Photonic crystals based on periodic arrays of aligned carbon nanotubes. *Nano Lett.* **3**(1), 13–18 (2003)
23. J. Rybczynski, K. Kempa, Y. Wang, Z.F. Ren, J.B. Carlson, B.R. Kimball, G. Benham, Visible light diffraction studies on periodically aligned arrays of carbon nanotubes: Experimental and theoretical comparison. *Appl. Phys. Lett.* **88**(20), 203122 (2006)
24. O. Glatter, O. Kratky (ed.), *Small Angle X-ray Scattering* (Academic Press, London, 1982)

25. B.N. Wang, R.D. Bennett, E. Verploegen, A.J. Hart, R.E. Cohen, Quantitative characterization of the morphology of multiwall carbon nanotube films by small-angle x-ray scattering. *J. Phys. Chem. C* **111**(16), 5859–5865 (2007)
26. N. C. Das, K. Yang, Y. Liu, P.E. Sokol, Z. Wang, H. Wang, Quantitative characterization of vertically aligned multi-walled carbon nanotube arrays using small angle x-ray scattering. *J. Nanosci. Nanotechnol.* **11**(6), 4995–5000 (2011)
27. P. Launois, A. Marucci, B. Vigolo, P. Bernier, A. Derre, P. Poulin, Structural characterization of nanotube fibers by x-ray scattering. *J. Nanosci. Nanotechnol.* **1**(2), 125–128 (2001)
28. B. Wei, R. Vajtai, Y.Y. Choi, P.M. Ajayan, H. Zhu, C. Xu, D. Wu, Structural characterizations of long single-walled carbon nanotube strands. *Nano Lett.* **2**(10), 1105–1107 (2002)
29. L.A. Hough, M.F. Islam, B. Hammouda, A.G. Yodh, P.A. Heiney, Structure of semidilute single-wall carbon nanotube suspensions and gels. *Nano Lett.* **6**(2), 313–317 (2006)
30. D.W. Schaefer, J. Zhao, J.M. Brown, D.P. Anderson, D.W. Tomlin, Morphology of dispersed carbon single-walled nanotubes. *Chem. Phys. Lett.* **375**(3–4), 369–375 (2003)
31. B. Finnigan, K. Jack, K. Campbell, P. Halley, R. Truss, P. Casey, D. Cookson, S. King, D. Martin, Segmented polyurethane nanocomposites: Impact of controlled particle size nanofillers on the morphological response to uniaxial deformation. *Macromolecules* **38**(17), 7386–7396 (2005)
32. H. Wang, J. Feng, X. Hu, K.M. Ng, Synthesis of aligned carbon nanotubes on double-sided metallic substrate by chemical vapor deposition. *J. Phys. Chem. C* **111**(34), 12617–12624 (2007)
33. H. Wang, Z. Xu, G. Eres, Order in vertically aligned carbon nanotube arrays. *Appl. Phys. Lett.* **88**(21), 213111 (2006)
34. H. Wang, W. Zhou, D.L. Ho, K.I. Winey, J.E. Fischer, C.J. Glinka, E.K. Hobbie, Dispersing single-walled carbon nanotubes with surfactants: A small angle neutron scattering study. *Nano Lett.* **4**(9), 1789–1793 (2004)
35. K. Yurekli, C.A. Mitchell, R. Krishnamoorti, Small-angle neutron scattering from surfactant-assisted aqueous dispersions of carbon nanotubes. *J. Am. Chem. Soc.* **126**(32), 9902–9903 (2004)
36. A. Smekal, Zur quantentheorie der dispersion. *Naturwissenschaften* **11**(43), 873–875 (1923)
37. C.V. Raman, K.S. Krishnan, A new radiation. *Indian J. Phys.* **2**, 387 (1928)
38. C.V. Raman, K.S. Krishnan, A new type of secondary radiation. *Nature* **121**, 501 (1928)
39. G. Landsberg, L. Mandelstam, Eine neue erscheinung bei der lichtzerstreuung in krystallen. *Naturwissenschaften* **16**(28), 557 (1928)
40. R. Saito, A. Grúneis, G.G. Samsonidze, V.W. Brar, G. Dresselhaus, M.S. Dresselhaus, A. Jorio, L.G. Cançado, C. Fantini, M.A. Pimenta, A.G.S. Filho, Double resonance raman spectroscopy of single-wall carbon nanotubes. *New J. Phys.* **5**(1), 157 (2003)
41. A. Jorio, M.A. Pimenta, A.G.S. Filho, R. Saito, G. Dresselhaus, M.S. Dresselhaus, Characterizing carbon nanotube samples with resonance raman scattering. *New J. Phys.* **5**(1), 139 (2003)
42. A.G.S. Filho, A. Jorio, G.G. Samsonidze, G. Dresselhaus, R. Saito, M.S. Dresselhaus, Raman spectroscopy for probing chemically/physically induced phenomena in carbon nanotubes. *Nanotechnology* **14**(10), 1130 (2003)
43. M. Dresselhaus, G. Dresselhaus, R. Saito, A. Jorio, Raman spectroscopy of carbon nanotubes. *Phys. Rep.* **409**(2), 47–99 (2005)
44. M.S. Dresselhaus, A. Jorio, M. Hofmann, G. Dresselhaus, R. Saito, Perspectives on carbon nanotubes and graphene raman spectroscopy. *Nano Lett.* **10**(3), 751–758 (2010)
45. R. Saito, M. Hofmann, G. Dresselhaus, A. Jorio, M.S. Dresselhaus, Raman spectroscopy of graphene and carbon nanotubes. *Adv. Phys.* **60**(3), 413–550 (2011)
46. B. Lei, K. Ryu, L.G. De-Arco, S. Han, A. Badmaev, D. Farmer, K. Kim, R. Gordon, K.L. Wang, C. Zhou, Raman characterization and polarity tuning of aligned single-walled carbon nanotubes on quartz. *Jpn. J. Appl. Phys.* **49**(2), 02BC02 (2010)
47. P. Hawkes (ed.), *The beginnings of Electron Microscopy* (Academic Press, London, 1985)
48. R. Erni, M.D. Rossell, C. Kisielowski, U. Dahmen, Atomic-resolution imaging with a sub-50-pm electron probe. *Phys. Rev. Lett.* **102**(9), 096101 (2009)

49. G. Thomas, *Transmission Electron Microscopy of Metals* (Wiley, New York, 1962)
50. P.B. Hirsch, A. Howie, R.B. Nicholson, D.W. Pashley, M.J. Whelan, *Electron microscopy of Thin Crystals* (Krieger, Huntington, New York, 1977)
51. M. von Heimendahl, *Electron Microscopy of Materials* (Academic Press, New York, 1980)
52. L. Reimer, *Transmission Electron Microscopy: Physics of Image Formation and Microanalysis* (Springer, New York, 1993)
53. C. Bower, W. Zhu, S. Jin, O. Zhou, Plasma-induced alignment of carbon nanotubes. *Appl. Phys. Lett.* **77**(6), 830–832 (2000)
54. J.G. Wen, Z.P. Huang, D.Z. Wang, J.H. Chen, S.X. Yang, Z.F. Ren, J.H. Wang, L.E. Calvet, J. Chen, J.F. Klemic, M. Reed, Growth and characterization of aligned carbon nanotubes from patterned nickel nanodots and uniform thin films. *J. Mater. Res.* **16**(11), 3246–3253 (2001)
55. G. Binnig, H. Rohrer, Scanning tunneling microscopy. *IBM J. Res. Dev.* **30**, 4 (1986)
56. C. Bai, *Scanning Tunneling Microscopy and Its Applications* (Springer, New York, 2000)
57. C.J. Chen, *Introduction to Scanning Tunneling Microscopy* (Oxford University Press, New York, 1993)
58. T.W. Odom, J.L. Huang, C.M. Lieber, Stm studies of single-walled carbon nanotubes. *J. Phys.-Condens. Mat.* **14**(6), R145–R167 (2002)
59. A.A. Almaqwashi, J.W. Kevek, R.M. Burton, T. DeBorde, E.D. Minot, Variable-force microscopy for advanced characterization of horizontally aligned carbon nanotubes. *Nanotechnology* **22**(27), 275717 (2011)
60. W. Yi, L. Lu, D.-I. Zhang, Z. W. Pan, and S. S. Xie, Linear specific heat of carbon nanotubes. *Phys. Rev. B* **59**(14), R9015–R9018 (1999)
61. T. Borca-Tasciuc, S. Vafaei, D.-A. Borca-Tasciuc, B.Q. Wei, R. Vajtai, P.M. Ajayan, Anisotropic thermal diffusivity of aligned multiwall carbon nanotube arrays. *J. Appl. Phys.* **98**(5), 054309 (2005)
62. R.B. Weisman, S.M. Bachilo, D. Tsyboulski, Fluorescence spectroscopy of single-walled carbon nanotubes in aqueous suspension. *Appl. Phys. A* **78**, 1111–1116 (2004)

Chapter 8

Properties and Applications of Aligned Carbon Nanotube Arrays

Individual CNTs have wide applications because of their unique properties, such as nanoprobe in scanning probe microscopes [1], tips of atomic force microscopes [2, 3], electron field emitters [4], mechanical memory elements [5, 6], SWCNT chemical sensors [7], quantum resistors [8], nanobalances to weigh nanoparticles [9], nanodevices [10], transistors [11–13], logic gates [14], nano-motors without friction (molecular linear motors and rotational motors [15]), nano-electronics [16, 17], nano test-tubes [18], high-pressure nano-cylinders [19], nanotweezers [20], pressure sensors [21], microwave rectification [22], molecular delivery to shuttle macromolecules into cells [23–25] or rapid transport of gold nanoparticles across the cell wall [25], etc. However, it is not the emphasis of this book to discuss these applications of individual CNTs. We refer the interested readers to the relevant reviews [16, 26–36] and books [6, 37–48] on the applications of individual CNTs, and the physics of CNT devices [42, 44, 47, 49–55] for detailed information.

Aligned CNT arrays have unique properties over individual CNTs and have wider applications, including field emission and flat screens, ultracapacitors, nanoelectrode arrays, fuel cells, solar cells, transistors, chemical and biological sensors, due to the ordering of their aligned structures. In this chapter, we focus on the applications of the well-aligned CNT arrays and talk about these applications in detail.

8.1 Field Emission Devices

A field emission occurs under intense electric fields with typical gradients higher than 1,000 V/m for pure metals and is strongly dependent on the work function of the emitting material.

In a parallel-plate arrangement, the macroscopic field E_{macro} between the plates is given by $E_{\text{macro}} = V/d$, where d is the plate separation and V the applied voltage. If a sharp object is created on a plate, then the local field E_{local} at its apex is greater than E_{macro} and can be related to E_{macro} by

$$E_{\text{local}} = \gamma \times E_{\text{macro}} \quad (8.1)$$

The parameter γ is called the *field-enhancement factor* and basically determined by the shape of the object. Because the field-emission characteristics are determined by the local field E_{local} , the higher the γ -value of the object, the lower the value of E_{macro} at which significant emission occurs.

CNTs have high aspect ratios (length divided by diameter) and induce very high local electric field around the CNT tips. So CNTs are considered as one of the best electron-emitting materials.

Emission of CNTs was first reported in 1994 [56] and several papers were published in the subsequent years [4, 57–69]. From 1998, interests in field-emission properties of CNTs undertook a very sharp increase all over the world [70] and thousands of papers have been published ever since, such as the field-emission property of aligned CNT arrays [71], due mainly to the successes in the alignment of CNTs. The early history of CNT field emission is reviewed recently [56] and applications can be found in some review literatures [72, 73].

The intrinsic field-enhancement factor γ_0 of an individual CNT in the planar diode configuration can be approximated by [74]

$$\gamma_0 = 1.2 \times \left(2.5 + \frac{l}{r} \right)^{0.9} \quad (8.2)$$

where l and r are the length and the radius of the CNT, respectively.

The typical field-enhancement factor γ_0 ranges from 30,000 to 50,000 for individual CNTs. The field-enhancement factors of CNT films consisting of random CNTs are much lower than those of individual CNTs because of the planar substrate supporting the CNT films. Usually $\gamma = 1,000$ – $3,000$ for CNT films [75]. A high field-enhancement factor of 1.88×10^4 was achieved when CNTs are grown on carbon clothes [67]. A recorded low turn-on electric field of less than $0.4 \text{ V}/\mu\text{m}$ was achieved to reach an emission current density of $1 \text{ mA}/\text{cm}^2$ [67].

The field emission of the CNT films consisting of random CNTs has been widely reviewed recently [76–78]. In this chapter we mainly focus on the field emission of aligned CNTs and their applications.

8.1.1 Field Emission of Aligned Carbon Nanotube Arrays

The field-enhancement factor γ of CNT arrays can be experimentally determined from the slope of Fowler–Nordheim plot if the work function ϕ is known. The extracted field-enhancement factor γ from the Fowler–Nordheim plot is affected by the adsorbates [79] and by the geometry of configuration [80].

The Fowler–Nordheim dependence of an aligned CNT array takes the form [56]

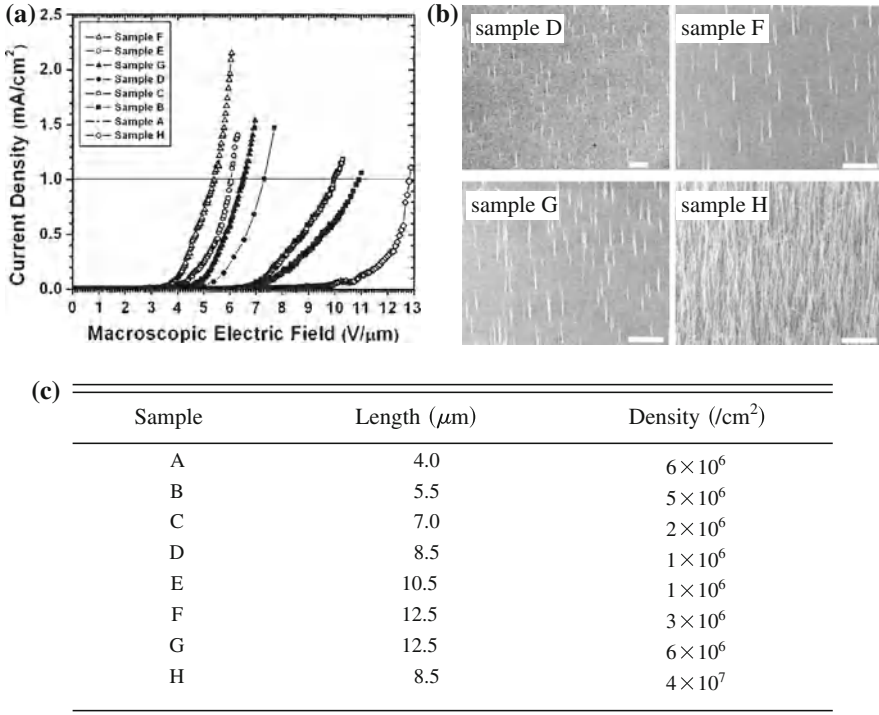


Fig. 8.1 **a** The measured current densities as a function of the macroscopic electric field for eight samples; **b** SEM micrograph at a grazing incidence of 45° to the substrate of the four samples. The white scale bar corresponds to $10\mu\text{m}$; **c** length and areal density of eight CNT arrays. From Jo et al. [81]. Reprinted with permission from American Institute of Physics

$$j \approx 1.56 \times 10^{-6} \times \frac{(\gamma E_{\text{macro}})^2}{\phi} \exp\left(-\frac{0.683 \times 10^7 \times \phi^{3/2}}{\gamma E_{\text{macro}}}\right) \quad (8.3)$$

where j is the current density (in A/cm^2), ϕ the work function (in eV ; it is assumed that $\phi = 4.7 \text{ eV}$ for carbon nanotubes), and E_{macro} the external applied electric field (in $\text{V}/\mu\text{m}$). In the Fowler–Nordheim coordinates of MWCNTs, $\ln[j/(E_{\text{macro}})^2] \propto 1/(\gamma E_{\text{macro}})$. So the field-enhancement factor γ can be experimentally determined from the slope of the Fowler–Nordheim plot.

In the typical measurements of Fowler–Nordheim plots, the field-emission currents of CNT arrays are measured in a simple diode configuration. The anode is a molybdenum disk with a diameter of 5 mm and the substrate on which the CNT arrays have grown works as a cathode. The gap between the silicon substrate and the anode is $300\mu\text{m}$ [81]. Figure 8.1 shows the field-emission current of CNT arrays measured by the diode method.

Figure 8.1 clearly shows that the field enhancement of CNT ensembles is affected by the length of CNTs and the spacing between them. So it is important to characterize

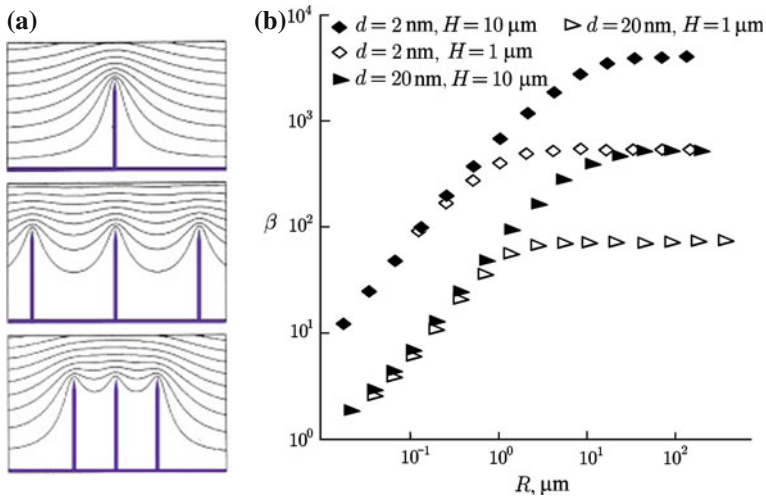


Fig. 8.2 **a** Simulation of the equipotential lines of the electrostatic field for CNTs of 1 μm height and 2 nm radius, for average nanotube spacings of 4, 1, and 0.5 μm; **b** the calculated field-enhancement factor γ of CNT arrays with a honeycomb structure. H is the height, d diameter of a CNT, and R the distance between the nearest CNT neighbors. **a** From Nilsson et al. [85]. Copyright (2000), American Institute of Physics. **b** From Zhanov et al. [56]. Copyright (2004), Springer

the effects of length and spacing on field-emission properties in order to obtain a large and uniform field-emission current at low electric fields. The studies on the effects of length and spacing have been reported for vertically aligned CNT arrays [58, 60, 81–84] as well as for randomly oriented CNT ensembles [85–87]. It is found that the field emission is critically affected by the CNT height that protruded from the surface because of the field-screening effect [83].

The field-enhancement factors γ of dense CNT arrays are lower than those of CNT arrays with lower site density because the local electric field near one nanotube is screened by the proximity of neighboring nanotubes (Fig. 8.2a). Through analyzing the vertically aligned MWCNT arrays, it is found that, for a given length of CNTs, γ increases as the spacing of CNTs is increased [81]. It is estimated that γ is nearly saturated when the site density is about 10^6 tubes/cm² and the length is longer than 10 μm. However, for the very-high-density CNT assemblies, the increase in length increases γ slightly, whereas for the very short CNT arrays, the increase in spacing does not effectively reduce γ .

The theoretical simulation indicates that the field emission is optimal when the nanotube height is close to the inter-nanotube distance (Fig. 8.2b), in agreement with experimental results.

Taking into consideration the effect of spacing between CNTs, the field-enhancement factor γ of CNT arrays can be approximated by [75]

$$\gamma = \gamma_0 \left(1 - \exp^{-2.3172 \times \frac{R}{l}} \right) \quad (8.4)$$

where R is the spacing between CNTs and l the height of CNTs.

The emission property of aligned CNT arrays is not satisfactory if the areal density is higher than 10^9 tubes/cm² because of small enhancement factors at the CNT tips [88]. An areal density of about 10^7 tubes/cm² has been estimated to be the optimal density for electron emission properties in terms of both emission site distribution and current density [85]. PECVD technique discussed in Chap. 5, and Sect. 6.1.6, provides a valuable approach for obtaining optimal emitter density of CNTs. The CNT forests grown by the thermal CVD method under crowding effect (see Sect. 6.1.1) is not good for field emission because of high site density.

To enhance the field-emission properties of aligned CNT arrays, some effective methods have been carried out, such as plasma treatments in H₂ [89], or in O₂ [90] after growth, controlling the site densities of CNTs during growth to decrease the electrostatic screening effect [91], laser treatment [92], annealing in oxygen or ozone to open the end of the CNTs [93], thermal oxidation in air [69], and ultra-low energy ion bombardment [94]. The field-emission current density can be significantly improved by a factor of 4 [69] or even 8 [93] after these treatments.

More detailed information on the physics of electron emission of CNT arrays can be found in the recent published reviews [70, 77, 95–97] and books [98].

Prototype devices using the superior field-emission properties of aligned CNT arrays have been demonstrated, including X-ray sources, flat-panel displays, and lamps. We will introduce some field-emission applications of vertically aligned CNT arrays in this section.

8.1.2 Carbon Nanotube Array Emitters

Based on the emission properties of aligned CNT arrays, CNT field emitters are produced [85, 99, 100]. At present, CNT emitters operate stably under moderate-vacuum conditions (10^{-8} Torr), which is an advantage over metal field emitters such as those made of tungsten and molybdenum requiring ultra-high vacuum environments (10^{-10} Torr) [101].

The underlying substrates affect the field-emission properties of CNT emitters. Figure 8.3 shows the typical current density versus the electric field strength for CNT emitters on stainless steel substrates and on nickel substrates, at 1×10^{-6} Pa and room temperature [102]. The inset in Fig. 8.3 shows the Fowler–Nordheim plot of the same emission data. CNTs on stainless steel (3×3 mm²) begin to emit electrons at a lower electric field level than CNTs on nickel, indicating that the emission property of CNTs depends also on the substrate material supporting the catalysts for CNT growth. The emission current density of the stainless steel substrate displays an onset field near 1.2 V/μm. A field-emission current density of 1 mA/cm², the critical value required for conventional flat-panel displays, is achieved at a field intensity

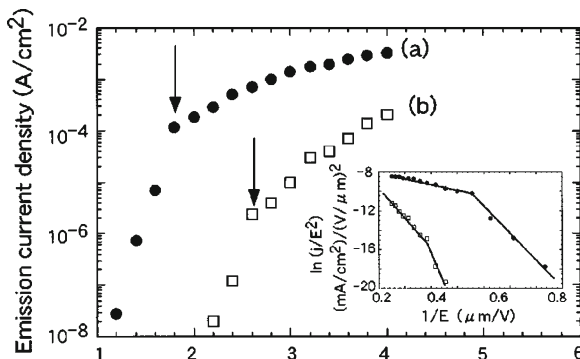


Fig. 8.3 Field-emission current density versus electric field of a CRT lighting device equipped with a flat-aligned CNT array cathode. CNTs grown on stainless steel substrates (*filled circle*) and on nickel substrates (*open square*). *Inset* corresponding Fowler–Nordheim plot. *Arrows* indicate the onsets of saturation. From Murakami et al. [102]. Copyright (2000), American Institute of Physics

level of about $3 \text{ V}/\mu\text{m}$. Strong saturations above $1 \text{ mA}/\text{cm}^2$ on nickel substrates and $10 \text{ mA}/\text{cm}^2$ on stainless steel substrates are observed, with the Fowler–Nordheim slope diminishing by a factor of 2 on nickel substrates and by a factor of 3 on stainless steel substrates. These current saturations for aligned CNT emitters are also reported in random CNT emitters [103, 104].

8.1.3 High-Intensity Electron Sources

Based on their field-emission properties, aligned CNT arrays can be used as high-intensity electron guns [58]. Such electron sources are air-stable and longtime reliable with field-emission current densities of $\sim 0.1 \text{ mA}/\text{cm}^2$ under an applied voltage as low as 200 V. Current densities greater than $100 \text{ mA}/\text{cm}^2$ have also been realized under 700 V, making such electron sources suitable for high-intensity applications.

In addition to the emission current density, the stabilities of aligned CNT arrays (the variation of emission current over time) are also critical to obtain a long-lasting reliable field-emission electron source. The field-emission current from CNT arrays usually shows a unstable behavior in air due to reaction with ambient gas. When the CNT arrays are coated by amorphous layers, the coated CNT arrays have stable emission current for more than 60 h in vacuum (Fig. 8.4), while the emission current of non-coated CNT arrays decreases with time [67]. The emission current of coated CNT arrays is decreased after an air exposure but recovers after re-evacuation.

The CNT electron sources are well reviewed recently [72, 105] and the interested readers are referred to these reviews.

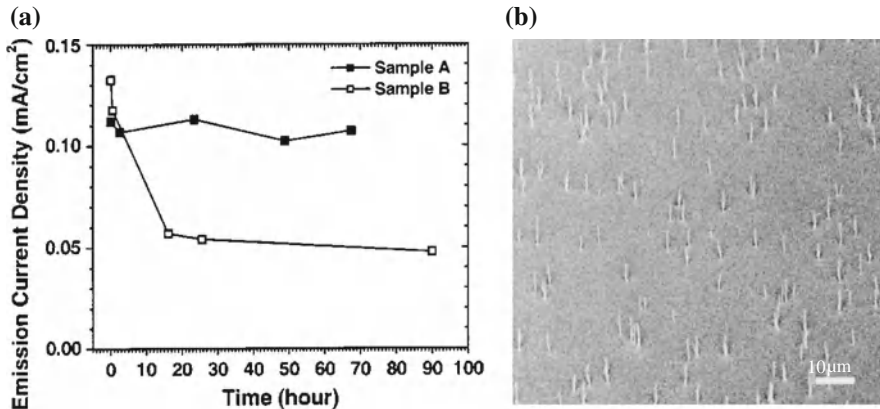


Fig. 8.4 **a** Stability of field-emission current with time in vacuum. The CNT arrays are covered with an amorphous layer of 10–25 nm thickness; **b** an SEM image of the CNT arrays. The average length and site density of CNTs are 8.5 μm and $1 \times 10^6/\text{cm}^2$, respectively. The diameter of the CNTs is in the range of 50–80 nm. From Jo et al. [67]. Reprinted with permission from American Institute of Physics

8.1.4 Lighting

When a bias potential is applied between a CNT array and an anode, a strong local field is produced at the small CNT tips, inducing electrons to tunnel from the CNT tips into the vacuum space toward the anode. When a phosphor layer is coated on the anode, the field-emitted electrons will bombard the phosphor to produce light, a useful process in flat-panel displays and lighting sources. Three kinds of CNT lighting devices have been demonstrated. One is the cathodoluminescent light-emitting element of cylindrical geometry [106, 107] (Fig. 8.5). MWCNTs are grown on a conductive cathode of radius r_1 , located on the symmetry axis of the cylindrical anode of inner radius r_2 . The anode is a glass tube with a conductive coating and a phosphor layer on the inner surface. When working at an operating voltage of 5.4 kV, the emitted current density is 0.5 mA/cm^2 on the cathode and 0.06 mA/cm^2 on the anode [106]. The emitted light intensity amounts to 10,000 cd/m^2 , comparable to a commercial fluorescent tube 11,000 cd/m^2 .

The second kind is the diode-structured flat-panel luminescent light source with a CNT array field-emission cathode [96, 101, 102, 108]. In such a flat-panel source, the CNT arrays as the cathode are vertically grown on a substrate with patterned catalyst particles (Fig. 8.6). Under high voltages, the electrons from CNT tips bombard onto a phosphor screen to generate light, similar to the first kind of light source to generate light.

CNT-based flat-panel lighting sources can emit white light as well as colored light. The CNT lighting sources can provide stable emission, long lifetimes (over 4,000 h), and low emission threshold voltages [96, 101]. For cathode ray tube (CRT) light-

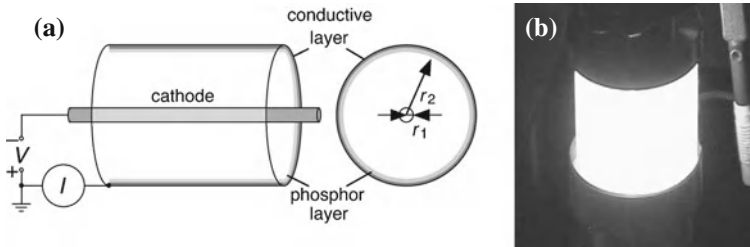


Fig. 8.5 Luminescent field-emission device in cylindrical geometry. **a** Schematic structure of the device; **b** product of the CNT field-emission device. From Bonard et al. [106]. Copyright (2001), American Institute of Physics

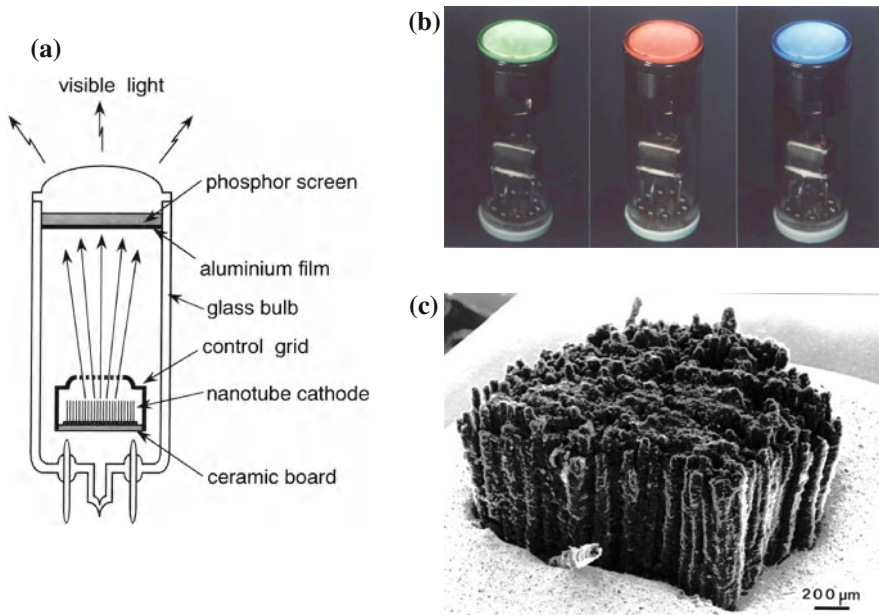


Fig. 8.6 CRT light source device with a flat-field-emission cathode composed of CNTs. **a** Schematic structure of a cross-section; **b** photographs of fluorescent displays emitting the three primary colors: *green, red, and blue*; **c** SEM micrograph of a cathode made of MWCNTs with columnar structure. From Saito et al. [101]

emitting-based electric lamps with various colors, the current density at the cathode is 10 mA/cm^2 , the average electric field intensity is $1.5 \text{ V}/\mu\text{m}$, and the luminance of elements of various colors range from 1.5×10^4 to $6.3 \times 10^4 \text{ cd/m}^2$ [96]. The emission current of a white-color CNT lighting device is stable with a fluctuation of 2% without bias resistors. The lifetime of such device exceeds 10,000 h recently [102]. The luminance of about $6 \times 10^4 \text{ cd/m}^2$ for green light is obtained using CNT cold cathodes [101]. The ultrahigh luminance light sources can be produced by

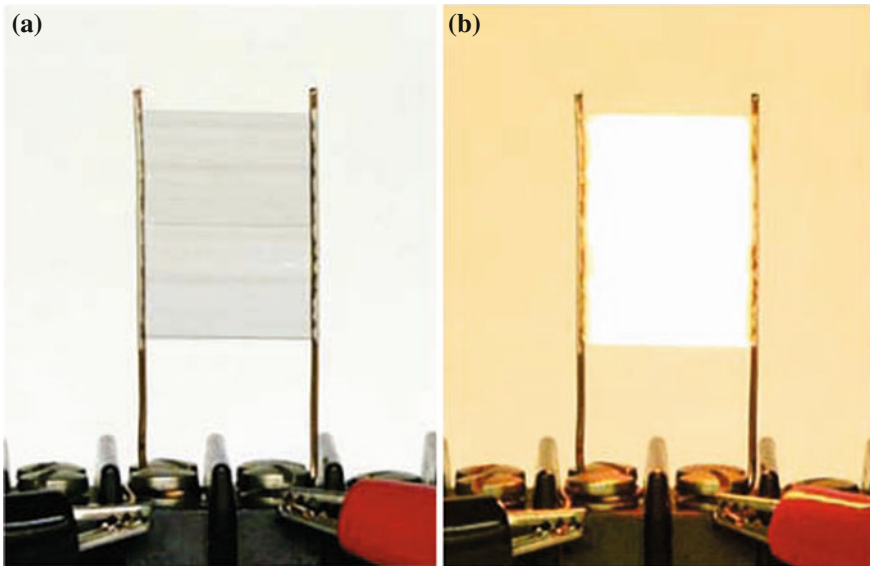


Fig. 8.7 Planar incandescent light source consisting of CNT sheets (16 mm \times 22 mm): **a** the unheated sheet; **b** the incandescent sheet. From Zhang et al. [109]. Copyright (2005), AAAS

employing special MWCNTs as field emitters in hydrogen gas. An extremely high luminance of 10^6 cd/m² is achieved for ZnS/Cu/Al green phosphor as a cathode with a DC voltage of 30 kV and a DC current of 400 μ A. The ultrahigh luminance light source is expected to emit luminous flux of more than 1,000 lm [108]. These data are comparable to those of CRT-based lamps.

The last kind is the planar incandescent light source consisting of CNT sheets [110]. CNT sheets are usually fabricated by the dry-spinning method described in Sect. 6.2.3.2. Figure 8.7 shows such a planar lighting source. Pure CNT sheets are connected to two electrodes. When a current passes through the CNT sheets, the CNTs are heated up to over 1,000 $^{\circ}$ C in less than 1 ms and then emit light.

8.1.5 Field Emission Flat Panel Displays

In conventional field-emission displays, metal tips with micron sizes have usually served as emission sources. When a voltage is applied between a gate electrode and a metal emitter, a higher electric field is generated at the apex of a metal tip, inducing electron emission from the metal tip. Emitted electrons are accelerated toward an anode and bombard a phosphor layer, producing visible light. Such metal field-emission displays perform as cathode ray tube (CRT)-like displays but their production cost is higher.

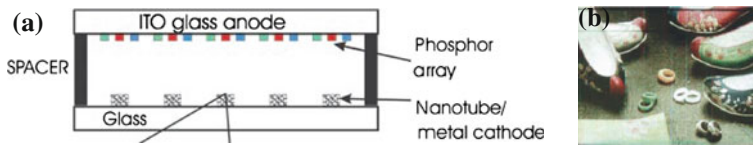


Fig. 8.8 **a** Schematic illustration of a flat-panel display based on well-separated SWCNT bundles protruding from the supporting metal base; **b** photograph of a 5 in CNT field-emission *red-blue-green* color display that can reproduce moving images. From Baughman et al. [26]. Copyright (2002), AAAS

CNTs have been spotlighted as one of the promising alternatives for new electron sources used in flat field-emission displays, due to their superior emission properties as discussed in Sect. 8.1.1, and their straightforward fabrication processes. CNTs are expected to produce field-emission displays with low cost, low power consumption, and high scalability [111]. Now the flat-panel display is one of the most lucrative CNT applications being developed in the commercial sector.

CNTs provide high current densities, stable emission, long lifetimes, and low emission threshold potentials [58, 96]. Current densities as high as 4 A/cm^2 have been obtained, compared with the 10 mA/cm^2 needed for flat-panel field-emission displays [112].

The short-term emission of CNT emitters is stable with a current density of 1 mA/cm^2 and a fluctuation of 2% without bias resistors. This emission current is sufficient for practical use in flat-panel displays. A lifetime exceeding 10,000 h is suggested under direct current driving and continuous electron emission without diminution [102]. These reliable results, i.e., high current densities and long-time stability, enable the commercialization potentials of large-area full-color flat-panel displays using CNT emitters in the near future. Based on the emission properties of the aligned CNT arrays, a series of flat-panel displays have been designed from CNT arrays.

The first CNT-based flat-panel display consisting of 32×32 matrix-addressable pixels was reported in 1998 using random CNTs as the electron emission source [113]. Later, 4.5 in [114, 115] and 9 in [111] colorful field-emission displays have been reported. At present, flat panel displays based on CNT field-emission cathodes are developed in hundreds of laboratories, and commercial displays have already been manufactured. The CNTs in the commercial flat panel displays are usually vertically aligned on cathode electrodes for better electron emission. At present, CVD technologies are employed to synthesize vertically aligned CNTs over a large area of substrates, as discussed in Sect. 6.1.6 and in Chap. 5.

Figure 8.8a shows a basic structure of a flat-panel display based on CNTs. CNTs are vertically grown on a substrate in the form of bundles, working as the cathode electron source. Indium tin oxide (ITO) is deposited on glass as the anode. By applying a bias voltage across the CNTs and the ITO anode, electrons are emitted from CNT tips and bombard onto the phosphor screen to emit light. Figure 8.8b illustrates an image produced by a CNT-based color flat-panel display.

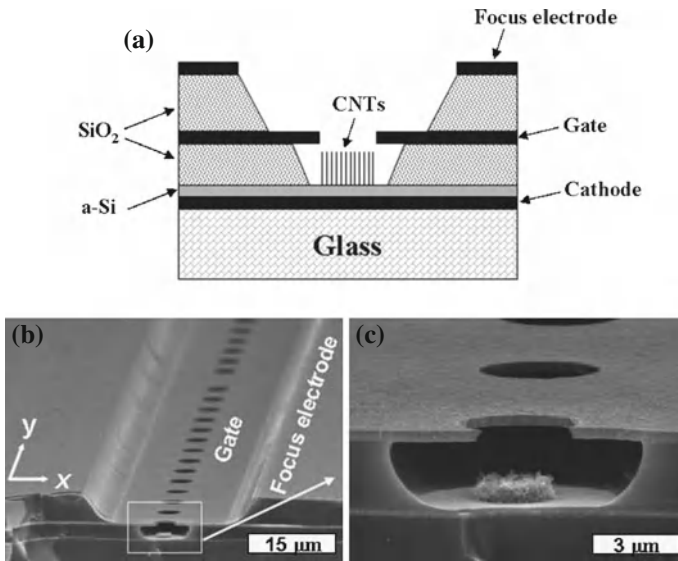


Fig. 8.9 Double-gated field emitter array. **a** Schematic diagram of the structure; **b** SEM image of the structure; **c** magnified image of the *white rectangular part* in (b). From Choi et al. [115]. Copyright (2006), American Institute of Physics

The commercial flat-panel displays have more complex structures. Figure 8.9 shows a double-gated CNT display. The emitted electrons are focused by a focusing electrode before arriving at the phosphor layers.

Compared with liquid crystal displays, the field-emission displays have a lower power consumption, a higher brightness, a wider viewing angle, a higher response rate, and a wider operating temperature range [26, 41].

8.1.6 Incandescent Displays

Besides the field-emission displays, CNT array displays can also be fabricated based on incandescence mechanisms [116]. Figure 8.10 illustrates an incandescent CNT array display fabricated from a CNT cloth. The CNT cloth is fabricated from aligned CNTs by the dry-spinning method (see Sect. 6.2.3.2). The superaligned CNT cloth (Fig. 8.10a) is suspended on the screen printed electrodes of several tens of microns. Then the CNT cloth is cut into separate $100\ \mu\text{m} \times 300\ \mu\text{m}$ units (Fig. 8.10b) as display pixels using a laser. When a current is applied through the cloth film on the electrodes, the CNT film is heated to incandescence in vacuum [117], similar to the CNT incandescent light discussed in Sect. 8.1.4. Figure 8.10c shows an image of one Chinese word displayed by the incandescent $16\ \text{pixel} \times 16\ \text{pixel}$ array.

The maximum brightness of an individual pixel is $6,400\ \text{cd}/\text{m}^2$ at about $0.08\ \text{W}$ heating power. The current and incandescent brightness stabilities of a pixel are 0.05 and 1.1%, respectively, at 1,740 K.

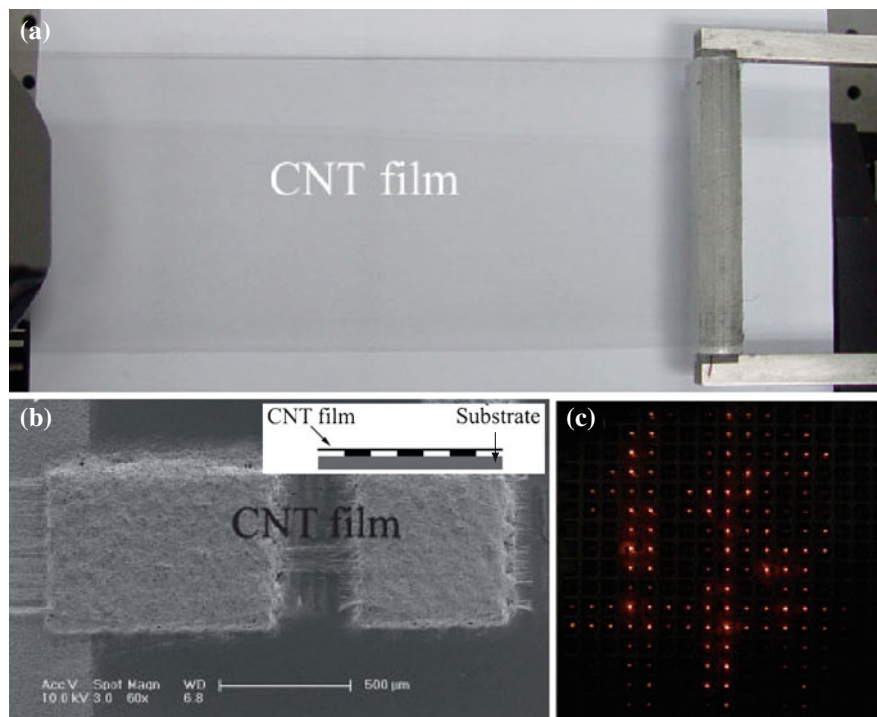


Fig. 8.10 Incandescent CNT array displays. **a** Superaligned CNT film used in the incandescent display; **b** top-view SEM image of the CNT film working as an individual pixel in the incandescent display. *Inset* schematic illustration (*side view*) of the pixels; **c** image of a Chinese character displayed by an incandescent display with a 16 pixel \times 16 pixel array. From Liu et al. [116]. Copyright John Wiley and Sons

The lifetime of the CNT incandescent display is estimated to be about 550h because of the evaporation of CNTs at high temperature. Compared with field-emission CNT displays, the turnon voltage of the CNT incandescent displays is about 4–7V, the response time is less than 1 ms, and there is no viewing-angle problems of LCDs.

8.1.7 X-Ray Generators

When the field-emitted electrons from CNT tips bombard onto a metal target, not a phosphorescent screen, X-rays are emitted instead of light [118]. So CNT arrays can be used for X-ray imaging tubes [119]. Figure 8.11a illustrates a circuit of X-ray CNT generator. The field-emitted electrons from CNT tips bombard on the Cu target to produce X-ray.

In a conventional X-ray tube, the X-ray intensity is limited by the focusing of the X-ray beam and the response time of the thermionic emission is slow. Therefore the

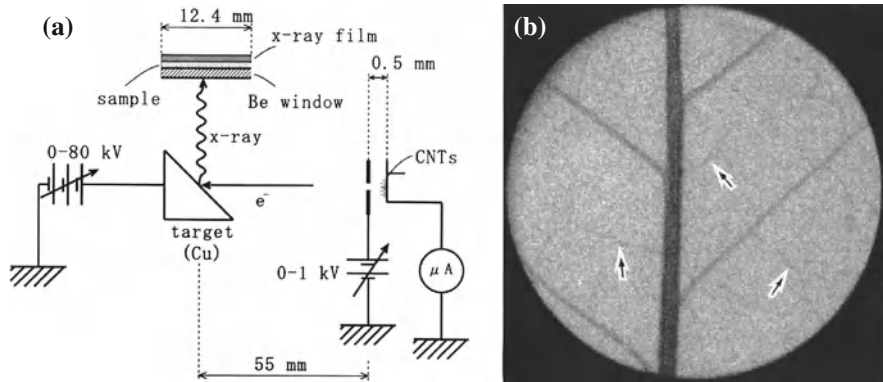


Fig. 8.11 **a** Diagram of the X-ray producing circuit; **b** fresh leaf imaged at 10kV using the CNT X-ray generator. From Sugie et al. [118]. Copyright (2001), American Institute of Physics

three-dimensional images of moving body parts, such as the heart and lungs, are not clear.

The X-ray intensity of CNT arrays increases exponentially with the linear increase in accelerating potential. When the CNT arrays are uniform, the emission energy distribution of emitted electrons is far more uniform than that of thermal electrons [118]. This near uniformity in electron energy provides higher resolution than thermionic electron sources do (see Fig. 8.11b).

At present, the high emission current density and stability of current is achieved for requirement of the commercialization of portable, lightweight CNT-based X-ray source. CNT-derived X-ray sources can create X-ray pulses of any duration and frequency, gate the X-ray pulse to any source and allow the placement of many sources of clinical and medical imaging [120], with specific advantages over traditional thermionic tubes.

Multi-pixel X-ray array sources generated by CNT cathode arrays can be used for microradiotherapy for cancer research. The developed multipixel X-ray array source has several distinct advantages over other irradiation sources including high-temporal resolution (millisecond level), the ability to electronically shape the form, and intensity distribution of the radiation fields [121].

8.1.8 Microwave Devices

High-frequency (30GHz and above) and high-power (10 W) amplifiers are used in satellites for telecommunication. The conventional semiconductor electronics and vacuum microelectronics are difficult to make small, lightweight, high-frequency, high-power devices because of dissipation heat. CNT array-based microwave devices provide the power amplification in this field.

The CNT arrays are constructed into a microwave diode [122], as shown in Fig. 8.12. The device consists of a cathode-grid design, similar to the structures

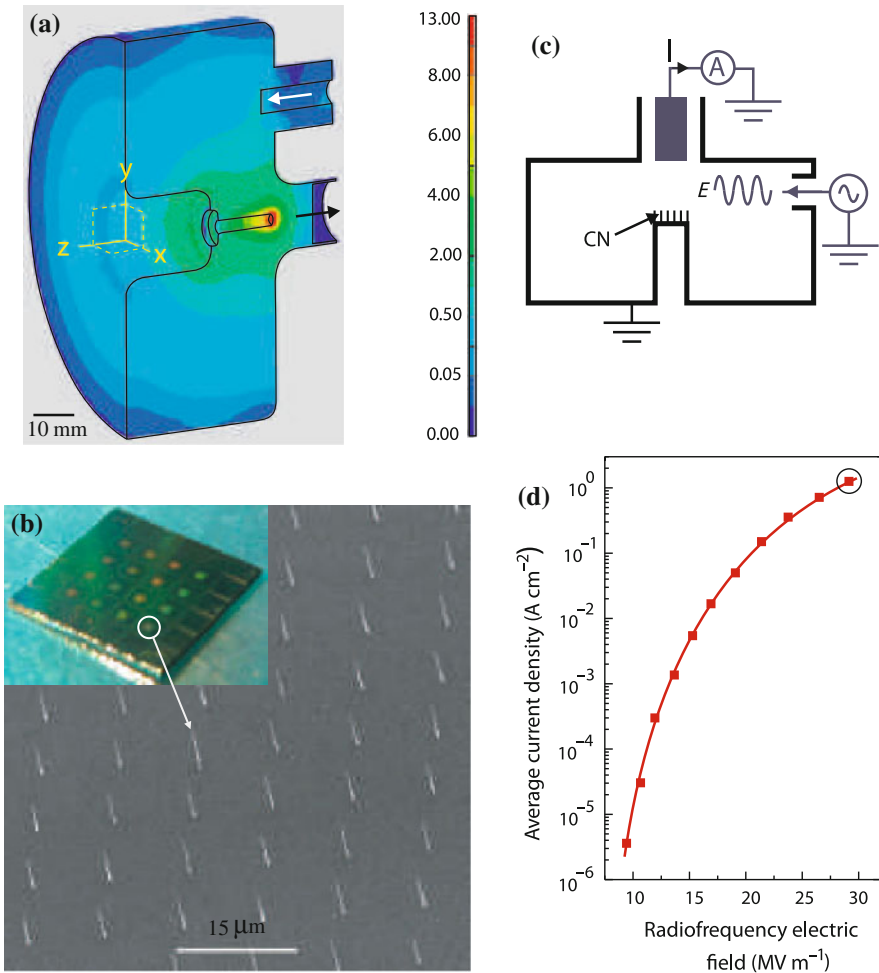


Fig. 8.12 **a** Simulation of the coaxial resonant cavity that was used to generate a high electric field (red) at the carbon-nanotube-array cathode from the radio-frequency input; color scale shows the applied macroscopic electric field in volts ($\sim 10^5$) per meter; **b** SEM images of the carbon-nanotube-array cold cathode at a tilt of 45° . The CNTs have an average diameter of 49 nm, height of 5.5 μm , and a spacing of 10 μm ; inset photograph of 16 cathodes; **c** representation of the equivalent electrical circuit, where E is the applied electric field and I the emitted current; CN carbon nanotube; **d** measured average current density plotted against applied radio-frequency electric field using 1.5 GHz sinusoidal input. The circled point corresponds to $I = 3.2$ mA. The cavity-quality factor is 3,160. From Teo et al. [122]. Copyright (2005), Macmillan Publishers Ltd

of conventional traveling wave tubes amplifiers. A traveling wave tube amplifier modulates the electron beam directly by introducing the radio-frequency (RF) signal onto a grid above the thermionic cathode. In CNT array devices, the CNT arrays consist of uniform individual CNTs (average diameter of 59 nm and height of 5.5 μm)

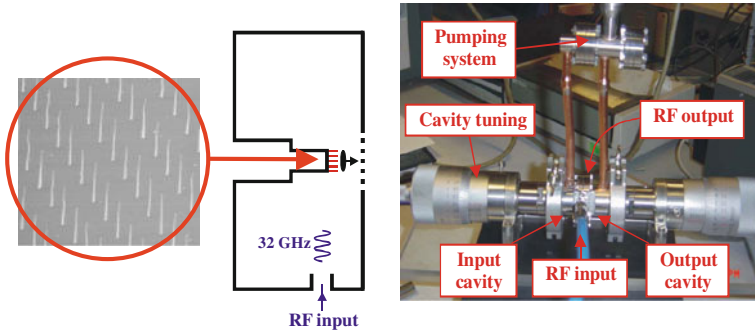


Fig. 8.13 32 GHz cathode-grid assembly (*left*) and experimental setup for 32 GHz modulation (*right*). From Legagneux et al. [126]

with a spacing of twice the CNT height, working as the cathode. The CNTs can be grown by the PECVD method from a catalytic pattern prepared by the e-beam lithography, as discussed in Sect. 6.1.6.2. Such diodes can operate at 1.5 GHz or even 32 GHz holding promises for a new generation of compact microwave devices for telecommunication.

Great care should be taken over the uniformity of the CNT arrays in terms of their height, diameter, spacing uniformity, and tips to ensure the uniform emission from these CNTs [123]. Otherwise, the emission current density from the non-uniform field enhancement factors would be low.

High current densities of 1 A/cm^2 can be obtained under direct current and 1.5 GHz direct modulation using such microwave amplifiers consisted of well aligned CNT arrays [124, 125]. These CNT microwave amplifiers offer considerable weight and size savings over conventional hot cathodes used in microwave applications.

Figure 8.13 shows a microwave amplifier. The triode is designed by associating two coaxial re-entrant cavities (facing each other) [126]. These cavities are separated by a grid, and sized to work at a frequency of 32 GHz. The distances of cathode-grid and grid-anode are, respectively, 100 and $500 \mu\text{m}$. Due to the re-entrant shape of the cathode-grid cavity, higher electric fields are generated at the post apex where a CNT cathode (consisted of CNT arrays with length of $5 \mu\text{m}$ and diameter of 50 nm) is placed. With the device, a 1.4 A/cm^2 peak current density with a 82 % modulation ratio is achieved at 32 GHz.

8.1.9 Other Field Emission Devices

Besides the field emission applications of CNT arrays talked about above, CNT arrays have many other applications based on their unique field emission properties, such as micro time-of-flight mass spectrometer [127].

8.2 Optical Devices

CNTs (with or without a surface coating) can interact with light strongly due to their nanoscale dimensions. The interaction is contributed to either Mie resonances or plasmonic resonances when the frequency of light is close to the CNT surface plasmon frequencies.

When an array of aligned CNTs of uniform sizes is incident with light, each CNT can be viewed as physically identical elements. The intra-CNT factor (interacting with light as individuals) and the inter-CNT factor (interacting with light as pairs or groups) will play a role in the overall interaction behaviors of the CNT array. These two factors can be adjusted by using arrays of different inter-CNT spacings and periodicities, to purposely suppress the other factor. More specifically, the inter-CNT factor is suppressed when the CNTs have a random spatial distribution among each other, where it is suitable to observe the intra-CNT factor in optical antennas and classical nanocoaxes. The intra-CNT factor is suppressed when the CNTs are arranged periodically in space where the inter-CNT factor prevails in the overall characteristics (2D photonic crystals, distributed nanocoaxes, etc.).

The semiconducting CNTs can also interact with light to generate photo-induced carriers in a photoelectric process and can be used in photoelectrochemical solar cells [128], but such effects would not significantly benefit from CNT alignment and are therefore beyond the scope of this book.

The aligned CNTs used for optical devices are 3D ordered. Such 3D ordered CNTs are usually fabricated by the PECVD method described in Sect. 6.1.6.2.

8.2.1 Photonic Crystals

It was reported that the periodic aligned CNTs can diffract light, behaving as polaritonic crystals with formation of polaritonic and photonic band gaps [129]. The photonic crystal behaviors lie in the high aspect ratio of individual CNTs, their alignment, and their wavelength-scale periodic distribution in the plane perpendicular to their alignment which causes high-contrast periodic modulations of the dielectric function of the system [130–135].

Figure 8.14 shows a laser diffraction pattern obtained from an aligned CNT array of hexagonal periodicity and lattice parameters close to the visible wavelengths. The diffraction pattern was obtained by shining a green (560 nm) and a blue (454 nm) laser light perpendicular to the plane of the lattice, and collecting the projection onto an almost flat screen, which allowed for an observation of a large portion of the projected reciprocal space but caused a distortion of the triangular symmetry of the pattern. Apart from this, the pattern is highly rotationally symmetric (except for the third-order blue diffraction spots), showing that the scatters (nanotubes) are circularly symmetric in the plane. Note that there is a rather small hexatic distortion of the pattern, indicating the presence of a possible formation of misaligned crystalline

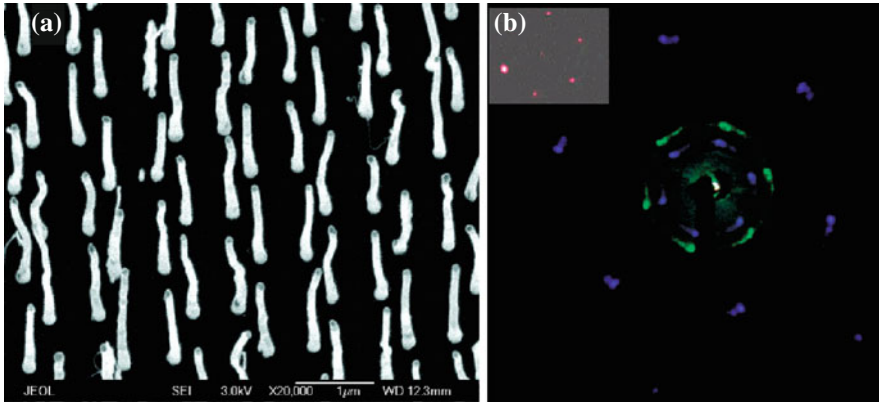


Fig. 8.14 **a** Periodically aligned CNTs arrays; **b** diffraction pattern of laser light at different frequencies by the nanotube arrays shown in **a**. The CNT height is 1 μm . *Inset* diffraction pattern of *red laser light*. From Kempa et al. [129]. Reprinted with permission from American Chemical Society

macro regions. There is also a small diffusive scattering (nonzero Ursell function) resulting from the fact that the nanotubes are not perfectly straight (see Fig. 8.14a). For perfectly straight CNTs, the diffraction spots would be points and the green background around the central spot would disappear. The amount of the spot broadening can be estimated using the Debye–Waller factor and assuming that bent nanotubes can be viewed as effectively displaced from the lattice sites. The inset in Fig. 8.14b shows the diffraction pattern for a red light (680 nm), obtained at an incidence angle of 45° . Note that there is an asymmetry of the spot intensity favoring the forward reflection. This reflects the fact that with increasing angle of incidence, the diffraction pattern must evolve into the in-plane scattering, which according to the Laue construction should consist of only one diffraction spot for a given incoming direction.

The CNTs can be coated to extend the variation scopes of the photonic crystal parameters. They can also be used as structural templates to obtain nonmetallic photonic arrays, including nonmetallic 2D band-gap crystals [129].

8.2.2 Optical Antennae

When individual CNTs in an aligned array have lengths of a few hundred nanometers (wavelength of visible light in air), the CNT array interacts with visible light so strongly that the reflection spectrum shows a series of peaks depending on the CNT length. Such interaction is due to the excited oscillation of the free electron gas of the CNTs by the electromagnetic field, which may further develop into a resonant state if the CNT length L (i.e., the cavity length of the electron oscillation) matches the field wavelength λ such that $L = m\lambda/2$, where m is an integer.

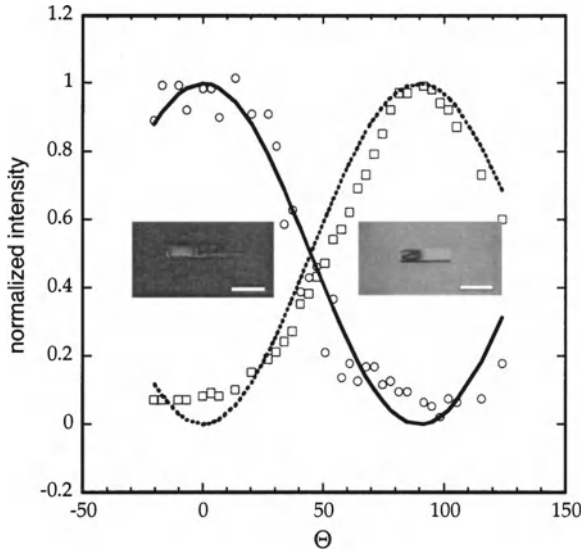


Fig. 8.15 Polarization effect. Reflected, normalized light intensity versus polarization angle θ for the sample shown in the *insets*. *Circles* represent the light intensity from the random array of nanotubes, and *squares* from the metallic film. *Lines* represent the expected functional dependencies: $I = \cos(2\theta)$ for nanotubes (*solid*), $I = \sin(2\theta)$ for the metallic film (*dotted*). *Left inset* sample viewed with the polarization plane parallel to nanotubes (*p*-polarization), $\theta = 0^\circ$. *Right inset* sample viewed through polarizer with the polarization plane perpendicular to nanotubes (*s*-polarization), $\theta = 90^\circ$. Scale bars 1 cm. From Wang et al. [136]. Reprinted with permission from American Institute of Physics

This is in great analogy with conventional dipole antennas reacting with radio waves except that here the operating frequency is much higher (optical frequencies). The CNTs therefore belong to the scope of optical antennas where metallic nanostructures show high scattering/absorption efficiencies with incident light. The alignment of the dipole optical CNT antennas in an array allows the orientation features in the reflection of individual CNT antennas to be preserved in the reflection of the macroscopic array. This means that the polarization effects of a dipole antenna, i.e., the antenna response is strong when the incident light is polarized in the antenna length direction, and suppressed in the perpendicular direction, can be fully observed on the array composed of millions of individual dipoles. Indeed, this is the case (shown in Fig. 8.15) as one observes the sinusoidal variation of the reflection intensity as the incident polarization is rotated with respect to the CNT length orientation [136].

The angular radiation patterns of aligned CNT antennas (Fig. 8.16) have also been recorded using arrays of lower areal densities and of different CNT lengths. Again, the alignment of the arrays allows for the probing of individual CNT characteristics. Using a projection method, the reflection patterns of CNT antennas

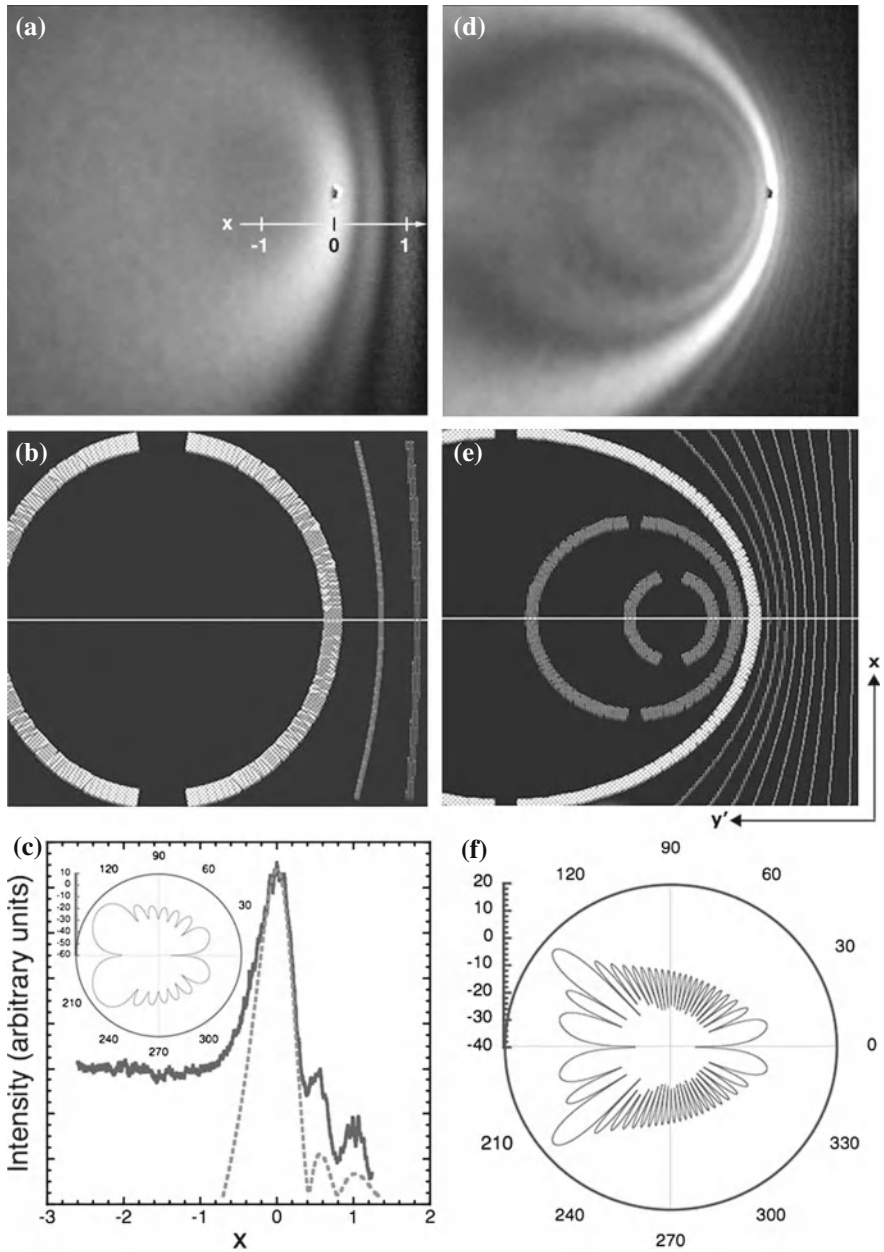


Fig. 8.16 A comparison of the measured (a, d) and calculated (b, e) radiation maps for the CNT antennas of length (a, b) $l = 850\text{ nm}$, and (d, e) for $l = 3.5\ \mu\text{m}$. The light wavelength is $\lambda = 543.5\text{ nm}$, and the angle of incidence is $\theta_i = 40^\circ$. The corresponding calculated freestanding antenna radiation patterns are shown in the *bottom panels* (inset in c and f) (in decibels, i.e., the \log_{10} of the ratio of the incident power to the emitted power). Each pattern was used to calculate the lobe angles for the corresponding middle panel maps. e) The experimental and calculated intensity profiles, taken along the line x indicated in a. From Kempa et al. [131]. Reprinted figure with permission from John Wiley and Sons

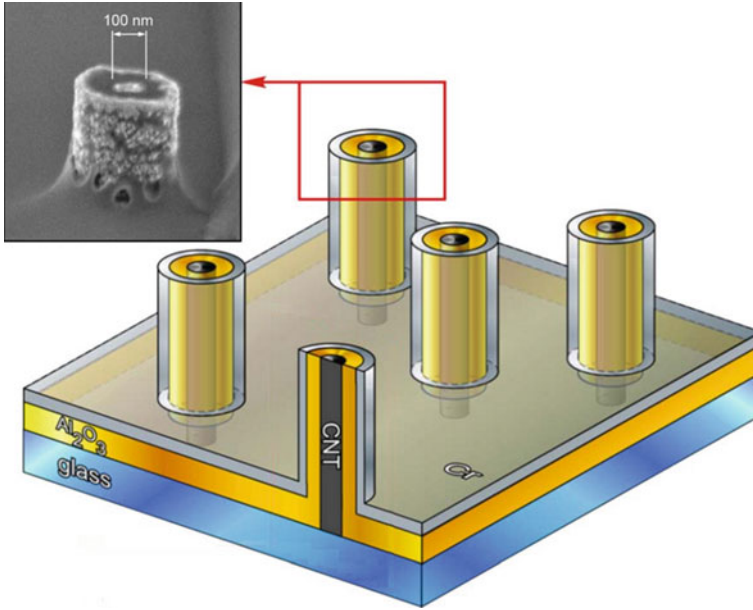


Fig. 8.17 Sketch of a nanocoax array, with SEM images of an exposed end of a nanocoax, a *side view* of a nanocoax with an open section at the substrate revealing the layered structure. From Ryczynski et al. [137]. Reprinted with permission from American Institute of Physics

show consistency with dipole or multipole antenna theories where multiple intensity lobes are confirmed and related to the antenna length. The discovery that arrays of aligned CNTs can work as optical antennas reveals tremendous potentials in future applications in optical and optoelectronic devices, such as optical polarizers, detectors, and solar cells which will be further discussed in the following sections.

8.2.3 Optical Waveguides

CNT coaxial cables (Fig. 8.17) can waveguide visible light. These nanocoaxes are optically long but have subwavelength channel with and they strongly transmit light in the entire visible frequency range without a frequency cutoff. With judicious choice of materials, the propagation is essentially via the conventional transmission electromagnetic mode of a common coaxial cable.

Figure 8.18 shows the results of optical reflection from, and transmission through, a nanocoax array shown in Fig. 8.17 [137]. In Fig. 8.18a, white light is reflected from the top surface of the sample, showing the topography, with dark spots due primarily to absorption of light by the nanocoaxes. When the light is incident from the backside,

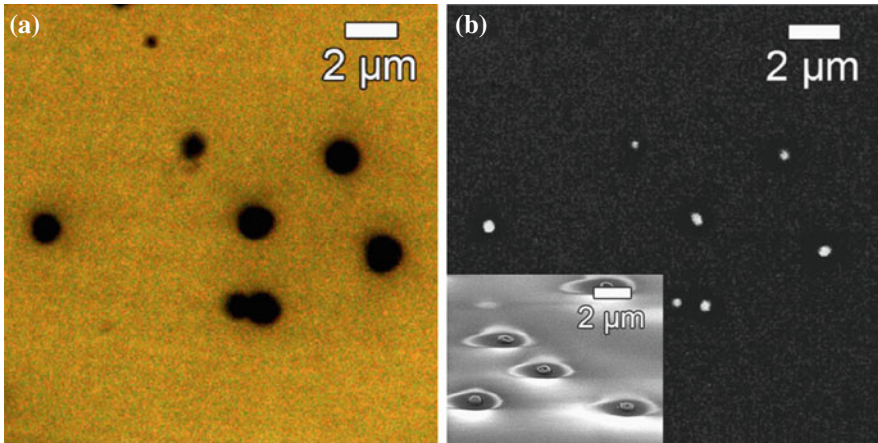


Fig. 8.18 High-resolution optical microscope image of *white light* **a** reflected from and **b** transmitted through the $\text{Al}_2\text{O}_3/\text{Cr}$ -coated CNT nanocoax array medium. *Inset in b*: SEM image of coated CNT nanocoax array (*tilted view*). From Rybczynski et al. [137]. Reprinted with permission from American Institute of Physics

it is absorbed and transmitted along the coaxes and emerges at the top surface, as seen by the spots in Fig. 8.18b for the same region of this sample. Note that the transmitted light remains white, suggesting that there is no cutoff frequency. The inset in Fig. 8.18b shows an SEM image of a nanocoax used for the experiment.

More experiments indicated that a laser beam ($\lambda = 680 \text{ nm}$) can transmit directly through the nanocoax array and the transmission is independent of nanocoax length [137]. Transmission at $\lambda = 532 \text{ nm}$ was obtained for various sample thicknesses (i.e., coax lengths). This length independence is fully consistent with the theoretical value for the photon propagation length ($50 \mu\text{m}$), which is much greater than each film thickness. There is also no cutoff frequency. The nanocoax medium is expected to process transmitted light in a discrete manner by breaking the incoming plane wave into wavelets, transmitting it to the other side, and then re-assembling the plane wave on the other side of the medium. For straight, identical coaxes, the re-assembled wave retains all the propagation characteristics of the incoming wave. This explains the observed lack of beam divergence.

By replacing the inter-electrode dielectric with a nonlinear material in each nanocoax, one may achieve light mixing, switching, or phase conjugation. The nanocoax structures described here can be fabricated from a wide variety of materials. The inner and outer conductors can be made from any appropriate metal, using soft (e.g., templated electrodeposition, CVD) or hard (electron or focused ion beam lithography) techniques, and the choice of dielectrics is extensive [137]. Moreover, the coupling of radiation (light) to the nanocoax can be achieved in ways other than the linear antenna described here.

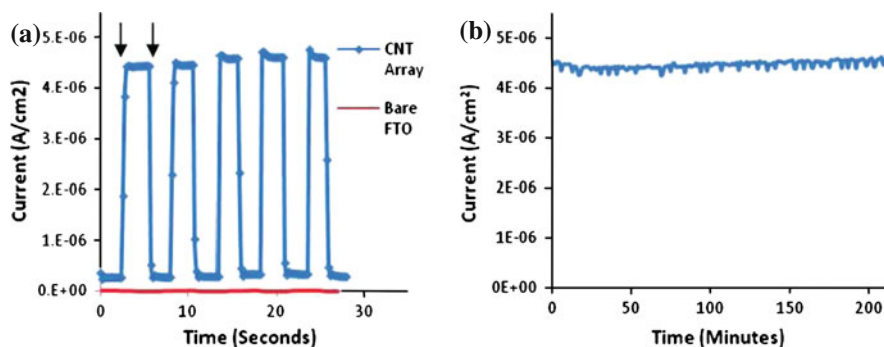


Fig. 8.19 **a** On–off light response from the FTO-CNT cell and blank cell containing no CNTs. The *arrows* indicate the light on and off cycles; **b** light-soaking response of the same cell left under illumination for over 200 min; *FTO* fluorine-doped tin oxide glass [142]

8.2.4 SWCNT Array Solar Cells

The photoresponse of carbon nanotubes was first observed in 1999 [138] and further photocurrent generation was investigated over the next decade. The unique density of states of carbon nanotubes allows for electron–hole generation when CNTs are exposed to light. Semiconducting SWCNTs with optimal chirality and tube diameter may have a band gap of about 1 eV, easily produce electron–holes under solar irradiation. Existing researches have confirmed the photoresponse of SWCNT films [139–141].

Vertically aligned SWCNT arrays are employed to produce photocurrent [142–144]. Figure 8.19 shows the photocurrent produced when a light source was switched on and off. Obviously, the SWCNT arrays produce noticeable photocurrent (Fig. 8.19a), approximately $4.5 \mu\text{A}/\text{cm}^2$, when exposed to light. The photocurrent response time to both the on and off cycles is about 200 ms, indicating that the photocurrent response is not a gradual response but a very quick and well-defined increase. Also, once exposed to light, the photocurrent appears to be constant over time (Fig. 8.19b). These data show that, over an extended period, there is a consistent photocurrent output by the SWCNT cells, with no noticeable drop in photocurrent. The produced photovoltage is 40 mV.

8.2.5 Solar Cells Based on MWCNT Nanocoaxes

Coated MWCNT arrays have also been employed as solar cells. The particular geometry of aligned CNTs allows a layer-by-layer deposition strategy to fabricate an array of nanocoaxes of various thin films in the CNT radial direction. One typical application example of such nanocoax structures is a new type of solar cells where active

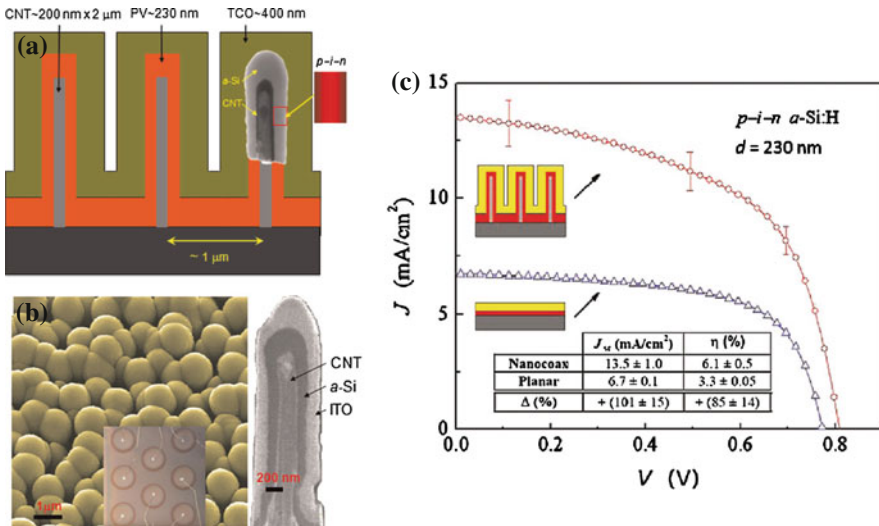


Fig. 8.20 **a** Schematic of the MWCNT nanocoax solar cell architecture and **b** an SEM image of the surface of a completed cell. In the schematic drawing of the coax, CNT means Ag coated MWCNT. *Inset in (a): (inside) TEM image of the coax, and (right) p-i-n junction sequence; inset in (b): (inside) photograph of a nanocoax cell (each circular contact is about 3 mm in diameter), and (right) TEM image of a single completed nanocoax, prepared by FIB.* From Paudel et al. [145]. Reprinted figure with permission from John Wiley and Sons

photoabsorbers such as *p-i-n* amorphous silicon thin films are sandwiched between two coaxial metallic layers.

A schematic of the MWCNT nanocoax solar cells based on multi-walled carbon nanotube arrays, is shown in Fig. 8.20a. Vertically aligned MWCNTs work as the pillars/inner electrodes. These are of 200 nm diameter and 2 mm height, grown on Cr-coated glass, and coated with Ag (gray pillars). The periodicity of the array is achieved by nanolithographically defining the catalyst sites for the MWCNT growth. Such MWCNT arrays have been coated with hydrogenated *a-Si* in a radial *p-i-n* (*p* closest to the core) configuration as the photovoltaic absorber by PECVD. Finally, ITO is deposited by sputtering, providing the outer coaxial conductor and completing the nanocoax structure. A transmission electron microscope image of a carbon nanotube coated with *a-Si* in a nanocoax is shown as the inset in Fig. 8.20a. Figure 8.20b shows a scanning electron microscope image of a completed nanocoax array. The inside inset shows a photograph of a 2 cm² nanocoax cell, with eight circles of deposited ITO for photovoltaic measurements. The right inset shows a single completed nanocoax, prepared by focused ion beam (FIB) to expose all three components of the coax. In this case, the nanotube was precoated with a thin (50 nm) layer of Ag (bright fringe around nanotube coax core) to enhance its electrical conductivity. The average absorber (*a-Si*) thickness for this cell is 230 nm.

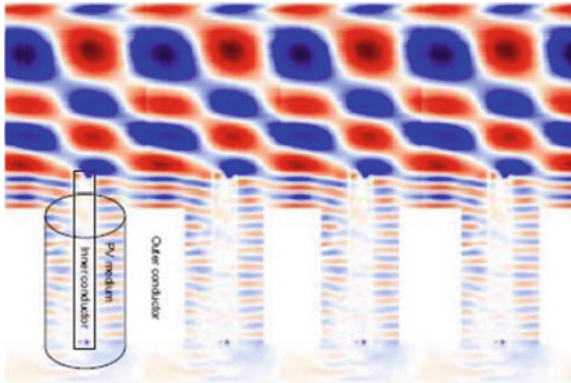


Fig. 8.21 Computer generated simulation of 500 nm light propagation (from above) into an array of nanocoaxial structures, plotting the electric field amplitude E (red and blue indicating + and – sign of E). The outline of one coax is shown on the left, where the components of the structure are indicated

This variation of the conventional thin-film amorphous silicon solar cell structure may allow separation of the photonic absorption length in the absorber from the photoexcited carrier collection distance to achieve superior energy conversion efficiencies [146]. The fabricated structure utilizes a distributed nanocoax scheme where, unlike in the classic nanocoax scheme [137, 147], each individual nanocoax does not have an opaque outer conductor shell, while the metallic cores of the neighbor nanocoaxes function effectively as its outer shell. Indeed, clear photocurrent enhancement has been observed in these nanocoax solar cell structures using very thin absorber layers (~ 180 nm).

It should be pointed out that in these devices, the aligned CNTs are mostly structural templates on which consecutive metallic and semiconducting layers are deposited. The low-cost nature of the CNT growth process gives the aligned CNTs an advantage over other similar templates such as etched single-crystalline silicon wafers.

The power conversion efficiency of an exemplary nanocoax solar cell (0.18 cm^2 total area) is $\eta = 6.1 \%$. As demonstrated in Fig. 8.20c, this performance well exceeds (about 50% higher) the efficiency of a planar cell with similar absorber thickness ($\eta = 3.3 \%$) [146].

Finite differential time domain (FDTD) simulations have been carried out on these nanocoax solar cell structures to show that light propagation will be highly confined to very thin absorber layers if the nanocoaxes are microns long and have subwavelength spacings. Figure 8.21 shows an example of the light intensity distribution of a typical nanocoax thin film solar cell.

FDTD simulations show the transverse electromagnetic waves propagates along the coax. The electric field strongly damped toward the base of the coaxes inside the

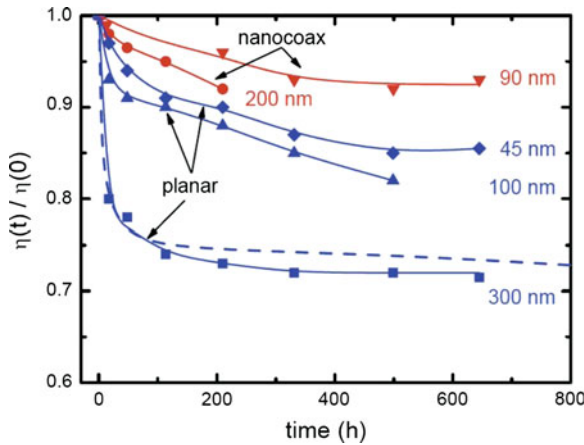


Fig. 8.22 Light-induced degradation of representative planar and nanocoax cells with various PV thickness. Note that the nanocoax cells have about half the degradation of their planar counterparts. *Dashed line* is Wronski's result for a conventional planar *a*-Si solar Cell. From Paudel et al. [145]. Reprinted figure with permission from John Wiley and Sons. The 200 nm nanocoax sample was inadvertently damaged after 200 h

a-Si absorber and in between the closely spaced coaxes. The open circuit voltages for the MWCNT solar cells is 0.81 V, comparable to that of planar cells, 0.78 V. On the other hand, the short-circuit current density for the MWCNT nanocoax cell (13.5 mA/cm^2) exceeds that of the planar control sample (6.7 mA/cm^2) by about a factor of 2, due to the increased path of photons in the nanocoax geometry. The initial energy conversion efficiency of the MWCNT nanocoax solar cells is 6.1 % and higher than 10 % is expected with improvements in the uniformity of the *a*-Si film coating, and change to a tighter, hexagonal geometry.

These cells were also shown to have less Staebler–Wronski degradations [145] due to their smaller absorber layer thicknesses (Fig. 8.22).

Similar solar cell fabrication schemes can be employed at a larger scale where the CNT towers can be used as templates to deposit the thin-film solar cell layers (Fig. 8.23). The efficiency can be doubled [148] from 3.5 % in a planar configuration to 7 % in the CNT tower configuration at 45° solar incidence with CdTe thin film absorbers (Fig. 8.23a). In another instance, a short-circuit current enhancement of 25 % has been achieved [149] over the conventional planar structure, owing to the highly effective light-trapping structure of the coaxial MWCNT/*a*-Si:H nanowire array (Fig. 8.23b). In this case, the nanocoax effect is absent due to the large dimensions of the structures and the performance enhancement is purely expected from the enlarged surface area of the absorber material and the higher ray scattering frequency for broad incident angles due to the 3D geometry.

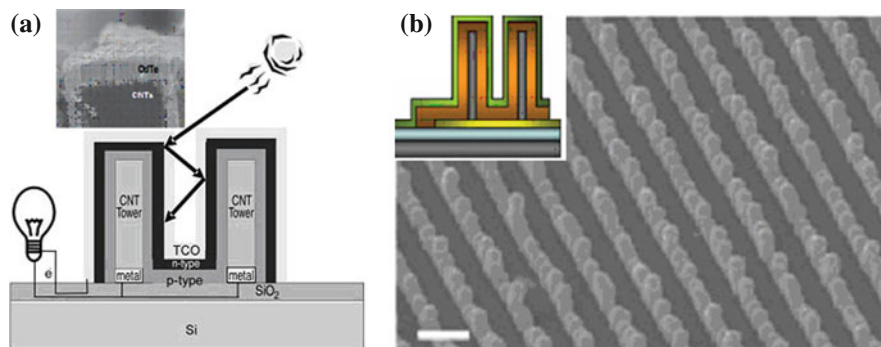


Fig. 8.23 **a** CdTe solar cell deposited on towers of aligned CNT arrays; *inset* SEM image of a cut tower; **b** SEM image of line-patterned array of coaxial MWCNTs (ITO and amorphous silicon-coated CNTs). *Inset* schematic of the coaxial MWCNTs. Scale bar: 2 μm . **a** From Camacho et al. [148]. Copyright (2007), Springer. **b** From Zhou et al. [149]. Copyright (2009), John Wiley and Sons

8.3 Nanoelectrode-Based Sensors

Individual CNTs can be semiconducting or metallic, and are good candidates for various sensors. Up to now, lots of sensors, such as the mass sensors, have been fabricated from individual CNTs. The unique electronic, chemical, and mechanical properties of CNTs make them extremely attractive for applications in chemical and biochemical sensors [26, 150]. Most CNT sensing platforms take advantage of the unique properties of CNTs, such as increased electrode surface areas [151] and high electron transfer rates [152]. It is well known that the electron transfer rate of the electrode is dominated by its surface structure. The sidewall atomic structure of MWCNTs is similar to the graphitic basal plane and the open-end of CNTs is similar to the edge-plane. Because the electron transfer on edge-plane graphite is faster than that on the basal-plane graphite, the open ends of the CNTs have higher electron transfer rates similar to a graphitic edge-plane electrode [153], while the sidewalls exhibit very low electron transfer rates similar to the graphitic basal plane. It is reported that the high-site-density CNT array and CNT forest show fast electron transfer characteristics [152, 154].

In this section, we review the CNT nanoelectrode arrays and their applications as sensors.

8.3.1 Nanoelectrode Arrays

Microelectrode arrays consisting of hundreds of metal microelectrodes with diameters of several micrometers have been fabricated by lithographic techniques [155]. The microelectrodes show many advantages over the conventional macroelectrodes such as high mass sensitivities, enhanced mass transport, and a decreased influence

from the solution resistance. Further size reductions of each individual electrode to nanometers and an increase in the density of electrodes can improve the detection limits and the signal-to-noise ratio [156] since the noise level depends on the active area of the individual electrode, whereas the signal strength depends on the total area of the electrodes [157]. Such 2D nanoelectrode arrays have been fabricated based on gold nanowires [158].

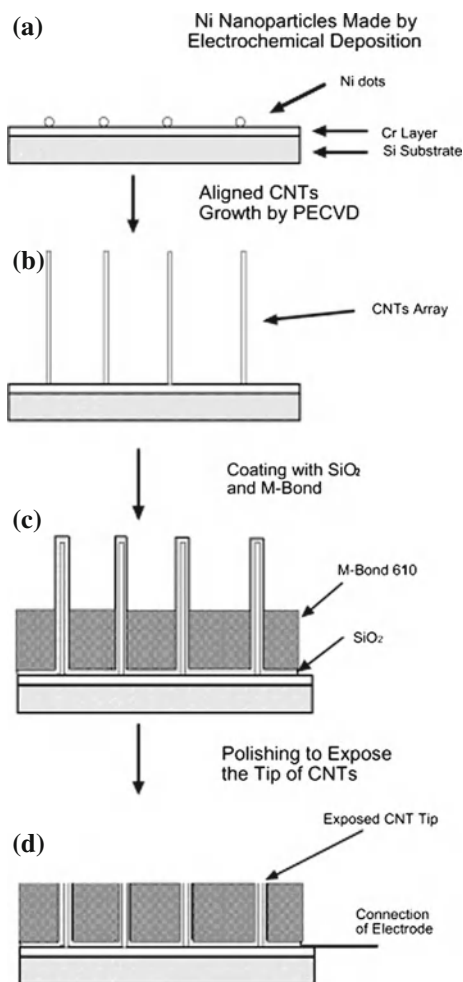
SWCNTs exhibit high electrical conductivities and are the most promising candidates for miniaturizing electrodes beyond the micrometer-scale electrodes currently used in electronics. Up to now, CNT-based nanoelectrodes have already been fabricated [156, 159–170]. These CNT nanoelectrode arrays are based on the advantages of CNT materials over conventional macroelectrodes such as enhanced mass transport and decreased influence from the solution resistance, which makes an excellent electrochemical transducer in various applications. The aligned CNT nanoelectrode has a high mass sensitivity, an increased mass-transport rate, a decreased influence from the solution resistance, and a higher signal-to-noise ratio, leading to a much lower background current than other electrode configurations. For example, the CNT array of nanoelectrodes can produce a much higher current than a single nanoelectrode [171] and bundles of CNTs [172, 173], which can improve the signal-to-noise ratio.

CNT nanoelectrode arrays are fabricated with aligned CNTs of low site densities. Such aligned CNTs can be grown by PECVD method from catalytic patterns, as described in Sect. 6.1.6. To make each CNT working as an individual nanoelectrode, the spacing needs to be sufficiently larger than the CNT diameter to prevent the diffusion layer from overlapping with the neighboring electrodes [174, 175].

The signal-to-noise ratio of an electrode array depends on the electrode area, the perimeter-to-area ratio of the electroactive portion of the surface, the mass transfer coefficient of the analyte—electrode combination, the measurement bandwidth, and the sources and magnitudes of the noises [157]. Previous work on microelectrode (5 μm -radius) arrays indicated that the signal-to-noise ratio is better for the electrode array than for a solid electrode [176]. Signal-to-noise ratio of an microelectrode array (millimeter dimension, consisting of about 1 % active surface) can improve an order of magnitude over solid electrodes [157], with a sensitivity of 10^{-10} M. CNT nanoelectrode arrays with low-site-density are consisted of millions of nanoelectrodes with each electrode being less than 100 nm in diameter. The size reduction of each individual CNT electrode and the increased total number of CNT electrodes should result in improvements in both the signal-to-noise ratio and the detection limits of CNT array-based nanoelectrode arrays.

The fabrication of CNT nanoelectrode arrays has been described in existing literatures [91, 156, 177]. Figure 8.24 shows the SiO_2 /epoxy-coated nanoelectrode arrays. The CNTs are directly grown on the conductive substrate to ensure good electrical conductivity to the external circuit. In a typical experiment, Ni catalytic nanoparticles are electrodeposited on a Cr-coated Si substrate of 1 cm^2 in area (Fig. 8.24a). The site density of the catalytic nanoparticles is low. Aligned CNT arrays are then grown from those Ni nanoparticles by PECVD (Fig. 8.24b). Next, the CNT spacings are filled by epoxy spin-coating or other coating methods (Fig. 8.24c). In a typical

Fig. 8.24 Fabrication scheme of the nanoelectrode arrays. **a** Ni nanoparticle electrodeposition; **b** growth of aligned CNT; **c** coating of SiO₂ and M-bond; **d** polishing to expose CNTs. From Tu et al. [156]. Reprinted with permission from American Chemical Society



filling process, an epoxy-based polymer with a curing agent is spin-coated on the substrate and covers up to half of the CNT length. The protruding parts of the CNTs are mechanically removed subsequently by polishing (Fig. 8.24d).

Figure 8.25 shows the SEM images of the CNT nanoelectrode array fabrication steps corresponding to the scheme shown in Fig. 8.24. The bright dots in Fig. 8.25a are the electrodeposited Ni nanoparticles that are randomly distributed on the substrate. Figure 8.25b shows the low density aligned CNT array grown by PECVD from the Ni nanoparticles. Figure 8.25c shows the morphology after coating with a thin layer of SiO₂ followed by a second layer of epoxy film. The CNT arrays are half-embedded in the polymer. Figure 8.25d provides a close-up look at a single half-embedded CNT. Figure 8.25e shows the topography after mechanical polishing. It is clearly shown that only the tips of the embedded CNTs are exposed. To prove that the tips

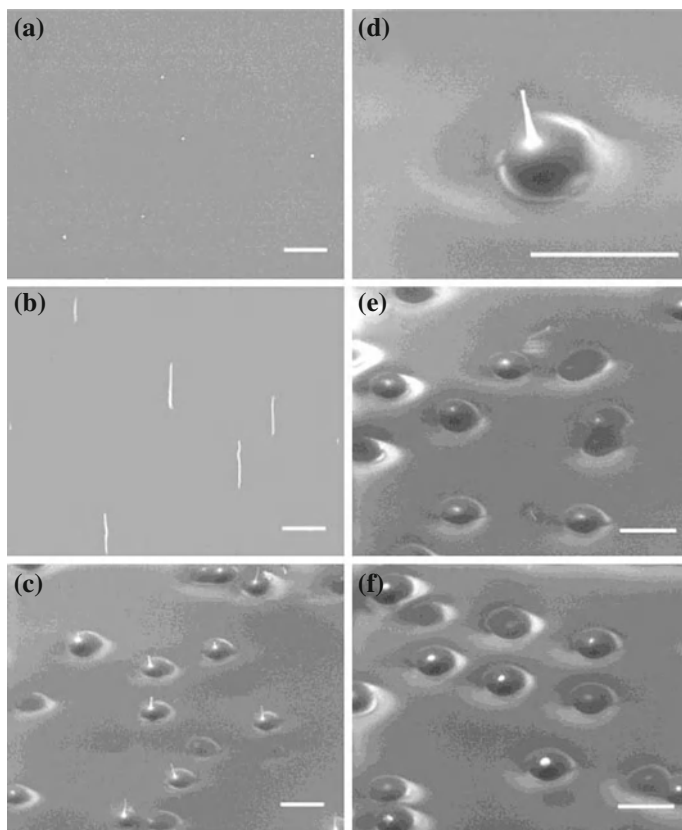


Fig. 8.25 Scanning electron microscope images of CNT nanoelectrode array fabrication. **a** *Top view*; **b–f** from a 45° *side view*. All of the scale bars represent $5\ \mu\text{m}$. **a** Electrodeposited Ni nanoparticles; **b** low-site-density-aligned CNT array; **c** CNT array coated with SiO_2 and an epoxy layer; **d** close-up look at a single half-embedded CNT; **e** CNTs after polishing; **f** second electrodeposition of Ni nanoparticles on the broken CNT tips only. From Tu et al. [156]. Reprinted with permission from American Chemical Society

of the CNTs are exposed and conducting, electrodeposition of Ni nanoparticles is repeated. Figure 8.25f shows that the Ni nanoparticles are deposited only on the CNT tips, nowhere else. This also indicates that the carbon nanoelectrode array could be used as a template to fabricate other metal nanoelectrodes.

For successful fabrication of nanoelectrode arrays, two important requirements exist. First, the inter-spacing of the individual electrodes should be much larger than the radius of each electrode; otherwise, a closely packed nanoelectrode array will behave similarly to a macroelectrode due to the diffusion layer overlap [155, 165, 178–181]. The cyclic voltammogram measurements indicate that [177] there is no

diffusion layer overlapping between the nanoelectrodes when the CNTs are separated from their nearest-neighbors by at least $5\mu\text{m}$, which is much larger than the diameter of each CNT (50–80 nm). Therefore, controlled low site density of aligned CNTs is the key for the fabrication of CNT nanoelectrode arrays, which can be done by tuning the site density of Ni nanoparticle catalysts, using an electrochemical deposition method [91].

The CNT forest electrodes or high-site-density CNT arrays do not act as individual nanoelectrodes because the high site density of the CNTs causes the overlapping of diffusion layers of individual nanoelectrodes, as discussed in Sect. 8.1.1. To make each CNT work as an individual nano-electrode, the spacing needs to be sufficiently larger than the CNT diameter to prevent diffusion layer from overlapping with the neighboring electrodes. The microsphere lithography method is a good technique to prepare nanoparticle catalysts with low site densities. The electrodeposition method is also suitable to prepare such catalysts for low-site-density growth. In order to take advantage of a high electron transfer rate, the CNT tips are always opened. To eliminate the background current leakage generated from the sidewalls of CNTs and the electrode capacitance, the sidewalls are sealed with an epoxy passivation layer. Such a structure provides a high signal-to-noise ratio.

Secondly, there must be a passivation layer that can protect the underlying conducting layer as well as prevent current leakage and corrosion. Both inorganic materials, such as SiO_2 and Si_3N_4 , and organic materials, such as epoxy and photo resist, have been previously tested [182]. The ideal passivation layer is captive and crack-free, long lasting in aqueous electrolyte solutions, adhering well to substrates and electrodes, mechanically strong, and easily processable. Insulating materials should be good enough to prevent the current leakage that results in the distortion of the cyclic voltammetry curve. Very low background current and leakage current are achieved when the CNT arrays are excellently sealed by the spin-coated epoxy resin, which enables the sensitivity analysis [177].

The cyclic voltammetry curve of the CNT nanoelectrode arrays (Fig. 8.26) indicates that the signal (in the range of microamperes) generated from the nanoelectrode arrays is much larger compared to the signal (a few picoamperes) generated from a couple of carbon electrodes with a similar disk shape [159] because the total current for the loosely packed electrode array is proportional to the number of individual electrodes [175]. The interested readers are referred to some review literatures [167, 183] on electrochemical properties of CNT array electrodes for more details.

Compared to the traditional macroelectrode, the aligned CNT nanoelectrode has a high mass sensitivity, an increased mass-transport rate, a decreased influence from the solution resistance, and a higher signal-to-noise ratio, leading to a much lower background current. Therefore the nanoelectrodes have many practical applications such as ultrasensitive electrochemical sensors for chemical and biological sensing. In the next several subsections we will talk about some of these applications.

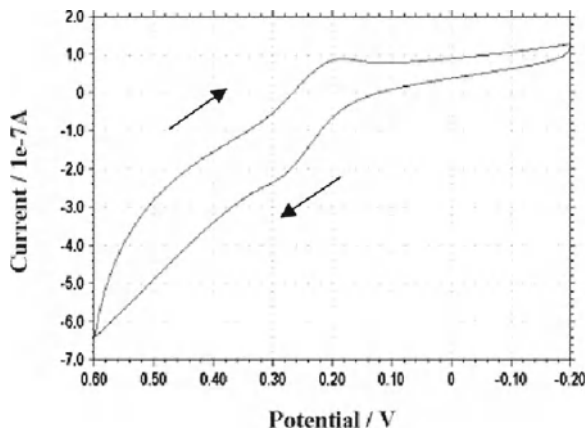


Fig. 8.26 Cyclic voltammetry curve of the carbon nanoelectrode arrays. The curve was taken in a solution of 4 mM $K_3Fe(CN)_6$ in 0.5 M KNO_3 . The scan rate was 40 mV/s. From Tu et al. [156]. Reprinted with permission from American Chemical Society

8.3.2 Ion Sensors

The low-site-density CNT arrays are usually employed as CNT ion-sensing platforms. The CNT sensing platforms are fabricated similarly to nanoelectrode arrays, as shown in Fig. 8.24. In a typical process, a CNT array is grown first by PECVD [166]. The site density of the aligned CNTs is controlled by tuning the site density of catalytic nanoparticles. The site density is typically $1\text{--}3 \times 10^6$ tubes/cm², depending on the final length of CNTs. An epoxy resin layer of microns thick is coated on the aligned CNT arrays grown on the substrate surface using a standard spin-coating method. The aligned CNTs show very good mechanical stabilities and preserve their vertical alignment. The CNTs are half-embedded in the resin with 2–3 μm of length protruding from the resin surface. By using a lens paper to gently polish the coated CNTs, the protruding parts are broken and removed by ultrasonication in water. Then an electrical connection is made to the CNT substrate to produce an ion-sensing platform.

Square-wave voltammetric measurements are carried out in an electrochemical cell containing a CNT-array working electrode, a Ag/AgCl reference electrode, and a platinum wire counterelectrode. A magnetic stirrer together with a magnetic bar provides the convective conditions when needed.

Figure 8.27a presents a typical square voltammogram for a mixture containing 5 $\mu\text{g/L}$ cadmium ions and lead ions. A well-defined, undistorted, sharp signal with a favorable resolution is obtained. The peak potentials of cadmium and lead are +0.75 and +0.55 V, respectively. The stripping signal for the selected target metals is surrounded with low background contributions, indicating effective sealing on the sidewalls of CNTs during the preparation of the nanoelectrode array. The very

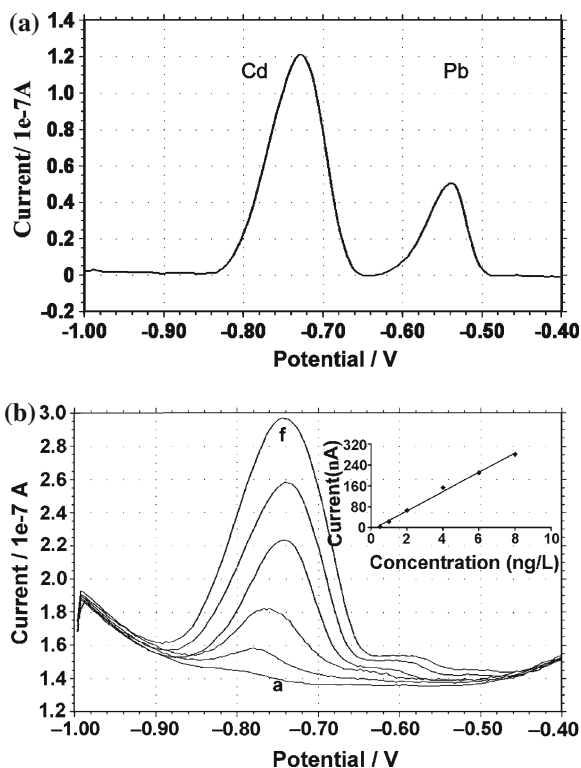


Fig. 8.27 **a** Typical square wave voltammogram of $5 \mu\text{g/L}$ cadmium and lead in 0.1M acetate buffer ($\text{pH} = 4.5$) in the presence of $500 \mu\text{g/L}$ bismuth; **b** square wave voltammograms response of cadmium solution with increasing concentration ($0.5, 1, 2, 4, 6, 8 \mu\text{g/L}$). The *small shoulder peaks* at -0.57V are attributed to a trace of lead in the blank solution. A square-wave voltammogram scan with step potential: 5mV ; amplitude: 20mV ; and frequency: 25Hz . From Liu et al. [184]. Reproduced with permission from The Royal Society of Chemistry

attractive signal-to-noise characteristics and peak resolution indicate that the aligned CNT array can be used as an excellent electrochemical sensing platform [184].

Figure 8.27b displays the square voltammograms response of an aligned CNT-array for increasing cadmium ion concentrations under the optimum experimental conditions. Well-defined peaks, proportional to the concentration of the corresponding cadmium, are observed. A linear relationship between the stripping current and cadmium concentration is obtained covering the concentration range from $0.5 \mu\text{g/L}$ to $8 \mu\text{g/L}$, as the linear regression equation being $I = 37.054 \times \phi - 10.486$, with a correlation coefficient of 0.9955 , where I in nA, concentration ϕ in $\mu\text{g/L}$. The detection limit is improved significantly by increasing the accumulation time. A detection limit of $0.04 \mu\text{g/L}$ (40ppm) is estimated on the basis of an $S/N = 3$ characteristic of the $0.1 \mu\text{g/L}$ data points in connection with a 240s accumulation time. Such

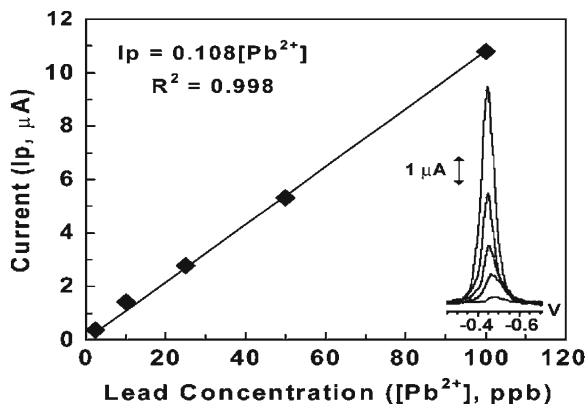


Fig. 8.28 The voltammetric response (current) of Pb^{2+} in 0.1 M NaNO_3 solution as a function of Pb^{2+} concentration, measured after 3 min of deposition. Pulse amplitude: 25 mV; step amplitude: 5 mV; frequency: 100 Hz. The voltammograms correspond to Pb^{2+} concentration of 2, 5, 25, 50, and 100 ppb. From Tu et al. [166]. Reprinted figure with permission from John Wiley and Sons

improvement of the stripping signal and extremely low detection limit benefit from the high signal-to-noise ratio of CNT arrays.

Lead is regarded as a highly toxic metal ion to a wide variety of organs in both human and animals, including nerves, immune, reproductive, and gastrointestinal systems. The ability to rapidly detect a trace amount of Pb^{2+} species on-site is very desirable. Figure 8.28 shows that the voltammetric response is a linear function of Pb^{2+} concentrations ranging from 2 to 100 ppb [166]. The lead concentration can be detected at a very low level of several parts per billion. The inset shows the response peaks of 2 to 100 ppb of Pb^{2+} .

The CNT array sensing platform shows potential to detect very low concentrations of heavy metal ions compared to a traditional bulk and macro-electrode sensing platform [184].

Besides trace Pb^{2+} and Cd^{2+} heavy metal ions, Cu^{+2} and Zn^{+2} ions can also be detected using highly aligned MWCNT electrodes [185]. The detection limits of 44 and 67 nM for Cu^{2+} and Zn^{2+} are achieved, respectively, for a deposition time of 120 s. The detectable limit can be as low as 0.5 nM for a 10 min deposition.

8.3.3 Gas Sensors

A gas chemical sensor can be defined as a device that responds to changes in the local gas environment. The response should be predictable such that it scales with the magnitude of change in the gas environment. Additionally, a gas sensor should be sensitive and selective to the chemical molecule concerned. CNTs are good candidates for chemical detection, because the nanoscale dimensions and exceptionally

large surface area of CNTs make them more environmentally sensitive than bulk materials.

CNT-based gas sensors were demonstrated as early as in 2000 when the responses of CNT field-effect transistor, mainly made of a single semiconducting SWCNT, to NO_2 and NH_3 gases were reported [7]. NH_3 exposure resulted in a shift in the transfer characteristic gate voltage of approximately -4 V , while NO_2 exposure created a shift of approximately $+4\text{ V}$. Alternatively, when the transistor was held at a constant gate voltage of $V_G = 0\text{ V}$, exposure to NH_3 resulted in a decrease in the device current, while NO_2 exposure ($V_G = +4\text{ V}$) resulted in an increase. The response time to 200 ppm NO_2 was a few seconds, and the sensitivity, defined as the resistance after exposure divided by the initial resistance, was approximately 100–1,000. The response time to approximately 1% NH_3 was a few minutes with a sensitivity between 10 and 100. A floodgate of interests in the development of CNT-based gas sensors was generated by these initial results of CNT gas-sensing capabilities.

Up to now, thousands of scientific papers focused on the CNT gas sensors have been published [186]. CNTs have shown sensitivities toward gases such as NH_3 , NO_2 , H_2 , C_2H_4 , CO , SO_2 , H_2S , and O_2 . In all these sensors, the excellent properties of CNT gas sensors depend on the unique properties of individual CNTs, such as large surface-to-volume ratio, high aspect ratio, and good electric properties, and on the alignment properties. To date, most of these demonstrated sensors are fabricated from random or individual CNTs in the configurations of CNT-based field-effect transistors [7, 13, 187, 188]. The gas sensors made of individual CNTs or random CNT networks are well reviewed recently [186, 189–195]. Some gas sensors are also fabricated from CNT arrays and reviewed recently [459]. Here, we focus on the application of CNT arrays in gas and vapor sensors.

The aligned CNTs should be a better candidate of gas sensors. The aligned CNTs can be 1D ordered, directly grown on random catalysts by PECVD method (see Sect. 6.1.6.1) or by thermal CVD method (see Sect. 6.1.1), or be 3D ordered, grown from 2D ordered catalysts by PECVD method (see Sect. 6.1.6.2). The expose of gas molecules causes the change in electrical properties (electron emission properties, resistivity, frequency, capacity) of aligned CNTs. The aligned CNT arrays amplify the changes to increase sensitivity of the CNT gas sensors. These CNT array gas sensors have an outstanding sensitivity at low temperatures of fast response and high selectivity [196].

Two types of gas sensors using CNT arrays have been proposed. One kind is the gas *ionization sensor*, in which CNTs are used as field-emission electrodes to ionize the analyzing gas, resulting in high gas selectivity and sensitivity [197]. Another type is *resistance-based sensors* based on a change of the electrical conductance of CNTs when adsorbing gas molecules. The mechanism of this kind of gas sensors is based on the dependence of CNT electrical resistance with ambient gas concentration. When the *p*-type semiconducting CNTs adsorb oxidizing molecules, electrical resistance of the CNTs decreases with the number increase of the adsorbed gas molecules. In other words, the electrical conductance of *p*-type semiconducting CNTs is modified by the electron transfer between CNTs and oxidizing or reducing gas molecules adsorbed on the CNT surfaces. This kind of a gas sensor has extremely high sensitivity and fast

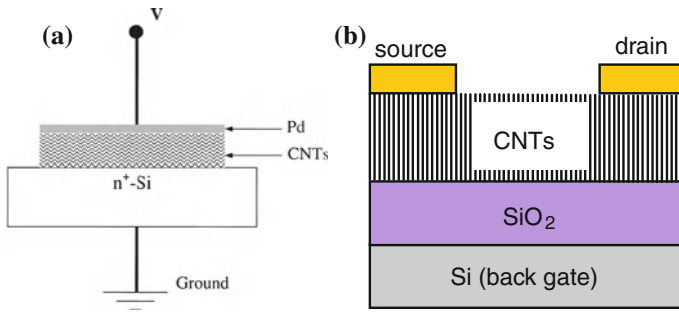


Fig. 8.29 Schematic cross-section views of **a**) two-terminal and **b**) three-terminal CNT gas sensors. **a**) From Wong et al. [203]. Copyright (2003), Elsevier. **b**) From Huang et al. [250]. Copyright (2005), Elsevier

response at room temperature and is compatible with integrated circuit fabrication, while it cannot detect several gases simultaneously.

The resistance-based sensors are the two-terminal (Fig. 8.29a) or three-terminal (Fig. 8.29b). The two-terminal sensors are simple, while the sensitivity of the three-terminal sensors is higher.

8.3.3.1 Hydrogen Gas Sensors

The risk of explosion is the primary reason for the needs to accurately measure H₂ levels in air since the air with hydrogen concentrations as low as 4% can become explosive. Bare CNTs do not show appreciable sensitivity to H₂ due to the weak binding energy of hydrogen to the surfaces of CNTs [198]. After being decorated or functionalized by Pd or Pt nanoparticles on their sidewalls, the CNTs can detect the ppm level of H₂ gas [199, 200]. It is believed that H₂ dissociates as atomic hydrogen on the Pd or Pt nanoparticle surface at room temperature to form PdH₂ or PtH₂, decreasing the Pd or Pt work function and leading to electron donation into the CNTs from the nanoparticles [201, 202]. As a result, the electrical resistance of the Pd- or Pt-decorated CNT decreases, yielding a response time of a few seconds.

Figure 8.30a shows an SEM image of a vertically aligned CNT array grown in an anodized aluminum oxide (AAO) template used for room-temperature detection of ppm concentrations of H₂. The CNTs are coated with a Pd film to form a two-terminal gas sensor to enhance the sensitivity of the H₂ gas sensors. The electrical resistance varies with the concentration of H₂ (Fig. 8.30b). The Pd-coated CNT array sensor is sensitive to hydrogen gas concentrations from 100 ppm to 1.5% at room temperature.

H₂ is also detected by a Pd/MWCNT Si thin-film sandwich structure [203]. The thin layer of Pd is sputtered on top of the MWCNT array. The current is reduced in the presence of hydrogen and the reduction is attributed to an increase in the barrier height between the Pd-CNT interface after H₂ adsorption.

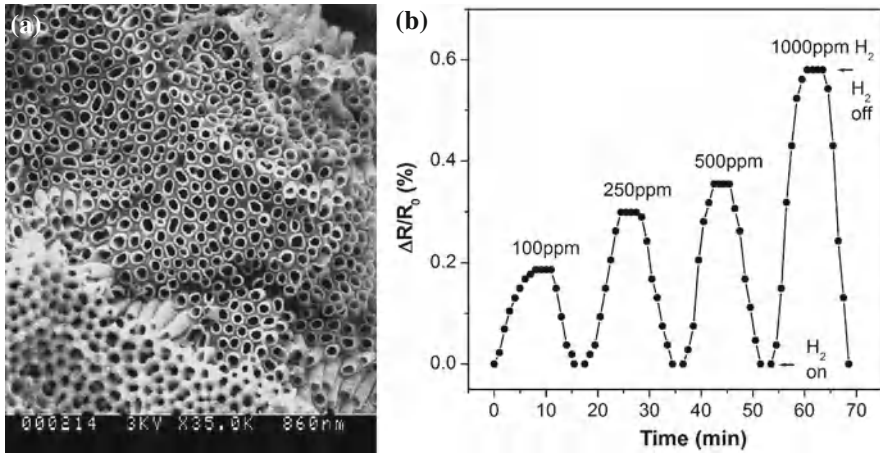


Fig. 8.30 **a** Aligned CNT array grown from an AAO template; **b** response of a CNT array coated with a Pt film to H_2 exposure expressed as the relative change of electrical resistance R/R_0 at zero gate voltage. From Ding et al. [202]. Copyright (2007), Elsevier

Besides the CNT arrays, CNT thin films and random CNT bulks can also be used for hydrogen sensors [200]. Here we do not cover the applications of random CNTs.

8.3.3.2 Nitrogen Gas Sensors

The electrical resistance of CNTs is found to increase when CNTs are exposed to the reducing N_2 gas [204]. Figure 8.31a shows the electrical resistance variations of a three-terminal sensor consisting of CNT arrays upon exposure to a N_2 filling and pumping environment. After CNT arrays are grown on a SiO_2/Si substrate from patterned catalysts, the silicon substrate on the backside acts as the gate of the sensor. The structure of the sensor is shown in Fig. 8.29. Source and drain electrodes are biased at 10 V with zero gate voltage. Since N_2 is a reducing gas [204], CNTs receive electrons due to a N_2 absorption process and the concentration of conducting holes on the CNTs decreases. As a result, the electrical resistance between source and drain electrodes increases when CNTs are exposed to N_2 . A higher N_2 pressure makes the electrical resistance higher. Because the N_2 is absorbed on CNT surfaces by the van der Waals force, almost all the N_2 molecules leave CNT surfaces after pumping and the electrical resistance returns to its initial value (Fig. 8.31a).

Experiments indicate that the gas sensor sensitivity increases with higher source drain bias voltages. Furthermore, the sensor sensitivity is also affected by the gate voltage. Figure 8.31b shows that the electrical resistance of a CNT array changes with various gate voltages at a fixed 5 V source-drain voltage in a 5 Torr N_2 pumping and filling environment. The initial electrical resistance increases when a positive gate voltage is applied and decreases with a negative gate voltage. The sensor sensitivity

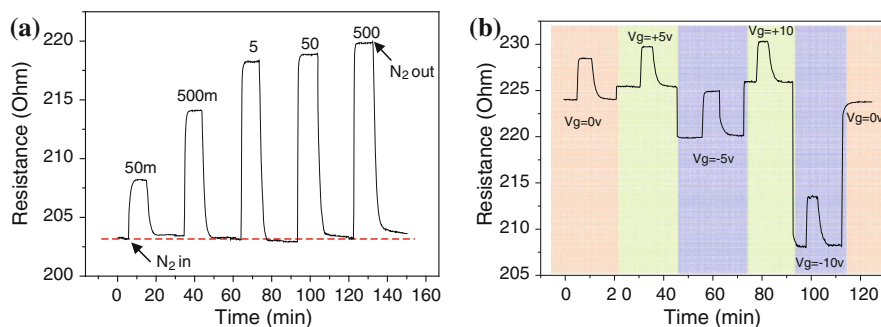


Fig. 8.31 Electrical resistance of a three-terminal gas sensor. **a** The electrical resistance between the source and the drain at 10 V bias voltage without any gate voltage under various N₂ filling pressure from 50 to 500 Torr; **b** the electrical resistance of a CNT array measured at a fixed 5 V source-drain bias voltage while applying various gate voltages V_g under a 5 Torr N₂ pumping and filling environment. From Huang et al. [250]. Copyright (2005), Elsevier

increases with the decrease in the gate voltage from positive to negative due to the increase in the gas-binding sites caused by a negative gate voltage. Similar to under zero drain-bias voltage, the resistance of CNT array restores its initial value after a cycle of N₂ filling and pumping under different positive and negative gate voltages.

8.3.3.3 Nitrous Oxide Gas Sensors

Nitrous oxides such as nitrogen monoxide (NO) and nitrogen dioxide (NO₂) are typical air pollutants that cause environmental problems. There are also demands for small and cheap gas sensors for NO detection in medical applications and scientific researches.

Figure 8.32 shows a two-terminal gas sensor with interdigitated electrodes. The platinum interdigitated electrodes are deposited on the CNT arrays (Fig. 8.32a) to provide larger sensing areas and sufficient contact areas between the electrodes and the coated CNTs. The resistance change of CNTs under gas exposure is detected by two-terminal resistors with a DC voltage. NO₂ exposure drastically decreases the electrical resistance of the CNT arrays and completely removing the gas exposure restores the initial resistance of CNT arrays (Fig. 8.32b). The conductance change of the sensors shows a linear response to the gas concentration upon exposure to NO₂, no matter MWCNT arrays [205, 206] or SWCNT arrays [165] are used.

Besides NO₂, NO can also be detected using the gas sensors with identical structures [205, 207].

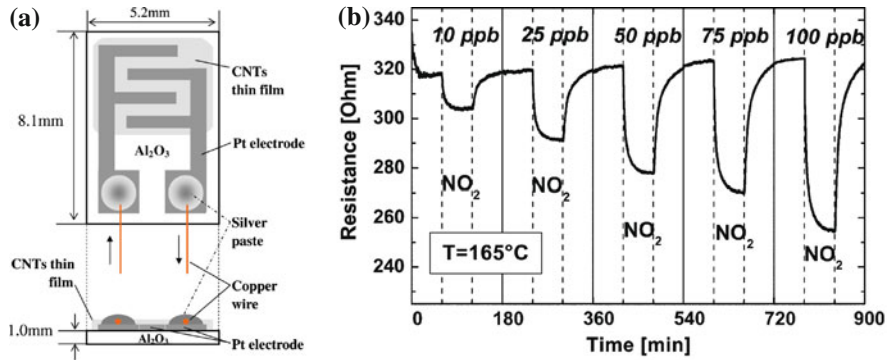


Fig. 8.32 Two-terminal NO_2 gas sensor. **a** Schematic diagram of CNTs patterned with platinum contacts; **b** electrical resistance variation of CNT arrays at an operating temperature of 165°C and NO_2 concentration between 10 and 100 ppb. **a** From Ueda et al. [205]. Copyright (2008), Elsevier. **b** From Valentini et al. [207]. Copyright (2004), Elsevier

8.3.3.4 Ammonia Gas Sensors

In the case of chemical gas sensors based on electrical resistance, it is difficult to detect gas molecules with low adsorption energy while the ionization sensors can easily detect the inert gases or gas mixture. Ionization gas sensors can detect the fingerprinting ionization characteristics of the detected gases. Therefore the ionization sensors can identify different kinds of gas molecules when the detected gas molecules are ionized. There are no limits to identify gases with low adsorption energy and poor charge transfer with the sensing materials. Therefore, the effect of gas adsorption on CNT field-emission properties has been investigated and the CNT ionization gas sensors have attracted a great amount of research interests.

Figure 8.33 shows a diagram of an ionization gas sensor with an aligned MWCNT array as the anode of sensors. The whole sensor consists of an MWCNT array anode, an Al plate cathode, and a $150\ \mu\text{m}$ thick glass insulator between them (Fig. 8.33a). The MWCNT anode is grown by thermal CVD technique (Fig. 8.33b). Under electric fields, individual MWCNTs create very high nonlinear electric fields near the CNT tips, resulting in the formation of highly ionized gases that surrounds the MWCNT tips and causing the formation of a self-sustaining interelectrode discharge at very low voltages.

The precise breakdown voltage provides a fingerprint to each kind of gas and indicates the potential for gas identification within a mixture of gases. The breakdown voltage is rarely affected by the concentration in the range of 10^{-5} – 10^{-1} mol/L. So the breakdown voltage of each kind of gas is unique (Fig. 8.34a). Therefore by monitoring the breakdown voltage of the gas, its identity can be determined. The discharge current of each gas increases logarithmically with the gas concentration. Therefore, the discharge current provides a convenient means to quantify the concentration of the gas being detected (Fig. 8.34b).

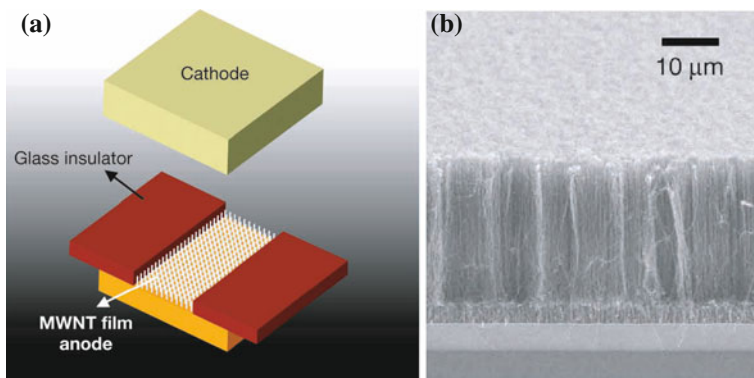


Fig. 8.33 Ionization gas sensors. **a** Schematic diagram of the CNT array ionization gas sensor device; **b** SEM micrograph of vertically aligned MWCNT arrays used as the anode of ionization sensors. From Modi et al. [197]. Copyright (2003), Macmillan Publishers Ltd

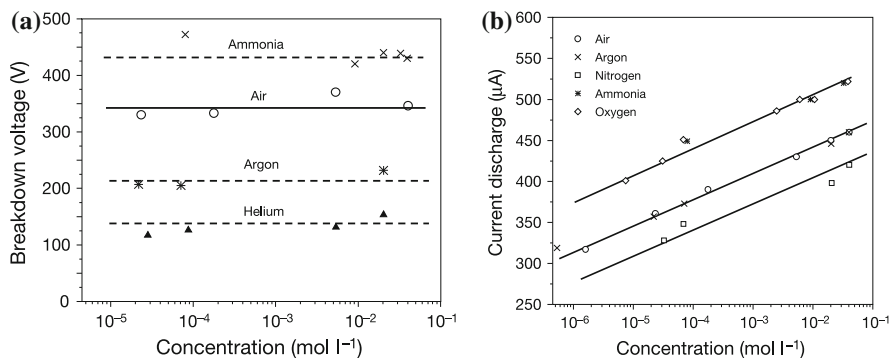


Fig. 8.34 Electrical properties of ionization gas sensors. **a** Breakdown voltage as a function of gas concentration. The breakdown voltage varies only slightly with gas concentration; **b** discharge current at breakdown voltage as a function of gas concentration. The discharge current varies logarithmically with concentration. From Modi et al. [197]. Copyright (2003), Macmillan Publishers Ltd

The ionization sensor works best in the concentration range of 10^{-5} – 10^{-1} mol/L. In the lower concentration, the breakdown voltage decreases with air or the argon concentration below 10^{-5} mol/L [208, 209] and varies slightly with the concentration above 10^{-5} mol/L [208].

Besides ammonia, argon and helium gases can also be detected using the ionization gas sensors while the resistance-based sensors can not detect these two kinds of gases.

NH_3 is also measured from the electrical resistance variation of CNT arrays using two-terminal CNT sensors [207, 210]. The electrical resistance of *p*-type CNT arrays increases with the ammonia concentration.

8.3.3.5 Other Gas Sensors

H₂O, C₂H₆, and ethanol exposures also increase the electrical resistance of a CNT array and can be determined by two-terminal sensors [207].

After being coated with conducting polymers such as polyvinyl acetate, the vertically aligned CNT arrays can also be used to detect cyclohexane and ethanol from electrical resistance variations [211].

Besides the CNT array gas sensors, more kinds of gases and liquids are detected by CNT-matrix sensors based on the electron emission, electrical resistivity change, frequency shift, and capacity changes of random CNTs. The interested readers are referred to some books [42, 191] and review papers.

8.3.4 Biosensors

CNTs can be functionalized with different biomolecules such as deoxyribonucleic acid (DNA) and protein [153, 173, 212, 213]. It was found that the electronic transport and thermopower of CNTs are very sensitive to substances that affect the amount of injected charge [7, 214]. Based on these unique properties including the high electron transfer rate [153] and the high electrocatalytic activity [215, 216], several research groups have demonstrated that bundles of CNTs [172, 173], CNT membranes [217], polymer-CNT composites [177, 215, 218, 219], and CNT-modified electrodes [150, 213, 220] can be used as effective electrochemical biosensors [221–223]. The main advantages of CNTs are the nanosize of the CNT-sensing element and the corresponding small amount of materials required for detectable response.

The well-aligned CNT arrays have been employed to work as ribonucleic acid (RNA) sensors [170], enzymes sensors [154], DNA sensors [224], and even protein sensors [152]. The biological applications of aligned CNT arrays are reviewed recently [225–233]. In this section we focus on the structure properties of these CNT array biosensors and their working mechanisms.

8.3.4.1 Glucose Sensors

Because of the high demand for blood glucose monitoring, significant researches and development efforts have been devoted to producing reliable glucose sensors for in vitro or in vivo applications. The measurement principle of oxidase-based amperometric biosensors previously relied on the immobilization of oxidase enzymes on the surface of various electrodes and the detection of the current associated with the redox product in the biological reaction. To increase the selectivity and sensitivity of amperometric biosensors, artificial mediators and permselective membranes are often used in the biosensor fabrication. Artificial mediators can shuttle electrons between the enzyme and the electrode to allow operation at low potentials, minimizing interferences with coexisting electro-active species. However the stability and the

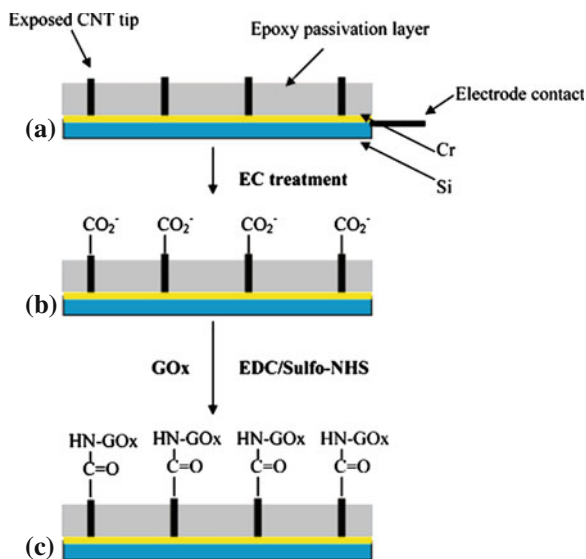


Fig. 8.35 Fabrication of a glucose biosensor based on CNT nanoelectrode arrays. **a** CNT nanoelectrode array with exposed CNT tips; **b** electrochemical treatment of the CNT nanoelectrode arrays for functionalization; **c** coupling of the enzyme (GO_x) to the functionalized CNT nanoelectrode arrays. From Lin et al. [177]. Reprinted with permission from American Chemical Society

toxicity of some mediators limit their *in vivo* applications. Permselective membranes are also used to eliminate interferences while also have some disadvantages.

A mediator- and membrane-free biosensor was invented using CNT arrays [177]. The idea of the mediator- and membrane-free biosensor is based on the reduction of hydrogen peroxide [234, 235], the strong electrocatalytic effect, and a high electron-transfer rate of CNTs [178]. The innovative method provides a means for measuring the cathodic current of enzymatically liberated hydrogen peroxide in metal-dispersed carbon paste biosensors and provides a new approach for biosensor development [234, 235].

The glucose sensors are fabricated from the CNT nanoelectrode arrays with low site densities. The aligned CNT arrays are first fabricated as the starting building block (Fig. 8.35a). The detailed fabrication procedure of the CNT nanoelectrode arrays is described in Sect. 8.3.1. The CNT nanoelectrode arrays are pre-treated for functionalization in 1.0 M NaOH at 1.5 V for 90 s. After the electrochemical treatment, some functional groups (e.g., carboxylic acid) are created at the CNT tips (Fig. 8.35b). Then enzymes are attached to the broken tips of the polished CNT arrays using standard water-soluble coupling agents 1-ethyl-3-(3-dimethylaminopropyl) carbodiimide (EDC) and *N*-hydroxy-sulfo-succinimide (sulfo-NHS) by forming amide linkages between their amine residues and carboxylic acid groups on the CNT tips [177, 178] (see Fig. 8.35c).

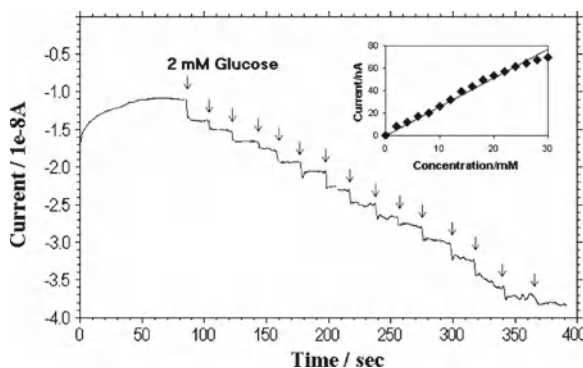


Fig. 8.36 Amperometric responses of a CNT nanoelectrode array biosensor to successive additions of 2 mM glucose. From Lin et al. [177]. Reprinted with permission from American Chemical Society

In a typical procedure, the activated CNT nanoelectrode arrays are then immersed in a freshly prepared 10 mL aqueous solution of EDC (10 mg/mL). With stirring, 300 mg of sulfo-NHS is added to the solution. The pH of the solution is adjusted to 7. The reaction is allowed to occur at room temperature for 2 h. Then the nanoelectrode is washed quickly with cold water and immediately immersed into a degassed solution (10 mL) with the desired amount of glucose oxidase enzyme (GO_x , 2 mg/mL in a 0.1 M phosphate buffer solution with $\text{pH} = 7.4$) with stirring. The resultant nanoelectrode array biosensor is stored at 4 °C before use.

The amperometric experiment was performed in a standard single-compartment electrochemical cell that contained a nanoelectrode array electrode, a Ag/AgCl reference electrode, and a platinum wire auxiliary electrode. The electrochemical detector is connected to a portable computer. The amperometric response of the glucose biosensor based on CNT nanoelectrode arrays to glucose was recorded under steady-state conditions in a 0.1 M phosphate buffer with $\text{pH} = 7.4$ by applying a desired potential (for interference experiments, +0.4 and -0.2 V; for the calibration experiment, -0.2 V) to the biosensor. The background response of the biosensor is allowed to decay to a steady state with stirring. When the background current becomes stable, a solution of glucose is injected into the electrolytic cell, and its response is measured and recorded.

The amperometric responses at the nanoelectrode array glucose biosensors for each successive addition of 2×10^{-3} M glucose are presented in Fig. 8.36. The inset is the calibration curve. Well-defined current responses for glucose were obtained by the nanoelectrode array biosensor. The occurring reaction at the biosensor is very fast to reach a dynamic equilibrium upon each addition of the sample solution, generating a steady-state current signal within 20–30 s. The linear response of the glucose biosensor to glucose is up to about 30 mM of glucose, which is higher than the 15 mM required for practical uses in the detection of blood glucose. The signal response curve is effective at low detection limits for glucose because of favorable

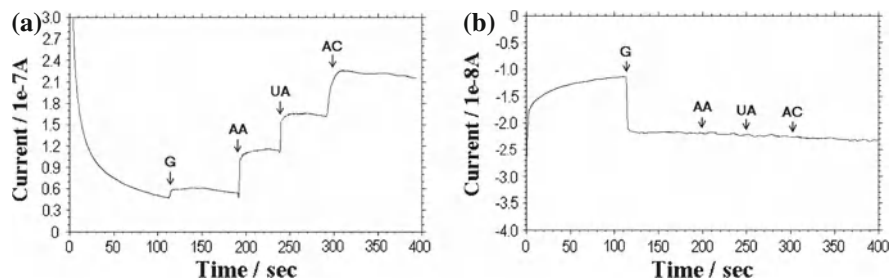


Fig. 8.37 Amperometric responses of a CNT nanoelectrode array glucose biosensor to glucose (G), ascorbic acid (AA), uric acid (UA), and acetaminophen (AC) at potentials of **a** +0.4 V and **b** -0.2 V. From Lin et al. [177]. Reprinted with permission from American Chemical Society

signal-to-noise ratio characteristics at -0.2 V. The limit of detection, based on a signal-to-noise ratio of 3, is 0.08 mM.

SWCNT arrays can also be used as glucose sensor after being coated by copper oxide nanoparticles [236]. The as-prepared copper-oxide-SWCNT electrodes exhibit synergistic electrocatalytic activity on the oxidation of glucose in alkaline media with a rapid response time of less than 2 s and a high sensitivity of $16.2 \mu\text{A}/\text{M}$. In the presence of physiological level ascorbic acid (0.1 mM), the experimental detection limit of glucose increases to 50 nM with a sensitivity of $1.31 \mu\text{A}/\text{M}$.

Besides the detection of glucose, such CNT nanoelectrode biosensors can also be used to detect ascorbic acid, uric acid, acetaminophen, and herbicide atrazine [237]. The selectivity advantage accrued from the hydrodynamic voltammograms is demonstrated in Fig. 8.37 which compares amperometric responses for relevant physiological levels of glucose, ascorbic acid, acetaminophen, and uric acid at the GO_x -modified nanoelectrode array at potentials of $+0.4$ and -0.2 V, respectively. Amperometric responses are obtained by a batch addition of interfering species (0.5 mM ascorbic acid, 0.5 mM uric acid, and 0.5 mM acetaminophen) after the 5 mM glucose addition at two different potentials ($+0.40$ and -0.2 V). Well-defined cathodic and anodic glucose responses are obtained by the nanoelectrode array biosensor at potentials of $+0.4$ and -0.2 V. At an operating potential of $+0.40$ V, the glucose response is overlapped by large anodic contributions from ascorbic acid, uric acid, and acetaminophen. The use of a lower operating potential greatly reduces these contributions. No interference is observed at a potential of -0.20 V for the interference species, indicating high selectivity toward the glucose substrate. Such a highly selective response to glucose is obtained by the nanoelectrode array biosensor without the use of mediators and permselective membranes [177].

Cyclic voltammetric experiments indicate that the oxidation of the interfering species at the nanoelectrode array starts at about $+0.20$ V (ascorbic acid) and $+0.30$ V (acetaminophen, uric acid) with no reduction until -0.2 V [177].

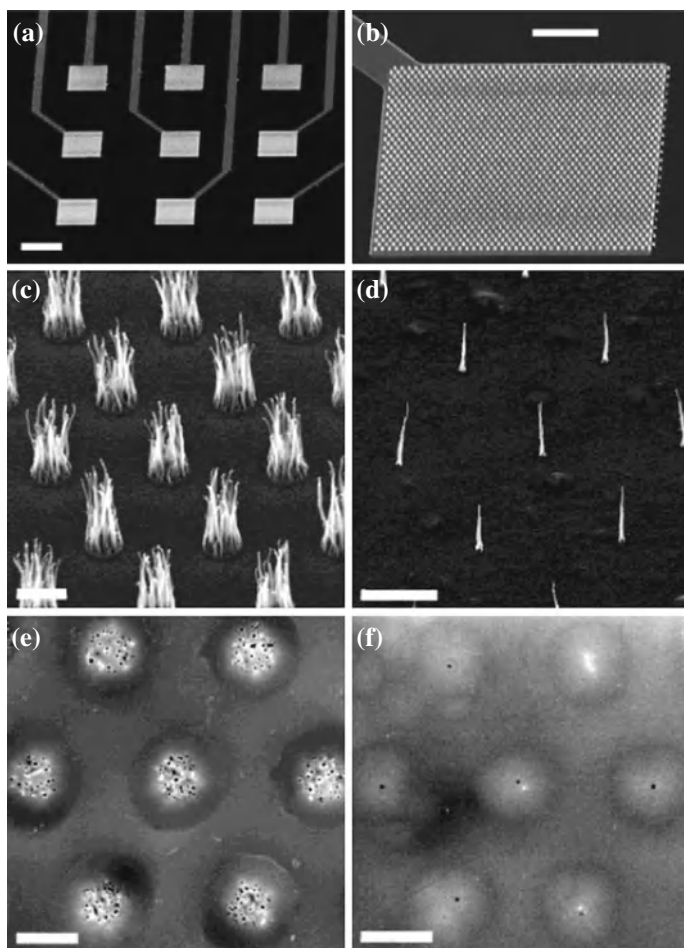


Fig. 8.38 SEM images of **a** 3×3 CNT electrode arrays; **b** Array of MWCNT bundles on one of the electrode pads. **c**, **d** array of MWCNTs grown from UV-lithography and e-beam patterned Ni catalytic spots, respectively; **e**, **f** surface of polished MWCNT electrode arrays grown on $2 \mu\text{m}$ and 200nm catalytic spots, respectively. **a–d** are 45° perspective views and **e** and **f** are top views. Scale bars **a** $200 \mu\text{m}$, **b** $50 \mu\text{m}$, **c** $2 \mu\text{m}$, **d** $5 \mu\text{m}$, **e** $2 \mu\text{m}$, and **f** $2 \mu\text{m}$. From Li et al. [178]. Copyright (2003) American Chemical Society

8.3.4.2 DNA Sensors

Coated CNT nanoelectrode arrays have also been employed as DNA sensors [170, 238, 239]. Each individual CNT works as an individual nanoelectrode. The smaller radius of CNT electrodes ($10\text{--}100 \text{nm}$) is close to the size of DNAs and makes the CNT nanoelectrode arrays applicable to detect individual DNA.

Figure 8.38 shows SEM images of a DNA sensor consisting of a 3×3 array of individually addressed CNT electrodes on a Si(100) wafer covered with a 500 nm thick thermal oxide. The electrodes and contact lines are 200 nm thick Cr patterned with UV-lithography. Each electrode can be varied from 2×2 to $200 \times 200 \mu\text{m}^2$ consisting of a vertically aligned MWCNT array grown by PECVD from 10 to 20 nm thick Ni catalyst films. Figure 8.38c, d shows MWCNT arrays grown on $2 \mu\text{m}$ and 200 nm diameter Ni catalytic spots prepared by UV and e-beam lithography, respectively. The spacing and spot size can be precisely controlled. The diameters of the MWCNTs are uniform over the whole chip and can be controlled between 30 and 100 nm by the PECVD growth process. The number of CNTs in each Ni catalytic spot can be varied as well by changing the thickness of the Ni film. The individual nanotube can be grown at each catalytic spot if the catalytic spot size is reduced below 100 nm. A tetraethoxysilane CVD process can encapsulate each nanotube and the substrate surface with a uniform SiO_2 film, resulting in a mechanically stable and well insulated matrix. Then the coated CNT arrays are mechanically polished for planarization and exposure of the ends of the CNTs. Figure 8.38e, f shows the embedded CNT array electrodes with different patterns after polishing. Clearly, CNTs retain their integrity and are separated from one another.

The aligned MWCNT nanoelectrodes shown in Fig. 8.38 can detect DNA at a sensitivity limit lower than a few attomoles of oligonucleotide targets. The sensitivity can be further improved to detect only thousands of target DNAs after optimization, which could provide faster, cheaper, and simpler solutions for molecular diagnosis particularly for early cancer detection, point-of care, and field uses.

8.3.4.3 Protein Sensors

Figure 8.39 shows the fabrication of a protein sensor from CNT arrays by nanoimprint. The supporting polymer (SU8-2002) is spin-coated onto a glass substrate containing nanotube arrays. The template protein is initially incorporated into the nanocoating and, upon extraction of protein from the accessible surfaces on the nanocoating, the electrical impedance of the CNT array is found to be greatly reduced due to electrical leakage through the surface imprints in the nanocoating. Subsequent recognition of the template protein is detected as an increase in impedance due to the relatively lower conductivity of the protein. A critical component for the assembly of the sensor architecture is comprised of electropolymerizing non-conductive polyphenol (PPn) nanocoating onto the tips of nanotubes. Such protein sensors can selectively recognize human papillomavirus E7 protein and is also useful for the detection of other pathogens and toxins, for diagnosing human diseases (through the detection of disease biomarkers), and for a host of proteomic applications.

In contrast to conventional protein sensors, a key architectural improvement of the CNT array sensors is the non-conductive PPn nanocoating on the nanotube tips. The level of detection (e.g., 10 pg/l was achieved for hFtn proteins [240]) surpasses that affordable by conventional sensors by a few orders of magnitude.

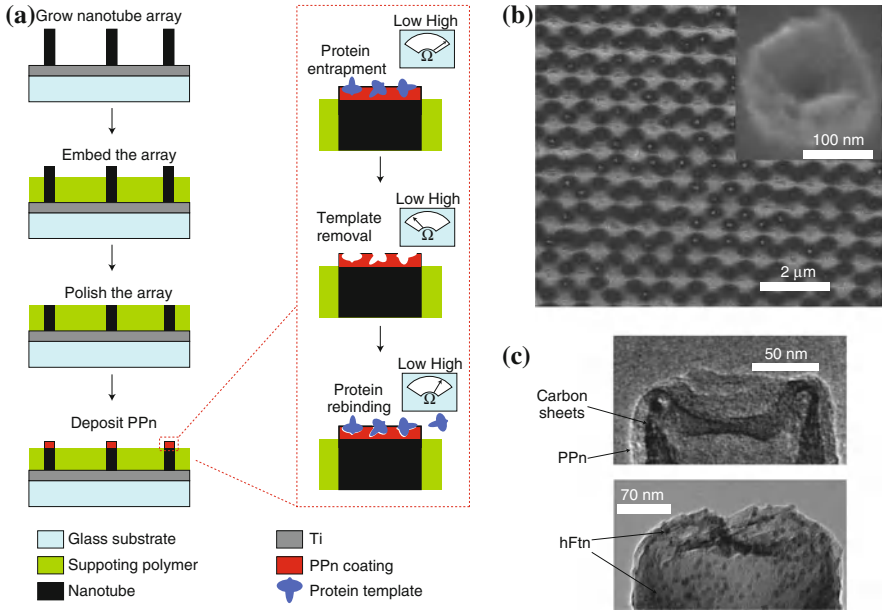


Fig. 8.39 Fabrication of a protein nanosensor. **a** Schematic of nanosensor fabrication and template protein detection. Template proteins trapped in the polyphenol (PPn) coating are removed to reveal the surface imprints. *Inset* hypothetical sensor impedance responses at critical stages of fabrication and detection; **b** Scanning electron microscopy image of a polished nanotube array after PPn coating. *Inset* cross-section of a nanotube tip after polishing; **c** TEM images of a PPn-coated nanotube tip without (*top*) and with (*bottom*) hFtn proteins. From Cai et al. [240]. Reprinted with permission from Macmillan Publishers Ltd

8.4 Thermal Devices: Thermal Interface Materials

Thermal interface materials (TIMs) play a key role in the heat dissipation at all levels within a microelectronic device, such as integrated chips (ICs). TIMs fill the microscopic gaps between two contacting materials to enhance the heat conduction through the interfaces. The heat from the ICs can be efficiently transferred to the heat sinks or ambient environment.

The total thermal resistance, R_{TIM} , of real TIMs can be expressed as [241]

$$R_{TIM} = \frac{B_{LT}}{\kappa_{TIM}} + R_{c1} + R_{c2} \tag{8.5}$$

where R_{c1} and R_{c2} represent the contact thermal resistances of a TIM with the two bounding surfaces at the interfaces, B_{LT} the bond line thickness of the TIM, and κ_{TIM} the thermal conductivity of the TIM.

CNTs have high thermal conductivities. The measured room-temperature thermal conductivity for an individual MWCNT (>3,000 W/m/K) is higher than that

of natural diamond and the basal plane of graphite (both 2,000 W/m/K) [242]. So CNTs are considered as one of the most promising TIMs due to their high thermal conductivities. Up to now, three kinds of CNT-based TIMs have been achieved. The first ones are TIMs with CNT filler. CNTs are suspending in a conventional TIMs or aligned in the TIMs after CNTs is mixed with conventional TIMs. The content of CNTs is usually low. The second ones are pure CNT arrays. The third ones are aligned CNT composites. CNT arrays are grown then filled with conventional TIMs. The content of CNT is usually higher than that of TIM fillers.

TIMs with CNT filler. CNTs are first used as a novel type of highly thermally conductive filler to modify micro- and nanoscale structures of the TIM materials to improve their thermal performance. After CNTs are randomly dispersed in conventional TIMs or liquids, the thermal conductivity of the composites is enhanced [243–246]. It is reported that the thermal conductivity is doubled with 1 wt.% SWCNTs loading [244]. Some literatures reviewed such composites with random CNTs [247, 248].

However, the thermal conductivity of the CNT-filler composites is much lower than the value estimated from the intrinsic thermal conductivity of the CNTs and their volume fraction [249]. If all the CNTs are vertically aligned well on the substrate, phonons propagate easily along the CNTs and the arrays are able to transport heat in one direction, along the alignment of the CNTs. Aligned CNT-based interfaces should conduct more heat than conventional thermal interface materials at the same temperatures.

The distribution and alignment of the thermally conductive CNT fillers are important factors to affect the phonon transport [250]. The composite with aligned CNTs shows an enhancement of 0.65 W/m/K with a 0.3 wt.% loading (Fig. 8.40). Comparably, the enhanced thermal conductivity of the randomly dispersed CNT composite is below 0.05 W/m/K at the same loading of 0.3 wt.%. Experiments indicate that the conductivity enhancement with aligned CNTs is at least two times higher than that without CNTs (inset in Fig. 8.40). So the vertically aligned CNT arrays are good candidates for TIM. At the same time, the CNT arrays have very low densities, 20 times lower than that of a similar copper structure with similar cooling properties. So recently various SWCNT and MWCNT array thermal interface materials have been fabricated using thermal CVD and PECVD methods [216–220, 226, 227, 231, 234, 235, 238–242, 244].

TIMs of Pure CNT arrays. Besides being used as fillers in the conventional TIMs, CNT arrays can also be used directly as TIMs [251–253] after growth. Compared with the conventional TIMs, the thermal resistances of the pure CNT arrays are lower (Fig. 8.41b). Experiments revealed that the thermal conductivity of the CNT array increases monotonically with both increasing CNT array height and CNT density [253]. The thermal conductivity of the CNT array is also higher for an interface material of lower thermal resistance. Increasing the contact pressure on the array free surface also results in higher array thermal conductivity values (Fig. 8.41a). The thermal conductivity also increase with increasing temperature for all heights and densities.

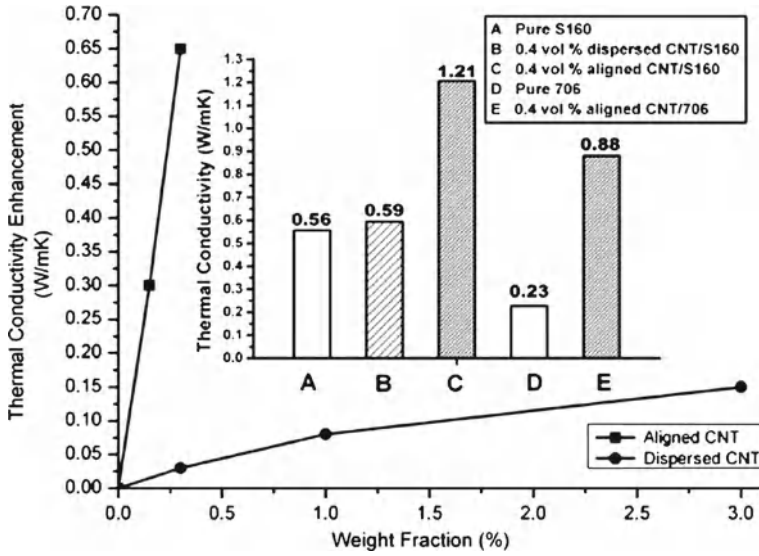


Fig. 8.40 The enhanced thermal conductivity versus weight fraction of CNTs. The *inset* is a comparison of measured thermal conductivity of different samples. 706: Silicone elastomer 706; S160: silicone elastomer Sylgard 160. Both pure 706 TIM and S160 TIM are thermally conductive TIMs. The CNTs are aligned under magnetic fields. From Huang et al. [250]. Copyright (2005), John Wiley and Sons

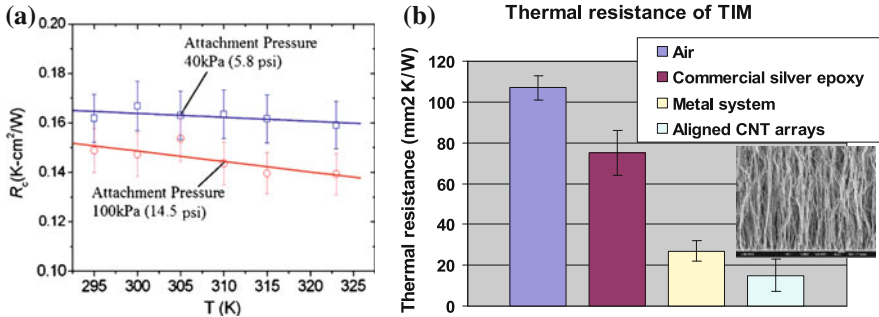


Fig. 8.41 **a** Thermal resistance of a CNT array on Si at different pressures; **b** thermal resistance of different materials. **a** From Hu et al. [251]. Copyright (2006), ASME. **b** From Zhang et al. [252]. Copyright (2006), IEEE

TIMs of CNT array composites. In order to enhance the thermal conductivity further and enforce the mechanical strength, the conventional TIMs can be filled into the gaps between CNTs. CNTs are usually fabricated by the thermal CVD method with the crowding effect (see Sect. 6.1.1) first, followed by the filling of the conventional TIMs. Such prepared CNT array composites have lower thermal resistances.

Despite the massive research efforts, the CNT TIMs are not commercialized yet. The performance of most of these novel TIMs is still not high enough to overtake the current high-end commercial products. Many of them even generate undesirable results when compared to commercial materials. Several technical barriers have to be solved before commercial applications. Firstly, the measured highest thermal conductivity of CNT TIMs is much lower than the highest value of individual CNTs of perfect atomic structures. Secondly, the contact thermal resistances between CNTs and other substances, e.g., the polymer matrix in composites and the substrates above or below the aligned CNT arrays, are very high and cause the low overall performance of the CNT TIMs. Another main technical barrier is the significant difficulty in achieving high filling ratio and better alignment of CNTs in the TIMs. In the case of CNT arrays, the gaps between the aligned CNTs are indeed quite large compared to their diameters, causing a rather low effective filling factor.

8.5 Electrical Interconnects and Vias

Semiconductor technologies with feature sizes of several tens of nanometers are currently in development and the future nanometer-scale circuits will contain more than a billion transistors in 1 cm^2 area and operate at clock speeds well over 10GHz. The performance of such a high-speed chip is highly dependent on interconnects/vias/contacts, which connect different microcells within a chip. The interconnects (local, semiglobal, and global) distribute power and signal across the chips. With the rapid down-scaling of feature sizes to submicron levels and the increase in the integration density of the complementary metal-oxide semiconductors (CMOS) and frequency, which result in a significant increase in current density and corresponding upgraded operating temperature, the requirements of high current carrying and thermal transport abilities are the major concerns in interconnect design besides the resistive capacitive (RC) delay for the interconnects/vias/contacts [254].

At present, copper is widely used in chips as interconnect/vias/contacts for advanced integrated circuits while facing serious challenges because of its electromigration, skin effect, dispersion, signal degradation, power dissipation, and electromagnetic interference at high frequencies and at the submicron level [255]. For example, the dimension of Cu interconnects has already reached the order of the electron mean free path in Cu (40 nm) at room temperature. The electrical resistivity of copper interconnects is increasing rapidly under the effects of grain scattering and surface scattering, longer interconnect length, and higher frequency operation [255]. The signal delay caused by the Cu interconnects becomes increasingly significant compared to the delay caused by the gates and thus affecting the circuit's reliability when the feature size is rapidly scaled down to deep submicron levels. The rising Cu electrical resistivity with decreasing size also leads to a significant rise in the metal temperature due to self-heating leading to electromigration problems which degrade the IC performance [256].

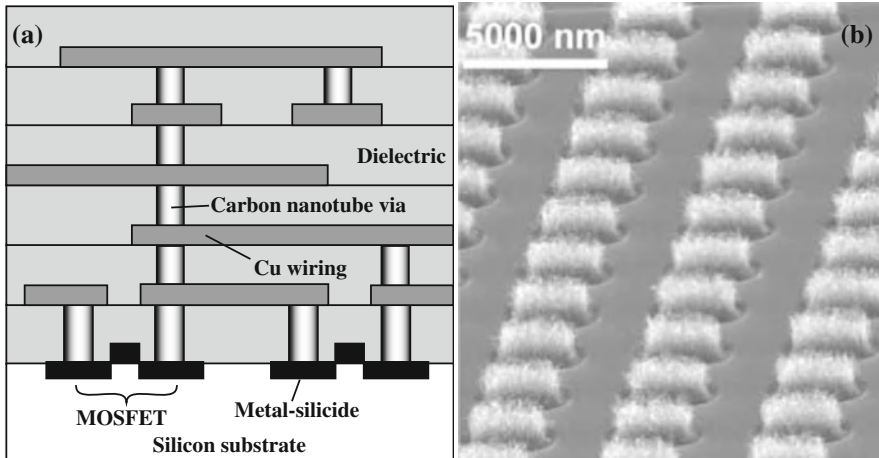


Fig. 8.42 **a** Schematic cross-sectional image of hybrid Cu interconnects/CNT vias; **b** SEM image of CNT via array before top electrodes are deposited. **a** From Nihei et al. [270]. **b** From Awano et al. [283]. Copyright (2006), John Wiley and Sons

The excellent electrical conductivity, high thermal conductivity, and good mechanical characteristics make CNTs a very promising candidate for interconnect applications. CNTs can conduct high current densities up to 10^9 A/cm² [257–261], 1,000 times higher than Cu. Metallic CNTs have a long electron mean free path of several microns [262] and exhibit ballistic transport properties [263]. Additionally, the excellent thermal conductivity of CNTs (5,800 W/m/K [262] or 3,500 W/m/K [264] while only 385 W/m/K for Cu) can remove the heat sufficiently from the chips. Significant research efforts are therefore underway to develop CNT interconnect technologies. The detailed semiglobal and global CNT interconnects are reviewed [265] and the physical properties of SWCNT interconnects are analyzed [254, 265–267] recently.

The current state-of-the-art on-chip integration of CNTs focuses on the hybrid Cu-interconnect/MWCNT-via systems [268–272]. The first reason is that the vias carry the highest current density among interconnects, vias, and contacts. The second is that there is no convincing method to grow dense CNT bundles of varying lengths for interconnects that are parallel to the chip surface in two perpendicular directions [273] although horizontally aligned CNTs have been grown using gas-flow methods [274, 275], electric field methods [276–280], fluidic assembly methods [281], or template selectivity growth methods [282]. The third is that MWCNTs show metallic behaviors while it is very challenging to grow dense bundles of metallic SWCNTs because of the lack of control on SWCNT chirality to ensure metallic properties. So, most present researches have focused on the hybrid Cu-interconnect/MWCNT-via systems.

Figure 8.42 shows the hybrid CNT interconnect/CNT via system. Each CNT bundle consists of many individual CNTs and conducts current in a parallel manner. The

CNT bundles are ideal electrical conductors when thousands of individual CNTs are tightly packed. Aligned CNT bundles can be manufactured by an in situ patterned growth of CNTs on a patterned substrate surface [269–271, 283–285] or by an ex situ transfer process of the CNT forests to foreign substrates [286]. In order to grow CNT bundles on Si ICs, it is necessary to grow CNTs below the microelectronics-compatible temperatures of 400–600 °C [283]. The hot-filament CVD method, discussed in Sect. 6.1.6 and Chap. 5, is a suitable way to grow CNT bundles. CNT bundles are first grown from catalyst particles in the vias, aligning perpendicularly to the silicon wafer surface. Subsequently, SiO₂ is deposited and the wafer is polished to open the nanotube ends for contacts.

Such prepared CNT-based vias potentially offer significant advantages: longer mean free path of electrons, higher current densities, and higher thermal conductivities over copper [266].

Electrical resistance of CNT vias. When an isolated CNT is shorter than its mean free path of electrons, its resistance during ballistic transport is independent of length [260, 287]. For longer isolated CNTs, the electrical resistance increases with length because of electron scattering. The experimentally measured resistance of an isolated CNT is usually much higher than the calculated resistance because of the presence of imperfect metal-CNT contacts, which gives rise to an additional contact resistance. The total resistance of a CNT via is a sum of the resistances: ballistic or scattering resistance and the imperfect contact resistance, typically in the range of 7 KΩ [288] to 100 KΩ [289] for an isolated CNT via. Such resistance is too high for actual via applications. Hence, a bundle or rope of CNTs is employed as an effective via to lower the resistance [269, 290]. The effective resistance of a CNT bundle is $R_{\text{bundle}} = R_{\text{CNT}}/n_{\text{CNT}}$, where R_{CNT} is the electrical resistance of a CNT and n_{CNT} the total number of CNTs in a via if it is assumed that all CNTs are metallic and conducting. The total resistance of an MWCNT via consisting of 1,000 MWCNTs can be decreased by three orders of magnitude from that of an isolated CNT, down to 100 Ω [291].

Figure 8.43 shows the interconnect resistances as a function of the length of CNT vias. The Cu resistance is measured based on ITRS and the Cu contact resistance are extrapolated from experimental data. Both the Cu ITRS resistance and the extrapolated Cu contact resistances are plotted for comparison. CNT vias could offer solutions for large aspect ratios, where copper plating can no longer fill the feature. A single MWCNT with a 11 nm diameter could perform better than copper when the aspect ratio is higher than 3 [285].

The resistance can be reduced further by increasing the CNT number in the via. The total resistance has been lowered to 0.59 Ω for 2 μm diameter vias with a CNT site density of 10¹¹ tubes/cm² [283] and 0.7 Ω for a 2 μm diameter via consisting of about 1,000 MWCNTs [284] when a TiN layer is employed in the metal-CNT contacts. Theoretical calculation indicates that the resistance of packed CNT array vias (assuming perfect contacts) formed from SWCNTs shows an improved resistance compared to Cu vias for 22–45 nm node technology or much lower than that of a Cu via of identical dimensions [266].

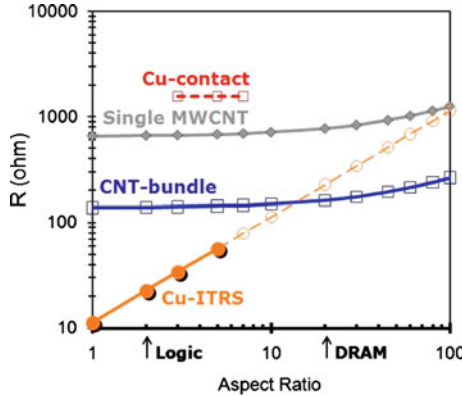


Fig. 8.43 Vertical interconnect resistance versus the aspect ratio of CNT via consisted of one MWCNT or one MWCNT bundle, compared with copper resistivity (Cu-ITRS) and Cu contact resistance (Cu-contact). From Chiodarelli et al. [285]

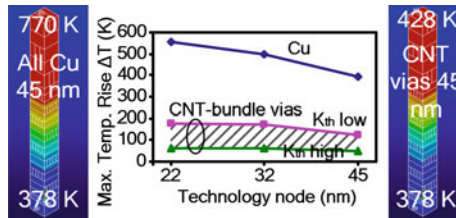


Fig. 8.44 Calculated maximum temperature rise for Cu-interconnects and Cu-vias (left) versus CNT bundle via integrated with Cu-interconnects (right) [262]. The middle figure indicates the effect of node size. CNT thermal conductivity range: $1\,750\text{ W/m/K} < K_{th} < 5,800\text{ W/m/K}$. The substrate temperature is 378 K [266]. From Srivastava et al. [266]. Copyright (2005) IEEE

Current density. At the same time, preliminary experimental researches show that an array of CNT vias can carry more than an order of magnitude higher current densities than conventional copper vias [269].

Temperature. CNTs can sufficiently remove heat from the chips due to their excellent thermal conductivity [242]. Because the typical via height is smaller than 300 nm, shorter than both the electron and phonon mean free paths of CNTs, CNT vias operate in both the electrical and thermal ballistic transport regimes. When CNT bundles are used only as vias integrated with Cu interconnects, the maximum interconnect temperature rise is much lower [266]. Figure 8.44 compares the temperature rises of Cu-interconnects/Cu-vias with Cu-interconnects/CNT-vias. The temperature of the chips rises to 428 K when CNT vias are employed while up to 770 K in traditional Cu-interconnects/Cu-vias. Such lower interconnect temperatures in hybrid CNT/Cu structures can lead to two orders of magnitude improvement in the mean-time-to-failure of Cu global interconnects [266]. The Cu wire delay is also improved

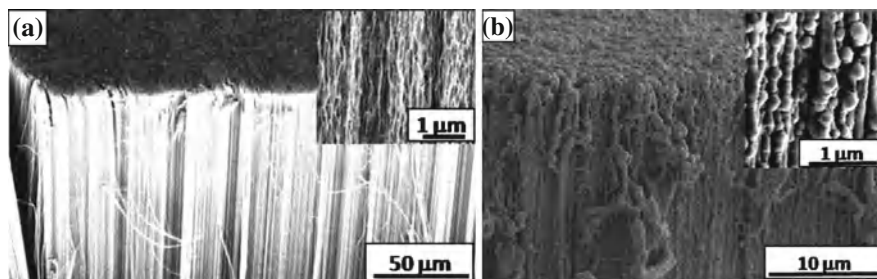


Fig. 8.45 Deposition of nanocrystalline nickel on the CNT array template. **a** SEM image of as-received vertically aligned carbon nanotubes grown by CVD process; **b** SEM image of nickel nanotube deposited by PVD process. From Hwang et al. [292]

by 30% [266]. In one word, the vias composed of MWCNT bundles serve as more effective heat conductors than Cu vias and can potentially reduce the temperature gradient at the backend.

8.6 Templates

The aligned CNT arrays are good templates to grow other ordered nanostructures. Other materials can directly deposited on CNT surface by physical vapor deposition (PVD). Such PVD processes such as sputter deposition offer a relatively simple and clean route to synthesize other nanotubes.

Figure 8.45 shows the Ni nanomaterials deposited on CNT arrays. The CNT array works as template. Ni atoms are deposited on the CNT surface using a DC magnetron sputtering at room temperature [292]. Figure 8.45b clearly exhibits the granular morphology of Ni nanocrystals uniformly coating the surface of the carbon nanotubes (higher magnification shown as an inset). TEM images show that the average crystalline size is about 5 nm. The electron diffraction confirms the polycrystalline nature of the vapor deposited nanocrystals on the surface of the carbon nanotubes.

Additionally the carbon nanotubes can act as the templates to confine the chemical reaction to grow nanorods. For example, the wurtzite gallium nitride nanorods having a diameter similar to that of the original carbon nanotube were synthesized from the Ga₂O vapor reacting with NH₃ gas inside carbon nanotubes [293]. The synthesized nitride nanorods have a diameter of 4–50 nm and a length of up to 25 μm.

8.7 Aligned-CNT Composites and Applications

Bulk CNT are also widely applied in many cases to improve the mechanical, thermal, electrical, and other physical properties of the target materials. The CNTs are random or aligned in these composites.

The random CNT bulks have already been used as composite fibers/reinforcing additives in polymers or ceramics [294–304], metal composites [294, 298, 299, 301, 304–307] to improve the mechanical, thermal, and electrical properties of the bulk products. In a fully dense SWCNTs/ Al_2O_3 composite without damaging the CNTs, a fracture toughness of $9.7 \text{ MPam}^{1/2}$, nearly three times higher than that of pure nanocrystalline alumina, was achieved in the spark plasma-sintered composites [308] and in hot-pressed samples [302, 306]. Random CNT bulks are also used as additives in liquids [243] to increase the thermal conductivities, used for solar cells [309, 310], fuel cells [311, 312], and hydrogen storage [313, 314]. The readers are referred to the respective literatures [247, 307, 315–332].

CNTs can also be aligned in the composites to form aligned-CNT composites. Such aligned-CNT composites can be produced by two methods. One is in situ method. Aligned CNTs are firstly grown as discussed in Sect. 6.1. Then polymers, ceramics, or metals are filled into the gap between CNTs using varied physical or chemical methods, such as infiltration method [333, 334], ALD deposition [335], polymerization [336]. Another is ex situ method. CNTs are firstly grown by various techniques described in Chap. 3. Then the random CNTs are dispersed into second phase to form CNT composites. At this stage, the CNTs are random in the composites. Then followed various ex situ alignment techniques described in Sect. 6.2, the CNTs are aligned along a certain direction. The ex situ technique includes high-shear blending [337], extrusion [338, 339], electric field processing [340], magnetic field processing [341], melt [342, 343], spark plasma sintering [297], capillary-action [344, 345], electrospinning [346], and hot-pressing or extrusion [300].

In this book, we did not discuss more on the composites with aligned CNTs. The interested readers are referred to some review literatures [247, 307, 315–319, 325–328, 330–332, 347–363] and research papers therefore.

References

1. H. Dai, J.H. Hafner, A.G. Rinzler, D.T. Colbert, R.E. Smalley, Nanotubes as nanoprobes in scanning probe microscopy. *Nature* **384**(6605), 147–150 (1996)
2. C.L. Cheung, J.H. Hafner, C.M. Lieber, Carbon nanotube atomic force microscopy tips: direct growth by chemical vapor deposition and application to high-resolution imaging. *Proc. Natl. Acad. Sci. USA* **97**(8), 3809–3913 (2000)
3. N.R. Wilson, J.V. Macpherson, Carbon nanotube tips for atomic force microscopy. *Nat. Nanotechnol.* **4**(8), 483–491 (2009)
4. A.G. Rinzler, J.H. Hafner, P. Nikolaev, P. Nordlander, D.T. Colbert, R.E. Smalley, L. Lou, S.G. Kim, D. Tománek, Unraveling nanotubes: field emission from an atomic wire. *Science* **269**(5230), 1550–1553 (1995)

5. H. Ko, Z. Zhang, J.C. Ho, K. Takei, R. Kapadia, Y.-L. Chueh, W. Cao, B.A. Cruden, A. Javey, Flexible carbon-nanofiber connectors with anisotropic adhesion properties. *Small* **6**(1), 22–26 (2010)
6. P.M. Ajayan, O.Z. Zhou, Applications of carbon nanotubes. in *Carbon Nanotubes: Synthesis, Structure, Properties, and Applications*. Topics in Applied Physics, vol. 80, ed. by M.S. Dresselhaus, G. Dresselhaus, P. Avouris (Springer, Berlin, 2001), pp. 391–425
7. J. Kong, N.R. Franklin, C. Zhou, M.G. Chapline, S. Peng, K. Cho, H. Dai, Nanotube molecular wires as chemical sensors. *Science* **287**(5453), 622–625 (2000)
8. S. Frank, P. Poncharal, Z.L. Wang, W.A. de Heer, Carbon nanotube quantum resistors. *Science* **280**(5370), 1744–1746 (1998)
9. P. Poncharal, Z.L. Wang, D. Ugarte, W.A. de Heer, Electrostatic deflections and electro-mechanical resonances of carbon nanotubes. *Science* **283**(5407), 1513–1516 (1999)
10. P.G. Collins, A. Zettl, H. Bando, A. Thess, R.E. Smalley, Nanotube nanodevice. *Science* **278**(5335), 100–102 (1997)
11. M.S. Fuhrer, J. Nygård, L. Shih, M. Forero, Y.-G. Yoon, M.S.C. Mazzoni, H.J. Choi, J. Ihm, S.G. Louie, A. Zettl, P.L. McEuen, Crossed nanotube junctions. *Science* **288**(5465), 494–497 (2000)
12. A. Javey, J. Guo, Q. Wang, M. Lundstrom, H. Dai, Ballistic carbon nanotube field-effect transistors. *Nature* **424**, 654–657 (2003)
13. S.J. Tans, A.R.M. Verschueren, C. Dekker, Room-temperature transistor based on a single carbon nanotube. *Nature* **393**, 49–52 (1998)
14. Z. Chen, J. Appenzeller, Y.-M. Lin, J. Sippel-Oakley, A.G. Rinzler, J. Tang, S.J. Wind, P.M. Solomon, P. Avouris, An integrated logic circuit assembled on a single carbon nanotube. *Science* **311**(5768), 1735 (2006)
15. Y. Takagi, T. Uda, T. Ohno, Carbon nanotube motors driven by carbon nanotube. *J. Chem. Phys.* **128**(19), 194704 (2008)
16. P. Avouris, Molecular electronics with carbon nanotubes. *Acc. Chem. Res.* **35**(12), 1026–1034 (2002)
17. P.L. McEuen, Nanotechnology: carbon-based electronics. *Nature* **393**(6680), 15–17 (1998)
18. H. Shiozawa, T. Pichler, C. Kramberger, M. Rütteli, D. Batchelor, Z. Liu, K. Suenaga, H. Kataura, S.R.P. Silva, Screening the missing electron: nanochemistry in action. *Phys. Rev. Lett.* **102**, 046804 (2009)
19. L. Sun, F. Banhart, A.V. Krashennnikov, J.A. Rodriguez-Manzo, M. Terrones, P.M. Ajayan, Carbon nanotubes as high-pressure cylinders and nanoextruders. *Science* **312**(5777), 1199–1202 (2006)
20. P. Kim, C.M. Lieber, Nanotube nanotweezers. *Science* **286**(5447), 2148–2150 (1999)
21. J.R. Wood, M.D. Frogley, E.R. Meurs, A.D. Prins, T. Peijs, D.J. Dunstan, H.D. Wagner, Mechanical response of carbon nanotubes under molecular and macroscopic pressures. *J. Phys. Chem. B* **103**(47), 10388–10392 (1999)
22. E. Cobas, M.S. Fuhrera, Microwave rectification by a carbon nanotube schottky diode. *Appl. Phys. Lett.* **93**, 043120 (2008)
23. D. Cai, J.M. Mataraza, Z.-H. Qin, Z. Huang, J. Huang, T.C. Chiles, D. Carnahan, K. Kempa, Z. Ren, Highly efficient molecular delivery into mammalian cells using carbon nanotube spearing. *Nat. Methods* **2**, 449–454 (2005)
24. D. Cai, C.A. Doughty, T.B. Potocky, F.J. Dufort, Z. Huang, D. Blair, K. Kempa, Z.F. Ren, T.C. Chiles, Carbon nanotube-mediated delivery of nucleic acids does not result in non-specific activation of B lymphocytes. *Nanotechnology* **18**(36), 365101 (2007)
25. J.A. Rojas-Chapana, M.A. Correa-Duarte, Z. Ren, K. Kempa, M. Giersig, Enhanced introduction of gold nanoparticles into vital acidothiobacillus ferrooxidans by carbon nanotube-based microwave electroporation. *Nano Lett.* **4**(5), 985–988 (2004)
26. R.H. Baughman, A.A. Zakhidov, W.A. de Heer, Carbon nanotubes—the route toward applications. *Science* **297**(5582), 787–792 (2002)
27. M. Terrones, Science and technology of the twenty-first century: synthesis, properties, and applications of carbon nanotubes. *Annu. Rev. Mater. Res.* **33**, 419–501 (2003)

28. Y. Nakayama, S. Akita, Nanoengineering of carbon nanotubes for nanotools. *New J. Phys.* **5**, 128 (2003)
29. J. Robertson, Realistic applications of CNTs. *Mater. Today* **7**(10), 46–52 (2004)
30. A. Merkoçi, M. Pumera, X. Llopis, B. Pérez, M. del Valle, S. Alegret, New materials for electrochemical sensing VI: carbon nanotubes. *TrAC* **24**(9), 826–838 (2005)
31. P.J. Burke, C. Rutherglen, Z. Yu, Single-walled carbon nanotubes: applications in high frequency electronics. *Int. J. High Speed Electron. Syst.* **16**(4), 977–999 (2006)
32. K. Ishibashi, S. Moriyama, D. Tsuya, T. Fuse, M. Suzuki, Quantum-dot nanodevices with carbon nanotubes. *J. Vac. Sci. Technol. A* **24**(4), 1349–1355 (2006)
33. B. Mahar, C. Laslau, R. Yip, Y. Sun, Development of carbon nanotube-based sensors—a review. *IEEE Sens. J.* **7**, 266–284 (2007)
34. B.L. Allen, P.D. Kichambare, A. Star, Carbon nanotube field-effect-transistor-based biosensors. *Adv. Mater.* **19**(11), 1439–1451 (2007)
35. D. Vairavapandian, P. Vichchulada, M.D. Lay, Preparation and modification of carbon nanotubes: review of recent advances and applications in catalysis and sensing. *Anal. Chim. Acta* **626**(2), 119–129 (2008)
36. H. Xie, L. Chen, Review on the preparation and thermal performances of carbon nanotube contained nanofluids. *J. Chem. Eng. Data* **56**, 1030–1041 (2011)
37. F. Kreupl, Carbon nanotubes in microelectronic applications. in *Carbon Nanotube Devices: Properties, Modeling, Integration and Applications*, ed. by C. Hierold (Wiley-VCH, Weinheim, 2008), pp. 1–41
38. C. Stampfer, C. Hierold, Electromechanical carbon nanotube transducers. in *Carbon Nanotube Devices: Properties, Modeling, Integration and Applications*. Advanced Micro and Nanosystems, vol. 8, ed. by C. Hierold (Wiley-VCH, Weinheim, 2008)
39. A. Jungen, C. Hierold, Carbon nanotube direct integration into microsystems. in *Carbon Nanotube Devices: Properties, Modeling, Integration and Applications*. Advanced Micro and Nanosystems, vol. 8, ed. by C. Hierold (Wiley-VCH, Weinheim, 2008)
40. C. Roman, S. Roche, A. Rubio, Modeling the properties of carbon nanotubes for sensor-based devices. in *Carbon Nanotube Devices: Properties, Modeling, Integration and Applications*. Advanced Micro and Nanosystems, vol. 8, ed. by C. Hierold (Wiley-VCH, Weinheim, 2008)
41. J. Robertson, Carbon nanotube field emission devices. in *Carbon Nanotube Devices: Properties, Modeling, Integration and Applications*. Advanced Micro and Nanosystems, vol. 8, ed. by C. Hierold (Wiley-VCH, Weinheim, 2008)
42. F. Léonard, *The Physics of Carbon Nanotube Devices*. Micro and Nano Technologies (William Andrew, Norwich, 2009)
43. E. ōsawa (ed.), *Perspectives of Fullerene Nanotechnology* (Kluwer Academic, Dordrecht, 2002)
44. P. Bernier, D. Carroll, G. Kim, S. Roth (eds.), *Nanotube-Based Devices*. Materials Research Society Symposium Proceedings, vol. 772 (Materials Research Society, Warrendale, 2003)
45. C.V. Nguyen, Applications in scanning probe microscopy, in *Carbon Nanotubes: Science and Applications*, ed. by M. Meyyappan (CRC Press, Boca Raton, 2004)
46. T. Yamada, Nanoelectronics applications. in *Carbon Nanotubes: Science and Applications*, ed. by M. Meyyappan (CRC Press, Boca Raton, 2004)
47. M. Freitag, Carbon nanotube electronics and devices. in *Carbon Nanotubes Properties and Applications*, ed. by M.J. O’Connell (CRC Press, Boca Raton, 2006)
48. P. Russer, N. Fichtner, Nanoelectronics in radio-frequency technology. *IEEE Microw. Mag.* **10**, 119–135 (2010)
49. M.P. Anantram, F. Léonard, Physics of carbon nanotube electronic devices. *Rep. Prog. Phys.* **69**(3), 507–561 (2006)
50. C. Hierold (ed.), *Carbon Nanotube Devices: Properties, Modeling, Integration and Applications*. Advanced Micro and Nanosystems, vol. 8 (Wiley-VCH, Weinheim, 2008)
51. A. Mandelis, C. Christofides, *Physics, Chemistry and Technology of Solid State Gas Sensor Devices* (Wiley, New York, 1993)

52. K. Balasubramanian, E.J.H. Lee, R.T. Weitz, M. Burghard, K. Kern, Carbon nanotube transistors—chemical functionalization and device characterization. *Phys. Stat. Sol. A* **205**(3), 633–646 (2008)
53. M. Burghard, H. Klauk, K. Kern, Carbon-based field-effect transistors for nanoelectronics. *Adv. Mater.* **21**(25–26), 2586–2600 (2009)
54. S. Ji, C. Liu, B. Zhang, F. Yang, J. Xu, J. Long, C. Jin, D. Fu, Q. Ni, X. Yu, Carbon nanotubes in cancer diagnosis and therapy. *BBA Rev. Cancer* **1806**(1), 29–35 (2010)
55. G. Lota, K. Fic, E. Frackowiak, Carbon nanotubes and their composites in electrochemical applications. *Energy Environ. Sci.* **4**(5), 1592–1605 (2011)
56. A.I. Zhanov, N.I. Sinitsyn, G.V. Torgashov, Nanoelectronic devices based on carbon nanotubes. *Radiophys. Quantum Electron.* **47**(5–6), 435–452 (2004)
57. L.A. Chernozatonskii, Y.V. Gulyaev, Z.J. Kosakovskaja, N.I. Sinitsyn, G.V. Torgashov, Y.F. Zakharchenko, E.A. Fedorov, V.P. Val'chuk, Electron field emission from nanofilament carbon films. *Chem. Phys. Lett.* **233**(1–2), 63–68 (1995)
58. W.A. de Heer, A. Châtelain, D. Ugarte, A carbon nanotube field-emission electron source. *Science* **270**(5239), 1179–1180 (1995)
59. L.A. Chernozatonskii, Z.Y. Kosakovskaya, Y.V. Gulyaev, N.I. Sinitsyn, G.V. Torgashov, Y.F. Zakharchenko, Influence of external factors on electron field emission from thin-film nanofilament carbon structures. *J. Vac. Sci. Technol. B* **14**(3), 2080–2082 (1996)
60. P.G. Collins, A. Zettl, A simple and robust electron beam source from carbon nanotubes. *Appl. Phys. Lett.* **69**(13), 1969–1971 (1996)
61. H. Schmid, H.-W. Fink, Carbon nanotubes are coherent electron sources. *Appl. Phys. Lett.* **70**(20), 2679–2680 (1997)
62. W.A. de Heer, J. Bonard, K. Fauth, A. Châtelain, D. Ugarte, L. Forró, Electron field emitters based on carbon nanotube films. *Adv. Mater.* **9**(1), 87–89 (1997)
63. Y.V. Gulyaev, N.I. Sinitsyn, G.V. Torgashov, S.T. Mevlyut, A.I. Zhanov, Y.F. Zakharchenko, Z.Y. Kosakovskaya, L.A. Chernozatonskii, O.E. Glukhova, I.G. Torgashov, Work function estimate for electrons emitted from nanotube carbon cluster films. *J. Vac. Sci. Technol. B* **15**(2), 422–424 (1997)
64. P.G. Collins, A. Zettl, Unique characteristics of cold cathode carbon-nanotube-matrix field emitters. *Phys. Rev. B* **55**(15), 9391–9399 (1997)
65. Y. Saito, K. Hamaguchi, K. Hata, K. Uchida, Y. Tasaka, F. Ikazaki, M. Yumura, A. Kasuya, Y. Nishina, Conical beams from open nanotubes. *Nature* **389**(6651), 554–555 (1997)
66. Y.H.L. Lee, S.G. Kim, D. Tomnek, Field-induced unraveling of carbon nanotubes. *Chem. Phys. Lett.* **265**(6), 667–672 (1997)
67. S.H. Jo, Y. Tu, Z.P. Huang, D.L. Carnahan, J.Y. Huang, D.Z. Wang, Z.F. Ren, Correlation of field emission and surface microstructure of vertically aligned carbon nanotubes. *Appl. Phys. Lett.* **84**(3), 413–415 (2004)
68. S.H. Jo, J.Y. Huang, S. Chen, G.Y. Xiong, D.Z. Wang, Z.F. Ren, Field emission of carbon nanotubes grown on carbon cloth. *J. Vac. Sci. Technol. B* **23**(6), 2363–2368 (2005)
69. B. Zeng, G. Xiong, S. Chen, W.Z. Wang, D.Z. Wang, Z.F. Ren, Enhancement of field emission of aligned carbon nanotubes by thermal oxidation. *Appl. Phys. Lett.* **89**(22), 223119 (2006)
70. J.-M. Bonard, H. Kind, T. Stekli, L.-O. Nilsson, Field emission from carbon nanotubes: the first five years. *Solid-State Electron.* **45**(6), 893–914 (2001)
71. S. Fan, M.G. Chapline, N.R. Franklin, T.W. Tomblor, A.M. Cassell, H. Dai, Self-oriented regular arrays of carbon nanotubes and their field emission properties. *Science* **283**(5401), 512–514 (1999)
72. N. de Jonge, J.M. Bonard, Carbon nanotube electron sources and applications. *Phil. Tr. R. Soc. S. A* **362**(1823), 2239–2266 (2004)
73. W.I. Milne, K.B.K. Teo, G.A.J. Amaratunga, P. Legagneux, L. Gangloff, J.P. Schnell, V. Semet, V.T. Binh, O. Groening, Carbon nanotubes as field emission sources. *J. Mater. Chem.* **14**(6), 933–943 (2004)
74. C.J. Edgcombe, U. Valdrè, Microscopy and computational modelling to elucidate the enhancement factor for field electron emitters. *J. Microsc.* **203**(2), 188–194 (2001)

75. J.-M. Bonard, F. Maier, T. Stöckli, A. Châtelain, W.A. de Heer, J.-P. Salvetat, L. Forró, Field emission properties of multiwalled carbon nanotubes. *Ultramicroscopy* **73**(1–4), 7–15 (1998)
76. P. Sarrazin, Field emission. in *Carbon Nanotubes: Science and Applications*, ed. by M. Meyyappan (CRC Press, Boca Raton, 2004)
77. J.M. Bonard, M. Croci, C. Klinke, R. Kurt, O. Noury, N. Weiss, Carbon nanotube films as electron field emitters. *Carbon* **40**(10), 1715–1728 (2002)
78. Y.H. Lee, S.C. Lim, K.H. An, W.S. Kim, H.J. Jeong, Y.M. Shin, H.-G. Lee, J.M. Kim, Applications of carbon nanotubes to electron emitters. *New Diam. Front. Carbon Technol.* **12**(4), 181–207 (2002)
79. K.A. Dean, B.R. Chalamala, Current saturation mechanisms in carbon nanotube field emitters. *Appl. Phys. Lett.* **76**(3), 375–377 (2000)
80. J.-M. Bonard, M. Croci, I. Arfaoui, O. Noury, D. Sarangi, A. Châtelain, Can we reliably estimate the emission field and field enhancement factor of carbon nanotube film field emitters? *Diam. Relat. Mater.* **11**(3–6), 763–768 (2002)
81. S.H. Jo, Y. Tu, Z.P. Huang, D.L. Carnahan, D.Z. Wang, Z.F. Ren, Effect of length and spacing of vertically aligned carbon nanotubes on field emission properties. *Appl. Phys. Lett.* **82**(20), 3520–3522 (2003)
82. M. Chhowalla, C. Ducati, N.L. Rupesinghe, K.B.K. Teo, G.A.J. Amaratunga, Field emission from short and stubby vertically aligned carbon nanotubes. *Appl. Phys. Lett.* **79**(13), 2079–2081 (2001)
83. J.S. Suh, K.S. Jeong, J.S. Lee, I. Han, Study of the field-screening effect of highly ordered carbon nanotube arrays. *Appl. Phys. Lett.* **80**(13), 2392–2394 (2002)
84. M.A. Guillorn, A.V. Melechko, V.I. Merkulov, D.K. Hensley, M.L. Simpson, D.H. Lowndes, Self-aligned gated field emission devices using single carbon nanofiber cathodes. *Appl. Phys. Lett.* **81**(19), 3660–3662 (2002)
85. L. Nilsson, O. Groening, C. Emmenegger, O. Kuettel, E. Schaller, L. Schlapbach, H. Kind, J.-M. Bonard, K. Kern, Scanning field emission from patterned carbon nanotube films. *Appl. Phys. Lett.* **76**(15), 2071–2073 (2000)
86. O. Gröning, O.M. Kützel, C. Emmenegger, P. Gröning, L. Schlapbach, Field emission properties of carbon nanotubes. *J. Vac. Sci. Technol. B* **18**(2), 665–678 (2000)
87. J.-M. Bonard, N. Weiss, H. Kind, T. Stöckli, L. Forró, K. Kern, A. Châtelain, Tuning the field emission properties of patterned carbon nanotube films. *Adv. Mater.* **13**(3), 184–188 (2001)
88. W.J. Yu, Y.S. Cho, G.S. Choi, D. Kim, Patterned carbon nanotube field emitter using the regular array of an anodic aluminium oxide template. *Nanotechnology* **16**(5), S291–S295 (2005)
89. T.C. Cheng, J. Shieh, W.J. Huang, M.C. Yang, M.H. Cheng, H.M. Lin, M.N. Chang, Hydrogen plasma dry etching method for field emission application. *Appl. Phys. Lett.* **88**(26), 263118 (2006)
90. Z. Chen, D. den Engelsen, P.K. Bachmann, V. van Elsbergen, I. Koehler, J. Merikhi, D.U. Wiechert, High emission current density microwave-plasma-grown carbon nanotube arrays by postdepositional radio-frequency oxygen plasma treatment. *Appl. Phys. Lett.* **87**(24), 243104 (2005)
91. Y. Tu, Z.P. Huang, D.Z. Wang, J.G. Wen, Z.F. Ren, Growth of aligned carbon nanotubes with controlled site density. *Appl. Phys. Lett.* **80**(21), 4018–4020 (2002)
92. Y. Liu, S. Fan, Enhancement of field emission properties of cyanoacrylate-carbon nanotube arrays by laser treatment. *Nanotechnology* **15**(8), 1033–1037 (2004)
93. S.-C. Kung, K.C. Hwang, I.N. Lin, Oxygen and ozone oxidation-enhanced field emission of carbon nanotubes. *Appl. Phys. Lett.* **80**(25), 4819–4821 (2002)
94. K.S. Hazra, N.A. Koratkar, D.S. Misra, Improved field emission from multiwall carbon nanotubes with nano-size defects produced by ultra-low energy ion bombardment. *Carbon* **49**, 4760–4766 (2011)
95. Y. Saito, Carbon nanotube field emitter. *J. Nanosci. Nanotechnol.* **3**(1–2), 39–50 (2003)
96. Y. Saito, S. Uemura, Field emission from carbon nanotubes and its application to electron sources. *Carbon* **38**(2), 169–182 (2000)

97. A.V. Eletsii, Carbon nanotube-based electron field emitters. *Phys. Usp.* **53**, 2010 (2010)
98. Y. Saitō (ed.), *Carbon Nanotube and Related Field Emitters: Fundamentals and Applications* (Wiley-VCH, Weinheim, 2010)
99. Y. Shiratori, H. Hiraoka, Y. Takeuchi, S. Itoh, M. Yamamoto, One-step formation of aligned carbon nanotube field emitters at 400 °C. *Appl. Phys. Lett.* **82**(15), 2485–2487 (2003)
100. S.-H. Jeong, H.-Y. Hwang, K.-H. Lee, Y. Jeong, Template-based carbon nanotubes and their application to a field emitter. *Appl. Phys. Lett.* **78**(14), 2052–2054 (2001)
101. Y. Saito, S. Uemura, K. Hamaguchi, Cathode ray tube lighting elements with carbon nanotube field emitters. *Jpn. J. Appl. Phys.* **37**, L346–L348 (1998)
102. H. Murakami, M. Hirakawa, C. Tanaka, H. Yamakawa, Field emission from well-aligned, patterned, carbon nanotube emitters. *Appl. Phys. Lett.* **76**(13), 1776–1778 (2000)
103. J.-M. Bonard, J.-P. Salvetat, T. Stöckli, W.A. de Heer, L. Forró, A. Châtelain, Field emission from single-wall carbon nanotube films. *Appl. Phys. Lett.* **73**(7), 918–920 (1998)
104. X. Xu, G.R. Brandes, A method for fabricating large-area, patterned, carbon nanotube field emitters. *Appl. Phys. Lett.* **74**(17), 2549–2551 (1999)
105. P. Gröning, P. Ruffieux, L. Schlapbach, O. Gröning, Carbon nanotubes for cold electron sources. *Adv. Eng. Mater.* **5**(8), 541–550 (2003)
106. J. Bonard, T. Stöckli, O. Noury, A. Châtelain, Field emission from cylindrical carbon nanotube cathodes: possibilities for luminescent tubes. *Appl. Phys. Lett.* **78**(18), 2775–2777 (2001)
107. J.X. Huang, J. Chen, S.Z. Deng, J.C. She, N.S. Xu, Field-emission fluorescent lamp using carbon nanotubes on a wire-type cold cathode and a reflecting anode. *J. Vac. Sci. Technol. B* **26**(5), 1700–1704 (2008)
108. Y. Saito, K. Hata, A. Takakura, J. Yotani, S. Uemura, Field emission of carbon nanotubes and its application as electron sources of ultra-high luminance light-source devices. *Phys. B Condens. Matter* **323**(1–4), 30–37 (2002)
109. M. Zhang, S. Fang, A.A. Zakhidov, S.B. Lee, A.E. Aliev, C.D. Williams, K.R. Atkinson, R.H. Baughman, Strong, transparent, multifunctional, carbon nanotube sheets. *Science* **309**(5738), 1215–1219 (2005)
110. L.M. Ericson, H. Fan, H. Peng, V.A. Davis, W. Zhou, J. Sulpizio, Y. Wang, R. Booker, J. Vavro, C. Guthy, A.N.G. Parra-Vasquez, M.J. Kim, S. Ramesh, R.K. Saini, C. Kittrell, G. Lavin, H. Schmidt, W.W. Adams, W.E. Billups, M. Pasquali, W.-F. Hwang, R.H. Hauge, J.E. Fischer, R.E. Smalley, Macroscopic, neat, single-walled carbon nanotube fibers. *Science* **305**(5689), 1447–1450 (2004)
111. N.S. Lee, D.S. Chung, I.T. Han, J.H. Kang, Y.S. Choi, H.Y. Kim, S.H. Park, Y.W. Jin, W.K. Yi, M.J. Yun, J.E. Jung, C.J. Lee, J.H. You, S.H. Jo, C.G. Lee, J.M. Kim, Application of carbon nanotubes to field emission displays. *Diam. Relat. Mater.* **10**(2), 265–270 (2001)
112. W. Zhu, C. Bower, O. Zhou, G. Kochanski, S. Jin, Large current density from carbon nanotube field emitters. *Appl. Phys. Lett.* **75**(6), 873–875 (1999)
113. Q.H. Wang, A.A. Setlur, J.M. Lauerhaas, J.Y. Dai, E.W. Seelig, R.P.H. Chang, A nanotube-based field-emission flat panel display. *Appl. Phys. Lett.* **72**(22), 2912–2913 (1998)
114. W.B. Choi, D.S. Chung, J.H. Kang, H.Y. Kim, Y.W. Jin, I.T. Han, Y.H. Lee, J.E. Jung, N.S. Lee, G.S. Park, J.M. Kim, Fully sealed, high-brightness carbon-nanotube field-emission display. *Appl. Phys. Lett.* **75**(20), 3129–3131 (1999)
115. Y.C. Choi, K.S. Jeong, I.T. Han, H.J. Kim, Y.W. Jin, J.M. Kim, B.G. Lee, J.H. Park, D.H. Choe, Double-gated field emitter array with carbon nanotubes grown by chemical vapor deposition. *Appl. Phys. Lett.* **88**(26), 263504 (2006)
116. P. Liu, L. Liu, Y. Wei, K. Liu, Z. Chen, K. Jiang, Q. Li, S. Fan, Fast high-temperature response of carbon nanotube film and its application as an incandescent display. *Adv. Mater.* **21**(35), 3563–3566 (2009)
117. Y. Wei, K. Jiang, X. Feng, P. Liu, L. Liu, S. Fan, Comparative studies of multiwalled carbon nanotube sheets before and after shrinking. *Phys. Rev. B* **76**(4), 045423 (2007)
118. H. Sugie, M. Tanemura, V. Filip, K. Iwata, K. Takahashi, F. Okuyama, Carbon nanotubes as electron source in an X-ray tubes. *Appl. Phys. Lett.* **78**(17), 2578–2580 (2001)

119. G.Z. Yue, Q. Qiu, B. Gao, Y. Cheng, J. Zhang, H. Shimoda, S. Chang, J.P. Lu, O. Zhou, Generation of continuous and pulsed diagnostic imaging X-ray radiation using a carbon-nanotube-based field-emission cathodes. *Appl. Phys. Lett.* **81**(2), 355–357 (2002)
120. Y.Z. Lee, L. Burk, K. han Wang, G. Cao, J. Lu, O. Zhou, Carbon nanotube based X-ray sources: applications in preclinical and medical imaging. *Nucl. Instrum. Meth. A* **648**, S281–S283 (2011)
121. S. Wang, X. Calderon, R. Peng, E.C. Schreiber, O. Zhou, S. Chang, A carbon nanotube field emission multipixel x-ray array source for microradiotherapy application. *Appl. Phys. Lett.* **98**(21), 213701 (2011)
122. K.B.K. Teo, E. Minoux, L. Hudanski, F. Peauger, J.-P. Schnell, L. Gangloff, P. Legagneux, D. Dieumegard, G.A.J. Amaratunga, W.I. Milne, Microwave devices: carbon nanotubes as cold cathodes. *Nature* **437**, 968 (2005)
123. K.B.K. Teo, S.-B. Lee, M. Chhowalla, V. Semet, V.T. Binh, O. Groening, M. Castignolles, A. Loiseau, G. Pirio, P. Legagneux, D. Pribat, D.G. Hasko, H. Ahmed, G.A.J. Amaratunga, W.I. Milne, Plasma enhanced chemical vapour deposition carbon nanotubes/nanofibres: how uniform do they grow? *Nanotechnology* **14**(2), 204–211 (2003)
124. W.I. Milne, K.B.K. Teo, E. Minoux, O. Groening, L. Gangloff, L. Hudanski, J.-P. Schnell, D. Dieumegard, F. Peauger, I.Y.Y. Bu, M.S. Bell, P. Legagneux, G. Hasko, G.A.J. Amaratunga, Aligned carbon nanotubes/fibers for applications in vacuum microwave amplifiers. *J. Vac. Sci. Technol. B* **24**(1), 345–348 (2006)
125. E. Minoux, L. Hudanski, K.B.K. Teo, O. Groening, F. Peauger, D. Dieumegard, J.-P. Schnell, L. Gangloff, G.A.J. Amaratunga, W.I. Milne, J. Robertson, P. Legagneux, Carbon nanotube cathodes as electron sources for microwave amplifiers. in *7th IEEE Conference on Nanotechnology, 2007. IEEE-NANO 2007*, pp. 1248–1251 (2007)
126. P. Legagneux, N. Le Sech, P. Guiset, L. Gangloff, C. Cojocar, J.P. Schnell, D. Pribat, K.B.K. Teo, J. Robertson, W.I. Milne, F. Andre, Y. Rozier, D. Dieumegard, Carbon nanotube based cathodes for microwave amplifiers. in *Vacuum Electronics Conference, 2009. IVEC '09. IEEE International*, pp. 80–81 (2009)
127. K. Han, Y. Lee, D. Jun, S. Lee, K.W. Jung, S.S. Yang, Field emission ion source using a carbon nanotube array for micro time-of-flight mass spectrometer. *Jpn. J. Appl. Phys.* **50**(6), 06GM04 (2011)
128. T. Hasobe, S. Fukuzumi, P.V. Kamat, Stacked-cup carbon nanotubes for photoelectrochemical solar cells. *Angew. Chem. Int. Edit.* **45**(5), 755–759 (2006)
129. K. Kempa, B. Kimball, J. Rybczynski, Z.P. Huang, P.F. Wu, D. Steeves, M. Sennett, M. Giersig, D.V.G.L.N. Rao, D.L. Carnahan, D.Z. Wang, J.Y. Lao, W.Z. Li, Z.F. Ren, Photonic crystals based on periodic arrays of aligned carbon nanotubes. *Nano Lett.* **3**(1), 13–18 (2003)
130. X. Wang, K. Kempa, Z.F. Ren, B. Kimball, Rapid photon flux switching in two-dimensional photonic crystals. *Appl. Phys. Lett.* **84**(11), 1817–1819 (2004)
131. K. Kempa, J. Rybczynski, Z. Huang, K. Gregorczyk, A. Vidan, B. Kimball, J. Carlson, G. Benham, Y. Wang, A. Herczynski, Z. Ren, Carbon nanotubes as optical antennae. *Adv. Mater.* **19**(3), 421–426 (2007)
132. X. Wang, Z. Ren, K. Kempa, Unrestricted superlensing in a triangular two dimensional photonic crystal. *Opt. Express* **12**(13), 2919–2924 (2004)
133. X. Wang, Z.F. Ren, K. Kempa, Improved superlensing in two-dimensional photonic crystals with a basis. *Appl. Phys. Lett.* **86**(6), 061105 (2005)
134. Y. Wang, X. Wang, J. Rybczynski, D.Z. Wang, K. Kempa, Z.F. Ren, Triangular lattice of carbon nanotube arrays for negative index of refraction and subwavelength lensing effect. *Appl. Phys. Lett.* **86**(15), 153120 (2005)
135. Y. Wang, J. Rybczynski, D.Z. Wang, Z.F. Ren, Large-scale triangular lattice arrays of sub-micron islands by microsphere self-assembly. *Nanotechnology* **16**(6), 819–822 (2005)
136. Y. Wang, K. Kempa, B. Kimball, J.B. Carlson, G. Benham, W.Z. Li, T. Kempa, J. Rybczynski, A. Herczynski, Z.F. Ren, Receiving and transmitting light-like radio waves: antenna effect in arrays of aligned carbon nanotubes. *Appl. Phys. Lett.* **85**(13), 2607–2609 (2004)

137. J. Rybczynski, K. Kempa, A. Herczynski, Y. Wang, M.J. Naughton, Z.F. Ren, Z.P. Huang, D. Cai, M. Giersig, Subwavelength waveguide for visible light. *Appl. Phys. Lett.* **90**(2), 021104 (2007)
138. Y. Zhang, S. Iijima, Elastic response of carbon nanotube bundles to visible light. *Phys. Rev. Lett.* **82**(17), 3472–3475 (1999)
139. Z. Li, V.P. Kunets, V. Saini, Y. Xu, E. Dervishi, G.J. Salamo, A.R. Biris, A.S. Biris, Light-harvesting using high density p-type single wall carbon nanotube/n-type silicon heterojunctions. *ACS Nano* **3**(6), 1407–1414 (2009)
140. S. Barazzouk, S. Hotchandani, K. Vinodgopal, P.V. Kamat, Single-wall carbon nanotube films for photocurrent generation: a prompt response to visible-light irradiation. *J. Phys. Chem. B* **108**(44), 17015–17018 (2004)
141. Y. Shi, D. Fu, D.H. Marsh, G.A. Rance, A.N. Khlobystov, L.-J. Li, Photoresponse in self-assembled films of carbon nanotubes. *J. Phys. Chem. C* **112**(33), 13004–13009 (2008)
142. M.A. Bissett, J.G. Shapter, Photocurrent response from vertically aligned single-walled carbon nanotube arrays. *J. Phys. Chem. C* **114**(14), 6778–6783 (2010)
143. M.A. Bissett, J.G. Shapter, Electrochemistry and photocurrent response from vertically-aligned chemically-functionalized single-walled carbon nanotube arrays. *J. Electrochem. Soc.* **158**(3), K53–K57 (2011)
144. M.A. Bissett, I. Koper, J.S. Quinton, J.G. Shapter, Dendron growth from vertically aligned single-walled carbon nanotube thin layer arrays for photovoltaic devices. *Phys. Chem. Chem. Phys.* **13**(13), 6059–6064 (2011)
145. T. Paudel, J. Rybczynski, Y.T. Gao, Y.C. Lan, Y. Peng, K. Kempa, M.J. Naughton, Z.F. Ren, Nanocoax solar cells based on aligned multiwalled carbon nanotube arrays. *Phys. Stat. Sol. (a)* **208**(4), 924–927 (2011)
146. M.J. Naughton, K. Kempa, Z.F. Ren, Y. Gao, J. Rybczynski, N. Argenti, W. Gao, Y. Wang, Y. Peng, J.R. Naughton, G. McMahon, T. Paudel, Y.C. Lan, M.J. Burns, A. Shepard, M. Clary, C. Ballif, F.-J. Haug, T. Söderström, O. Cubero, C. Eminian, Efficient nanocoax-based solar cells. *Phys. Stat. Sol. (Rapid Res. Lett.)* **4**(7), 181–183 (2010)
147. M. Tang, S.-T. Chang, T.-C. Chen, Z. Pei, W.-C. Wang, J. Huang, Simulation of nanorod structures for an amorphous silicon-based solar cell. *Thin Solid Films* **518**(6, Suppl. 1), S259–S261 (2010)
148. R. Camacho, A. Morgan, M. Flores, T. McLeod, V. Kumsomboone, B. Mordecai, R. Bhattacharjea, W. Tong, B. Wagner, J. Flicker, S. Turano, W. Ready, Carbon nanotube arrays for photovoltaic applications. *JOM-J MET* **59**(3), 39–42 (2007)
149. H. Zhou, A. Colli, A. Ahnood, Y. Yang, N. Rupesinghe, T. Butler, I. Haneef, P. Hiralal, A. Nathan, G.A.J. Amaratunga, Arrays of parallel connected coaxial multiwall-carbon-nanotube: amorphous-silicon solar cells. *Adv. Mater.* **21**(38–39), 3919–3923 (2009)
150. Y. Lin, F. Lu, J. Wang, Disposable carbon nanotube modified screen-printed biosensor for amperometric detection of organophosphorus pesticides and nerve agents. *Electroanalysis* **16**(1–2), 145–149 (2004)
151. J. Wang, G. Liu, M.R. Jan, Ultrasensitive electrical biosensing of proteins and dna: carbon-nanotube derived amplification of the recognition and transduction events. *J. Am. Chem. Soc.* **126**(10), 3010–3011 (2004)
152. J.J. Gooding, R. Wibowo, J. Liu, W. Yang, D. Losic, S. Orbons, F.J. Mearns, J.G. Shapter, D.B. Hibbert, Protein electrochemistry using aligned carbon nanotube arrays. *J. Am. Chem. Soc.* **125**(30), 9006–9007 (2003)
153. J.M. Nugent, K.S.V. Santhanam, A. Rubio, P.M. Ajayan, Fast electron transfer kinetics on multiwalled carbon nanotube microbundle electrodes. *Nano Lett.* **1**(2), 87–91 (2001)
154. X. Yu, D. Chattopadhyay, I. Galeska, F. Papadimitrakopoulos, J.F. Rusling, Peroxidase activity of enzymes bound to the ends of single-wall carbon nanotube forest electrodes. *Electrochem. Commun.* **5**(5), 408–411 (2003)
155. R. Feeney, S.P. Kounaves, Microfabricated ultramicroelectrode arrays: developments, advances, and applications in environmental analysis. *Electroanalysis* **12**(9), 677–684 (2000)

156. Y. Tu, Y. Lin, Z.F. Ren, Nanoelectrode arrays based on low site density aligned carbon nanotubes. *Nano Lett.* **3**(1), 107–109 (2003)
157. S.G. Weber, Signal-to-noise ratio in microelectrode-array-based electrochemical detectors. *Anal. Chem.* **61**(4), 295–302 (1989)
158. V.P. Menon, C.R. Martin, Fabrication and evaluation of nanoelectrode ensembles. *Anal. Chem.* **67**(13), 1920–1928 (1995)
159. M.A. Guillorn, T.E. McKnight, A. Melechko, V.I. Merkulov, P.F. Britt, D.W. Austin, D.H. Lowndes, M.L. Simpson, Individually addressable vertically aligned carbon nanofiber-based electrochemical probes. *J. Appl. Phys.* **91**(6), 3824–3828 (2002)
160. J. Li, A. Cassell, L. Delzeit, J. Han, M. Meyyappan, Novel three-dimensional electrodes: electrochemical properties of carbon nanotube ensembles. *J. Phys. Chem. B* **106**(36), 9299–9305 (2002)
161. W. Li, C. Liang, J. Qiu, W. Zhou, H. Han, Z. Wei, G. Sun, Q. Xin, Carbon nanotubes as support for cathode catalyst of a direct methanol fuel cell. *Carbon* **40**(5), 791–794 (2002)
162. J.H. Chen, W.Z. Li, D.Z. Wang, S.X. Yang, J.G. Wen, Z.F. Ren, Electrochemical characterization of carbon nanotubes as electrode in electrochemical double-layer capacitors. *Carbon* **40**(8), 1193–1197 (2002)
163. X.Q. Chen, T. Saito, H. Yamada, K. Matsushige, Aligning single-wall carbon nanotubes with an alternating-current electric field. *Appl. Phys. Lett.* **78**(23), 3714–3716 (2001)
164. J.H. Chen, Z.P. Huang, D.Z. Wang, S.X. Yang, W.Z. Li, J.G. Wen, Z.F. Ren, Electrochemical synthesis of polypyrrole films over each of well-aligned carbon nanotubes. *Synth. Met.* **125**(3), 289–294 (2002)
165. J. Li, Y. Lu, Q. Ye, M. Cinke, J. Han, M. Meyyappan, Carbon nanotube sensors for gas and organic vapor detection. *Nano Lett.* **3**, 929–933 (July 2003)
166. Y. Tu, Y. Lin, W. Yantasee, Z. Ren, Carbon nanotubes based nanoelectrode arrays: fabrication, evaluation, and application in voltammetric analysis. *Electroanalysis* **17**(1), 79–84 (2005)
167. J. Li, J.E. Koehne, A.M. Cassell, H. Chen, H.T. Ng, Q. Ye, W. Fan, J. Han, M. Meyyappan, Inlaid multi-walled carbon nanotube nanoelectrode arrays for electroanalysis. *Electroanalysis* **17**(1), 15–27 (2005)
168. A. Misra, J. Giri, C. Daraio, Hydrogen evolution on hydrophobic aligned carbon nanotube arrays. *ACS Nano* **3**, 3903–3908 (2009)
169. C.V. Nguyen, L. Delzeit, A.M. Cassell, J. Li, J. Han, M. Meyyappan, Preparation of nucleic acid functionalized carbon nanotube arrays. *Nano Lett.* **2**(10), 1079–1081 (2002)
170. J. Koehne, J. Li, A.M. Cassell, H. Chen, Q. Ye, H.T. Ng, J. Han, M. Meyyappan, The fabrication and electrochemical characterization of carbon nanotube nanoelectrode arrays. *J. Mater. Chem.* **14**(4), 676–684 (2004)
171. J.K. Campbell, L. Sun, R.M. Crooks, Electrochemistry using single carbon nanotubes. *J. Am. Chem. Soc.* **121**(15), 3779–3780 (1999)
172. P. Britto, K. Santhanam, P. Ajayan, Carbon nanotube electrode for oxidation of dopamine. *Bioelectrochem. Bioenerg.* **41**(1), 121–125 (1996)
173. J.J. Davis, R.J. Coles, H. Allen, O. Hill, Protein electrochemistry at carbon nanotube electrodes. *J. Electroanal. Chem.* **440**(1–2), 279–282 (1997)
174. P. Ugo, L.M. Moretto, F. Vezzà, Ionomer-coated electrodes and nanoelectrode ensembles as electrochemical environmental sensors: recent advances and prospects. *Chem. Phys. Chem.* **3**(11), 917–925 (2002)
175. W.E. Morf, N.F. de Rooij, Performance of amperometric sensors based on multiple microelectrode arrays. *Sens. Actuat. B Chem.* **44**(1–3), 538–541 (1997)
176. W.L. Caudill, J.O. Howell, R.M. Wightman, Flow rate independent amperometric cell. *Anal. Chem.* **54**(14), 2532–2535 (1982)
177. Y. Lin, F. Lu, Y. Tu, Z. Ren, Glucose biosensors based on carbon nanotube nanoelectrode ensembles. *Nano Lett.* **4**(2), 191–195 (2004)
178. J. Li, H.T. Ng, A. Cassell, W. Fan, H. Chen, Q. Ye, J. Koehne, J. Han, M. Meyyappan, Carbon nanotube nanoelectrode array for ultrasensitive dna detection. *Nano Lett.* **3**, 597–602 (May 2003)

179. S. Fletcher, M.D. Horne, Random assemblies of microelectrodes (RAM(TM) electrodes) for electrochemical studies. *Electrochem. Commun.* **1**(10), 502–512 (1999)
180. M.E. Sandison, N. Anicet, A. Glidle, J.M. Cooper, Optimization of the geometry and porosity of microelectrode arrays for sensor design. *Anal. Chem.* **74**(22), 5717–5725 (2002)
181. H.J. Lee, C. Beriet, R. Ferrigno, H.H. Girault, Cyclic voltammetry at a regular microdisc electrode array. *J. Electroanal. Chem.* **502**(1–2), 138–145 (2001)
182. F. Faßbender, G. Schmitt, M. J. Schöning, H. Lüth, G. Buß, J.W. Schultze, Optimization of passivation layers for corrosion protection of silicon-based microelectrode arrays. *Sens. Actuat. B Chem.* **68**(1–3), 128–133 (2000)
183. J.J. Gooding, Nanostructuring electrodes with carbon nanotubes: a review on electrochemistry and applications for sensing. *Electrochim. Acta* **50**(15), 3049–3060 (2005)
184. G. Liu, Y. Lin, Y. Tu, Z. Ren, Ultrasensitive voltammetric detection of trace heavy metal ions using carbon nanotube nanoelectrode array. *Analyst* **130**(7), 1098–1101 (2005)
185. X. Guo, Y. Yun, V.N. Shanov, H.B. Halsall, W.R. Heineman, Determination of trace metals by anodic stripping voltammetry using a carbon nanotube tower electrode. *Electroanalysis* **23**(5), 1252–1259 (2011)
186. D. Kauffman, A. Star, Carbon nanotube gas and vapor sensors. *Angew. Chem. Int. Edit.* **47**(35), 6550–6570 (2008)
187. R. Martel, T. Schmidt, H.R. Shea, T. Hertel, P. Avouris, Single- and multi-wall carbon nanotube field-effect transistors. *Appl. Phys. Lett.* **73**(17), 2447–2449 (1998)
188. E.S. Snow, J.P. Novak, P.M. Campbell, D. Park, Random networks of carbon nanotubes as an electronic material. *Appl. Phys. Lett.* **82**(13), 2145–2147 (2003)
189. H.E. Katz, Chemically sensitive field-effect transistors and chemiresistors: new materials and device structures. *Electroanalysis* **16**(22), 1837–1842 (2004)
190. E.S. Snow, F.K. Perkins, J.A. Robinson, Chemical vapor detection using single-walled carbon nanotubes. *Chem. Soc. Rev.* **35**(9), 790–798 (2006)
191. J.T.W. Yeow, Carbon nanotube gas sensors. in *Carbon Nanotube Devices: Properties, Modeling, Integration and Applications*. Advanced Micro and Nanosystems, vol. 8, ed. by C. Hierold (Wiley-VCH, Weinheim, 2008)
192. T. Zhang, S. Mubeen, N.V. Myung, M.A. Deshusses, Recent progress in carbon nanotube-based gas sensors. *Nanotechnology* **19**(33), 332001 (2008)
193. P. Bondavalli, P. Legagneux, D. Pribat, Carbon nanotubes based transistors as gas sensors: state of the art and critical review. *Sens. Actuat. B Chem.* **140**(1), 304–318 (2009)
194. Y. Wang, J.T.W. Yeow, A review of carbon nanotubes-based gas sensors. *J. Sens.* **2009**, 493904 (2009)
195. M. Lee, K.Y. Baik, M. Noah, Y.K. Kwon, J.O. Lee, S. Hong, Nanowire and nanotube transistors for lab-on-a-chip applications. *Lab Chip* **9**(16), 2267–2280 (2009)
196. C. Cantalini, L. Valentini, I. Armentano, J.M. Kenny, L. Lozzi, S. Santucci, Carbon nanotubes as new materials for gas sensing applications. *J. Eur. Ceram. Soc.* **24**(6), 1405–1408 (2004)
197. A. Modi, N. Koratkar, E. Lass, B. Wei, P.M. Ajayan, Miniaturized gas ionization sensors using carbon nanotubes. *Nature* **424**, 171–174 (2003)
198. S. Dag, Y. Ozturk, S. Ciraci, T. Yildirim, Adsorption and dissociation of hydrogen molecules on bare and functionalized carbon nanotubes. *Phys. Rev. B* **72**(15), 155404 (2005)
199. J. Kong, M.G. Chapline, H. Dai, Functionalized carbon nanotubes for molecular hydrogen sensors. *Adv. Mater.* **13**(18), 1384–1386 (2001)
200. I. Sayago, E. Terrado, E. Lafuente, M. Horrillo, W. Maser, A. Benito, R. Navarro, E. Urriolabeitia, M. Martinez, J. Gutierrez, Hydrogen sensors based on carbon nanotubes thin films. *Synth. Met.* **148**(1), 15–19 (2005)
201. A.T. Gee, B.E. Hayden, C. Mormiche, T.S. Nunney, The role of steps in the dynamics of hydrogen dissociation on Pt(533). *J. Chem. Phys.* **112**(17), 7660–7668 (2000)
202. R.A. Olsen, Ş.C. Bădescu, S.C. Ying, E.J. Baerends, Adsorption and diffusion on a stepped surface: atomic hydrogen on Pt(211). *J. Chem. Phys.* **120**(24), 11852–11863 (2004)
203. Y.M. Wong, W.P. Kang, J.L. Davidson, A. Wisitsora-at, K.L. Soh, A novel microelectronic gas sensor utilizing carbon nanotubes for hydrogen gas detection. *Sens. Actuat. B Chem.* **93**(1–3), 327–332 (2003)

204. J. Zhao, A. Buldum, J. Han, J.P. Lu, Gas molecule adsorption in carbon nanotubes and nanotube bundles. *Nanotechnology* **13**(2), 195 (2002)
205. T. Ueda, S. Katsuki, K. Takahashi, H. Narges, T. Ikegami, F. Mitsugi, Fabrication and characterization of carbon nanotube based high sensitive gas sensors operable at room temperature. *Diam. Relat. Mater.* **17**(7–10), 1586–1589 (2008)
206. M. Penza, R. Rossi, M. Alvisi, E. Serra, Metal-modified and vertically aligned carbon nanotube sensors array for landfill gas monitoring applications. *Nanotechnology* **21**(10), 105501 (2010)
207. L. Valentini, C. Cantalini, I. Armentano, J.M. Kenny, L. Lozzi, S. Santucci, Highly sensitive and selective sensors based on carbon nanotubes thin films for molecular detection. *Diamond Relat. Mater.* **13**(4–8), 1301–1305 (2004)
208. S. Kim, CNT sensors for detecting gases with low adsorption energy by ionization. *Sensors* **6**(5), 503–513 (2006)
209. S.J. Kim, Gas sensors based on paschen's law using carbon nanotubes as electron emitters. *J. Phys. D Appl. Phys.* **39**(14), 3026 (2006)
210. M. Arab, F. Berger, F. Picaud, C. Ramseyer, J. Glory, M. Mayne-L'Hermite, Direct growth of the multi-walled carbon nanotubes as a tool to detect ammonia at room temperature. *Chem. Phys. Lett.* **433**(1–3), 175–181 (2006)
211. C. Wei, L. Dai, A. Roy, T.B. Tolle, Multifunctional chemical vapor sensors of aligned carbon nanotube and polymer composites. *J. Am. Chem. Soc.* **128**(5), 1412–1413 (2006)
212. R.J. Chen, Y. Zhang, D. Wang, H. Dai, Noncovalent sidewall functionalization of single-walled carbon nanotubes for protein immobilization. *J. Am. Chem. Soc.* **123**(16), 3838–3839 (2001)
213. B.R. Azamian, J.J. Davis, K.S. Coleman, C.B. Bagshaw, M.L.H. Green, Bioelectrochemical single-walled carbon nanotubes. *J. Am. Chem. Soc.* **124**(43), 12664–12665 (2002)
214. A. Thess, R. Lee, P. Nikolaev, H. Dai, P. Petit, J. Robert, C. Xu, Y.H. Lee, S.G. Kim, A.G. Rinzler, D.T. Colbert, G.E. Scuseria, D. Tománek, J.E. Fischer, R.E. Smalley, Crystalline ropes of metallic carbon nanotubes. *Science* **273**(5274), 483–487 (1996)
215. J. Wang, M. Musameh, Y. Lin, Solubilization of carbon nanotubes by Nafion toward the preparation of amperometric biosensors. *J. Am. Chem. Soc.* **125**(9), 2408–2409 (2003)
216. H. Luo, Z. Shi, N. Li, Z. Gu, Q. Zhuang, Investigation of the electrochemical and electrocatalytic behavior of single-wall carbon nanotube film on a glassy carbon electrode. *Anal. Chem.* **73**(5), 915–920 (2001)
217. G. Che, B.B. Lakshmi, E.R. Fisher, C.R. Martin, Carbon nanotubule membranes for electrochemical energy storage and production. *Nature* **393**(6683), 346–349 (1998)
218. Y. Yu, A. Cimen, Y. Lan, J. Rybczynski, D. Wang, T. Paudel, Z. Ren, D. Wagner, M. Qiu, T. Chiles, D. Cai, Assembly of multi-functional nanocomponents on periodic nanotube array for biosensors. *Micro Nano Lett.* **4**, 27–33 (Mar. 2009)
219. M. Gao, L. Dai, G.G. Wallace, Biosensors based on aligned carbon nanotubes coated with inherently conducting polymers. *Electroanalysis* **15**(13), 1089–1094 (2003)
220. M. Musameh, J. Wang, A. Merkoci, Y. Lin, Low-potential stable nadh detection at carbon-nanotube-modified glassy carbon electrodes. *Electrochem. Commun.* **4**(10), 743–746 (2002)
221. D.R. Kauffman, A. Star, Electronically monitoring biological interactions with carbon nanotube field-effect transistors. *Chem. Soc. Rev.* **37**(6), 1197–1206 (2008)
222. S.N. Kim, J.F. Rusling, F. Papadimitrakopoulos, Carbon nanotubes for electronic and electrochemical detection of biomolecules. *Adv. Mater.* **19**, 3214–3228 (2007)
223. G. Sánchez-Pomales, L. Santiago-Rodríguez, C.R. Cabrera, DNA-functionalized carbon nanotubes for biosensing applications. *J. Nanosci. Nanotechnol.* **9**(4), 2175–2188 (2009)
224. P. He, Y. Xu, Y. Fang, Applications of carbon nanotubes in electrochemical DNA biosensors. *Microchim. Acta* **152**, 175–186 (2006)
225. Y. Lin, S. Taylor, H.P. Li, K.A.S. Fernando, L.W. Qu, W. Wang, L.R. Gu, B. Zhou, Y.P. Sun, Advances toward bioapplications of carbon nanotubes. *J. Mater. Chem.* **14**(4), 527–541 (2004)
226. J. Wang, Carbon-nanotube based electrochemical biosensors: a review. *Electroanalysis* **17**(1), 7–14 (2005)

227. M. Sinha, J. Ma, J.T.W. Yeow, Carbon nanotube-based sensors. *J. Nanosci. Nanotechnol.* **6**(3), 573–590 (2006)
228. K. Balasubramanian, M. Burghard, Biosensors based on carbon nanotubes. *Anal. Bioanal. Chem.* **385**(3), 452–468 (2006)
229. M.U. Ahmed, M.M. Hossain, E. Tamiya, Electrochemical biosensors for medical and food applications. *Electroanalysis* **20**(6), 616–626 (2008)
230. J. Koh, B. Kim, S. Hong, H. Lim, H.C. Choi, Nanotube-based chemical and biomolecular sensors. *J. Mater. Sci. Technol.* **24**(4), 578–588 (2008)
231. K. Maehashi, K. Matsumoto, Label-free electrical detection using carbon nanotube-based biosensors. *Sensors* **9**(7), 5368–5378 (2009)
232. C.B. Jacobs, M.J. Peairs, B.J. Venton, Review: carbon nanotube based electrochemical sensors for biomolecules. *Anal. Chim. Acta* **662**(2), 105–127 (2010)
233. D. Fam, A. Palaniappan, A. Tok, B. Liedberg, S. Moochhala, A review on technological aspects influencing commercialization of carbon nanotube sensors. *Sens. Actuat. B Chem.* **157**(1), 1–7 (2011)
234. J. Wang, J. Liu, L. Chen, F. Lu, Highly selective membrane-free, mediator-free glucose biosensor. *Anal. Chem.* **66**(21), 3600–3603 (1994)
235. J. Wang, F. Lu, L. Angnes, J. Liu, H. Sakslund, Q. Chen, M. Pedrero, L. Chen, O. Hammerich, Remarkably selective metallized-carbon amperometric biosensors. *Anal. Chim. Acta* **305** (1–3), 3–7 (1995)
236. F. Jiang, S. Wang, J. Lin, H. Jin, L. Zhang, S. Huang, J. Wang, Aligned SWCNT-copper oxide array as a nonenzymatic electrochemical probe of glucose. *Electrochem. Commun.* **13**(4), 363–365 (2011)
237. Q. Yang, Y. Qu, Y. Bo, Y. Wen, S. Huang, Biosensor for atrazin based on aligned carbon nanotubes modified with glucose oxidase. *Microchim. Acta* **168**(3), 197–203 (2010)
238. Y. Li, T. Kaneko, Y. Hirotsu, R. Hatakeyama, Light-induced electron transfer through DNA-decorated single-walled carbon nanotubes. *Small* **6**(1), 27–30 (2010)
239. F. Patolsky, C.M. Lieber, Nanowire nanosensors. *Mater. Today* **8**(4), 20–28 (2005)
240. D. Cai, L. Ren, H. Zhao, C. Xu, L. Zhang, Y. Yu, H. Wang, Y. Lan, M.F. Roberts, J.H. Chuang, M.J. Naughton, Z. Ren, T.C. Chiles, A molecular-imprint nanosensor for ultrasensitive detection of proteins. *Nat. Nanotechnol.* **5**, 597–601 (2010)
241. R.S. Prasher, Surface chemistry and characteristics based model for the thermal contact resistance of fluidic interstitial thermal interface materials. *J. Heat Transf.* **123**(5), 969–975 (2001)
242. P. Kim, L. Shi, A. Majumdar, P.L. McEuen, Thermal transport measurements of individual multiwalled nanotubes. *Phys. Rev. Lett.* **87**, 215502 (Oct 2001)
243. S.U.S. Choi, Z.G. Zhang, W. Yu, F.E. Lockwood, E.A. Grulke, Anomalous thermal conductivity enhancement in nanotube suspensions. *Appl. Phys. Lett.* **79**(14), 2252–2254 (2001)
244. M.J. Biercuk, M.C. Llaguno, M. Radosavljevic, J.K. Hyun, A.T. Johnson, J.E. Fischer, Carbon nanotube composites for thermal management. *Appl. Phys. Lett.* **80**(15), 2767–2769 (2002)
245. C.H. Liu, H. Huang, Y. Wu, S.S. Fan, Thermal conductivity improvement of silicone elastomer with carbon nanotube loading. *Appl. Phys. Lett.* **84**(21), 4248–4250 (2004)
246. C.-W. Nan, G. Liu, Y. Lin, M. Li, Interface effect on thermal conductivity of carbon nanotube composites. *Appl. Phys. Lett.* **85**(16), 3549–3551 (2004)
247. O. Breuer, U. Sundararaj, Big returns from small fibers: a review of polymer/carbon nanotube composites. *Polym. Compos.* **25**, 630–645 (2004)
248. J. Liu, B. Michel, M. Rencz, C. Tantolin, C. Sarno, R. Miessners, K.V. Schuetts, X.H. Tang, S. Demoustier, A. Ziaei, Recent progress of thermal interface material research—an overview, in *14th International Workshop on Thermal Investigation Of ICs And Systems*, pp. 156–162 (2008)
249. S.T. Huxtable, D.G. Cahill, S. Shenogin, L. Xue, R. Ozisik, P. Barone, M. Usrey, M.S. Strano, G. Siddons, M. Shim, P. Koblinski, Interfacial heat flow in carbon nanotube suspensions. *Nat. Mater.* **2**, 731–734 (Nov. 2003)

250. H. Huang, C.H. Liu, Y. Wu, S. Fan, Aligned carbon nanotube composite films for thermal management. *Adv. Mater.* **17**(13), 1652–1656 (2005)
251. X.J. Hu, A.A. Padilla, J. Xu, T.S. Fisher, K.E. Goodson, 3-omega measurements of vertically oriented carbon nanotubes on silicon. *J. Heat Transf.* **128**(11), 1109–1113 (2006)
252. K. Zhang, M.M.F. Yuen, N. Wang, J.Y. Miao, D.G.W. Xiao, H.B. Fan, Thermal interface material with aligned CNT and its application in HB-LED packaging, in *Electronic Components and Technology Conference, 2006. Proceedings. 56th*, p. 177 (2006)
253. J.L. Abot, V. Raghavan, G. Li, E.L. Thomas, Effect of interface, height and density of long vertically aligned carbon nanotube arrays on their thermal conductivity: an experimental study. *J. Nanosci. Nanotechnol.* **11**(1), 115–124 (2011)
254. B.K. Kaushik, S. Goel, G. Rauthan, Future VLSI interconnects: optical fiber or carbon nanotube—a review. *Microelectron. Int.* **24**(2), 53–63 (2007)
255. W. Steinhögl, G. Schindler, G. Steinlesberger, M. Engelhardt, Size-dependent resistivity of metallic wires in the mesoscopic range. *Phys. Rev. B* **66**, 075414, (2002)
256. S. Im, N. Srivastava, K. Banerjee, K. Goodson, Scaling analysis of multilevel interconnect temperatures for high-performance ICs. *IEEE Trans. Electron Dev.* **52**(12), 2710–2719 (2005)
257. Y.Y. Wei, G. Eres, V.I. Merkulov, D.H. Lowndes, Effect of catalyst film thickness on carbon nanotube growth by selective area chemical vapor deposition. *Appl. Phys. Lett.* **78**(10), 1394–1396 (2001)
258. M. Radosavljević, J. Lefebvre, A.T. Johnson, High-field electrical transport and breakdown in bundles of single-wall carbon nanotubes. *Phys. Rev. B* **64**, 241307 (Dec 2001)
259. P.G. Collins, M.S. Arnold, P. Avouris, Engineering carbon nanotubes and nanotube circuits using electrical breakdown. *Science* **292**(5517), 706–709 (2001)
260. C.T. White, T.N. Todorov, Carbon nanotubes as long ballistic conductors. *Nature* **393**, 240–242 (1998)
261. Z. Yao, C.L. Kane, C. Dekker, High-field electrical transport in single-wall carbon nanotubes. *Phys. Rev. Lett.* **84**, 2941–2944 (2000)
262. J. Hone, M. Whitney, C. Piskoti, A. Zettl, Thermal conductivity of single-walled carbon nanotubes. *Phys. Rev. B* **59**(4), R2514–R2516 (1999)
263. J. Kong, E. Yenilmez, T.W. Tomblor, W. Kim, H. Dai, R.B. Laughlin, L. Liu, C.S. Jayanthi, S.Y. Wu, Quantum interference and ballistic transmission in nanotube electron waveguides. *Phys. Rev. Lett.* **87**, 106801 (Aug 2001)
264. E. Pop, D. Mann, Q. Wang, K. Goodson, H. Dai, Thermal conductance of an individual single-wall carbon nanotube above room temperature. *Nano Lett.* **6**(1), 96–100 (2006)
265. A. Naemi, J.D. Meindl, Carbon nanotube interconnects. *Annu. Rev. Mater. Res.* **39**(1), 255–275 (2009)
266. N. Srivastava, R.V. Joshi, K. Banerjee, Carbon nanotube interconnects: implications for performance, power dissipation and thermal management, in *Electron Devices Meeting, 2005. IEDM Technical Digest. IEEE International*, pp. 249–252 (2005)
267. X. Zhang, T. Wang, J. Liu, C. Andersson, Overview of carbon nanotubes as off-chip interconnects, in *Electronics System-Integration Technology Conference, 2008. ESTC 2008, 2nd*, Greenwich, UK, pp. 633–638 (2008)
268. J. Li, Q. Ye, A. Cassell, H.T. Ng, R. Stevens, J. Han, M. Meyyappan, Bottom-up approach for carbon nanotube interconnects. *Appl. Phys. Lett.* **82**(15), 2491–2493 (2003)
269. F. Kreupl, A.P. Graham, G.S. Duesberg, W. Steinhögl, M. Liebau, E. Unger, W. Hönlein, Carbon nanotubes in interconnect applications. *Microelectron. Eng.* **64**(1–4), 399–408 (2002)
270. M. Nihei, A. Kawabata, Y. Awano, Direct diameter-controlled growth of multiwall carbon nanotubes on nickel-silicide layer. *Jpn. J. Appl. Phys.* **42**(Part 2, 6B), L721–L723 (2003)
271. Y.-M. Choi, S. Lee, H.S. Yoon, M.-S. Lee, H. Kim, I. Han, Y. Son, I.-S. Yeo, U.-I. Chung, J.-T. Moon, Integration and electrical properties of carbon nanotube array for interconnect applications, in *Nanotechnology, 2006. IEEE-NANO 2006. Sixth IEEE Conference*, vol. 1, pp. 262–265 (2006)
272. Y. Chai, M. Sun, Z. Xiao, Y. Li, M. Zhang, P. Chan, Pursuit of future interconnect technology with aligned carbon nanotube arrays [nanopackaging]. *IEEE Nanotechnol. Mag.* **5**(1), 22–26 (2011)

273. F. Kreupl, Carbon nanotubes in microelectronic applications. *Adv. Micro Nanosyst.* **8**, 1–41 (2008)
274. S. Huang, X. Cai, J. Liu, Growth of millimeter-long and horizontally aligned single-walled carbon nanotubes on flat substrates. *J. Am. Chem. Soc.* **125**(19), 5636–5637 (2003)
275. H. Xin, A.T. Woolley, Directional orientation of carbon nanotubes on surfaces using a gas flow cell. *Nano Lett.* **4**(8), 1481–1484 (2004)
276. Y. Zhang, A. Chang, J. Cao, Q. Wang, W. Kim, Y. Li, N. Morris, E. Yenilmez, J. Kong, H. Dai, Electric-field-directed growth of aligned single-walled carbon nanotubes. *Appl. Phys. Lett.* **79**(19), 3155–3157 (2001)
277. A. Ural, Y. Li, H. Dai, Electric-field-aligned growth of single-walled carbon nanotubes on surfaces. *Appl. Phys. Lett.* **81**(18), 3464–3466 (2002)
278. E. Joselevich, C.M. Lieber, Vectorial growth of metallic and semiconducting single-wall carbon nanotubes. *Nano Lett.* **2**(10), 1137–1141 (2002)
279. A. Nojeh, A. Ural, R.F. Pease, H. Dai, Electric-field-directed growth of carbon nanotubes in two dimensions. *J. Vac. Sci. Technol. B* **22**(6), 3421–3425 (2004)
280. Y. Li, D. Mann, M. Rolandi, W. Kim, A. Ural, S. Hung, A. Javey, J. Cao, D. Wang, E. Yenilmez, Q. Wang, J.F. Gibbons, Y. Nishi, H. Dai, Preferential growth of semiconducting single-walled carbon nanotubes by a plasma enhanced CVD method. *Nano Lett.* **4**(2), 317–321 (2004)
281. Y.H. Yan, S. Li, L.Q. Chen, M.B. Chan-Park, Q. Zhang, Large-scale submicron horizontally aligned single-walled carbon nanotube surface arrays on various substrates produced by a fluidic assembly method. *Nanotechnology* **17**(22), 5696 (2006)
282. B.Q. Wei, R. Vajtai, Y. Jung, J. Ward, R. Zhang, G. Ramanath, P.M. Ajayan, Microfabrication technology: organized assembly of carbon nanotubes. *Nature* **416**(6880), 495–496 (2002)
283. Y. Awano, S. Sato, D. Kondo, M. Ohfuti, A. Kawabata, M. Nihei, N. Yokoyama, Carbon nanotube via interconnect technologies: size-classified catalyst nanoparticles and low-resistance ohmic contact formation. *Phys. Stat. (a)* **203**(14), 3611–3616 (2006)
284. M. Nihei, D. Kondo, A. Kawabata, S. Sato, H. Shioya, M. Sakauae, T. Iwai, M. Ohfuti, Y. Awano, Low-resistance multi-walled carbon nanotube vias with parallel channel conduction of inner shells [IC interconnect applications], in *Interconnect Technology Conference, 2005. Proceedings of the IEEE 2005 International*, pp. 234–236 (2005)
285. N. Chiodarelli, K. Kellens, D.J. Cott, N. Peys, K. Arstila, M. Heyns, S.D. Gendt, G. Groeseneken, P.M. Vereecken, Integration of vertical carbon nanotube bundles for interconnects. *J. Electrochem. Soc.* **157**(10), K211–K217 (2010)
286. Z. Liu, N. Bajwa, L. Ci, S.H. Lee, S. Kar, P.M. Ajayan, J.-Q. Lu, Densification of carbon nanotube bundles for interconnect application, in *International Interconnect Technology Conference, IEEE 2007*, pp. 201–203 (2007)
287. P.L. McEuen, M. Bockrath, D.H. Cobden, Y.-G. Yoon, S. G. Louie, Disorder, pseudospins, and backscattering in carbon nanotubes. *Phys. Rev. Lett.* **83**(24), 5098–5101 (1999)
288. W. Liang, M. Bockrath, D. Bozovic, J.H. Hafner, M. Tinkham, H. Park, Fabry–Perot interference in a nanotube electron waveguide. *Nature* **411**(6838), 665–669 (2001)
289. T. Hunger, B. Lengeler, J. Appenzeller, Transport in ropes of carbon nanotubes: contact barriers and lutjtinger liquid theory. *Phys. Rev. B* **69**(19), 195406 (2004)
290. T. Wang, K. Jeppson, N. Olofsson, E.E.B. Campbell, J. Liu, Through silicon vias filled with planarized carbon nanotube bundles. *Nanotechnology* **20**(48), 485203 (2009)
291. M. Nihei, M. Horibe, A. Kawabata, Y. Awano, Carbon nanotube vias for future LSI interconnects. *IEEE* **2004**, 251–253 (2004)
292. J.Y. Hwang, A.R.P. Singh, M. Chaudhari, J. Tiley, Y. Zhu, J. Du, R. Banerjee, Templated growth of hexagonal nickel carbide nanocrystals on vertically aligned carbon nanotubes. *J. Phys. Chem. C* **114**(23), 10424–10429 (2010)
293. W. Han, S. Fan, Q. Li, Y. Hu, Synthesis of gallium nitride nanorods through a carbon nanotube-confined reaction. *Science* **277**(5330), 1287–1289 (1997)
294. T. Kuzumaki, K. Miyazawa, H. Ichinose, K. Ito, Processing of carbon nanotube reinforced aluminum composite. *J. Mater. Res.* **13**(9), 2445–2449 (1998)

295. J.W. An, D.H. You, D.S. Lim, Tribological properties of hot-pressed alumina-CNT composites. *Wear* **255**(1–6), 677–681 (2003)
296. L. Chen, B.-L. Zhang, M.-Z. Qu, Z.-L. Yu, Preparation and characterization of CNTS-TiO₂ composites. *Powder Technol.* **154**(1), 70–72 (2005)
297. F.L. Garcia, C. Estournès, A. Peigney, A. Weibel, E. Flahaut, C. Laurent, Spark-plasma-sintering of double-walled carbon nanotube-magnesia nanocomposites. *Scr. Mater.* **60**(9), 741–744 (2009)
298. E. Flahaut, A. Peigney, C. Laurent, C. Marlière, F. Chastel, A. Rousset, Carbon nanotube-metal-oxide nanocomposites: microstructure, electrical conductivity and mechanical properties. *Acta Mater.* **48**(14), 3803–3812 (2000)
299. C. Laurent, A. Peigney, O. Dumortier, A. Rousset, Carbon nanotubes-Fe-alumina nanocomposites. Part II: microstructure and mechanical properties of the hot-pressed composites. *J. Eur. Ceram. Soc.* **18**(14), 2005–2013 (1998)
300. A. Peigney, E. Flahaut, C. Laurent, F. Chastel, A. Rousset, Aligned carbon nanotubes in ceramic-matrix nanocomposites prepared by high-temperature extrusion. *Chem. Phys. Lett.* **352**(1–2), 20–25 (2002)
301. S. Cha, K. Kim, S. Arshad, C. Mo, S. Hong, Extraordinary strengthening effect of carbon nanotubes in metal-matrix nanocomposites processed by molecular-level mixing. *Adv. Mater.* **17**(11), 1377–1381 (2005)
302. Y. Guo, H. Cho, D. Shi, J. Lian, Y. Song, J. Abot, B. Poudel, Z. Ren, L. Wang, R.C. Ewing, Effects of plasma surface modification on interfacial behaviors and mechanical properties of carbon nanotube-Al₂O₃ nanocomposites. *Appl. Phys. Lett.* **91**(26), 261903 (2007)
303. A. Peigney, Composite materials: tougher ceramics with nanotubes. *Nat. Mater.* **2**, 15–16 (Jan. 2003)
304. W.A. Curtin, B.W. Sheldon, CNT-reinforced ceramics and metals. *Mater. Today* **7**(11), 44–49 (2004)
305. K.T. Kim, S.I. Cha, S.H. Hong, Hardness and wear resistance of carbon nanotube reinforced Cu matrix nanocomposites. *Mat. Sci. Eng. A Struct.* **449–451**, 46–50 (2007)
306. H. Cho, D. Shi, Y. Guo, J. Lian, Z. Ren, B. Poudel, Y. Song, J.L. Abot, D. Singh, J. Routbort, L. Wang, R.C. Ewing, Enhanced thermal stability of carbon nanotubes by plasma surface modification in Al₂O₃ composites. *J. Appl. Phys.* **104**(7), 074302 (2008)
307. A. Peigney, C. Laurent, E. Flahaut, A. Rousset, Carbon nanotubes in novel ceramic matrix nanocomposites. *Ceram. Int.* **26**(6), 677–683 (2000)
308. G.-D. Zhan, J.D. Kuntz, J. Wan, A.K. Mukherjee, Single-wall carbon nanotubes as attractive toughening agents in alumina-based nanocomposites. *Nat. Mater.* **2**, 38–42 (2003)
309. B. Landi, S. Castro, H. Ruf, C. Evans, S. Bailey, R. Raffaele, CdSe quantum dot-single wall carbon nanotube complexes for polymeric solar cells. *Sol. Energy Mater. Sol. Cells* **87**(1–4), 733–746 (2005)
310. I. Robel, B. Bunker, P. Kamat, Single-walled carbon nanotube-CdS nanocomposites as light-harvesting assemblies: photoinduced charge-transfer interactions. *Adv. Mater.* **17**(20), 2458–2463 (2005)
311. P. Santhosh, A. Gopalan, K.-P. Lee, Gold nanoparticles dispersed polyaniline grafted multi-wall carbon nanotubes as newer electrocatalysts: preparation and performances for methanol oxidation. *J. Catal.* **238**(1), 177–185 (2006)
312. I. Robel, G. Girishkumar, B.A. Bunker, P.V. Kamat, K. Vinodgopal, Structural changes and catalytic activity of platinum nanoparticles supported on C₆₀ and carbon nanotube films during the operation of direct methanol fuel cells. *Appl. Phys. Lett.* **88**(7), 073113 (2006)
313. T. Yildirim, S. Ciraci, Titanium-decorated carbon nanotubes as a potential high-capacity hydrogen storage medium. *Phys. Rev. Lett.* **94**(17), 175501 (2005)
314. A. Ansón, E. Lafuente, E. Urriolabeitia, R. Navarro, A.M. Benito, W.K. Maser, M.T. Martínez, Hydrogen capacity of palladium-loaded carbon materials. *J. Phys. Chem. B* **110**(13), 6643–6648 (2006)
315. W. Bauhofer, J.Z. Kovacs, A review and analysis of electrical percolation in carbon nanotube polymer composites. *Compos. Sci. Technol.* **69**(10), 1486–1498 (2009)

316. L. Bokobza, Multiwall carbon nanotube elastomeric composites: a review. *Polymer* **48**(17), 4907–4920 (2007)
317. J.N. Coleman, U. Khan, W.J. Blau, Y.K. Gun'ko, Small but strong: a review of the mechanical properties of carbon nanotube-polymer composites. *Carbon* **44**, 1624–1652 (2006)
318. J.N. Coleman, U. Khan, Y.K. Gun'ko, Mechanical reinforcement of polymers using carbon nanotubes. *Adv. Mater.* **18**(6), 689–706 (2006)
319. A.V. Desai, M.A. Haque, Mechanics of the interface for carbon nanotube-polymer composites. *Thin Wall Struct.* **43**(11), 1787–1803 (2005)
320. Y. Ear, E. Silverman, Challenges and opportunities in multifunctional nanocomposite structures for aerospace applications. *MRS Bull.* **32**(4), 328–334 (2007)
321. K.-T. Lau, M. Chipara, H.-Y. Ling, D. Hui, On the effective elastic moduli of carbon nanotubes for nanocomposite structures. *Compos. Part B Eng.* **35B**(2), 95–101 (2004)
322. K. Lau, C. Gu, D. Hui, A critical review on nanotube and nanotube/nanoclay related polymer composite materials. *Compos. Part B Eng.* **37**(6), 425–36 (2006)
323. K.T. Lau, M. Lu, D. Hui, Coiled carbon nanotubes: synthesis and their potential applications in advanced composite structures. *Compos. Part B Eng.* **37**(6), 437–48 (2006)
324. C. Li, E.T. Thostenson, T.W. Chou, Sensors and actuators based on carbon nanotubes and their composites: a review. *Compos. Sci. Technol.* **68**(6), 1227–1249 (2008)
325. C. McClory, S.J. Chin, T. McNally, Polymer/carbon nanotube composites. *Aust. J. Chem.* **62**(8), 762–785 (2009)
326. H. Miyagawa, M. Misra, A.K. Mohanty, Mechanical properties of carbon nanotubes and their polymer nanocomposites. *J. Nanosci. Nanotechnol.* **5**(10), 1593–1615 (2005)
327. M. Moniruzzaman, K.I. Winey, Polymer nanocomposites containing carbon nanotubes. *Macromolecules* **39**(16), 5194–5205 (2006)
328. P. Podsiadlo, B.S. Shim, N.A. Kotov, Polymer/clay and polymer/carbon nanotube hybrid organic-inorganic multilayered composites made by sequential layering of nanometer scale films. *Coord. Chem. Rev.* **253**(23–24), 2835–2851 (2009)
329. M. Singh, P.K. Kathuroju, N. Jampana, Polypyrrole based amperometric glucose biosensors. *Sens. Actuat. B Chem.* **143**(1), 430–443 (2009)
330. E.T. Thostenson, Z.F. Ren, T.W. Chou, Advances in the science and technology of carbon nanotubes and their composites: a review. *Compos. Sci. Technol.* **61**(13), 1899–1912 (2001)
331. E.V. Barrera, M.L. Shofner, E.L. Corral, Applications: composites, in *Carbon Nanotubes: Science and Applications*, ed. by M. Meyyappan (CRC Press, Boca Raton, 2004)
332. C.A. Dyke, J.M. Tour, Functionalized carbon nanotubes in composites, in *Carbon Nanotubes Properties and Applications*, ed. by M.J. O'Connell (CRC Press, Boca Raton, 2006)
333. S. Boncel, K.K. Koziol, K.Z. Walczak, A.H. Windle, M.S. Shaffer, Infiltration of highly aligned carbon nanotube arrays with molten polystyrene. *Mater. Lett.* **65**(14), 2299–2303 (2011)
334. P. Mahanandia, J.J. Schneider, M. Khanefit, B. Stuhn, T.P. Peixoto, B. Drossel, Polymer confinement effects in aligned carbon nanotubes arrays. *Phys. Chem. Chem. Phys.* **12**(17), 4407–4417 (2010)
335. C.J. Hu, Y.H. Lin, C.W. Tang, M.Y. Tsai, W.K. Hsu, H.F. Kuo, ZnO-coated carbon nanotubes: flexible piezoelectric generators. *Adv. Mater.* **23**(26), 2941–2945 (2011)
336. K.K. Koziol, S. Boncel, M.S. Shaffer, A.H. Windle, Aligned carbon nanotube-polystyrene composites prepared by in situ polymerisation of stacked layers. *Compos. Sci. Technol.* **71**(13), 1606–1611 (2011)
337. J. Sandler, J. Kirk, I. Kinloch, M. Shaffer, A. Windle, Ultra-low electrical percolation threshold in carbon-nanotube-epoxy composites. *Polymer* **44**(19), 5893–5899 (2003)
338. E.T. Thostenson, T.W. Chou, Aligned multi-walled carbon nanotube-reinforced composites: processing and mechanical characterization. *J. Phys. D Appl Phys* **35**, 77–80 (2002)
339. B.H. Cipriano, A.K. Kota, A.L. Gershon, C.J. Laskowski, T. Kashiwagi, H.A. Bruck, S.R. Raghavan, Conductivity enhancement of carbon nanotube and nanofiber-based polymer nanocomposites by melt annealing. *Polymer* **49**, 4846–4851 (2008)

340. C.A. Martin, J.K.W. Sandler, A.H. Windle, M.K. Schwarz, W. Bauhofer, K. Schulte, M.S.P. Shaffer, Electric field-induced aligned multi-wall carbon nanotube networks in epoxy composites. *Polymer* **46**, 877–886 (2005)
341. E.S. Choi, J.S. Brooks, D.L. Eaton, M.S. Al-Haik, M.Y. Hussaini, H. Garmestani, D. Li, K. Dahmen, Enhancement of thermal and electrical properties of carbon nanotube polymer composites by magnetic field processing. *J. Appl. Phys.* **94**(9), 6034–6039 (2003)
342. R. Haggemueller, H.H. Gommans, A.G. Rinzler, J.E. Fischer, K.I. Winey, Aligned single-wall carbon nanotubes in composites by melt processing methods. *Chem. Phys. Lett.* **330**(3–4), 219–225 (2000)
343. P. Pötschke, H. Brüning, A. Janke, D. Fischer, D. Jehnichen, Orientation of multiwalled carbon nanotubes in composites with polycarbonate by melt spinning. *Polymer* **46**, 10355–10363 (2005)
344. E.J. García, A.J. Hart, B.L. Wardle, A.H. Slocum, Fabrication of composite microstructures by capillarity-driven wetting of aligned carbon nanotubes with polymers. *Nanotechnology* **18**, 165602 (2007)
345. E.J. García, D.S. Saito, L. Megalini, A.J. Hart, R. Guzman de Villoria, B.L. Wardle, Fabrication and multifunctional properties of high volume fraction aligned carbon nanotube thermoset composites. *J. Nano Syst. Tech.* **1**, 1–11 (2009)
346. S. Sarkar, J. Zou, J. Liu, C. Xu, L. An, L. Zhai, Polymer-derived ceramic composite fibers with aligned pristine multiwalled carbon nanotubes. *ACS Appl. Mater. Interfaces* **2**, 1150–1156 (2010)
347. S.V. Ahir, Y.Y. Huang, E.M. Terentjev, Polymers with aligned carbon nanotubes: active composite materials. *Polymer* **49**(18), 3841–3854 (2008)
348. P.M. Ajayan, J.M. Tour, Nanotube composites. *Nature* **447**, 1066–1068 (2007)
349. M.H. Al-Saleh, U. Sundararaj, A review of vapor grown carbon nanofiber/polymer conductive composites. *Carbon* **47**(1), 2–22 (2009)
350. M. Panzer, G. Zhang, D. Mann, X. Hu, E. Pop, H. Dai, K.E. Goodson, Thermal properties of metal-coated vertically-aligned single wall nanotube films, in *The Tenth Intersociety Conference on Thermal and Thermomechanical Phenomena in Electronics Systems, 2006. IThERM'06*, pp. 1306–1313, June 2006
351. M. Baibarac, P. Gomez-Romero, Nanocomposites based on conducting polymers and carbon nanotubes: from fancy materials to functional applications. *J. Nanosci. Nanotechnol.* **6**(2), 289–302 (2006)
352. P. Dubois, M. Alexandre, Performant clay/carbon nanotube polymer nanocomposites. *Adv. Eng. Mater.* **8**(3), 147–154 (2006)
353. N. Fujita, M. Asai, T. Yamashita, S. Shinkai, Sol-gel transcription of silica-based hybrid nanostructures using poly(*n*-vinylpyrrolidone)-coated [60] fullerene, single-walled carbon nanotube and block copolymer templates. *J. Mater. Chem.* **14**, 2106–2114 (2004)
354. P.J.F. Harris, Carbon nanotube composites. *Int. Mater. Rev.* **49**(1), 31–43 (2004)
355. T. Hasan, Z.P. Sun, F.Q. Wang, F. Bonaccorso, P.H. Tan, A.G. Rozhin, A.C. Ferrari, Nanotube-polymer composites for ultrafast photonics. *Adv. Mater.* **21**(38–39), 3874–3899 (2009)
356. P. Liu, Modifications of carbon nanotubes with polymers. *Eur. Polym. J.* **41**(11), 2693–2703 (2005)
357. S.S. Samal, S. Bal, Carbon nanotube reinforced ceramic matrix composites—a review. *J. Miner. Mater. Charact. Eng.* **7**(4), 355–370 (2008)
358. D. Srivastava, C. Wei, K. Cho, Nanomechanics of carbon nanotubes and composites. *Appl. Mech. Rev.* **56**(2), 215–230 (2003)
359. J. Suhr, N.A. Koratkar, Energy dissipation in carbon nanotube composites: a review. *J. Mater. Sci.* **43**(13), 4370–4382 (2008)
360. J. Wang, Y. Chen, W.J. Blau, Carbon nanotubes and nanotube composites for nonlinear optical devices. *J. Mater. Chem.* **19**(40), 7425–7443 (2009)
361. A.A. White, S.M. Best, I.A. Kinloch, Hydroxyapatite-carbon nanotube composites for biomedical applications: a review. *Int. J. Appl. Ceram. Technol.* **4**(1), 1–13 (2007)

362. S. Wijewardane, Potential applicability of CNT and CNT/composites to implement ASEC concept: a review article. *Sol. Energy* **83**(8), 1379–1389 (2009)
363. X.L. Xie, Y.W. Mai, X.P. Zhou, Dispersion and alignment of carbon nanotubes in polymer matrix: a review. *Mater. Sci. Eng. R Rep.* **49**(4), 89–112 (2005)

Chapter 9

Potential Applications of Carbon Nanotube Arrays

Besides the above applications described in Chap. 8, there are additional potential applications of CNT arrays which are relatively further away from commercialization and major progresses are still needed. We talk about these applications altogether in this chapter.

9.1 Mechanical Devices

CNTs possess extremely high tensile strengths. The yield strength of SWCNTs exceeds 45 GPa [1] with an average strength of 30 GPa [2], over 20 times the yield strength of typical high strength steels. The highest tensile strength of an individual MWCNT has been recorded to be 63 GPa. The measured Youngs modulus of SWCNTs is over 1 TPa [2, 3], lower than that of MWCNTs 1.3 TPa [4] or 1.8 TPa [5]. The strain at tensile failure has been measured to be as high as 5.3 % for SWCNTs [2] and 12 % for MWCNTs [6] at room temperature. The theoretical yield strain is up to 9 % or higher [7, 8] for defect-free SWCNTs. The unique strength and flexibility of CNTs make them potentially useful in many mechanical applications, ranging from everyday items such as clothes and sport gears to fictional combat jackets and space elevators. The aligned CNT ropes, CNT sheets, and aligned CNT composites would preserve the superb mechanical properties of the individual CNTs.

There are two kinds of aligned CNT materials used for mechanical devices. One kind is aligned CNT composites where the CNTs are used as additive and embedded in a matrix. Such aligned CNTs are usually fabricated by *ex situ* methods discussed in Sect. 6.2. After CNTs are synthesized as described in Chap. 3, CNTs are collected, purified if needed, and mixed with polymeric, ceramic, or other materials. In order to improve the dispersion of CNTs in the processing composites, the surfaces of CNTs are chemically functionalized or some surfactants are used as a dispersing agent. If the CNTs are randomly dispersed in the matrix, the mechanical properties of such composites are slightly enhanced. For example, random CNTs have been employed

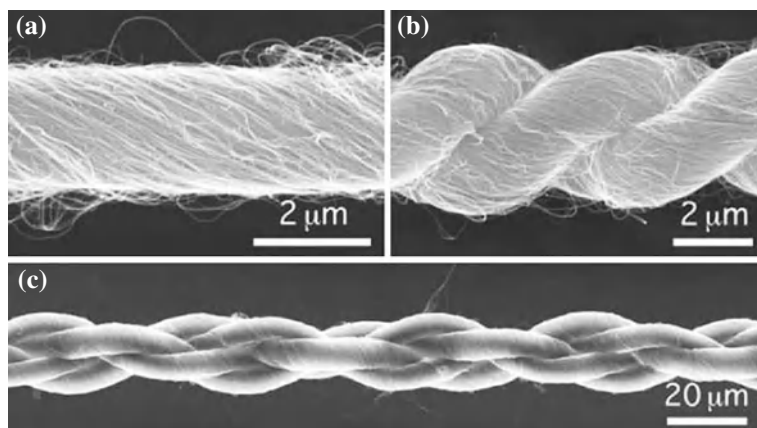


Fig. 9.1 SEM images of polymer-free CNT ropes. **a** Single-ply MWCNT rope. **b** Two-ply MWCNT rope. **c** Four-ply MWCNT rope. From Zhang et al. [24]. Copyright (2004), AAAS

to enhance the mechanical strength of swords [9, 10]. In order to align the CNTs in the matrix, force fields, [11–15], magnetic fields [16], or electric fields [17–22] are applied on the liquid-like mixture. CNTs are aligned along a certain direction. The alignment methods for CNTs in matrices were reviewed [23] and discussed in Sect. 6.2.

Another is the aligned CNTs without matrices. The aligned CNTs can be synthesized first and then mechanically aligned to achieve an ordered structure, such as CNT ropes, CNT clothes, CNT films, etc. The details of the alignment methods are discussed in Sect. 6.2.3.2. The aligned CNTs can also be in situ grown directly on a substrate (see Sect. 6.1).

In this subchapter, we talk about the potential mechanical applications of both kinds of aligned CNT materials.

9.1.1 Carbon Nanotube Ropes

The CNT ropes are usually fabricated by spinning methods, including the wet-spinning method and the dry-spinning methods, as described in Sect. 6.2.3.2. The mechanical properties of these CNT ropes or bundles are reviewed recently [25].

Experimental data indicate that the mechanical properties of CNT ropes are lower than those of the individual CNTs. The CNTs in ropes are aligned parallel to one another [24] or twisted [26]. In the untwisted ropes, the CNTs are held together by van der Waals interactions and the untwisted ropes tensile strength is so weak that the rope breaks once the untwisted ropes are pulled [26]. So the CNT ropes are usually twisted to increase the strength [26]. The twisted pure CNT ropes can be fabricated by wet-spinning from CNT solvents [27] or dry-spinning directly from CVD-grown

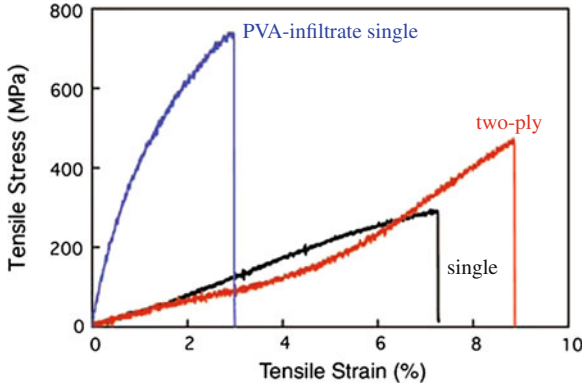


Fig. 9.2 Stress–strain curves of single-ply (black), two-ply (red), and PVA-infiltrated single-ply (blue) ropes at a strain rate of 1% min for a centimeter gauge length. From Zhang et al. [24]. Copyright (2004), AAAS

CNTs [26, 28]. The fabrication details are discussed in Sect. 6.2.3.2. Figure 9.1 shows MWCNT ropes prepared by the dry-spinning method from CVD-synthesized CNT forests. Its stress–strain curve is shown in Fig. 9.2.

Detailed experimental results indicate that the CNTs in the twisted ropes are arranged in a helical structure [29]. The mechanical properties of CNT helical ropes depend on the microstructure of the ropes, such as the helix angle and the frictional force between CNTs. The tensile strength of twisted CNT ropes, σ_{rope} , follows the mechanical properties of textile fiber yarns [26, 29] and can be expressed as [30]

$$\sigma_{\text{rope}} \approx \sigma_{\text{CNT}} \cos^2 \alpha \left[1 - \frac{\sqrt{dQ/u}}{2L} \cos \alpha \right] \tag{9.1}$$

where σ_{CNT} is the tensile strength of the CNT, α the helix angle that CNTs make with the rope axis, d the CNT diameter, L the CNT length, Q the CNT migration length, and u the friction coefficient between the CNTs. The CNTs in the twisted rope are inclined at the angle α with respect to the tensile axis. The tensile strength decreases with the helix angle α [29] according to Eq. 9.1. For short CNTs, however, there is little strength in the absence of twist because there are no significant transverse forces to bind the CNT assembly together. The transverse forces are generated by transfer of the tensile load to the rope surface, which locks the fibers together forming a coherent structure [26]. The tensile strength of a twisted rope increases with increasing coefficient of friction between CNTs, with CNT length, and with decreasing CNT diameter and CNT migration length.

Figure 9.3 shows Youngs modulus of CNT ropes with different diameters. Both experimental data [31] and theoretical analysis [32] indicate that the tensile modulus depends strongly on the diameter of the CNT ropes because of the creeping

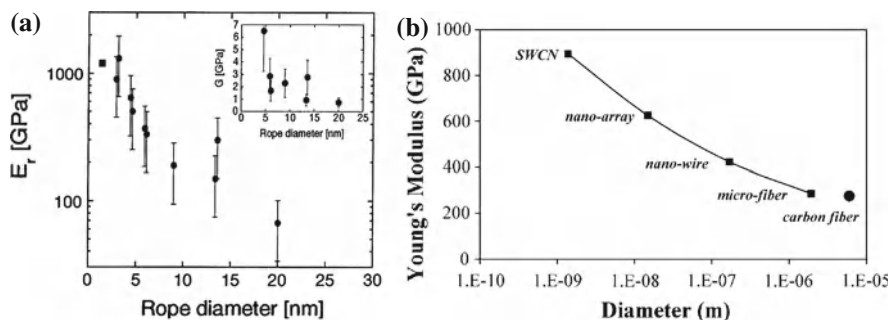


Fig. 9.3 Young's modulus of SWCNT ropes with helical array geometry. **a** Experimental data and **b** theoretical data. **a** From Salvetat et al. [31]. Copyright (1999), American Physical Society. **b** From Pipes and Hubert [32]. Copyright (2003), American Chemical Society

between CNTs. With the increase in rope diameters, Young's modulus is diminished by approximately 68% when upscaling from nanoscale to microscale.

In order to increase the friction between CNTs, CNTs can be embedded in a polymer with high strength and high modulus like polyvinyl alcohol (PVA). The CNT/polymer ropes can be fabricated by wet-spinning or dry-spinning followed by soaking in a polymer solution. The tensile strength of SWCNT/PVA yarns increases to 850 MPa from 150 to 300 MPa of PVA-free yarns. The strength is still much lower than that of individual SWCNTs. Creep is a major problem for these CNT composite ropes.

The highest Young's modulus of the helical SWCNT ropes is about 15 GPa [33] for CNT ropes spun from coagulation solution (polymer is removed and CNT ropes mainly consist of CNTs), with a yield stress of 8.8 GPa. The highest stiffness is 357 GPa for CNT ropes spun directly from an aerogel CNTs [34]. The reported highest tensile strength is 150–300 MPa for MWCNT ropes fabricated directly from CNT forests [26]. The tensile strength is higher than most of commercial high-performance fibers while still more than an order of magnitude lower than the intrinsic modulus of individual SWCNTs of 37 GPa.

Twisted polymer fibers consisting of CNTs at less than 10 wt% have also been fabricated. The mechanical strength and modulus are enhanced compared with pure polymer fibers [13]. It is reported that the tensile strength and Young's modulus have reached 4.2 and 167 GPa, respectively, in the dry-jet wet-spinning poly(*p*-phenylene benzobisoxazole)/SWCNT ropes (SWCNT: 10 wt%) [35]. When the SWCNTs are lower than 2.1 wt%, the additive of SWCNTs does not enhance the mechanical properties [36].

In order to avoid creeping, two-ply ropes are fabricated by over-twisting a single rope (Fig. 9.1b), and four-ply ropes by oppositely twisting a two-ply rope (Fig. 9.1c), and even knitted or knotted ropes are fabricated [24]. Higher tensile strength values of 250–460 MPa are measured for two-ply yarns, while only 150–300 MPa for single-ply yarns (Fig. 9.2).

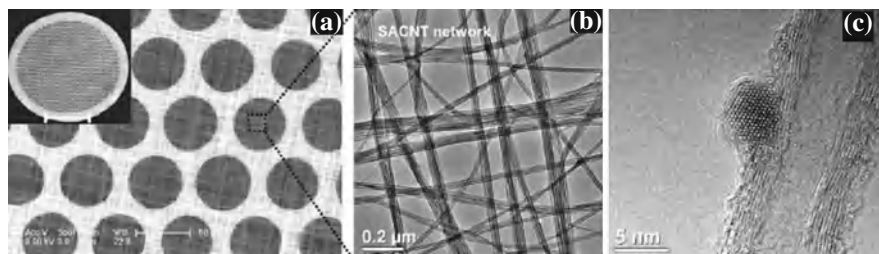


Fig. 9.4 Morphologies of a TEM grid with CNT sheet as a supporting film. **a** SEM image of the CNT sheet over the holes of a copper grid. Inset: optical image of the coated TEM grid with a diameter of 3 mm. **b** TEM image of the CNT sheet covering a hole showing a network morphology. **c** HRTEM image of a Cu_2S nanoparticle on one side of a nanotube of the TEM grid. From Zhang et al. [41]. Copyright (2008) American Chemical Society

Recent experimental data indicate that the parameters of the nanotubes, such as tube diameter, CNT wall thickness, tube length, and level of defects, play a more important role in the mechanical properties of the fibers than the initial tube arrangement do [37]. To improve the fiber strength, as well as the modulus, the tubes must be long and have a small diameter and thin walls.

9.1.2 TEM Grids

The continuous CNT sheets with centimeters in width and tens of nanometers in thickness can be fabricated by spinning methods [24, 28, 38] as described in Sect. 6.2.3.2. The CNTs are parallel-aligned in the drawing direction and end-to-end joined to form a continuous thin film, having a much better alignment than the as-synthesized CNT arrays [38]. These aligned CNT sheets are transparent and highly conductive [38–40], as a good candidate for TEM grid supporting films.

Figure 9.4 shows the morphologies of a TEM grid. In the fabrication of TEM grids, four layers of CNT thin sheets are directly cross-stacked layer by layer on TEM copper grids, then an organic solvent is dispensed on the sheets to bond the sheets onto the copper grid, following a CNT sheet cutting by a focused laser beam. The ultrathin CNT sheets cover the copper grid and regular networks with numerous holes are formed. The holes are mostly less than $1\ \mu\text{m}$ in diameter, and the nanometer-sized holes are more than 60% of all holes. Considering the good electrical conductivity and mechanical strength of CNTs, these TEM grids are ideal tools for the characterization of nanomaterials [41]. The fine structures of individual nanoparticles can be clearly observed on HRTEM (Fig. 9.4c) when the nanoparticles are attached to a CNT on TEM grids.

In comparison with conventional TEM holey carbon grids, the TEM grids with CNT sheets have some advanced characteristics resulting from the excellent intrinsic physical properties of CNTs [41]. First, the CNT has strong adsorbability to adsorb

small nanoparticles and ensure them to be suspended stably during TEM observation. Second, due to good electrical conductivity of MWCNTs, the CNT sheet also has good electrical conductivity (bulk resistivity is about $3.8 \times 10^{-4} \Omega\text{m}$). Third, because of the fixed interspace between sidewalls of the MWCNTs, i.e., $\sim 0.34 \text{ nm}$, the CNT grid can be a standard sample for calibration of HRTEM magnification and size measurement of nanoparticles. In addition, the CNT sheets have better thermal stability than that of the conventional amorphous carbon film.

9.1.3 Artificial Setae

Replicating the multiscale structure of micron-size setae and nanometer-size spatulas of gecko lizard feet using microfabricated MWCNTs, CNT arrays can translate weak van der Waals interactions into enormous attractive forces [42]. The CNT block arrays ($50\text{--}500 \mu\text{m}$ patches) are synthesized from photolithographic patterns. Each block array works as micron-size setae and consists of thousands of individual MWCNTs, the nano-sized spatulas. These patterned CNT arrays can stick to both hydrophobic and hydrophilic surfaces with a maximum shear stress of 36 N/cm^2 , nearly four times higher than the gecko foot and 10 times higher than polymer pillars. The shear forces supported by the patterned CNT arrays are very stable and time independent.

9.1.4 Piezoresistive Effects: Pressure and Strain Sensors

MWCNT arrays are also very effective sensing element for pressure and strain sensors operating at elevated temperature [43]. When a CNT array is compressed, individual carbon nanotube starts to buckle, which in turn decreases the array's electrical resistance. The behavior is almost fully recoverable because of the high elasticity of the covalent carbon-carbon bond. The MWCNT array exhibits a significant increase in the change of resistance with increasing temperature of $20\text{--}80^\circ\text{C}$.

Experimental data of SWCNT arrays show that the normalized resistance changes in response to the changes in strain [44]. The resistance ratio $\Delta R/R$ increases linearly with the strain, with a linearity of 0.991. The gauge factor, ratio of normalized change in piezoresistance to the change of strain, calculated from $(\Delta R/R)/\varepsilon$ or $(I_0 - I)/(I\varepsilon)$ (where I is the current and ε is the strain), is 248. Figure 9.5 plots the dynamic response of the sensor device at a frequency of 0.1 Hz for three different strain intervals. When the strain of the suspended SWCNT array is located in the scope of $0.0267\text{--}0.0497$ and $0.0450\text{--}0.0769\%$, the response curve reveals separate top-flat and bottom-flat appearances. A perfect triangular wave shows the strain in the linear changes in the rate of resistance ($\Delta R/R$) as a response to the changes in strain. Such SWCNT array devices with high sensitivity have potential application as strain gauges.

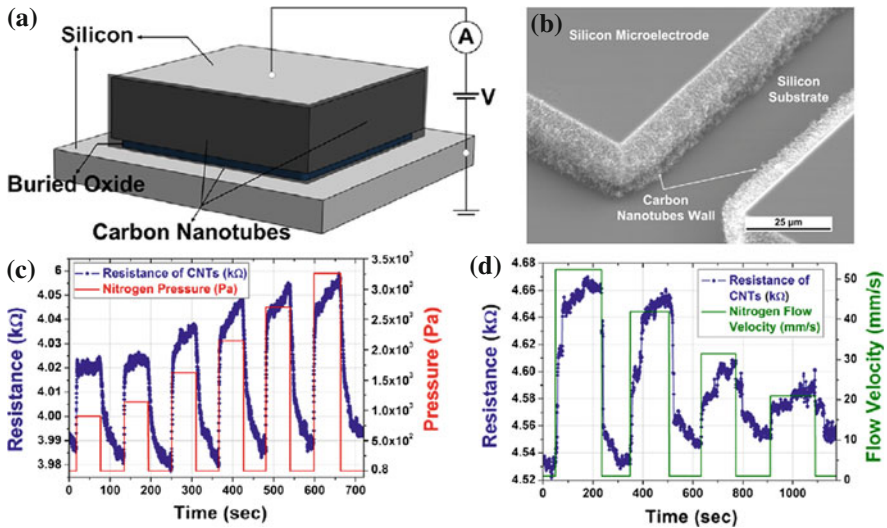


Fig. 9.6 **a** Schematic structure of a pressure and flow velocity sensor consisted of aligned CNTs based on the electrothermal-thermistor effect. The CNTs are grown on the silicon microelectrode, and the bias voltage and the current are applied and monitored through the CNTs. **b** SEM image of the silicon microelectrode, silicon substrate, and aligned CNTs. **c** Dynamic responses of different nitrogen pressure with a bias of 25 V applied to the sensor. The electric resistance of the sensor increases as the nitrogen pressure is elevated. **d** Nitrogen flow velocity sensing results with 25 V bias voltage. The resistance of the sensor increases with increasing nitrogen flow velocity. From Choi et al. [45]

cules when the supply of constant electrical energy on the CNTs is maintained [45]. Hence, the pressure and flow velocity change induces a temperature change in the CNTs and at the interface between the CNTs and silicon that is monitored by measuring the resistance change.

The responses of the CNT pressure sensor to various nitrogen pressure are presented in Fig. 9.6c. The resistance increases under the elevated pressure and recovered when the pressure is lowered, exhibiting slight signal drift, when the applied bias of 25 V between the microelectrode and substrate is maintained as constant during the experiment. The responsiveness, $\Delta R/R$, increases monotonically as a function of pressure increase. The flow velocity sensing capability of the CNTs is also demonstrated in Fig. 9.6d, based on the same mechanism as pressure sensing, wherein the resistance of the CNTs increases with an increase in flow velocity. The resistance of the CNTs immediately increases with respect to an abruptly increased nitrogen flow velocity as the baseline nitrogen flow velocity of 1 mm/s is sequentially modulated to 52.4, 41.9, 31.4 and 20.9 mm/s.

Coated CNT arrays can also be used as flow-rate sensors. Experimental results show that, after a thin Al_2O_3 coating on CNTs, the CNT array flow-rate sensor has higher sensitivity and faster response than a conventional platinum hot-wire flow-rate

sensors [46]. Such coated CNT flow-rate sensor has better repeatability than its bare counterpart due to insulation from the surrounding environment.

9.2 Electrical Devices

SWCNTs are metallic or semiconducting according to their structures. The electronic properties of perfect MWCNTs are rather similar to those of perfect SWCNTs. In the 1D electronic structure, electrons transport in metallic SWCNTs and MWCNTs over long nanotube lengths, carrying high current densities [47]. Such electrical properties make CNTs having important applications in electronics.

Many researches have been carried out to add random CNTs into various composites to enhance electrical conductivity. Depending on the composite matrix, conductivities of 0.01–10 S/m can be obtained for 5 wt% MWCNT loading or 0.1–0.2 wt% SWCNT loading in polymers. Such CNT composites with high conductivities can dissipate electrostatic charges [48, 49], having potential applications in electrostatic discharge and electromagnetic radio interference protection. The preparation and electrical properties of random CNT composites are reviewed [50] and the readers are referred to the research papers in the review.

The electrical conductivity of CNT composites also depends on the alignment as well as the concentration of CNTs [51, 52]. Here, we review several electrical applications of aligned CNTs without matrices.

9.2.1 *Random Access Memory*

Aligned CNTs can serve as addressable electromechanical switches arrayed across the surface of a microchip, storing hundreds of gigabits of information as random access memory (RAM) (Fig. 9.7). When an electric field is applied to a nanotube, the electric field causes the CNT flex downward into a depression onto the chip surface, where it contacts metal electrodes (in another design, the CNTs touch other nanotubes [54]). The binary 0 state corresponds to the nanotubes suspended and not making contact with the electrode (Fig. 9.7b). When a transistor turns on, the electrode produces an electric field that causes the aligned CNTs to bend and touch an electrode, a configuration that denotes a 1 state (Fig. 9.7c). Van der Waals forces hold the switch in place until application of a field of different polarity causes the nanotubes to return to their straightened positions.

Compared with conventional memories, dynamic random access memory, static random access memory, and flash memory, the CNT-based data storage devices have higher cell density, lower programming voltage, 22 nm process technology while both reading speed and writing speed are fast [53].

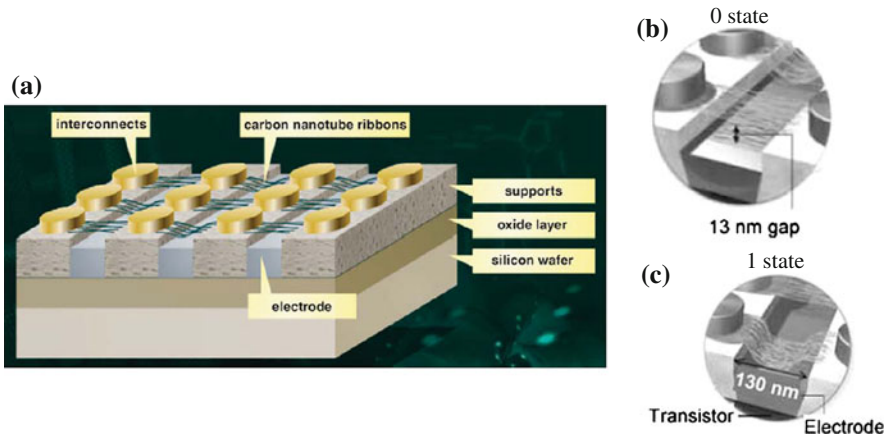


Fig. 9.7 a RAM made with aligned CNTs. b 0 state. c 1 state. From Bichoutskaia et al. [53]. Copyright (2008), Elsevier

9.2.2 Low κ Dielectrics

Electrically insulating layers are required in integrated circuits on semiconductor substrates to reduce the coupling capacitance of interconnects. The low κ materials are employed as the insulating layers in integrated circuits to reduce the coupling capacitance. Amorphous silicon dioxide with or without fluorine, hydrogen, or alkyl groups is often used as the dielectric to electrically insulate the metallic interconnects from one another.

The relative dielectric constant of electrically insulating layers can be reduced further by introducing cavities into the low κ materials. The κ value decreases linearly with the cavity volume fraction. The simulation calculations demonstrate that the effective κ value is also affected by the morphology of the cavities. If elongated and oriented pores are used, it is possible to reduce significantly the effective κ value without increasing the proportion of the cavity volume in a dielectric. With the same proportion of cavity volume, a reduction of 13% is achieved with a cavity aspect ratio of 4:1 and a reduction of 20% is achieved with a cavity aspect ratio of 24:1 when the cavities are oriented perpendicularly to an electric field.

CNTs have a high aspect ratio and can be used to introduce elongated, oriented pores into a low κ dielectric to further reduce the effective κ value of the dielectric.

In a typical procedure, aligned CNT forests are grown on a desired surface using PECVD methods as described in Sect. 6.1. Silicon dioxide is deposited between and on top of CNTs. The top oxide is removed by mechanical polishing or by a dry-etch process to expose the CNTs. Then the CNTs are subsequently removed by high-temperature oxidation and/or oxygen or hydrogen plasma.

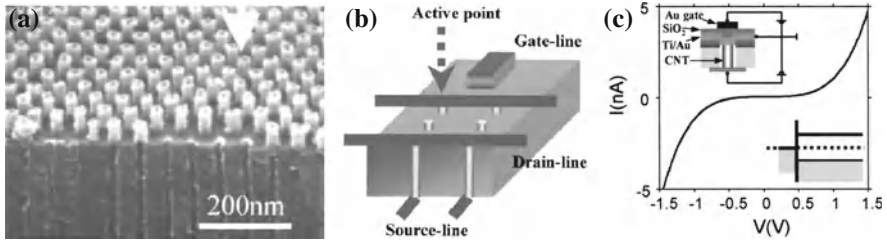


Fig. 9.8 Architecture of a CNT transistor array. (a) Vertically grown CNTs with diameter of 20 nm and height of 40 nm. (b) Structure of a CNT transistor. (c) Current-voltage diagram of a vertically oriented CNT transistor at a temperature of 4.2 K. No bias is applied to the gate. From Choi et al. [55]. Copyright (2001), American Institute of Physics

9.2.3 Transistors

Figure 9.8 shows a transistor array made from vertically aligned CNTs grown on a template of porous aluminum oxide described in Sect. 6.1.6.2. In the integrated device, each CNT is electrically attached to a source electrode (lower electrode in Fig. 9.8b) and a drain electrode (upper electrode in Fig. 9.8b). The gate electrode is located close to the nanotubes. Current flows from the source electrode to the drain electrode and can be switched on or off by applying a voltage to the gate. Figure 9.8c shows a current-voltage curve of the CNT transistor.

Recently, the effects of CNT lengths, CNT diameters, source and drain contacts have been systematically investigated [56].

9.3 Acoustic Sensors

9.3.1 Artificial Ears

CNT arrays are also used to detect sound as an ear [57]. The CNT arrays bend in response to acoustic energy. The motion of CNTs is transformed to an electrical signal that can be received by a standard electrical sensor. Such sensors can detect much fainter sounds than ears and provide directional information of sounds.

9.3.2 Thermoacoustic Loudspeakers

The thermoacoustic phenomenon was discovered in the late nineteenth century. When an alternating current passes through a thin conducting plate or wire, a periodic heating takes place in the conductor because of Joules effect, following the periodic

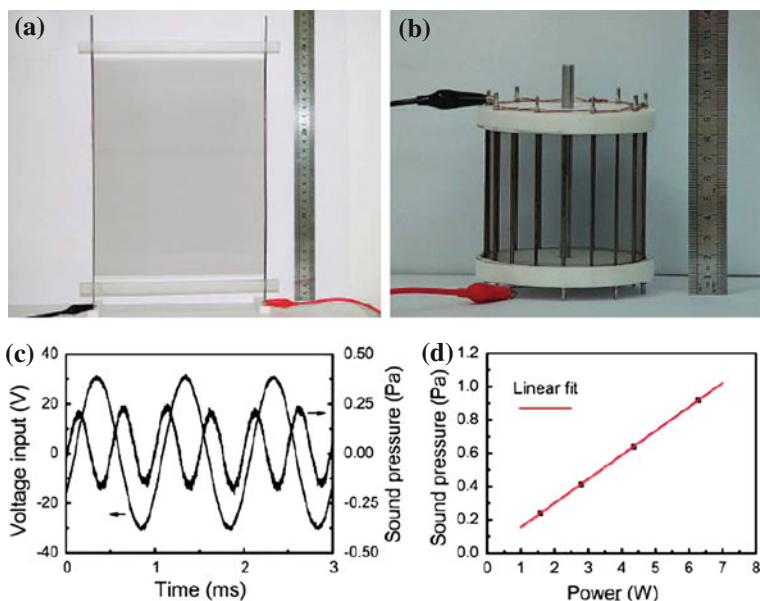


Fig. 9.9 Thermoacoustic CNT loudspeaker. Optical images of thermoacoustic CNT sheet loudspeakers with **a** planar structure and **b** cage structure. **c** Real-time signals of the input voltage of a CNT thin-film loudspeaker and the output sound pressure. The phase shift between the input voltage and the output sound pressure signal is primarily due to the sound propagation from the CNT sheet to the microphone detector. **d** Sound pressure versus power of CNT thermoacoustic speaker. From Xiao et al. [61]. Copyright (2008) American Chemical Society

change of the current amplitude. This periodic heating causes a periodic temperature oscillation that heats the surrounding medium (usually air) near the conductor surface, resulting in the contraction and expansion of molecules near the conductor while the conductor remains static. The vibrating movement of the molecules results in the generation of an acoustic wave. In a conventional thermoacoustic device (thermophone), the acoustic element is a thin metal film such as a gold film with a thickness of 285 nm [58] and a platinum strip with a thickness of 1.8 μm [59].

To obtain appreciable amplitudes of acoustic waves, it is essential that the conductor be very thin and its heat capacity be very low to conduct the produced heat at a high rate [59]. CNTs have an extremely low heat capacity and good thermal conductivity. CNT sheets can be heated up to 2000 $^{\circ}\text{C}$ in less than 1 ms, and the sheet temperature synchronizes with electrical currents in a wide frequency range of 1–10⁵ Hz [60] because of extremely low heat capacity and high thermal conductivity of CNTs. The thickness of present CNT sheets is less than microns. So CNT sheets are one of the best candidates for thermoacoustic devices.

Figure 9.9a, b shows CNT sheet loudspeakers. The CNT sheets are directly drawn out from CNT forests consisting of super aligned CNTs with diameters of 10 nm. The dry-spinning method is described in Sect. 6.2. The thickness of the CNT sheet

is of tens of nanometers. The CNT sheet loudspeaker is formed by directly putting the CNT sheet on two electrodes. When a sinusoidal voltage is applied across the two electrodes, clear and loud tones are emitted from the CNT sheet.

Figure 9.9c shows the input voltage and the output sound pressure. The output sound pressure is measured by a microphone near the CNT sheet. It is noted that the frequency of the sound pressure doubles that of the input voltage, as observed in a conventional thermophone. When an alternating current passes through the CNT sheet, the CNT sheet is heated twice, once during positive and once during negative half-cycles of the alternating current, resulting in a double frequency temperature oscillation, as well as a double frequency sound pressure [61]. The output sound with doubled frequency always sounds strange. In order to reproduce human voice and music with normal frequency without introducing the double frequency effect, a direct current bias must be superimposed to the alternating current. When the strength of the direct current is several times higher than that of the alternating current, the double frequency effect can be negligible [59]. Then the CNT sheet loudspeaker can possess all the functions of a voice-coil loudspeaker [61].

The CNT sheet loudspeaker can generate sound in a wide frequency range 1–10⁵ Hz. The high sound pressure level increases with increasing frequency and the sound pressure is proportional to the input power (Fig. 9.9d). The sound pressure produced by the CNT sheet under an alternating current can be expressed as [61]

$$P_{rms} = \left(\frac{\sqrt{\alpha} \rho_0}{2\sqrt{\pi} T_0} \times \frac{\sqrt{f}}{C_s} \right) \frac{P_{input}}{r} \quad (9.2)$$

in an open system (a more accurate while more complex expression is derived in some references [61, 62]), in which C_s is the heat capacity per unit area of the CNT sheet, f the frequency of sound, $P_{input} = I^2 R$ the input electrical power proportional to the square of applied root-mean-square (rms) current $I = I_0 \sin(\omega t)$, R the resistance of the CNT sheet, r the distance between the thin CNT sheet conductor and the sound pressure detector (microphone), ρ_0 , T_0 , and α the density, average temperature, and thermal diffusivity of the surrounding medium, respectively, and P_{rms} the rms sound pressure.

Equation 9.2 indicates that the produced sound pressure decreases rapidly with distance. Usually, the temperature of the CNT sheet is a sinusoid of time, and the temperature waves propagate into the atmosphere on either side. The periodic temperature change in the thin boundary layer near the CNT sheets accounts for the sound vibration. Calculation shows that the temperature waves propagate into the working medium and are practically extinguished after one wavelength (27 μm in air and 2.0 μm in water) has been traversed [59].

According to Eq. 9.2, the sound pressure generated by CNT sheet loudspeaker is 260 times higher than that generated by a conventional thermophone with a 700 nm-thick Pt film as the acoustic element, corresponding to a 48 dB difference in the sound pressure level [61]. The measured sound pressure level of the CNT loudspeaker is over 100 dB at high frequencies, higher than the conventional thermoacoustic device with a gold film of 285 nm in thickness as the acoustic element (63 dB) [58].

More detailed works indicate that the heat capacity of the gas also affects the generated sound pressure. Theoretical derivations show that the sound pressure generated by CNT thin films is approximately proportional to the inverse of the heat capacity of the gas within the audible frequency range of human hearing [63].

Besides the freestanding CNT sheet loudspeaker, CNT sheets are also encapsulated into an argon- or air-filled chamber. Such encapsulated CNT loudspeakers can be used in liquids, such as water [64]. In the small enclosure, the sound pressure is

$$P_{\text{rms}} = \frac{\sqrt{\alpha} \rho_0 T_{\text{surf}}^{1/4}}{V_0 T_{\text{ave}} C_s f^{3/2}} \times P_{\text{input}} \quad (9.3)$$

where T_{surf} is the temperature of the surface of the CNT sheet, T_{ave} the average temperature of the filled gas, and V_0 the volume of the enclosure [59]. The produced pressure causes a vibration of the attached enclosure windows with a resonant frequency f_r ($f_r = 3.28 \text{ kHz}$ when working in air and 1050 Hz when immersed in water [64]). The highest sound pressure level is over 130 dB, 30 dB higher than that exposed to air.

The pressure generation efficiency coefficient

$$\xi = (\sqrt{\alpha} \rho_0 / 2 \sqrt{\pi} T_0) (\sqrt{f} / C_s) \quad (9.4)$$

is affected by many parameters [64], such as (1) the ability of the CNT sheet to be rapidly electrically heated and then to transfer heat to the surrounding medium at high rates, thereby returning to a starting temperature within the excitation cycle; (2) the working medium, which enables rapid heat transfer while minimizing effective increase in the heat capacity of the projector material, and surviving the possible extreme temperature of the CNT sheets; and (3) possible packaging, which provides protection for the CNT sheets and efficient transmission of internal acoustic oscillation to external locations. Theoretical calculation indicates that a CNT sheet working in argon has a higher generation coefficient than that in air or in helium while 100 times higher than that working in liquids, such as water, methanol, and ethanol [64]. The total energy conversion efficiency of the argon-encapsulated thermoacoustic device is 0%, while that of CNT freestanding sheet device in air does not exceed 0.001%.

Additionally, the experimental efficiency of nanoscale thermophones is one order of magnitude below the theoretical expectation [65]. At low frequencies this mainly results from the presence of a substrate. At high frequencies, on the other hand, the efficiency is limited by the heat capacity of the nanowires.

Similar thermoacoustic CNT speakers made of CNT networks are also demonstrated recently [66]. A strong acoustic output was observed in a wide frequency range from 100 Hz to 100 kHz. Sound pressure level measured from 0.5 m away was extremely broad and flat in the ultrasonic region from 40 to 100 kHz.

Based on the same principle, graphene can also be used as speaker to produce sound in the wide ultrasound range 20–50 kHz [67]. The sound pressure depends

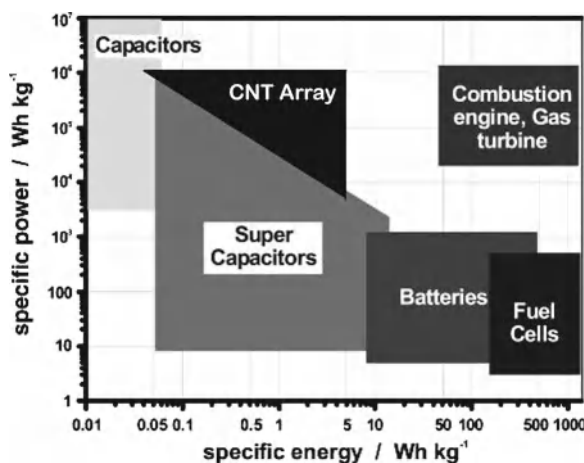


Fig. 9.10 Simplified Ragone diagram of the energy storage domains for the electrochemical energy conversion systems compared to the internal combustion engine, turbines, and conventional capacitors. From Winter and Brodd [69]. Copyright (2004) American Chemical Society

linearly with frequency of the signal generator from 3 to 20 kHz while independent on the frequency in the ultrasonic region, ranging from 20 to 50 kHz.

Besides the AC electric fields, laser can also generate ultrasound by exploiting the high frequency spectra of laser pulses to achieve broad acoustic bandwidths [68]. Such optoacoustic transmitters made of CNT arrays generate very strong optoacoustic pressure: 18 times stronger than a Cr film reference and five times stronger than a gold nanoparticle composite with the same polymer under pulsed laser excitation. The frequency of the produced strong and high sound covers the DC frequency up to 120 MHz.

9.4 Electrochemical and Chemical Storage Devices

Systems for electrochemical energy storage and conversion include batteries, fuel cells, and electrochemical capacitors [69]. Although the mechanisms are different, the common features are that the energy-providing processes take place at the phase boundary of the electrode/electrolyte interface and that electron and ion transports are separated. All of them consist of two electrodes in contact with an electrolyte solution. Figure 9.10 is a simplified Ragone-diagram disclosing the specific power and specific energy of these three electrochemical storage systems. Fuel cells can be considered to be high-energy systems and capacitors to be high-power systems while batteries have intermediate power and energy characteristics. Although no single electrochemical power source can match the characteristics of the internal combustion

engine (high power and high energy), some hybrid electrochemical power sources combining fuel cells (deliver high energy) and capacitors (provide high power) will be competitive with regard to the combustion engines and turbines in the future.

Here, we talk about the applications of CNT arrays in batteries, fuel cells, and capacities as electrodes.

Most favorable electrodes in these electrochemical storage systems are porous electrodes with large surface areas and low polarization. The porous structures of electrodes increase the surface area for reaction and shorten the diffusion path lengths to the reaction sites [69]. The effectiveness of a porous electrode can be estimated from the active surface area and the penetration depth of the reaction process into the porous electrode.

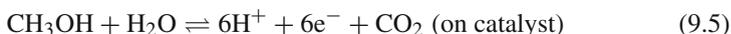
CNTs are the electrode material of choice because a CNT combines a large surface area wetted by an electrolyte, a high electrical conductivity, and a high chemical, mechanical, and electrochemical stability. So the electrochemical behaviors of CNTs have been studied [70–79] because of good electrical conductivity/chemical inertness/wide potential range.

Below, we discuss the application of aligned CNT arrays as porous electrodes in these chemical storage devices. Because of the large electrochemically accessible surface area of CNT arrays, combined with their high electrical conductivity and useful mechanical properties, CNT arrays are attractive as electrodes for devices that use electrochemical double-layer charge injection [48].

9.4.1 Fuel Cells

Fuel cells, one kind of electrochemical energy storage devices, are made up of three sandwiched segments similar to ultracapacitors and batteries: an anode, an electrolyte, and a cathode, in a reaction cell. Different from ultracapacitors and batteries in which the energy is stored in the cells and consumed, electricity is produced inside the fuel cells through the reactions between an external fuel and an oxidant in the presence of an electrolyte. At the anode, a catalyst, usually Pt nanoparticles, oxidizes the fuel, usually hydrogen, hydrocarbons, and alcohols, turning the fuel into positively charged ions and negatively charged electrons. The electrolyte (usually composed of aqueous alkaline solution, polymer membrane, phosphoric acid, molten carbonate, and solid oxide substrates) blocks the transportation of electrons while conducting ions. On the cathode, the ions traveling through the electrolyte are reunited with the electrons passing through a load during a reaction with an oxidant, such as oxygen, chlorine, and chlorine dioxide, to produce water or carbon dioxide.

In a typical fuel cell using methanol as the fuel, methanol is oxidized to produce ions and electrons at the anode in a polymer electrolyte:



and oxygen combines with electrons and H^+ ions at the cathode catalyst surface to form water:



Fuel cells can operate continuously as long as the fuels and the oxidants are well maintained [69].

Platinum and platinum alloys seem to be the best choice of catalysts for the electroreduction of oxygen in an acidic media [80]. The catalytic nanoparticles are deposited on porous materials, such as activated carbon, as electrodes. The electrocatalytic activity of platinum catalyst is dependent on many factors [81]. Among them, the good properties of the catalyst supports, such as high surface area and good electrical properties, are essential for a Pt catalyst to highly promote catalytic activities [82].

The large accessible surface area, low resistance, and high stability of CNTs [83, 84] suggest that CNTs are suitable materials for electrodes and catalyst supports in fuel cells. The nanoparticles with electrocatalytic activities may decorate the external walls or be encapsulated in the interior of the CNTs [85]. Several papers have studied the electrocatalytic properties of tangled and substrate-free CNTs [86–91]. More details of electrocatalytic activities using CNT electrodes are reviewed recently [92, 93]. Pt has been deposited on activated SWCNTs or MWCNTs by chemical reduction methods and the resultant electrodes show good electrocatalytic properties for hydrogenation [87], and oxygen reduction [86, 89]. Below we review the electrocatalytic properties of CNT arrays.

Experiments show that no O_2 reduction current is observed using CNT array electrodes or using graphite electrodes over the studied potential range [83]. This means that the CNT arrays and the graphite substrate result in no obvious electrocatalytic activities.

After Pt coating, electrocatalytic activity of CNT is observed. Pt nanoparticles can be deposited on the as-grown CNT arrays by a DC sputtering method [94] or other methods. Figure 9.11 shows the electrocatalytic properties of a Pt/CNT electrode for oxygen reduction reaction investigated by linear sweep voltammetry in a 0.1M H_2SO_4 aqueous solution. The well-aligned CNT arrays are synthesized by the PECVD method (see Chap. 5) on a titanium substrate as the working electrode. The CNT diameters are 50–70 nm and the lengths are 3–4 μm [83]. Pt catalysts are deposited on the CNT arrays using a potential-step electrodeposition method.

For Pt/CNT electrodes, a large oxygen reduction current is observed at 0.36 V, which is the typical potential for oxygen electroreduction on platinum catalysts in a H_2SO_4 solution [83]. The specific current, defined by peak current density (mA/cm^2) per unit of deposition charge (C/cm^2) [83] is used to evaluate the electrocatalytic activity of Pt catalysts for oxygen reduction activities. When the Pt loading mass is low (deposition charge: $9.744 C/cm^2$), the specific current of the Pt/CNT electrode (solid curve in Fig. 9.11a) is $0.41 mA/\mu C$, which is 1.4 times as large as that of a Pt/graphite electrode (dashed curve in Fig. 9.11a). At a high deposition charge ($572.5 \mu C/cm^2$), the specific current of the Pt/CNT electrode (solid curve in Fig. 9.11b) is almost twice as large as that of a Pt/graphite electrode (dashed curve

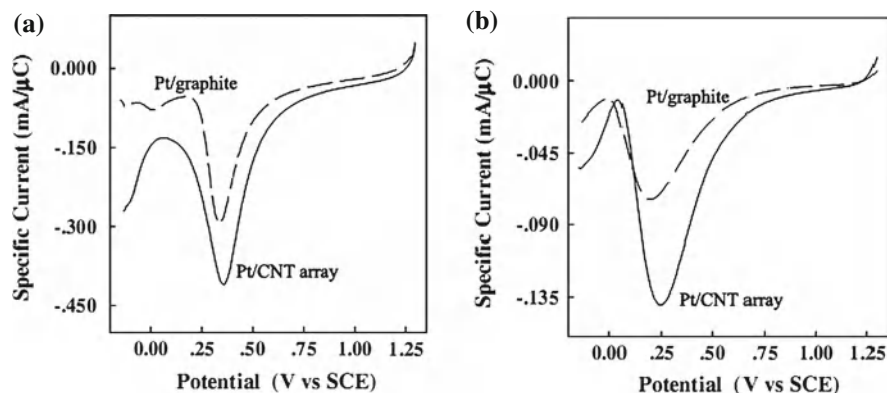


Fig. 9.11 The linear sweep voltammograms of Pt/CNT arrays in N_2 saturated $0.1\text{ M H}_2\text{SO}_4$ aqueous solution. For comparison, the voltammograms of platinum-electrodeposited graphite disk electrode (geometry area 1.71 cm^2 prepared at the same conditions) are also plotted as dashed curves. (a) Pt nanoparticles disperse individually on CNT walls with a deposition charge of $9.744\text{ }\mu\text{C}/\text{cm}^2$. (b) Pt nanofilm is deposited on individual CNTs with a deposition charge of $572.5\text{ }\mu\text{C}/\text{cm}^2$ while the coated CNTs huddle together to form bundles of 2–10 CNTs. Linear sweep rate is 200 mV/s . Pt catalytic nanoparticles are also deposited on a conventional graphite electrode for comparison. From Tang et al. [83]. Reprinted with permission from Elsevier

in Fig. 9.11b). These results imply that the Pt/CNT electrodes possess higher electrocatalytic activities for oxygen reduction.

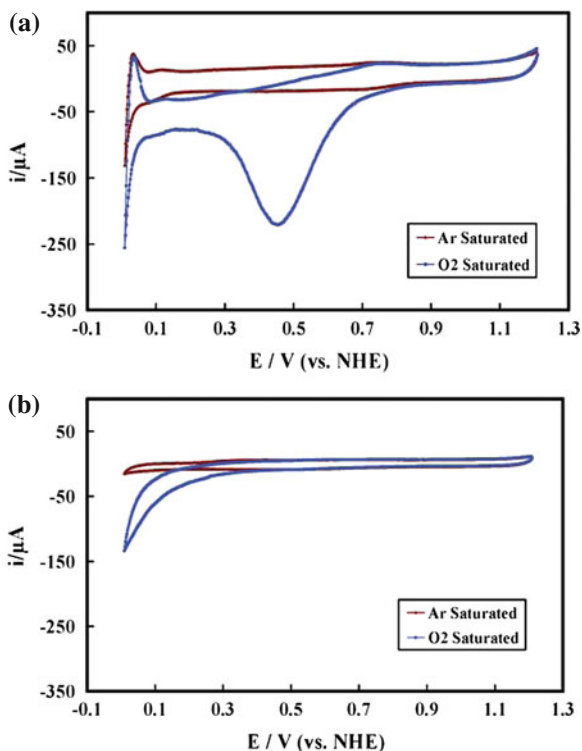
The increase in the O_2 reduction activity of Pt/CNT array electrodes may be attributed to the following two factors: (1) high dispersion of Pt nanoparticles on the 3D structure of CNT electrodes can provide large acceptable surface areas of Pt nanoparticles for oxygen reduction; (2) the particular structure and electrical properties of CNT arrays may be beneficial to the electrocatalytic reduction of oxygen. A previous study on the dissociation of adsorptive oxygen on the surface of CNTs suggested that CNTs have the ability to promote electron-transfer reactions [79]. Additionally, the activity of the catalyst, which could be involved in the interaction between metallic catalyst and catalyst support, can be strongly affected by the properties of the supporting materials. These results imply that well-aligned CNT arrays may be a good candidate for the cathodic catalyst supports in fuel cells.

More detailed studies on the kinetics of oxygen reduction reaction at Pt/CNT electrodes indicated that the activation energy of Pt/CNT electrodes is lower than that of Pt/graphite electrodes at the same cathodic over potential [83]. This suggests that CNTs have a beneficial effect on the kinetics of oxygen reduction.

Pt/CNT arrays can also oxidize methanol [95]. Additionally the oxidation activity of the Pt/CNT electrodes is increased after nitrogen doping.

Besides working as novel catalyst supports (including random CNTs [91, 96] and CNT arrays [83]), CNT arrays with iron catalyst may highly promote electrocatalytic activity themselves after nitrogen doping and can replace Pt catalysts [84, 87, 97, 98]. Figure 9.12 shows the cyclic voltammograms for CNT arrays taken in either argon- or

Fig. 9.12 Cyclic voltammograms of (a) nitrogen-doped CNT arrays and (b) CNT arrays without nitrogen measured in a 0.6M HCl electrolyte saturated with argon or oxygen at a scan rate of 10 mV/s. Ferrocene is used for CNT catalyst and not removed from CNTs. From Yang et al. [96]. Copyright (2008), The Royal Society of Chemistry



oxygen-saturated aqueous electrolytes. CNT arrays are synthesized using ferrocene as the source of catalyst and ammonia as the nitrogen dopant. The catalytic iron nanoparticles are kept on the CNT tips and the as-synthesized CNT arrays are used as cathodes. The CNTs are doped by nitrogen from ammonia during the CNT growth. The average content of nitrogen of the nitrogen-doped CNT arrays is 3.44 atomic%. Compared with the undoped CNT arrays (Fig. 9.12b), the electrocatalytic activity of the nitrogen-doped CNT arrays is enhanced significantly (Fig. 9.12a), as observed in random CNTs [99]. It is believed that active sites of nitrogen and iron with carbon have contributed to the oxygen reduction reaction.

Recently, it is found that the nitrogen-containing CNT arrays without metal inclusions also promote good electrocatalytic activities. Figure 9.13 plots the cyclic voltammogram for the oxygen reduction reaction of nitrogen-doped CNT array electrodes. The CNT arrays are free of iron catalysts and have a nitrogen content of 4–6 atomic%. Compared to Pt/carbon electrodes, the CNT array electrodes result in a much better electrocatalytic activity, long-term operation stability, and more tolerance to crossover effects than platinum for oxygen reduction in alkaline fuel cells. The vertically aligned CNTs reduce oxygen more effectively in alkaline solutions.

The ends of CNT arrays can be open by femtosecond laser. This Pd-coated end-opened CNT array electrodes perform significantly better than the unprocessed

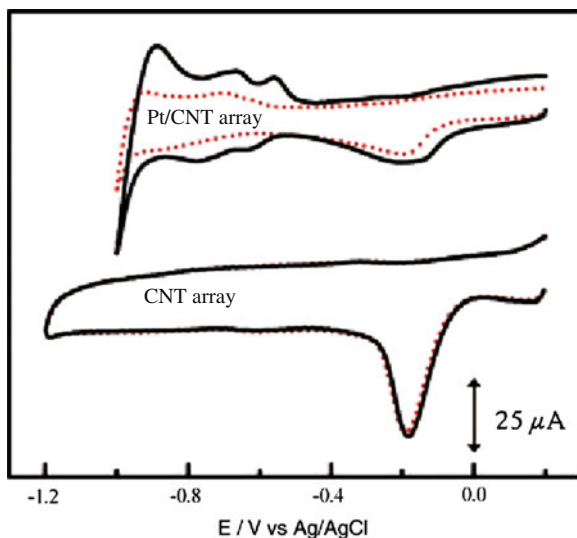


Fig. 9.13 The cyclic voltammogram for the oxygen reduction reaction of CNT array electrodes before (*solid curves*) and after (*dotted curves*) a continuous potentiodynamic swept for 100,000 cycles in an air-saturated 0.1 M KOH solution at 25 °C. The CNT array electrodes are free of iron catalysts. The properties of Pt/carbon electrodes are also plotted as a reference. From Gong et al. [98]. Copyright (2009), AAAS

Pd-coated CNT array electrodes [100]. Such treated Pd/CNT arrays can oxidate alcohol better in alkaline fuel cells.

9.4.2 Supercapacitors

Supercapacitors, also termed as electric double-layer capacitors or ultracapacitors, are electrochemical capacitors that store the electrostatic charges through adsorbing electrolytic ions onto a conductive electrode material with a large accessible specific surface area. The high capacitance of supercapacitors depends on the accessible specific surface area and the double layer adsorbing ions. Supercapacitors can be fully charged or discharged in seconds and achieve a high power output (10 kW/kg) in a few seconds [101] while their energy density (~ 5 kWh/kg) is lower than that of batteries. Supercapacitors currently bridge the conventional electrolytic capacitors and traditional batteries because they combine the unique properties of conventional capacitors (high power density) and that of traditional batteries (high energy density) [102].

Supercapacitors consist of two electrodes immersed in or impregnated with an electrolyte solution with a semi-permeable membrane serving as a separator that prevents electrical contact between the two electrodes. Figure 9.14 schematically

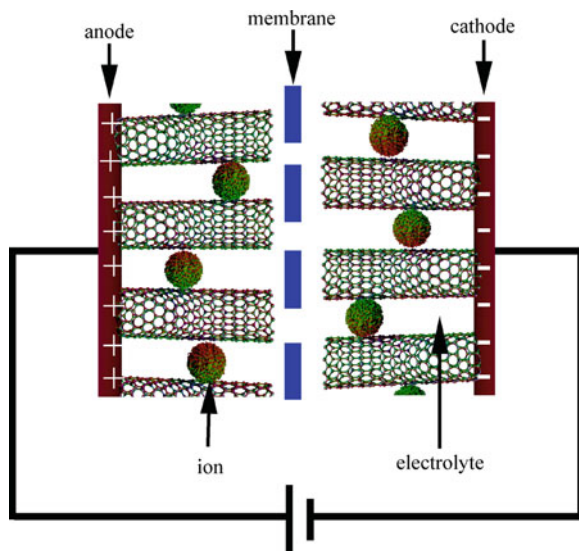


Fig. 9.14 Schematic of electrochemical double-layer capacitor. The membrane thickness is several nanometers. The potential difference is only several volts

illustrates a supercapacitor made of CNT array electrodes. CNT supercapacitors typically comprise two electrodes separated by an electrically insulating material, which is ionically conducting in electrochemical devices [103, 104]. The capacitance depends on the separation between the charges on the electrodes and the counter-charges in the electrolyte that contributed mostly to the capacitance. Very large capacitances result from the large CNT surface area accessible to the electrolyte.

The CNT array electrodes can be fabricated ex situ or in situ. In ex situ procedures, CNT arrays are grown by CVD methods. Then they are detached from the substrates, re-attached onto an electrically conductive current collector by binding [105], soldering, or surface tension, to form a CNT array electrode. The CNT array electrodes can also be fabricated from random CNTs by self-assembly processes [106]. In in situ procedures, a CNT array can be directly grown on a current collector to form an electrode [107, 108]. The procedure is a one-step process, and the electrical resistance between the CNT array and the current collector is relatively low.

The supercapacitors store the electrostatic charges by reversible absorption of electrolytic ions on active materials with large accessible specific surface areas. When an electric potential is applied to the electrodes, a potential difference is created at the electrode–electrolyte interface because of the charge separation from polarization. This electrostatic interface consists of a double-layer between the ions in the electrolyte and the electrical charges on the electrode.

The capacitance of a supercapacitor is generally assumed to follow that of a parallel-plate capacitor based on the Helmholtz model [109]:

$$C = \frac{\varepsilon_0 \varepsilon_r A}{d} \quad (9.7)$$

where ε_r is the dielectric constant of the electrolyte, ε_0 the permittivity of vacuum, A the specific surface area of the electrode accessible to the electrolyte ions, and d the effective thickness of the electrical double layer.

In fact, the structure of the electric double-layer is more complex than the Helmholtz model. The Helmholtz model states that two layers of opposite charges are formed at the electrode–electrolyte interface and are separated by an atomic distance. Besides the Helmholtz model, a modified Gouy-Chapman model refers to a diffuse layer consisting of continuous distribution of electrolyte ions (both cations and anions), not a layer consisting of only cations or only anions, in the electrolyte solution. The modern Stern model combines the Helmholtz model with the Gouy-Chapman model to structure two regions of ion distribution: the inner compact layer (Stern layer) where ions are strongly absorbed by the electrode and an outer diffuse layer defined in the Gouy-Chapman model. The more accurate capacitance is a sum of the capacitances from the two regions:

$$\frac{1}{C} = \frac{1}{C_{\text{Stern}}} + \frac{1}{C_{\text{diff}}} \quad (9.8)$$

Both Stern layer contribution C_{Stern} and diffuse layer contribution C_{diff} are proportional to the specific surface area and depend on the pore size.

In the supercapacitors, the electrical energy is stored as the electrostatic charges based on the separation of charged species in an electrical double-layer across the electrode-solution interfaces and there is no faradic (redox) reaction.

The active materials with high specific surface area and electrically conducting electron collectors produce high capacitances. In conventional supercapacitors, in which activated carbon or glassy carbon are employed as electrodes, the double-layer capacitance reaches 100–200 F/g in organic electrolytes, and exceeds 370 F/g in aqueous electrolytes [110], storing more energy than the conventional capacitors [111].

CNT arrays store energy by the electrochemical double-layer formed on the surfaces of each CNT in the array. Since the capacitive properties of the array-like CNT membranes were studied [76], capacitance of 18 F/g was obtained in 6 M KOH electrolytes using a 400 μm long CNT array directly grown on a metallic alloy [108], and 35 F/g was obtained in 6 M KOH using a CNT array embedded in cellulose [112].

It is observed that the capacitance of supercapacitors is maximum when the electrode size is close to the ion size [113], confirming the capacitance contribution from pores with sizes smaller than the solvated ion size. CNTs are aligned regularly, possessing regular pore structures, and adjustable pore sizes, and therefore are the best candidates for supercapacitor electrodes. The CNT arrays have larger surface areas than activated carbon to store electron charges in supercapacitors. In addition, the CNT site density can be adjusted to store elementary charges, such as electrons, and consequently the capacitance may be increased considerably.

The capacitances of 180 and 102 F/g are achieved for random SWCNT electrodes and MWCNT electrodes, respectively. It is typically between 15 and 200 F/g when random CNTs are employed [103, 104]. The capacitances come from the large amounts of charge injection when only a few volts are applied.

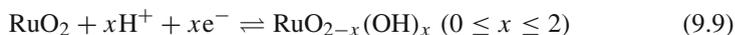
The CNT array electrodes possess lower ion diffusion resistance, higher electrical conductivity, larger pores, and more regular pore structure than the electrodes consisting of random CNTs. Therefore, the CNT array electrodes have higher capacitances, lower resistances, and better rate performances [114]. The application of CNT arrays as capacitors are reviewed recently [102, 110, 114, 115].

Besides aqueous electrolytes, organic electrolytes are also tested. Capacitances of 22 F/g in ionic liquid electrolyte [112], 80 F/g in 1 M tetra-ethylammonium tetrafluoroborate (Et₄NBF₄)/propylene carbonate (PC) electrolyte using SWCNT arrays [116], 10–15 F/g in organic electrolytes at an extremely high current density of 200 A/g [117], 83 F/g in organic electrolytes using a DWCNT array of 300 μm in length grown on a conductive Si substrate [118], and 27 F/g in organic electrolytes are reported.

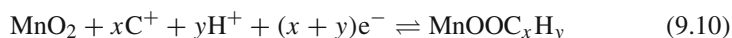
Experimental results indicate that the CNT array electrodes possess lower ion diffusivity resistances and higher electrical conductivities, better rate performances, and higher capacitances than random CNTs because of the regular pore structure and the large pore size of CNT arrays.

Although CNT array electrodes possess a higher rate capability than any other electrochemical electrode materials, their capacitances are moderate, i.e., 10–80 F/g [118, 119], lower than the activated carbon and pseudo-capacitive materials. The moderate capacitance should come from the medium specific surface area of CNTs (120–500 m²/g), lower than that of active carbon (1000–3500 m²/g) [110]. In order to improve the power and cycle performances of CNT array electrodes, pseudo-capacitive materials (including conducting polymers, such as polyaniline [120], polypyrrole, and polythiophene, metal oxides, such as ruthenium oxide (RuO₂), manganese oxide (MnO₂) [121], NiO, Fe₃O₄, and nitrides, (such as vanadium nitride) are deposited on the CNT surface to form CNT composite electrodes. In these CNT composite capacitors, CNTs serve as an effective support for pseudo-capacitive materials because of the excellent mechanical properties of CNTs.

At the same time, the CNTs conduct electrons due to superior electrical properties. These pseudocapacitive (or termed redox supercapacitive) materials can be fast and reversible redoxed on the CNT surfaces or near-surface for charge storage and the pseudo-capacitance is faradic. For example, the ruthenium oxidation states in ruthenium oxide can react in electrolyte as [101]



The continuous change of x during H^+ insertion leads to a pseudo-capacitive behavior with ion adsorption. The charge storage mechanism of manganese oxide is based on the surface absorption of electrolyte cations and proton incorporation:



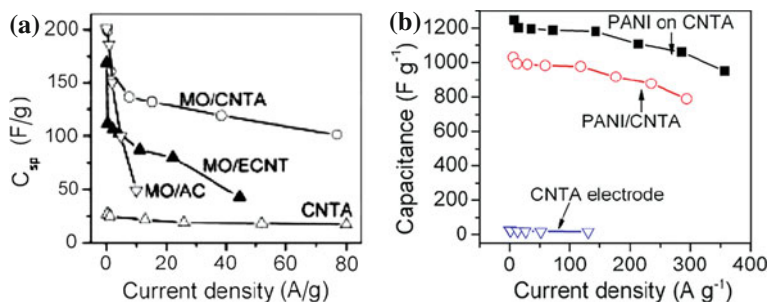


Fig. 9.15 Specific capacitance of (a) manganese oxide-CNT array (MO/CNTA), manganese oxide-entangled CNT(MO/ECNT), manganese oxide-active carbon (MO/AC), and CNTA versus discharge current density. From Zhang et al. [121]. Copyright (2008) American Chemical Society. (b) Polyaniline (PANI) on CNT array compared with polyaniline/CNTA. From Zhang et al. [120]. Copyright (2008), Elsevier

A study in an electrolyte ionic liquid shows that maximum capacitance is produced when the pore size is close to the ionic radius [113]. So the density of CNT array is usually very high with the gap between CNTs being a few nanometers. So, the conducting polymers and inorganic materials are usually electrodeposited on CNT arrays, like polyaniline (PANI) [120] and MnO_x [121].

Such CNT array composites have higher capacitances than CNT arrays and pseudo-capacitive materials due to the contribution of both double-layer capacitance and pseudo-capacitance (Fig. 9.15). The capacitance of the PANI/CNTA composite is 1030 F/g at a low current density of 5.9 A/g [120], higher than the PANI materials. Compared to the best results from commercial products (about 130 F/g), the pseudo-capacitors have much higher energy storage capabilities.

SWCNT arrays are also coated by Al_2O_3 to fabricate solid-state dielectric energy storage materials. The solid-state dielectric architecture enables the operation of such devices at substantially higher frequencies than conventional electrolyte-based capacitor designs [122]. Furthermore, modeling of supercapacitor architectures utilizing other dielectric layers suggests the ability to achieve energy densities above 10 Wh/kg while still exhibiting power densities comparable to conventional solid-state capacitor devices.

The SWCNT films were also uniformly spreaded onto the separators serving as both electrodes and charge collectors without metallic current collectors, leading to a simplified and lightweight assembling compact-designed supercapacitor [123]. High energy density of 43.7 Wh/kg and power density of 197.3 kW/kg were achieved from the SWCNT film-based compact-designed supercapacitors with small equivalent series resistance. The specific capacitance of this kind of compact-designed SWCNT film supercapacitor is about 35 F/g.

The advantages of CNT arrays as capacitors come from their excellent mechanical properties, electrical conductivity, and good ion conduction owing to the straight

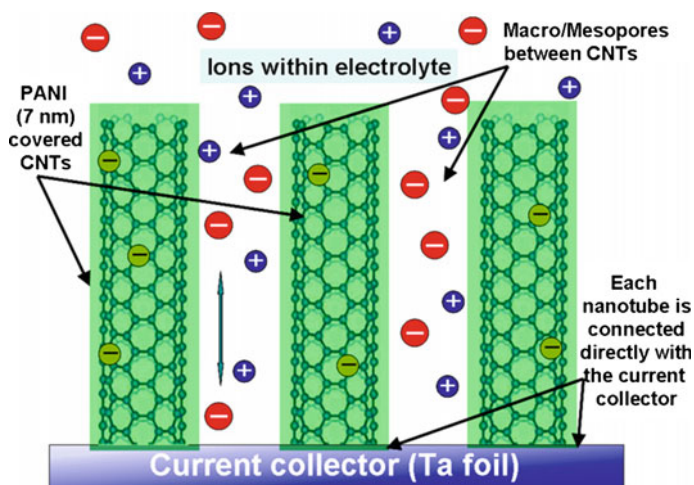


Fig. 9.16 Schematic diagram showing the Li-ion battery devices with CNT array electrodes as anodes. From Zhang et al. [120]. Copyright (2008), Elsevier

conduction pathways [116]. More detailed applications of CNTs as supercapacitors are reviewed in some literatures [109].

Additionally, the vertical CNT arrays can form effective CNT membranes, which can be electrostatically actuated like the conventional metal plates used in MEMS capacitors [124]. A maximum capacitance of 400 fF and maximum tunability of 5.8% is extracted.

9.4.3 Lithium Ion Batteries

In batteries, electrical energy is generated by conversion of chemical energy via a redox reaction at the anode and the cathode in a closed system. Unlike in ultracapacitors where the solvent of the electrolyte is not involved in the charge storage mechanism, the solvent of the electrolyte contributes to the solid-electrolyte interphase in batteries. The Li-ion batteries, one kind of rechargeable batteries, usually consist of an active carbon anode, a lithium-cobalt oxide cathode, and an organic electrolyte.

Activated carbon is used in the commercial lithium-ion batteries as electrodes. In order to obtain better performance of electrodes, CNT arrays and CNT array composites are recently studied as electrodes besides the random CNTs and random CNT composites.

Figure 9.16 illustrates such a Li-ion battery consisting of CNT array (composite) electrodes and a Li electrode. The CNT arrays are prepared by the PECVD method described in Chap. 5. Then a PANI layer is coated on CNTs. Then the PANI/CNT

array composite can be used as the lithium-ion battery cathode [120]. The capacity of such PANI/CNT array composite electrode 98 mAh/g is higher than that of the PANI/random CNT composite electrode 86 mAh/g [125]. MnO_x /CNT array composite electrodes are also used as cathodes [121]. The capacity of MnO_x /CNT array composite (246 mAh/g) is also higher than that of MnO_x -based nanostructures. In the CNT array composites, the CNT array framework enhances the rate performance of the electrode materials by providing good electrical conductivity and preserving the benefits of the electrochemical properties of supercapacitive nanomaterials. The CNT array electrodes can also be used as lithium-ion battery anodes [76, 114]. The rate and cycle performance of CNT array electrodes are superior to random CNT electrodes.

9.4.4 Hydrogen Storage

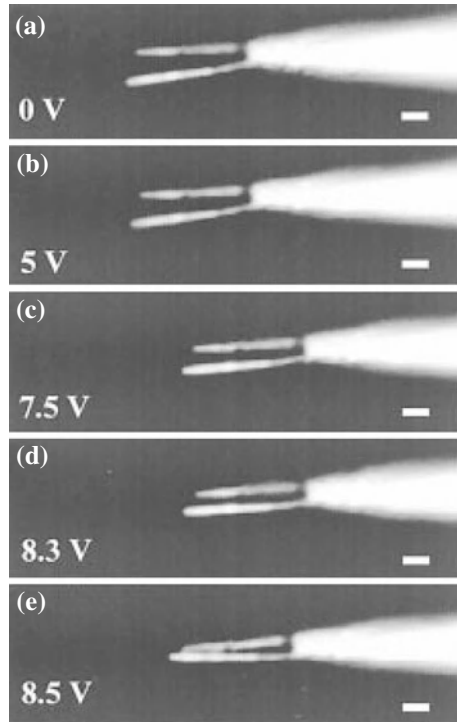
CNTs have been long heralded as potentially useful for hydrogen storage. It was reported that the amount of hydrogen desorbed on SWCNTs is 5–10 wt% at room temperature [126–128], close to the reasonable automotive target of 6.5 wt%. A higher hydrogen storage capacity was also reported in many published papers. For example, it was reported that lithium-doped SWCNTs can absorb 20 wt% of hydrogen at room temperatures under ambient pressures [129]. However, experimental reports of high storage capacities are so controversial [130] that it is impossible to assess the true potential [48]. Careful experiments indicate that the highest absorption percentage of hydrogen is less than 0.1 wt% at room temperature in SWCNTs [131, 132], in MWCNTs [131], and in carbon fibers [133]. More efforts are needed in the field, and the application of CNT arrays in hydrogen storage is still far away from practical applications.

9.5 Electromechanical Devices: Actuators

Actuator materials can convert electrical, chemical, thermal, or photonic energies to mechanical energy. Electromechanical actuators are frequently used in robots and typically comprised of two electrodes separated by an electrically insulating material, similar to the supercapacitors. The charge injection causes electrode expansions and contractions that can do mechanical work in the electromechanical actuators [135]. Electrostatic attraction and repulsion between two CNTs were used for cantilever-based nanotweezers [134] (Fig. 9.17) and electromechanically based logic elements [54] and nanoswitches [136].

Macroscaled CNT actuators powered by electricity [135, 137, 138] or fuel [139] can provide a hundred times higher stress generation than natural muscles [140]. The maximum observed isometric actuator stress of SWCNT-sheet actuators is about 26 MPa, 100 times that of the stress generation capability of natural muscles. Aligned

Fig. 9.17 Electromechanical response of the nanotube nanotweezers. From Kim and Lieber [134]. Scale bar 1 μm



CNT composites can also be actuators powered by IR irradiation [141] or by electricity [142], and be of shape memory functions [143, 144].

Figure 9.18 shows the CNT aerogel sheets used as the sole component of artificial muscles. The CNT aerogel sheets are fabricated by the spinning method described in Chap. 6. Such muscles can provide giant elongations and elongation rates of 220% and 3.7×10^4 % per second, respectively, at operating temperatures from 80 to 1900K. The width expansion ratio, W/W_0 , increases approximately quadratically with applied voltage V , while a crossover occurs at higher voltages to a weaker dependence, $\sim V^{3/2}$.

9.6 Terahertz Sources

CNTs have many properties, from their unique dimensions to an unusual current conduction mechanism, that make them ideal components of electrical circuits. For example, they have shown to exhibit strong electron-phonon resonances. Under certain direct current bias and doping conditions their current and the average electron

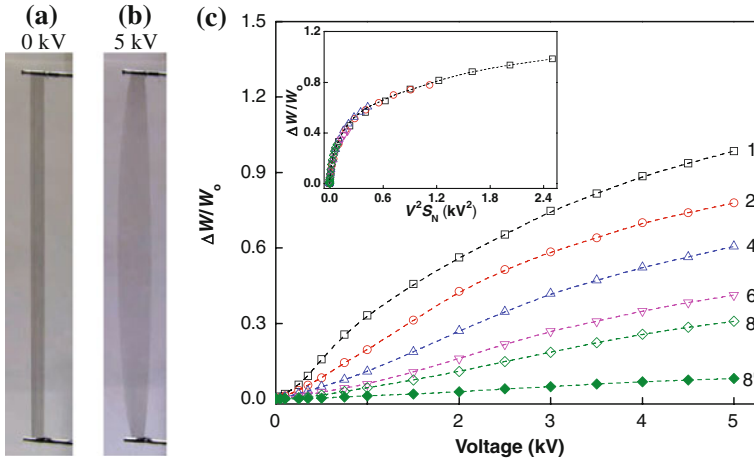


Fig. 9.18 Artificial muscles. (a) Photograph of a rigidly end-supported nanotube sheet strip with length of 50 mm and width of 2 mm. (b) Same sheet strip expanded by applying a 5 kV voltage with respect to ground. (c) Width direction actuation strain, W/W_0 versus applied voltage V for $N = 1 - 8$ stacks of single aerogel sheets and for a densified eight-sheet stack, labeled 1 to 8, respectively. From Aliev et al. [145]. Copyright (2009), AAAS

velocity, as well as the electron concentration on the tube, CNTs can oscillate at terahertz frequencies. These resonances could potentially be used to make terahertz sources or sensors.

9.7 Other Applications

There are a handful of other applications of assembled CNTs, such as blackbody absorbers to absorb light perfectly across a very wide spectral range (0.2–200 μm) [147], and infrared (IR) detectors [148, 146] as shown in Fig. 9.19, filters and membranes [149–152], hydrophilicity [153], micro-electro-mechanical-systems [154], gate MOS transistor [155], varactor [156], piezoelectric generators [157], platelet hybrid microstructured reactor [158], ion source in mass spectrometry [159, 160], organic electronic devices [161], microtransducers [162], hazardous industrial chemical gas sensors [163], temperature sensors [164]. As a demonstration, nanotube transistor radios are also fabricated [165], in which SWCNT array devices provide all of the key functions, including resonant antennas, fixed RF amplifiers, RF mixers, and audio amplifiers.

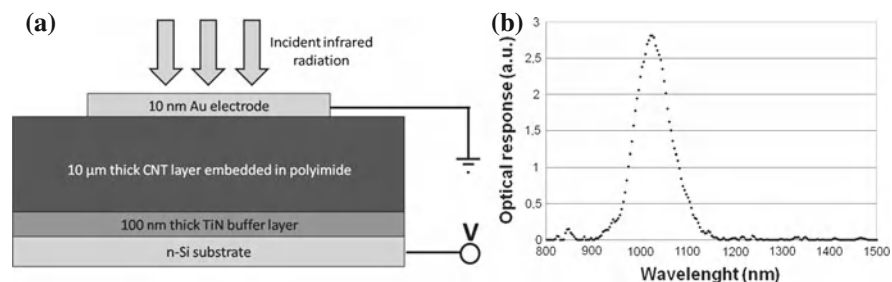


Fig. 9.19 Infrared sensors. (a) Representation and (b) Spectral response of the CNT IR sensors on silicon (bias voltage of -0.18 V). From Mérel et al. [146]

References

1. D.A. Walters, L.M. Ericson, M.J. Casavant, J. Liu, D.T. Colbert, K.A. Smith, R.E. Smalley, Elastic strain of freely suspended single-wall carbon nanotube ropes. *Appl. Phys. Lett.* **74**(25), 3803–3805 (1999)
2. M.-F. Yu, B.S. Files, S. Arepalli, R.S. Ruoff, Tensile loading of ropes of single wall carbon nanotubes and their mechanical properties. *Phys. Rev. Lett.* **84**(24), 5552–5555 (2000)
3. A. Krishnan, E. Dujardin, T.W. Ebbesen, P.N. Yianilos, M.M.J. Treacy, Young's modulus of single-walled nanotubes. *Phys. Rev. B* **58**, 14013–14019 (Nov 1998)
4. E.W. Wong, P.E. Sheehan, C.M. Lieber, Nanobeam mechanics: elasticity, strength, and toughness of nanorods and nanotubes. *Science* **277**(5334), 1971–1975 (1997)
5. M.M.J. Treacy, T.W. Ebbesen, J.M. Gibson, Exceptionally high Young's modulus observed for individual carbon nanotubes. *Nature* **381**(6584), 678–680 (1996)
6. M.-F. Yu, O. Lourie, M.J. Dyer, K. Moloni, T.F. Kelly, R.S. Ruoff, Strength and breaking mechanism of multiwalled carbon nanotubes under tensile load. *Science* **287**(5453), 637–640 (2000)
7. C. Wei, K. Cho, D. Srivastava, Tensile strength of carbon nanotubes under realistic temperature and strain rate. *Phys. Rev. B* **67**(11), 115407 (2003)
8. B.M. Nardelli, B.I. Yakobson, J. Bernholc, Mechanism of strain release in carbon nanotubes. *Phys. Rev. B* **57**(8), R4277–R4280 (1998)
9. M. Reibold, P. Paufler, A.A. Levin, W. Kochmann, N. Patzke, D.C. Meyer, Materials: carbon nanotubes in an ancient damascus sabre. *Nature* **444**(7117), 286–286 (2006)
10. K. Sanderson, Sharpest cut from nanotube sword. *Nature* (2006). News at <http://dx.doi.org/10.1038/news061113-11>
11. E.T. Thostenson, W.Z. Li, D.Z. Wang, Z.F. Ren, T.W. Chou, Carbon nanotube/carbon fiber hybrid multiscale composites. *J. Appl. Phys.* **91**(9), 6034–6037 (2002)
12. L. Jin, C. Bower, O. Zhou, Alignment of carbon nanotubes in a polymer matrix by mechanical stretching. *Appl. Phys. Lett.* **73**(9), 1197–1199 (1998)
13. R. Hagenmueller, H.H. Gommans, A.G. Rinzler, J.E. Fischer, K.I. Winey, Aligned single-wall carbon nanotubes in composites by melt processing methods. *Chem. Phys. Lett.* **330**(3–4), 219–225 (2000)
14. B. Safadi, R. Andrews, E.A. Grulke, Multiwalled carbon nanotube polymer composites: synthesis and characterization of thin films. *J. Appl. Polym. Sci.* **84**(14), 2660–2669 (2002)
15. A.R. Bhattacharyya, T. Sreekumar, T. Liu, S. Kumar, L.M. Ericson, R.H. Hauge, R.E. Smalley, Crystallization and orientation studies in polypropylene/single wall carbon nanotube composite. *Polymer* **44**(8), 2373–2377 (2003)

16. E.S. Choi, J.S. Brooks, D.L. Eaton, M.S. Al-Haik, M.Y. Hussaini, H. Garmestani, D. Li, K. Dahmen, Enhancement of thermal and electrical properties of carbon nanotube polymer composites by magnetic field processing. *J. Appl. Phys.* **94**(9), 6034–6039 (2003)
17. X. Zhang, Q. Li, T.G. Holesinger, P.N. Arendt, J. Huang, P.D. Kirven, T.G. Clapp, R.F. DePaula, X. Liao, Y. Zhao, L. Zheng, D. Peterson, Y. Zhu, Ultrastrong, stiff, and lightweight carbon-nanotube fibers. *Adv. Mater.* **19**(23), 4198–4201 (2007)
18. Y. Dror, W. Salalha, R.L. Khalfin, Y. Cohen, A.L. Yarin, E. Zussman, Carbon nanotubes embedded in oriented polymer nanofibers by electrospinning. *Langmuir* **19**(17), 7012–7020 (2003)
19. R. Sen, B. Zhao, D. Perea, M.E. Itkis, H. Hu, J. Love, E. Bekyarova, R.C. Haddon, Preparation of single-walled carbon nanotube reinforced polystyrene and polyurethane nanofibers and membranes by electrospinning. *Nano Lett.* **4**(3), 459–464 (2004)
20. J. Gao, A. Yu, M.E. Itkis, E. Bekyarova, B. Zhao, S. Niyogi, R.C. Haddon, Large-scale fabrication of aligned single-walled carbon nanotube array and hierarchical single-walled carbon nanotube assembly. *J. Am. Chem. Soc.* **126**(51), 16698–16699 (2004)
21. J.J. Ge, H. Hou, Q. Li, M.J. Graham, A. Greiner, D.H. Reneker, F.W. Harris, S.Z.D. Cheng, Assembly of well-aligned multiwalled carbon nanotubes in confined polyacrylonitrile environments: electrospun composite nanofiber sheets. *J. Am. Chem. Soc.* **126**(48), 15754–15761 (2004)
22. M.D. Lynch, D.L. Patrick, Organizing carbon nanotubes with liquid crystals. *Nano Lett.* **2**(11), 1197–1201 (2002)
23. X.L. Xie, Y.W. Mai, X.P. Zhou, Dispersion and alignment of carbon nanotubes in polymer matrix: a review. *Mat. Sci. Eng. R-Rep.* **49**(4), 89–112 (2005)
24. M. Zhang, K.R. Atkinson, R.H. Baughman, Multifunctional carbon nanotube yarns by downsizing an ancient technology. *Science* **306**(5700), 1358–1361 (2004)
25. M.B. Bazbouz, G.K. Stylios, Novel mechanism for spinning continuous twisted composite nanofiber yarns. *Eur. Polym. J.* **44**(1), 1–12 (2008)
26. K. Jiang, Q. Li, S. Fan, Nanotechnology: spinning continuous carbon nanotube yarns. *Nature* **419**(6909), 801–801 (2002)
27. Y.-L. Li, I.A. Kinloch, A.H. Windle, Direct spinning of carbon nanotube fibers from chemical vapor deposition synthesis. *Science* **304**(5668), 276–278 (2004)
28. F. Ko, Y. Gogotsi, A. Ali, N. Naguib, H. Ye, G. Yang, C. Li, P. Willis, Electrospinning of continuous carbon nanotube-filled nanofiber yarns. *Adv. Mater.* **15**(14), 1161–1165 (2003)
29. R.B. Pipes, P. Hubert, Helical carbon nanotube arrays: mechanical properties. *Compos. Sci. Technol.* **62**(3), 419–428 (2002)
30. J.W.S. Hearle, P. Grosberg, S. Backer, *Structural Mechanics of Fibers, Yarns, and Fabrics* (Wiley-Interscience, New York, 1969)
31. J.-P. Salvetat, G.A.D. Briggs, J.-M. Bonard, R.R. Bacsá, A.J. Kulik, T. Stöckli, N.A. Burnham, L. Forró, Elastic and shear moduli of single-walled carbon nanotube ropes. *Phys. Rev. Lett.* **82**, 944–947 (Feb 1999)
32. R.B. Pipes, P. Hubert, Scale effects in carbon nanostructures: self-similar analysis. *Nano Lett.* **3**(2), 239–243 (2003)
33. B. Vigolo, A. Pénicaud, C. Coulon, C. Sauder, R. Pailler, C. Journet, P. Bernier, P. Poulin, Macroscopic fibers and ribbons of oriented carbon nanotubes. *Science* **290**(5495), 1331–1334 (2000)
34. K. Koziol, J. Vilatela, A. Moisala, M. Motta, P. Cuniff, M. Sennett, A. Windle, High-performance carbon nanotube fiber. *Science* **318**(5858), 1892–1895 (2007)
35. S. Kumar, T.D. Dang, F.E. Arnold, A.R. Bhattacharyya, B.G. Min, X. Zhang, R.A. Vaia, C. Park, W.W. Adams, R.H. Hauge, R.E. Smalley, S. Ramesh, P.A. Willis, Synthesis, structure, and properties of PBO/SWNT composites. *Macromolecules* **35**(24), 9039–9043 (2002)
36. L.-Q. Liu, M. Eder, I. Burgert, D. Tasis, M. Prato, H.D. Wagner, One-step electrospun nanofiber-based composite ropes. *Appl. Phys. Lett.*, **90**(8), 083108 (2007)
37. J. Jia, J. Zhao, G. Xu, J. Di, Z. Yong, Y. Tao, C. Fang, Z. Zhang, X. Zhang, L. Zheng, Q. Li, A comparison of the mechanical properties of fibers spun from different carbon nanotubes. *Carbon* **49**(4), 1333–1339 (2011)

38. K. Liu, Y. Sun, L. Chen, C. Feng, X. Feng, K. Jiang, Y. Zhao, S. Fan, Controlled growth of super-aligned carbon nanotube arrays for spinning continuous unidirectional sheets with tunable physical properties. *Nano Lett.* **8**(2), 700–705 (2008)
39. L.M. Ericson, H. Fan, H. Peng, V.A. Davis, W. Zhou, J. Sulpizio, Y. Wang, R. Booker, J. Vavro, C. Guthy, A.N.G. Parra-Vasquez, M.J. Kim, S. Ramesh, R.K. Saini, C. Kittrell, G. Lavin, H. Schmidt, W.W. Adams, W.E. Billups, M. Pasquali, W.-F. Hwang, R.H. Hauge, J.E. Fischer, R.E. Smalley, Macroscopic, neat, single-walled carbon nanotube fibers. *Science* **305**(5689), 1447–1450 (2004)
40. Z. Wu, Z. Chen, X. Du, J.M. Logan, J. Sippel, M. Nikolou, K. Kamaras, J.R. Reynolds, D.B. Tanner, A.F. Hebard, A.G. Rinzler, Transparent, conductive carbon nanotube films. *Science* **305**(5688), 1273–1276 (2004)
41. L. Zhang, C. Feng, Z. Chen, L. Liu, K. Jiang, Q. Li, S. Fan, Superaligned carbon nanotube grid for high resolution transmission electron microscopy of nanomaterials. *Nano Lett.* **8**(8), 2564–2569 (2008)
42. L. Ge, S. Sethi, L. Ci, P.M. Ajayan, A. Dhinojwala, Carbon nanotube-based synthetic gecko tapes. *Proc. Natl. Acad. Sci. U S A* **104**(26), 10792–10795 (2007)
43. N.M. Mohamed, L.M. Kou, Piezoresistive effect of aligned multiwalled carbon nanotubes array. *J. Appl. Sci.* **11**(8), 1386–1390 (2011)
44. F.-Z. Zheng, Z.-Y. Zhou, X. Yang, Y.-K. Tang, Y. Wu, Investigation on strain-sensing suspended single-walled carbon nanotube arrays. *IEEE Trans. Nanotechnol.* **10**(4), 694–698 (2011)
45. J. Choi, J. Kim, Batch-processed carbon nanotube wall as pressure and flow sensor. *Nanotechnology* **21**(10), 105502 (2010)
46. X. Yang, Z. Zhou, D. Wang, X. Liu, High sensitivity carbon nanotubes flow-rate sensors and their performance improvement by coating. *Sensors* **10**(5), 4898–4906 (2010)
47. S. Frank, P. Poncharal, Z.L. Wang, W.A. de Heer, Carbon nanotube quantum resistors. *Science* **280**(5370), 1744–1746 (1998)
48. R.H. Baughman, A.A. Zakhidov, W.A. de Heer, Carbon nanotubes—the route toward applications. *Science* **297**(5582), 787–792 (2002)
49. M.J. Biercuk, M.C. Llaguno, M. Radosavljevic, J.K. Hyun, A.T. Johnson, J.E. Fischer, Carbon nanotube composites for thermal management. *Appl. Phys. Lett.* **80**(15), 2767–2769 (2002)
50. W. Bauhofer, J.Z. Kovacs, A review and analysis of electrical percolation in carbon nanotube polymer composites. *Compos. Sci. Technol.* **69**(10), 1486–1498 (2009)
51. F. Du, J.E. Fischer, K.I. Winey, Effect of nanotube alignment on percolation conductivity in carbon nanotube/polymer composites. *Phys. Rev. B* **72**(12), 121404 (2005)
52. J. Sandler, J. Kirk, I. Kinloch, M. Shaffer, A. Windle, Ultra-low electrical percolation threshold in carbon-nanotube-epoxy composites. *Polymer* **44**(19), 5893–5899 (2003)
53. E. Bichoutskaia, A.M. Popov, Y.E. Lozovik, Nanotube-based data storage devices. *Mater. Today* **11**(6), 38–43 (2008)
54. T. Rueckes, K. Kim, E. Joselevich, G.Y. Tseng, C.-L. Cheung, C.M. Lieber, Carbon nanotube-based nonvolatile random access memory for molecular computing. *Science* **289**(5476), 94–97 (2000)
55. W.B. Choi, J.U. Chu, K.S. Jeong, E.J. Bae, J.-W. Lee, J.-J. Kim, J.-O. Lee, Ultrahigh-density nanotransistors by using selectively grown vertical carbon nanotubes. *Appl. Phys. Lett.* **79**(22), 3696–3698 (2001)
56. X. Ho, L. Ye, S.V. Rotkin, Q. Cao, S. Unarunotai, S. Salamat, M.A. Alam, J.A. Rogers, Scaling properties in transistors that use aligned arrays of single-walled carbon nanotubes. *Nano Lett.* **10**(2), 499–503 (2010)
57. F. Noca, J. Xu, P. Koumoutsakos, T. Werder, J. Walther, in *Nanoscale ears based on artificial stereocilia*, in *The 140th Meeting of the Acoustical Society of America/NOISE-CON*, Newport Beach, California (2000)
58. R.R. Bouillosa, A.O. Santillá, A note on the use of novel thermoacoustic radiators for ultrasonic experiments: the importance of phase in a focused field. *Eur. J. Phys.* **27**(1), 95 (2006)

59. H.D. Arnold, I.B. Crandall, The thermophone as a precision source of sound. *Phys. Rev.* **10**(1) 22–38 (1917)
60. P. Liu, L. Liu, Y. Wei, K. Liu, Z. Chen, K. Jiang, Q. Li, S. Fan, Fast high-temperature response of carbon nanotube film and its application as an incandescent display. *Adv. Mater.* **21**(35), 3563–3566 (2009)
61. L. Xiao, Z. Chen, C. Feng, L. Liu, Z.-Q. Bai, Y. Wang, L. Qian, Y. Zhang, Q. Li, K. Jiang, S. Fan, Flexible, stretchable, transparent carbon nanotube thin film loudspeakers. *Nano Lett.* **8**(12), 4539–4545 (2008)
62. E.C. Wentz, The thermophone. *Phys. Rev.* **19**(4), 333–345 (1922)
63. L. Xiao, P. Liu, L. Liu, Q. Li, Z. Feng, S. Fan, K. Jiang, High frequency response of carbon nanotube thin film speaker in gases. *J. Appl. Phys.* **110**(8), 084311 (2011)
64. A.E. Aliev, M.D. Lima, S. Fang, R.H. Baughman, Underwater sound generation using carbon nanotube projectors. *Nano Lett.* **10**(7), 2374–2380 (2010)
65. V. Vesterinen, A.O. Niskanen, J. Hassel, P. Helistö, Fundamental efficiency of nanothermophones: modeling and experiments. *Nano Lett.* **10**, 5020–5024 (2010)
66. K. Suzuki, S. Sakakibara, M. Okada, Y. Neo, H. Mimura, Y. Inoue, T. Murata, Study of carbon-nanotube web thermoacoustic loud speakers. *Jpn. J. Appl. Phys.* **50**(1), 01BJ10 (2011)
67. H. Tian, T.-L. Ren, D. Xie, Y.-F. Wang, C.-J. Zhou, T.-T. Feng, D. Fu, Y. Yang, P.-G. Peng, L.-G. Wang, L.-T. Liu, Graphene-on-paper sound source devices. *ACS Nano* **5**(6), 4878–4885 (2011)
68. H.W. Baac, J.G. Ok, H.J. Park, T. Ling, S.-L. Chen, A.J. Hart, L.J. Guo, Carbon nanotube composite optoacoustic transmitters for strong and high frequency ultrasound generation. *Appl. Phys. Lett.* **97**(23), 234104 (2010)
69. M. Winter, R.J. Brodd, What are batteries, fuel cells, and supercapacitors? *Chem. Rev.* **104**(10), 4245–4270 (2004)
70. J. Li, A. Cassell, L. Delzeit, J. Han, M. Meyyappan, Novel three-dimensional electrodes: electrochemical properties of carbon nanotube ensembles. *J. Phys. Chem. B* **106**(36), 9299–9305 (2002)
71. J.K. Campbell, L. Sun, R.M. Crooks, Electrochemistry using single carbon nanotubes. *J. Am. Chem. Soc.* **121**(15), 3779–3780 (1999)
72. P. Britto, K. Santhanam, P. Ajayan, Carbon nanotube electrode for oxidation of dopamine. *Bioelectrochem. Bioenerg.* **41**(1), 121–125 (1996)
73. J.M. Nugent, K.S.V. Santhanam, A. Rubio, P.M. Ajayan, Fast electron transfer kinetics on multiwalled carbon nanotube microbundle electrodes. *Nano Lett.* **1**(2), 87–91 (2001)
74. J. Wang, M. Musameh, Y. Lin, Solubilization of carbon nanotubes by Nafion toward the preparation of amperometric biosensors. *J. Am. Chem. Soc.* **125**(9), 2408–2409 (2003)
75. H. Luo, Z. Shi, N. Li, Z. Gu, Q. Zhuang, Investigation of the electrochemical and electrocatalytic behavior of single-wall carbon nanotube film on a glassy carbon electrode. *Anal. Chem.* **73**(5), 915–920 (2001)
76. G. Che, B.B. Lakshmi, E.R. Fisher, C.R. Martin, Carbon nanotubule membranes for electrochemical energy storage and production. *Nature* **393**(6683), 346–349 (1998)
77. M. Musameh, J. Wang, A. Merkoci, Y. Lin, Low-potential stable nadh detection at carbon-nanotube-modified glassy carbon electrodes. *Electrochem. Commun.* **4**(10), 743–746 (2002)
78. Y. Lin, S. Taylor, H.P. Li, K.A.S. Fernando, L.W. Qu, W. Wang, L.R. Gu, B. Zhou, Y.P. Sun, Advances toward bioapplications of carbon nanotubes. *J. Mater. Chem.* **14**(4), 527–541 (2004)
79. P. J. Britto, K.S.V. Santhanam, A. Rubio, J.A. Alonso, P.M. Ajayan, Improved charge transfer at carbon nanotube electrodes. *Adv. Mater.* **11**(2), 154–157 (1999)
80. B.D. McNicol, D.A.J. Rand, K.R. Williams, Direct methanol-air fuel cells for road transportation. *J. Power Sources* **83**(1–2), 15–31 (1999)
81. A. Gamez, D. Richard, P. Gallezot, F. Gloaguen, R. Faure, R. Durand, Oxygen reduction on well-defined platinum nanoparticles inside recast ionomer. *Electrochim. Acta.* **41**(2), 307–314 (1996)

82. J.-S. Yu, S. Kang, S.B. Yoon, G. Chai, Fabrication of ordered uniform porous carbon networks and their application to a catalyst supporter. *J. Am. Chem. Soc.* **124**, 9382–9383 (2002)
83. H. Tang, J.H. Chen, Z.P. Huang, D.Z. Wang, Z.F. Ren, L.H. Nie, Y.F. Kuang, S.Z. Yao, High dispersion and electrocatalytic properties of platinum on well-aligned carbon nanotube arrays. *Carbon* **42**(1), 191–197 (2004)
84. H. Dai, E.W. Wong, C.M. Lieber, Probing electrical transport in nanomaterials: conductivity of individual carbon nanotubes. *Science* **272**(5261), 523–526 (1996)
85. T.W. Ebbesen, P.M. Ajayan, Large-scale synthesis of carbon nanotubes. *Nature* **358**(6383), 220–222 (1992)
86. W. Li, C. Liang, J. Qiu, W. Zhou, H. Han, Z. Wei, G. Sun, Q. Xin, Carbon nanotubes as support for cathode catalyst of a direct methanol fuel cell. *Carbon* **40**(5), 791–794 (2002)
87. V. Lordi, N. Yao, J. Wei, Method for supporting platinum on single-walled carbon nanotubes for a selective hydrogenation catalyst. *Chem. Mater.* **13**, 733–737 (2001)
88. N. Jha, A.L.M. Reddy, M. Shaijumon, N. Rajalakshmi, S. Ramaprabhu, Pt-Ru/multi-walled carbon nanotubes as electrocatalysts for direct methanol fuel cell. *Int. J. Hydrogen Energy* **33**(1), 427–433 (2008)
89. Z. Liu, X. Lin, J.Y. Lee, W. Zhang, M. Han, L.M. Gan, Preparation and characterization of platinum-based electrocatalysts on multiwalled carbon nanotubes for proton exchange membrane fuel cells. *Langmuir* **18**(10), 4054–4060 (2002)
90. R. Yu, L. Chen, Q. Liu, J. Lin, K.-L. Tan, S.C. Ng, H.S.O. Chan, G.-Q. Xu, T.S.A. Hor, Platinum deposition on carbon nanotubes via chemical modification. *Chem. Mater.* **10**, 718–722 (Mar. 1998)
91. J.M. Planeix, N. Coustel, B. Coq, V. Brotons, P.S. Kumbhar, R. Dutartre, P. Geneste, P. Bernier, P.M. Ajayan, Application of carbon nanotubes as supports in heterogeneous catalysis. *J. Am. Chem. Soc.* **116**, 7935–7936 (1994)
92. I. Dumitrescu, P.R. Unwin, J.V. Macpherson, Electrochemistry at carbon nanotubes: perspective and issues. *Chem. Commun.* **2009**(45), 6886–6901 (2009)
93. J.J. Gooding, Nanostructuring electrodes with carbon nanotubes: a review on electrochemistry and applications for sensing. *Electrochim. Acta* **50**(15), 3049–3060 (2005)
94. N. Soin, S. Roy, L. Karlsson, J. McLaughlin, Sputter deposition of highly dispersed platinum nanoparticles on carbon nanotube arrays for fuel cell electrode material. *Diamond Relat. Mater.* **19**(5–6), 595–598 (2010)
95. W.-C. Fang, High methanol oxidation activity of well-dispersed Pt nanoparticles on carbon nanotubes using nitrogen doping. *Nanoscale Res. Lett.* **5**(1), 68–73 (2010)
96. J. Yang, D.-J. Liu, N.N. Kariuki, L.X. Chen, Aligned carbon nanotubes with built-in FeN₄ active sites for electrocatalytic reduction of oxygen. *Chem. Commun.* **2008**(3), 329–331 (2008)
97. H.B. Zhang, X.L. Liang, X. Dong, H.Y. Li, G.D. Lin, Multi-walled carbon nanotubes as a novel promoter of catalysts for CO/CO₂ hydrogenation to alcohols. *Catal. Surv. Asia* **13**(1), 41–58 (2009)
98. K. Gong, F. Du, Z. Xia, M. Durstock, L. Dai, Nitrogen-doped carbon nanotube arrays with high electrocatalytic activity for oxygen reduction. *Science* **323**(5915), 760–764 (2009)
99. P. Matter, U. Ozkan, Non-metal catalysts for dioxygen reduction in an acidic electrolyte. *Catal. Lett.* **109**(3), 115–123 (2006)
100. F. Hu, W. Chen, End-opened carbon nanotube array supported Pd as anode for alkaline fuel cells. *Electrochem. Commun.* **13**(9), 955–958 (2011)
101. B. Conway, *Electrochemical Supercapacitors: Scientific Fundamentals and Technological Applications* (Kluwer, Boston, 1999)
102. J.M. Boyea, R.E. Camacho, S.P. Turano, W.J. Ready, Carbon nanotube-based supercapacitors: technologies and markets. *Nanotechnol. Law Bus.* **4**(1), 585–593 (2007)
103. C. Niu, E.K. Sichel, R. Hoch, D. Moy, H. Tennent, High power electrochemical capacitors based on carbon nanotube electrodes. *Appl. Phys. Lett.* **70**(11), 1480–1482 (1997)
104. K.H. An, W.S. Kim, Y.S. Park, J.-M. Moon, D.J. Bae, S.C. Lim, Y.S. Lee, Y.H. Lee, Electrochemical properties of high-power supercapacitors using single-walled carbon nanotube electrodes. *Adv. Funct. Mater.* **11**(5), 387–392 (2001)

105. H. Zhang, G.P. Cao, Y.S. Yang, Using a cut-paste method to prepare a carbon nanotube fur electrode. *Nanotechnology* **18**(19), 195607 (2007)
106. D. Nkosi, K.I. Ozoemena, Self-assembled nano-arrays of single-walled carbon nanotube-octa(hydroxyethylthio)phthalocyaninatoiron(II) on gold surfaces: impacts of SWCNT and solution pH on electron transfer kinetics. *Electrochim. Acta* **53**(6), 2782–2793 (2008)
107. T. Hiraoka, T. Yamada, K. Hata, D.N. Futaba, H. Kurachi, S. Uemura, M. Yumura, S. Iijima, Synthesis of single- and double-walled carbon nanotube forests on conducting metal foils. *J. Am. Chem. Soc.* **128**(41), 13338–13339 (2006)
108. S. Talapatra, S. Kar, S.K. Pal, R. Vajtai, L. Ci, P. Victor, M.M. Shaijumon, S. Kaur, O. Nalamasu, M.P. Ajayan, Direct growth of aligned carbon nanotubes on bulk metals. *Nat. Nanotechnol.* **1**(2), 112–116 (2006)
109. E. Frackowiak, Carbon materials for supercapacitor application. *Phys. Chem. Chem. Phys.* **9**, 1774–1785 (2007)
110. L.L. Zhang, X.S. Zhao, Carbon-based materials as supercapacitor electrodes. *Chem. Soc. Rev.* **38**(9), 2520–2531 (2009)
111. E. Raymundo-Piñero, K. Kierzek, J. Machnikowski, F. Béguin, Relationship between the nanoporous texture of activated carbons and their capacitance properties in different electrolytes. *Carbon* **44**(12), 2498–2507 (2006)
112. V.L. Pushparaj, M.M. Shaijumon, A. Kumar, S. Murugesan, L. Ci, R. Vajtai, R.J. Linhardt, O. Nalamasu, P.M. Ajayan, Flexible energy storage devices based on nanocomposite paper. *Proc. Natl. Acad. Sci. U S A* **104**(34), 13574–13577 (2007)
113. C. Largeot, C. Portet, J. Chmiola, P.-L. Taberna, Y. Gogotsi, P. Simon, Relation between the ion size and pore size for an electric double-layer capacitor. *J. Am. Chem. Soc.* **130**(9), 730–2731 (2008)
114. H. Zhang, G.P. Cao, Y.S. Yang, Carbon nanotube arrays and their composites for electrochemical capacitors and lithium-ion batteries. *Energy Environ. Sci.* **2**(9), 932–943 (2009)
115. P. Simon, Y. Gogotsi, Materials for electrochemical capacitors. *Nat. Mater.* **7**, 845–854 (2008)
116. D.N. Futaba, K. Hata, T. Yamada, T. Hiraoka, Y. Hayamizu, Y. Kakudate, O. Tanaike, H. Hatori, M. Yumura, S. Iijima, Shape-engineerable and highly densely packed single-walled carbon nanotubes and their application as super-capacitor electrodes. *Nat. Mater.* **5**, 987–994 (2006)
117. Y. Honda, T. Haramoto, M. Takeshige, H. Shiozaki, T. Kitamura, M. Ishikawa, Aligned mwcnt sheet electrodes prepared by transfer methodology providing high-power capacitor performance. *Electrochem. Solid-State Lett.* **10**(4), A106–A110 (2007)
118. T. Iwasaki, T. Maki, D. Yokoyama, H. Kumagai, Y. Hashimoto, T. Asari, H. Kawarada, Highly selective growth of vertically aligned double-walled carbon nanotubes by a controlled heating method and their electric double-layer capacitor properties. *Phys. Stat. Sol. (RRL)* **2**(2), 53–55 (2008)
119. L. Gao, A. Peng, Z.Y. Wang, H. Zhang, Z. Shi, Z. Gu, G. Cao, B. Ding, Growth of aligned carbon nanotube arrays on metallic substrate and its application to supercapacitors. *Solid State Commun.* **146**(9–10), 380–383 (2008)
120. H. Zhang, G. Cao, Z. Wang, Y. Yang, Z. Shi, Z. Gu, Tube-covering-tube nanostructured polyaniline/carbon nanotube array composite electrode with high capacitance and superior rate performance as well as good cycling stability. *Electrochem. Commun.* **10**(7), 1056–1059 (2008)
121. H. Zhang, G. Cao, Z. Wang, Y. Yang, Z. Shi, Growth of manganese oxide nanoflowers on vertically-aligned carbon nanotube arrays for high-rate electrochemical capacitive energy storage. *Nano Lett.* **8**(9), 2664–2668 (2008)
122. C.L. Pint, N.W. Nicholas, S. Xu, Z. Sun, J.M. Tour, H.K. Schmidt, R.G. Gordon, R.H. Hauge, Three dimensional solid-state supercapacitors from aligned single-walled carbon nanotube array templates. *Carbon* **49**(14), 4890–4897 (2011)
123. Z. Niu, W. Zhou, J. Chen, G. Feng, H. Li, W. Ma, J. Li, H. Dong, Y. Ren, D. Zhao, S. Xie, Compact-designed supercapacitors using free-standing single-walled carbon nanotube films. *Energy Environ. Sci.* **4**(4), 1440–1446 (2011)

124. A. Arun, H.L. Poche, T. Idda, D. Acquaviva, M.F.-B. Badia, P. Pantigny, P. Salet, A.M. Ionescu, Tunable MEMS capacitors using vertical carbon nanotube arrays grown on metal lines. *Nanotechnology* **22**(2), 025203 (2011)
125. S.R. Sivakkumar, D.-W. Kim, Polyaniline/carbon nanotube composite cathode for rechargeable lithium polymer batteries assembled with gel polymer electrolyte. *J. Electrochem. Soc.* **154**(2), A134–A139 (2007)
126. A.C. Dillon, K.M. Jones, T.A. Bekkedahl, C.H. Kiang, D.S. Bethune, M.J. Heben, Storage of hydrogen in single-walled carbon nanotubes. *Nature* **386**, 3770–3779 (1997)
127. Y. Ye, C.C. Ahn, C. Witham, B. Fultz, J. Liu, A.G. Rinzler, D. Colbert, K.A. Smith, R.E. Smalley, Hydrogen adsorption and cohesive energy of single-walled carbon nanotubes. *Appl. Phys. Lett.* **74**(16), 2307–2309 (1999)
128. C. Liu, Y.Y. Fan, M. Liu, H.T. Cong, H.M. Cheng, M.S. Dresselhaus, Hydrogen storage in single-walled carbon nanotubes at room temperature. *Science* **286**(5442), 1127–1129 (1999)
129. P. Chen, X. Wu, J. Lin, K.L. Tan, High H₂ uptake by alkali-doped carbon nanotubes under ambient pressure and moderate temperatures. *Science* **285**(5424), 91–93 (1999)
130. M.S. Dresselhaus, K.A. Williams, P.C. Eklund, Hydrogen adsorption in carbon materials. *MRS Bull.* **24**(11), 45 (1999)
131. G.G. Tibbetts, G.P. Meisner, C.H. Olk, Hydrogen storage capacity of carbon nanotubes, filaments, and vapor-grown fibers. *Carbon* **39**(15), 2291–2301 (2001)
132. M. Hirscher, M. Becher, M. Haluska, A. Quintel, V. Skakalova, Y.-M. Choi, U. Dettlaff-Weglikowska, S. Roth, I. Stepanek, P. Bernier, A. Leonhardt, J. Fink, Hydrogen storage in carbon nanostructures. *J. Alloys Compd.* **330–332**, 654–658 (2002)
133. C.C. Ahn, Y. Ye, B.V. Ratnakumar, C. Witham, J.R.C. Bowman, B. Fultz, Hydrogen desorption and adsorption measurements on graphite nanofibers. *Appl. Phys. Lett.* **73**(23), pp. 3378–3380 (1998)
134. P. Kim, C.M. Lieber, Nanotube nanotweezers. *Science* **286**(5447), 2148–2150 (1999)
135. R.H. Baughman, C. Cui, A.A. Zakhidov, Z. Iqbal, J.N. Barisci, G.M. Spinks, G.G. Wallace, A. Mazzoldi, D.D. Rossi, A.G. Rinzler, O. Jaschinski, S. Roth, M. Kertesz, Carbon nanotube actuators. *Science* **284**(5418), 1340–1344 (1999)
136. V.V. Deshpande, H.-Y. Chiu, H.W.C. Postma, C. Mikó, L. Forró, M. Bockrath, Carbon nanotube linear bearing nanoswitches. *Nano Lett.* **6**(6), 1092–1095 (2006)
137. U. Vohrer, I. Kolaric, M.H. Haque, S. Roth, U. Dettlaff-Weglikowska, Carbon nanotube sheets for the use as artificial muscles. *Carbon* **42**(5–6), 1159–1164 (2004)
138. S. Gupta, M. Hughes, A.H. Windle, J. Robertson, Charge transfer in carbon nanotube actuators investigated using in situ raman spectroscopy. *J. Appl. Phys.* **95**(4), 2038–2048 (2004)
139. V.H. Ebron, Z. Yang, D.J. Seyer, M.E. Kozlov, J. Oh, H. Xie, J. Razal, L.J. Hall, J.P. Ferraris, A.G. MacDiarmid, R.H. Baughman, Fuel-powered artificial muscles. *Science* **311**(5767), 1580–1583 (2006)
140. G. Spinks, G. Wallace, L. Fifield, L. Dalton, A. Mazzoldi, D. De Rossi, I. Khayrullin, R. Baughman, Pneumatic carbon nanotube actuators. *Adv. Mater.* **14**(23), 1728–1732 (2002)
141. S.V. Ahir, E.M. Terentjev, Photomechanical actuation in polymer-nanotube composites. *Nat. Mater.* **4**(6), 491–495 (2005)
142. A.R.T.S. Courty, J. Mine, E.M. Terentjev, Nematic elastomers with aligned carbon nanotubes: New electromechanical actuators. *Europhys. Lett.* **64**(5), 654–660 (2003)
143. H. Koerner, G. Price, N.A. Pearce, M. Alexander, R.A. Vaia, Remotely actuated polymer nanocomposites: stress-recovery of carbon-nanotube-filled thermoplastic elastomers. *Nat. Mater.* **3**, 115–120 (2004)
144. P. Miaudet, A. Derré, M. Maugey, C. Zakri, P.M. Piccione, R. Inoubli, P. Poulin, Shape and temperature memory of nanocomposites with broadened glass transition. *Science* **318**(5854), 1294–1296 (2007)
145. A.E. Aliev, J. Oh, M.E. Kozlov, A.A. Kuznetsov, S. Fang, A.F. Fonseca, R. Ovalle, M.D. Lima, M.H. Haque, Y.N. Gartstein, M. Zhang, A.A. Zakhidov, R.H. Baughman, Giant-stroke, superelastic carbon nanotube aerogel muscles. *Science* **323**(5921), 1575–1578 (2009)

146. P. Mérel, J.A. Kpetsu, C. Koechlin, S. Maine, R. Haidar, J. Pélouard, A. Sarkissian, M.I. Ionescu, X. Sun, P. Laou, S. Paradis, Infrared sensors based on multi-wall carbon nanotube films. *C. R. Phys.* **11**(5–6), 375–380 (2010)
147. K. Mizuno, J. Ishii, H. Kishida, Y. Hayamizu, S. Yasuda, D.N. Futaba, M. Yumura, K. Hata, A black body absorber from vertically aligned single-walled carbon nanotubes. *Proc. Natl. Acad. Sci. U S A* **106**(15), 6044–6047 (2009)
148. J.M. Xu, Highly ordered carbon nanotube arrays and IR detection. *Infrared Phys. Technol.* **42**(3–5), 485–491 (2001)
149. B.J. Hinds, N. Chopra, T. Rantell, R. Andrews, V. Gavalas, L.G. Bachas, Aligned multiwalled carbon nanotube membranes. *Science* **303**(5654), 62–65 (2004)
150. V.K.K. Upadhyayula, S.G. Deng, M.C. Mitchell, G.B. Smith, Application of carbon nanotube technology for removal of contaminants in drinking water: A review. *Sci. Total Environ.* **408**(1), 1–13 (2009)
151. B. Hinds, Dramatic transport properties of carbon nanotube membranes for a robust protein channel mimetic platform. *Curr. Opin. Solid St. M.* **16**(1), 1–9 (2011)
152. F. Du, L. Qu, Z. Xia, L. Feng, L. Dai, Membranes of vertically aligned superlong carbon nanotubes. *Langmuir* **27**(13), 8437–8443 (2011)
153. Y. Abdi, M. Khalilian, E. Arzi, Enhancement in photo-induced hydrophilicity of TiO_2 /CNT nanostructures by applying voltage. *J. Phys. D: Appl. Phys.* **44**(25), 255405 (2011)
154. A. Arun, D. Acquaviva, M. Fernández-Bolaós, P. Salet, H. Le-Poche, P. Pantigny, T. Idda, A. Ionescu, Carbon nanotube vertical membranes for electrostatically actuated micro-electromechanical devices. *Microelectron. Eng.* **87**(5–8), 1281–1283 (2010)
155. A. Arun, S. Campidelli, A. Filoramo, V. Derycke, P. Salet, A.M. Ionescu, M.F. Goffman, SWNT array resonant gate MOS transistors. *Nanotechnology* **22**(5), 055204 (2011)
156. F.A. Ghavanini, P. Enoksson, S. Bengtsson, P. Lundgren, Vertically aligned carbon based varactors. *J. Appl. Phys.* **110**(2), 021101 (2011)
157. C.J. Hu, Y.H. Lin, C.W. Tang, M.Y. Tsai, W.K. Hsu, H.F. Kuo, ZnO-coated carbon nanotubes: Flexible piezoelectric generators. *Adv. Mater.* **23**(26), 2941–2945 (2011)
158. Y. Liu, I. Janowska, T. Romero, D. Edouard, L.D. Nguyen, O. Ersen, V. Keller, N. Keller, C. Pham-Huu, High surface-to-volume hybrid platelet reactor filled with catalytically grown vertically aligned carbon nanotubes. *Catal. Today* **150**(1–2), 133–139 (2010)
159. J. Luo, L.P. Mark, A.E. Giannakopoulos, A.W. Colburn, J.V. Macpherson, T. Drewello, P.J. Derrick, A.S. Teh, K.B. Teo, W.I. Milne, Field ionization using densely spaced arrays of nickel-tipped carbon nanotubes. *Chem. Phys. Lett.* **505**(4–6), 126–129 (2011)
160. K. Han, Y. Lee, D. Jun, S. Lee, K.W. Jung, S.S. Yang, Field emission ion source using a carbon nanotube array for micro time-of-flight mass spectrometer. *Jpn. J. Appl. Phys.* **50**(6), 06GM04, (2011)
161. B.K. Sarker, M.R. Islam, F. Alzubi, S.I. Khondaker, Fabrication of aligned carbon nanotube array electrodes for organic electronic devices. *Mater. Exp.* **1**(1), 80–85 (2011)
162. M. De Volder, S.H. Tawfik, D. Copic, A.J. Hart, Hydrogel-driven carbon nanotube micro-transducers. *Soft Matter* **7**(21), 9844–9847 (2011)
163. C. Yuana, C. Chang, Y. Song, Hazardous industrial gases identified using a novel polymer/MWNT composite resistance sensor array. *Mat. Sci. Eng. B: Solid* **176**(11), 821–829 (2011)
164. A. Di Bartolomeo, M. Sarno, F. Giubileo, C. Altavilla, L. Lemmo, S. Piano, F. Bobba, M. Longobardi, A. Scarfato, D. Sannino, A.M. Cucolo, P. Ciambelli, Multiwalled carbon nanotube films as small-sized temperature sensors. *J. Appl. Phys.* **105**, 064518 (2009)
165. C. Kocabas, H. sik Kim, T. Banks, J.A. Rogers, A.A. Pesetski, J.E. Baumgardner, S.V. Krishnaswamy, H. Zhang, Radio frequency analog electronics based on carbonnanotube transistors. *Proc. Natl. Acad. Sci. U S A* **105**(5), 1405–1409 (2008)

Epilogue

In summary, the in situ and ex situ fabrication methods, the physics for alignment, the unique physical properties, and the broad applications of aligned CNTs are introduced. It has been clearly demonstrated by numerous publications that PECVD and thermal CVD are frequently the most effective methods to in situ grow aligned CNT arrays with a predetermined orientation, diameter, length, location, and site density. Depending on the spatial distribution of catalytic nanoparticles on substrates, the aligned CNTs may have 1D or 3D orderings. The mechanisms for achieving alignment are discussed. Aligned CNTs have found their edges for applications in thermal, electrical, photonic, mechanical, chemical, and biological devices as well as various types of sensors for gas and bio-species detections. These applications are reviewed and illustrated based on the uniqueness of the aligned CNT geometry and the corresponding physical properties due to alignment. It is the hope of the authors that this book can generate broader interests from researchers of all related fields and from academic and industrial funding institutions to further explore various applications of aligned CNTs with the grand goal of improving our fundamental scientific understandings and everyday life.

Although relatively extensive research efforts have been made to achieve superb CNT alignment, to study the physics of the alignment and the CNT properties, and to explore various application possibilities, there still remain tremendous unfinished work and unexplored territories to make use of the full potentials of aligned CNT systems. We need to emphasize the difference between studying and utilizing the aligned CNT arrays and individual CNTs. When a single CNT structure is to be studied or put to use in an application, the details of its atomic structure such as chirality and wall number become extremely important and critical. So far, after years of intense research by numerous scientists around the globe, it turns out to be still prohibitively difficult to control the chirality of an SWCNT during its formation. This difficulty has largely hindered the progress of many of the latest research efforts concerning individual CNTs and has even sometimes discouraged researchers and sponsors in this field. However, the subject

of aligned CNT arrays can be very different since they are large ensembles composed of thousands or millions of individual CNTs all with common orientation and sizes. Although every individual CNT in the array might not have the same exact properties, it is the statistical similarity among all CNTs and the anisotropy induced by alignment that make the aligned CNT systems intriguing and useful. This similarity and anisotropy have been repeatedly confirmed experimentally, and are to be merely enhanced and optimized by continued efforts on incremental improvements in various aspects such as uniformity and scale. Therefore, no major obstacle is in sight to prevent aligned CNT arrays from fully maturing into dominantly used materials in large-scale and advanced applications.

The real challenge for the future development of aligned CNTs, in our opinion, is to find the very suitable application that benefits more from the unique properties of the aligned CNTs than any other alternative materials. Among all the potential applications we have reviewed such as field emitters, photonic crystals, optical antennas, nanoelectrode sensors, electrical interconnects, supercapacitors, and so on, it seems none of them has yet to demonstrate the uniqueness and superiority in utilizing aligned CNTs instead of other materials. Among many of the reasons, an important one is, as we believe, a lack of in-depth understanding of the particular characteristics of aligned CNT systems and how they are different and unique from other similar materials. And if one can combine multiple property features of aligned CNTs including the optical, electrical, mechanical, chemical properties, etc., and not just one or two of them, and appreciate the fact that the aligned CNTs as ensembles that are very different from individual CNTs, he may find fascinating new applications where aligned CNTs are the only and/or the best choice available. We will leave it to the readers to think of such applications and to experience the excitement of important new findings. This also conveys our opinion that major efforts for future aligned CNT research should probably be devoted to searching for the most suitable applications instead of immersing into the work of optimizing the structures towards better and better ordering. We realize that this future task cannot be done without the cohesive joint efforts from researchers with vastly different and broad backgrounds.

Aligned CNTs provide a rare chance for us all to bridge the gap between atomically small systems and the macroscopic world. One truly has to think both microscopically and macroscopically to fully understand and make good use of them. The ability to perform effective research on different length scales is critical when aligned CNTs are the subject of interest. Imagine holding a pen of centimeters scale and write letters on a nanometer or micrometerscale. That line of thought is what we think will find you the fruitful returns in your research on aligned CNTs. Maybe we should ask an average machinist to learn the knowledge about the properties of the aligned CNTs on the microscopic scale and he will easily find a better mechanical application which doesn't require precisely manipulating atoms in the nanomaterial using the most delicate STMs (Scanning Tunneling Microscope) or TEMs (Transmission Electron Microscope), shouldn't we?

Index

- 1D ordered CNT, 130
3D, 135
3D CNT architecture, 115
- A**
AAO template, 55, 138
Absorber, 207
Acetaminophen sensor, 225
Acoustic energy, 265
Acoustic wave, 266
Activation energy, 96
Actuator, 280, 281
Aligned CNT, 11, 13, 48, 198, 229, 256, 265
Aligned composite, 236
Alignment, 111, 142
 manipulation, 102
 mechanism, 81
 model, 106
Alkali halide, 59
Allotrope, 1
Ammonia gas sensor, 220
Ammonia sensor, 222
Amorphous, 1, 24
 array, 25
 carbon, 104
Angular radiation pattern, 200
Anisotropic polarizability, 117
Annealing, 137
Anode, 94
Anodized aluminum oxide, 138
Antenna, 200
Anti-Stokes scattering, 174
Apex, 191
Apparatus DC PECVD, 93
Application, 21
Arc discharge, 45, 46
Argon sensor, 221
Armchair, 17
Array electrode, 273
Arrhenius plots, 96
Artificial muscle, 281
Ascorbic acid sensor, 225
Aspect ratio, 30
Assembly, 140, 186
Atmosphere thermal CVD, 68
Atomic
 force microscopy, 179
 layer deposition, 134
 resolution, 179
 step, 124, 125
Azimuth degree, 162
- B**
Ballistic transport, 233
Bamboo-like CNT, 19, 75
Barrier layer, 84
Beam divergence, 203
Bending angle, 127
Bias potential, 187
Biosensor, 222, 223
Block copolymer micelles, 140
Bottom diffusion, 51
Boudouard equilibrium, 57
Bragg diffraction, 160
Bragg's law, 160
Brightness, 193

B (cont.)

Bundle, 232
 Buoyant effect, 120
 Buoyant force, 121

C

C₆₀, 2
 Capacitance, 275, 277
 Capacitor, 274
 Capacity, 275
 Carbon, 1
 fiber, 8
 filament, 8
 monoxide, 57
 nanotube, 3, 7
 Catalyst, 13, 50, 71–73, 83, 120, 128, 130, 132, 272
 diameter, 73
 thermal CVD, 71
 Catalytic
 activity, 75, 131
 decomposition, 60
 growth mechanism, 74
 Cathode ray tube, 191
 Cavity, 264
 Cd ion sensor, 214
 Characterization method, 157
 Chemical reaction, 76
 Chemical Vapor Deposition, 48
 Chiral, 17
 Chiral vector, 17
 CNT, 7, 30
 array, 11, 13, 14, 49, 56, 57, 102, 183, 271, 273
 display, 193
 filler, 229
 growth, 102
 rope, 11, 256
 stability, 55
 tower, 207
 CNT array
 history, 13
 electrode, 275
 growth, 73
 Coagulant, 145
 Coated CNT arrays, 226
 Coaxial cable, 202
 Color, 190
 Color flat-panel display, 192

Composite, 231, 236
 Connection, 20
 Convection flow, 119
 Conversion efficiency, 206
 Cosahedral, 2
 Creeping, 258
 Crossbar array, 126
 Crowding effect, 112
 Crystal lattice, 17
 Crystallization, 24
 Current
 bias, 267
 density, 77, 192, 234
 leakage, 212
 stability, 195
 Cutoff frequency, 203
 CVD, 67
 Cyclic voltammetry curve, 212
 Cyclic voltammogram, 273
 Cyclohexane sensor, 222
 Cylindrical, 3

D

Dark discharge, 100
 DC PECVD, 76, 93
 de Broglie equation, 164
 de Broglie wavelength, 176
 Debye-Waller factor, 168
 Decomposition, 59
 Degree of alignment, 162, 169, 176
 Deposition, 136
 Depth of field, 160
 Dewetting, 112
 Diameter, 171
 Diamond, 1
 Dielectric, 34
 constant, 264
 mismatch, 141
 Diffraction, 166
 pattern, 198
 spot, 199
 Diffusion, 100
 layer, 211
 rate, 128
 Diode configuration, 185
 Diode method, 185
 Dipole moment, 117
 Directed growth, 117
 Discharge, 99

- Discovery, 8
- Display, 192
- Disproportionation, 57
- DNA sensor, 226
- Dry spinning, 145
- DWCNT, 18
- Dynamic growth, 73

- E**
- E-beam, 13
- Efficiency coefficient, 268
- Electric dipole, 116
- Electric field, 101, 116, 141
- Electrical, 17
 - device, 263
 - resistance, 233
 - resistivity, 31
- Electrocatalytic, 271
- Electrochemical
 - cell, 213, 224
 - deposition, 132, 133
 - energy storage, 269
- Electrode, 208, 279
- Electrolysis, 59
- Electrolyte, 270
- Electron, 176
 - lithography, 138
 - diffraction, 164
 - source, 188
 - transfer, 208
 - transfer rate, 208
 - wavelength, 176
- Electroreduction, 271
- Electrostatic force, 81
- Ellipsoidal, 2
- Emission current density, 188
- Emitter, 187
- Encapsulate, 29
- Energy distribution, 195
- Entangled CNT, 102
- Epitaxy, 123
- Ethanol sensor, 222
- Everhart-Thornley detector, 159
- Ex situ, 111
 - method, 147
 - technique, 236

- F**
- Fabrication, 210
- Faradic, 277
- Fast heating growth, 119
- Femtosecond laser, 273

- Ferromagnetic, 128
- Field emission, 22, 183, 184
- Field-emission current, 188
- Field-enhancement factor, 184, 186
- Fishbone, 20
- Flame, 56, 57
- Flat-panel, 189
- Flat-panel display, 192
- Flatten, 26
- Flattened CNT, 27
- Flow velocity, 262
- Flow-rate sensor, 262
- Flux, 60
- Forest, 264
- Four-circle diffractometer, 161
- Fowler-Nordheim plot, 184, 187
- Friction, 258
- Fuel cell, 270
- Full width at half maximum, 162
- Fullerene, 2, 10
- Functionalization, 18

- G**
- Gas, 74, 83
 - flow, 119
 - sensor, 215
- Gate voltage, 216, 219
- Gauge factor, 260
- Glow discharge, 85, 99, 100
- Glucose, 224
- Glucose sensor, 222, 225
- Gouy-Chapman model, 276
- Graphene, 3, 268
- Graphite, 1, 16
- Graphoepitaxial growth, 127
- Graphoepitaxy growth, 125
- Grid, 259
- Growth, 21, 27, 45, 50, 68, 69, 75, 78, 82, 94, 105
- Growth mechanism, 48, 50, 80

- H**
- Heating source, 75
- Helical, 26
- Helium sensor, 221
- Helix angle, 257
- Helmholtz model, 276
- Hermans orientation parameter, 170
- Hexagonal array, 136
- High pressure, 52
- High-energy electron, 158
- Histogram distribution, 128

H (*cont.*)

History, 8, 10
 Hollow carbon filament, 8
 Honeycomb lattice pattern, 13
 Horizontal array, 117
 Hot-filament PECVD, 76
 Hot-wall CVD, 68
 Hot-wire CVD, 70
 Three-point junction, 21
 Hydrogen, 217
 gas sensor, 217
 storage, 280
 Hydrothermal, 52, 54
 Hydrothermal synthesis, 54

I

In situ, 111, 112
 In situ alignment, 128
 Incandescent
 displays, 193
 light, 191
 light source, 191
 Inelastic scatter, 158
 Infrared sensor, 282
 Integrated circuit, 231
 Interconnect, 231, 232
 resistances, 233
 Ion
 bombardment, 99, 105
 concentrations, 214
 milling, 178
 sensor, 213
 Ionization gas sensor, 221
 Ionization sensor, 216

L

Laminar flow, 121
 Laminar gas, 120
 Large-scale, 12
 Laser
 ablation, 47
 diffraction, 198
 vaporization, 11
 Lattice directed growth, 123
 Laue construction, 199
 Lead concentration, 215
 Ledge directed growth, 124
 Lifetime, 194
 Light diffraction, 166
 Light propagation, 206
 Lighting, 189
 Lithium chloride, 59

Lithium ion battery, 279
 Local field, 101
 Loudspeaker, 266, 267
 Low k dielectric, 264
 Luminescent light source, 189

M

Magnetic, 34
 dipole moment, 142
 easy axis, 128
 field, 128, 141, 142
 susceptibility, 34
 Magnetization, 142
 Magnetron sputtering deposition, 131
 Mass spectrometer, 197
 Mechanical, 22, 31
 Mechanical device, 255
 Mechanism, 81, 102
 Micro-contact printing, 140
 Micro-diffraction, 164
 Micro-stamp method, 140
 Microelectrode array, 208
 Microsphere lithography, 13
 Microtrench, 121
 Microtube, 23
 Microwave, 78
 amplifier, 197
 device, 195
 magnetron, 78
 Mie resonance, 198
 Milestone, 9
 Mineralizer, 52
 Molten salt, 59
 Monoxide disproportionation, 57
 Morphology, 210
 Mosaic angle, 162
 MWCNT, 12
 array, 57, 205
 nanocoax, 205

N

Nano-onion, 29
 Nano-radio, 282
 Nanobrush, 114
 Nanobud, 22
 Nanocoax, 203
 Nanocoax array, 203
 Nanocoax cell, 205
 Nano-cone, 30
 Nanoelectrode, 208
 Nanoelectrode array, 208, 209, 223, 224
 Nanoelectrode arrays, 209

- Nanofiber, 20, 29
- Nanogroove, 125
- Nanohorn, 30
- Nanoimprint, 226
- Nanosphere, 135
- Nanostep, 125, 126
- Nanotorus, 23
- Nanotweezer, 280
- Neutron diffraction, 164
- Nitrogen gas sensor, 218
- Nitrous oxide gas sensor, 219
- Node density, 127
- Nucleation, 52

- O**
- One-step procedure, 122, 126
- Optical antennae, 199
- Optical reflection, 202
- Organic electrolyte, 277
- Orientation, 100, 111, 128
- Over-etch, 132
- Over-heat, 132
- Oxidant, 113
- Oxygen reduction, 271, 273
- Oxygen-assisted CVD, 112

- P**
- Parallel, 139
- Paramagnetic, 141
- Parchment model, 19
- Parr reactor, 54
- Partially aligned CNT, 104
- Paschen curve, 97
- Passivation layer, 212
- Pattern, 13
- Pb ion sensor, 215
- Peapod, 28
- PECVD, 13, 75, 78, 93
- Periodic, 13
- Phase diagram, 71
- Phosphor screen, 189
- Photocurrent, 204
- Photoelectric, 198
- Photolithography, 138
- Photomultiplier tube, 159
- Photonic, 199
- Photonic crystal, 198
- Photoresponse, 204
- Photovoltage, 204
- Photovoltaic, 205
- Piezoresistance, 260
- Plasma, 84, 94, 105, 132
 - etching, 98, 99, 104
 - heating, 98
 - source, 75
- Polarizability, 117
- Polarization, 141
- Polyphenol, 227
- Polystyrene nanosphere lithography, 135
- Pore size, 278
- Porous anodic alumina template, 139
- Porous electrode, 270
- PPn, 227
- Pressure, 77, 85
- Pressure sensor, 261
- Protein sensor, 226
- Pseudo-capacitive material, 277
- Purification, 11, 45
- Pyrolysis, 13, 59
- Pyrolytic, 60
- Pyrolytic processes, 60

- Q**
- Quantum tunneling, 179

- R**
- Radiation map, 200
- Radii, 172
- Ragone diagram, 269
- Raman scattering, 173
- Random access memory, 263
- Random CNT, 117
- Rayleigh instability, 112, 131
- Rayleigh scattering, 173
- Reflection, 199
- Reflection high-energy electron diffraction, 165
- Regrowth technique, 115
- Remote-plasma, 96
- Resistance, 234
- Resistance-based sensors, 216
- Resonant cavity, 196
- Reynolds number, 120
- RF PECVD, 78
- Root-mean-square, 267
- Rope, 146
- Rotation, 27
- Russian Doll model, 16, 19

- S**
- SAXS, 169
- Scanning
 - electron microscopy, 157

S (*cont.*)

probe microscopy, 179
tunneling microscopy, 178
Scattering pattern, 169, 172
Scattering vector, 169
Secondary electron, 158, 159
Secondary electron imaging, 158
Seebeck coefficient, 33
Segregate, 59
Selected area electron diffraction, 166
Self-assembly, 136
Sensitivity, 212, 226
Separator, 278
Setae, 260
Setup, 47
Shadow mask, 135
Shear field, 143
Sheath electric field, 82
Sheet, 147, 259, 266
SiC, 79
Signal-to-noise ratio, 209, 225
Site density, 133, 212, 213
Small-angle neutron scattering, 172
Small-angle scattering, 168
Small-angle X-ray scattering, 168
Sodium dodecyl sulfate, 144
Solar, 60
Solar cell, 204
Solution, 147
Solution method, 130
Sound, 265
Sound pressure, 267
Spatulas, 260
Specific current, 271
Spining, 145
Spinning, 144
Square voltammogram, 213, 214
Square wave voltammogram, 213
Stiffness, 258
Stack pillar, 116
Stacked-cup, 20
Staebler-Wronski degradation, 207
Stern layer, 276
Stern model, 276
Stokes scattering, 174
Strain, 257, 260
Stretching, 143
Stripping signal, 213
Structure, 16, 19
Substrate, 84, 123
Supercapacitor, 274
Supercritical, 52

Surface diffusion, 50
Surfactant, 144
Susceptibility, 142, 143
SWCNT, 10, 17
array, 204
bundle, 176
rope, 11, 48
sheets, 114
tower, 114
Synthesis efficiency, 70

T

TEM, 178
Temperature, 53, 73, 74, 84, 96, 235, 261
Temperature wave, 267
Template, 235
Tensile, 257
Tensile strength, 257
Terahertz source, 282
Thermal
conductivity, 32, 229, 231
CVD, 67, 112
diffusivity, 33
interface materials, 228
resistance, 228, 229
Thermoacoustic, 265
Thermodiffusivity, 33
Thermophone, 266, 267
Thermopower, 35
Tip-mode growth, 105
Tori, 23
Torque, 117, 142
Tower, 115
Transistor, 265
Transmission electron
microscopy, 176
Triode, 197
Tube axis, 24
Tubular nanostructure, 8
Turbulence, 120
Twisted rope, 257
Two-step growth, 122
Two-terminal gas sensor, 219

U

Ultracapacitors, 274
Ultrasonication, 136
Uncompensated surface dipole, 125
Underlayer, 95
Underlying substrate, 187

Uric acid sensor, 225
Ursell function, 166

V

Van der Waals force, 118, 260
Vapor-liquid-solid model, 72
Vertical bundles, 113
Via, 231
Viscous shear, 142
Visible light, 199

W

Water sensor, 222
Water-assisted CVD, 113
Water-assisted thermal CVD, 69
Waveguide, 78, 202
Wavelet, 203
Wet spinning, 144
White light, 189
Work function, 184, 185

X

X-ray, 194
 diffraction, 160
 diffraction pattern, 161
 diffractometer, 161
 generator, 194
 lithography, 138

Y

Y-junction, 20
Yarn, 146, 258
Yield, 45, 112
Yield strength, 255
Y-junction, 21
Young's modulus, 31, 258

Z

Zigzag, 17